INMATEH –

AGRICULTURAL ENGINEERING

JANUARY - APRIL

CONTENT

EFFECT OF SOWING SPEED AND WIDTH ON SPACING UNIFORMITY OF PRECISION SEED DRILLS
/
EFFETTO DELLA VELOCITÀ DI SEMINA SULL'UNIFORMITÀ DI DEPOSIZIONE DEL SEME DI SEMINATRICI PER LA SEMINA DI MAIS E BARBABIETOLA

**Roberto FANIGLIULO*), Renato GRILLI, Stefano BENIGNI, Laura FORNACIARI,
Marcello BIOCCA, Daniele POCHI**

Consiglio per la ricerca in agricoltura e l'analisi dell'economia agraria (CREA), Centro di ricerca Ingegneria e Trasformazioni agroalimentari (Research Centre for Engineering and Agro-Food Processing), Monterotondo (Rome), Italy
Tel: +39 0690675233; E-mail: roberto.fanigliulo@crea.gov.it
DOI: https://doi.org/10.35633/inmateh-66-01

ABSTRACT

The precision seed drills significantly improve the competitiveness of farms, in terms of sowing quality and yield. This paper refers to the field performance of the tractor-seed drill system and the seed spacing uniformity with reference to three precision drills with 4, 6 and 8 sowing units, respectively. The tests have been conducted using graded maize and sugar beet seeds, according to ISO 7256-1:1984 standard, under three speed conditions (5.0, 6.5 and 8.0 km h^{-1}). The seed drills showed high values of the quality of feed index (> 90%) even at the higher speed. The multiples index and the miss index were very low.

ABSTRACT

Le seminatrici pneumatiche di precisione migliorano significativamente la competitività delle aziende agricole, in termini di qualità della semina e resa del raccolto. Questo lavoro ha verificato le prestazioni in campo dell'accoppiamento trattore-operatrice e l'uniformità di deposizione del seme di tre seminatrici dotate, rispettivamente, di 4, 6 e 8 unità di semina. I test sono stati condotti a tre velocità di semina (5.0 ,6.5 e 8.0 km h^{-1}) in accordo allo standard ISO 7256-1:1984, utilizzando sementi certificate di mais e bietola. Le seminatrici testate hanno mostrato elevati valori dell'indice delle deposizioni regolari (> 90%), anche alla velocità più elevata. Gli indici delle deposizioni multiple e delle deposizioni mancate sono risultati molto bassi.

INTRODUCTION

In a background of increasing input of high technology solutions in agricultural mechanization, the diffusion of pneumatic precision seed drills for the sowing of spring-summer crops, significantly contributes to improve the competitiveness of farms by ameliorating sowing quality and yield *(Gondal et al., 2017)*. The productivity of crops like maize and sugar beet depends not only on the cultivation method, but also on the respect of the plant investment per area unit, which is realized through the spaced sowing. For this reason, the efficiency and the proper use of precision seed drills is a crucial point *(Fanigliulo and Pochi, 2011)*. The optimal planting density per unit area increases the yield of agricultural products while preventing the overuse of such inputs as seeds, water, fertilizers, pesticides, and herbicides. Especially for sugar beet, under suitable plant spacing in vertical and horizontal levels, the roots can grow to the size requested from the sugar industries and they can fill the row, without reducing the space available to the adjacent roots *(Findura et al., 2008)*.

The aim of the precision seed drill manufacturers and researchers is to improve seed drill design and the accuracy of seed placement, often electronically controlled *(Karimi et al., 2019)*, according to cultivation standard requirements. The main objective of precision seeding is ensuring that the seeds are put at the desired depth and spacing within the row. Soil pulverization *(Fanigliulo et al., 2018)*, seed metering device *(Cujbescu et al., 2021)*, sowing depth *(Karayel and Özmerzi, 2008)* and sowing speed *(Vučajnk et al., 2020)*, represent the main factors affecting performance of seed drills. As the sowing speed increases, the sowing accuracy decreases because of the enhanced seed bounce and rolling effect occurring even with reduced distance between seed drop tube and the furrow. Also, the seed drop tube condition, new or worn, influence the seed spacing uniformity *(Kocher et al., 2011)*.

Regularity of seed spacing can also be affected by the vibrations induced by excessive soil surface roughness, particularly at high sowing speed, and by specifications of the seeding unit (type of seeder opener, final speed of the seed at the outlet from the seeding disc, acceleration of the seeding unit in vertical direction).

The distance between plants within a row could be influenced by some factors, such as failure of dropping seed, multiple seeds dropped at the same time, failure of seeds to emerge, and the variability of seed placement around the drop point *(Kachman and Smith, 1995)*. In compliance with the ISO 7256-1:1984 standard (ISO, 1984), CREA, developed a test system and a series of devices and instruments aimed at evaluating the precision seed drills field performance, the qualitative aspects of the sowing and the dust drift of dressed seed from the machine vacuum fan *(Pochi et al., 2015a; Biocca et al., 2015; Biocca et al., 2017)*, potentially harming for the health of honeybees and agricultural workers (*Pochi et al., 2015b; Biocca et al.*, 2019). The CREA test system represents an instrument useful to the manufacturers that can quantify the performance of their products, the effects of some modifications and the differences with other machines. The tests provided detailed information about the performances of the machines, allowing their comparison. Moreover, the system has the function to provide the users with the elements necessary for a correct choice of the machine, depending on their sowing requirements.

This paper reports the results of tests aimed at the comparison of the field performance of three precision seed drills, equipped with double furrow-opener disks, respectively with 4, 6, 8 sowing units. These machinery are widespread in Northern and Central Italy and have different mechanic solutions of the seed metering device.

MATERIALS AND METHODS

The dynamic-energetic behaviour of the tractor-seed drill system and the quality of sowing were tested. The tests were carried out using graded maize and sugar beet seeds, evaluating the accuracy of the single seed metering mechanism, in terms of distance among the seeds along the furrows, at three working speed values (5.0, 6.5 and 8.0 km h^{-1}), representative of normal sowing conditions. In the field tests, three rear semi-mounted pneumatic precision seed drills (indicated as A, B and C) with a different number of sowing units (4, 6 and 8) were used (Fig. 1). In each seed drill, the deposition of a single seed at a predefined distance was operated by tractor's power-take-off. Table 1 shows their technical characteristics and their dimensions.

Fig. 1 - The precision drills used in the tests.
(A) with four sowing units; (B) with six sowing units; (C) with eight sowing units

Table 1

Main technical characteristics of the tested precision seed drills

Technical data	Seed drill A		Seed drill B		Seed drill C	
	Maize	**Sugar beet**	**Maize**	**Sugar beet**	**Maize**	**Sugar beet**
Total width in sowing position (m)	3.0		4.5		6.0	
Sowing units (n)	4		6		8	
Pneumatic wheel drives (n)	2		2		4	
Hopper capacity (dm^3)	37		37		32	
Seed disks diameter (mm)	240		240		220	240
Number of gathering holes (n)	24	36	24	36	26	36
Hole diameter (mm)	4.5	2.5	4.5	2.5	4.75	2.10
Mass with empty hoppers (kg)	840	796	1415	1349	1600	1499

Each sowing unit consists of a hopper, a single-seed metering mechanism and of the devices devoted to furrow opening and closing and to sowing depth adjustment. An articulated parallel link hitch connects the sowing units to the main frame, allowing the vertical movements due to the soil unevenness and keeping the sowing depth constant. The bottom of the hopper directly communicates with the vertical sowing disk that shows, on its peripheral part, equidistant holes with diameter slightly smaller than the seeds. A vacuum fan provides each sowing unit with the required vacuum. Flexible pipes starting directly from the fan have the

function of making uniform the air flow created by the vacuum in all sowing units. The furrow is opened by a double disk equipped with a soil scraper and a coulter. A clod pusher precedes the disks to remove the biggest clods from the row. The sowing depth is controlled by two lateral steel wheels with rubber coating and soil scraper. In seed drills B and C, a small seed-presser wheel after each sowing unit ensures the contact between soil and seeds, operating the seed compression immediately after its deposition. In these seed drills, the furrow is closed by a couple of convergent small wheels. The precision seed drills were operated by a 4WD tractor (Landini Legend 145, Reggio Emilia, Italy) with nominal power of 110 kW and total mass of 6420 kg. The P.T.O. speed was 540 min⁻¹ corresponding to an engine speed of 1.944 min⁻¹. All tests were performed with diesel fuel in compliance with the EN 590, which was always provided by the same supplier. Consequently, its quality was assumed to be constant, with a Low Heating Value of 42.7 MJ kg⁻¹. Before sowing tests, the tractor's engine performance was verified at the dynamometric brake that provided the updated characteristic curves of the engine *(Pochi et al., 2013)*. After field tests, the tractor was connected again to the dynamometric brake to reproduce the work conditions: the engine speed was set on the same values adopted at the start of each test. Then, the engine load was increased in such a way that the resulting engine speed reductions were equal to the average speeds measured during the field test. This method provided the average values of the total torque and power required to the engine and the corresponding fuel consumption.

The efficiency of the seed metering mechanism was evaluated in the experimental farm of CREA in Monterotondo (Rome, Italy; 42°5'51.26"N; 12°37'3.52"E; 24 m a.s.l.), on flat surface plots (< 1% slope) classified as silty-clay (clay 543 g kg⁻¹, silt 434 g kg⁻¹, sand 23 g kg⁻¹) according to the USDA soil classification system. The soil was previously ploughed at medium depth and subsequently pulverized by means of a power harrow equipped with a packer roll *(Fanigliulo et al., 2016)*. Tests were conducted at near optimum soil moisture for tillage and sowing. Table 2 shows the main characteristics of the test field.

Table 2

Physical-mechanic characteristics of the soil

Moisture contents at the depth range of 0-0.2 m (%)	18.6
Dry bulk density at the depth range of 0-0.2 m (g cm⁻³)	1.21
Clod-breaking index	0.85
Surface roughness index	2.34

The quality of the seedbed was evaluated through the determination, before the sowing, of the clod-breaking index (CBI) and of soil surface roughness index (SRI) *(Fanigliulo et al., 2021)*. The cloddiness was measured digging a 0.5 m side square trench to the working depth. The soil aggregates were removed from the trench avoiding any manipulation and left to dry for at least 20 min. Then they were divided into six size classes by means of hand-operated standard sieves and weighed. An index (I_{ai}), ranging from 0 for the biggest class to 1 for the smallest class, was attributed to each class. The cloddiness results as the percent of each size class mass referred to total mass of the sample.

From the cloddiness, the CBI (I_a) is calculated as follows:

$$I_a = \sum_{i=1}^{6} \frac{M_i \cdot I_{ai}}{M_t} \ [mm] \tag{1}$$

where:

$M_i \cdot I_{ai}$ is the product of the index assigned to a clod size class and the mass (kg) of ground belonging to the same class; M_t is the total mass of the sample (kg).

The SRI was calculated as the standard deviations (σ) of the series of data provided by an in-house designed profile-meter *(Fanigliulo et al., 2020)*: a laser sensor, moving along a horizontal rail, measures its distance from the soil surface at steps of 10 mm. A personal computer collected and processed the data, by means of a software program (in Microsoft Visual Basic 6.0) which controls the movement of the laser probe and the sampling rate per unit of distance. This determination was made after the passage of the power harrow. The tests on the performance of the tractor-operating machine system have been performed according to ENAMA test protocol *(ENAMA, 2003)*. To find the correct working parameters (sowing speed and gear box ratio; P.T.O. and vacuum fan speed; air depression value, etc.) some preliminary tests were carried out. For each tested regulation, three replications were carried out, determining the following operative parameters: actual working time, width and depth of sowing; sowing speed; P.T.O. torque, speed and power; force of traction required by the sowing machines and corresponding power under the measured sowing speed conditions; tractor's slip; fuel consumption. Each measurement refers to a 100 m reference working distance, within the 150 x 20 m experimental fields.

The data of the mentioned parameters were collected by an integrated system based on two units, a field unit and a support unit *(Fanigliulo et al., 2004)*. The tractor (equipped with sensors and a personal computer with a PCI card for real time data acquisition and an LCD monitor) and a photocell system (placed in each test plot and indicating the start and stop of the test) represent the field unit. The sensors' signals were recorded at a scan rate of 10 Hz. The support unit consists of a van equipped as a mobile laboratory which is parked on the field border during the tests. Its PC communicates with the field unit's PC by means of a radio-modem system, exchanging data and allowing to monitor the behaviour of critical parameters and the efficiency of the instruments. The sensors used in the tests consisted of a 500 Nm full scale torque meter mounted on the tractor P.T.O. shaft, measuring the torque and speed during the work (to calculate the required P.T.O. power); a digital encoder measuring the number of revolutions of the tractor rear wheels on a reference distance (to calculate its peripheral velocity and the slip); a 49 kN full scale load cell, fitted in a suitable drawbar connecting a dynamometric vehicle and the tractor-seed drill system in neutral, pulled at the same sowing speed (for the measurement of the force of traction). The three precision drills underwent sowing tests using certified maize and sugar beet seeds. The main characteristics of the seeds are reported in Table 3.

Table 3

Physical characteristics of maize and sugar beet seeds utilized during the field tests

Characteristics	Maize	Sugar beet
Seed emergence (%)	92	80
Seed purity (%)	99	97
Average calibre (mm)	GR2	4.1
Cultivation cycle length (Days)	135	-
Bulk density (g dm^{-3})	801	480
Thousand seed mass (g)	445	28.2

The three machines have been set to carry out the sowing according to the data reported in the Table 4.

Table 4

Sowing conditions and seed drills setting

Seed	Maize			Sugar beet		
Seed drill	A	B	C	A	B	C
Mass of seed with full hoppers (kg)	115	173	224	71	107	123
Distance between rows (m)	0.75			0.75		
Theoretical seed spacing (mm)	175	190	173	120		
Investment (seeds m^{-2})	7.6	7.0	7.7	11.1		
Theoretical seed distribution (kg ha^{-1})	33.9	31.2	34.9	3.1		
Sowing depth (mm)	40			20		
Sowing speed (km h^{-1})	6.4–8.1	6.6-8.3	6.6-8.2	4.9-8.0	5.1-8.1	4.9-8.0

The air depression for maize and sugar beet seeds, measured by a vacuum gauge installed on each seed drill, was set on the values indicated by the manufacturers on the instruction manuals. As to the evaluation of the sowing quality, according to the ISO 7256-1:1984 standard, the actual spacing along the row between adjacent seeds must be determined and related to the theoretical spacing indicated by the manufacturer in the calibration chart. After the sowing, seeds spacing was measured on random row portions 20 m long, by measuring the distance between contiguous seeds in the furrow. Referring to the theoretical spacing, the actual spacing measurement is classified in the mentioned ISO standard as: DS (double sowing), when it is 0 to 0.5 times the theoretical spacing; AS (correct sowing), when it is 0.5 to 1.5 times the theoretical spacing; MS (missing sowing), when it is higher than 1.5 times the theoretical spacing. Since the actual seed spacing is the key-parameter in the evaluation of a precision drill, its deviations from the theoretical spacing values underwent the statistical test ANOVA (analysis of variance). The test was carried out separately for maize and sugar beet datasets, considering as variability factors: three machines, two speeds, two hoppers for each machine (one lateral hopper and one central hopper) and their interaction. The test was based on five replicates, each with ten values of deviation.

The percent frequency of measurements occurring in each class allows to define several quality indices characterizing the machine, as the multiple index, the quality of feed index, the miss index and the precision sowing index (CS), ratio between the standard deviation of AS measurements and the theoretical spacing. These indices measure the degradation of the performances within the target range. Low values of DS, CS, and MS and high AS values indicate good performance of the machine. According to the standard, at least 250 depositions on the same row must be considered, repeating the counting on three sowing units (two lateral and one central sowing unit). Lastly, the uniformity of transversal distribution was evaluated for all the sowing units of the tested machines. The quantity of seed distributed by each of them, along the reference distance, was properly collected and weighted, providing the behaviour of the transversal distribution and the transversal unevenness index. Moreover, the total mass of seeds collected during each replication allowed the calculation of the actual seed dose (kg ha^{-1}) and, by referring to the theoretical dose, the efficiency of distribution (coefficient of irregularity, %). Basing on the above indices relating to the quality of sowing, the performances can be synthetically judged as "insufficient", "sufficient", "good", and "excellent".

RESULTS

The data of the dynamic-energetic performances of each tractor-sowing machine system are reported in Table 5. The results of the measurements aimed at evaluating the quality of sowing are reported in Table 6.

Table 5

Average values of the parameters describing the technical performance of each tractor-seed drill system

Parameters	Seed drill A				Seed drill B				Seed drill C			
	Maize		Sugar beet		Maize		Sugar beet		Maize		Sugar beet	
Actual sowing speed (km h^{-1})	6.4	8.1	4.9	8.0	6.6	8.3	5.1	8.1	6.6	8.2	4.9	8.0
Actual sowing capacity (ha h^{-1})	1.9	2.4	1.5	2.4	3.0	3.8	2.3	3.6	3.8	4.9	3.0	4.8
Operative sowing capacity (ha h^{-1})	1.1	1.3	0.9	1.3	1.7	2.0	2.5	2.0	3.3	3.7	2.4	3.5
Fuel consumption per hour (kg h^{-1})	6.4	6.9	4.8	6.4	7.5	8.3	6.6	7.4	11.8	12.6	14.3	15.8
Surface unit fuel consumption (kg ha^{-1})	3.3	2.8	3.2	2.6	2.5	2.2	2.8	2.0	3.1	2.6	4.9	3.3
Average force of traction (kN)	2.2	2.4	1.8	2.1	3.0	3.2	2.5	3.0	5.7	6.2	5.2	6.0
Power required for the traction (kW)	3.9	5.4	2.4	4.8	5.5	7.4	3.5	6.7	10.5	14.1	7.1	13.4
Specific resistance to traction (kN row^{-1})	0.5	0.6	0.4	0.5	0.5	0.5	0.4	0.5	0.7	0.8	0.6	0.8
Average P.T.O. speed (min^{-1})	516	509	402	395	533	523	440	420	503	506	455	435
Average torque at the P.T.O. (daNm)	1.7	2.0	1.9	1.7	3.0	2.6	3.2	2.9	6.9	7.3	6.6	7.7
Average power at the P.T.O. (kW)	0.9	1.1	0.8	0.7	1.7	1.4	1.5	1.3	3.6	3.9	3.1	3.5
Slip (%)	1.6	2.3	1.5	2.3	2.2	2.5	1.8	2.4	3.3	3.6	1.9	3.3
Power losses for slip (kW)	0.2	0.4	0.1	0.3	0.3	0.4	0.2	0.4	0.4	0.6	0.3	0.9
Total power required (kW)	4.8	6.4	3.2	5.5	7.1	8.8	5.0	8.0	14.6	18.6	10.5	17.8
Tractor's total engine power (kW)	9.8	14.3	7.6	15.0	16.3	22.1	15.9	20.1	28.2	35.5	19.3	34.3
Energy per surface unit (MJ ha^{-1})	18.5	21.5	18.8	22.7	20.1	21.5	25.0	20.1	25.6	26.0	23.7	25.8

Table 6

Uniformity and accuracy indices resulting from the tests with the precision drills

Technical parameters	Seed drill A				Seed drill B				Seed drill C			
	Maize		Sugar beet		Maize		Sugar beet		Maize		Sugar beet	
Average seed spacing (mm)	182	185	138	129	205	216	146	138	196	179	145	139
Coefficient of Variation	21.4	26.5	40.2	24.9	14.4	15.6	36.5	22.0	16.6	29.1	35.4	23.6
Average depth of seed placement (mm)	38.1	41.2	13.8	12.9	40.9	41.8	14.6	13.8	41.0	42.1	13.9	13.2
Transversal unevenness index (%)	2.1	2.4	2.6	0.9	0.6	3.7	5.9	6.1	0.9	1.6	6.6	6.9
Coefficient of irregularity (%)*	-0.9	-6.5	-3.9	-2.4	-3.6	-5.1	-8.3	-7.3	-5.9	-6.4	-8.5	-8.1
Multiple index (%)	1.0	0	2.5	0	0	0	0.4	0	0	2.3	1.7	1.3
Quality of feed index (%)	96.1	95.2	82.3	93.8	98.8	97.9	84.0	93.5	95.1	90.4	85.3	90.6

Technical parameters	Seed drill A				Seed drill B				Seed drill C			
	Maize		Sugar beet		Maize		Sugar beet		Maize		Sugar beet	
Miss index (%)	2.9	4.8	15.2	6.2	1.2	2.1	15.6	6.5	4.9	7.3	13.0	8.1
Precision sowing index (%)	15.0	18.2	19.3	18.3	12.1	12.5	20.0	17.5	19.2	22.4	19.9	17.3

* Referring to the theoretical dose

Among the data reported in Table 5, modest values of specific resistance to traction can be noticed, with corresponding low traction power requests. Tractor's slip and fuel consumption values are normal for this typology of machines. The dynamic and energetic parameters clearly increase with speed, for all machines that, because of the reduced run-out time (turning, manoeuvres, hoppers' refills), showed high sowing capacity.

Maize sowing test

The actual sowing depth was similar to the pre-set value, as some differences can be observed between theoretical and actual seed spacing (4.1% and 5.9% for seed drill A; 7.9% and 13.6% for B; 13.0% and 3.6% for C). According to the results of the ANOVA carried out on the deviations of actual seed spacing from theoretical seed spacing (Table 7), said differences seem mostly caused by the factor "machines" ($p = 0.05$) probably due to their different design, type of sowing disks, number of hoppers. The differences relating to the speed and hopper's position were not significant. However, those due to the interaction of factors were significant ($p = 0.05$).

Table 7

Results of the ANOVA carried out on the deviations of the actual spacing values from the theoretical spacing values (Table 4) observed after the sowing of maize seed with the three pneumatic precision drills

Variability factors	Deviance	Degree of freedom	Variance	F Calculated	Probability		
					p = 0.05	p = 0.01	p = 0.001
Replicates	15.60	4	3.90	0.27	2.37	3.32	4.62
Seed	87.5	2	43.74	<u>3.08</u>	3.00	4.61	6.91
Speed	7.8	1	7.81	0.55	3.84	6.63	10.83
Hoppers	2.9	1	2.87	0.20	3.84	6.63	10.83
Interaction	270.2	11	24.57	<u>1.73</u>	1.72	2.20	2.68
Error	8384.9	591	14.19	-	-	-	-
Total	8768.9	599	-	-	-	-	-

Based on the results of the ANOVA, the minimum significant differences, MSD, between the average deviations of the three machines, reported in Table 8, indicate that only the difference A-B is significant (p=0.01) and is mostly responsible of the variability observed in the ANOVA among seed drills. This means that the seed drill A has a smaller average deviation than B from the theoretical distance between the seeds. A can be considered better than B, but not better than C, just as C cannot be considered better than B, despite its smaller mean deviation.

Table 8

Minimum Significant Differences between the means relating to the results of the ANOVA reported in Table 7

Mean spacing			Difference between means			t values		
A	B	C	A-B	A-C	B-C	p = 0.05	p = 0.01	p = 0.001
0.843	1.763	1.157	**-0.920**	-0.315	0.605	1.645	2.326	3.090
Standard error of the difference between two means						0.377		
Minimum Significant Differences (MSD)						0.620	0.876	1.164
Significance						A-B	A-B	n.s.

Increasing the sowing speed, the actual seed distribution decreased from 33.5 to 31.5 kg ha⁻¹ for the machine A, from 32.5 to 31.9 kg ha⁻¹ for the machine B and from 34.8 to 32.6 kg ha⁻¹ for the machine C, with a variation of 5.8, 1.7 and 6.2%, respectively. Considering the transversal unevenness index, as it shows very low values in all conditions, it can always be classified as "excellent".

The coefficient of irregularity always resulted "excellent" in all tests but two: for the machines A and C at 8 km h^{-1} it has been judged "good". A similar behaviour has been observed for the quality of feed index, the values of which resulted "excellent" for the machine B, as they were "good" for the machine A. For the machine C, the values resulted "acceptable" at lower speed and "insufficient" at 8.2 km h^{-1}. The histograms of Figures 2, 3, and 4 show the distribution of frequency of the seed spacing values.
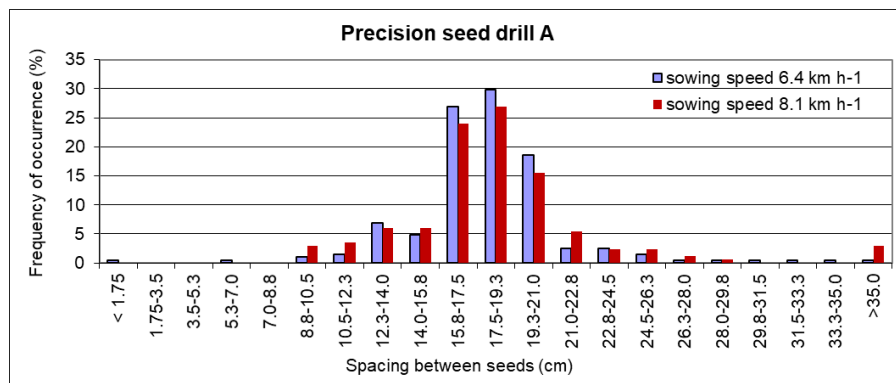
Fig. 2 - Frequency distribution of the seed maize spacing values for the machine A (theoretical value: 17.5 cm)
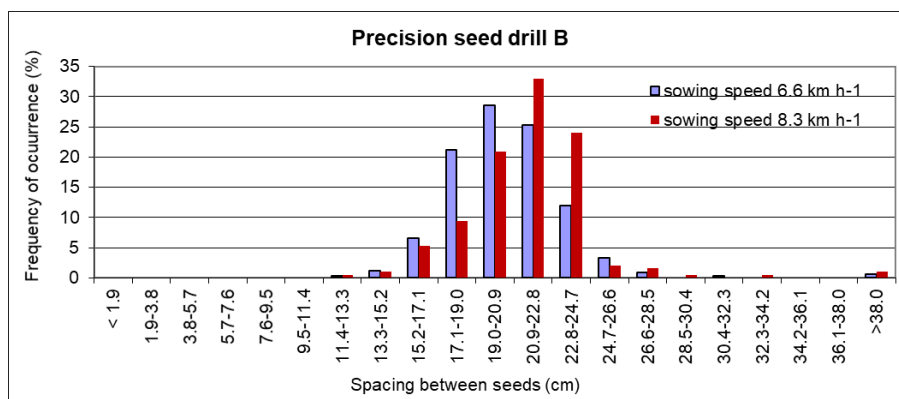
Fig. 3 - Frequency distribution of the seed maize spacing values for the machine B (theoretical value: 19.0 cm)
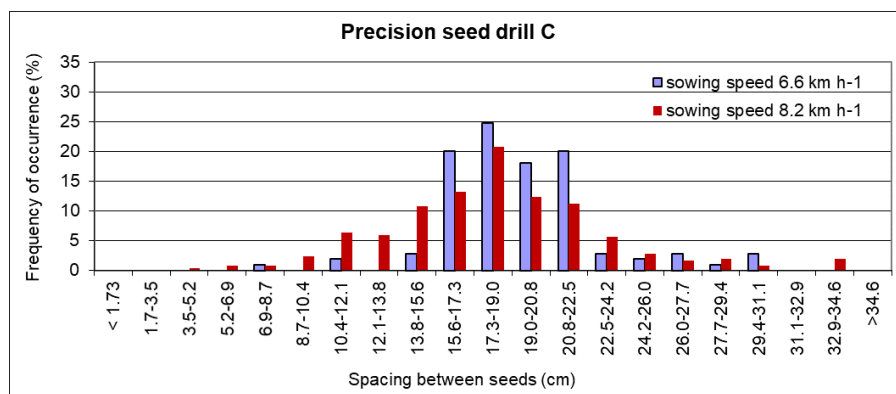
Fig. 4 - Frequency distribution of the seed maize spacing values for the machine C (theoretical value: 17.3 cm)

It can be noticed that, in the class corresponding to the theoretical spacing, the variability increased with the speed and the frequency of the values decreased. The highest frequencies inside the theoretical spacing classes have been observed for the machine A, under both sowing speed conditions. The histograms of the machine B also showed a lower number of classes than A and C: considering a ± 30 mm interval around the theoretical spacing, the depositions occurred in it have been, for A, B and C, respectively 80.4%, 81.5% and 65.7% at the lower speed and 72.5%, 68.6% and 57.2% at the higher speed.

Sugar beet sowing test

As observed for maize, also in this case the actual sowing depth was similar to the pre-set value. Some differences occurred between theoretical seed spacing (Table 4, constant for the three machines) and actual seed spacing (15.3% and 7.3% for A; 21.9% and 14.9% for B; 20.4% and 15.6% for C).

The ANOVA carried out on the deviations of actual seed spacing from theoretical seed spacing (Table 9) did not show any significant differences in the deviations due to the considered variability factors.

Table 9

Results of the ANOVA carried out on the deviations of the actual spacing values from the theoretical spacing values (Table 4) observed after the sowing of sugar beet seed with the three pneumatic precision drills

Variability factors	Deviance	Degree of freedom	Variance	F Calculated	Probability		
					p = 0.05	p = 0.01	p = 0.001
Replicates	158.01	4	39.50	2.03	2.37	3.32	4.62
Seed	27.3	2	13.63	0.70	3.00	4.61	6.91
Speed	12.2	1	12.16	0.63	3.84	6.63	10.83
Hoppers	15.2	1	15.23	0.78	3.84	6.63	10.83
Interaction	229.2	11	20.83	1.07	1.72	2.20	2.68
Error	11493.6	591	19.45	-	-	-	-
Total	11935.4	599	-	-	-	-	-

Increasing the sowing speed, the actual seed distribution increases from 3.01 to 3.06 kg ha^{-1} for the machine A, from 2.87 to 2.90 kg ha^{-1} for the machine B and from 2.86 to 2.88 kg ha^{-1} for the machine C, with a variation respectively of 1.6, 1.0 and 0.4%. Considering the transversal unevenness index and the coefficient of irregularity, since they show very low values in all conditions, they can always be classified as excellent for seed drill A and good for seed drills B and C. A similar behaviour was observed for the quality of feed index values that resulted acceptable at 8.0 km h^{-1} for all machines, as it was not sufficient at lower speed. The histograms of Figures 5, 6, and 7 show the frequency distribution of the seed spacing values.
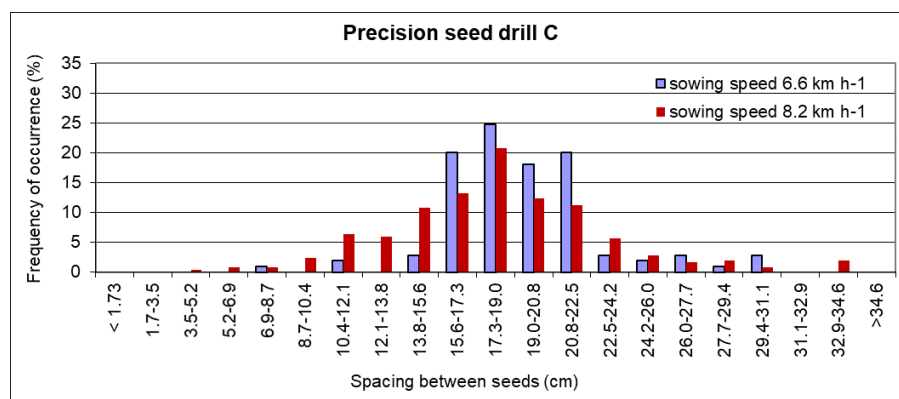
Fig. 5 - Frequency distribution of the sugar beet seed spacing values for the machine A
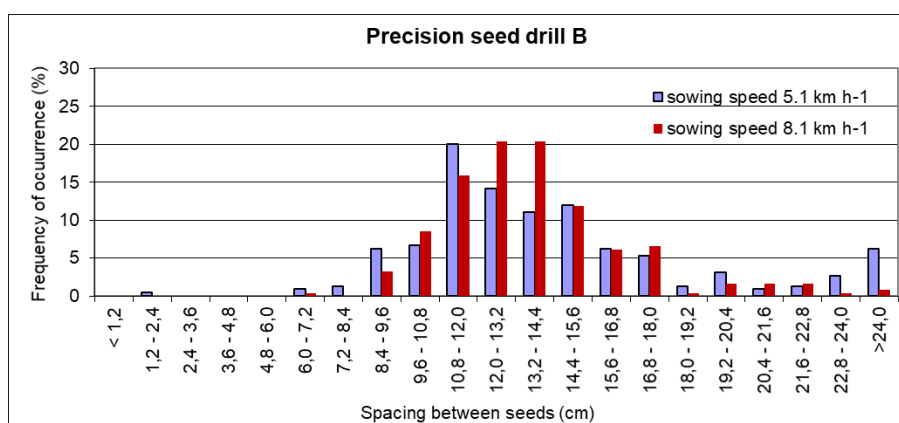
Fig. 6 - Frequency distribution of the sugar beet seed spacing values for the machine B
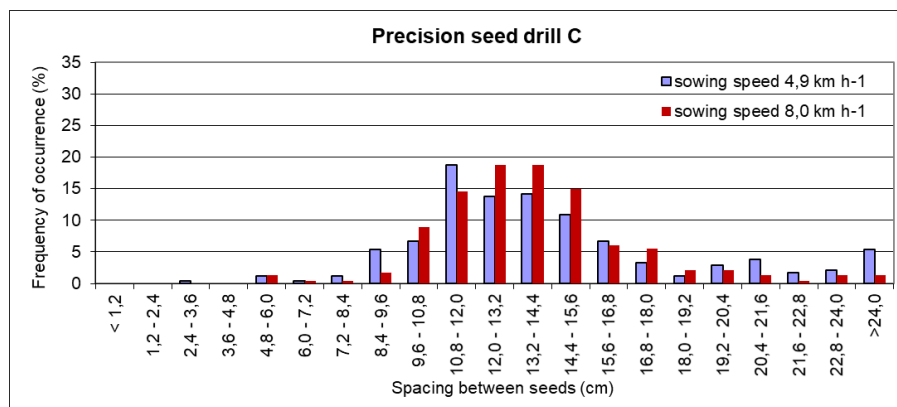
Fig. 7 - Frequency distribution of the sugar beet seed spacing values for the machine C

The variability decreases with the sowing speed and the frequency of values in the class corresponding to the theoretical spacing decrease except for the seed drill A. The highest frequencies inside the theoretical spacing classes were observed for the machine A, under both speed conditions. The histograms of the seed drill A also showed a lower number of classes than B and C: considering a ± 24 mm interval around the theoretical spacing, the depositions occurred in it have been, for A, B and C, respectively 40.5%, 34.2% and 32.5% at the lower speed and 38.1%, 36.3% and 33.3% at the higher speed.

CONCLUSIONS

During the field experiments of sowing of maize and sugar beet, carried out according to ISO 7256-1:1984 standard*,* we compared three pneumatic precision seed drills with a different number of sowing units (4, 6 and 8) and under two sowing speed conditions. The tested seed drills showed good performances in sowing operations, which are strictly connected to the optimal setting of the seed selector of the metering system and to the correct choice of disks with the most suitable hole diameter. The sowing speed and the sowing width represent the main factors affecting precision seed drill performance. As they increase, the vibrations induced by any soil unevenness could affect the uniformity of seed spacing. As for the sowing capacity, it was found to be fair due to the good manoeuvrability of the machines and the ease of filling the hoppers. With full hoppers and at the highest speed, the sowed surfaces were about 3.8, 5.6, 6.3 ha for maize and 23.2, 36.7, 42.7 ha for sugar beet, respectively for the machines A, B and C. Moreover, the accuracy of the devices regulating the pressure of burying allowed to maintain constant sowing depth, corresponding to the pre-set values. The increasing of sowing speed seems to induce opposite results in the two crops: in fact, the quantity of maize seed distributed per hectare decreased, while the sugar beet seed quantity per hectare increased. The missing deposition value (MS) was affected in a similar way. This was probably caused by an irregular seed feeding due to a not optimum time of contact between seeds and disk, also due to the different size and mass of the tested seeds. No effect was observed on the multiple depositions (DS). Consequently, the average actual spacing was increased for all machines and particularly for B. The good values of quality-of-feed index testify the accuracy of the distribution system and its efficiency even at higher speed for seed drill (beyond 90%). The precision sowing index observed in the tests ranged from 12.1% up to 22.4% in maize sowing, and from 17.5% up to 20.0% in sugar beet sowing, indicating that the spacing values were uniformly distributed within the target range. As to the frequency distribution of the spacing values, the machine A showed the best performance. This can be explained by the presence, in each metering system, of the anti-filling-up plate aimed at avoiding multiple depositions.

REFERENCES
[1]   Biocca, M., Fanigliulo, R., Gallo, P., Pulcini, P., & Pochi, D. (2015). The assessment of dust drift from pneumatic drills using static tests and in-field validation, *Crop Protection*, *71,* 109-115. https://doi.org/10.1016/j.cropro.2015.02.006
[2]   Biocca, M., Pochi, D., Fanigliulo, R., Gallo, P., Pulcini, P., Marcovecchio, F., & Perrino, C. (2017). Evaluating a filtering and recirculating system to reduce dust drift in simulated sowing of dressed seed

and abraded dust particle characteristics, *Pest Management Science*, *73*(6), 1134–1142. https://doi.org/10.1002/ps.4428

[3] Biocca, M., Fanigliulo, R., Pochi, D., & Gallo, P. (2019). Dust drift mitigating devices applied on precision pneumatic seed drills: a mini-review. *INMATEH-Agricultural Engineering*, *58*(2), 273-284. https://doi.org/10.35633/inmateh-58-30

[4] Cujbescu, D., Găgeanu, I., Persu, C., Matache, M., Vlăduţ, V., Voicea, I., Paraschiv, G., Biriş, Ş, Ungureanu, N., Voicu, G., & Ipate, G. (2021). Simulation of sowing precision in laboratory conditions. *Applied Sciences*, *11*, 6264. https://doi.org/10.3390/app11146264

[5] ENAMA. (2003). *Agricultural Machinery Functional and Safety Testing Service. (Test Protocol No. 04 rev. 2 - Sowing Machines)*. Rome, Italy.

[6] Fanigliulo, R., Pochi, D., Volpi, C., & Santoro, G. (2004). A mobile system to evaluate the performances of agricultural machinery under field conditions. *Journal of Agricultural Engineering*, *4*, 89-95.

[7] Fanigliulo, R., & Pochi, D. (2011), Air-flow distribution efficiency of a precision drill used in the sowing of different graded seeds, *Journal of Agricultural Science and Technology B 1*, *1*(5), 655-662.

[8] Fanigliulo, R., Biocca, M., & Pochi, D. (2016). Effects of six primary tillage implements on energy inputs and residue cover in Central Italy. *Journal of Agricultural Engineering*, *47*(3), 177-180. https://doi.org/10.4081/jae.2016.519

[9] Fanigliulo, R., Biocca, M., & Pochi, D. (2018). An analysis of eight tillage methods in a silty-clay soil: proposal for flexible tillage cycles. *INMATEH - Agricultural Engineering*, *56*(3), 49-58.

[10] Fanigliulo, R., Antonucci, F., Figorilli, S., Pochi, D., Pallottino, F., Fornaciari, L., Grilli, R., Costa, & C. (2020). Light drone-based application to assess soil tillage quality parameters. *Sensors*, *20*(3), 728. https://doi.org/10.3390/s20030728

[11] Fanigliulo, R., Pochi, D., & Servadio, P. (2021). Conventional and conservation seedbed preparation systems for wheat planting in silty-clay soil. *Sustainability*, *13*(11), 6506. https://doi.org/10.3390/su13116506

[12] Findura, P., Nozdrovický, L., Tóth, P., & Mrázová, Ľ. (2008). Evaluation of the work quality of the sugar beet planter in relation to the sugar beet seed parameters. *Research in Agricultural Engineering*, *54*(3), 148–154. https://doi.org/10.17221/713-RAE

[13] Gondal, M. R., Hussain, A., Yasin, S., Musa, M., & Rehman, H. S. (2017). Effect of seed rate and row spacing on grain yield of sorghum. *SAARC Journal of Agriculture*, *15*(2), 81-91. https://doi.org/10.3329/sja.v15i2.35154

[14] Kachman, S. D., & Smith, J. A. (1995). Alternative measures of accuracy in plant spacing for planters using single seed metering. *Transactions of the ASAE*, *38*(2), 379-387.

[15] Karayel, D., & Özmerzi, A. (2008). Evaluation of three depth-control components on seed placement accuracy and emergence for a precision planter. *Applied Engineering in Agriculture*, *24*(3), 271-276. https://doi.org/10.13031/2013.24494

[16] Karimi, H., Navid, H., Besharati, B., & Eskandari, I. (2019). Assessing an infrared-based seed drill monitoring system under field operating conditions. *Computer and Electronics in Agriculture*, *162*, 543-554. https://doi.org/10.1016/j.compag.2019.04.045

[17] Kocher, M. F., Lan, Y., Chen, C., & Smith, J. A. (1998). Opto-electronic sensor system for rapid evaluation of planter seed spacing uniformity. *Transactions of the ASAE*, *41*(1), 237-245.

[18] International Organization for Standardization. (1984). *Sowing equipment – Test methods. Part 1: single seed drills (precision drills)*. (ISO Standard No. 7256-1:1984). https://www.iso.org/standard/13910.html

[19] Pochi, D., Fanigliulo, R., Pagano, M., Grilli, R., Fedrizzi, M., & Fornaciari, L. (2013). Dynamic-energetic balance of agricultural tractors: active systems for the measurement of the power requirements in static tests and under field conditions. *Journal of Agricultural Engineering*, *44*, 415-420.

[20] Pochi, D., Biocca, M., Fanigliulo, R., Gallo, P., Fedrizzi, M., Pulcini, P., Perrino, C., & Marcovecchio, F. (2015a). A device for pneumatic precision drills reducing the drift of the abrasion dust from dressed seed. *Crop Protection*, *74*, 56-64. http://dx.doi.org/10.1016/j.cropro.2015.02.026

[21] Pochi, D., Biocca, M., Fanigliulo, R., Gallo, P., & Pulcini, P. (2015b). Sowing of seed dressed with thiacloprid using a pneumatic drill modified for reducing abrasion emissions. *Bulletin of Insectology* *68*(2), 273-279.

[22] Vučajnk, F., Šantavec, I., Kocjan Ačko, D., Rakun, J., Verbič, J., Bernik, R., Trdan, S., & Vidrih, M. (2020). Increased planting speed did not affect silage and grain yield of maize, while saving seed and energy. *Italian Journal of Agronomy*, *15*(3), 206-213. https://doi.org/10.4081/ija.2020.1612

ESTABLISHMENT AND CALIBRATION OF DISCRETE ELEMENT MODEL OF KING GRASS STALK BASED ON THROWING TEST
/
基于抛送试验的王草茎秆离散元模型参数标定

Xiaolong HUAN[1)], Decheng WANG*[1)], Yong YOU*[1)], Wenpeng MA[2)], Lu ZHU [1)], Sibiao LI[1)]
[1)]China Agricultural University, College of Engineering, Beijing / China
[2)]Shandong University of Technology，College of Agricultural Engineering and Food Science, Shandong/China
Tel: +86 10 010-62737208, +86 10 010-62737977; E-mail: wdc@cau.edu.cn, youyong@cau.edu.cn
Corresponding authors: Decheng Wang, Yong You
DOI: https://doi.org/10.35633/inmateh-66-02

ABSTRACT

In order to better use the discrete element method (DEM) to study the cutting and throwing process of King Grass (KG) stalk in mechanical harvesting, the DEM model and contact parameters of KG stalk were studied in this paper. By using the Multi-sphere method, the DEM model of KG stalk was established in EDEM software. Through the impact bounce test and slope sliding test, the stalk-steel coefficient of static friction, stalk-steel coefficient of restitution and stalk-stalk coefficient of restitution were calibrated as 0.372, 0.656 and 0.523, respectively. Based on the stacking test, using the response surface methodology, the optimal values of stalk-stalk coefficient of static friction, stalk-stalk coefficient of rolling friction, stalk-steel coefficient of rolling friction were calibrated as 0.393, 0.072 and 0.144, respectively. The throwing test bench of stalk was designed, and the actual and simulation throwing test were carried out. The relative error of throwing distance in bench test and simulation test under four throwing speeds was 1.15%, 7.76%, 8.88% and 10.46%, respectively. The throwing trajectory curve of the simulation test is consistent with that of the actual test, which verifies the accuracy of the DEM model and contact parameters of KG stalk.

摘要

为更好的应用离散元法研究王草茎秆与收获机械的作用机理，寻求王草茎秆离散元模型的最优接触参数组合。论文对王草茎秆的物理参数进行测量，并基于多球粘结颗粒模型在 EDEM 软件中建立了王草茎秆的离散元模型；采用台架试验和仿真试验相结合的方式，通过碰撞弹跳试验和斜面滑动试验，得到茎秆-钢板静摩擦因数、王草茎秆-钢板碰撞恢复系数和茎秆-茎秆碰撞恢复系数依次为 0.372、0.656 和 0.523；基于堆积试验，利用响应面优化方法，以 EDEM 仿真堆积角与实际堆积角的相对误差为指标，确定茎秆-茎秆静摩擦因数、茎秆-茎秆滚动摩擦因数以及茎秆-钢板滚动摩擦因数的最优数值分别为 0.393、0.072 和 0.144；进行王草茎秆实际抛送试验和CFD-DEM 气固耦合仿真抛送试验，得到不同抛送板转速（400、500、600 和 700 r·min⁻¹）条件下，台架试验和仿真试验抛送距离的相对误差分别为 1.15%、7.76%、8.88%和 10.46%，仿真试验的茎秆抛送轨迹曲线与台架试验抛送轨迹曲线相吻合，验证了王草茎秆离散元模型和接触参数的准确性。

INTRODUCTION

King Grass (Pennisetum Americanum × P. purpureum, KG) is mainly planted in south of China and other tropical and subtropical regions globally (*Zhao et al., 2019*). KG is a high-yield biological resources and it is extensively used in ecological environmental protection, bioenergy industry, and animal husbandry (*Li et al., 2019*). In order to improve the harvest level and economic benefit, it is necessary to develop suitable mechanical equipment for KG harvest. In recent years, simulation software EDEM based on discrete element method (DEM) has been widely used in agricultural equipment research. The chopped KG stalk can be regarded as granular. The application of DEM to study the mechanism of KG stalk and harvester in the process of cutting and throwing can provide a theoretical basis for machine design and optimization. In the DEM simulation, it is necessary to establish a DEM model and define the contact parameters of the model, including coefficient of static friction (CSF), coefficient of rolling friction (CRF) and coefficient of restitution (CR). Many scholars had carried out extensive research on the DEM model and contact parameters of soil (*Tran et al.,*

---

[1] *Xiaolong, Huan, Ph.D. Stud. Eng.; Decheng Wang, Prof. Ph.D. Eng.; Yong You, Assoc. Prof. Ph.D. Eng.;*

Wenpeng Ma, Ph.D. Stud. Eng.; Sibiao Li, M.S. Stud. Eng Lu Zhu, Ph.D. Stud. Eng.

2020), fertilizer (*Bangura et al., 2020*), seed (*Guzman et al., 2021; Ma et al., 2020*) and other materials. In recent years, the research on the DEM model of stalk has also been reported. *Liao et al. (2020)* took forage rape as the research object, determined the main parameters of DEM model through stalk bending failure simulation test and response surface analysis, such as normal contact stiffness, tangential contact stiffness, critical normal stress and critical tangential stress. Based on the results of Alfalfa straw physical test, *Ma et al. (2020)* determined the parameters of Alfalfa stalk DEM model by using Plackett-Burman test, steepest climbing test and Box-Behnken test. *Zhang et al. (2020)* determined the optimal combination of corn straw parameters by using results of mechanical corn stalk tests, DEM simulations of impact fracture, compression fracture.

Compared with soil, fertilizer, seeds and other materials, the size and mass of KG stalk are different. At the same time, compared with alfalfa, forage rape and other forages, its stalk diameter is larger, and the DEM model is more difficult to calibrate. In this research, the KG stalk after cutting was taken as the research object. The DEM model of KG stalk was established in EDEM software. The contact parameters were calibrated by bench test and simulation test. The stalk throwing test bench was built to carry out the actual throwing test. The CFD-DEM coupling method was used to carry out the simulation throwing test. By comparing the results of actual test and simulation test, the accuracy of DEM model and contact parameters was verified. The objective of this study is to provide model and parameter support for the application of DEM to study the interaction mechanism between KG stalk and harvester, and provide a DEM model verification method for stalk based on throwing test.

MATERIALS AND METHODS
Physical model of KG stalk

In order to make the DEM model of KG stalk more accurate, it is necessary to establish the stalk profile model of KG through measurement. The stalk of KG was collected from the experimental field of Hebei Xinnong Machinery Co., Ltd. (E:114.822º, N:38.157º), the average plant height was 1.8m during the harvesting period. According to the harvesting requirements, 9FDRFX cutter was used to cut KG, and the average cutting length was 24mm. In order to determine the physical model of KG stalk, 200 stalk segments were randomly selected to observe the stalk shape and measure the stalk diameter with vernier calliper. It was found that the stalk of KG was mainly cylindrical, and some of the stalks were broken along the axis to be semi-cylindrical, and the ratio of cylinder to semi-cylinder was about 4:1. The diameter distribution of cylindrical stalk is shown in Fig. 1. According to the diameter distribution, the cylindrical stalk is divided into small diameter (14 mm < d < 17 mm), medium diameter (17 mm < d < 20 mm) and large diameter (20 mm < d < 23 mm). The average diameter of the three is 15.7 mm, 18.3 mm and 21.2 mm, and the approximate ratio of quantity is 2:5:1.
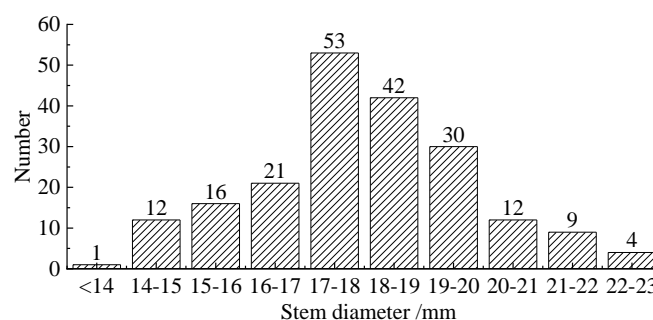
Fig. 1 - Stalk diameter distribution

The DEM model of KG stalk

DEM is a kind of analytical method based on molecular dynamics. During the simulation test, according to the material characteristics of KG stalk, its surface adhesion force is small. Hertz-Mindlin (no-slip) model is adopted for the contact model of KG stalk particles (*Grima et al., 2011*).

The shape of spherical particles is simple, which can be limited by radius and coordinate parameters, and there is only one contact state between spherical particles, which can shorten the simulation time. Therefore, the DEM model of materials is usually established in the form of spherical particle accumulation. When the diameter of spherical particles is smaller, the number of spherical particles required is more, and the shape of DEM model is closer to the actual shape of stalk, but the corresponding computer calculation processing time is longer. Considering comprehensively, using the Multi-sphere method (MSM), the small-diameter stalk, medium diameter stalk and large-diameter stalk were filled with spherical particles with radius of 4 mm, 4.5 mm and 5 mm respectively. The semi cylindrical stalk structure was filled with spherical particles

with radius of 2.25 mm and 4.5 mm. Finally, the optimized DEM model of KG stalk was formed, as shown in Fig. 2.

| a. Small diameter stalk （15.7mm） | b. Medium diameter stalk （18.3mm） | c. Large diameter stalk （21.2mm） | d. Semi-cylinder stalk （18.3mm） |
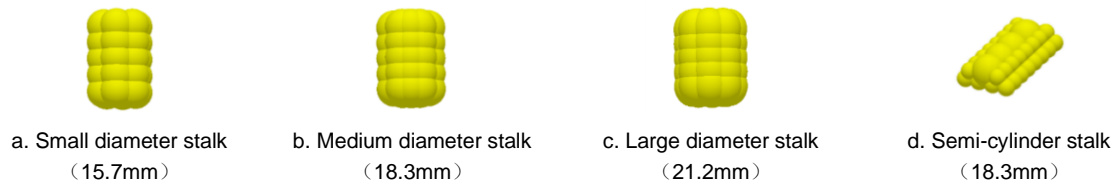
Fig. 2 - DEM model of KG stalk

Calibration of contact parameters

Due to the difference between the DEM model and the actual shape of stalk, the direct application of the contact parameters measured in the test to the simulation will cause test error. In order to improve the accuracy of the DEM simulation test, this section calibrates the DEM model parameters through the combination of bench test and simulation test.

In the process of harvesting and processing, in addition to the contact and interaction between KG stalks, stalks and mechanical equipment will also have contact. Q235 steel commonly used in agricultural machinery was selected as the contact material in this study. The intrinsic parameters of KG stalk and Q235 are shown in Table 1 (*Rong, 2014; Ma et al., 2020*).

Table 1

Intrinsic parameters

Moisture content of KG	Poisson's ratio of KG	Shear modulus of KG	Density of KG	Poisson's ratio of Q235	Shear modulus of Q235	Density of Q235
[%]	—	[Pa]	[kg/m³]	—	[Pa]	[kg/m³]
72±2	0.34	10.45×10⁶	1090	0.28	8.2×10¹⁰	7850

Calibration of Stalk-Steel CSF

CSF is one of the main contact parameters of DEM model, which can be expressed as the ratio of the maximum static friction force (f) to the contact positive pressure (F_N). In this study, the stalk-steel CSF was measured by inclined plane method. The test device is shown in Fig. 3a. The steel plate was fixed on the inclined plate, and the inclined plate was placed horizontally at the beginning. In order to prevent the stalk from rolling and reduce the test error, two sections of stalk were connected in series with pins and placed on the steel plate smoothly. Slowly lift one side of the inclined plate by pulling rope to gradually increase the inclined angle. When they begin to slide, stop lifting, and measure the inclined angle with the angle digital display instrument (Weidu, 4 * 90⁰, 0.05⁰, Wenzhou Weidu Electronics Co., Ltd.).

The relation between coefficient of static friction (μ_1) and inclination angle (α) is written as Eq. 1,

$$\mu_1 = f/F_N = tan\alpha \qquad (1)$$

In order to improve the accuracy of the test results, considering the influence of the placing state of the stalks, the stalks were placed on the steel plate in transverse, longitudinal and oblique directions. The average value was calculated by seven repeated tests. The results showed that the inclination angles were 22.42°, 22.38° and 22.41° when the stalk was placed horizontally, longitudinally and obliquely. It can be seen that the state of stalk placement had no significant influence on the friction angle. The average friction angle of the three states was 22.40°, and the static friction factor was calculated as 0.41.

| (a) Practical test | (b) Simulation test |
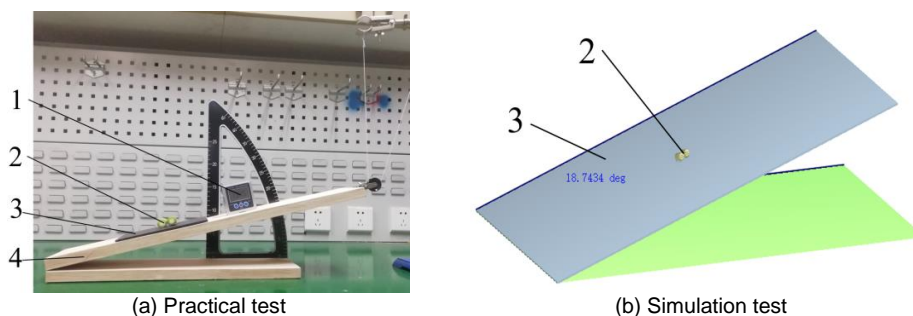
Fig. 3 - Practical test and simulation test of CSF
1 – Angle digital display instrument; 2 – KG stalk; 3 – Steel plate; 4 – Inclined plate;

Setting the physical parameters of stalk particles and plate in the EDEM simulation test (Fig. 3b). CRF, CR and stalk-steel CSF have no effect on the inclination angle of steel plate, so these parameters were set to 0 in order to reduce interference. According to the pre-simulation test, the stalk-steel CSF ranged from 0.25 to 0.55. Seven groups of simulation tests were conducted with step size as 0.05, and each group of tests was repeated for three times to take the average value. The test design scheme and results are shown in Table 2. Using Origin 2018 software to fit the data, the fitting curve is shown in Fig. 6, and the fitting equations for the stalk-steel CSF (x_1) and the steel plate inclination angle (y_1) was established as:

$$y_1 = 7.6856x_1^2 + 46.36x_1 + 4.0672 \tag{2}$$

Table 2

Design scheme and results of simulation test for stalk-steel CR

Stalk-steel CSF x_1	0.25	0.30	0.35	0.40	0.45	0.50	0.55
Inclination angle y_1 [°]	1.17	1.05	0.78	0.52	0.47	0.39	0.37

The determination coefficient R^2 of Eq. 2 was 0.9999，indicating that the fitting equation is highly reliable. The steel plate inclination angle of 22.40° measured by bench test was substituted into Eq. 2 to obtain x_1=0.372. The simulation test was carried out with CSF of 0.372, and the value of steel plate inclination angle was measured as 22.373°. The relative error between this result and bench test was 0.12%, which indicates that the calibrated stalk-steel CSF can be used for EDEM simulation, so the stalk-steel CSF was selected as 0.372.

Calibration of stalk-steel CR

The stalk-steel CR was determined by impact bounce test, and the test environment is shown in Fig. 4. KG was released from the initial position, and bounced to the highest point after colliding with the steel plate. The whole process of collision bounce was recorded by high-speed camera (Vision Research, Inc. Phantom v 9.1). The collision process is shown in Fig. 5.

Fig. 4 - Impact recovery test
1 – Fill light; 2 – High-speed camera; 3 – Coordinate paper; 4– Steel plate; 5– Computer

Initial height   Impact steel plate   Highest jumping point
(a) Bounce test

Initial height   Impact steel plate   Highest jumping point
(b) Simulation test
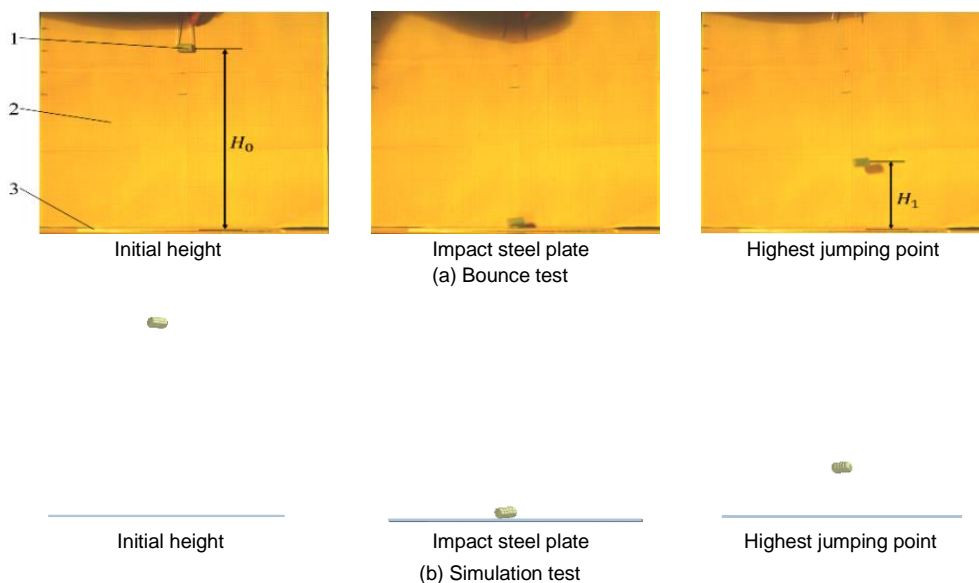
Fig. 5 - Test for CR
1– KG stalk; 2– Coordinate paper; 3– Steel plate

The maximum jumping height of the straw was measured by using the image processing software Fiji (ImageJ) with the reference length of coordinate paper dimension. The stalk-steel CR (e_1) can be calculated according to formula 3,

$$e_1 = \frac{v_1}{v_0} = \frac{\sqrt{2gH_1}}{\sqrt{2gH_0}} = \sqrt{\frac{H_1}{H_0}} \tag{3}$$

where:

v_0 is the instantaneous contact velocity, v_1 is the instantaneous separation velocity, H_0 is the initial falling height, H_1 is the maximum jumping height and *g* is the acceleration of gravity.

It was assumed that in the process of collision, the stalk and steel plate have small deformation at the contact point of collision and the collision time is very short. In order to verify whether the initial release height has influence on the test results, bench impact bounce tests were carried out with initial heights of 300 mm, 350 mm and 400 mm, respectively. The maximum bounce heights of stalk were 83.8 mm, 99.8 mm and 112.7 mm and the stalk-steel CR were calculated as 0.529, 0.534 and 0.531, respectively. The initial release height had no significant effect on the CR. The simulation experiment was carried out with H_0 as 350 mm. The CSF, CRF and stalk-stalk CR have no effect on the rebound height. In order to reduce the interference, the above parameters were set to 0 in EDEM simulation. The results of pre-simulation test showed that the range of stalk-steel CR was 0.40-0.70. Therefore, the step length was set to 0.05, and 7 groups of simulation tests were conducted, and each test was repeated for 3 times. The design scheme and results of the test are shown in Table 3. Using Origin 2018 software to fit the data, the fitting curve is shown in Fig. 7, and the fitting equation of the CR (x_2) and bounce height (y_2) was established as:

$$y_2 = 338.81x_2^2 - 139.66x_2 + 45.337 \tag{4}$$

Table 3

Design scheme and results of simulation test for coefficient of restitution

Stalk-steel CR x_2	0.40	0.45	0.50	0.55	0.60	0.65	0.70
Bounce height y_2 [mm]	44.23	50.36	59.83	70.64	86.15	95.51	114.10

The determination coefficient R^2 of Eq. 4 was 0.9966, which indicates that the fitting equation has high reliability. Substituting H_1=99.8 mm measured in the 350 mm bench test into Eq. 10, it can be obtained that x_2 was 0.656. Then the CR was set to 0.656 in EDEM, and the simulation tests with release heights of 300, 350 and 400mm were carried out. The rebound heights of simulation tests were 80.85 mm, 97.88 mm and 110.41 mm, and the relative errors with the actual experimental rebound heights were 3.65%, 1.96% and 2.07%. It showed that the simulation results after calibration are basically consistent with the bench test, so the stalk-steel coefficient of restitution was selected as 0.656.

Calibration of stalk-stalk coefficient of restitution

Similar to the method of measuring the stalk-steel coefficient of restitution, the steel plate is replaced by the stalk row which was neatly strung together. The KG stalk was clamped with tweezers and releases from the initial position. The stalk fell freely and bounced to the highest point after colliding with the stalk row. The whole process of collision bounce was recorded by high-speed camera. The calculation formula of the stalk-stalk coefficient of restitution is the same as that of formula 3.

The initial release height of stalk was selected as 300 mm, 350 mm and 400 mm respectively. Each group was tested for 10 times and the average value was taken. The average height of stalk bounce was 63.4 mm, 76.7 mm and 85.5 mm respectively. The stalk-stalk CR under the three release heights were 0.459, 0.468 and 0.462, respectively. The initial release height of the stalk had no significant effect on the CR, so the simulation experiment was carried out with H_0=350mm. The CRF and the stalk-stalk CSF have no effect on the bouncing height of stalk. In order to reduce the interference, the above parameters were set to 0 in EDEM simulation. The stalk-steel CSF was set as 0.372, and the stalk-steel CR was set as 0.656. After the pre-simulation test, it was determined that the value range of stalk-stalk CR was 0.30 ~ 0.60. The design scheme of simulation test is shown in Table 4.

Table 4

Design scheme and results of simulation test for CR

Stalk-stalk CR x_3	0.30	0.35	0.40	0.45	0.50	0.55	0.60
Bounce height y_3 [mm]	37.69	45.68	55.41	57.17	72.69	82.52	96.75

Fitting the data in Table 4, the fitting curve is shown in Fig. 8, and the fitting equation of the stalk-stalk CR (x_3) and rebound height (y_3) was established as :

$$y_3 = 281.98x_3^2 - 62.241x_3 + 32.073 \tag{5}$$

The determination coefficient R^2 of Eq. 5 was 0.9887, which indicates that the fitting equation has high reliability. By substituting the measured value of 76.7 mm in the 350 mm bench test into Eq. 5, it can be obtained that x_3=0.523. Then the stalk-stalk CR was set as 0.523 in EDEM, and the simulation tests with release heights of 300 mm, 350 mm and 400 mm were carried out. The rebound heights of the simulation tests were 60.36 mm, 73.51 mm and 79.68 mm, and the relative errors with the actual experiments were 4.80%, 4.16% and 6.81%. It showed that the simulation results after calibration were basically consistent with the bench test, so the stalk-stalk coefficient of restitution was selected as 0.523.

y_1=7.6856x_1^2=46.36x_1+4.0672, R^2=0.9999	y_2=338.81x_2^2-139.66x_2+45.337, R^2=0.9966	y_3=289.98x_3^2-62.241x_3+32.073, R^2=0.9887
Fig. 6 - The fitting curve of Eq.12	**Fig. 7 - The fitting curve of Eq.12**	**Fig. 8 - The fitting curve of Eq.12**
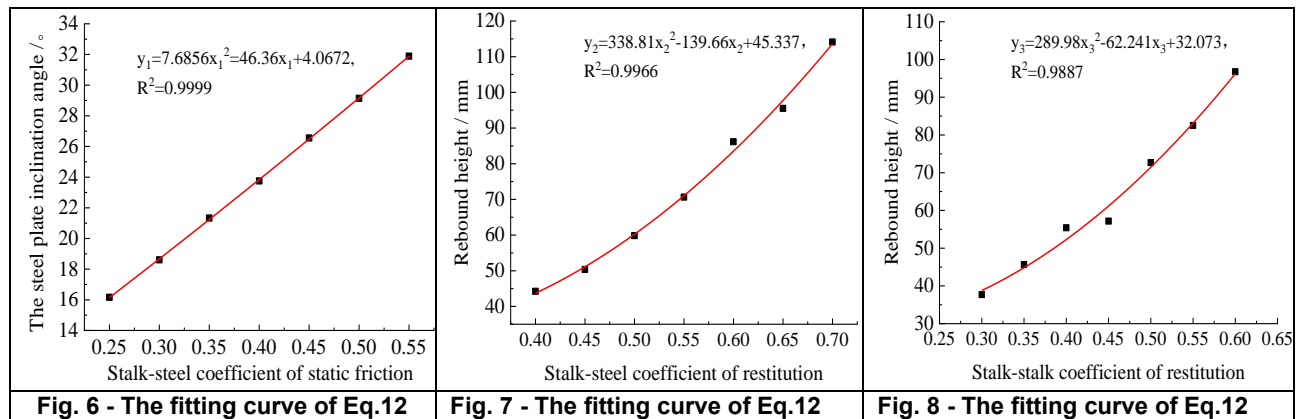
Calibration of contact parameters based on stacking test

It is difficult to measure and calibrate the stalk-stalk CSF, stalk-stalk CRF and the stalk-steel CRF. The measurement error of traditional bench test is large. Stacking angle is a macro parameter to characterize the flow and friction characteristics of discrete materials. During the process of stalk falling and stacking on the surface of steel plate, the value of contact parameter significantly affects the shape of stalk stacking (*Ghodk et al., 2017*). In this section, by analysing and comparing the results of bench stacking test and simulation stacking test, the response surface methodology (RSM) based on central composite design (CCD) was used to calibrate the above three parameters (*Wang et al., 2021*).

The stacking test is shown in Fig. 9. The funnel and steel plate were made of Q235, and the distance between the lower end face of the funnel and the steel plate was 75 mm. The stalk fell freely from the centre of the funnel and accumulated on the surface of steel plate. After all the stalks fell on the steel plate and stood still, using the camera to take the front view picture of the stalk pile, the image was binarized, and the contour curve was extracted by edge detection using MATLAB. The edge points of the contour curve were fitted linearly.
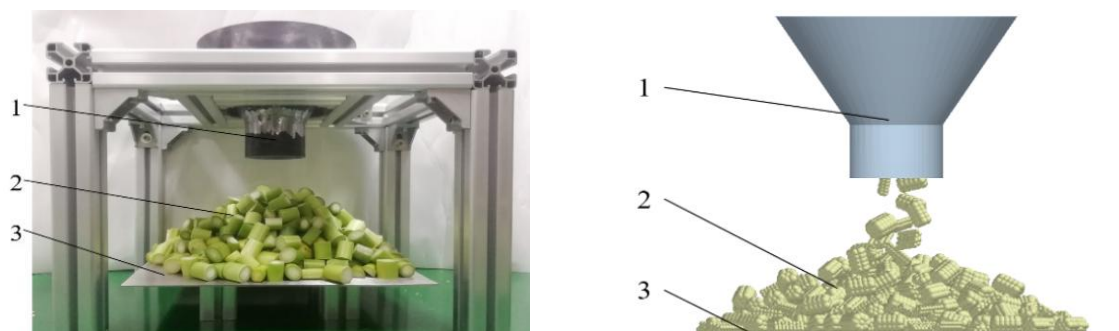
Fig. 9 - Stacking test of KG stalk
1– Funnel; 2– KG stalk; 3– Steel plate

The arctangent value of the slope of the fitting line was calculated, which was the stacking angle. The image processing is shown in Fig. 10. The stacking test was repeated 5 times, and the average value was taken. The measured value of stacking angle of KG stalk was 26.22°.

(a) Binary image   (b) Fitting line diagram
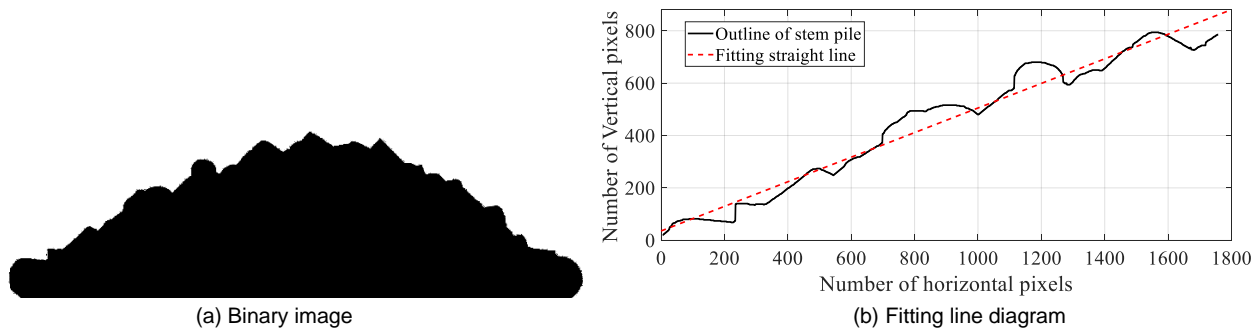
Fig. 10 - Image processing of stalk pile

When setting simulation parameters, select the calibrated parameters: μ_1=0.372、e_1=0.656、e_2=0.523. The DEM models of small diameter stalk, medium diameter stalk, large diameter stalk and semi cylindrical stalk were added in EDEM. According to the shape distribution of KG stalk after cutting, the generation rate ratio of four models was set as 6:15:3:7. The stalk-stalk CSF (X_1), stalk-stalk CRF (X_2) and stalk-steel CRF (X_3) were selected as test factors. And the relative error (δ) of simulation test stacking angle (θ') and bench test stacking angle (θ) was taken as test index. The relative error (δ) was calculated according to Eq. 6,

$$\delta = \frac{|\theta' - \theta|}{\theta} \times 100\% \qquad (6)$$

The steepest ascent test was used to determine the value range of CCD factors. According to the pre-test results, the stalk-stalk CSF (X_1) ranged from 0.3 to 0.6, the stalk-stalk CRF (X_2) ranged from 0.01 to 0.19, and the stalk-steel CRF (X_3) ranged from 0.05 to 0.35. The steepest ascent test was used to determine the 0 level and optimal value interval of factors for CCD.

Verification test

After CCD test, in order to further verify the reliability of the DEM model and contact parameters of KG stalk, a stalk throwing test bench was designed for throwing test, and the CFD-DEM coupling simulation throwing test was carried out by using the established DEM model and calibrated contact parameters. Under different rotating speed of throwing plate (400、500、600 and 700 r/min), the trajectory curves of straw throwing in bench test and simulation test were compared, and the relative error of throwing distance was calculated. The throwing test bench of KG stalk was shown in Fig. 11. The funnel was connected with the throwing room, and the stalk in the funnel can enter the throwing room under the action of gravity. A high-speed rotating throwing plate was installed in the throwing room. The throwing plate was powered by a stepping motor. The stalks entering the throwing room were thrown out under the action of the throwing plate. At the beginning of the test, the baffle was inserted into the connection between the funnel and the throwing chamber, and the cut KG stalks were put into the funnel. The frequency converter was adjusted to make the throwing plate reach the speed set in the test. After the speed was stable, the baffle was drawn out to make the stalks enter the throwing room to start the throwing operation. The pictures of the throwing trajectory of the stalks were taken by using the camera (DJI POCKTE 2).

Fig. 11 – Test bed for KG throwing
1– KG stalk; 2– Funnel; 3– Baffle; 4– Throwing chamber; 5– Stepping motor

According to the design dimension of throwing test bench, the 3D model was established by UG NX 8.5. In order to simplify the analysis, the model was imported into ANSYS-SCDM software for preparation. The 3D model was imported into Fluent software. By using Fluent for simulation calculation, the vector distribution of fluid velocity in the throwing room was obtained, as shown in Figure 12a. The 3D of the throwing test bench was imported into EDEM. Particle factory was added in the funnel and the ratio of small diameter stalk, medium diameter stalk, large diameter stalk and semi cylindrical stalk were set as 6:15:3:7. The rotation speed of the throwing plate was set according to the test requirements. Then CFD-DEM coupling simulation throwing test was carried out in EDEM. After the end of the simulation, the simulation throwing trajectory pictures were obtained in the post-processing. The stalk throwing simulation experiment is shown in Fig. 12b.

(a) Velocity vector distribution	(b) CFD-DEM coupling simulation throwing test
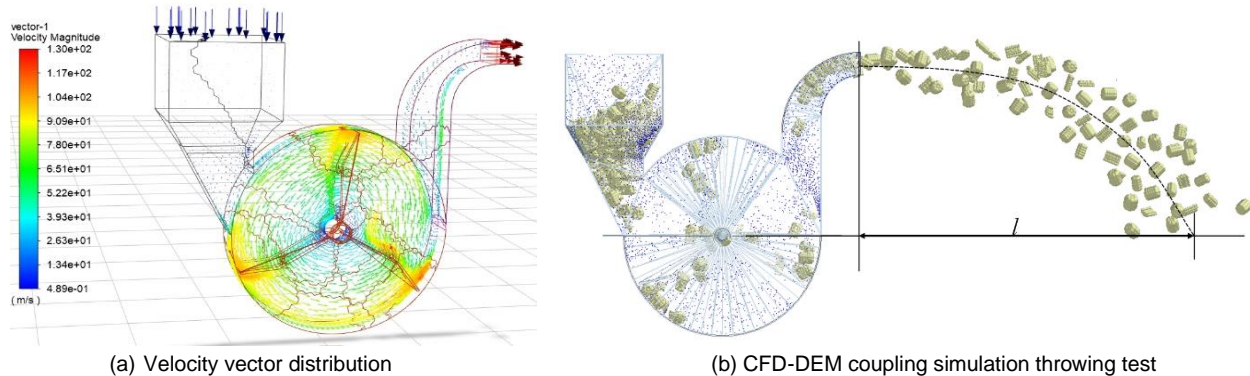
Fig. 12 – KG stalk Simulation test

RESULTS

Result of steepest ascent test

The steepest ascent test scheme and results are shown in table 5. According to the analysis of table 5, the relative error of simulation test 3 was the smallest. So, test 3 was selected as medium level, test 2 and 4 were selected as low level and high level respectively for CCD test. The low, middle and high levels of each variable were designated as -1, 0 and 1, respectively, and 1.682 is the axial distance from the centre point. The stalk-stalk CSF (X_1), stalk-stalk CRF (X_2) and stalk-steel CRF (X_3) were taken as test factors, the optimization ranges were 0.35 ~ 0.45, 0.04 ~ 0.10 and 0.10 ~ 0.20 respectively.

Table 5

Steepest ascent test scheme and results

Test No.	X_1	X_2	X_3	θ' /°	δ /%
1	0.30	0.01	0.05	18.63	28.93
2	0.35	0.04	0.10	21.58	17.69
3	0.40	0.07	0.15	23.73	9.50
4	0.45	0.10	0.20	29.52	12.58
5	0.50	0.13	0.25	31.49	20.10
6	0.55	0.16	0.30	33.02	25.95
7	0.60	0.19	0.35	34.91	33.16

Result of CCD test

The coding of CCD test factors is shown in Table 6, and the design scheme and results of simulation test are shown in Table 7. The study of RSM and the optimization of results were carried out by using the software Design expert 10.0.7. A quadratic polynomial regression model was assumed for predicting the response. The regression equation of stacking angle relative error (δ) was obtained as:

$$\delta = -1563.72X_1 - 220.42X_2 - 744.36X_3 - 1661.7X_1X_2 + 637.81X_1X_3 - 1034.73X_2X_3 + 2023.51X_1^2$$
$$+ 7093.08X_2^2 + 1947.51X_3^2 + 345.77$$

(7)

Table 6

Code table of simulation test factors

Code	X_1	X_2	X_3
-1.628	0.35	0.04	0.10
-1	0.37	0.05	0.12
0	0.40	0.07	0.15
1	0.43	0.09	0.18
1.628	0.45	0.10	0.20

Table 7

Test scheme and results

Test No.	Factor level			Index
	X_1	X_2	X_3	δ /%
1	-1(0.37)	-1(0.05)	-1(0.12)	7.5
2	1(0.43)	-1	-1	11.39
3	-1	1(0.09)	-1	8.96
4	1	1	-1	7.67
5	-1	-1	1(0.18)	9.11
6	1	-1	1	13.6
7	-1	1	1	6.72
8	1	1	1	9.34
9	-1.682(0.35)	0(0.07)	0(0.15)	8.03
10	1.682(0.45)	0	0	10.57
11	0(0.40)	-1.682(0.04)	0	11.4
12	0	1.682(0.10)	0	9.85
13	0	0	-1.682(0.10)	7.35
14	0	0	1.682(0.20)	10.87
15	0	0	0	4.29
16	0	0	0	3.66
17	0	0	0	2.89
18	0	0	0	4.7
19	0	0	0	3.35
20	0	0	0	4.44
21	0	0	0	2.85
22	0	0	0	4.69
23	0	0	0	3.35

The analysis of variance of Eq.7 is shown in Table 8. The quadratic regression model for stacking angle relative error were significant (P < 0.05) and the R^2 were higher than 0.9518. Among these model variables, X_1、X_2、X_1^2、X_2^2 and X_3^2 all had a very significant impact (P < 0.01), X_3 and X_1X_2 both had a significant impact (P<0.05). The effect of X_1X_3 and X_2X_3 on stacking angle error (δ) were not significant. The non-significant factors were eliminated and the optimized quadratic regression model was obtained as Eq. 8

$$\delta = -1468.05X_1\text{-}375.63X_2\text{-}561.67X_3\text{-}1661.7X_1X_2 + 2023.51X_1^2$$
$$+ 7093.08X_2^2 + 1947.51X_3^2 + 345.77$$

(8)

Through using Design Expert 10.0.7, the influence of the interaction between stalk-stalk CSF X_1 and stalk-stalk CRE X_2 on the relative error of stacking angle can be obtained, and the response surface graph is shown in Figure 13a. It can be seen from Figure 13b that the contour line presents ellipse with larger curvature, and the interaction was significant. When the stalk-stalk CSF is 0.39 ~ 0.41 and the stalk-stalk CRF is 0.06 ~ 0.08, the relative error of stacking angle is small.

Table 8

Analysis of variance of regression equation

Source	Sum of square	df	Sum of mean square	F-value	P-value
model	217.82	9	24.20	28.51	< 0.0001**
X_1	14.31	1	14.31	16.86	0.0012**
X_2	9.71	1	9.71	11.44	0.0049**

X_3	6.16	1	6.16	7.25	0.0184*
$X_1 X_2$	6.21	1	6.21	7.32	0.0180*
$X_1 X_3$	2.54	1	2.54	3.00	0.1072
$X_2 X_3$	2.41	1	2.41	2.84	0.1159
X_1^2	50.83	1	50.83	59.88	< 0.0001**
X_2^2	80.94	1	80.94	95.35	< 0.0001**
X_3^2	47.08	1	47.08	55.47	< 0.0001**
Residual	11.04	13	0.85		
Lack of fit	6.63	5	1.33	2.41	0.1293
Pure Error	4.41	8	0.55		
Total	228.85	22			

Note: * indicates that this item has significant effect on the result (P≤0.05), * * indicates that this item has extremely significant effect on the result (P≤0.01).

(a) Response surface graph   (b) Contour map
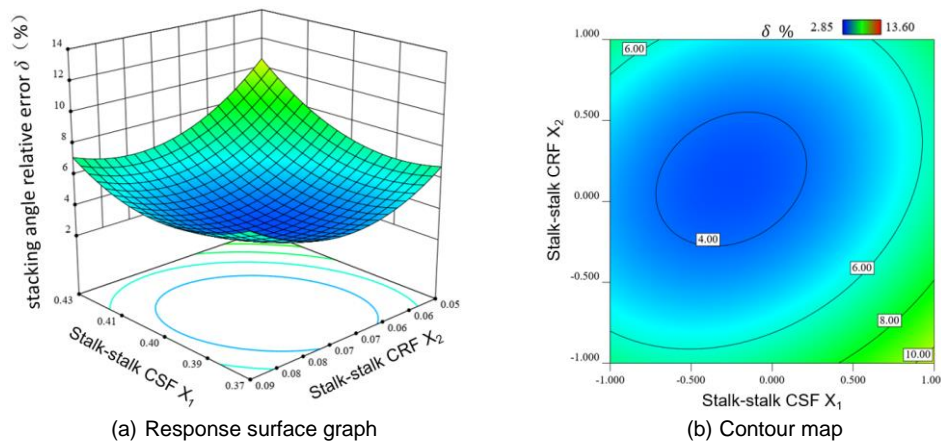
Fig. 13 – Effect of interaction between X_1 and X_2 on relative error of stacking angle

Using the optimization module of Design expert 10.0.7 software, taking the minimum relative error of stacking angle as the objective, the regression equation was solved, the response surface is analysed. The objective and constraint equations were shown as:

$$\begin{cases} \min \delta(X_1, X_2, X_3) \\ s.t. \begin{cases} 0.35 \le X_1 \le 0.45 \\ 0.04 \le X_2 \le 0.10 \\ 0.10 \le X_3 \le 0.20 \end{cases} \end{cases} \tag{9}$$

Through data processing, the optimal parameter combination of regression model was obtained as follows: the stalk-stalk CSF was 0.393, the stalk-stalk CRF was 0.072, the stalk-steel CRF was 0.144. The calibrated contact parameters were substituted into EDEM software for stacking simulation test. The average stacking angle was 26.91° and the relative error with bench test was 2.63%. It showed that the optimal combination of simulated contact parameters was basically consistent with the actual value, which can be used for subsequent simulation test.

Result of verification test

Python was used to process the images of throwing trajectory in bench test and simulation test, and the coordinates of throwing trajectory points were extracted. By using Origin 2018 to fit the coordinate data of trajectory points, the trajectory curves and fitting equations of bench test and simulation test under different throwing speeds were obtained, as shown in Fig. 14. It can be seen that the throwing trajectory curves of the two experiments were relatively consistent. The measured and simulated values of throwing distance of stalk under four throwing speeds (400, 500, 600 and 700 R / min) were shown in table 9 and the relative errors of throwing distance were 3.46%, 8.26%, 8.82% and 10.46% respectively. The above results show that the optimized DEM model and contact parameters can be used in the discrete element simulation experiment, which can provide theoretical support for the follow-up simulation.

$y_1=-0.0013x_1^2+0.0333x_1+476.1$
$R^2=0.8523$
$y_2=-0.0014x_2^2+0.149x_2+452.31$
$R^2=0.8971$

(a) 400 r/min

$y_3=-0.0011x_3^2+0.0447x_3+456.3$,
$R^2=0.9002$
$y_4=-0.0098x_4^2+0.0635x_4+461.82$,
$R^2=0.8528$

(b) 500 r/min

$y_5=-0.0003x^2+0.0457x+465.54$
$R^2=0.8705$
$y_6=-0.0004x^2+0.1022x+459.69$
$R^2=0.9066$

(c) 600 r/min

$y_7=-0.0003x^2+0.085x+455.32$
$R^2=0.8975$
$y_8=-0.0003x^2+0.153x+465.36$
$R^2=0.8548$

(d) 700 r/min
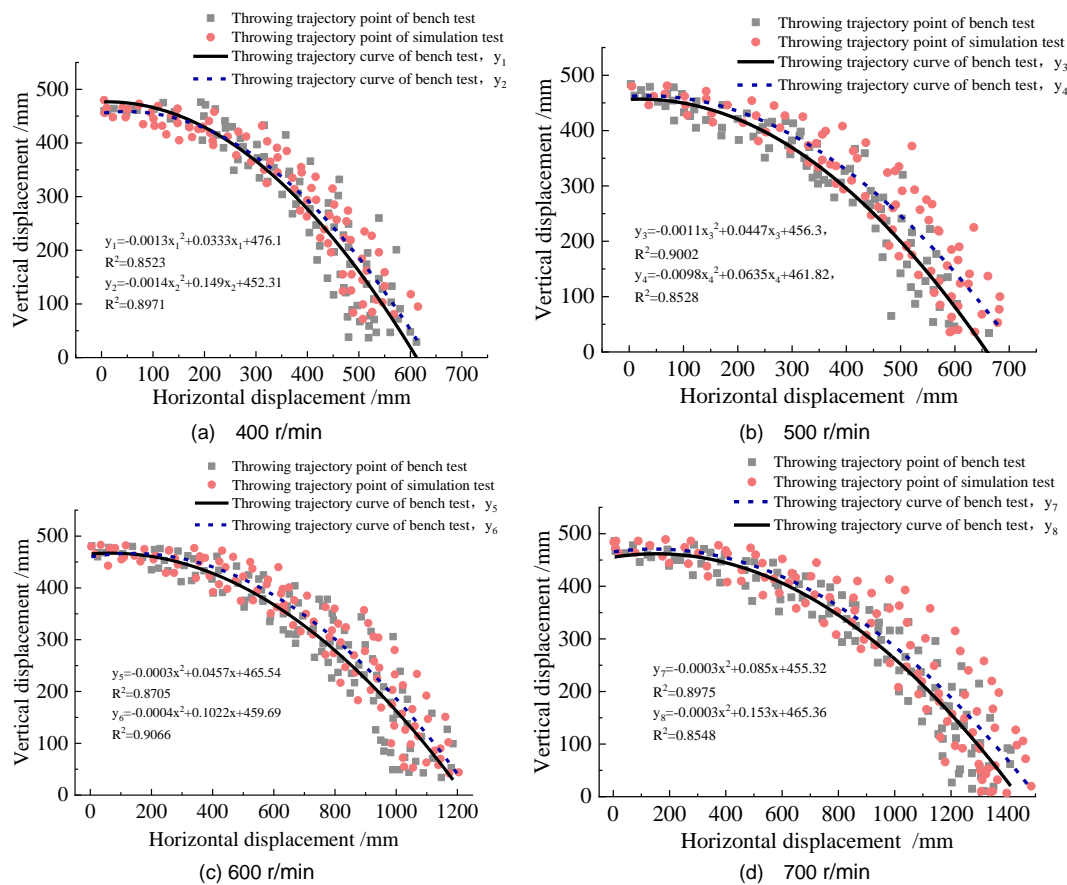
Fig. 14 - Fitting curve of stalk throwing trajectory

Table 9

Scheme and results of verification experiment

Parameters		Speed [r/min]			
		400	**500**	**600**	**700**
Distance throwing [mm]	Bench test	603.24	664.70	1324.21	1381.75
	Simulation test	624.10	719.63	1207.35	1526.31
Relative error /%		3.46	8.26	8.82	10.46

CONCLUSIONS

Compared with soil, fertilizer, seeds and other forages, the DEM model of KG stalk is more complex and more difficult to establish and calibrate. In this paper, the parameters of DEM model were calibrated by the combination of bench test and simulation test. Through the slope sliding test between stalk and steel plate, the stalk-steel coefficient of static friction was calibrated as 0.372. Through the collision bounce test between stalk and stalk, stalk and steel plate, the stalk-steel coefficient of restitution and stalk-stalk coefficient of restitution were calibrated as 0.656 and 0.523. Through the stalk stacking test of KG stalk, the actual stacking angle of stalk was measured as 26.22°. Based on the steepest ascent test and CCD test, the optimal values of stalk-stalk coefficient of static friction, stalk-stalk coefficient of rolling friction, stalk-steel coefficient of rolling friction were calibrated as 0.393, 0.072 and 0.144, respectively. In order to verify the accuracy of the model and parameters, the test bench of KG stalk throwing was designed, and the actual and simulation throwing test were carried out. The throwing trajectory curve of the simulation test is consistent with that of the actual test, which verifies the accuracy of the DEM model and contact parameters of KG stalk.

There were differences between the simulation model parameters and the actual parameters, but there was no obvious difference in the test results, which also showed the significance of parameter calibration. This study provides model and parameter support for the application of DEM to study the interaction mechanism between KG stalk and harvester, and provides a stalk DEM model verification method based on throwing test. It is worth noting that this study only established the DEM model of KG stalk, and the leaves will also be affected in the actual harvest. In further research, the DEM model under the mixed state of stalk and leaf should be established.

REFERENCES

[1]   Bangura K., Gong, H., Deng RL., Tao M., Liu C., Cai YH., Liao KF., Liu JW. & Qi L., (2020). Simulation analysis of fertilizer discharge process using the Discrete Element Method [J]. *PLoS ONE*, 15(7):e0235872. https://journals.plos.org/plosone/article?id=10.1371/journal.pone.0235872.

[2]   Ghodk B. M., and Goswami, T. K. (2017). DEM simulation of flow of black pepper seeds in cry ogenic grinding system. *Journal of Food Engineering*, England, 196,36–51. https://doi.org/10.1016/j. jfoodeng.2016.09.026.

[3]   Grima A.P., Wypych P.W., (2011), Development and validation of calibration methods for discret e element modeling. *Granular Matter*, 13(2),127-132, Berlin/Germany.

[4]   Guzman L., Chen Y., Landry, H., (2021). Coupled CFD-DEM simulation of seed flow in an air seeder distributor tube. *Processes*, Switzerland, 8(12). Switzerland, https://www.mdpi.com/2227-9 717/8/12/1597.

[5]   Li, M., Zi, X., Tang, J., Zhou, H., and Cai, Y. (2019). Silage fermentation, chemical composition and ruminal degradation of king grass, cassava foliage and their mixture. *Grassland Science*, *Japan*, *65*(4), 210–215. https://doi.org/10.1111/grs.12235.

[6]   Liao, Y. T., Liao, Q. X., Zhou, Y., Wang, Z. P., Jiang, Y. J., & Liang, F. (2020). Parameters calibration of discrete element model of fodder rape crop harvest in bolting stage (饲料油菜薹期收获茎秆破碎离散元仿真参数标定). *Transactions of the Chinese Society of Agricultural Machinery*, *China*, *51*(06), 73–82. DOI:10.6041/j.issn.1000-1298.2020.06.008.

[7]   Ma, W. P., You, Y., Wang, D. C., Yin, S. J., & Huan, X. L. (2020). Parameter calibration of alfalfa seed discrete element model based on RSM and NSGA-Ⅱ (基于 RSM 和 NSGA-Ⅱ的苜蓿种子离散元模型参数标定). *Transactions of the Chinese Society of Agricultural Machinery*, *China*, *51*(08), 136–144. DOI：10.6041/j.issn.1000-1298.2020.08.015.

[8]   Ma, Y. H., Song, C. D., Xuan, C. Z., Wang, H. Y., Yang, S., & Wu, P. (2020). Parameters calibration of discrete element model for alfalfa straw compression simulation (苜蓿秸秆压缩仿真离散元模型参数标定). *Transactions of the Chinese Society of Agricultural Engineering*, *China*, *36*(11), 22–30. DOI:10.11975/j. issn.1002-6819.2020.11.003.

[9]   Rong, X. (2014). *Optimization of Rotor Cutter Cutting Technics for King Grass* [Unpublished Master's dissertation]. China Agricultural University.

[10]   Tran, KM., Bui, H., Sanchez, M., & Kodikara, J., (2020). A DEM approach to study desiccation processes in slurry soils. *Computers and Geotechnics*, 120, 103448. DOI:10.1016/j.compgeo.2020.103448.

[11]   Wang, L., Hu, C., He, X. W., Guo, W. S., Wang, X., F., Hou, S. L. (2021). A general modelling approach for coated cotton-seeds based on the discrete element method. *INMATEH Agricultural Engineering*, 63(01), 219–228, Romania. https://doi.org/10.35633/inmateh-63-22.

[12]   Xie, Q.J., Liu, F.Y., Yang, M.J., Liu, J., Yang, S.H., & Xie, S.Y., (2021). DEM simulation and evaluation of well cellar making performance of opener with large socket. *INMATEH Agricultural Engineering*, 63(01), 41–50. Romania. https://doi.org/10.35633/inmateh-63-04.

[13]   Xu B., Zhang Y., Cui Q., Ye S., & Zhao F., (2021). Construction of a discrete element model of buckwheat seeds and calibration of parameters. *INMATEH Agricultural Engineering*, 64(02), 175-184. Romania. https://dx.doi.org/10.35633/inmateh-64-17.

[14]   Zhang, T., Zhao, M., Liu, F., Tian, H. & Li, D., (2020). A discrete element method model of corn stalk and its mechanical characteristic parameters. *Bioresources*, *USA*, 1*5*(4), 9337–9350. DOI: 10.15376/biores.15.4.9337-9350.

[15]   Zhao, J. M., Xiao, B., Meng, Y., Yang, Z. F., Pang, L., Zhou, M., & Zhang, X. Q. (2019). Transcriptome analysis to shed light on the molecular mechanisms of early responses to cadmium in roots and leaves of King Grass (Pennisetum Americanum ×P. purpureum). *International journal of molecular sciences*, *USA, 20*(10), 2532. https://doi.org/10.3390/ijms20102532.

DROPPING EAR DETECTION METHOD FOR CORN HARVERSTER
BASED ON IMPROVED Mask-RCNN
/
基于改进 *Mask-RCNN* 的玉米果穗损失检测方法

Geng AIJUN [1,2)], **Gao ANG** [1)], **Yong CHUNMING** [3)], **Zhang ZHILONG** [1,2*)], **Zhang JI** [1)], **Zheng JINGLONG** [1)]
[1)] Shandong Agricultural University, College of Mechanical and Electrical Engineering/ China;
[2)] Shandong Provincial Engineering Laboratory of Agricultural Equipment Intelligence/ China;
[3)] Shandong Wuzheng Group, Agricultural Equipment Research Institute/ China
Tel: +86-0538-8242500; E-mail: sdauzzl@163.com
DOI: https://doi.org/10.35633/inmateh-66-03

ABSTRACT

In order to quickly and accurately identify the corn ears lost during the corn harvesting process, a corn ear loss detection method based on the improved Mask-RCNN model was proposed. The lost corn ears in the field were taken as research objects, the images of the lost corn ears were collected and the fallen ears data set was established. The size ratio of the Anchor Box of the area recommendation network was changed by changing the K-means algorithm to reduce the influence of artificial setting intervention. The group convolution was introduced into the residual unit and the channel dimension was divided into 3 equal parts to reduce the model parameters in the basic feature extraction network ResNet. A Convolutional Block Attention Module (CBAM) was introduced to improve the accuracy of the model in the last layer of the ResNet network. Results showed that the average target recognition accuracy of the method on the test set in this study was 94.3%, which was better than that of the previous model, and the average time to recognize a single image was 0.320 s. The proposed method could detect the lost corn ears during the harvesting process under the complicated background, and provide a reference for the corn ear loss detection of the corn harvester.

摘要

为快速准确识别玉米收获过程果穗损失，本文以玉米收获机田间收获掉落的果穗为研究对象，进行图像采集并建立掉落果穗数据集，提出一种基于改进 Mask-RCNN 的果穗损失检测方法。将 Mask-RCNN 深度学习模型引入玉米果穗图像识别中并提出一种优化方法，通过 K-means 算法改变区域建议网络 Anchor Box 尺寸比例以减少人为设置干预影响，在基础特征提取网络 ResNet 中将分组卷积引入残差单元并将通道分为 3 等份以减少模型参数，在 ResNet 网络层最后一层引入卷积注意力模块(CBAM)以提高模型的准确率。结果表明：本文方法在测试集上平均目标识别准确率为 94.3%，优于改进前的模型，识别单幅图像的平均耗时为 0.320 s。所提方法对复杂背景下玉米收获机掉落的果穗有较好的检测效果，可为玉米收获机掉穗损失检测提供参考。

INTRODUCTION

The North China Plain (NCP) is the main grain production area in China and the mechanized harvesting of corn in NCP has been dominated by ear harvesting. Due to the shocks and vibrations in the working process of corn harvesters, it is inevitable for a small number of ears to be omitted. The high corn ear loss rate indicates that there are some problems with the working quality of the corn harvester and the harvester should be inspected and adjusted in time to avoid greater economic losses. Therefore, corn ear loss rate is regarded as an important index to measure the working performance of the corn harvester, and it is of great significance to determine the ear loss rate of corn harvester in real time.

With the development of deep learning, more and more target detection methods have been developed and applied in agricultural production (*Kamilaris et al., 2018*). The role of target detection is to identify targeted targets and non-targeted targets. Compared with traditional algorithms, deep learning algorithms are highly adaptable, easy to migrate, and do not require feature engineering. As a mainstream model, Mask Region Convolutional Neural Network (Mask-RCNN) has been widely applied in the field of agriculture. *Jesus et al., (2020),* adopted the Mask-RCNN model to segment 10 different types of microalgae with an average accuracy of 85%. *Yu et al., (2019),* used Mask-RCNN with ResNet50 as the basic network to visually locate the strawberry picking points, and the average detection accuracy was 95.41%. *Xiong et al., (2020),* used the Mask-RCNN model to segment soybean leaves under a complex background, and used the migration learning

method of the VGG network to extract the leaf features to obtain the leaf element classification method, and the average accuracy of the classification was 89.42%. *Li et al., (2019),* proposed a pig crawling behavior recognition algorithm based on Mask R-CNN, introduced a migration learning method to train the ResNet-FPN network, the segmentation accuracy rate of the pig segmentation network model was 94%, and the accuracy rate of the crawling behavior recognition algorithm was 94.5%. In spite of this, there were still few reports on the detection of missing ears in corn harvesting process based on the Mask-RCNN model.

In this paper, the lost corn ears in the working process of corn harvester were taken as the research object and the images of the lost corn ears were collected. The improved Mask-RCNN was adopted to recognize the corn ears of different sizes and shapes. A visual detection method was proposed to detect the lost corn ears in the working process of corn harvesting, which could provide reliable feedback to ensure the consistent performance of the corn harvester.

MATERIALS AND METHODS

IMAGE ACQUISITION AND PROCESSING
Image acquisition
The images of corn ears were collected in October 2019 twice under the conditions of suitable corn harvesting and good weather from the experimental field which was located in Nanqiu village, Feicheng City. The collection tool was an iPhone 6S smartphone with a 12-million-pixel camera which was used to collect 1500 sample images at different angles and shooting distance ranging from 0.3 to 0.5m.
Image preprocessing
The data set was augmented to improve the generalization ability of the training model and prevent the occurrence of overfitting for the small number of images about the data set. The existing data enhancement methods could be classified into three different categories: spatial transformation, such as rotation, flip, etc.; color transformation, such as changing brightness, changing image color, etc.; message deletion, such as random deletion, hide-and-seek (HAS), etc.

a. Original pictures

b. Increasing image contrast

c. Gaussian noises

Fig. 1 - Data enhancement results

In order to facilitate the computer to process the data set, the collected images were uniformly scaled to 720*406 pixels, and the images were processed by means of rotation, brightness enhancement, Gaussian noise, and Hide-and-Seek (HAS) data enhancement (*Singh et al., 2019*). The results of data enhancement were shown in Fig. 1. Finally, there were 6000 images included in the expanded data set. The data set was split into training sets (4800 pieces) and verification sets (1200 pieces) based on the ratio of 8:2.

DETECTION METHOD FOR FALLING CORN EARS

Corn ear detection model based on Mask-RCNN

The flowchart of the corn ear detection model based on Mask R-CNN was shown in Fig. 2. The image data was firstly performed data preprocessing after collection, involving the scaling of images in data set, the data enhancement processing and the conversion of data sets into MS coco format. Then, the Mask R-CNN model was used to train the preprocessed data, and the initial weight and the number of training iteration were set. The corn ear detection was completed by using the images in the test set to test and assess the trained model after the model training was completed.
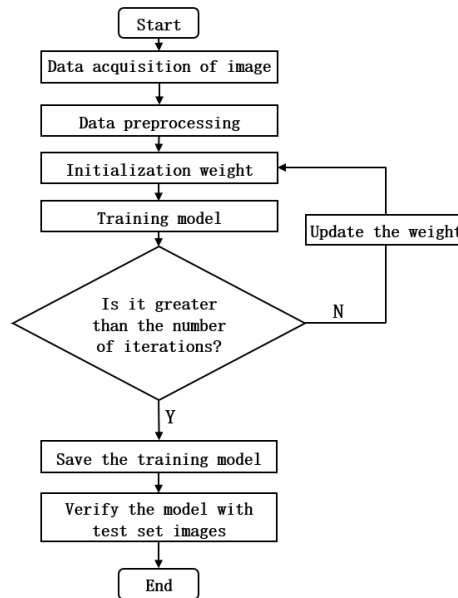
Fig. 2 - Flow chart of corn ear detection model

As an improvement to the Faster R-CNN model, Mask R-CNN consisted of target location, category and segmentation mask prediction. The structure and working process of the algorithm were illustrated in Fig. 3. In the Mask R-CNN model, the input images with length P and width Q was first scaled to an image with length M and width N, and then the feature maps were extracted by the convolutional neural network embedded in the backbone network. The feature maps were shared by the region proposal network (RPN) and Mask R-CNN network, and the candidate frame generated by the feature image and RPN was input to ROI pooling layer. The corresponding target features in the shared feature mapping were extracted after pooling processing, and then output to FC layer and FCN layer respectively for target classification and segmentation mask prediction.
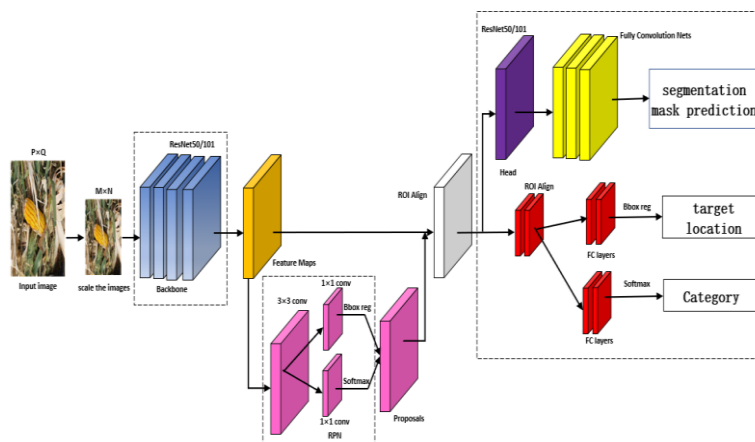
Fig. 3 - Network structure of Mask R-CNN

The convolutional neural network of the backbone network adopted the residual network (ResNet) in this paper *(He al., 2016)*. In order to expand the main network at multiple scales, the feature pyramid network (FPN) was introduced *(Lin al., 2016)*, and the top and bottom features of the feature pyramid network structure were fused through up-sampling to generate feature graphs of different levels *(Lin al., 2019)*.

TEST SOFTWARE AND HARDWARE

The processing platform was a desktop computer, the processor was Intel Pentium G4560, the main frequency was 3.5GHz, and the GPU was GeForce GTX 2080. The operating environment was Ubuntu (18.04) Linux system, the machine learning library was Tensorflow1.5.0, and the parallel computing architecture was CUDA 9.0.

TEST EVALUATION INDEX

Average precision (AP) was treated as the evaluation index of corn ear recognition, so that the calculation formula is written as follows.

$$P = \frac{T_P}{T_P + F_P} \times 100\% \tag{4}$$

$$R = \frac{T_P}{T_P + F_N} \times 100\% \tag{5}$$

$$AP = \int_0^1 P(R)\,\mathrm{d}R \tag{6}$$

where:

P –precision rate; R–recall rate;

T_P—the number of positive samples correctly predicted;

F_P—the number of negative samples predicted as positive;

F_N— the number of positive samples predicted as negative;

AP— average accuracy.

Improved model

Although Mask R-CNN was an advanced example segmentation model, there were still problems in the application of Mask R-CNN to the detection and segmentation of the fallen corn ears, because the model could not perform target detection and Mask segmentation well due to the influence of the outdoor environment and the complex background of images. Therefore, the model needs to be improved to enhance the detection accuracy and mask segmentation effect.

In order to solve the above problems, the K-means algorithm was used to cluster the targets in the regional recommendation network, and the reasonable recommendation size was set to reduce the interference of artificial design recommendation size. The attention mechanism was added in the feature extraction network to make the convolutional neural network pay Convolutional Block Attention Module (CBAM) to feature extraction and improve the classification ability. The residual structure was optimized to reduce the model parameters in the residual element.

(1) Size regression of area recommendation network Anchor Box based on K-means Algorithm

In the Mask R-CNN model, the RPN scanned the image through a sliding window to search the target area of the Anchor. Anchor was a rectangular box of different sizes and different proportions distributed on the image, and the Anchor Box was designed in 3 sizes and 3 aspect ratios of 1:2, 1:1, 2:1 in the original model. Image tests were carried out by using the Coco dataset, which has 80 categories and more than 330,000 images. The data set in this paper was self-made, and the category and target size were different from the original Coco data set. Therefore, modifying the proportional size of Anchor Box was helpful to improve the target detection accuracy.

K-means algorithm was a typical unsupervised learning algorithm, which could automatically divide different clusters. If the Euclidean distance in standard K-means was directly used as a measure, different clusters would produce different errors, and the larger the cluster, the greater the error. Therefore, the IOU value was used as the distance measure, and the measurement formula was shown below.

$$\mathrm{d}(box, anchor) = 1 - \mathrm{IOU}(box, anchor) \tag{1}$$

According to the location box of the target region of the data set in this paper, the values of k were clustered several times in the interval of 2-10 to obtain the change curves of the average IOU and k values, as shown in Fig. 4. The optimal k value was estimated using the Elbow method (*Dhanachandra, 2015*), that was, the optimal k value was the one with the most obvious change in the slope of the curve.
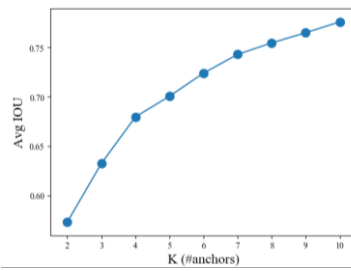
Fig. 4 - Variation curves of average IOU and *k* values

Finally, *k* =4 was selected for cluster analysis, and the clustering results were shown in Fig. 5. Four clustering centers were obtained (236.96, 80.12), (132.52, 157.78), (113.03, 66.96) and (544.55, 111.34). The aspect ratio of Anchor was determined to be (0.8, 1.6, 3.0, 4.9), and the size was not changed.
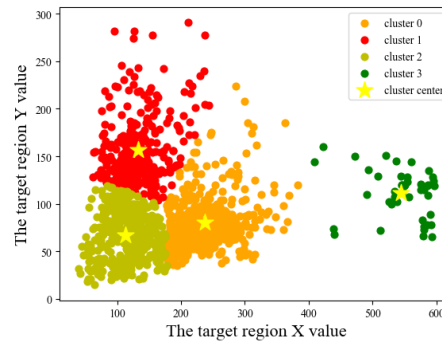
Fig. 5 - Clustering visualization diagram when *k*=4

(2) Residual network and attention mechanism

A large number of machine learning experiments showed that different feature extraction networks had a certain impact on the accuracy and speed of model detection, and the popular feature extraction networks were the VGG network and the ResNet network (*Simonyan, 2016*). As the number of network layers increased, however, the level of accuracy would drop even though a more complex process of feature extraction could be carried out. Based on the mapping relationship shown by the identity transformation, He et al. (2016) proposed a residual network structure (ResNet). Fig. 6 showed the residual unit, where X indicated the input of the neural network, while (X) denoted the expected output. Then, the function could be expressed as $F(X)= H(X)-X$, let $F(X)=0$, and constituted identity mapping $H(X)=X$, the learning goal of the ResNet network became the residual of input $H(X)$ and output X. In this way, it was easier to fit residuals and more sensitive to changes in the mapping output. Thus, the ResNet series were taken as the feature extraction network in this paper for the model.
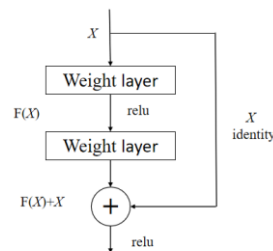
Fig. 6 - Schematic diagram of residual structure

In order to increase the recognition ability of the network and reduce the network parameters (*Li et al*), the residual module was optimized and the grouped convolution was introduced into the residual unit. After the feature map was dimensioned through the 1×1 convolutional layer, the channel dimension was divided into 3 equal parts, and the original 3×3 convolutional layer was replaced with a 3×1 convolution kernel and a 1×3 convolution layer. The optimized residual unit structure was shown in Fig. 7, the input X_1, X_2, X_3 corresponded to the output Y_1, Y_2, Y_3, and the output of the previous channel was used as the input K_2 and K_3 of the next channel. Assuming that the feature map of size $n×n×h$ passed through the 3×3 convolutional layer, the parameter A was $h×3×3×h=9h^2$, then the optimized parameter B was 3×($h/3 ×3×1×h/3+ h/3×1×3×h/3)= 2h^2$. It was pointed out that the optimized design greatly reduced the number of parameters of the convolutional layer, and could make up for the computational expenses of adding the CBAM module.
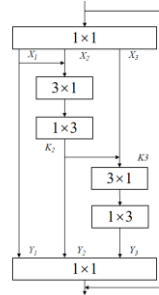
Fig. 7 - Structure diagram of residual after optimization

Inspired by the attention mechanism of deep learning, the CBAM module was introduced into ResNet of the Mask R-CNN feature extraction network to construct the channel attention module and the spatial attention module. Given an intermediate feature map, the CBAM module would infer the attention weight along the spatial and channel dimensions successively, and adjust the features flexibly through multiplication with the original feature map. The performance of the model was significantly improved and the cost incurred by the model was kept low in the meantime.

The channel attention module relied on maximum pooling and average pooling to compress the feature map in spatial dimensions, and two different spatial background descriptions could be obtained including *Fc max* and *Fc avg*. Then, it was evaluated and computed element-by-element through a shared network composed of MLPs to produce the channel attention map $M_c \in R^{c \times 1 \times 1}$. The channel attention mechanism could be expressed as:

$$M_S(F) = \sigma(f^{7 \times 7}([\text{AvgPool}(F); \text{MaxPool}(F)])) = \sigma(f^{7 \times 7}([F_{avg}^S; F_{max}^S])) \qquad (2)$$

where, $f^{7 \times 7}$ represented a 7×7 convolution layer.

ResNet had four layers with different parameters. We only added channel attention module and spatial attention module in the last layer, and then connected with average pooling and full connection layer. The improved structure was shown in Fig. 8.
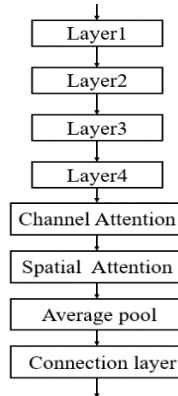
Fig. 8 - CBAM insert structure diagram

RESULTS

EXPERIMENTAL DESIGN AND ANSLYSIS

Experiment and analysis of different feature extraction networks

In order to validate the proposed method, the same data set would be used in this paper to conduct comparative experiments on the speed and accuracy of different feature extraction network models through the same processing platform. Resnet50 and resnet101 feature extraction networks were used to train and test the Mask R-CNN model. The recognition accuracy of Mask R-CNN -ResNet50 model was 88.5%, and the average recognition accuracy of Mask R-CNN -ResNet101 model was 90.0%. Therefore, the Mask-Rcnn-ResNet101 model was chosen as the object of further research in this paper.

Hyperparameter selection experiment and analysis

Through the above-mentioned experiments, the Mask R-CNN model based on ResNet101 was selected to further optimize the hyperparameters. Plenty of deep learning experiments showed that batch processing (minibatch), learning rate and learning decay rate had different impacts on the accuracy of model detection. Empirical batch processing value was set as 32 and 64, learning rate was set as 0.01 and 0.001, and learning decay rate was set as 0.001 and 0.0001. The test results were listed in Table 1. As shown in Table 1, *a* was batch processing value, *b* was learning rate and *c* was learning decay rate.

Comparison test results of different parameter combinations   Table 1

Serial number	Parameter	Average accuracy / %
1	a= 32, b=0.01, c=0.001	87.6
2	a= 32, b=0.001, c=0.001	88.2
3	a= 32, b=0.01, c=0.0001	86.6
4	a= 32, b=0.001, c=0.0001	87.4
5	a= 64, b=0.01, c=0.001	88.1
6	a= 64, b=0.001, c=0.001	90.8
7	a= 64, b=0.001, c=0.001	89.6
8	a= 64, b=0.001, c=0.001	88.7

The effects that different combinations of learning rate and learning decay rate on the average accuracy of the model were tested based on the different batch processing values as 32 and 64. Compared with the results of the third group and the fifth group in Table 1, the average accuracy of the model test with batch processing value of 64 was higher than that of the model with batch processing value of 32. Compared with the first group and the second group, the sixth group and the eighth group, the model with a learning rate of 0.001 and a learning decay rate of 0.001 had a higher accuracy than the model with a learning rate of 0.01 and a learning decay rate of 0.0001. The average accuracy of the sixth group reached 90.8%, which was the highest among the six groups. Therefore, the model with batch processing value as 64, the learning rate as 0.001 and the learning decay rate as 0.001 was finally adopted.

Comparative test and analysis of the improved model

In order to further demonstrate the effectiveness of this algorithm, a comparison experiment was conducted between the Mask R-CNN model with batch processing value as 64, learning rate as 0.001, learning decay rate as 0.001 based on ResNet101 and the Mask R-CNN model with enhanced data set, improved Anchor Box ratio, residual optimization module and the CBAM. Table 2 shows that the improved Mask R-CNN model without enhanced datasets was 2.4% higher than before, and our model was 3.5% higher than before. In comparison with SharpMask and Scoring R-CNN, SharpMask had the lowest recognition accuracy and Mask Scoring R-CNN had higher recognition accuracy than Mask Scoring R-CNN, but 1.6 % lower than this method. However, with the increase of the average detection time when the convolutional Block Attention Module (CBAM) model was added, it can still meet the practical application requirements.

Comparison test results of improved model   Table 2

Model	Data enhancement	Average accuracy /%	Average detection time /s
Mask R-CNN	No	90.8	0.282
SharpMask	Yes	87.6	0.262
Mask Scoring R-CNN	Yes	92.7	0.292
Improved model	No	93.2	0.317
Improved model	Yes	94.3	0.320

Thermal diagram analysis

The Gradient-weighted Class Activation Mapping (Grad-CAM) (*Selvaraju, 2018*) was performed to visualize the results of model classification in this paper, and the effect of Convolutional Block Attention Module (CBAM) on the model classification process was demonstrated. The global average of the gradient was used by Gard-Cam to calculate the weight, so that the local feature map was generated in the last layer of the convolutional neural network, and the important feature region of the target prediction was highlighted through the point-by-point multiplication of the thermal map and the back propagation.

The basic network of ResNet101 in the Mask R-CNN model and the improved method in this paper were selected to visualize the classification results. As shown in Figure 9, the red part indicated the high credibility of the feature area. Upon comparison, it was found out that the heat map of ResNet101 with the CBAM paid more attention to the feature area. When there are two objects in an image, the thermal map of the attention mechanism module with convolution focused on two objects, while the original thermal map only focused on one object, indicating that it was helpful for the classification and extraction of feature regions, making the feature extraction network more accurate and improving the accuracy of the overall model.

| Original picture | Resnet101 | Resnet101 | Improved model | Improved model |
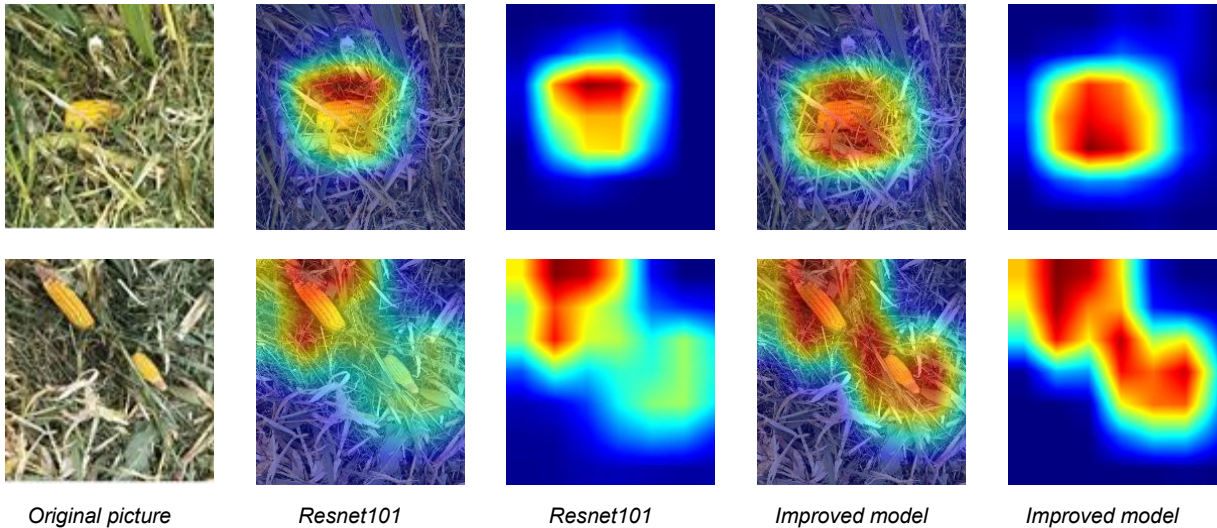
Fig. 9 - Gard-CAM thermal diagram

Results analysis

a.   Mask R-CNN

b.   Mask Scoring R-CNN

c.   SharpMask

d.   Improved model

Fig. 10 - Comparison of corn ear recognition results

The recognition result of the fallen corn ear was shown in Fig. 10. It can be seen that the SharpMask method had an incomplete segmentation of the corn ear. The accuracy of the Mask R-CNN method was above 0.9, and the Mask contour of a single ear was clearly identified and accurate. However, the contour of partial Mask segmentation deviated from the actual target, and the Mask segmentation error occurred when there was ear peel next to the ear. The segmentation contour of Mask Scoring R-CNN was relatively accurate, but it was slightly inferior to the accuracy of the improved method in this paper. It could be seen that the improved model had a more complete mask segmentation wheel for incomplete ears and occluded ears. There was no mask segmentation error when there were ear peels nearby, and good results had been achieved in recognition and segmentation. Therefore, the improved method in this paper could be used to identify and segment the corn ears dropped by the harvester.

CONCLUSIONS

A method based on the improved Mask R-CNN model to detect the corn ears lost by the corn harvester was proposed in our study. Data processing for the recognition and segmentation of the ears lost by the corn harvester were enhanced, the Anchor Box size ratio of the RPN sliding window was improved, and the grouping convolution was introduced into the residual unit in this method. Moreover, the original 3×3 convolution layer was replaced by a 3×1 convolution kernel and a 1×3 convolution layer and the CBAM was added to the last layer of the feature extraction network ResNet101, which improved the detection and segmentation accuracy of the model.

Different advanced model tests were performed on the images of the lost corn ears in the test set. Results showed that the average recognition accuracy of the improved method in our study on the test set was 94.3%, which was 4.3% higher than that of the original model. In addition, the method was better than average accuracy of 87.6% by SharpMask and average accuracy of 92.7% by Mask Scoring R-CNN. The method not only had good recognition accuracy and contour segmentation for a single corn ear, but also could identify the interference and overlapping corn ears under the complicated background. It was predicted that the time required for each image was 0.320 s, which met the identification requirements of fallen corn ears.

The reliable recognition of corn ears could be ensured to assist the intelligent detection of the ears lost by corn combine harvester by the dropped corn ear detection method based on the improved Mask R-CNN model.

REFERENCES

[1] Dhanachandra N., Manglem K., & Chanu Y. J. (2015). Image segmentation using K-means clustering algorithm and subtractive clustering algorithm. *Procedia Computer Science*, Vol.54, pp.764-771, Manipur/India.

[2] He K., Gkioxari G., Piotr Dollár, & Girshick R. (2017). Mask R-CNN. *Proceedings of the IEEE International Conference on Computer Vision (ICCV)*, pp. 2961-2969, Venice / Italy.

[3] Huang Z., Huang L., Gong Y., Huang C., & Wang X. (2019). Mask Scoring R-CNN. *2019 IEEE/CVF Conference on Computer Vision and Pattern Recognition (CVPR)*. *IEEE*, Long Beach / USA.

[4] Jesus R.S., Gloria B., Oscar D., Noelia V., & Gabriel C. (2020). Semantic versus instance segmentation in microscopic algae detection. *Engineering Applications of Artificial Intelligence*, Vol.87, pp.1-15, Ciudad Real / Spain.

[5] Kamilaris A., Prenafeta-Boldu F. X. (2018). Deep learning in agriculture: a survey. *Computers and Electronics in Agriculture*, Vol.147, pp. 70-90, Catalonia / Spain.

[6] Lin T. Y., Dollár P., Girshick R., He K., Hariharan B., Belongie S. (2017, July). Feature pyramid networks for object detection. In *Proceedings of the IEEE conference on computer vision and pattern recognition (CVPR)*, Honolulu.

[7] Li D., Zhang K., Li X., Chen Y., Li Z., & Pu D. (2019). Mounting behavior recognition for pigs based on Mask R-CNN. *Transactions of the Chinese Society for Agricultural Machinery*, Vol.50, Issue (Supp), pp.261-266+275, Beijing/China.

[8]   Ren S., He K., Girshick R., & Sun J. (2017). Faster R-CNN: towards real-time object detection with region proposal networks. *IEEE Transactions on Pattern Analysis & Machine Intelligence*, Vol.39, Issue 6, pp.1137-1149, Anhui / China.

[9]   Sun H., Li S., Li M., Liu H., Qiao L., & Zhang Y. (2020). Research progress of image sensing and deep learning in agriculture. *Transactions of the Chinese Society for Agricultural Machinery*, Vol.51, Issue 5, pp.1-17, Beijing / China.

[10]   Singh K. K., Yu H., Sarmasi A., Pradeep G., & Lee Y. (2018). Hide-and-Seek: A data augmentation technique for weakly-supervised localization and beyond. *ArXiv*, 1811.02545, Davis / USA.

[11]   Simonyan K., & Zisserman A. (2014). Very deep convolutional networks for large-scale image recognition. ArXiv, 1409.1556. https://doi.org/10.48550/arXiv.1409.1556. Cornel University / USA.

[12]   Selvaraju R. R., Cogswell M., Das A., Vedantam R., & Batra D. (2020). Grad-cam: visual explanations from deep networks via gradient-based localization. *International Journal of Computer Vision*. Vol.128, issue 2, pp. 336-359, Atlanta / USA.

[13]   Trullo, R., Petitjean, C., Ruan, S., Dubray, B., Nie, D., & Shen, D. (2017). Segmentation of organs at risk in thoracic CT images using a SharpMask architecture and conditional random fields. *IEEE International Symposium on Biomedical Imaging,* Vol.2017, pp.1003-1006. Melbourne / Australia.

[14]   Wang C., Guo X., Wu S., Xiao B., & Du J. (2014). Three dimensional reconstruction of maize ear based on computer vision. *Transactions of the Chinese Society for Agricultural Machinery*, Vol.45, Issue 9, pp.274-279, Beijing/China.

[15]   Wang H., Sun Y., Zhang T., Zhang G., & Li Y. (2010). Appearance quality grading for fresh corn ear using computer vision. *Transactions of the Chinese Society for Agricultural Machinery*, Vol.41, issue 8, pp.156-159, Changchun / China.

[16]   Woo S., Park J., Lee J. Y., & Kweon, I. S (2018, September). CBAM: convolutional block attention module, *ECCV*, Vol.11211, pp. 3-19, Munich / Germany.

[17]   Xiong J., Dai S., Ou J., Lin X., Huang Q., & Yang Z. (2020). Leaf deficiency symptoms detection method of soybean based on Deep learning. *Transactions of the Chinese Society for Agricultural Machinery*, Vol.51, Issue1, pp.195-202, Guangzhou / China.

[18]   Yu Y., Zhang K., Yang L., & Zhang D. (2019). Fruit detection for strawberry harvesting robot in non-structural environment based on Mask R-CNN. *Computers and Electronics in Agriculture*, Vol.163, Issue (2019), pp.1-9, Beijing/China.

NUMERICAL SIMULATION OF SEED DISTRIBUTION OF
A PNEUMATIC SEED METER
/
SIMULAREA NUMERICĂ A PROCESULUI DE LUCRU AL
UNUI DISTRIBUITOR PNEUMATIC

Dan CUJBESCU, Iuliana GĂGEANU *), Cătălin PERSU, Gabriel GHEORGHE
INMA Bucharest / Romania
E-mail: iulia.gageanu@gmail.com
DOI: https://doi.org/10.35633/inmateh-66-04

ABSTRACT
Studies and research carried out on seed meters of precision planters whose operating principle is based on the depression / suction of the air created during the work by the exhauster (vacuum generator) in the vacuum chamber have the role of helping to improve their performance. With the advancement of sowing technology, the emphasis on the ability of seed meters to accurately and consistently distribute seeds in the soil increases. The singularization of the seeds by means of the seed meters and their distance along the channels opened by the coulter is essential to ensure the achievement of the maximum yield of the crop sown on a certain area of land. The paper presents the numerical simulation of the working process for a pneumatic seed meter by means of a mathematical model, analysing the movement of the seeds according to the angle of detachment, the height of detachment of the seed, as well as the speed of the seed in its trajectory towards the channel opened by the coulter.

REZUMAT
Studiile şi cercetările efectuate pe distribuitoarele semănătorilor de precizie al căror principiu de funcţionare are la bază depresiunea/aspiraţia aerului creată în timpul lucrului de către exhaustor în camera vacuumatică au rolul de a ajuta la îmbunătăţirea performanţelor acestora. Odată cu avansarea tehnologiei de semănat, accentul pus pe capacitatea aparatelor de distribuţie a seminţelor de a distribui cu precizie și în mod consecvent seminţele în sol, creşte. Singularizarea seminţelor prin intermediul aparatelor de distribuţie şi distanţarea acestora de-a lungul şanţurilor deschise de brăzdare este esenţială pentru a asigura obţinerea producţiei maxime a culturii semănate pe o anumită suprafaţă de teren. În lucrare este prezentată simularea numerică a procesului de lucru pentru un distribuitor pneumatic prin intermediul unui model matematic, analizându-se deplasarea seminţelor în funcţie de unghiul de desprindere, înălţimea de desprindere a seminţei, precum şi de viteza seminţei în traiectoria sa spre şanţul deschis de brăzdar.

INTRODUCTION

Precision sowing is a phenomenon in which two processes must be carried out, the objective being the precise placement of seeds in a row at the distance required by the agrotechnical norms. The first process consists in aspirating the seeds in the orifices of the distributor disc, without them doubling or missing from the orifices in the disc, the second process consisting in releasing the seeds from the orifices of the distribution disc and incorporating them into the soil (*Han et al., 2020; Staggenborg et al., 2004; Yazgi et al, 2010*).

Engineering calculation is the scientific tool used for the design, development and verification of technical systems. Mathematical modelling was developed through the means of experimental research performed on real models or laboratory models, the aim being to verify the analytical calculation, as well as to confirm the hypotheses and calculation models used (*Marin C., 2009*). The engineering language represented by mathematical modelling aims to describe the different aspects of the real world, their interaction and dynamics. It can be said, therefore, that mathematical modelling and scientific calculus are gradually and steadily expanding into various fields, becoming a unique tool for qualitative and quantitative analysis (*Biriş et al., 2018; Gupta et al., 2020; Quarteroni and Valli, 1999*).

In the analysis of the sowing process, improving the performance of seed meters is a constant concern for researchers in mechanical engineering and beyond. (*Kornienko et al., 2016, Zubrilina et al., 2019*). By uniformly spacing the sown seeds, the roots of future plants can reach uniform sizes that will fill the spaces on the sown rows without the risk of being pushed outside of the row of adjacent roots (*Li et al., 2013*, *Marin et al., 2014*). Precision planters are designed to place the seeds evenly, on the row, if properly operated and adjusted. The quality of the sowing work conducted using precision equipment is constantly analysed during the operation, in order to be able to quickly remove any deficiencies, because after sowing it is no longer possible to intervene (*Miller et al., 2012*; *Soyoye, 2020*).

The lateral distribution of seeds is registered perpendicular to the working direction of the precision planter, this being influenced by the mass of the seeds reaching each coulter of the row unit. In contrast, the basis for the longitudinal distribution of seeds is constituted by the distances between seeds in a row. Therefore, it will be recorded in the working direction of the precision planter (*Heege, 1985*).

In general, the lateral distribution does not constitute a problem, its coefficient of variation being less than 4%. Exceptions may occur for planters with pneumatic seed meters, when sowing on a sloping ground, the sowing norm for row units at the bottom of the slope being higher than for those at the top of the slope. This effect depends not only on the slope, but also on the speed of the air, as well as the size of the seeds. The effect of the slope on sowing accuracy decreases when air speed increases and when the seeds are smaller (*Heege, 1975*).

Precision sowing seeds are generally dredged to facilitate handling, singularization, precise placement and incorporation of beneficial chemicals, being larger, more rounded, finer, heavier and more uniform than unedged ones (*Kaufman, 1991, Sauder and Schaefer, 2016*).

Usually, several sets of distribution discs are used in precision planters, each with orifices adapted to the size of the seed to be planted. There are several factors that contribute to maintaining the distance between seeds sown on a row. In the design process, it is assumed that the distance between the seeds will probably be uniform, but the uniformity may differ depending on the degree of tillage, the sowing characteristics, but the most important are the physical properties of the seeds (*Srivastava, 1993*).

The spacing of the seeds in the channel is controlled by varying the rotational speed of the distribution disc. Most often, the drive of the seed distribution discs is done by means of a common drive shaft. The drive shaft transmits the movement of each row unit of the planter, being driven by a single electric motor or a wheel in contact with the ground. In this configuration, the sowing norm can be adjusted for all rows of the row units by adjusting the rotational speed of the common drive shaft. In general, an optimal sowing rate for a certain area is selected before the sowing work is conducted and maintained at that rate, regardless of the soil conditions.

In the paper, a mathematical model was developed for the distribution process of a pneumatic seed meter for weeding plants, provided with a vertical distribution disc with orifices, and then the simulation of the distribution process was performed according to the detachment angle which was varied between 0-90°, taking into account three values of the seed height of detachment (0.10-0.20 m), and the speed of the seed in its trajectory towards the channel opened by the coulter had values between 0.5-4.44 m/s.

MATERIAL AND METHODS

The working process of the pneumatic seed meter is as follows: the vertical distribution disc (with orifices) is driven by means of a chain transmission from a drive wheel of the seed drill, the depression in the working chamber of the seed meter being achieved through the suction pipe (vacuum socket). The row unit is supported on the ground on the compaction wheel and on the coulter.

Each orifice on the distribution disc drives a seed, as a result of the depression that is created near the orifice. The evacuation of the seeds from the seed meter is done under the action of their own weight, when the orifices of the distribution disc (to which the seeds have adhered) are no longer in the area where the depression is created.

The development of the mathematical model for the distribution process of the pneumatic seed meter for weeding plants has a key role for a deeper understanding of the phenomena at the basis of this process.

Considering a sequence of the seed distribution phenomenon (Fig. 1), the seed detached from the orifice of the distribution disc, after passing the depression chamber, in its trajectory towards the channel opened by the coulter, has a horizontal movement Δ_x relative to the point of detachment, analysis based on the xOy reference system.
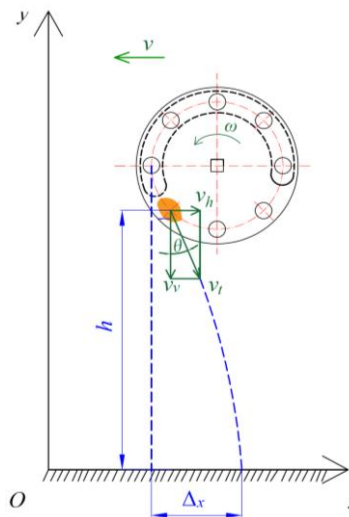
Fig. 1 - Schematic diagram of the distribution kinematics

V_h − the horizontal component of seed speed in its trajectory toward the open channel; V_v − *the vertical component of seed speed in its trajectory toward the open channel;* V_t − *seed speed in its trajectory towards the open channel before colliding with the soil;* θ − the angle of seed detachment relative to the vertical; ω − angular speed of the distribution disc

The components of the seed's speed in its trajectory towards the channel opened by the coulter will be:

$$v_h = v_t \cdot \sin\theta \tag{1}$$

$$v_v = v_t \cdot \cos\theta \tag{2}$$

$$v_t = v \cdot i_{tr} \cdot \frac{R_{dd}}{R_{rs}} \tag{3}$$

where:

i_{tr} – gear ratio, [-];

R_{dd} – distribution disc pinion radius, [mm];

R_{rs} − the radius of the pinion of the seed drill support wheel, [mm].

The equations of movement of the seed having the speed v_t will be:

$$\Delta_x = v_t \cdot t_i \cdot \sin\theta \tag{4}$$

$$h = v_t \cdot t_i \cdot \cos\theta + g \cdot \frac{t_i^2}{2} \tag{5}$$

where:

t_i – time for the seed to fall into the channel opened by the coulter, [s];

g - gravitational acceleration, [m/s^2].

From formula (4) results:

$$t_i = \frac{\Delta_x}{v_t \cdot \sin\theta} \tag{6}$$

From formulae (4) and (5) results:

$$h = \frac{\Delta_x}{tg\theta} + g \cdot \frac{\Delta_x^2}{2 \cdot v_t^2 \sin^2\theta} \tag{7}$$

Formula (7) becomes:

$$\frac{g}{2 \cdot v_t^2 \sin^2\theta} \cdot \Delta_x^2 + \frac{1}{tg\theta} \cdot \Delta_x - h = 0 \tag{8}$$

Solving formula (8) we obtain:

$$\Delta_{x_{1,2}} = \frac{-\dfrac{1}{tg\theta} \pm \sqrt{\dfrac{1}{tg^2\theta} + \dfrac{2 \cdot g \cdot h}{v_t^2 \cdot \sin^2\theta}}}{\dfrac{g}{v_t^2 \cdot \sin^2\theta}} \tag{9}$$

The negative solution is adopted so that the horizontal movement of the seed is in the opposite direction to the movement of the tractor-seed drill aggregate, so that the relative speed of the horizontal component of the seed relative to the ground tends towards zero.

Therefore:

$$\Delta_x = \frac{-\dfrac{1}{tg\theta} - \sqrt{\dfrac{1}{tg^2\theta} + \dfrac{2 \cdot g \cdot h}{v_t^2 \cdot \sin^2\theta}}}{\dfrac{g}{v_t^2 \cdot \sin^2\theta}} \tag{10}$$

It is observed that Δ_x is a function dependent on the angle of detachment, the seed detachment height, as well as the seed speed in its trajectory towards the channel opened by the coulter.

RESULTS

The solving of the mathematical model is done by giving successive values to the influencing factors responsible for its operation.

The mathematical model presented in relation (10) in the form of a computer processable program was used for the analysis of multiple versions of entry data sets.

The numerical simulation for the evolution of the value of movement depending on the influence factors θ, v_t and h is achieved using Excel program.

Table 1 presents the evolution of seed movement depending on the angle of detachment, replacing in equation (10) the height of seed detachment h=0.1 m and the speed of the seed in its trajectory towards the channel opened by the coulter v_t=0.55 – 4.44 m/s.

Table 1

Seed movement Δ_x depending on the angle of detachment θ for h=0.1 m and v_t =0.55 – 4.44 m/s

Angle θ [º]	Angle θ [rad]	h [m]	Movement Δ_x [m]							
			v_t=0.55 [m/s]	v_t=1.11 [m/s]	v_t=1.66 [m/s]	v_t=2.22 [m/s]	v_t=2.77 [m/s]	v_t=3.33 [m/s]	v_t=3.88 [m/s]	v_t=4.44 [m/s]
0	0		0	0	0	0	0	0	0	0
10	0.174		0.009	0.013	0.015	0.016	0.016	0.016	0.017	0.017
20	0.349		0.018	0.027	0.031	0.033	0.034	0.034	0.035	0.035
30	0.523		0.028	0.041	0.048	0.051	0.053	0.054	0.055	0.055
40	0.698	0.1	0.037	0.057	0.067	0.073	0.076	0.078	0.079	0.080
50	0.872		0.047	0.074	0.090	0.099	0.104	0.108	0.111	0.112
60	1.047		0.056	0.093	0.117	0.132	0.143	0.150	0.155	0.158
70	1.221		0.065	0.114	0.150	0.177	0.197	0.212	0.224	0.232
80	1.396		0.072	0.136	0.190	0.238	0.278	0.313	0.343	0.369
90	1.570		0.079	0.158	0.238	0.317	0.396	0.476	0.555	0.634

Figure 2 shows the dependency of seed movement on the horizontal depending on the angle of detachment and the seed's speed in its trajectory towards the channel opened by the coulter for h=0.1 m.
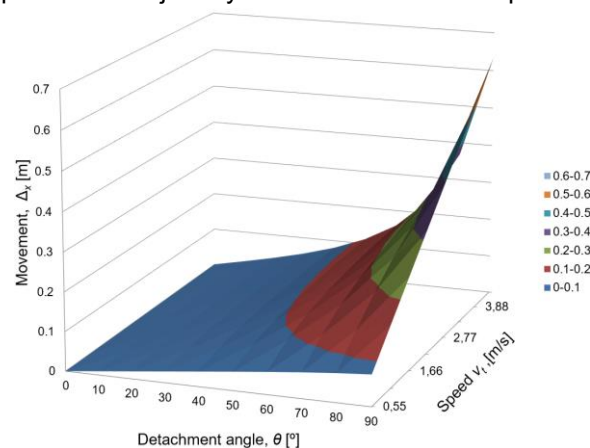
Fig. 2 - Dependence of the horizontal movement of the seed depending on the angle of detachment and on the speed of the seed in its trajectory towards the open channel for h=0.1 m

Table 2 presents the evolution of seed movement depending on the angle of detachment for the height of seed detachment h=0.15 m and the speed of the seed in its trajectory towards the channel opened by the coulter v_t=0.55 – 4.44 m/s.

Table 2

Seed movement Δ_x depending on the angle of detachment θ for h=0.15 m and v_t=0.55 – 4.44 m/s

Angle θ [º]	Angle θ [rad]	h [m]	Movement Δ_x [m]							
			v_t=0.55 [m/s]	v_t=1.11 [m/s]	v_t=1.66 [m/s]	v_t=2.22 [m/s]	v_t=2.77 [m/s]	v_t=3.33 [m/s]	v_t=3.88 [m/s]	v_t=4.44 [m/s]
0	0		0	0	0	0	0	0	0	0
10	0.174		0.012	0.018	0.021	0.023	0.024	0.024	0.025	0.026
20	0.349		0.024	0.037	0.043	0.047	0.049	0.051	0.051	0.052
30	0.523		0.036	0.056	0.067	0.074	0.077	0.080	0.081	0.082
40	0.698	0.15	0.048	0.077	0.094	0.104	0.110	0.114	0.116	0.118
50	0.872		0.060	0.099	0.123	0.139	0.149	0.156	0.161	0.165
60	1.047		0.071	0.122	0.158	0.183	0.200	0.213	0.222	0.229
70	1.221		0.081	0.146	0.197	0.237	0.269	0.293	0.313	0.328
80	1.396		0.090	0.171	0.242	0.306	0.362	0.412	0.456	0.495
90	1.570		0.097	0.194	0.291	0.388	0.486	0.583	0.680	0.777

Figure 3 shows the dependency of seed movement on the horizontal depending on the angle of detachment and the seed's speed in its trajectory towards the channel opened by the coulter for h=0.15 m.
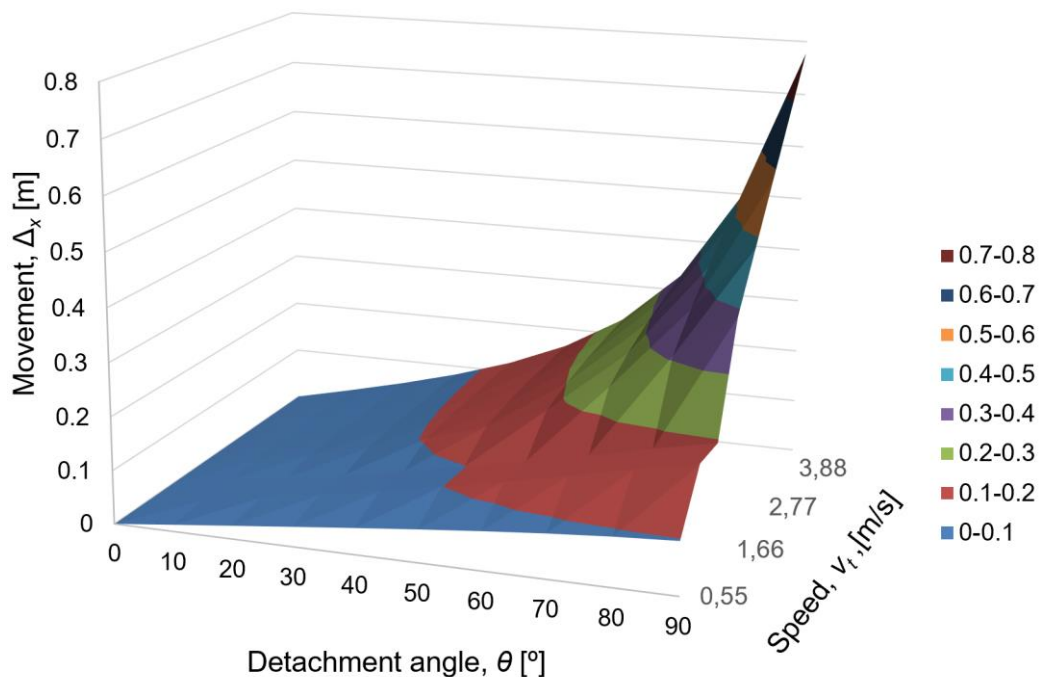
Fig. 3 - Dependence of the horizontal movement of the seed depending on the angle of detachment and on the speed of the seed in its trajectory towards the open channel for h=0.15 m

Table 3 presents the evolution of seed movement depending on the angle of detachment for the height of seed detachment h=0.2 m and the speed of the seed in its trajectory towards the channel opened by the coulter v_t=0.55 – 4.44 m/s.

Table 3

Seed movement Δ_x depending on the angle of detachment θ for h=0.2 m and v_t=0.55 – 4.44 m/s

Angle θ [º]	Angle θ [rad]	h [m]	Movement Δ_x [m]							
			v_t=0.55 [m/s]	v_t=1.11 [m/s]	v_t=1.66 [m/s]	v_t=2.22 [m/s]	v_t=2.77 [m/s]	v_t=3.33 [m/s]	v_t=3.88 [m/s]	v_t=4.44 [m/s]
0	0		0	0	0	0	0	0	0	0
10	0.174		0.014	0.022	0.027	0.030	0.031	0.032	0.033	0.033
20	0.349		0.029	0.046	0.055	0.061	0.064	0.066	0.068	0.069
30	0.523		0.044	0.070	0.085	0.094	0.100	0.104	0.106	0.108
40	0.698	0.2	0.058	0.095	0.117	0.132	0.141	0.148	0.152	0.155
50	0.872		0.071	0.120	0.153	0.175	0.191	0.201	0.209	0.215
60	1.047		0.084	0.147	0.193	0.227	0.252	0.271	0.285	0.296
70	1.221		0.095	0.174	0.238	0.289	0.331	0.365	0.393	0.415
80	1.396		0.105	0.200	0.286	0.364	0.434	0.497	0.553	0.604
90	1.570		0.112	0.224	0.336	0.448	0.561	0.673	0.785	0.897

Figure 4 shows the dependency of seed movement on the horizontal depending on the angle of detachment and the seed's speed in its trajectory towards the channel opened by the coulter for h=0.2 m.
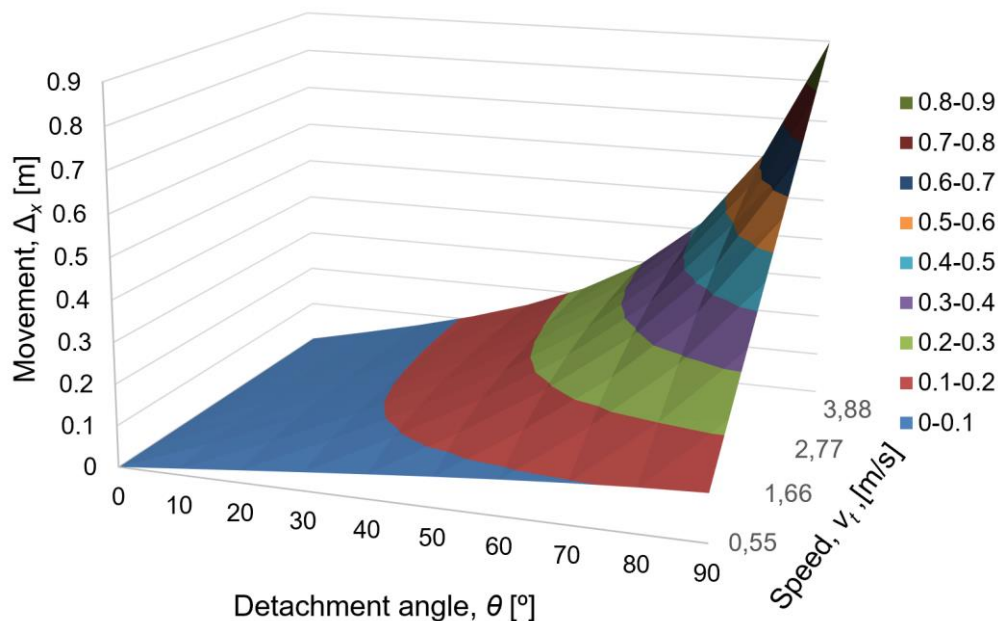
Fig. 4 - Dependence of the horizontal movement of the seed depending on the angle of detachment and on the speed of the seed in its trajectory towards the open channel for h=0.2 m

The numerical simulation program of the distribution process offers the possibility to study it with the help of the mathematical model using the method of modification produced by each disturbing factor, as well as by the method of modifications produced by all disturbing factors.

CONCLUSIONS

From a mathematical point of view, certain constructive requirements must be met to obtain a calculated production on a given area of land, thus, there should be a certain distance between the row units of the planter and between the seeds sown on each row (rows of seeds) the distance should be constant to achieve the norms/densities specific to each crop.

Taking into account these specifications, it can be concluded that:

- a method of studying the phenomena underlying the distribution process is the development of a mathematical model of distribution;

- the achieved mathematical model regards kinematically the seed distribution process, taking into consideration the kinematic factors that interfere in its disturbance;

- the studied factors influencing the distribution process were: the speed of the seed in its trajectory towards the channel opened by the coulter; the height of seed detachment relative to the ground; the angle of seed detachment.

- the numerical simulation results of the mathematical model show an obvious tendency of increase for the horizontal movement of the seeds with the increase of the angle of detachment and also with the increase of the detachment speed;

- by varying the seed detachment height (similar to the sowing on uneven ground) between 0.1 m and 0.2 m, it is noted that the horizontal movement of the seeds increases as the height increases. This increase is observed for all seed detachment speeds;

- for minimum values of the detachment speed, the horizontal seed movement is minimal (0.009 m for a detachment speed of 0.55 m / s, and a seed detachment height of 0.10 m);

- increasing the speed of detachment leads to an increase of horizontal seed movement (0.897 m for a detachment speed of 4.44 m / s, at a seed height detachment of 0.20 m);

- the increase of the angle of detachment leads to an increase in the horizontal movement of the seeds resulting in a decrease of the sowing precision (0.897 m for a 90° detachment angle, for a seed separation height of 0.20 m);

- around the value of 60° of the seed detachment angle, there is a high increase in the horizontal movement of the seeds, a common aspect for all the detachment heights;

- the mathematical model for estimating the real interval between two consecutive seeds includes kinematic factors that interfere with its disruption, as well as the geometry of some constructive elements of the mechanical system used to conduct the sowing work;

- the soil profile and the geometry of some constructive elements of the row unit used have a role in estimating the rotational effect on the row unit and implicitly the effect on the seed detachment angle.

REFERENCES

[1] Gupta, M., Abdelsalam, M., Khorsandroo S., Mittal, S., (2020), Security and Privacy in Smart Farming: Challenges and Opportunities, *IEEE Access*, vol. 8, pp. 34564-34584, doi: 10.1109/ACCESS.2020.2975142;

[2] Han T., Changsu X., Wang Z., Wang Q., Wang J., (2020), Optimized Design, Monitoring System Development and Experiment for a Long-Belt Finger-Clip Precision Corn Seed Metering Device, *Frontiers in Plant Science,* DOI=10.3389/fpls.2022.814747;

[3] Heege H. J., (1975), Zaehres W. Pneumatic seed distribution with bulk drilling, *Grundlagen der Landtechnik*: Dusseldorf 25(4), pp. 111–115;

[4] Biriş, S. Şt; Ungureanu, N.; Vlăduţ, V. (2016), Study on the influence of mechanical vibrations to the energy required for soil tillage, *5th International Conference on Thermal Equipment, Renewable Energy and Rural Development*, TE-RE-RD, ISSN 2359-7941, pp. 203-208;

[5] Heege H. J., (1985), Seed distribution over the soil surface with drilled and broadcast cereals, *Translation No. 529 of the National Institute of Agricultural Engineering*, Wrest Park, Silsoe: England;

[6] Kaufman G., (1991), Seed coating: A Tool for Stand Establishment; a Stimulus to Seed Quality, *HortTechnology*, (1), pp. 98–102, 1991;

[7] Kornienko S., Pashenko V., Melnik V., Kharchenko S., Khramov N., (2016), Developing the method of constructing mathematical models of soil condition under the action of a wedge, *Eastern-European Journal of Enterprise Technologies*, Vol. 5, Issue 7, pp. 34–43;

[8]   Li D., Geng D., Ma B., Li Q., Wang Zh., (2013), Study on Performance Monitoring System of Corn Precision Seeder, *Journal of Agricultural Mechanization Research*, Vol 11, pp.71–74;

[9]   Marin C., (2009), *Modern methods of analysis of mechanical structures (Metode moderne de analiză a structurilor mecanice)*, Valahia University of Târgoviște Faculty of Materials Engineering, Mechatronics and Robotics, Master's course;

[10]   Marin E., Bolintineanu Gh., Sorică C., Manea D., Herak D., Croitoru Ş., Grigore I., (2014), Scientific researches on the qualitative working indexes of the sowing body of a modern technical hoeing plants sowing equipment, *INMATEH - Agricultural Engineering*, Vol. 42 (1), pp. 19–26;

[11]   Miller E. A., Rascon J., Koller A., Porter W. M., Taylor R. K., Raun W. R., Kochenower R., (2012), Evaluation of Corn Seed Vacuum Metering Systems, *ASABE Annual International Meeting*, Dallas, Texas, July 29 – August 1, Paper Number: 12–1337167;

[12]   Sauder D. A., Schaefer T., (2016), *Seed meter*, Patent No. US 2016/0128272 Al;

[13]   Soyoye, B., (2020), Development of the Instrumentation Unit of a Motorized Precision Planter, *European Journal of Engineering and Technology*, Research 5, (4), pp. 403-407, doi.org/10.24018/ejers.2020.5.4.1815;

[14]   Srivastava A. K., Goering C. E., Rohrbach R. P., (1993), Engineering Principles of Agricultural Machines. *American Society of Agricultural Engineers: ASAE*, St. Joseph-Michigan;

[15]   Staggenborg S. A., Taylor R. K., Maddux L. D., (2004), Effect of planter speed and seed firmers on corn stand establishment, *Appl. Eng. in Agric*, 20(5), pp. 573–580;

[16]   Stout B. A., Cheze B., (1999), *CIGR Handbook of Agricultural Engineering*, Volume III Plant Production Engineering, Published by the American Society of Agricultural Engineers;

[17]   Quarteroni A., Valli A., (1999), *Domain Decomposition Methods for Partial Differential Equations*, Oxford University Press, Oxford;

[18]   Zubrilina, E.; Markvo, I.; Novikov, V.; Beskopylny, A.; Vysochkina, L.; Rudoy, D.; Butovchenko, A., (2019), Precise seeding planter with automated monitoring and control system, *IOP Conf. Ser.: Earth Environ*. Sci. 403 012063, pp. 1-10;

[19]   Yazgi A., Degirmencioglu A., Bayram E., (2010), Optimisation of the Seed Spacing Uniformity Performance of a Precision Seeder Using Spherical Materials and Response Surface Methodology, *An ASABE Meeting Presentation*, Paper Number: 1008560; DOI: 10.13031/2013.29653.

SIMULATIONS AND EXPERIMENTS OF THE SEEDBED STRAW AND SOIL DISTURBANCE AS AFFECTED BY THE STRIP-TILLAGE OF ROWCLEANER (DEM)
/
带状耕作对种床秸秆清除率和土壤扰动的仿真与试验

Weiwei WANG, Jiale SONG, Guoan ZHOU, Beituo PAN, Qingqing WANG, Liqing CHEN *)

1) College of Engineering, Anhui Agricultural University, Hefei 230036, China
2) Laboratory of Engineering of Agricultural Machinery Equipment of Anhui Province, Hefei 230036, China

Keywords: *biomimetic; vertical rotary tillage; row clean; anti-blocking*

ABSTRACT

Strip-tillage is an effective option for proper seedbed preparation because it ensures the suitable conditions for seed germination and has been widely implemented. This study developed a strip-tillage of corn planter row cleaner using bionic vertical rotary blades to remove seedbed straw and ideal soil for no tillage sowing can be created. Through the qualitative analysis of the serrated arrangement contour of the praying mantis foreleg tip, the characteristic curve of the praying mantis foreleg tip was extracted and fitted, and the bionic geometric structure surface of the vertical rotary blade was constructed. The model and interaction system were established in EDEM 2.6 simulation environment, and their physical properties were calibrated with the real properties of lime concretion black soil and wheat straw. According to theoretical design to set simulation parameters, the radius of the cutter head was set to 120 mm, the driving speed of the cutter shaft was set to 500 r/min, and the depth of the cutting edge was set to 10 mm, the operating velocity of the active anti-blocking device was set to 5 km/h. The experiment results show that when the moving speed ratio is increased from 2.8 to 4.5, compared with the traditional vertical rotary blades, the straw removal rate and soil uniformity of seed bed are increased by 6.4% and 9.3%, and the average torque of the rotary tiller has been reduced by 12.3% respectively, the process effect and sowing quality being effectively improved. The study can provide theoretical reference for realization of no-tillage sowing vertical rotary tillage blade to reduce resistance and consumption and improve the quality.

摘要

带状耕作是可以为种子发芽提供良好环境的一种途径，已经被广泛应用。本文设计了一种基于螳螂趾多段锯齿状结构的立式仿生清茬防堵装置。通过对螳螂前肢尖锯齿状排列轮廓进行了定性分析，提取并拟合出螳螂前肢尖特征曲线，构建了立式旋耕刀的仿生几何结构曲面。运用 EDEM 软件构建无支撑秸秆全覆盖土壤离散元模型，在秸秆-土壤-仿生立式清茬防堵装置系统中进行秸秆移位虚拟仿真，设了仿生立式清茬防堵装置的刀轴驱动转速为 500r/min、回转半径为 150 mm 及刀齿入土深度为 10mm，利用仿真数据对秸秆扰动位移、清茬率进行分析，检验仿生立式清茬防堵装置结构参数和运动参数设计的合理性，试验结果表明，当移动速度比由 2.8 提高到 4.5 时，与传统的立式旋耕刀相比，秸秆清理率和种床土壤均匀度分别提高了 6.4%和 9.3%，旋耕机的平均扭矩降低了 12.3%。本文的研究结果为实现免耕播种立式清茬防堵装置减少阻力和消耗，提高种床耕作质量提供了理论参考。

INTRODUCTION

No-till (less-till, direct-seeding) sowing is a kind of protective farming technical operation, which has the advantages of maintaining soil moisture and saving labor and cost than traditional farming *(Sale et al., 2015; Li et al., 2019)*. However, the return of large quantities of crop residues to farmland also exposes disadvantages, as other equipment components can block and interfere with the process flow. Many studies have shown that crop residues thrown on the soil surface represent one of the main sources of interference in ensuring the process of strip-tillage and direct drilling *(Dikgwatlhe et al., 2014; Li et al., 2016)*. Therefore, it is urgent to research on a new type strip-tillage technology, which includes the advantage of full rotary-tillage seeding inasmuch as narrow soil strips can be removed residue and tilled rather deeply, having sown seeds and fertilizers into the strips cleaning area of tilled soil, subsequent seeds can grow under optimal condition similar to those of the fully rotary tillage. Moreover, strip-tillage combines the advantage of direct drilling, which facilitates the reduction of soil degradation processes and nutrient leaching, increases soil biological activity,

improves composition, conserves water, etc. *(Licht et al. 2010; Bilen et al., 2010; Jia et al., 2019)*. Therefore, to achieve the balance between soil conservation and organic matter content, it is necessary to take appropriate straw returning management measures, improve soil fertility and promote sustainable grain production.

Row cleaner is a very important working part of no-tillage planter. It can ensure that all crop residues are removed from the soil strip, and do not mix the plant seeds into these residues, which prevent the good interaction between the seeds and soil, which has an adverse impact on seed germination *(Fallahi et al., 2008; Laufer et al., 2017)*. Compared with the soil part without seed metering device in direct drilling, the removal of crop residues from the soil part incorporated by plant seeds can improve the emergence rate and yield. In addition, removing crop residues from seed rows facilitates reducing the incidence of disease *(He et al., 2007)*. Many experts point out that the quantity of the previous crop left on the soil surface after harvest determines the operation quality of the no-till planter. The working quality of no-tillage planter is improved by adjusting the driving speed and working depth *(Celik et al., 2016; Vaitauskiene et al., 2017)*.

Wang et al, (2017), found that the traditional vertical rotary blade was used for cleaning the plant residues in the strip cultivation. Based on previous research, this paper combines the working principle of the no-tillage planter's straw removal, anti-blocking mechanism with the mantis toe characteristic and efficient cutting principle to design a bionic device that can realize the dual-cutter counter-rotating straw removal operation. Theory Analysis, test verification and other methods are used to clarify the influence of the operating parameters of the mechanism on the stubble removal and cutting performance so as to provide theoretical and technical support for the design of high-performance straw removal and anti-blocking devices.

MATERIALS AND METHODS
Structure and working principle

2BYQD-4A type active anti-blocking type corn no-tillage pneumatic planter is mainly composed of frame, suspension mechanism, row cleaners, layered fertilization device, wind pressure system, sowing device, ditching device, soil covering, pressing device and others, as shown in Fig.1. The technical parameters of corn no-tillage pneumatic planter are shown in Table 1.
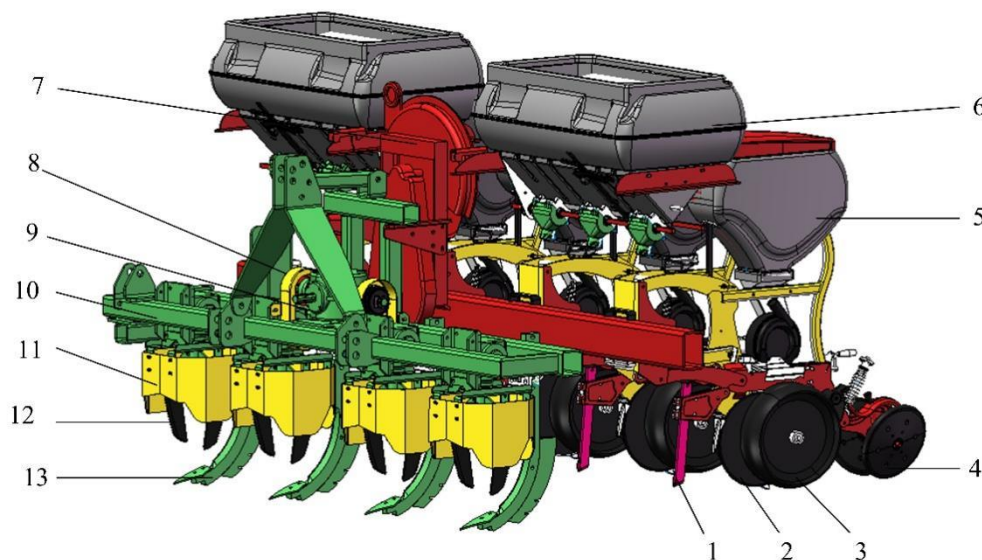
Fig. 1 - Physical drawing of no-tillage air suction planter for corn
1- Opening share；2- Double disc trencher; 3- Earth covering device; 4- Depth limiting device; 5- Seed metering system;
6- Fertilizer discharge system; 7- Air pressure system; 8- Transmission case; 9- Chain power conveyor; 10- Frame;
11- Straw separator; 12- Row cleaner; 13- Layered fertilization subsoiler

Table 1

Main technical parameters of integration machine

Indexes	Parameters
Overall dimension (L×W×H) / (mm)	1960×2830×1620
Overall quality / kg	1000
Operation width / mm	1600-2800

Auxiliary power / kw	51.45-66.15
Speed of straw cleaner / (r/min)	450-600
Number of row cleaner	4
Straw cleaning radius / mm	15
Number of rows sown	4
Row spacing / mm	60
Sowing depth / mm	5-10
Depth of fertilization / mm	5-30
Theoretical plant spacing / mm	20-30
Operation speed / (m/s)	4-7

In this paper, the strip-tillage of row cleaner will be the research focus, which is mainly composed of double L-shaped rotary blades, rotary discs and bearings, which are vertically driven by the gearbox and commutator. The total length of the edge line of L-shaped rotary tiller is 200 mm and the length of soil cutting edge is 30mm, the radius of rotation is 150 mm, and the width of cutter head is 216 mm. According to the agronomic requirements of summer corn sowing, the sowing row spacing and depth were 400~600 mm and 30~50 mm, respectively. The lateral application of deep base fertilizer was generally applied to the sowing side 40~60 mm. The strip width of row cleaner was 240 mm, which was greater than the horizontal distance of the seed-fertilizer openers.

Feature extraction of mantis foot tooth contour curve

Many experts have carried out bionics research based on the peculiar physiological parts of animals (mole, locust, cricket, mole cricket), and designed a series of straw cutting parts and soil breaking parts of agricultural machinery with reference to the variable curvature contour characteristics of their toes, which effectively improves the straw breaking rate and reduces the cutting resistance *(Jia et al., 2018; Wang et al., 2019; Guo et al., 2017)*. As shown in Fig. 2, the leg and tibia of the mantis's forefoot are covered with hard and sharp serrations, which makes it have excellent predation ability. The unique physiological structure provides a reference for the design of soil crushing and straw breaking parts of agricultural machinery.

Fig. 2 - Tooth-shaped structure of mantis toes

Using MATLAB software in the rgb2gray, imerode, imdilate, im2bw, imfill, edge, bwperim function command in turn of the mantis front section photos on gray treatment, corrosion and expansion processing, binarization processing, hole filling, extract the boundary curves, the last frame expansion method is used to analyze the boundary curve connection, toes silhouette reconstructing CAD model, image after image processing using MATLAB software; the reconstructed model structure is clear, complete with the original sawtooth curves is shown in Fig. 3.

Original image of a Mantis toe → Im2bm → Imfill、edge → Get the toe outline CAD model
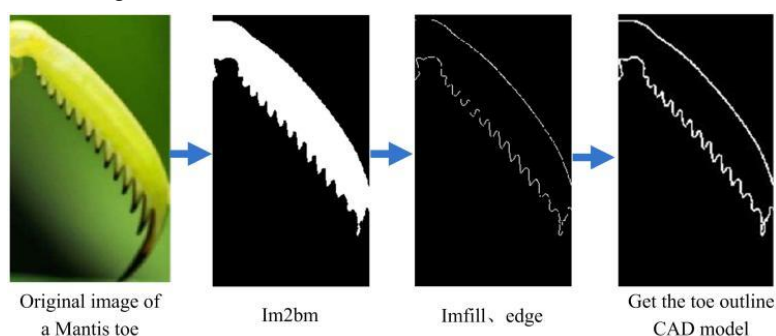
Fig. 3 - Extraction process of mantis toe curve

Extract the X and Y coordinates of the mantis toe model in the two-dimensional coordinate system, and fit a smooth serrated "edge" curve according to the coordinates of each point, as shown in Fig. 4. Due to the small cutting angle in the circle of the main cutting edge of the traditional vertical rotary tillage blade, the secondary cutting of soil and straw is formed when the rotary main cutting edge moves to the radian range [π, 2π], resulting in large resistance and increased vibration amplitude. However, too large internal cutting angle requires large blade width, which makes it difficult to balance the lateral force on the cutter head. At the same time, the straw is unsupported and irregularly sorted in the field, which will increase the difficulty of removing straw. The rotary operation process of the vertical rotary tillage knife should reduce the contact slip rate between the cutting edge and the straw layer to achieve rotary cutting and separation of straw, therefore the bionic vertical rotary tillage knife designed in this paper consists of a stubble breaking device, the increased serrations will make the longitudinal and horizontal straw not easy to slip from the cutting edge of the serrated blade, and at the same time increase the slip cutting effect between the blade and the straw, which can complete the rotary cutting of straw and separation of straw . The sawtooth "cutting edge" curve was applied to the cutting edge of the vertical clear straw blade, and the particularity of the "cutting edge" curve of the mantis toes arrangement provided a basis for the cutting efficiency.
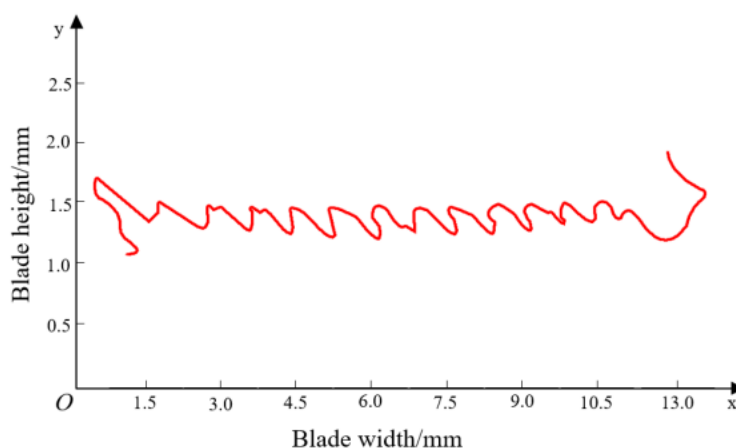
Fig. 4 - Sawtooth contour extraction and curve fitting

According to the fitted "cutting edge" curve and the idea of sawtooth for woodworking, the sharp "cutting edge" at the front end of tibia is selected as the sawtooth design model. The width of saw tooth is 1 ~ 1.5mm, the depth of saw tooth is 4.2mm, and the width of saw tooth bottom is 3.5 mm, because the sawtooth width and depth are too large in the actual operation process, it is easy to wind the straw, and too small causing severe wear and tear. The parameters of the bionic vertical rotary tillage blade were determined by repeated tests combined with the structural characteristics of the actual straw, as shown in Table 2. Its physical object is shown in Fig. 5.

Table 2

Mantis toes structure position

Name	*X*-axis coordinate position	*Y*-axis coordinate position
Convex starting point of first toe	2.78	1.46
Bottom of first toe	3.64	1.22
Convex starting point of second toe	3.75	1.42
Bottom of second toe	4.48	1.21
Convex starting point of third toe	4.45	1.42
Bottom of third toe	4.71	1.18
Convex starting point of fourth toe	5.25	1.45
Bottom of fourth toe	6.12	1.16
Convex starting point of fifth toe	6.14	1.43
Bottom of fifth toe	6.32	1.21

Fig. 5 - Sawtooth contour extraction and curve fitting

Movement analysis of bionic straw cutting device

Two bionic vertical rotary blades are installed and fixed on the cutter head in a dual way to form a straw breaking device. The center point O of the axis of the device makes a circular motion, and a fixed coordinate system is established with the rotation center of the straw breaking device as the origin. The positive direction of the X axis is consistent with the forward direction of the working planter, and the positive direction of the Y axis is vertical downward. Then, the trajectory equation of any point of the bionic straw breaking device is:

$$\begin{cases} x = R\cos\omega t + v_m t = R(\cos\alpha + \alpha/\lambda) \\ y = R\sin\omega t = R\sin\alpha \end{cases} \tag{1}$$

Where:

x and y are the position coordinates of the L-shaped blades at any point;

ω is the rotating angular velocity of the row cleaner;

φ is the rotation angle of the L-shaped blades;

v_d is the circumferential tangential velocity of point A;

v_m is operational speed of the planter forward direction;

λ is rotary tillage speed ratio, $\lambda = v_d/v_m$.
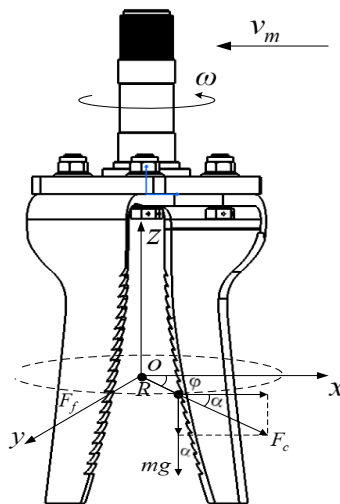
Fig. 6 - Cutting straw unit with the bionic rotary tillage blades

The movement track of the vertical rotary tillage blades is a trochoid, forcing the straw layer to circular flow in a strip. It was assumed that the flowing straw layer instantaneously subjected to the sliding cutting force *(Zhang et al., 2017)*. The flowing straw particles were thrown along the tangent direction at the linear velocity, when the sliding cutting force disappears. In order to obtain the critical condition that the straw-flow was thrown away from the row in the tangent direction of the blade trajectory, it was necessary to ensure that the tangent

direction component of rotary centrifugal force Fc was greater than the straw-flow unit by the soil layer rolling friction force. The force analysis of cutting straw layer trajectory was shown in Fig. 6. The rolling frictional force on the flowing straw particles was expressed as follows:

$$F_f = fmg + \frac{fmv_d^2 \sin \alpha}{R} \tag{2}$$

The condition under which the flowing straw layer can be centrifugally thrown to both sides of the seedbed is calculated using Eq. (3).

$$\frac{mv_d^2 \cos \alpha}{R} \geq fmg + \frac{fmv_d^2 \sin \alpha}{R} \tag{3}$$

Where:

m is the mass of flowing straw layer, [kg];

f is the friction coefficient between straw layer and soil layer;

α is slide-cutting angle of the straight blades.
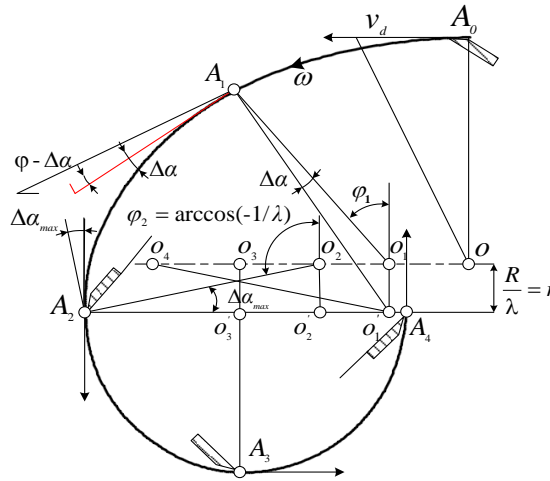
Fig. 7 - The moving trail of cutting edge at rotary tillage speed

When the rotation angle φ of the blades roll is from 0 to 2π (Fig. 7), as the tangential velocity decreases with increasing φ, the tangential velocity v_d at the point A_1 is calculated using Eq. (4):

$$v_d = \omega R \cos \Delta \alpha + \frac{\omega R}{\lambda} \cos (\phi - \Delta \alpha) \tag{4}$$

where $\Delta \alpha$ is the angle between the cutting velocity of point A and the peripheral velocity, the dynamic cutting angle $\Delta \alpha$ at points A_0 and A_3 approaches 0, respectively.

where the absolute velocity of point A_0 is the sum of the vector of circumferential velocity and forward velocity, the absolute velocity of point A_3 is the vector difference between them. Eq. (5) is obtained from Fig.7 as follows:

$$\frac{\omega R}{\sin(\varphi - \Delta \alpha)} = \frac{\omega R}{\lambda \sin(\Delta \alpha)} \tag{5}$$

Dynamic cutting angle calculated from Eq. (6)

$$\Delta \alpha = \arctg \frac{\sin \phi}{\lambda + \cos \phi} \tag{6}$$

Eq. (6) shows that the maximum value of dynamic slide-cutting angle depends on the slide-cutting angle of the straight blade, the rotary speed ratio λ of the row cleaner.

By formula (6) to solve the blade roller corner:

$$\varphi_2 = \arccos(-\frac{1}{\lambda})$$ (7)

The maximum cutting angle can be obtained by the value of:

$$\Delta\alpha_{max} = arc\sin\frac{1}{\lambda}$$ (8)

Analysis of the relationship between $\Delta\alpha$ and $f(\lambda)$ type, combined with anti-blocking type corn no-tillage pneumatic planter field operations 4 to 7 km/h and bench test on the basis of qualitative straw transfer required cutting speed, the concluded reasonable value of speed ratio is 2.8 to 4.5.

Bench test

Test preparation and testing

The experiments were conducted using the laboratory soil bin facility (6 m length × 1 m width × 0.6 m height), and a custom-built experimental single row cleaner using double L-shaped rotary blades was shown in Fig. 8. The forward speed of the electric sliding track was adjustable from 0 to 3 m/s. The soil environment covered with wheat straws was manually prepared before the experiment. Each experiment ensures that the straw coverage, surface roughness, moisture content and compactness were consistent. Basic data on straw and soil displacement were obtained by tracer in Fig. 9, and straw and soil from cultivated soil strips were removed for future development of the model *(Liu et al., 2010)*. At the speed of 1.5 m/s, the ridge clearing machine was used to plough once.
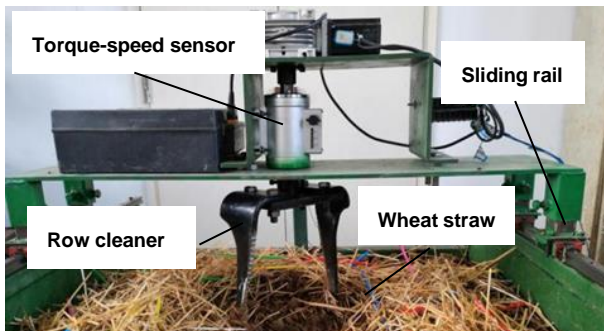
Fig. 8 - Soil and test
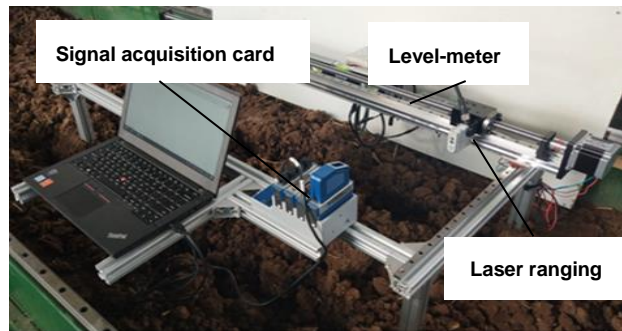
Fig. 9 - The soil surface measuring device

Evaluation indicators

(1) Straw removal rate

Straw removal rate refers to the percentage of straw removed in the total mass after seed metering device operation, a total of 20 groups of experiment data were collected. The effect of the technological parameters of the seed metering device on the distance between the straw and the center of the cultivated belt was studied. The actual straw amount was counted and weighed using the electronic balance in the straw cleaning area before and after the operation in the soil bin.

The arithmetic average values were m_1 and m_2, respectively. The straw removal rate is calculated as follows:

$$\eta = \left(1 - \frac{m_2}{m_1}\right) \times 100\%$$ (9)

Where:

η is straw removal rate, [%];

m_1 is the number of straw particles after simulation, [kg];

m_2 is the number of straw particles before simulation, [kg].

(2) Seedbed soil evenness

Seedbed soil evenness is a measure of the degree of soil concavity and convexity, and it plays an important role in mechanical sowing, irrigation and surface water accumulation, which directly affects the high and stable yield of crops and the water use efficiency of farmland. The soil surface micro-topography measuring device is a frame structure composed of aluminum profiles, as shown in Fig. 9. By measuring the spatial coordinates of the vertical axis, the device can determine the spatial position of the micro landform on the soil surface. According to the experimental method stipulated in GB/T 5668-2008 rotary tiller, the mean value of the standard deviation of the vertical axis height with m × n ranges was defined as the soil evenness of the tilled soil strip row, which was calculated as Eq. (10)

$$S_{mn} = \sqrt{\frac{\sum\limits_{j=1}^{m}\sum\limits_{i=1}^{n}(h_{i,j}-\overline{h})^2}{mn-1}} \tag{10}$$

Where:

$h_{i,j}$ is vertical axis distance from arbitrary scanning point to datum level, mm;`

h is average vertical axis height of strip width, mm;

m is the number of forward scanning points in the measured area;

n is the number of lateral scanning points of the measured area;

S_{mn} is the soil evenness of the scanned area, mm.

RESULTS
Simulation analysis of bionic vertical rotary tillage blade
Simulation model building

In this paper, when using the discrete meta-analysis software EDEM to build the straw covering soil model, the parameters of the simulation model are shown in Table 3, following pre-tests and references to the literature *(Zhang et al., 2017)*, the working width of the simulation model of the cleaner unit is constructed according to the dimensions 3200mm×1000mm×400mm virtual soil bin covered with wheat straw. Set the soil thickness of the tillage layer to 250mm (321600 particles), the thickness of straw cover to 120 mm (11000 particles), and use layer-by-layer generation. Among them, in the process of soil particle generation, after free subsiding, it is loaded vertically above the soil particle group to ensure that the soil model is basically consistent with the actual tightness. The row cleaner model of the vertical rotary tillage device established by CATIA software was imported into EDEM, the tool was grounded at a depth of 10 mm, the speed was 500 r/min, the simulation fixed time step was $4.0×10^{-5}$s, and Rayleigh time step was 25% and the total time was 3.5 s. The mesh unit is 3 times the minimum particle radius.
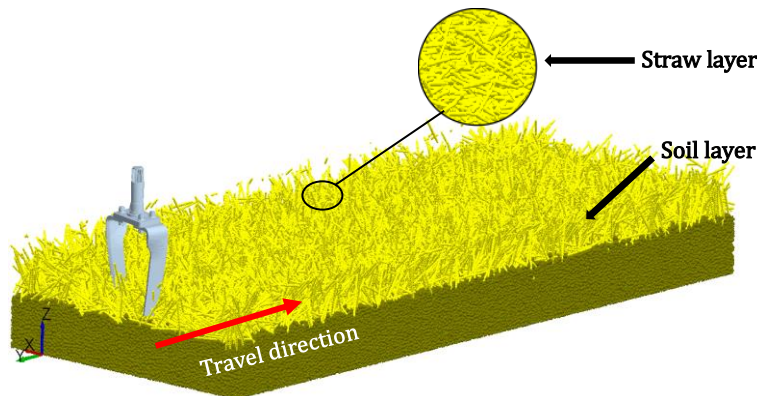
Fig. 10 - The straw-cleaner-soil model of with an enlarged image of straw clumps covered soil layers

Table 3

Calibration results of simulation experiment parameters

Parameters	Material			Parameters	Contact				
	Soil	Straw	Steel		Soil-Soil	Straw-Straw	Soil-Straw	Soil-Steel	Straw-Steel
Density, ρ /(kg·m⁻³)	1 850	30	7861	**Restitution(e)**	0.6	0.6	0.6	0.6	0.6
Poisson's ratio, v/m·s⁻¹	0.3	0.4	0.3	**Static friction (f_s)**	0.7	0.5	0.35	0.5	0.3
Shear modulus, G/Pa	$5×10^7$	$1×10^6$	$7.9×10^{10}$	**Rolling friction (f_r)**	0.225	0.01	0.015	0.05	0.01

Analysis of simulation results

Using the calibrated micro-parameters, the performance of the straw-cleaner-soil model was evaluated in terms of the straw displacement and cleaning rate. After the row-cleaner passage, the tangential force and displacement curves of each of the five straw tracers were plotted against the time. The straw moved laterally and forwardly when it was subjected to circumferential tangential force instantaneously. Fig. 11(a) shows that the average value of tangential force was 142 m·N, which decreased to 0 m·N with the friction resistance between the straw particles. *Zeng et al., (2020)* found that straw movement during tillage was modeled as three phases, namely forced, projectile, and overturning displacement, by means of video recording, mathematical modelling, and experimental validation. The moving trajectory of the five straw tracers shown nonlinear semi arc shape, which were away from a tilled soil strip row in Fig. 11(b).

(a)   (b)
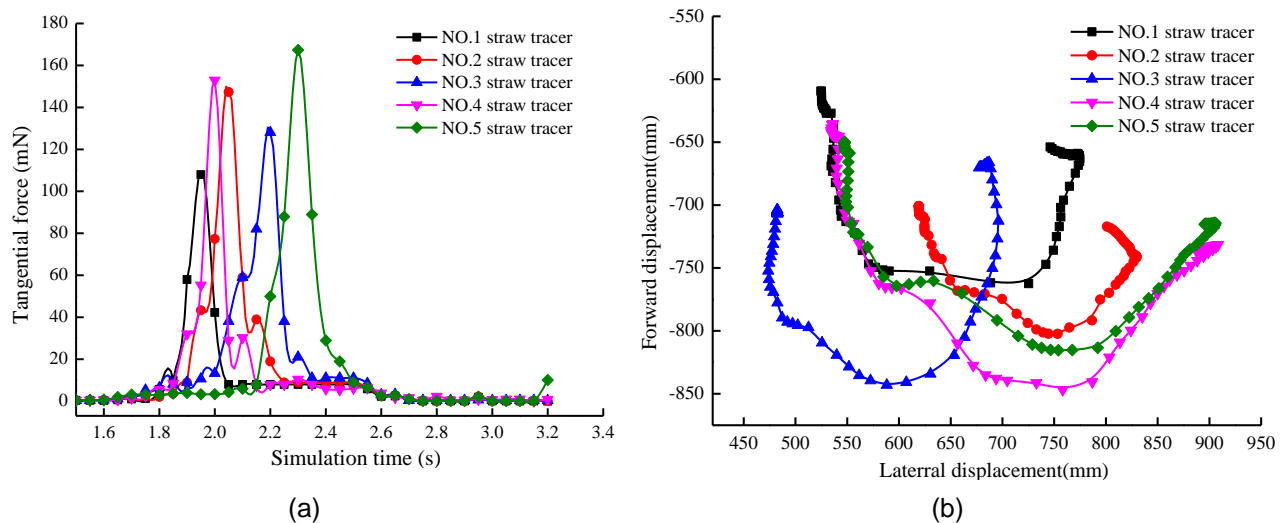
Fig. 11 -The force and displacement curve of five straw tracers

The length of straw and the mass of surface straws were 135 mm and 352 g·m⁻² respectively. The tillage speed of planter was 5 kw/h. Regardless of the situation that the straw particles were cut off, the position of the straw particle changed with the disturbance of the row cleaner during the simulation process. The simulation results showed that the covered straws were cleared from the travel path almost entirely on both sides of the seedbed, the straw displacement effect at different times are shown in Fig.12. The number of straw particles were statistically in the initial and ending positions of the simulated operation area, where the displacement of the straw particles was tracked, the average value of removal rate was 94.3% in the row sowing strip area.

From these simulation results, it can be clearly validated that using bionic vertical rotary tillage blades realized the anti-blocking idea of straws removal from a tilled soil strip row.

a. T=2.0   b. T=2.2

c. T=2.4   d. T=2.6
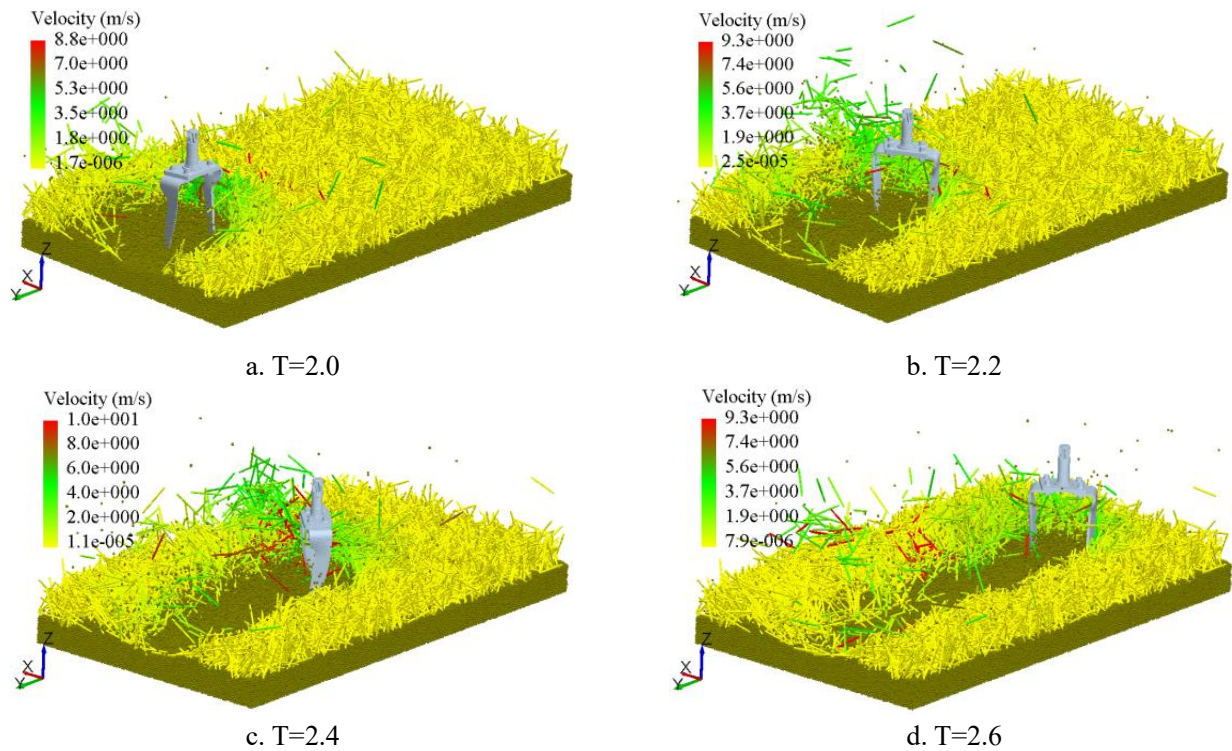
Fig. 12 - Straw displacement effect at different simulation times

Experiment results

The effects of rotation speed on straw removal rate and soil surface flatness were studied by bench test. According to the characteristics of wheat straw rhizome and theoretical consideration *(Zhou et al.,2020)*, the tillage depth of row cleaners in the range of 0~40 mm was selected as the controllable treatment factor, each factor being divided into five levels. In every trial, the length of the soil bin was separated into three parts, and randomly assigned 20 with the same straw coverage. The selection of evaluation index is the same as the simulation, in the course of bench test, the calculation of straw removal rate is the quality change within the width of tool work before and after the operation, and soil flatness is obtained by using the measurement system developed independently in the previous period *(Wang et al., 2019)*. Fig.13 showed straw removal rate and soil evenness after operation under different parameters.

$\lambda_1 = 2.8$ $\lambda_2 = 3.6$ $\lambda_3 = 4.5$
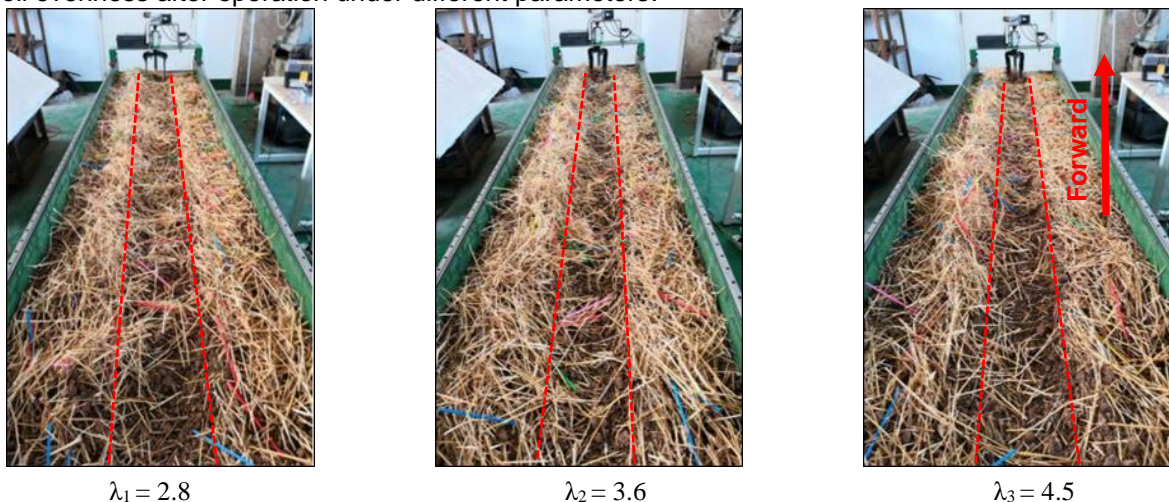
Fig. 13 - Straw removal rate and soil evenness after operation under different parameters

All the obtained spatial coordinates of soil surface can be imported into the software MATLAB to generate the three-dimensional figure of soil surface in the sample. Fig.14 showed the surface microrelief of a tilled soil strip row under tillage depth of 20 mm in the soil bin. This indicates that a flat "U" type shallow furrow with a width of 240 mm was formed by bionic vertical rotary blades for strip-tillage, the values of soil evenness were calculated by Eq. 10, which was reduced from 25.3 mm to 8.5 mm before and after operation.

The three section profiles were randomly selected from a tilled soil strip row, Fig.15 showed that the bottom curve of groove profile fluctuates less, all groove contour curves coincide basically. From these results, when cutting seedbed using bionic vertical rotary blades, it can be clearly seen a flat "U" type shallow furrow to improve the stability of sowing depth.
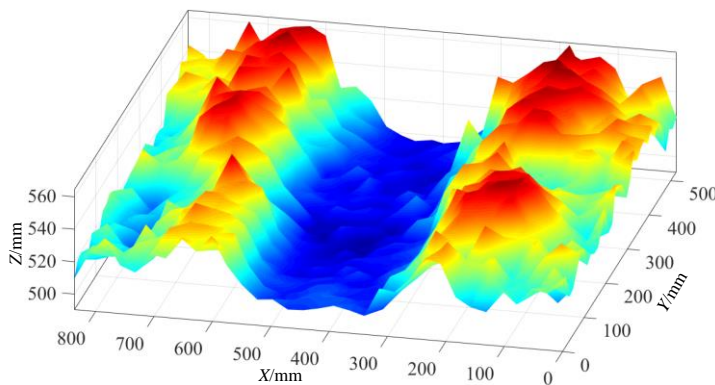
Fig. 14 - The flat "U" type shallow furrow with a width of 250 mm was formed after strip-tillage
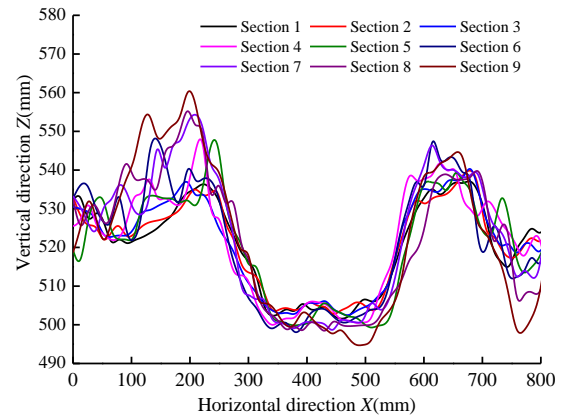
Fig. 15 - Groove section profile superposition curve from a tilled soil strip row

Fig.16 shows the measured values of straw cleaning rate and soil flatness under different motion speed ratios of three anti-blocking mechanisms during the experiment. The experimental results show that the straw cleaning rate increases with the increase of λ (the horizontal displacement and lateral displacement of straw increase), under the three speed ratios, the straw cleaning rate of the anti-blocking mechanism of the spiral sawtooth blade is higher than that of the traditional vertical straight blade and spiral blade, λ from 2.8 to 4.5, the straw removal rate in the operation area of the three anti blocking mechanisms increased by 8.3%, 6% and 4.8% respectively, and the difference among the three speed ratios was significant (P < 0.05); this is because the straw particles are in a discrete state, which is different from the volume of soil cutting block. When the motion speed ratio is 2.8, the horizontal displacement and transverse displacement of straw in the residual cycloid missed tillage area are relatively small, resulting in a large amount of straw residue in the strip tillage area.

As shown in Fig. 17, the soil flatness after three cutter operations under different speed ratios increases with the moving speed ratio λ the lower the flatness of the increased surface (the better the leveling effect), λ from 2.8 to 4.5, the surface roughness of the farming area decreased by 1.13mm, 0.46mm and 0.77mm respectively after the operation of the three anti blocking mechanisms, and the difference among the three motion speed ratios was significant (P < 0.01). Compared with the traditional vertical straight blade, soil uniformity of seed bed has been improved 9.3%.
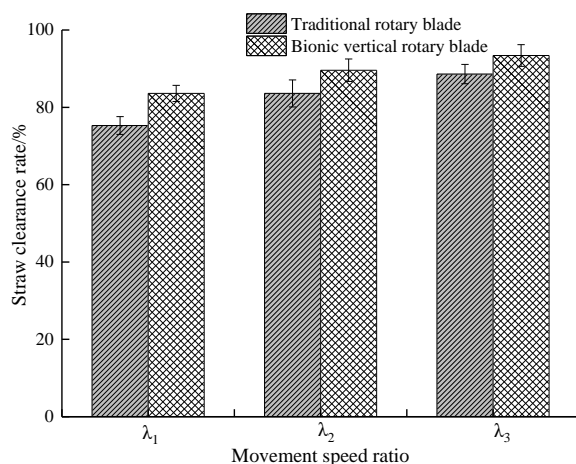
Fig. 16 - Straw removal rate under different speed ratios
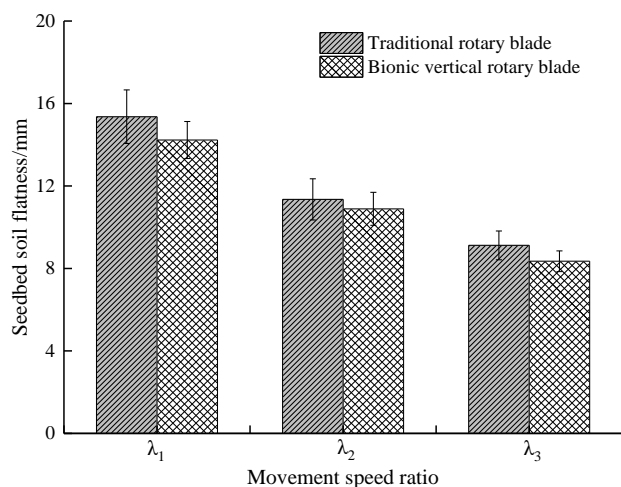
Fig. 17 - Soil flatness under different speed ratios

According to the power consumption comparison at different times in Fig.18, the torque of bionic vertical rotary blades under the same conditions is mostly lower than that of traditional vertical rotary blades, and the power consumption of bionic vertical rotary blades can be reduced by 12.3% compared to traditional vertical rotary blades by the average calculation.
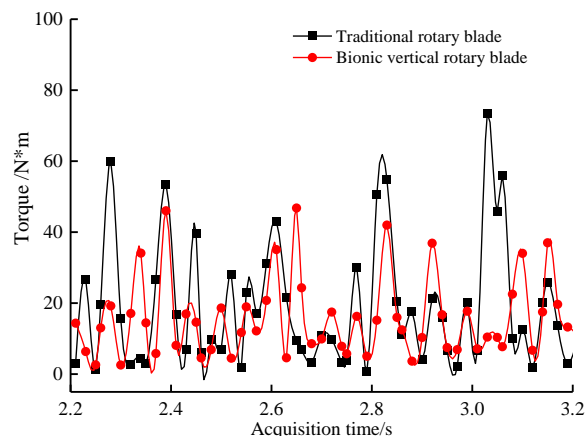
Fig. 18 - Comparison of power consumption at different acquisition times

CONCLUSIONS

The development of corn planter row cleaner using bionic vertical rotary tillage blades to remove seedbed straw and create ideal soil for no-tillage sowing, produce high-quality seedbeds for strip-tillage and production, so as to obtain the best seed germination and early seedling vigor. In this paper, an in-depth study of the rotation process of the bionic vertical rotating tillage blades has been carried out and compared with the rotation effect of conventional rotating blades through experimental verification. The specific conclusions were as follows:

In this study, the EDM simulations and experiments were used to collect and process the data, the hypothesis of the influence of some parameters on the straw removal rate and soil evenness was put forward, which was verified by simulations and bench experiment. Tillage speed have significant influence on the cutting process and results of straw and soil.

The experiments results showed that the straw removal rate of the anti-blocking mechanism of the spiral sawtooth blade is higher than that of the traditional vertical straight blade and spiral blade, the straw removal rate and soil level were improved by 6.4% and 9.3%, and the average torque of the rotary tiller has been reduced by 12.3%. Respectively, this design can provide reference for the design of no-tillage planter.

ACKNOWLEDGEMENT

REFERENCES

[1]   Bilen S., Celik A., Altikat S., (2010), Effects of strip and full–width tillage on soil carbon IV oxide–carbon (CO_2–C) fluxes and on bacterial and fungal populations in sunflower, *Afr. J. Bio technol*, 2010, 9 (38), 6312–6319.

[2]   Celik A., Altikat S., (2010), Effects of various strip widths and tractor forward speeds in strip tillage on soil physical properties and yield of corn, *J. Agric. Sci.*, 2010,16,169－179.

[3]   Dikgwatlhe S.B., Chen Z.D., Lal R., Zhang H.L., Chen F., (2014), Changes in soil organic carbon and nitrogen as affected by tillage and residue management under wheat-corn cropping system in the North China Plain, *Soil Tillage Res.* ,144, 110–118.

[4]   Fallahi S., Raoufat M.H., (2008), Row-crop planter attachments in a conservation tillage system: a comparative study, *Soil Tillage Res.*, 2008, 98, 27–34, https://doi.org/10.1016/j. still.2007.10.005.

[5] Guo J., Zhang Q.Y., Song J.N., et al., (2017), Design and experiment of bionic mole's toe arrangement serrated blade for soil-rototilling and straw-shattering, *Transactions of the Chinese Society of Agricultural Engineering (Transactions of the CSAE).*,33(6):43-50;

[6] He J., Li H.W., Wang X.Y., McHugh A. D., Li W. Y., Gao H.W., Kuhn N.J., (2007), The adoption of annual subsoiling as conservation tillage in dryland corn and wheat cultivation in northern China, *Soil Tillage Res.*, 2007,94, 493－502.

[7] Jia H.L., Guo M.Z., Guo C.J., et al., (2017), Design of Dynamic Bionic Straw Cutting Device and Optimization Test of Parameters, *Transactions of the Chinese Society for Agricultural Machinery.*, 49(10):103-114;

[8] Jia H. L., Wang Q., Huang D.Y., Zhu L. T., Li M. W., & Zhao, J.L. (2019), Design of bionic mole forelimb intelligent row cleaners, *Int J Agric & Biol Eng.*, 2019, 12(3), 27–35.

[9] Laufer D., Koch H.J., (2017), Growth and yield formation of sugar beet (Beta vulgaris L.) under strip tillage compared to full width tillage on silt loam soil in Central Europe, *Eur. J. Agric.*, 2017,82, 182–189. https://doi.org/10.1016/j.eja.2016.10.017.

[10] Li L.D., Wilson C.B., He H.B., Zhang X.D., Zhou F., Schaeffer S.M. (2 019), Physical, biochemical, and microbial controls on amino sugar accumulation in soils under long-term cover cropping and no-tillage farming, *Soil Biology & Biochemistry.*, 135, 369–378. https://doi.org/10.1016/j.soilbio.2019.05.017.

[11] Li S.Y., Gu X., Zhuang J. An T.T., Pei J.B., Xie H.T., Li H., Fu S.F., Wang J.K., (2016), Distribution and storage of crop residue carbon in aggregates and its contribution to organic carbon of soil with low fertility, *Soil Tillage Res.*,155, 199–206.

[12] Licht M.A., Al-Kaisi., (2010), Strip-tillage effect on seedbed soil temperature and other soil physical properties, *Soil Tillage Res.*, 80(1), 233–249.

[13] Liu J., Chen Y., & Kushwaha R. L., (2017), Effect of tillage speed and straw length on soil and straw movement by a sweep, *Soil Tillage Res*, 109, 9–17. https://doi.org/10. 1016/j.still.2010.03.014;

[14] Sale V., Aguilera P., Laczko E., Mäder P., Berner A., Zihlmann U., Marcel V.D.H., Oehl F., (2015), Impact of conservation tillage and organic farming on the diversity of arbuscular mycorrhizal fungi, *Soil Biology & Biochemistry.*, 84 ,38–52. http://dx.doi.org/10.1016/j.soilbio.2015.02.005.

[15] Vaitauskienė K., Šarauskis E., Romaneckas K., Jasinskas A., (2017), Design development and field evaluation of row-cleaners for strip tillage in conservation farming, *Soil Tillage Res*, 2017,174, 139–146. https://doi.org/10.1016/j.still.2017.07.006.

[16] Wang Q., Jia H.L, Zhu L.T, et al., (2017), Design and Experiment of Star-toothed Concave Disk Row Cleaners for No-till Planter, *Transactions of the Chinese Society for Agricultural Machinery.*, 50(2):68-77;

[17] Wang W.W., Li J., Wang Q.Q., et al., (2019), Chen L.Q. Design and Experiment for Tillage Soil Groove Measurement System, *Transactions of the Chinese Society for Agricultural Machinery*, 50(7):93-99;

[18] Wang W.W., Zhu C.X., Chen L.Q., et al., (2017), Design and experiment of active straw-removing anti-blocking device for maize no-tillage planter, *Transactions of the Chinese Society of Agricultural Engineering (Transactions of the CSAE).*, 33(24):10-17;

[19] Zeng Z. W., Chen Y., Zhang X. R., (2020), Modelling the interaction of a deep tillage tool with heterogeneous soil, *Computers and Electronics in Agriculture*, 2020,143, 130–138.

[20] Zhang X.R., Chen Y., (2017), Soil disturbance and cutting forces of four different sweeps for mechanical weeding, *Soil Tillage Res.*, 168, 167–175;

[21] Zhou H., Zhang C, L., Zhang, W, L., et al., (2020), Evaluation of straw spatial distribution after straw incorporation into soil for different tillage tools, *Soil Tillage Res.*, 196,104440. https://doi.org/10.1016/j.still.2019.104440;

DESIGN AND EXPERIMENT OF RECOGNITION SYSTEM FOR COATED RED CLOVER SEEDS BASED ON MACHINE VISION
/
基于机器视觉的包衣红三叶种子识别系统的设计与试验

Xiwen ZHANG, Zhanfeng HOU*), Chuanzhong XUAN
Inner Mongolia Agricultural University, College of Mechanical and Electrical Engineering, Inner Mongolia, China
Tel: 04714309215; *)Corresponding author E-mail: njau-hzf@163.com

ABSTRACT

While studying the coating theory, due to the lack of the support of the rapid identification and detection device for coated red clover seeds, for a long time, we have mainly relied on manual visual inspection to sort qualified coated seeds, only relying on human eyes to identify the cause of low efficiency, high wrong classification rate and high labor intensity. In order to identify the coated red clover seeds quickly and efficiently, a set of intelligent identification and detection system for coated red clover seeds was designed. First of all, by building a machine vision shooting platform to ensure that the light source and other shooting conditions are consistent, the images are transmitted to Vision Assistant 2018 for image processing. Secondly, two image processing algorithms are designed to process qualified coated seeds and damaged coated seeds respectively. Finally, an identification and detection algorithm is proposed, which uses LabVIEW2018 as the host computer to identify the qualified number and the damaged number. Taking red clover seeds as the test object, the test results show that the entire system takes about 1 second to collect and process a single image; the recognition accuracy of qualified coated seeds and damaged coated seeds is above 96% and 85%. The identification and detection system realizes the nondestructive detection of coated seeds, and provides theoretical basis and technical support for the later research on the optimal seed coating process, deepening the theoretical research of the coating machine and improving the degree of automation.

摘要

在对包衣理论进行研究的同时，由于缺少包衣红三叶种子快速识别检测装置的支持，长期以来主要依靠人工目测分选合格的包衣种子，仅靠人眼识别效率低、错分率高、劳动强度高，为此设计了一套包衣红三叶种子智能识别检测系统，针对包衣红三叶种子进行识别。首先，通过搭建机械视觉拍摄平台，保证光源等拍摄条件一致，传输图像至Vision Assistant 2018 进行图像处理。其次，设计两种图像处理算法，分别对合格包衣种子以及破损包衣种子进行处理。最后提出了一种识别检测算法,采用LabVIEW2018 作为上位机对合格数以及破损数进行识别。以红三叶种子为试验对象，试验结果表明：整套系统对单幅图像采集和处理时间约为1s；对合格包衣种子以及破损包衣种子识别准确率分别在96%和85%以上。该识别检测系统实现了对包衣种子的无损检测，为后期研究种子最佳包衣工艺，深化包衣机理论研究以及提高自动化程度提供了理论基础与技术支持。

INTRODUCTION

Red clover is one of the most widely cultivated legume pastures in the world, and is a famous high-quality pasture. Red clover has a high nutritional value. According to measurement, when flowering, the dry matter contains 17.1% crude protein, 3.6% crude fat, 21.5% crude fiber, 47.6% of nitrogen-free extract, 10.2% crude ash. It is also rich in various amino acids and vitamins, the grass is soft and the palatability is good, all kinds of livestock like to eat. In addition, red clover has strong resistance to extreme weather and its colorful flowers are excellent ornamental grass, and its medicinal value cannot be ignored.

Seed coating is a technique to cover seeds with external agents to upgrade their performance, handling, and plant establishment (*Li, 2016*). A specific coating process is used to make the surface of the seed and the coating agent evenly contact, and wrap it to form a smooth and firm medicinal film. Through mechanical processing, small spheres of uniform size and regular shape (including true circle, ellipse, oblate, etc.) are made. The coating agent can contain a variety of ingredients. According to specific environmental factors, proper adjustment of the dosage of ingredients can improve the ability of seeds to resist drought, cold, salt and alkali, and prevent soil-borne diseases (*Shao, 2018*).

Experiments have proved that the germination rate of red clover coated seeds is higher than that of ordinary red clover seeds, and the adaptability is stronger. Theoretically, the germination rate can reach more than 90. While studying the qualified rate of coating under different parameters, due to the lack of support for rapid identification and detection of coated seeds, we have mainly relied on manual visual inspection to sort qualified coated seeds and calculate the qualified rate of coating for a long time, relying only on human eyes has low recognition efficiency, high misclassification rate, and high labor intensity (*Xing, 2019*). The development and design of an intelligent identification and detection system for coated red clover seeds to improve the efficiency of coating research is a problem that needs to be solved urgently (*P.T, 2016*).

In this paper, a real-time algorithm based on LabVIEW was proposed to improve the detection speed and accuracy. A machine vision test platform to take real-time images of images is built (*Xiong, 2019*). Two image processing algorithms are designed to process qualified coated seeds and damaged coated seeds respectively. Transfer the image to system, identify the seeds, and calculate the qualified rate of coating, so as to explore the best coating process and enrich the theoretical research of the coating machine.

MATERIALS AND METHODS
Structure of coating machine

The seed coating machine is composed of a coating pot, an inclination adjusting device, a rotary motor and a vibrating table (*Sun, 2017*). The overall structure of seed coating machine is shown in Fig.1.
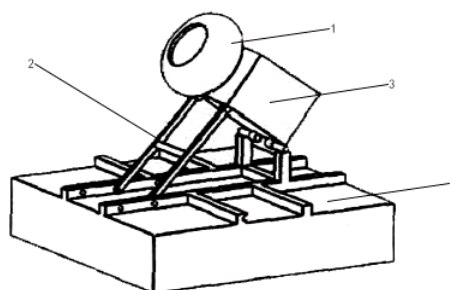
Fig.1 - The overall structure of seed coating machine
1- Coating pot; 2- Inclination adjusting device; 3- Rotary motor; 4- Vibrating table

Before coating, the inclination angle of the coating pot is adjusted by the inclination angle adjusting device, and the seeds and powder are respectively sent into the coating pot. When coating, the rotating motor starts to rotate, thus driving the coating pot to rotate at high speed. The shaking table vibrates continuously to make the seed coated quickly under the action of vibration force field (*Zhu, 2012*). During the coating process, the liquid is continuously supplied. Finally, the whole coating process is completed.

Machine vision experiment platform

In the process of shooting coated seeds, different light conditions and shooting angles have a great impact on the recognition effect (*Deng, 2017*). In order to improve the accuracy of recognition algorithm, a machine vision experimental platform is built. The mechanical vision experiment platform consists of USB camera, chassis, light source, bracket and image processing system. The mechanical vision experiment platform is shown in Fig.2**.**
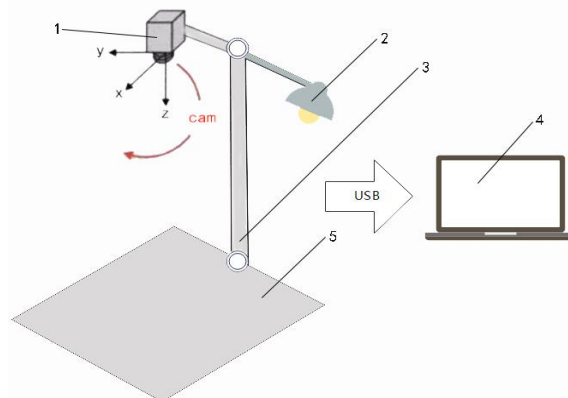
Fig. 2 - The mechanical vision experiment platform
1- USB camera; 2- Light source; 3- Bracket; 4- Image processing system; 5- Chassis

Red clover coated seed model template

Taking red clover seeds of leguminous forage as the object, the coating material is phosphorus potassium compound fertilizer. During the growth of seeds, the compound fertilizer dissolves in water, which not only does not affect the growth of seeds, but also creates nutritional conditions for their growth. Through the coating machine, adding water and adhesive properly, under the joint action of vibration force and rotation force, the compound fertilizer fully contacts with the seed, and finally evenly wraps the surface of the seed, forming a small sphere with uniform size and regular shape (*Taylor A.G, 2008*). The coated seeds are divided into qualified coated seeds and damaged coated seeds. The qualified coated seeds are shown in Fig. 3a, and the damaged coated seeds are shown in Fig. 3b.

Fig. 3 - The model of Red Clover Coated Seed

After coating, 100 red clover coated seeds were randomly selected as samples, and they were randomly placed on the shooting chassis, which contained three damaged coated seeds. The sample of image processing is shown in Fig. 4.

Fig. 4 - The sample of image processing

Image processing algorithm for qualified coated seeds

The effect of image preprocessing directly affects the recognition error of qualified coated seeds. In order to facilitate feature extraction and improve the accuracy of recognition, before extracting features, the captured images are subjected to ROI extraction, saturation adjustment, filtering, threshold segmentation, and morphological analysis. Finally, the contact area between the seeds is eliminated, so that each seed forms an independent individual for identification. In addition, based on the original image processing, advanced morphological analysis is used to retain qualified coated seeds, and broken coated seeds are eliminated to improve the accuracy of subsequent identification (*Meng, 2021*).

The image processing flow chart of qualified coated seeds is shown in Fig. 5.
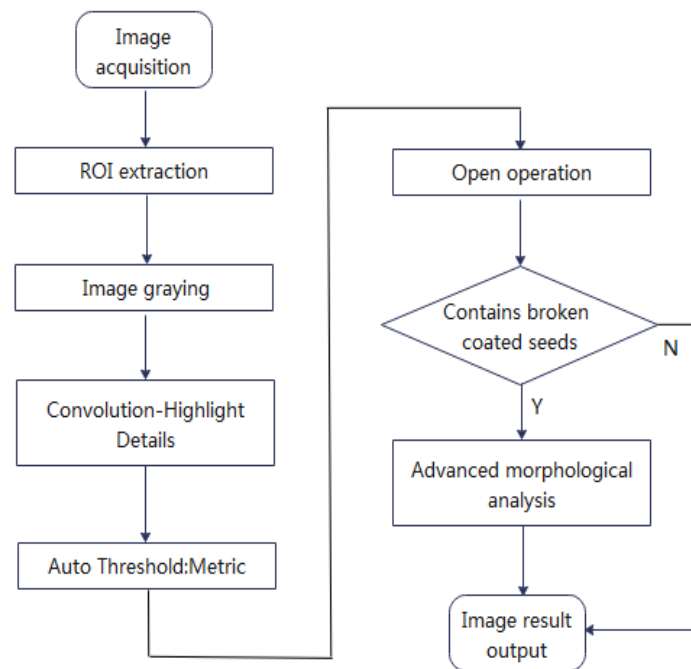
Fig. 5 - The image processing flow chart of qualified coated seeds

Image processing software is Vision Assistant 2018 developed by NI Company, which contains a complete set of image processing function library, which has rich and powerful functions, and can efficiently and quickly process images. Compared with other visual products, the software greatly simplifies the processing process and shortens the time of algorithm development and debugging.

The coated seeds are khaki. Considering that the background of the chassis is white, in order to better segment and highlight the contour of the seed, extract the color plane of the image, extract the saturation plane, and convert the image from color image to black and white image, which effectively removes background interference, highlight the outline of the seed, and facilitate subsequent processing. The gray-scale processing effect is shown in Fig. 6a.

Image shooting and processing are often contaminated by noise, and these noises will affect the visual effect of the image in the form of isolated pixels or pixel blocks. Noise is generally expressed as a large or small extreme value, which acts on the gray value of pixels in the image through addition and subtraction operations, causing bright or dark spot interference to the image. It not only affects the quality of captured images, but also affects the accuracy of seed feature recognition. Therefore, the use of convolution-highlight filter to highlight the details of the seed, make the image sharper, to solve the problem caused by noise. In the filtering process, the 3×3 square array is selected, and the type of the convolution kernel determines how the pixels in the image are transformed. In the calculation process, the convolution kernel slides point by point from the upper left corner to the lower right corner of the image, and each time it slides to a new pixel, the new value is obtained through the convolution operation, and the original pixel value of the image is overwritten. The pixel value corresponding to the central position of the template after convolution operation is P_5', with the following form:

$$P_5' = \sum_{i=1}^{9} WP_i = -P_1 - P_2 - P_3 - P_4 + 10P_5 - P_6 - P_7 - P_8 - P_9 \tag{1}$$

where: P_i -the pixel value, [-]; W -convolution kernel template, [-];

The design of image processing algorithm uses two convolutions highlight filtering, and the parameter settings are the same. The filtering effect is shown in Fig. 6b.

Automatic threshold segmentation method is a widely used segmentation technology. It can determine the gray threshold according to the gray histogram of the image, which has strong applicability. The image is divided into two categories: background and target. Those whose pixel gray values meet the uniformity distribution are classified into one category. The uniformity of pixel gray values is calculated to segment the image.

The principle of uniformity measurement is that if the initial threshold can divide the image into "background" and "target", then the distribution of gray values belonging to the same category should be uniform. Variance is used to measure uniformity. Let the gray value of any point in the original image be $f(x, y)$. The image to be segmented is divided into two categories: background C_1 and target C_2.

Given an initial threshold Th (in this paper, the initial threshold is set as the median), the width pixel value of the image to be segmented is represented by m, and the height pixel value is represented by n. The gray mean value μ_1 and within class variance value σ_1^2 corresponding to C_1 after segmentation are calculated respectively. The gray mean value μ_2 and within class variance value σ_2^2 corresponding to C_2 after segmentation are calculated respectively.

Both are calculated as follows:

$$\begin{cases} \mu_1 = \dfrac{1}{N_{C_1}} \sum_{f(x,y) \in C_1} f(x, y) \\ \sigma_1^2 = \sum_{f(x,y) \in C_1} \left(f(x, y) - \mu_1 \right)^2 \end{cases} \tag{2}$$

$$\begin{cases} \mu_2 = \dfrac{1}{N_{C_2}} \sum_{f(x,y) \in C_2} f(x, y) \\ \sigma_2^2 = \sum_{f(x,y) \in C_2} \left(f(x, y) - \mu_2 \right)^2 \end{cases} \tag{3}$$

where: N_{C_i} - the number of pixels in class i, [-];

The distribution probabilities p_1 and p_2 of the two types in the image are calculated respectively. The calculation formula of distribution probability is

$$\begin{cases} p_1 = \dfrac{C_{c1}}{m \times n} \\ p_2 = \dfrac{C_{c2}}{m \times n} \end{cases} \tag{4}$$

Substituting the distribution probability, gray mean value and intra-class variance corresponding to the background and the target, the optimal segmentation threshold Th^* which meet the conditions is Th.

The formula for calculating the optimal segmentation threshold is:

$$\left[p_1 \sigma_1^2 + p_2 \sigma_2^2 \right]_{Th=Th^*} = \min \left\{ p_1 \sigma_1^2 + p_2 \sigma_2^2 \right\} \tag{5}$$

The image after thresholding has the problem of poor edge area segmentation of some seeds.

The threshold processing effect is shown in Fig. 6c.

Expansion and corrosion are not reciprocal operations, so they can be combined step by step. After thresholding, the binary image first erodes and then dilates, carries on the open operation to remove the unnecessary information in the image, such as noise, overlapping areas. After morphological processing, the coated seeds eliminate the contact between each other and become an independent particle, which improves the accuracy of the recognition algorithm. The particle refers to a group of connected non-zero or high gray pixels in the image.

The formula of erode objects operation is as follows:

$$P_0 = and(P_i) \tag{6}$$

where: P_o - center pixel, [-];

P_i - the pixels involved in the calculation in the image corresponding to the structural element, [-];

The dilate objects operation is as follows:

$$P_o = or(P_i) \tag{7}$$

After morphological processing, the coated seeds eliminate the contact area and are divided into independent individuals. The effect of morphological processing is shown in Fig. 6d.
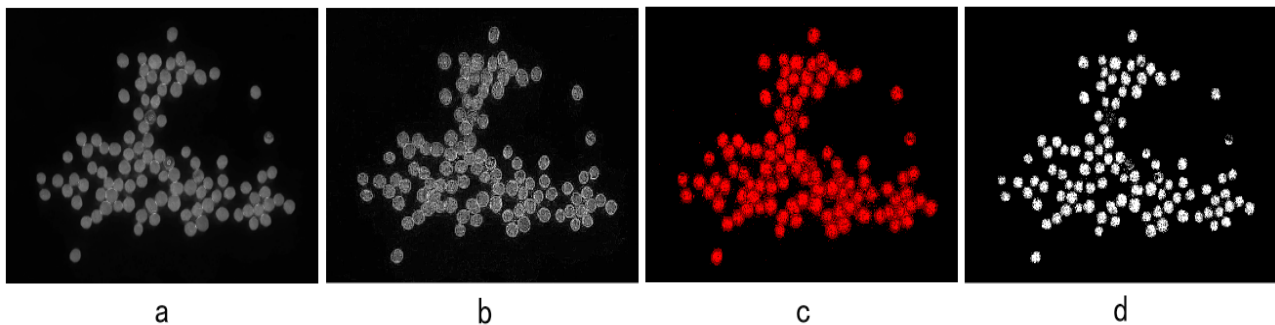
Fig. 6 - Image processing of qualified coated seeds

Advanced morphological processing algorithm is specially used for particle processing in binary image. The image processed by the algorithm is more suitable for quantitative analysis based on particle, extraction of target model and target recognition. The seed processed by the algorithm is a group of independent white pixels with high gray value. Through the pre-experiment, it is found that there is less powder on the surface of the damaged coated seeds, and the total value of white pixels after treatment is far less than the qualified coated seeds. Therefore, the operation of removing small objects in the advanced morphological algorithm can effectively remove the damaged coated seeds when the number of iterations is 3. The effect of advanced morphological processing is shown in Fig. 7.
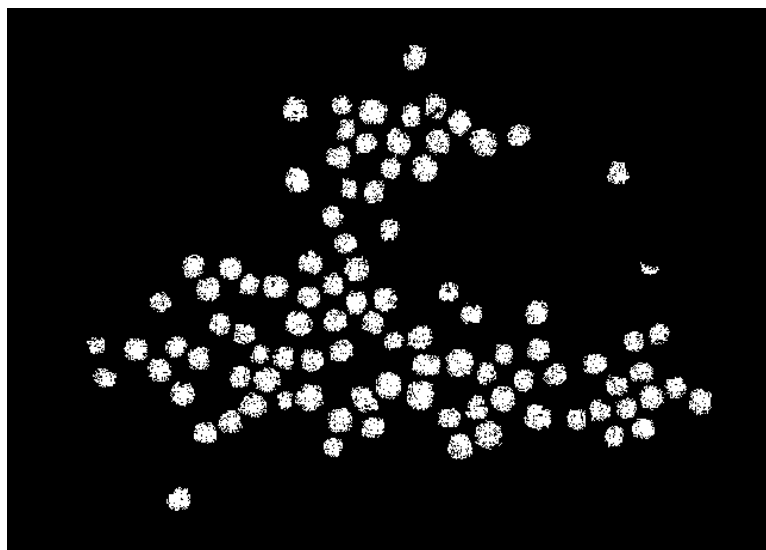
Fig. 7 - The effect of advanced morphological processing

Image processing algorithm for damaged coated seeds

A set of image processing algorithm was designed to identify the number of damaged coated seeds. Firstly, ROI extraction, saturation adjustment, Convolution-highlight Details filtering and Auto threshold segmentation are performed on the captured image. The preliminary process is similar to the algorithm of qualified coated seed map, and the threshold segmentation adopts the OTSU maximum between-class variance method. Secondly, the proper open operation and erode objects operation in morphological analysis are used to perform the close operation. Remove small objects operation in advanced morphological analysis is used to remove the interference in the image, and dilate objects is used to enhance the image effect. Finally, the qualified coated seeds are eliminated and the damaged coated seeds are retained for quantity identification.

The image processing flow chart of damaged coated seeds is shown in Fig. 8.
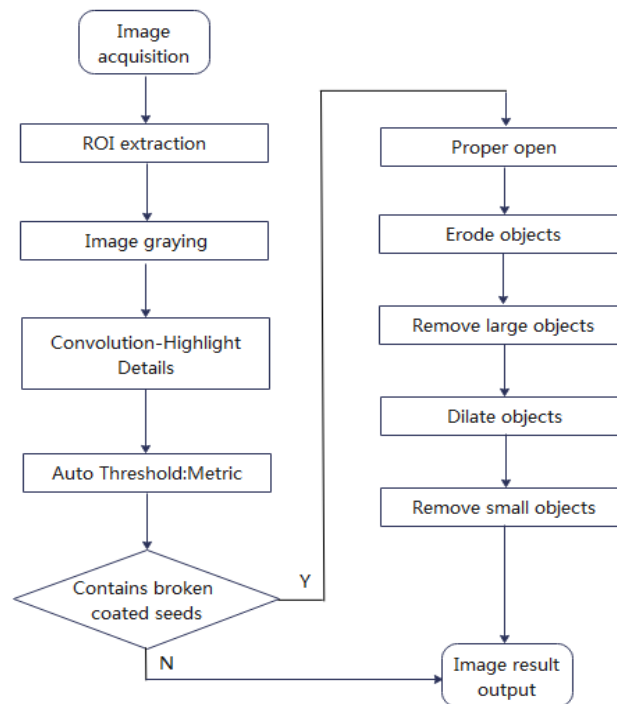
Fig. 8 - The image processing flow chart of damaged coated seeds

After image processing, the qualified coated seeds in the image can be effectively removed, and the damaged coated seeds can be retained. The image processing effect of damaged coated seeds is shown in Fig. 9.
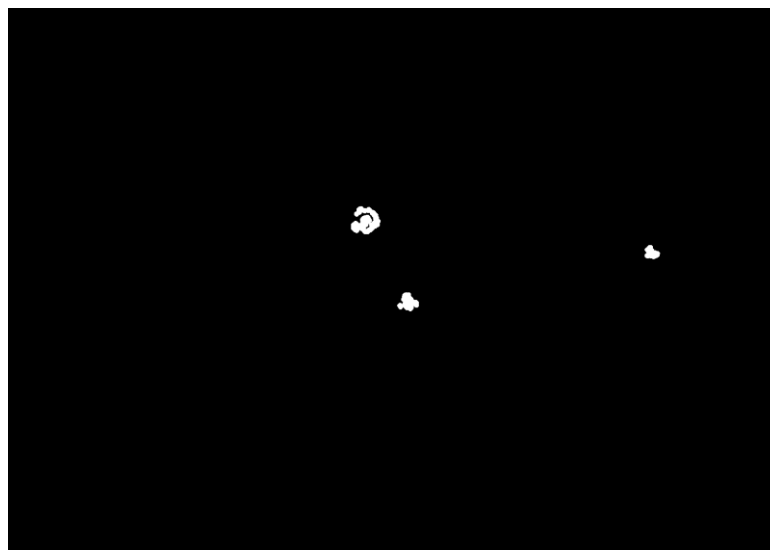
Fig. 9 - The image processing effect of damaged coated seeds

Identification control system

Using LabVIEW2018 to design a complete set of intelligent recognition system. The processed image is loaded into the Red Clover Seed intelligent recognition system for recognition. The modular design method is adopted, and each module is designed and written independently (*Bai, 2020*). The functional modules include parameter setting, image recognition, target marking and calculation processing. Initially the image path is selected, including the processed images of qualified coated seeds and the processed images of damaged coated seeds. Secondly, the appropriate threshold of the recognition function is determined through preliminary experiments. After the system runs, the identified image is generated, and the number of qualified coated seeds and the number of damaged coated seeds are obtained. Finally, the qualified rate of coating is obtained by calculation, and the results can be saved. The processing time of a single image is less than 1s. The intelligent recognition system of red clover coated seeds is shown in Fig. 10.
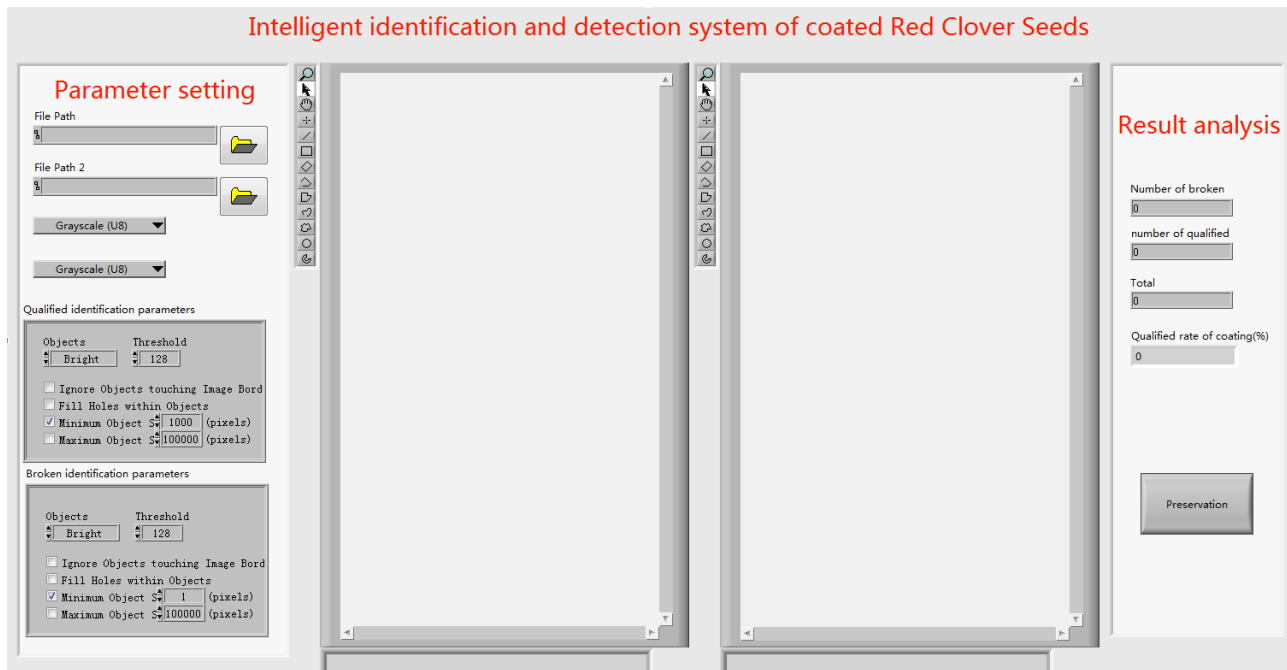
Fig. 10 - The intelligent recognition system of red clover coated seeds

The target seeds were identified by the identification function, and the number of two types of red clover coated seeds under a single group of coating parameters was obtained. Finally, the qualified coating rate was calculated. The system work flow chart is shown in Fig. 11.
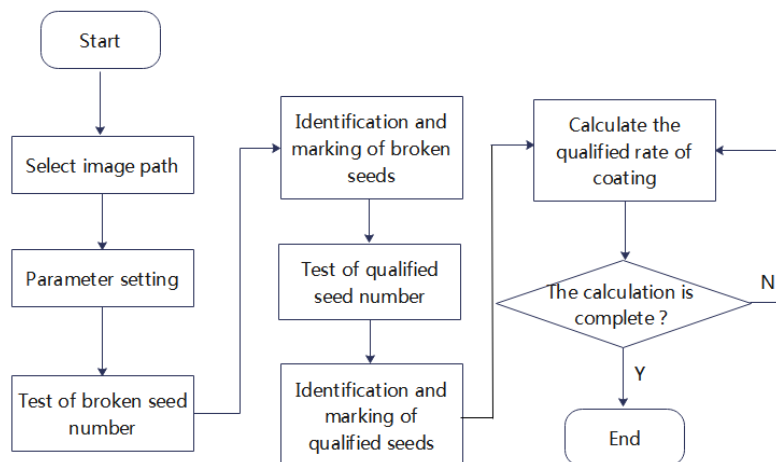
Fig. 11 - The system work flow chart

According to the total value of white pixels, the qualified number recognition algorithm uses the visual recognition function to recognize the white pixel target, sets the recognition threshold of the total number of pixels, identifies the coated seeds of the target in the image, and marks the number.

After advanced morphological analysis, the interference of small pixels is eliminated. When identifying the qualified number of coated seeds, because of the small error of the image processing algorithm of qualified coated seeds, some pixels of damaged coated seeds have not been removed. Therefore, the minimum total value of recognized pixels is adjusted to 1000, and all the targets with the total value of white pixels greater than 1000 in the image are identified by frame selection. Taking the sample image as an example, the total number of qualified coated seeds is 97. The recognition process is from the top to the bottom of the image, and the box is selected and numbered. The number starts from 0 and ends at 96, and the recognition success rate reaches 100%. The effect picture of qualified quantity identification is shown in Fig. 12.
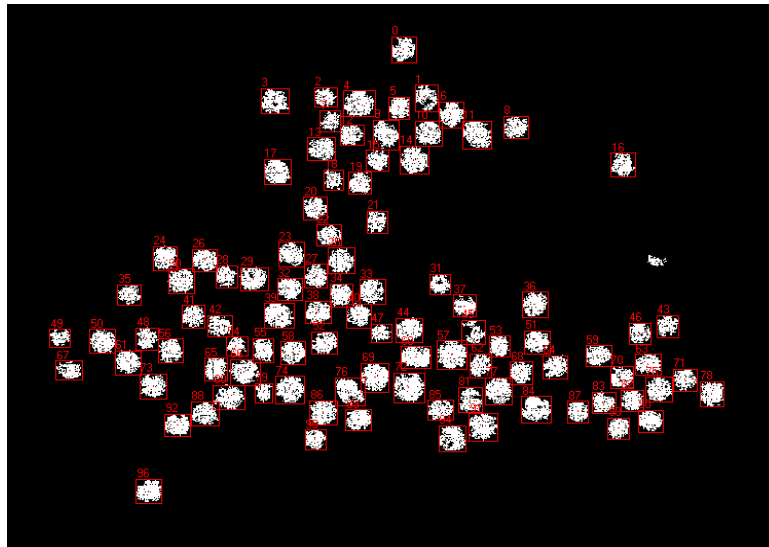
Fig. 12 - The effect picture of qualified quantity identification

The image processed by the image processing algorithm of damaged coated seeds is transmitted to the host computer in real time to identify the damaged coated seeds. Adjust the minimum total value of recognized pixels to 1, and recognize all the targets with white pixels in the image. Taking the sample image as an example, the number of damaged coated seeds is 3, and the recognition result is consistent with it. The effect picture of damage quantity identification is shown in Fig. 13.
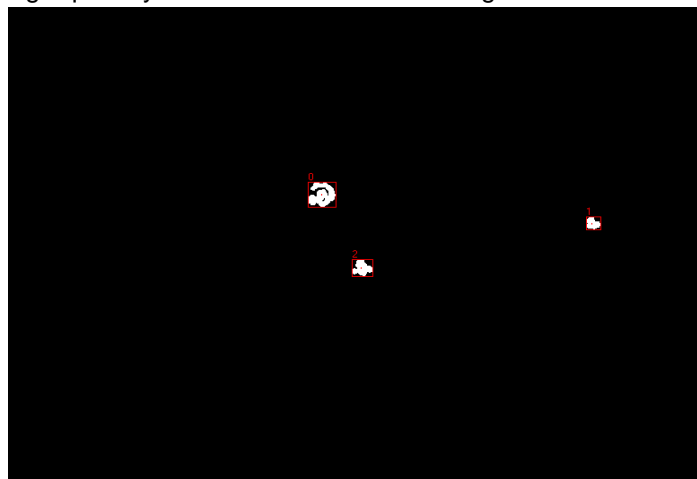
Fig. 13 - The effect picture of damage quantity identification

Before the system runs, the path of recognition image is initially selected, the recognition process is carried out at the same time, and the recognition results are displayed in real time. The total number of identification is equal to the number of qualified seeds plus the number of damaged seeds, and the qualified rate of coating is equal to the number of qualified seeds divided by the total number of identification. The generated results can be saved in Excel in real time to facilitate the comparative analysis of coating qualification rate of different coating parameters.

RESULTS AND DISCUSSIONS
Test and result analysis

In order to verify the stability and reliability of the device, a vibrating rotary coating machine was selected for test coating. The prototype of the device is shown in Fig. 14. Red clover seeds were used as the test sample to be coated, and then dried after coating (*Rogovskii I.L., 2020)*. The finished coated products are randomly selected and placed on the visual experiment platform for image shooting, followed by image processing and visual recognition. The experiment tests the reliability and accuracy of the coated seed recognition algorithm (*Wang, 2021*).

Fig. 14 - The prototype of the device

In order to verify the accuracy of the total number recognition algorithm and the seed recognition algorithm, a large number of coated products are randomly selected for the test. Considering that the optimal chassis capacity of the visual experiment platform is within 500, the number of test samples is 100 to 500, and the coated products are randomly selected to be placed on the chassis. The results are obtained by the traditional manual visual method and compared with the recognition results of the recognition system. Finally, the accuracy of identifying qualified coated seeds and multi-seed coated seeds was obtained. The test results are shown in Table 1.

Table 1

Experimental results of recognition algorithm

Total number of coated seeds	Number of qualified coated seeds	Number of damaged coated seeds	Detection of qualified coated seeds	Detection of damaged coated seeds	Detection accuracy of qualified coated seeds (%)	Detection accuracy of damaged coated seeds (%)
100	97	3	97	3	100.0	100.0
200	195	5	194	5	99.5	100.0
300	290	10	287	9	99.0	90.0
400	386	14	378	12	97.9	85.7
500	480	20	465	17	96.9	85.0

According to the data in Table 1, the accuracy rate of the identification system designed this time in detecting the number of qualified coated seeds reaches more than 96%. With the fewer seeds placed, the higher the accuracy. Due to the small number of damaged coated seeds, the identification error of damaged coated seeds is large. The experimental results show that the accuracy of detecting damaged coated seeds is more than 85%. As the number of identified seeds increases, the error increases relatively. Before shooting, the overlap can be reduced by gently moving to improve the recognition success rate and reduce the error. Experiments show that this method greatly improves work efficiency, reduces work intensity, and can effectively replace the traditional manual visual inspection method.

CONCLUSIONS

In this paper, through machine vision and image processing technology, an intelligent recognition and detection system of coated red clover seed is designed, including the visual experiment shooting platform and the upper computer detection system. Aiming at the red clover coated seeds, two unique image processing algorithms were designed to process the qualified coated seeds and damaged coated seeds respectively. The qualified number, damaged number and coating qualified rate were calculated by the upper computer detection system. A large number of experiments were carried out on the coated red clover seeds, and the following conclusions were drawn: the recognition accuracy of qualified coated seeds and damaged coated seeds were above 96% and 85% respectively, and the single image acquisition and processing time was about 1 s, which met the design requirements.

REFERENCES

[1] Bai Y., Zhang C., Zeng L.., (2020), Design of photoacoustic microscope system based on LabVIEW platform. *MATEC Web of Conferences*, Vol 309, Issue4, pp. 4-16, China;

[2] Deng K., Liu Z., Deng J., Zhao Y., (2017), Variation of Surface Profile Topography Based on W-M Function Model. *Mechanical design and manufacturing*, Vol.1, Issue 1, pp. 47-50, China;

[3] Li Y., Wei C., Ding W., Yi Y., (2016), Study on the detection method of cleft glume hybrid rice seeds based on acoustic characteristics. *Transactions of the Chinese Society of Agricultural Machinery*, Vol 47, Issue 5, pp. 263-269, China;

[4] Meng F., Luo S., Sun H., Li M., (2021), Design and experiment of real-time detection and sorting device for corn seeds. *Transactions of the Chinese Society of Agricultural Machinery*, Vol 52, Issue3, pp. 153-159+177, China;

[5] Tamilselvi P., Manohar Jesudas D., (2016), A Study on Physical Properties of Pelleted Carrot (*Daucus carota.* L) Seeds. *Advances in Life Sciences*, Vol. 4, pp. 1220-1224, India;

[6] Rogovskii I.L., Titova L.L., Trokhaniak V.I., Marinina, L.I. Lavrinenko, O.T. Bannyi O.O.., (2020) Engineering management of machine for formation of artificial shell on seed vegetable cultures. *INMATEH - Agricultural Engineering*, Vol.61, Issue 2, pp. 165-174, Romania;

[7] Shao Z., Chen Z., Hou Z., Mi L., Qiu Y., (2018), Seed pelletizing movement characteristics of BYW-400 wheatgrass seed vibration pelletizing coating machine. *Transactions of the Chinese Society of Agricultural Engineering,* Vol.34, Issue 3, pp. 57-64, China;

[8] Sun Z., Li S., Yuan Y., (2017), Design and experiment of pelleting device for tomato seed coating. *Agricultural Mechanization Research*, Vol.39, Issue 6, pp. 162-169, China;

[9] Taylor A.G., Allen P.S., (2008), Bennett M. A. Seed enhancements. *Seed science research*, Vol.8, Issue 2, pp.245-246, USA;

[10] Xiong T., Lin Q., Feng X., (2019), Degradation dynamics of chlorfenapyr after pelleting and its control on Phyllotreta striolata. *Acta Entomologica Sinica*, Vol 56, Issue4, pp. 826-831, China;

[11] Xing J., Xu L., Ma S., Yuan Q., Chen C., Zeng J., Niu C., (2019), Development of laser orientation and embryo recognition device for horse-tooth shaped corn seed tip. *Transactions of the Chinese Society of Agricultural Engineering*, Vol.35, Issue 3, pp. 52-59, China;

[12] Zhu M., Chen H., Li Y., (2012), Retrospect and prospect of seed processing industry in China. *Transactions of the Chinese Society of Agricultural Engineering*, Vol 28, Issue2, pp. 1-6, China;

[13] Wang L., Hu C., He X., Guo W., Wang X., Hou S., (2021) A general modelling approach for coated cotton-seeds based on the discrete element method. *INMATEH - Agricultural Engineering*, Vol 63, Issue1, pp. 221 -230, Romania.

EXPERIMENTAL STUDY ON NON-PLANAR SCREENING DEVICE FOR BUCKWHEAT THRESHING MATERIAL
/
荞麦混合脱出物非平面筛分装置试验研究

Rong FAN [1], Qingliang CUI [1*)], Qi LU [2], Huaming HOU [1], Decong ZHENG [1,3]
[1)] College of Agricultural Engineering, Shanxi Agricultural University, Taigu 030801, / China;
[2)] Chinese Academy of Agricultural Mechanization Science, Beijing 100083, / China;
[3)] Research centre of Shanxi modern agricultural facilities and equipment, Taiyuan 030031, / China
Corresponding author: Qingliang CUI
Tel: +(86)18404981210.; E-mail: sxau_fr@126.com

ABSTRACT

Structural and motion parameters of screen surface have an important impact on the screening quality. In order to reduce the loss rate and impurity rate of buckwheat threshing material in the screening process and improve the screening performance of the vibrating screen, the planar square hole sieve, round hole sieve, non-planar convex-column sieve, pit sieve, and wave sieve were designed. Screening test was conducted on buckwheat threshing material under different screen structure based on the discrete element method (DEM). The results showed that the screening effect of convex-column sieve was the best, followed by pit sieve, and they were better than the traditional planar sieve. In single factor screening test of convex-column sieve, the ratio and height of convex column have significant influence on screening performance. Convex column rate, convex column height in a certain range were advantageous for screening. The results can lay a foundation for the determination of optimal parameter of screen structure and motion, and also provide a theoretical basis for the design of screening and cleaning equipment for buckwheat.

ABSTRACT

筛面结构参数和运动参数对筛分质量有重要影响。为了进一步降低荞麦混合脱出物在筛分过程的损失率、含杂率，提高振动筛的筛分性能，本文设计了平面方孔筛、圆孔筛，非平面凸柱筛、凹坑筛、波浪筛，并基于离散元法进行了荞麦混合脱出物不同筛面结构下的筛分试验。结果表明：在振动参数相同的情况下，非平面凸柱筛面的筛分效果最好，凹坑筛面次之，但均优于传统的平面圆孔筛和方孔筛。在凸柱筛面筛分试验中，凸柱率和凸柱高度对筛分性能影响显著。凸柱率、凸柱高度在一定范围内对筛分有利。所得结论可为最优筛面结构和运动参数组合的确定奠定基础，同时，亦能为荞麦混合脱出物的筛分、清选装置的设计提供理论依据。

INTRODUCTION

Buckwheat has a high nutritional value and health function, recognized by FAO as a crop used for food and medicine *(FAO, 2014)*. The improvement of its yield and quality has been a concern at world level *(Germ M. et al., 2020)*. The planting area and yield in China rank second in the world. The demand for buckwheat is increasing year by year, but the corresponding development of industrialization and mechanization is slow. The existing harvesting machinery is challenging to meet the needs of buckwheat harvesting; significantly, the quality of the cleaning process should be enhanced *(Ji J. et al., 2016)*.

Buckwheat is an infinite raceme crop so that its growth and development are different from those of cereal crops. In harvesting process, the maturity of the same plant is not consistent, so it is difficult for the combine to harvest. Especially in the cleaning process, the threshing material of high moisture content can be easily accumulated on the sieve surface, and it is not easy to stratify and penetrate through the sieve, resulting in poor screening quality. Even an air-screen cleaning device broadly exploited in grain harvesting is difficult to accomplish an effective screening for buckwheat threshing material. The problems of high screening loss and impurity in buckwheat mechanical harvesting still exist, which seriously affects the economic benefits and restrict the growth of buckwheat industry.

---

[1] *Rong FAN, M.S. Stud. Eng.; Qingliang CUI, Prof. Ph.D. Eng.; Huaming HOU, Lecturer M.S. Eng.; Decong ZHENG, Prof. Eng.*

[2] *Qi LU, M.S. PhD candidate. Eng.;*

[3] *Decong ZHENG, Prof. Eng. Chief of Research Centre*

Generally, material screening is a complex random process. Many factors are affecting the material passing through the screen. The most critical factors are the material properties, structures, and kinematic parameters of the screening device *(Zhao Y. et al., 1999)*. At present, the vibrating screening device mostly adopts a crank connecting rod mechanism *(Li H. et al., 2011; Li J. et al., 1997)*. The motion track of the sieve surface is single, easy to block, so it has poor adaptability to materials. Considering these problems, both homeland and abroad investigators have carried out much research on changing the motion form of the sieve body as well as the screening surface structure.

Regarding alternating the movement form of sieve, *Shen et al., (2012; 2011),* and *Wang et al., (2012),* had proposed and developed multi-dimensional parallel vibrating sieve with variable degrees of freedom, and carried out methodical research on the motion law and the screen motion trajectory. *Li et al., (2016),* examined the movement process of particles on the screening surface of a multi-dimensional vibrating sieve and stated that the four-dimensional vibrating sieve would have the best screening permeability.

Concerning research on the sieve structure, *Deng et al., (2013),* and *Li et al., (2016),* elaborated the design of non-planar sieve surface and its multi-dimensional penetration principle. Subsequently, they compared the screening performance of parallel vibrating sieve and traditional linear vibrating sieve by experiment. Both conventional planar and non-planar sieve surfaces were taken into account in their studies. The obtained results showed that the screening efficiency of the combination of parallel vibrating screen and non-planar sieve would be higher than that of the combination of straight and planar screens. *Cleary et al. (2009)*, simulated the operation of an industrial double-layer banana screen by DEM to examine the influence of energy transfer and absorption between particles on the screening efficiency. *Bellocp et al., (2017)*, proved that the rotary sieve would have a higher screening efficiency for materials with soft wet agglomeration such as millet.

The screening efficiency of the parallel vibrating sieve mentioned above has been improved, however, its structure is complex and the costs are high. Additionally, sieve of other forms applied to screening operation for coarse cereals has not been addressed in the literature. Herein, screening of buckwheat threshing material based on three kinds of non-planar sieves is planned to be examined, focusing on the sieving performance of convex-column sieve. The main aim is to reduce the loss rate and impurity rate in buckwheat-combined harvest cleaning, and thereby, a theoretical basis for the design of buckwheat combined harvester is established.

MATERIALS AND METHODS
Structural Design and Operation Principle

The structure model of the screening device has been presented in Fig.1. During the screening, the vibrating screen vibrated to and from under the drive of the vibrating mechanism. The buckwheat mixture came into the screen surface from the stepped shaking plate and moved backward. In the movement process, the grains in the mixture fell into the grain collecting box through the sieve, while the short stems moved to the outlet along the sieve and slid into the residual collecting box. The separation of grain and stem was realized, and the screening operation was completed.
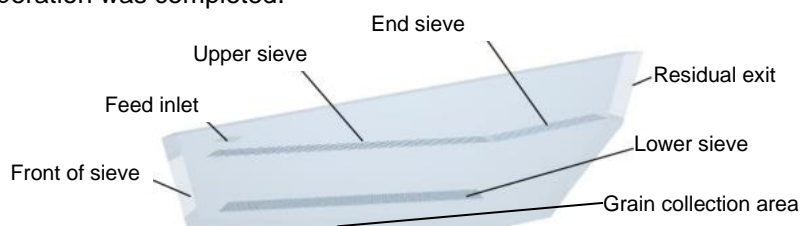
Fig. 1 - Cleaning device

Test materials

The understudy buckwheat threshing material (Heifeng No.1) consisted of test materials taken from the school experimental field. A complete feed combine harvester (XG788S) was exploited for harvesting. The harvested grains were obtained in the silo during the harvesting process, and the mixture was received under the threshing drum. It was found that the combine harvester could remove leaves, petals, dust, and other impurities effectively, however it was difficult to eliminate short stems. Therefore, this experiment only considered the separation of the mixture composed of grains and short stems.

Based on the material analyses, the weight ratio of the buckwheat grain and short stem in the mixture to be cleaned was 2.14:1. According to this ratio, the test materials were obtained (Fig. 2c).

In the mixture, the water content of buckwheat grains was 17.68%, and the grain density was 2540 kg/m³, while the water content of stems was 61.11%, and the density was 570 kg/m³. The grains and stems are shown in Fig. 2(a), 2(b). The buckwheat grains had triangular pyramid shape, and the shape of short stems was elliptical cylinder. By measurement and statistical analysis, the average dimension of the buckwheat grains was 5.90 mm in height, 3.94, 3.92, and 3.93 mm in three bottom edges. The average sizes of the stems in length, width, and thickness were 79.0, 2.95, and 2.77 mm, respectively.

| (a)Buckwheat grain | (b) Short stems | (c) Buckwheat threshing material |
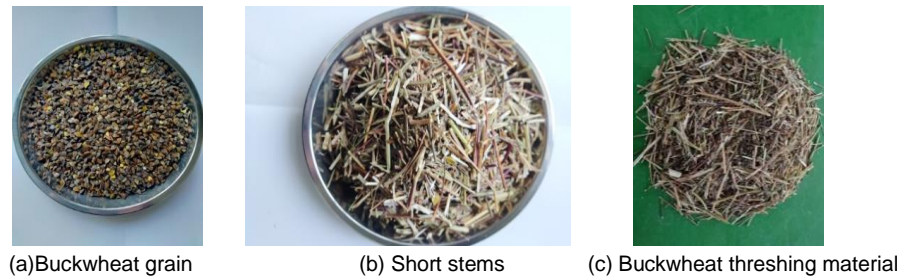
Fig. 2 - Test materials

The sieve structure

In this test, the upper sieve was designed. The round hole sieve (RS) and the square hole sieve (SS) were of planar punching screening surface. Three kinds of non-planar sieve surfaces (convex-column, pit, and wave sieves) were taken into account. According to the specifications of the testbed, Pro/E was employed to design the sieves. The screen frame was made from stainless steel with dimensions 1600×860 mm, its surrounding was covered with a 15 mm edge, and the screen surface's thickness was 2 mm. Let us consider the triaxial dimensions of the buckwheat grains would be less than 8 mm. By this view, the hole size of the upper sieve was controlled to be 8 mm in diameter or length, and the opening rate would be 62%. The lower sieve adopted a round hole sieve of 6 mm diameter. The screen models of the round and square hole sieves have been presented in Fig. 3(a) and 3(b).

| (a) Round hole sieve | (b) Square hole sieve | (c) Concave sieve |

| (d) Convex-column sieve | (e) Object of convex-column sieve | (f) Wave sieve |
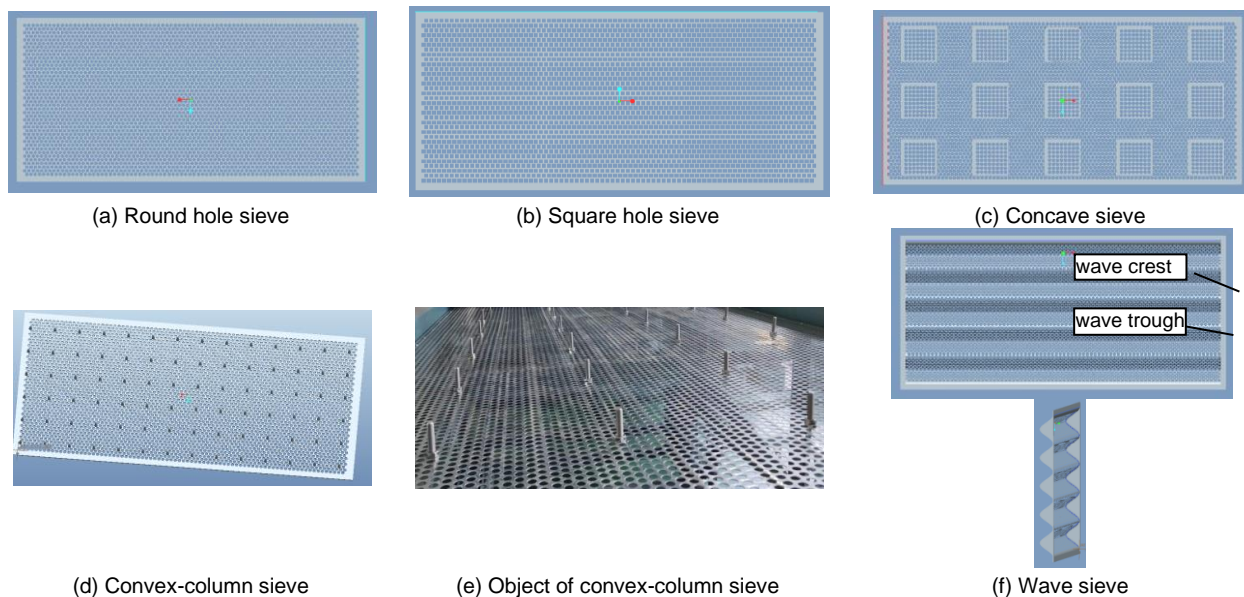
Fig. 3 - Physical models of vibrating screen

The non-planar convex-column sieve

The non-plane convex-column sieve (CCS) was composed of a flat baseplate (i.e., a round hole screen), convex columns, and a screen frame. The convex columns (bolts of M8) were arrayed on the baseplate and fixed by nuts through the screen holes. The layout of the convex columns would have a specific impact on the screening operation; hence, the convex column ratio and the height were commonly exploited to characterize the convex-column screen structure. The convex-column ratio (ρ) was defined as the ratio of the total number of convex columns to the total number of sieve holes:

$$\rho = M / N \times 100\% \tag{1}$$

where: M was the number of convex columns and N was the total number of sieve holes. The convex column height represented the length of the bolt higher than the screen surface, denoted by h.

According to the pre-test results, the convex-column ratio was about 1.0% (one convex column was arranged with 18 holes and 9 holes in order along the length and width directions of the sieve), and the convex-column height was 23 mm. The simulation model as well as the physical drawings were also demonstrated in Fig. 3(d), 3(e).

The non-plane concave sieve

The concave sieve (CS) was a screen with an array of square pits processed on the square hole sieve. In the present scrutiny, 15 square pits of side length 180 mm and of depth 10 mm were designed on the square hole sieve to form a concave screen surface. The simulation model had been shown in Fig. 3(c).

The non-planar wave sieve

The longitudinal section of the wave sieve (WS) was wavy, usually formed by bending a round hole screen with an appropriate width. It formed a curvy surface with five crests and five troughs of radius 30 mm. The simulation model was presented in Fig. 3(f).

Screening performance evaluation

The screening loss rate (S) and the grain impurity rate (H) are usually used as evaluation indexes for screening performance. In the simulation experiment, the grain quantity was counted by using grid cell group instead of grain collecting box and miscellaneous collecting box, and the particle quality was calculated indirectly. The screening loss rate (S) and the grain impurity rate (H) were defined by:

$$S = m_a / (m_a + m_b) \times 100\% \tag{2}$$

$$H = m_c / (m_c + m_b) \times 100\% \tag{3}$$

Where: m_a was the weight of grains discharged from the residual outlet, g. m_b represented the weight of grains under the sieve, g. m_c denoted the weight of stem under the sieve, g.

Methods of DEM simulation tests

Simulation model and parameter setting

The simulation models (Fig.4) for the buckwheat grains and stems were established in EDEM 2.7 according to the material dimensions given in "Test materials". Hertz-Mindlin (no-slip) contact model was implemented, which had been successfully exploited in grain screening and cleaning *(Li Y. et al., 2007; Wu Z. et al., 2019; Li J. et al., 2013).* The simulation parameters were determined by combining the results of the discrete element simulation of agricultural materials at homeland and abroad and the parameters of stainless steel *(Fan R. et al., 2021; Hou H., 2019; Sun J., 2019; Keppler I. et al., 2012; Boac J., 2010).* (See Table 1)
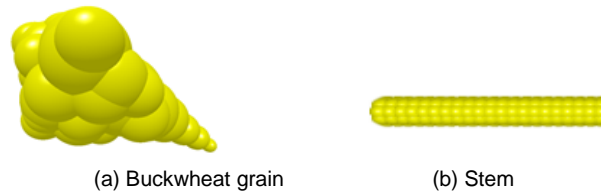
(a) Buckwheat grain   (b) Stem
Fig. 4 - Models of simulation

Table 1

Simulation parameters and values

Parameters	Values	Parameters	Values
Poisson's ratio of buckwheat	0.290	Restitution coefficient of buckwheat-buckwheat	0.260
Poisson's ratio of stem	0.400	Restitution coefficient of stem-screen	0.360
Poisson's ratio of screen	0.300	Coefficient of static friction of buckwheat-buckwheat	0.482
Shear modulus of buckwheat [MPa]	34.325	Coefficient of static friction of buckwheat-stem	0.611
Shear modulus of stem [MPa]	5.500	Coefficient of static friction of buckwheat-screen	0.446
Shear modulus of screen [MPa]	70000	Coefficient of static friction of stem-stem	0.600
Density of buckwheat [kg/m^3]	2540	Coefficient of static friction of stem- screen	0.500
Density of stem [kg/m^3]	570	Coefficient of rolling friction of buckwheat-buckwheat	0.290
Density of screen [kg/m^3]	7800	Coefficient of rolling friction of buckwheat-stem	0.505
Restitution coefficient of stem-stem	0.160	Coefficient of rolling friction of buckwheat-screen	0.235
Restitution coefficient of buckwheat-stem	0.220	Coefficient of rolling friction of stem-stem	0.460
Restitution coefficient of buckwheat-screen	0.500	Coefficient of rolling friction of stem-screen	0.300

Sieving simulation test for different sieve surface types

The established models were imported into EDEM2.7 one by one. The material properties, contact parameters, and motion parameters were added. Let us set the surface inclination angle to 5°, screen surface

amplitude to 25 mm, vibration direction angle to 6°, and vibration frequency to 3.33 Hz (corresponding crank speed 200 r/min). When the feeding amount rate was set to 0.5 kg/s, the production rate of grains and stems in order were 0.34 and 0.16 kg/s. According to the motion of the stepped shaking plate, the speeds of the material that went into the screen were determined (the horizontal and the vertical sub-speed were 0.433 and 0.25 m/s, respectively). The particle generation and the simulation times in order were 1 s and 5 s. Fig. 5 presents the screening simulation process of the convex-column sieve.
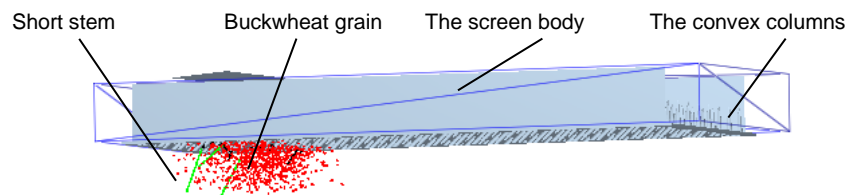
Fig. 5 - Screening simulation process of convex-column sieve

Simulation test of single factor screening based on convex-column sieve

      The screening tests were performed according to Table 2. The factors and levels were preliminarily determined by production practice. For instance, the convex-column ratio was determined by pre-test results. The empirical values of other three factors were selected to make the screening process proceed smoothly and had the slightest influence on the dependent variables. The test procedure and other parameters were the same as the sieving simulation test of different screen surfaces in the previous section.

Table 2

Factors and levels of screening test of convex-column sieve surface

No.	Convex-column ratio / (%)	Convex-column height / (mm)	Amplitude / (mm)	Vibration frequency / (r/min)
1	0.267, 1.000, 1.714, 2.500, 3.286	23	25	200
2	1.000	3, 13, 23, 33, 43	25	200
3	1.000	23	15, 20, 25, 30, 35	200
4	1.000	23	25	160, 180, 200, 220, 240

RESULTS

Simulation tests of various sieve surfaces

      The screening test results of buckwheat threshing material for five types of screening surface are provided in Fig. 7.
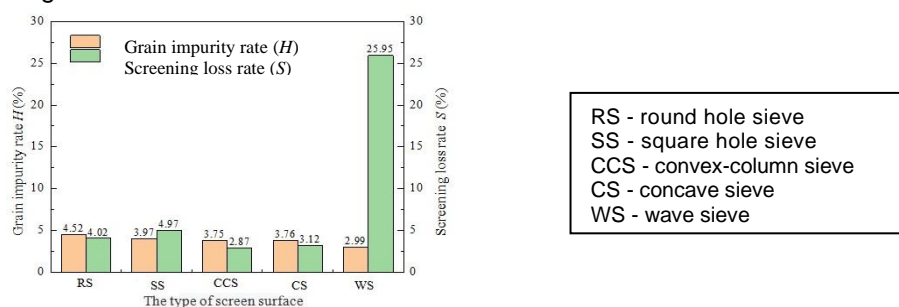
Fig. 7 - Simulation results of five screening surface types

      In the figure, we can see that the wave sieve had a smaller impurity rate but the largest loss rate. The impurity rate and loss rate of convex column sieve and pit screen were smaller, they were smaller than the round and square hole screen. On the whole, the screening performance of a non-planar sieve (except wave sieve) would be obviously better than that of a planar sieve under the current test conditions. It is worth mentioning that the wave sieve had a larger loss rate, as high as 25.95%, while the convex-column and the pit sieves had a lower loss and impurity rate. For the case of wave sieve, the stems were primarily concentrated in the trough of the wave sieve, which blocked the sieve holes. As a result, the grains in the trough could not pass through the sieve and mixed in the stems, flowing out of the cleaning chamber and resulting in a considerable loss rate. During pit sieve operation, the whole sieve box evolved into a large screen box composed of several small shallow sieve boxes, which could provide three directions (up and down, front and back, left and right) for materials to pass through the screen, that was, the sieve had three-dimensional sieve penetration *(Shen H. et al., 2012)*.

This structure indirectly lead to the growth of the effective screening area, resulting in a significant reduction of the congestion of the screen; however, it is challenging to design, process, and it is not economical.

In the operation of the convex-column sieve, although the effective screening area was reduced by the convex columns, it loosened and prevented the accumulation of crops with high moisture content during screening. Particularly in the sieve's forepart, the convex column's loose effect was significant since the materials can be easily stratified, not simply blocked, and the screening effect was good.

Single-factor tests based on the convex-column sieve

The screening test results of convex-column screen under single-factor are shown in Fig.8-11. According to Fig. 8, by increasing the convex-column ratio, the screening loss firstly decreased and then grew. Additionally, the grain impurity rate increased considerably for the convex-column ratio in the range of 0.267%~2.5% and slightly lessens when the convex-column ratio varied from 2.5% to 3.286%. For the case of the convex column ratio equal to 2.5%, the maximum impurity rate and the minimum loss rate in order were 3.9% and 2.64%.

In the simulation process, it is found that the loosening effect of the convex column on the material became weak as the convex column ratio increased, and the grains easily mixed in the stems with the screen to push back and out of the cleaning room, resulting in growing losses.
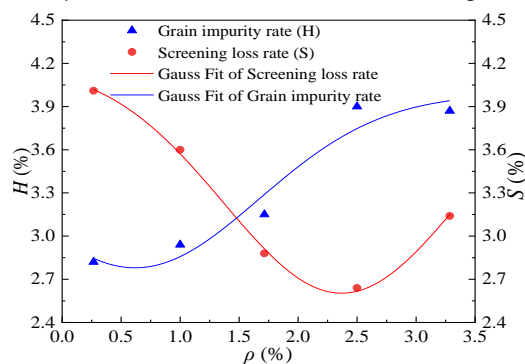
Fig. 8 - Loss and impurity rates under different convex-column ratio
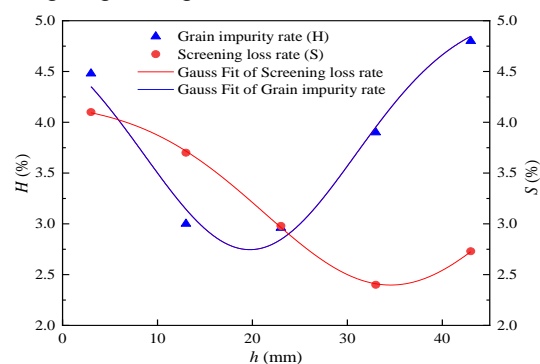
Fig. 9 - Loss rate and impurity rate under different convex-column height

Based on Fig.9, when the height of the convex column was equal to 3 mm, the impurity rate and the loss rate would be 4.48% and 4.10%, respectively, and the screening effect was close to that of the round hole sieve. When the convex column height was 3 mm, the loose effect on the material was not noticeable, and the convex-column sieve was similar to the punching sieve. A short-term accumulation of mixed materials was observed during the simulation when they fell on the vibrating screen. Some stems passed through the sieve due to the applied vibration, while some grains moved to the end sieve under the sieve pushing and fell into the impurity collecting box, causing losses. As a result, the rates of both impurities and losses were high. By growing the convex-column height, the material layer is loose in the height direction, and the material is stratified and screened better; therefore, the amount of loss is reduced, and the impurity became slightly high.

However, when the height increases to a specific range, the movement resistance of the material would increase, and some parts of stems would penetrate the sieve pore openings, growing the impurity yield. At the same time, a tiny part of the grain mix in the stem and finally enter into the impurity collecting box with the stem, resulting in a slight rise of the loss.

As can be seen from Fig.10, when the amplitude varied from 15 mm to 35 mm, both loss and impurity rates decreased in the first branch and then increased as the amplitude magnified. For the case of amplitude equal to 25 mm, the impurity and loss rates were small.

By increasing the vibration amplitude, the movement amplitude of the material on the sieve surface increased as well, and the material would be in a better motion state. The grain went through the sieve holes, the stem moved to the end of the sieve, went into the impurity collection box; therefore, the rates of both impurities and losses would be low.

When the amplitude continued to increase, the movement range of the material on the sieve surface was getting bigger and bigger. The grains jumped to the end of the sieve and jumped out of the cleaning chamber, while parts of the short stem fell into the collecting box through the sieve due to the vibration effect; hence, the grain loss rate increased significantly while the impurity rate slightly grew.
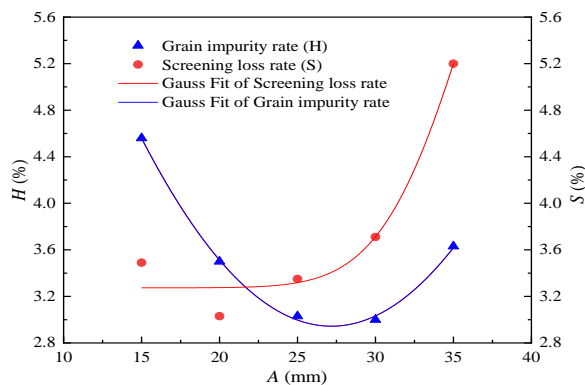
Fig. 10 - Loss rate and impurity content under different amplitude
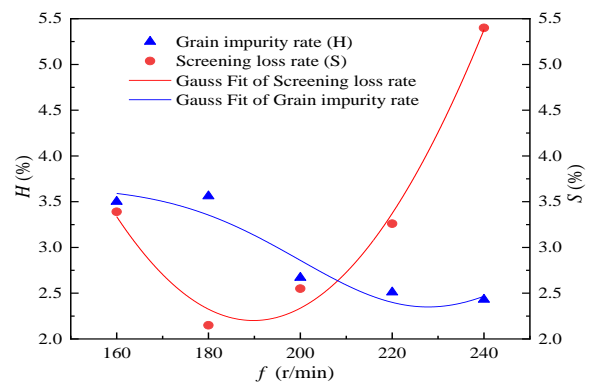
Fig. 11 - Loss rate and impurity rate under different frequency

During the screening process based on the plotted results in Fig. 11, by an increase of the vibrating screen frequency from 160 r/min to 240 r/min, the plot of the grain impurity rate demonstrated a decreasing branch after a slight increase, while the grain loss first decreased and then increased.

For the case of vibration frequency equal to 160 r/min, a considerable loss rate was detectable. This was mainly because of the fact that the smaller frequency resulted in fewer grain beat on the sieve surface and a lower chance of passage through the sieve. By increasing the vibration frequency, the collision times of materials and sieve surface increased. Hence, the probability of sieve penetration increased, the loss rate decreased, while the impurity rate would slightly increase. With the further increase of frequency, the movement of the material on the sieve surface would intensify; that is, the retention time of the stem on the sieve surface would lessen, and the short stem cannot easily penetrate the sieve pores, so the impurity rate would continuously reduce. Nevertheless, buckwheat grains moved faster and faster to the end of the sieve, leading to the loss of grains directly, and thereby, the loss rate rose sharply.

CONCLUSIONS

(1) The performance of the non-planar sieve (excluding wave sieve) was generally better than that of the planar circular hole sieve and square hole sieve under the same motion parameters. The screening effect of non-planar convex column sieve was the best, its impurity rate and loss rate were 3.75%, 2.87%, respectively, followed by the pit sieve, its impurity rate and loss rate were 3.76%, 3.12%, respectively.

(2) The convex-column height, convex-column ratio, vibration frequency, and amplitude all had a certain influence on the quality of screening operation. The convex-column ratio and height significantly influenced the screening performance, and they were of high benefit to the sieving in a particular range. For the sieving of buckwheat threshing material at the harvest stage, the appropriate ranges of the height and the convex-column ratio in order were 13~33 mm and 1.0%~2.5%.

(3) As the moisture content of the mixture decreased in the test, the sieving performance of the convex-column sieve would lessen and even hinder the screening of materials. The moisture content range of the material associated with the superior screening performance of the convex-column sieve is still required to be determined through further tests.

ACKNOWLEDGEMENT

REFERENCES

[1] Bellocq B., Ruiz T., Delaplace G., (2017), Screening efficiency and rolling effects of a rotating screen drum used to process wet soft agglomerates. *Journal of Food Engineering*, Iss.195, pp.235-246. USA.

[2] Cleary P.W., Sinnott M.D., Morrison R.D., (2009), Separation performance of double deck banana screens-part 2: quantitative predictions. *Minerals Engineering*. Vol.22, Issue 14, pp.1230-1244, Cornwall/UK.

[3]   Dai F., Zhao W.Y, Song X.F., et al., Parameters Optimization and Experiment on Separating and Cleaning Machine for Flax Threshing Material. *(胡麻脱粒物料分离清选作业机参数优化与试验)*, *Transactions of the Chinese Society for Agricultural Machinery*, 2020, Vol.51, Issue 7, pp.100-108, Beijing/China.

[4]   Deng J.M., Shen H.P., Li J., (2013), Design and experiment for three-dimensional parallel kinematics vibration sieve. *Transactions of the Chinese Society for Agricultural Machinery*, Vol.44, Issue 11, pp.342-346,328, Beijing/China.

[5]   Fan R., Cui Q.L., Zhang Y.Q. et al., (2021), Analysis and calibration of parameters of buckwheat grain. *INMATEH - Agricultural Engineering*, Vol.64, No. 2, pp.467-476, Bucharest/Romania.

[6]   Germ M., Rvay J., A Vollmannová, et al., (2020), Hydrothermal treatments affecting the concentration of neochlorogenic acid in dough of Tartary buckwheat. *Agriculture*, Vol.10, Issue 12, pp.601-608, USA.

[7]   Hou H.M., (2019), *Experimental study on cleaning dynamic characteristics of coarse cereals crops harvested by machinery (杂粮作物机械收获清选动力学特性研究)*, PhD Dissertation. Shanxi Agricultural University, Taiyuan/China.

[8]   Ji J.T., Li X.P., Ji X. et al. (2016). Present Situation, Technical Analysis and Equipment Demand of Harvesting Mechanization for Characteristic Coarse Cereals. *(特色杂粮收获机械化现状、技术分析及装备需求)*, *Agricultural Engineering*, Vol.6, Issue 6, pp.1-3, Beijing/China.

[9]   Keppler I., Kocsis L., Oldal I., (2012), Grain velocity distribution in a mixed flow dryer. *Advanced Powder Technology*, Vol.23, Issue 6, pp.824-832, Amsterdam/Netherlands.

[10]   Li H.C., Li Y.M., Tang Z., (2011), Numerical simulation and analysis of vibration screening based on EDEM. *(基于 EDEM 的振动筛分数值模拟与分析)*, *Transactions of the CSAE*, Vol.27, Iss.5, 117-121, Beijing/China.

[11]   Li J.P., Zhao Y. (1997). Experiment and Computer Simulation of Tossing Motion of Agricultural Materials on Oscillating Sieve. *(物料在振动筛面上抛起的计算机模拟和实验研究)*, *Transactions of the CSAE*. Vol.13, Issue 4, pp.46-48, Beijing/China.

[12]   Li J., Wang Z.B., Shen H.P., (2016), Experiment and analysis of parallel vibrating sieve with convex column screen surface on grain screen. *Machine Design and Research*, Vol.23, Issue 9, pp.150-154,158, Beijing/China.

[13]   Li J., Zhao D.A., Shen H.P., Deng, J. M. (2008). Research on Screening Effect of Grain Three Dimensional Parallel Vibrating Screen Based on DEM. *China Mechanical Engineering*, Vol.23, Issue 9, pp.28-32, Beijing/China.

[14]   Li J., Zeng Q.F., Deng J.M., (2016), Screening Process Analysis for Multi-dimensional Parallel Vibrating Screen and Optimization of Screen Surface Movement. *Transactions of the Chinese Society for Agricultural Machinery*, Vol.47, Issue 17, pp.399-407, Beijing/China.

[15]   Li Y.M., Wang Z.H., Xu L.Z., (2007), Motion analysis and experimental research of rape extractions on vibration sieve. *Transactions of the CSAE*, Vol.23, Issue 9, pp.111-114, Beijing/China.

[16]   Shen H.P., Wang X.X., Deng J.M., (2012), Experimental comparison study on screening performance between parallel vibrating screen and linear vibrating screen. *Mining & Processing Equipment*, 40, 79-83.

[17]   Shen H.P., Xue C.Y., Zhang J.T., (2011), A Novel PKM Based Vibrating Sifter and Its Screening Efficiency Experimental Study, *13th World Congress in Mechanism and Machine Science*. pp. 19-25, Guanajuato/México.

[18]   Shen H.P., Zhang J.T., He B.X., et al., (2011), Sifter efficiency and experimental study on a new type of vibrating sifter based on PKM. *Mechanical Design*, Vol.28, Issue 2, pp.83-86, Beijing/China.

[19]   Sun J.X. (2019). *Study on biomechanical characteristics and damage mechanism of coarse grain. (杂粮籽粒生物力学特性及损伤机理研究)*, PhD Dissertation, Shanxi Agricultural University, Taiyuan/China.

[20]   UN Food & Agriculture Organization (FAO). (2014), *Production of Buckwheat by countries*. http://faostat.fao.org/site/339/default.aspx.

[21]   Wang X.X., (2012), *Experimental Study on Screening of Parallel Vibrating Screen with Non-planar Screen Surface. (非平面筛面并联振动筛的筛分实验研究)*, MSc dissertation. Changzhou University, Jiangsu/China.

[22]   Wu, Z.C. (2019). *Design and Experiment of Curved Screen for Cleaning Maize in Harvester. (玉米收获机曲面清选筛设计与试验)* PhD Dissertation. Northeast Agricultural University, Harbin, Heilongjiang, China.

OPTIMAL DESIGN OF THE SURFACE OF THE HIGH-SPEED REVERSIBLE PLOW
/
高速翻转犁犁体曲面优化设计

Yichuan HE[1), Can HU[1,2), Qiaonan YANG[1), Xufeng WANG*[1), Xuan ZHENG[3), Huanjun YANG[3), Yaming LIU[1)   [1]

[1) College of Mechanical and Electrical Engineering, Tarim University, Alar 843300 / China;
[2) College of Engineering, China Agricultural University, Beijing 100085 / China;
[3) Mechanical Equipment Research Institute, Xinjiang Academy of Agricultural and Reclamation Science, Shihezi 832000 / China
Tel: +86 13779803762; E-mail: wxfwyq@126.com

ABSTRACT

The farmland in Xinjiang of China is mainly sandy loam soil, on which the crops are subject to flat planting with mulched film. Before planting, the soil should go through deep ploughing in a short operation period, thus there is high demand on the high-speed plow and it is necessary to optimize the plow based on tillage resistivity to improve its working performance. In view of optimal design of the surface of high-speed reversible plow, simulation test was adopted to optimize the resistivity model, then finite element method was used to test the force condition of the plow. At last, the tillage resistivity of the plow after optimization was tested by soil bin test. Test results showed that, at tilling depth of 300 mm, tilling speed of 12 km/hm, and when the plow height was 250 mm with cutting angle of 37° and dozer angle of 84°, the plow achieved the optimal tillage resistivity and the optimal combination was 2.85 N/cm²; at tilling depth of 300 mm, soil moisture content of 17%, and soil compactness of 220 N/cm², the maximum tensile stress on the surface of the plow was 115.61 MPa and total deformation was 2.869 mm; the maximum flexible strain of the plow was 9.38×10^{-4}. Soil bin test showed that, at tilling depth of 300 mm, dozer angle of 84°, the optimized high-speed reversible plow reduced the tillage resistance by 17.9% compared with common high-speed reversible plow made in China, and can provide reference to the design of high-horsepower tractors.

摘要

新疆农田以沙壤土为主，农作物采用覆膜平作方式，播前土壤均需要深耕作业，作业周期短，对高速犁体有较大需求，需要针对耕作比阻进行高速犁体优化，以提升国产犁的作业性能。本文针对高速翻转犁犁体曲面优化设计问题，采用仿真试验方法优化犁体比阻模型，利用有限元方法验证犁体受力情况，最后，通过土槽试验测试优化后犁体的耕作比阻。结果表明：当耕深深度为 300mm，耕作速度为 12km/h，犁体高度为 250mm，起土角为 37°，推土角为 84°，犁体具有最佳的耕作比阻，最优组合为 2.85 N/cm²；在作业深度为 300mm，土壤含水率为 17%，土壤坚实度为 220N/cm²，犁体曲面所受最大拉应力为 115.61Mpa，犁体总变形为 2.869mm，犁体最大弹性应变为 9.38×10⁻⁴；土槽试验结果也表明，当作业深度为 300mm，耕作速度为 12km/h，犁体高度为 250mm，起土角为 37°，推土角为 84°，优化后的高速翻转犁犁体比普通国产高速翻转犁犁体的耕作阻力低 17.9%，优化后的高速翻转犁犁体可为国产大马力拖拉机犁提供设计参考。

INTRODUCTION

Plow body is the main working component of reversible plow in high-speed working, and the parameter optimization of plow surface (*Yang & Yang, 2003*) directly affects tillage quality and traction resistance and affects the working speed of plow. Experts in China and abroad have carried out a great deal of studies on the optimization design of plow surface (*Hou, 1981*). *A. Ibrahmi et al. (2015)* studied the surface of plow body and did force analysis on the plow bottom by computer by taking Bezier surface as the basic construction model; *Mouazen et al. (2010)* did simulation analysis on the performance of moldboard plow. *Zhao & Mei (2010)* did simulation analysis on the surface of high-speed plow body; Gan, Sun, & Cheng (2008) developed 1FFSL-5 type reversible plow to realize shallow ploughing and deep digging in tillage. *He et al. (2016)* designed a 1LF-550 grille type hydraulic overturn and amplitude modulation plow, which has simple structure and results in low resistance and avoids soil blocking.

---

[1] *He Yichuan, A. Prof.; Hu Can, A. Prof. Ph.D.; Yang Qiaonan ; Wang Xufeng, Prof. Ph.D.; Zheng Xuan, Prof.;
Yang Huanjun , A. Prof.; Liu Yaming*

The surface of the plow is a complicated multi-space geometric surface (*Lin et al., 2016*), thus it is difficult to study the characteristics of the surface based on digital soil bin laboratory and field tests. The farmland in Xinjiang of China is mainly sandy loam soil, and plants such as cotton are subject to flat planting with mulched film. Before planting, the soil should go through deep ploughing in a short operation period, thus high-powered high-speed plow should be chosen in tillage. At present, plow body made by developed countries such as Reken (*Hu et al., 2020*) and Gregoire Besson were mainly adopted in Xinjiang for high horsepower tractors, and the agricultural machinery market in China lacks such advanced plows. Besides, the plows developed in other countries are not specially designed according to the soil conditions in Xinjiang, so totally optimized plow body has not been adopted in high-speed operation and thus it is not suitable for the plow operation in Xinjiang. It is of great significance to design a kind of high-speed plow suitable for farmland in Xinjiang and optimize the structural parameters and improve the working performance of the plow body of high horsepower tractors.

By taking the plow body of high-speed reversible plow as the object of study, resistivity parameters of the plow were adopted for orthogonal test, then the significance of force factors of the plow were analyzed by MATLAB and the optimal parameter values of different factors were obtained to analyze the force condition of the plow under specific soil humidity, compactness and adhesive force. Then the plow surface model was drawn by Solidworks, and simulation analysis was done on the plow surface by ANSYS, and the stress distribution diagram of the plow surface was established to analyze the shape variation of the surface and the influence of different factors on traction resistance, at last, the plow was designed to reduce the specific resistance of the plow body tillage and increase the plow body tillage speed.

MATERIALS AND METHODS
Optimization model of the plow surface
The main factors affecting the tillage resistivity of the plow include dozer angle, cutting angle, soil covering angle and plow height. It has been proved that the tillage resistivity of the plow is closely associated with parameters such as plow height, soil covering angle, cutting angle and dozer angle, and the equation of tillage resistivity is:

$$F_T = C_0 + C_1 x_1 + C_2 x_2^2 + C_3 x_1 x_2 + C_4 x_2 x_3 + C_5 x_2 + C_6 x_3 \qquad (1)$$

where F_T is tillage resistivity; x_1 is cutting angle; x_2 is dozer angle; x_3 is plow height; and $C_0, C_1, C_2, C_3, C_4, C_5, C_6$ are constants.

By taking the tillage resistivity on the plow during stable tillage operation as test index, and plow height A, soil covering angle B, cutting angle C, dozer angle D were taken as test factors, the software Solidworks was used for modeling and the model was imported into ANSYS for four-factor three-level orthogonal test (Zhang et al., 2019; Li & Hu, 2005). Without considering the interaction, the ANSYS simulation experiment analysis was carried out. In the simulation test, the tillage speed was 12 km/h and the tillage depth was 300 mm. According to theoretical analysis, the variation ranges of the four factors were: plow height in 200-240 mm, soil covering angle in 55°-750°, cutting angle in 30°-36°, dozer angle in 74°-90°; the test was repeated three times to calculate test errors. The factors and levels of the orthogonal test are shown in Table 1, and test result analysis is shown in Table 2.

Table 1

Factors and levels of the orthogonal test

Level	Plow height [mm]	Soil covering angle [°]	Cutting angle [°]	Dozer angle [°]
1	240	75	36	90
2	220	65	33	82
3	200	55	30	74

Table 2

Test result analysis

Test No.	A	B	C	D	Tillage resistivity (N·cm⁻²)
1	1	1	1	1	0.90
2	2	2	2	1	0.84

Test No.	A	B	C	D	Tillage resistivity (N·cm^{-2})
3	3	3	3	1	0.82
4	3	2	1	2	0.73
5	1	3	2	2	0.92
6	2	1	3	2	0.89
7	2	3	1	3	0.85
8	3	1	2	3	0.76
9	1	2	3	3	0.94
K_1	2.79	2.57	2.51	2.56	
K_2	2.59	2.54	2.54	2.84	
K_3	2.32	2.61	2.65	2.88	
k_1	0.93	0.86	0.84	0.85	
k_2	0.86	0.85	0.86	0.95	
k_3	0.77	0.88	0.90	0.96	
Range Rj	0.16	0.03	0.04	0.11	
Influence order of factors	A>D>C>B				
Optimal level	A_3	B_2	C_1	D_1	
Optimal combination	$A_3D_1C_1 B_2$				

It can be seen from the range analysis in Table 2 that, the influence order of factors is A, D, C, B, and the optimal combination is $A_3B_2C_1D_1$. Since the soil covering angle had the slightest influence on tillage resistivity, in order to simplify analysis, soil covering angle can be ignored, in this way, the relationship between plow height A, cutting angle C and dozer angle D with tillage resistivity should only be considered. Therefore, the following regression equation can be established:

$$y = 1.43704 + 0.08332x_1 + 0.00007x_2^2 - 0.00113x_1x_2 + 0.00049x_2x_3 + 0.01391x_2 + 0.00344x_3 \quad (2)$$

where, x_1 is cutting angle, x_2 is dozer angle and x_3 is plow height.

The software origin was used to establish the regression equation, and results showed that the significance level was 95%, showing great significance. The regression equation of tillage resistivity is shown in Table 3.

Table 3

Results of coefficients of regression equation

Tillage resistance	b6	b5	b4	b3	b2	b1	b0
Regression coefficient	0.00344	0.01391	0.00049	-0.00113	0.00007	0.08332	1.43704

Establishment of the target function

Taking the tillage resistivity of the high-speed reversible plow as the object of study, and the design variables being: plow height, cutting angle and dozer angle, then the regression equation was established after simulation analysis and the objective function was obtained.

The design variable X=[x_1,x_2,x_3]^T=[cutting angle, dozer angle, plow height]^T

Minf(x)=y=1.43704+0.08332x_1+0.00007x_2^2-0.00113x_1x_2+0.00049x_2x_3+0.01391x_2+0.00344x_3

Constraint conditions

Plow height: g6(x)=200-x_3≤0 ; g5(x)=x_3-240≤0.

Dozer angle: g4(x)=74°-x_2≤0 ; g3(x)=x_2-90°≤0.

Cutting angle: g1(x)=x_1-36°≤0 ; g2(x)=30°-x_1≤0.

Mathematical model of the tillage resistivity of the plow

     $Minf(x) = y = 1.43704 + 0.08332x_1 + 0.00007x_2^2 - 0.00113x_1x_2 + 0.00049x_2x_3 + 0.01391x_2 + 0.00344x_3$

     $X = [x_1, x_2, x_3]^T$

     $s.t.\,g_m(x) = 0 (m = 1,2,3……6)$

Advantages of the tillage resistivity of the plow

     The edited codes are imported into the code editor of MATLAB and:

     Function f=fun(x)

     $F(x) = y = 1.43704 + 0.08332x_1 + 0.00007x_2^2 - 0.00113x_1x_2 + 0.00049x_2x_3 + 0.01391x_2 + 0.00344x_3$

     The edited codes are saved into the fun.m text, and the MATLAB software was used to solve the optimal combination of tillage resistivity, and:

     1b=[30;75;25];

     ub=[37;84;20];

     x0=[33;83;27]

     [x,fn]=fmincon(@fun,x,[],[],[],[],1b,ub}

     fprintf(1,`f=%3.4f\n`,fn)

     fprintf(1,`x3=%3.4f\n`,x(3))

     fprintf(1,`x2=%3.4f\n`,x(2))

     fprintf(1,`x1=%3.4f\n`,x(1))

     And the optimal solution is: $X_3 = 20.0000$; $X_2 = 84.0000$; $X_1 = 37.0000$; f=2.85KPa。

     Results showed that, when limit depth was 300 mm, tillage speed was 12 km/h, plow height was 250 mm, cutting angle was 37°, dozer angle was 84°, the plow had optimal tillage resistivity, which was 2.85N·cm-2. It can be obtained after comparing with the analysis table that, the optimized tillage resistivity was reduced by 22.7% at most, and 8.96% at least.

Design of the plow surface
Lead curve graphing

     In order to reduce the resistivity of the high-speed reversible plow, taking the high-speed reversible plow, made in China, as an example, and by referring to the plow surface design method in the Agricultural Machinery Design Manual (*Chinese Academy of Agricultural Mechanization Sciences, 2007*) and the conclusion drawn in section 2 of this paper, the maximum designed tilling depth was 300 mm, the maximum cutting angle was 37°, the maximum dozer angle was 84°, the maximum plow height was 250 mm, and the maximum tillage speed was 12 km/h. Lead curve is the guide line to determine the location of the horizontal straight line, and lead curve in the shape of parabola is mainly used in the design of plow surface. In this paper, according to tilling depth, the straight-line segment length S was determined to be 45 mm, and the parabola part of the lead curve was drawn based on the envelop method (*He, He, & Yang, 2019; Zhou et al., 2019*), as shown in Fig.1.
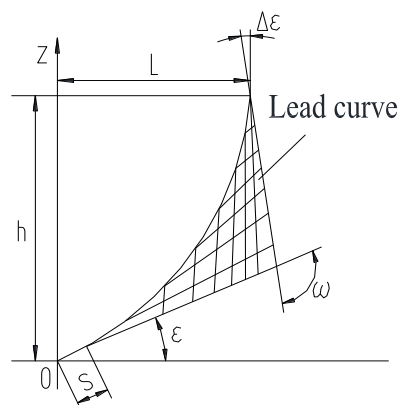
Fig. 1 - Lead curve

$$L = C_7 b(cos\,\Delta\varepsilon - sin\,\varepsilon) \tag{3}$$

$$h = l\left(\frac{cos\,\varepsilon + sin\,\Delta\varepsilon}{cos\,\Delta\varepsilon - sin\,\epsilon}\right) \tag{4}$$

$$\omega = \frac{\pi}{2} + \varepsilon - \Delta\varepsilon \tag{5}$$

where: L is the openness degree;

C_7 is a constant;

b is width;

$\Delta\varepsilon$ is the buckling angle of the lead curve;

ε is the installation angle of the plow blade;

h is the height of the lead curve;

ω is the angularity of tangent line of the end point. In order to improve the ground-breaking efficiency of the plow, reduce the tillage resistivity, improve the tillage speed and reduce tillage wastage,

ε was determined to be 37°.

C_7 is a constant, generally in the range of 1.0-1.7. If smaller value is taken, the soil crushing effect would be enhanced, however, the soil turning effect is reduced with higher resistance.

In order to ensure the tillage quality, C_7=1.2.

Establishment of a 3D model

The software SOLIDWORKS was used to establish a 3D model of the plow surface. First, a reference datum was chosen to draw the sketch for plough blade line and the lead curve, then the "boundary-surface" command was used to generate a smooth surface, and finally a 3D model of the plow surface is finished, as shown in Fig. 2.

Fig. 2 - 3D model of the plow

Finite element modeling

The 3D model of the plow surface drawn in SOLIDWORKS was converted into x-t format, and imported into the ANSYS workbench platform for finite element static analysis. In ANSYS software, the material property of the plow body was determined to be carbon steel and the material property was rigid body, as shown in Fig 2. In analysis, the range of tillage speed was set to be 10-12 km/h, and limit depth was 300 mm, and on this basis, the force analysis was carried out on the plow surface. Then mesh generation was carried out to generate 6129 quadrilateral meshes with 13365 mesh points, as shown in Fig. 3; then a load of 2572 N was applied to the surface of the plow body, as shown in Fig. 4.
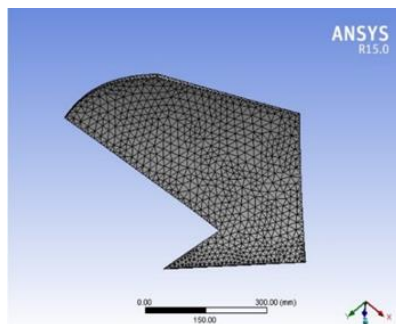
Fig. 3 - Mesh generation diagram   **Fig. 4 - Load application to the plow body**
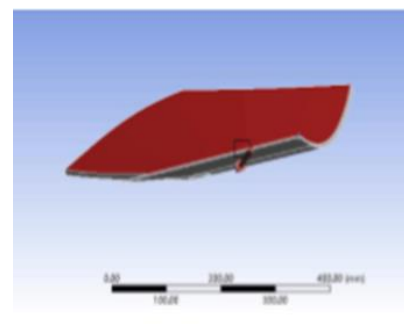
Static characteristics analysis of the plow body

The plow body model was solved by the Block Lanczos method in ANSYS software by modal analysis. The Block Lanczos method has high calculation accuracy and requires short convergence time. According to (*Sun, Liu, & Yang, 2020; Zhao et al., 2019*), the low-order modal may have a relatively large impact on the vibration of the system, and only the first few natural frequencies and modal shape cloud nephograms are required.

The modal diagrams of each order of the plow body were solved by ANSYS software, the natural frequencies of the first 6-order plow body are shown in Table 4.

Table 4

Natural frequencies of first 1-6 orders of the plow body

Orders	Natural frequency (Hz)
1	71.54
2	111.66
3	167.80
4	237.52
5	341.59
6	374.06

The plow modal shape nephogram of the first six orders is shown in Fig. 5.

(a) First order modal shape nephogram

(b) Second order modal shape nephogram

(c) Third order modal shape nephogram

(d) Fourth order modal shape nephogram

(e) Fifth order modal shape nephogram

(f) Sixth order modal shape nephogram
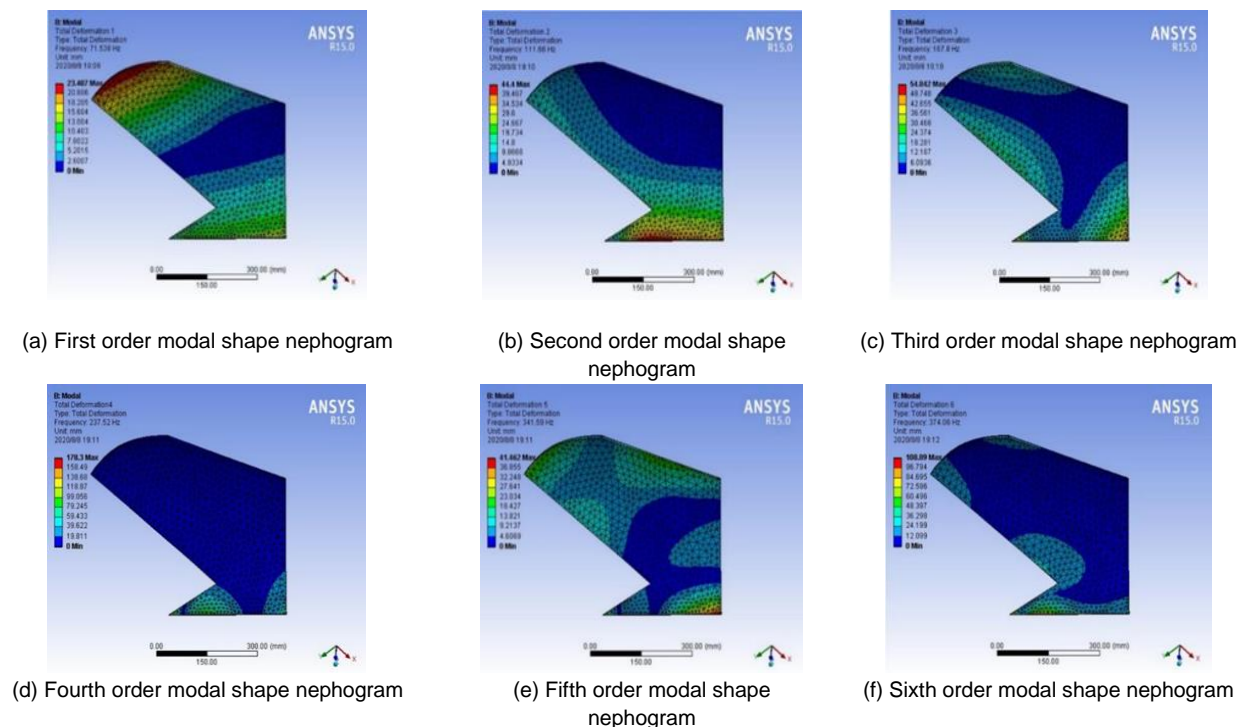
Fig. 5 - Plow shape nephogram of the first six orders of modals

The stress and strain analysis of the plow body was carried out by the ANSYS software. When the tillage speed was 12 km/h, the limit depth was 300 mm, the soil moisture content was 17%, and the soil compactness was 220 KPa, stress distribution of the plow body surface is shown in Fig. 6.

(a) Total deformation nephogram of the plow body

(b) Equivalent strain nephogram of the plow body

(c) Equivalent stress nephogram of the plow body
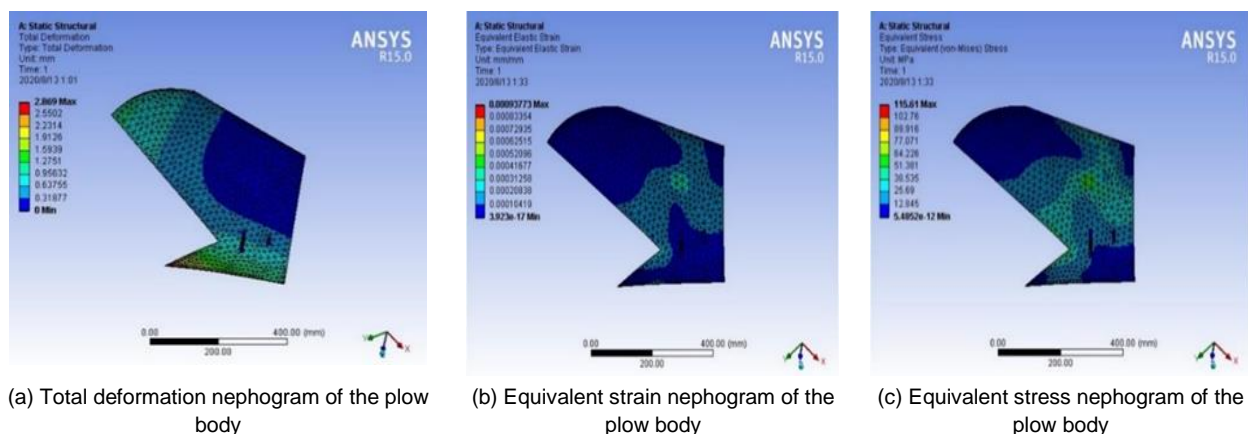
Fig. 6 - Stress distribution of the plow surface

According to Fig. 6a, the nephogram for the first order modal shape, the total deformation of the plow body was 2.869 mm, and according to the analysis of the equivalent strain nephogram of the plow body in Fig. 6b, the maximum elastic strain was 9.38×10^{-4}; according to the equivalent stress nephogram of the plow body in Fig. 6c, the maximum equivalent stress of the plow body was 115.61 MPa.

RESULTS AND DISCUSSIONS
SOIL BIN TEST

In order to verify the results of the ANSYS static simulation test and the working performance of the optimized high-speed reversible plow, the soil bin test was carried out in the soil bin laboratory of Tarim University, Alar, Xinjiang, China. As shown in Fig. 7, the test sample machine was the optimized high-speed reversible plow. As shown in Fig. 8, the power of the test was driven by the soil bin vehicle (*Zhao et al., 2020*), and the soil bin size was 120m×8m×1m (length×width×height), the test soil was the sandy loam, which is common in south Xinjiang. The average surface flatness was 23.9 mm, the average plant density was 305 g/m^2, and average soil compactness was 225 KPa, and average absolute moisture content of soil was 14.6%.

Test instruments include a straightedge (1 m), a tape measure (5 m), RL-AL type electronic level (Qingdao Rulan Electronics Co., Ltd., with accuracy of 0.002°), portable intelligent tension meter, balance, soil compactness meter (Zhejiang TOP Instrument Co., Ltd., TJSD-750Ⅱ type, ±0.5%FS), soil moisture content meter (Zhejiang TOP Instrument Co., Ltd., TZS-2X type, ±0.01%), fuel consumption meter (Hai-land Intelligent Technology Co., Ltd., with comprehensive accuracy ±0.05%), and electronic second chronograph.

At the beginning of the test, the tillage depth was controlled to be 300 mm by adjusting the depth wheel, the test was carried out based on National standard Moldboard Plough-Test Method (GB/14225.3-93) and Moldboard Plough-Technical Requirements (GB/T14225.2-93) and related reference (*Wei et al., 2020*).

Fig. 7 - Ground surface condition before the test

Fig. 8 - Optimized high-speed reversible plow

The test results obtained in the soil bin laboratory showed that, the traction on the optimized high-speed reversible plow and common high-speed reversible plow made in China was 2227 N and 2572 N, respectively; and the tillage resistances were 34.2 KPa and 40.3 KPa respectively; the tillage resistance on the optimized high-speed reversible plow was 17.9% lower than that on the common high-speed reversible plow made in China. The tillage quality indexes such as coverage rate, soil crushing rate, oil consumption of the optimized high-speed reversible plow was better than that of the common high-speed reversible plow made in China, thus the optimized plow could meet the national standard in terms of working performance.

Table 5

Soil bin test of the optimized high-speed reversible plow

No.	Tillage resistance (kPa)	Traction force (N)	Tilling width (mm)	Tilling depth (mm)	Soil crushing rate (%)	Tillage speed (km/h)
1	33.5	2254	314	297	79.1	10.25
2	348.	2184	315	298	80.1	10.25
3	33.6	2279	320	295	79.6	10.26

Table 5
(continuation)

Soil bin test of the optimized high-speed reversible plow

4	35.1	2365	315	294	79.4	10.25
5	34.3	2279	310	296	79.3	10.24
6	33.9	1985	315	290	79.4	10.25
7	34.5	2019	316	285	78.5	10.25
8	35.2	2308	318	301	78.9	10.24
9	33.1	2281	315	300	79.2	10.24
Mean value	34.2	2227	315	295	79.2	10.25
Extreme value	2.1	380	10	11	0.16	0.02

Table 6

Soil bin test results of the common high-speed reversible plow made in China

No.	Tillage resistance (KPa)	Traction force (N)	Tilling width (mm)	Tilling depth (mm)	Soil crushing rate (%)	Tillage speed (Km/h)
1	40.1	2497	311	284	75.8	10.25
2	40.5	2563	305	298	73.4	10.25
3	39.6	2580	308	286	74.8	10.26
4	39.8	2631	301	294	74.2	10.25
5	42.2	2587	302	296	75.4	10.24
6	40.7	2491	311	292	75.1	10.25
7	40.5	2581	304	297	74.4	10.25
8	38.9	2687	304	298	76.3	10.24
9	40.3	2534	297	292	75.1	10.24
Mean value	40.3	2572	304	293	74.9	10.25
Extreme value	3.3	196	14	14	0.29	0.02

CONCLUSIONS

(1) In this paper, a kind of high-speed reversible plow suitable for tillage in farmlands in South Xinjiang in China was designed. The plow can reduce tillage resistivity through changing the structure of the plow. When the limit depth was 300 mm, tillage speed was 12 km/h, the influence of different factors of the plow body on tillage resistivity was analyzed, and plow height had very significant influence on tillage resistivity. Both dozer angle and cutting angle had significant influence on tillage resistivity.

(2) The established quadratic response surface regression equation for the resistivity showed that, in tillage, when depth limit was 300 mm, tillage speed was 12 km/h, cutting angle was 37°, dozer angle was 84°, plow height was 250 mm, then the plow had the optimal tillage resistivity, which was 2.85 N·cm^{-2}. Compared with the results of numerical analysis, the tillage resistivity could reduce resistance by 8.96%~22.7%, showing that the structural parameters could meet the processing requirements.

(3) The finite element static simulation test showed that, when tillage speed was 12 km/h, depth limit was 300 mm, soil moisture content was 17% and soil compactness was 220 KPa, the total deformation of the plow surface was 2.869 mm, and the maximum elastic strain on the plow surface was 9.38×10^{-4}, the maximum stress on the plow surface was 115.61 MPa.

(4) Soil bin test showed that, the actual depth of the plow was basically consistent with the depth limit, also, the stability of the tilling depth was kept above 95%, so the working performance could meet the agronomic requirements.

ACKNOWLEDGEMENT

REFERENCES

[1]　Chinese Academy of Agricultural Mechanization Sciences. (2007). *Agricultural Machinery Manual (Vol. I)*. Beijing: China Agricultural Machinery Press.

[2]　Ibrahmi, H. Bentaher, M. Hbaieb, et al. (2015). Study the effect of tool geometry and operational conditions on moldboard plough forces and energy requirement: Part 2. Experimental validation with soil bin test. *Computers & Electronics in Agriculture, 117*(C):268-275.

[3]　Gan, L., Sun, D., & Cheng, H. (2008). Design of 1FFSL-5 type shallow-deep flip plow. *Journal of Agricultural Mechanization Research*, (05),136-138. (in Chinese)

[4]　Gao, H., Chen, X., Xue, J., & Gao, Q. (2020). Factor analysis of influencing factors of tractor operating resistance. *Journal of Agricultural Mechanization Research*, *42*(10):17-22. (in Chinese)

[5]　He, J., Chen, X., Zheng, X., & Wen, H. (2016). Design of 1LFT-550 modulated hydraulic turnover strip plough. *Journal of Chinese Agricultural Mechanization, 37*(05), 27-30. (in Chinese).

[6]　He, Y., He, J., & Yang, Z. (2019). Discrete element simulation and parameter optimization of plow surface. *Journal of Agricultural Mechanization Research, 41*(12):189-193+257. (in Chinese)

[7]　Hou, Z. (1981). Some issues in the study of plow surface. *Transactions of the Chinese Society of Agricultural Engineering,* 03, 74-85.

[8]　Hu, C., Shi, G., Liu, Y., Wang, X., & Zheng, X. (2020). Field testing test of Reiken 1LFTT-550 hydraulic turn-over high speed plough. *Journal of Agricultural Mechanization Research, 42*(06):160-165. (in Chinese).

[9]　Lan, F., Cui, Y., Su, Z., et al. (2012). Design and test on shelling and sorting machine of camellia oleifera fruit. *Transactions of the Chinese Society of Agricultural Engineering (Transactions of the CSAE), 28*(15), 33-39. (in Chinese with English abstract)

[10]　Li, Y., & Hu, C. (2005). Test design and data processing. Beijing: Chemical Industrial Press.

[11]　Li, Y., Meng, P., Geng, D., He, K., Meng, F., & Jiang, M. (2016). Intelligent system for adjusting and controlling corn seeding depth. *Transactions of the Chinese Society for Agricultural Machinery, 47*(s1): 62-68. (in Chinese)

[12]　Lin, J., Wang, L., Li, B., et al. (2016). Design and test of 2ZZ-3 type deep scarification-terrace ridge-fertilization combine intertill machine. *Transactions of the Chinese Society of Agricultural Engineering (Transactions of the CSAE), 32*(24):9-17. (in Chinese)

[13]　Lin, J., Zhang, T., Chen, B., Han, W., Lv, Q., & Wang, J. (2019). *Transactions of the Chinese Society for Agricultural Machinery, 50*(02):28-39. (in Chinese)

[14]　Liu, M., Li, C., Zhang, Y., Yang, M., Hou, Y., & Gao, L. (2013). Performance Test of Walnut Shelling Using Flexible-belt and Differential Velocity Extrusion. *Transactions of the Chinese Society for Agricultural Machinery, 47*(9):99-107. (in Chinese with English abstract)

[15]　Mahmoodi-Eshkaftaki M, Ebrahimi R, Ghanbarian D, et al. (2017). Geometric characterization of moldboard plough using coupled close photography and surface fitting model. *Soil and Tillage Research*, 170:122-129.

[16]　Mouazen A M, Miklós Neményi, Schwanghart H , et al. (1999). Tillage Tool Design by the Finite Element Method: Part 2. Experimental Validation of the Finite Element Results with Soil Bin Test. *Journal of Agricultural Engineering Research, 72*(1):53-58.

[17]　Song, P., Zhang, J., Li, W., Zhang, X., & Fang, X. (2011). Real-time monitoring system for accuracy of precision seeder. *Transactions of the Chinese Society for Agricultural Machinery, 42*(2), 71-74. (in Chinese)

[18]　Wei, G., Zhang, Q., Liu, L., Xiao, W., Sun, W., & Liao, Q. (2020). Design and Experiment of Plowing and Rotary Tillage Buckle Device for Rapeseed Direct Seeder. *Transactions of the Chinese Society for Agricultural Machinery, 51*(6), 38-46. (in Chinese)

[19]　Yang, M., Yang, L., Li, Q., & Chen, J. (2003). Agricultural mechanization system of rice production of Japan and proposal for China. *Transactions of the Chinese Society of Agricultural Engineering, 19*(5), 77-82 (in Chinese with English abstract).

[20]　Yang, Q., & Yang, W. (2003). Working out optimization model of high-speed moldboard plow surface by using improved genetic algorithm. *Transactions of the Chinese Society of Agricultural Engineering (Transactions of the CSAE),* (01):80-83. (in Chinese).

[21]　Yang, Y., Ye, Y., Xie, J., Cao, X., & Sun, C. (2016). Study on the Tensile Test and Analysis of Winter Mulching. *Journal of Agricultural Mechanization Research, 38*(06): 215-218 (in Chinese with English abstract).

[22] Zhai, L., Ji, C., Ding, Q., & Yu, Y. (2013). Optimized design of plough body structural and working parameters. *Transactions of the Chinese Society for Agricultural Machinery, 2013,44*(08):57-62. (in Chinese)

[23] Zhang, K., Li, J., Song, Z., Liu, X., & Liu, L. (2019). Optimum design and test of variable diameter double disc air suction precision seeder. *Transactions of the Chinese Society for Agricultural Machinery, 51*(06):38-46. (in Chinese)

[24] Zhao, J., Wang, A., Ma, Y., Li, J., Hao, J., Nie, Q., Long, S., & Yang, Q. (2019). Design and test of soil preparation machine combined subsoiling, rotary tillage and soil breaking. *Transactions of the Chinese Society of Agricultural Engineering (Transactions of the CSAE), 35*(08):46-54. (in Chinese).

[25] Zhao, W., Huo, X., Wang, W., Wang, H., Tang, J., & Wu, Y. (2020). Design and test of subsoil shovel strain acquisition system. *Journal of Chinese Agricultural Mechanization, 41*(03), 147-151+200. (in Chinese)

[26] Zhao, Y., & Mei, W. (2010). On parametric design of plough body surface by using VC and Pro/Toolkit. *Journal of Chinese Agricultural Mechanization*, (03), 71-74. (in Chinese)

[27] Zhou, J., Zhang, L., Tan, L., He, Z., & Zhong, G. (2019). *Journal of Mechanical Strength, 41*(02):400-406. (in Chinese)

[28] Sun, J., Liu, C., & Yang, P. (2020). Structure analysis of paver frame based on finite element method. *Journal of Mechanical & Electrical Engineering, 37*(07):841-844. (in Chinese)

DESIGN AND EXPERIMENTAL OPTIMIZATION OF VEGETABLE SURFACE RESIDUAL FILM RECYCLING MACHINE

/

蔬菜地表层残膜回收机的设计与试验研究

Peng WANG, Xiongwei LIU, Jianming JIAN*), Jinyan TIAN, Renjie XING, Shulin HOU
College of Engineering, China Agricultural University, Beijing 100083 / China;
Tel: +86-18701535953.; E-mail: jamesjian@126.com

ABSTRACT

To solve the problems such as low film recovery rate and high soil content of the recovered film of the surface residual film recycling machine, the parameters of the vegetable surface residue recycling machine were optimized. After modelling and theoretical analysis of the loosening shovel and film sweeping device, the key structural parameters of the machine were determined. The Box-Behnken Design analysis test results in Design-Expert were used to establish the comprehensive effects of speed, rotational speed, and angle of membrane picking device on the recovery and soil content. Then MATLAB was adopted to analyse the law of the comprehensive influence of three factors on two responses. The most significant factor affecting pickup net rate J was rotational speed Y_2, and the most significant factor affecting soil percentage was the angle Y_3 of the film picking device. By optimizing the experimental results by Design-Expert, the optimum operating parameters of the machine were obtained as follows: the forward speed of the machine was 3.2 km/h, the revolution speed was 10.5 r/s, the angle of the film picking device was 65.4°, the scavenging rate J and soil rate H of the residual film recycling machine were 87.084% and 10.382%, respectively.

摘要

为解决残膜回收机起膜率低、回收的残膜含土率高等问题，对蔬菜地表层残膜回收机进行参数优化。对起膜铲和扫膜装置建模和理论分析，确定该机具关键结构参数。利用 Design-Expert 中的 Box-Behnken Design 分析试验结果，建立速度、转速和挑膜装置角度对回收率和含土率的综合影响效应。运用 MATLAB 对三因素对两响应的综合影响规律进行分析得出结论：对拾净率 J 影响最显著的因素为转速 Y_2，对含土率影响最显著的因素是挑膜装置角度 Y_3。通过 Design-Expert 对实验结果进行优化，得到机具的最佳作业参数：机具前进速度为 3.2km/h，转速为 10.5 r/s，挑膜装置的角度为 65.4°，残膜回收机的拾净率 J 和含土率 H 分别为 87.084%、10.382%。

INTRODUCTION

Since the 1970s, plastic film mulching technology has been introduced from abroad to China and applied to agricultural production, providing China's solutions and strength for solving world food security problems *(Zhao et al., 2017; Li &Ma, 2014)*. The application of plastic film mulching technology has the function of heat preservation and moisture preservation, which is conducive to the propagation of microorganisms in the soil, speeding up the conversion of organic matters into inorganic matters, preventing waterlogging, and inhibiting the growth of weeds in plum rain season, so as to improve the crop yield *(Zhou, Tang & Xie, 2019; Zhang et al., 2013)*. So far, plastic film covering technology has been popularized and used in China for 40 years, and the usage and coverage area of plastic film rank first in the world *(Li, 2017)*. However, residual film pollution causes serious damage to the ecosystem. When seen from a microscopic perspective, the plastic film forms microplastics after weathering and decomposition, and then it is absorbed into the crops through the root system of plants, and some of the microplastics remain in the body after being eaten by humans, which harms human health *(An, 1996)*. When seen from a macroscopic perspective, the residual film winds the machine in the seeding process, which reduces the working efficiency.

At the same time, due to the inability to recover the residual film exposed on the soil surface, the problems such as choking caused by accidental ingestion of livestock often occur, bringing serious economic losses to farmers.

In the current Chinese market, there are many different types of residual film recycling machines, which can be divided into residual film recycling machines before seeding, residual film recycling machines during the seedling stage as well as residual film recycling machines after autumn according to different film lifting operation time *(Tian et al., 2018)*. The residual film recycling machine before seeding has been widely used, but because the residual film is seriously damaged in this stage, the residual film picking up rate is relative and the recovered residual film contains a large number of straws *(Chen et al., 2020)*. In China, residual film recycling mainly adopts two methods, including manual picking up and mechanized recycling. Manual picking up is characterized by high labour intensity and low efficiency, while mechanized recycling is characterized by high soil content and low scavenging rate. To solve the above problems, a film-soil separation residual film recycling machine was proposed, which can effectively reduce the soil content of the residual film and improve the cleaning rate of the machine.

MATERIALS AND METHODS
Overall structure

According to the characteristics of the vegetable land surface residual film *(Zhang et al., 2019)*, a surface residual film recycling machine was designed and manufactured. The structure of the whole machine was shown in Fig. 1. The residual film recycling machine mainly includes the reducer, loosening shovel, film sweeping device, traction device, film-soil separation device, film picking device, machine frame, machine box, film collection box, as well as depth-controlled device.

The tractor was connected with the power source tractor Dongfanghong-404 by using the mode of traction. The rear output shaft of the tractor was connected with the reducer of the residual film recycling machine to provide power, and the whole machine was powered by a chain drive and belt drive. When the machine was working, the loosening shovel scooped up the mixture of film and soil on the surface and swept the mixture to the film-soil separation device through the film sweeping device. Then the soil adhered to the film was shaken off by using the inertia of the device produced by the shaking. The film-soil separation machine moved upward and threw the residual film to the film picking device and caught the residual film through the film picking teeth on the device, and then the residual film was transported to the film collecting box as the film picking device moves upward. Since the film-soil separation device threw the residual film to the film picking device, the problem of difficult removal of the residual film due to the elastic tooth piercing was solved. When the film picking device transported the residual film to the upper end of the film collecting box, it fell off and into the film collecting box, thus improving the problem that the residual film winds the machine.
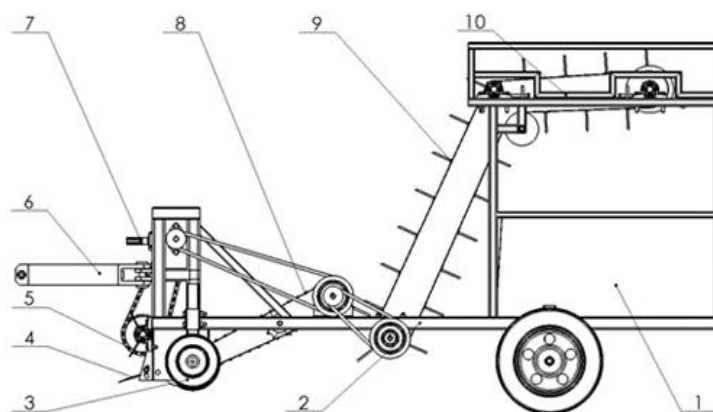
Fig. 1 - Schematic diagram of the physical design of vegetable surface residual film recycling machine
1. Film collecting box; 2. The frame of the machine; 3. Depth limiting device; 4. Loosening shovel; 5. Film sweeping device;
6. Traction device; 7. Reducer; 8. Film soil separation device; 9. Film picking device; 10. Machine box

Analysis of the angle of the loosening shovel

The stress diagram of the loosening shovel during the operation was shown in Fig. 2. The stress model of the loosening shovel unit was established by analysing the force of the loosening shovel unit. Taking the forward direction of the machine as the X-axis and the vertical direction as the Y-axis, the coordinate system was established, as shown in Figure 2, and then the stress analysis was conducted to the loosening shovel.

According to the analysis in Fig. 2, the gravity imposed on the film-soil mixture was G; the frictional force between the upper surface of the loosening shovel and the film-soil mixture was f. The normal load generated by the membrane soil mixture on the upper surface of the loosening shovel was Fn. The force needed to dig up the film-soil mixture along the loosening shovel was Ft. By analysing the stress condition during the operation of the loosening shovel, the stress balance equation of the loosening shovel was obtained as follows:

$$\begin{cases} f \sin\alpha - Fn \cos\alpha - G = 0 \\ Ft - Fn \sin\alpha - f \cos\alpha = 0 \\ f - \mu Fn = 0 \end{cases} \tag{1}$$
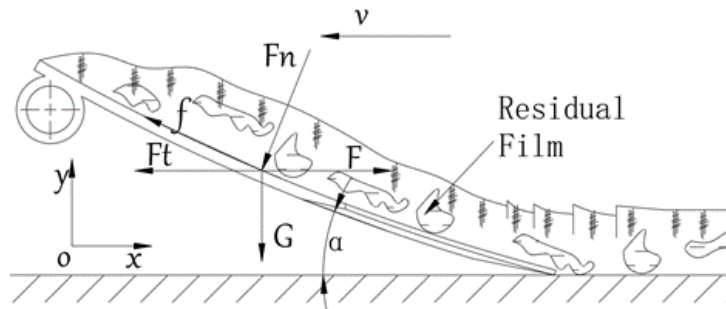
Fig. 2 - Schematic diagram of the entry angle of the loosening shovel
f - frictional force between the film-soil mixture and the upper surface of the loosening shovel, N;
F_n - normal load generated by the film-soil mixture on the upper surface of the loosening shovel, N;
G-gravity of the film-soil mixture itself, N; Ft - The force required to move along the loosening shovel to scoop up the film-soil mixture, N;

After analysing the resistance imposed on the loosening shovel, the soil resistivity was K, and the harder the soil texture was, the larger the coefficient would be. The soil area cut by the loosening shovel was S; the friction coefficient of the film-soil mixture on the loosening shovel $\mu = \tan\varphi$; the frictional angle of the film-soil mixture to the loosening shovel was φ, which was usually 30 ° ~ 36 °; the force required by the film-soil mixture to slip through the loosening shovel surface was P; the length of the loosening shovel was L; the soil density was ρ; by ignoring the impact of the moving speed of the machine on the resistance of the loosening shovel, resistance Ft could be expressed as *(Zhai et al., 2018)*:

$$Ft = P + Ps = SL\rho \tan(\alpha + \varphi) + Ks \tag{2}$$

By combining Formula (1) with Formula (2), the following formula could be obtained:

$$\alpha = \cot^{-1} \frac{\mu\ (SL\rho \tan(\alpha + \varphi) + Ks\ ) - G}{SL\rho \tan(\alpha + \varphi) + Ks - \mu G} \tag{3}$$

As shown in Formula (3), when the machines conduct residual film recycling, the larger the entry angle α was, the more the film-soil mixture scooped up by the loosening shovel would be, the greater the resistance generated would be, and the greater the force Ft required by the machine to dig up the film-soil mixture would be. When the buried angle was less than 25°, and at this time the resistance was relatively small *(Wang, 2010; Xue et al., 1987; Liu et al. 2018)*.

If the angle was too small, the soil breaking ability of the loosening shovel would be relatively poor *(Li, 2017)*. To adapt to different regions, soil texture, and soil moisture, the loosening shovel was designed into a fine-tuning structure, with an angle adjustment range of 23°~26°.

Analysis of the motion process of the film sweeping device

The heap soil condition is a common problem existing in the residual film recycling machine. To solve this problem, a film sweeping device was designed, as shown in Fig. 3.

By analysing the motion process of the film sweeping device, the influence laws of the film sweeping blades on the film-soil mixture were determined.
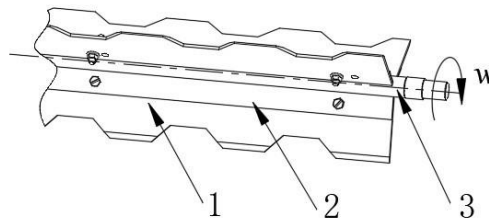
Fig. 3 - Partial diagram of the film sweeping device
1. Film sweeping blade; 2. Blade base; 3. Film sweeping spindle

Taking the axis of the film sweeping spindle as the origin, the operation direction of the machine as *X*-axis, and the direction perpendicular to the ground as Y-axis, the xoy rectangular coordinate system was established to analyse its motion process. In the process of residual film recycling operation, the machine moved along a straight line, and the film sweeping device carried out the film sweeping operation by rotating motion. The absolute motion of the film sweeping blade was synthesized by the above two motions.

By analysing Fig. 4, the absolute velocity of the film sweeping blades was obtained as follows:

$$v_1 + v_2 = v_0 \tag{4}$$

According to the basic principle of kinematics, the trajectory of point B of the film sweeping blade at any time could be obtained. Based on the analysis, the motion trajectory equation of the film sweeping blade at point B with time T could be obtained as follows:

$$\begin{cases} x = v_1 t + l\sin(\omega t) \\ y = -l\cos(\omega t) \end{cases} \tag{5}$$
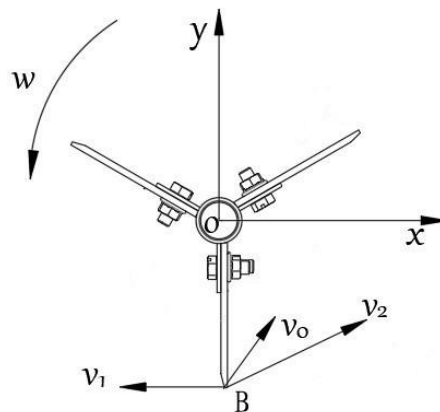
Fig. 4 - Motion trajectory analysis diagram of the film sweeping device
ω - angular velocity of the structure moving; v_1- the forward speed of the implement;
v_2- the rotating speed of film sweeping blades moving.

To obtain the motion velocity of point B of the film sweeping blade at time T, the derivative of t in formula (5) was obtained, and the motion velocity equation of point B of the film sweeping blade at any time was obtained as follows:

$$\begin{cases} v_x = v_1 + l\sin(\omega t) \\ v_y = \omega l\sin(\omega t) \end{cases} \tag{6}$$

By combining the above equations, the relationship among velocity v_x of point B at any time and the horizontal motion velocity v_1, angular velocity ω, and the distance l between point B of the film sweeping blade and the axis were as follows:

$$v_x = v_1 + \omega l \cos\cos^{-1}\frac{v_y}{\omega l} \tag{7}$$

According to Equation (7), the velocity v_x of point B at any time was mainly related to the machine's horizontal movement velocity v_1 and angular velocity ω. To further analyse the motion trajectory of point B of the film sweeping device, the film sweeping velocity ratio λ was introduced *(Deng et al., 2016; Zhao, & Wu, 2019).*

$$\lambda = \frac{v_2}{v_1} = \frac{\omega l}{v_1} \tag{8}$$

Substituting Formula (8) into Formula (5), then the following formula could be obtained:

$$x = \sqrt{l^2 - y^2} + \frac{l}{\lambda} cos^{-1} \left(-\frac{y}{l} \right) \tag{9}$$

According to Formula (9), point B of the film sweeping blade of the film sweeping device moved in a way of cycloid, and the sweeping velocity ratio λ was the determinant factor of the cycloid trajectory. Different velocity ratios would form different cycloid diagrams, thus affecting the film sweeping effect. Next, the cycloid diagrams under the situation for λ >1, B =1, and B <1 would be analysed. When v_2 was greater than v_1, namely, B >1, the trajectory was a trochoid. At this time, the film-soil mixture was thrown above the rear of the film sweeping device, which swept the film and alleviated the heap soil phenomenon, but the large amount of dust pollution generated by the throwing of a large amount of soil damaged the environment. When v_2 was smaller than v_1, the track was a short cycloid, namely, B <1, and at this time, the film sweeping effect could not be achieved as the angle and distance of the throwing of the film-soil mixture. When v_2 was equal to v_1, namely, B =1, the film sweeping blade could drop the film-soil mixture onto the separation device at a height of 45° to achieve the film sweeping effect.

Experimental materials

This prototype test was conducted in Gu'an County, Langfang City, Hebei Province. The harvested vegetable fields were selected as the test pilots, and the plastic film remaining on the surface of the field was mainly recovered. Fig. 5 shows the field experiment scene. The plastic film laid in the test field is a black plastic film with a thickness of 0.008 mm. The surface of the land contained a small number of weeds and vegetable leaves. The average moisture content of the soil was about 10.1%, and the test field was cohesive soil. After field investigation, the residual film was mainly buried in the surface soil or exposed on the surface, so in the test process, the machine mainly carried out the recycling test on the residual film on the surface.

Fig. 5 - Field test diagram

The main testing equipment includes a tractor Dongfanghong-404, vegetable surface film recycling machine, shovel, rotational speed meter, tape measure, electronic balance as well as an adjustable wrench.

Test indexes

To analyse the operation effect of the machine and test the stability and reliability of the operation, the picking up rate of the machine and the soil content of the residual film were taken as the test indexes *(Li, 2017)*, denoted as J and H, respectively. Next, these two indexes will be introduced, respectively.

Picking up rate: The ratio of the total film mass recovered by the machine and the total film mass in the soil before recycling is called picking up rate, which can be expressed in Formula (10):

$$J = (1 - D_1/D_2) \times 100\% \tag{10}$$

where:

J is the residual film pickup rate, %, D_1 is the total surface residual film mass after the residual film recycling operation, g, D_2 is the total surface residual film mass before the residual film recycling operation, g.

Soil content: The mass ratio of the total mass of the soil in the film collecting box to the residual film and soil is called soil content, which can be expressed by Formula (11):

$$H = (D_4 - D_3)/D_4 \times 100\% \tag{11}$$

where: H is soil content, %, D_4 is the total mass of soil and residual film in the film collecting box in a test field, g. D_3 is the total mass of residual film in the film collecting box in a test field, g.

Test parameters and methods

Table 1

Test factors and test levels

Level	Factor		
	Machine forward velocity (km/h)	rotational speed (r·s⁻¹)	The angle of PVC conveyer belt (°)
1	5	12	66
0	4	10.5	64.5
-1	3	9	63

According to the content described above, we took pickup rate J (%) and soil content rate H (%) as the two response values of the test. The forward speed of the machine (km/h), the rotational speed of the tractor (r/s), and the angle of the film picking device (°) were selected as the factors for the prototype test, which were denoted as Y_1, Y_2, and Y_3, respectively.

The speed of the output shaft of the Dongfanghong tractor was 9~12 r/s. The designed operating speed of the machine was 3 ~ 5 km/h, and the angle of the film picking device was 63°~66°. The test factors and horizontal coding table were determined based on the above data, as shown in Table 1. By combining different test factors, 17 groups of experiments were designed.

RESULTS
Experimental results

According to the three factors and two responses designed before, the test model of the three factors to the two responses was set up. Through analysing the influence laws of the three factors on the machine's performance, the main factors affecting the machine's pickup rate and soil content were obtained. Then the experimental results were optimized through the function Optimization in Design-Expert to optimize the experimental results, thus improving the operation effect of the residual film recycling machine.

Table 2

Field test results

Test number	Y₁ (km·h⁻¹)	Y₂ (r·s⁻¹)	Y₃ (°)	J (%)	H (%)
1	4	10.5	64.5	84.7	12.5
2	5	10.5	66	81.3	10.8
3	5	9	64.5	79.7	14.1
4	4	10.5	64.5	85.1	12.8
5	5	12	64.5	81.6	12.7
6	4	10.5	64.5	85.3	12.5
7	4	10.5	64.5	85.5	12.3
8	3	10.5	66	86.8	9.4
9	3	10.5	63	83.8	14.5
10	3	9	64.5	82.5	13.2
11	4	12	66	86.7	8.5
12	4	9	66	83.1	10.1
13	4	12	63	86.2	14.6
14	4	9	63	80.5	15.8
15	5	10.5	63	81.4	16.1
16	3	12	64.5	88.6	11.9
17	4	10.5	64.5	85.7	12.7

Y₁ - the machine's forward speed; Y₂ - revolving speed; Y₃ - Angle of the film picking device; J - pickup rate; H - soil content

By analysing the experimental design and results in Table 2, it could be found that by adjusting the level of the three experimental factors, the pickup rate of the machine fluctuated between 79.7% and 88.6%, and the soil content rate between 9.4%~16.1%, so it could be seen from the test data that the prototype basically met the design requirements. To further analyse the comprehensive influential effect of the three factors on the machine's operation performance, Plackett-Burman designs (PB) in Design-Expert were adopted to build the regression model and regression equation of the three factors to the two responses *(Geng, 2019; Zhao & Wu, 2019)*, and then the factors which decided the test results were selected from the experimental factors to further adjust the machine's parameters to achieve the best-operating conditions.

Regression analysis of test results

Through Design-Expert fitting, the regression equation of the three factors to the pickup rate J and the regression equation of the three factors to soil content H were obtained, as shown in Formulas (12) and (13).

$$J = -828.1375 + 48.8625A + 23.95833B + 20.78333C - 0.7AB - 0.51667AC$$
$$- 0.23333BC - 1.3A^2 - 0.22222B^2 - 0.12222C^2 \tag{12}$$

$$H = -382.4625 - 0.7875A + 2.38533B + 13.8C - 0.01667AB - 0.033333AC$$
$$- 0.044444BC + 0.4625A^2 + 0.00555556B^2 - 0.11667C^2 \tag{13}$$

Table 3

Significance test on the regression analysis model of the recovery rate of film residues and potato damage rate

Sources	Degree of freedom	Residual film recovery rate			soil content rate		
		Sum of square	Values of F	Values of P	Sum of square	Values of F	Values of P
Model	9	98.06	51.97	< 0.0001	69.34	117.89	< 0.0001
Y_1	1	39.16	186.80	< 0.0001	2.76	42.5	0.0003
Y_2	1	37.41	178.45	< 0.0001	3.78	57.86	0.0001
Y_3	1	4.50	21.47	0.0024	61.61	942.59	< 0.0001
$Y_1 Y_2$	1	4.41	21.04	0.0025	2.5×10^{-3}	0.038	0.8505
$Y_1 Y_3$	1	2.40	11.46	0.0117	0.010	0.15	0.7073
$Y_2 Y_3$	1	1.10	5.26	0.0555	0.040	0.61	0.4597
Y_{12}	1	7.12	33.49	0.0006	0.9	13.78	0.0075
Y_{22}	1	1.05	5.02	0.06	6.6×10^{-4}	0.01	0.9229
Y_{32}	1	0.32	1.52	0.2576	0.29	4.44	0.0731
Residual	7	1.47			0.46		
Pure Error	4	0.80			0		
Cor Total	16	99.53			69.80		

p < 0.01, Extremely significant; 0.01 < p < 0.05, Significant; p > 0.05, Not significant

Table 3 shows the variance analysis of the prototype's pickup rate regression model. The fitting degree of the regression model was judged by analysing P value, F value, P value of the misfit term, determination coefficient R^2 value as well as P value of the test factors *(Zhang et al, 2019; Deng et al, 2016).* The significance test of the pickup rate model was $F = 51.97$ and $P < 0.0001$, indicating that the pickup rate regression equation had a high significance. The significance test of the soil content model was $F = 117.89$ and $P < 0.0001$, indicating the regression equation had a higher significance.

A four-dimensional slice figure was drawn with MATLAB to depict the comprehensive influential effects of the three factors on the pickup rate. By analysing the comprehensive influential effects of the three factors in Fig. 6 on the pickup rate, it could be seen that the pickup rate basically did not change with the change of the angle of the film picking device Y_3, but increased with the increase of revolving speed Y_2 and the decrease of the machine's forward speed Y_1, among which the change of revolving speed was more significant to the pickup rate.

Based on the analysis of the comprehensive influential effects of the three factors in Fig. 7 on the soil content, it could be seen that the soil content gradually decreased rapidly with the increase of the angle of the film picking device Y_3, while the soil content basically remained unchanged with the changes of the operating speed of the machine Y_1 and Y_2. Based on analysing the comprehensive influential effects of the three factors on the pickup rate and soil content, it could be seen that the significance of the three factors to the pickup rate is the rotational speed Y_2 > speed Y_1 > the angle of the film pickup device Y_3. Among the three factors, the most significant one on the pickup rate is the angle of the film pickup device.
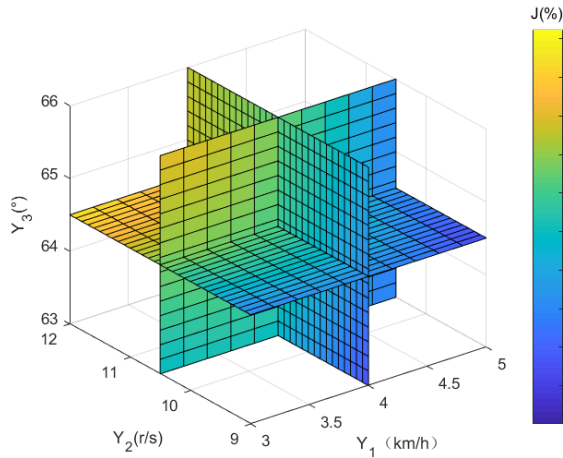
Fig. 6 - Comprehensive influential effects of three factors on pickup net rate
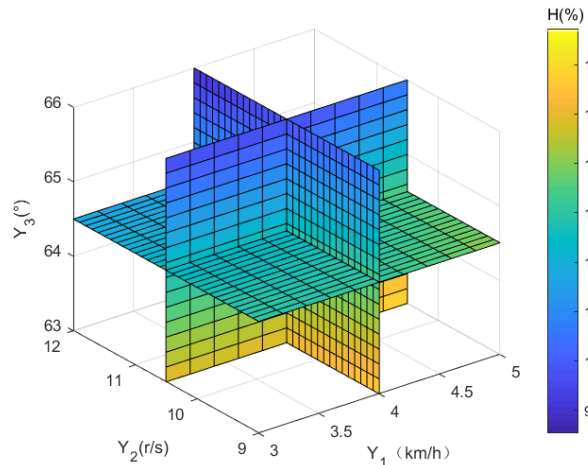
Fig. 7 - Comprehensive influential effects of three factors on soil content

Parameter optimization

To improve the operating performance of the residual film recycling machine *(Sun et al., 2018; Wu, J. 2018)*, the function Optimization in Design-Expert was used to optimize the test results, and the constraint conditions were selected according to the operational requirements, working conditions and relevant theoretical analysis of the high pickup rate and low soil content, and then the objective function (14) was established:

$$\begin{cases} max\,J\ (Y_1,\ Y_2,\ Y_3) \\ minH\ (Y_1,\ Y_2,\ Y_3) \end{cases}$$

$$(14)$$

and

$$\begin{cases} 3\ km/h \leq Y_1 \leq 5\ km/h \\ 9\ r/s \leq Y_2 \leq 12\ r/s \\ \quad 63° \leq Y_3 \leq 66° \end{cases}$$

The optimization range of objective function J was 80~100%, the optimization range of objective function R was a range of 0~2%, and the optimization of objective function H was 0~20%. Then the experimental results were optimized and solved, and the optimal parameters of the machine were obtained as follows: the machine's forward speed was 3.2 km/h; the revolving speed was 10.5 r/s, the angle of the film pickup device was 65.4 °, the film pickup rate J of the residual film recycling machine under these parameters was 87.084 %, and the soil content H was 10.382 %.

Experimental verification

To verify the performance of the machine under the optimized parameters, the experiment was carried out again in the harvested vegetable fields in Hebei Province. The test was conducted according to the standard of Residual Plastic Film Recycling Machine. The soil firmness of the test field was 3.82 MPa and the average moisture content of the soil was 12.3%.

Table 4

Results of the field test

Test number	Y₁ (km/h)	Y₂ (r/s)	Y₃ (°)	J (%)	H (%)
1	3.2	10.5	65.4	87.3	11.5
2	3.2	10.5	65.4	86.6	10.8
3	3.2	10.5	65.4	86.2	11.1
4	3.2	10.5	65.4	86.9	11.3
5	3.2	10.5	65.4	86.7	10.6
6	3.2	10.5	65.4	87.1	11.4

The operating effectiveness of the machine was obtained by averaging the results of the six tests. Test results are shown in Table 4. The average pickup rate J was 86.6%, and the average soil rate H was 11.12%, which was close to the optimization solution results. In the experiment, the pickup rate was slightly lower than the optimization solution, and the soil content was slightly higher than the optimization solution. This was because there were weeds, sand, and residual vegetables in the vegetable field recycling process, leading to a slight difference between the experimental value and the theoretical value, so it indicated that the model was reliable to a certain extent.

CONCLUSIONS

In this paper, the processing and production process of the machine was briefly introduced, and then the field experiment was carried out on the prototype. The comprehensive influential effects of the three factors on the two responses were established by using Design-Expert on the experimental data, and the following conclusions were drawn:

(1) The comprehensive influential laws of the three factors on the two responses were reflected by drawing the contour line and response surface of the two responses and the four-dimensional slice figure of the three factors on the two responses. The factor with the most significant influence on the pickup rate J was revolving speed Y_2, and the factor with the most significant influence on the soil content rate was the angle of the film picking device Y_2.

(2) The optimum operating parameters of the machine were obtained by using Design-Expert to optimize the experimental results: the machine's forward speed was 3.2 km/h, the revolving speed was 10.5 r/s, the angle of the film picking device was 65.4°, the pickup rate of the residual film recycling machine J was 86.6%, and the soil rate H was 11.12%.

ACKNOWLEDGEMENT

REFERENCES

[1]   An Q. (1996). The Effect of Pollution on Farm Ecosystem and the Control Countermeasures. *Journal of Ecology and Rural Environment*, (02):44-47.

[2]   Chen X.H., Chen X.G., Li J.B., Li C.S., Yang Y.K., (2020). Design and test of nail-teeth roller-type residual film recovery device before sowing. *Transactions of the Chinese Society of Agricultural Engineering*, 36(02):30-39.

[3]   Yanjie Li, Yong Xu, Colin Thornton. A comparison of discrete element simulations and experiments for 'sandpiles' composed of spherical particles [J]. *Powder Technology*. 2005 (3)

[4]   Geng X. (2020). Study on fume diffusion laws and analysis on response surface of welding workshop. *Journal of Safety Science and Technology*, 16(03):177-182.

[5]   Xr Wang, Kr Wang, Yc Li, Wang B., Liu J., Wang F.l., Zong Hy, Li Sj, Song Nn, (2020), Analysis on Pollution Situation of Mulch Film Residual in Farmland Soils in Qingdao City [J]. *Fresenius Environmental Bulletin*, 29(7A): 5822-5829.

[6]   Gang Li, Linhai Zhang, Yu Fu, Dangqin Xue, Shulin Hou, (2014), Crank-rocker Mechanism for Collecting Plastic Film [J]. *Transactions of the Chinese Society for Agricultural Machinery*,45(S1):63-67.

[7]   Liu W.F., Xu W., Li B., Li Y. (2018). Measurement and Simulation of Rolling Friction Coefficient. *Machinery Design & Manufacture*, (09):132-135.

[8]   Sun Y., Jian J., Tian Y., Sun F., Zhang M., Wang S. (2018). Analysis and Experiment of Filming Mechanism of Rotary Film-lifting Device of Residual Film *Recycling Machine. Transactions of the Chinese Society for Agricultural Machinery*, 49(S1):304-310.

[9]   Tian X., Zhao Y., Chen X., Yan L., Wen H., Gou H., Ji C. (2018). Development of 4JSM-2000A type combined operation machine for cotton stalk chopping and residual plastic film collecting. *Transactions of the Chinese Society of Agricultural Engineering*, 34(10):25-35.

[10]   Cleary P.W., Sinnott M.D., (2015)., Simulation of particle flows and breakage in crushers using DEM: Part 1 – Compression crushers. Minerals Engineering, 74: p. 178-197.

[11]   Fangyan Wang, Guangquan Sun, Shuqi Shang, (2019), Development of 4CL-1 self-propelled combine harvester for green onion [J]. *Transactions of the Chinese Society of Agricultural Engineering*, 35(24): 39 − 47

[12]   Xue H., Yang L., Lian D., Lu B. (1987). Test of Designing Parameters of Double-Wing Subsoiler. *Journal of Northwest A & F University* (Natural Science Edition), (01):24-29.

[13]   Zhou L., Tang W., Xie J., (2019). Present Research Situation and Existing Problems of Residue Film Collectors. *Xinjiang Agricultural Mechanization*, (5):13-15+32.

[14]   Zhang J., Xie J., Xue D., Han J., Hou S. (2013). Development Status of Applying Plastic Film and the Residue Mulching Film Collecting Machine at Domestic and Overseas. *Journal of Agricultural Mechanization Research*, 35(12):237-240.

[15]   Zhao Y., Chen X., Wen H., Zhen X., Ni Q., Kang J., (2017). Research Status and Prospect of Control Technology for Residual Plastic Film Pollution in Farmland. *Transactions of the Chinese Society for Agricultural Machinery*, 48(06):1-14.

[16]   Zhai H., Jian J., Hou S., San Y., Guo W., Sun Y., Gao M., (2018), The design and test of collecting device and film purge device joint work of residual film recovery machine based on Solidworks & Adams [J]. *IOP Conference Series: Materials Science and Engineering,* 324(1).

[17]   Zhai H., Jian J., Hou S., San Y., Guo W., Sun Y., Gao M., (2018). The design and test of collecting device and film purge device joint work of residual film recovery machine based on SolidWorks & Adams. *IOP Conference Series: Materials Science and Engineering*, 324(1).

[18]   Barrios G.K.P., Carvalho R.M., Kwade A., Tavares L.M., (2015), Contact parameter estimation for DEM simulation of iron ore pellet handling[J]. *Powder Technology*. 84-93.

[19]   Zhang M., Jian J., Wang F., Li W., San Y., Guo W., Hou S., Xue D. (2019). Design and Experimental Study on Belt-Tooth Type Collector for Potato Film Residues [J]. *Earth and Environmental Science*, 252(4).

RESEARCH ON DEM CALIBRATION OF CONTACT PARAMETERS
OF COATED FERTILIZER
/
包膜肥料接触参数 DEM 标定研究

Xin DU, Cailing LIU*⁾, Meng JIANG, Hao YUAN, Lei DAI, Fanglin LI, Zhanpeng GAO
College of Engineering, China Agricultural University, Beijing 100083/ China;
Tel: 0086-010-62737502; E-mail: cailingliu@163.com
Corresponding author: Cailing Liu

ABSTRACT

To simulate the interactions between the coated fertilizer particles and the fertilizer discharging components accurately, the coated fertilizer contact parameters were calibrated using the discrete element method (DEM). Based on the angle of repose test, single-factor simulations were performed on the coefficient of restitution (COR), coefficient of static friction (COSF) and coefficient of rolling friction (CORF) between particles, and the internal relationship between the level change of each factor and the static angle of repose (SAOR) was determined. The CCD test was used to calibrate the contact parameters between particles. When the COR, COSF and CORF between particles are 0.625, 0.175, and 0.037, respectively, the simulation value of SAOR is 24.173°, and the relative error from the real value is 1.230%, which indicates that the calibrated fertilizer particle contact parameters are accurate and reliable.

摘要

为准确模拟包膜肥料颗粒与排肥部件之间的相互作用，采用离散元法校准了包膜肥料颗粒的接触参数。通过跌落试验、斜板滑动试验和斜板滚动试验测得肥料颗粒与 ABS 间的碰撞恢复系数、静摩擦系数和滚动摩擦系数分别为 0.47、0.42 和 0.095；基于休止角试验分别对颗粒间碰撞恢复系数、静摩擦系数和滚动摩擦系数进行单因素仿真，确定各因素水平范围与堆积角的作用关系。采用 CCD 试验标定颗粒间接触参数，对试验数据进行多元二次回归拟合，建立肥料颗粒堆积角与颗粒间接触参数的回归模型并进行最优参数求解，得到颗粒间碰撞恢复系数、静摩擦系数和滚动摩擦系数分别为 0.625、0.175 和 0.037 时，堆积角仿真值为 24.173°，与真实值相对误差为 1.230%，表明标定所得肥料颗粒接触参数准确可靠。

INTRODUCTION

Fertilizer is the "food" of crops and has an irreplaceable role in agricultural production (*Chen et al., 2014*; *Hvistendahl, 2010*). To improve fertilizer utilization and reduce the environmental hazards of fertilizer loss, coated controlled-release fertilizers and variable amount fertilizer discharge application technologies have received widespread attention (*Chojnacka et al., 2020*; *Dimkpa et al., 2020*; *Kornei, 2017*). The outer groove wheel fertilizer discharger is a key carrier in the process of implementing precise variable fertilizer application, which has the advantages of simple structure and a large control range of fertilizer amount discharge but has problems such as large pulsation and poor stability of fertilizer discharge (*Zhu et al., 2018*; *Wang et al., 2017*). Therefore, it is of great importance to research the uniformity of fertilizer discharging by external slotted wheel dischargers.

Three methods are usually used to study the fertilizer discharge process of the outer groove wheel: experimental study, theoretical analysis, and numerical simulation. Experimental studies are the most direct and reliable research method, but it is difficult to obtain information on the internal forces and displacements of the particles. The theoretical analysis is often different from the actual results because it cannot fully consider all the practical complexities. Numerical simulation methods can make up for the shortcomings of theoretical analysis and experimental studies (*Lv et al., 2013*; *Zhao et al., 2012*; *Landry et al., 2006*).

Xin Du, Ph.D. Stud.; Cailing Liu*, Prof. Ph.D.; Meng Jiang, Ph.D. Stud.; Hao Yuan, Ph.D. Stud.; Lei Dai, Ph.D. Stud.;
Fanglin Li, Ph.D. Stud.; Zhanpeng Gao Ph.D. Stud.

The DEM method was proposed by *Cundall* and *Strack* (*1979*) and has been widely used to simulate the mixing, stirring, conveying, filling, and crushing of bulk materials in mining, geotechnical, pharmaceutical, chemical, and agricultural fields (*Lu et al., 2015*; *Shen et al., 2016*; *Gao et al., 2016*). To make the simulation match the real situation, it is necessary to calibrate its meso-parameters firstly. Most of the existing studies on the calibration of discrete element parameters of fertilizer particles are based on conventional fertilizers such as urea (*Liu et al., 2018*), compound fertilizers (*Wen et al., 2020*), and organic fertilizers (*Yuan et al., 2018*; *Han et al., 2021*; *Luo et al., 2018*), and there are few studies on the calibration of parameters of coated fertilizer particles. Coated fertilizers are influenced by the coating material and differ significantly from conventional fertilizers in terms of frictional characteristics. The improvement of the calibration process has been a subject of scientific research for many years (*Coetzee, 2017*). Researchers have tried several methods to calibrate or measure discrete element parameters, one is to directly measure the parameters of the particles through experiments, which is suitable for parameters that reflect the properties of the particles, such as Poisson's ratio, density, and shear modulus. One is to experimentally measure the macroscopic phenomena of the particles and then reverse calibrate them. In the inverse calibration process, the traditional method is "trial and error", which is inefficient and inaccurate (*Chen, 2017*). To make up for the above disadvantages, Zhao (*Zhao, et al., 2012*) tried to explore the complex relationship between micro and macro mechanical behavior and parameters through experience or theoretical formulas. In the calibration process, the method of experimental design is used to generate samples, such as Kevin (*Hanley et al., 2011*) used the Taguchi method and orthogonal experiment, and Rackl (*Rackl and Hanley, 2017*) used Latin hypercube sampling and Kriging method. Then, the optimized algorithm was used to process the data and get the calibration result, specifically, Do (*Do et al., 2018*) used genetic algorithm, Benvenuti (*Benvenuti et al., 2016*) used an artificial neural network, and Zhou (*Zhou et al., 2018*) used radial basis neural network method. Compared with the above methods, the experimental design based on response surface model theory has unique advantages in building regression models and analyzing the significance of factors. The method includes central combined design (CCD) and Box-Behnken design (BBD), and CCD is used in this study because it can fit the response surface better and with higher accuracy (*Myers et al., 2016*). Therefore, in this paper, a CCD-based repose angle test was chosen to calibrate the discrete element parameters of coated fertilizer particles and to study the uniformity of fertilizer discharge of the outer groove wheel discharger based on this.

In this study, the coated fertilizer particles were used as the research object, and the actual static angle of repose (SAOR) of the coated fertilizer particles was measured by the image processing method, and the contact parameters of the coated fertilizer particles in the discrete element simulation software EDEM were reverse-calibrated based on the actual SAOR. The simulated SAOR of the coated fertilizer particles in EDEM was quickly determined by the EDEMpy post-processing procedure.

MATERIALS AND METHODS
DEM MODELING OF FERTILIZER GRANULES
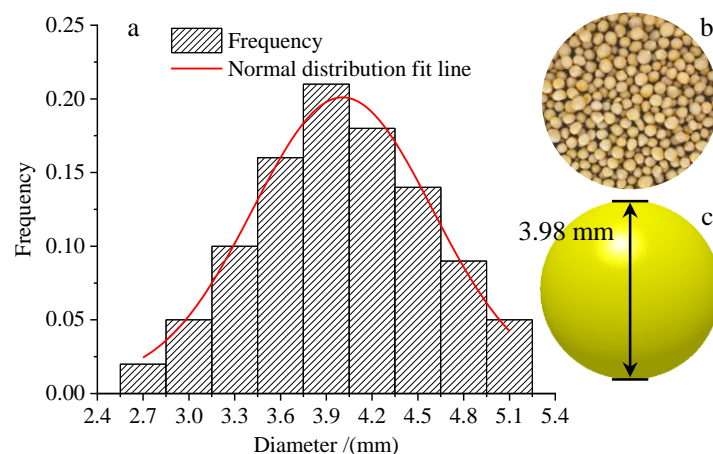
Fig. 1 - Fertilizers and discrete element model

In this paper, the coated controlled-release fertilizers were sourced from Shandong Nongyang Biological Technology Co., Ltd., China. (Fig.1b), 100 randomly selected fertilizer granule samples were measured in three directions: length, width, and thickness using digital calipers (accuracy 0.01 mm), and the average triaxial dimensions of fertilizer particles were 4.08 mm×3.97 mm×3.89 mm.

The equivalent diameter D and sphericity S_p were calculated using Equation (1), the equivalent diameter and sphericity are 3.98 mm and 0.975, respectively, and its size distribution is shown in Fig. 1a. A single sphere with a diameter of 3.98 mm was used in the DEM simulation to build the fertilizer granule simulation model (Fig.1c).

$$
\begin{cases}
D = \sqrt[3]{LWT} \\
S_p = \dfrac{D}{L}
\end{cases}
\tag{1}
$$

Where:

D is the equivalent diameter of fertilizer granules, [mm]; L is the length of fertilizer granules, [mm]; W is the width of fertilizer granules, [mm]; T is the thickness of fertilizer granules, [mm]; S_p is the sphericity.

A random sample of 300 fertilizer granules was selected, and the mass and volume were measured using a digital balance (accuracy 0.001 g) and a measuring cylinder (accuracy 0.01 mL), respectively (drainage method), and the true density of fertilizer granules was calculated as 1.46 g/cm^3 using equation (2). The moisture content of fertilizer granules was measured as 0.88% using a rapid moisture analyzer (accuracy 0.001 g).

$$
\rho_{real} = \frac{m_0}{V_1 - V_0}
\tag{2}
$$

Where:

ρ_{real} is the true density of fertilizer particles, [g/cm^3]; m_0 is the mass of fertilizer particles, [g]; V_1 is the total volume of fertilizer particles and water in the measuring cylinder, [cm^3]; V_0 is the volume of water in the measuring cylinder, [cm^3].

Due to the extremely low moisture content of the coated fertilizer particles and the lack of adhesion between the particles, the Herzt-Mindlin model was used in the EDEM software for DEM parameter calibration. Based on the drop test, the inclined plate sliding test and the inclined plate rolling test, the COR, COSF and CORF between the fertilizer particles and the ABS were measured to be 0.47, 0.42 and 0.095, respectively. Due to the limited space of the article, the process of determining the contact parameters between fertilizer particles and ABS will not be explained. Other parameters used in the simulation are Poisson's ratio 0.225 and shear modulus 1.528×10^8 Pa.

THE STATIC ANGLE OF REPOSE (SAOR) TEST

The inter-particle contact coefficient was calibrated using the SAOR test, and the actual SAOR of the fertilizer particles was measured first (as shown in Fig. 2), and the Fiji-ImageJ image processing software was used to process the fertilizer particles and extract the contour line after the stacked particles were stabilized, and the actual SAOR of the fertilizer particles was deduced from the slope of the contour line, and the test was repeated 10 times to take the average value.
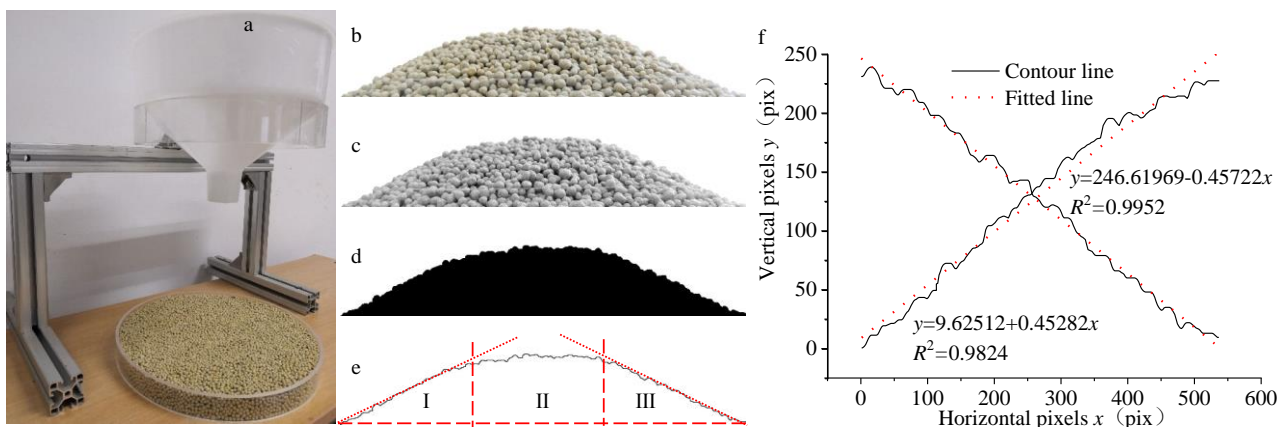
Fig. 2 - Schematic diagram of SAR of fertilizer particles

EDEM2018 was used to numerically simulate the SAOR of fertilizer particles (Fig.3). To accurately reflect the interaction between fertilizer particles, the funnel shown in Fig. 3a was used to perform SAOR test on the fertilizer particles. The total amount of particles in the bottom cylinder was 2500 g, and the total amount of particles in the funnel is 1000 g, the total simulation time is 4 s, and the time step is 5×10^{-6} s. After the simulation has been completed, use Python 3.6 to call the EDEMpy library, run the SAOR post-processing program, as shown in Fig. 3b, set up 18 sampling surfaces on the fertilizer particle surface, read the fertilizer particle position information on the accumulation surface and perform linear fitting, output the average and standard deviation of the SAOR.

a. Simulation diagram b. Edge particle detection diagram
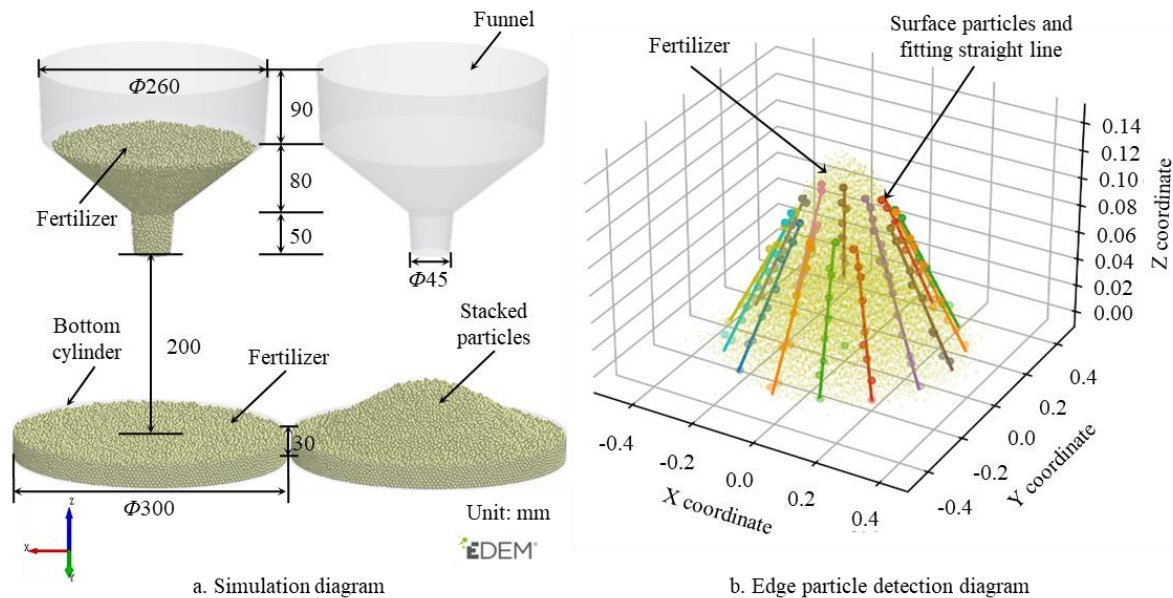
Fig. 3 – Simulation test diagram

Coefficient of restitution (COR)
Set the coefficient of static friction (COSF) and coefficient of rolling friction (CORF) between fertilizer particles 0.18 and 0.035, respectively. The horizontal range of the COR is 0.3 to 0.7, and the horizontal gradient is 0.1.

(a) SAOR (b) Kinetic energy
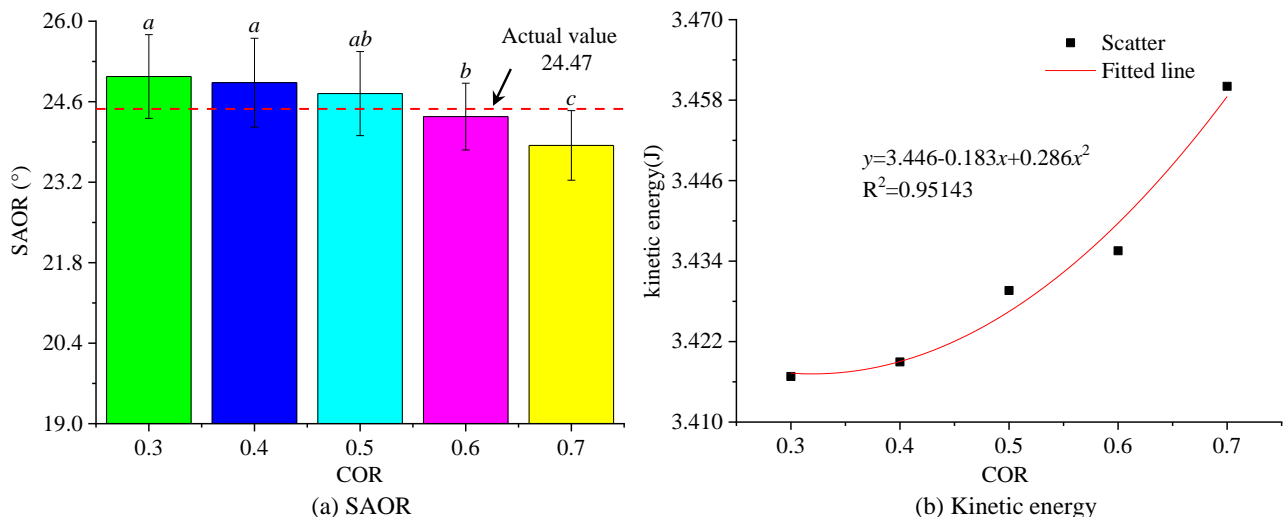
Fig. 4 – Effects of COR on SAOR and total kinetic energy of particles

The variation of SAOR of fertilizer particles under each COR gradient between fertilizer particles is shown in Fig. 4(a). One-way ANOVA was performed using SPSS 25.0, and the homogeneity of the variance test result was significant at 0.694>0.05, the analysis of variance could be performed; ANOVA results showed $P<0.0001$, indicating significant differences in the effects of different inter-granule COR on the SAOR.

From Fig. 4(a), it can be seen that the SAOR decreases with the increase of the inter-particle COR, and the difference between the SAOR groups is not significant when the inter-particle COR is 0.3, 0.4, and 0.5, and the difference between the SAOR groups is significant when the inter-particle COR is 0.6 and 0.7, and the COR corresponding to the actual value of the SAOR is between 0.5 and 0.6.

The variation of the total kinetic energy of fertilizer particles with the inter-particle COR is shown in Fig. 4(b). The larger COR, the greater the total kinetic energy of fertilizer particles, indicating that as the COR increases, the particles increase their collision bounce and fall more easily to a position far from the center of the fertilizer pile, and the particles on the surface of the fertilizer pile become more dispersed, resulting in a smaller pile-up angle.

Coefficient of static friction (COSF)

Set the COR and CORF between fertilizer particles to 0.5 and 0.035, respectively. The COSF between fertilizer particles ranges from 0.12 to 0.24, and the horizontal gradient is 0.03.

(a) SAOR   (b) Force chain strength
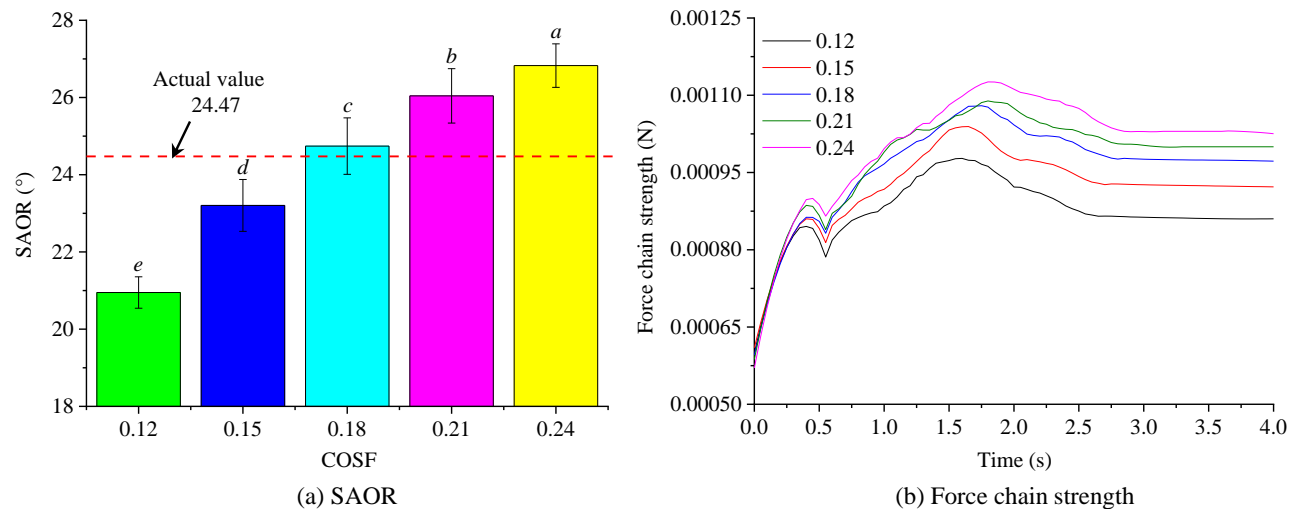
Fig. 5 – Effects of COSF on SAOR and force chain strength of particles

The variation of the SAOR of fertilizer particles under each COSF gradient between fertilizer particles is shown in Fig. 5(a). One-way ANOVA was performed using SPSS 25.0, and the homogeneity of the variance test result was significant at 0.265>0.05, the analysis of variance could be performed; ANOVA results showed $P<0.0001$, indicating significant differences in the effects of different inter-granule COSF on the SAOR.

(a) COSF 0.12   (b) COSF 0.15   (c) COSF 0.18   (d) COSF 0.21   (e) COSF 0.24
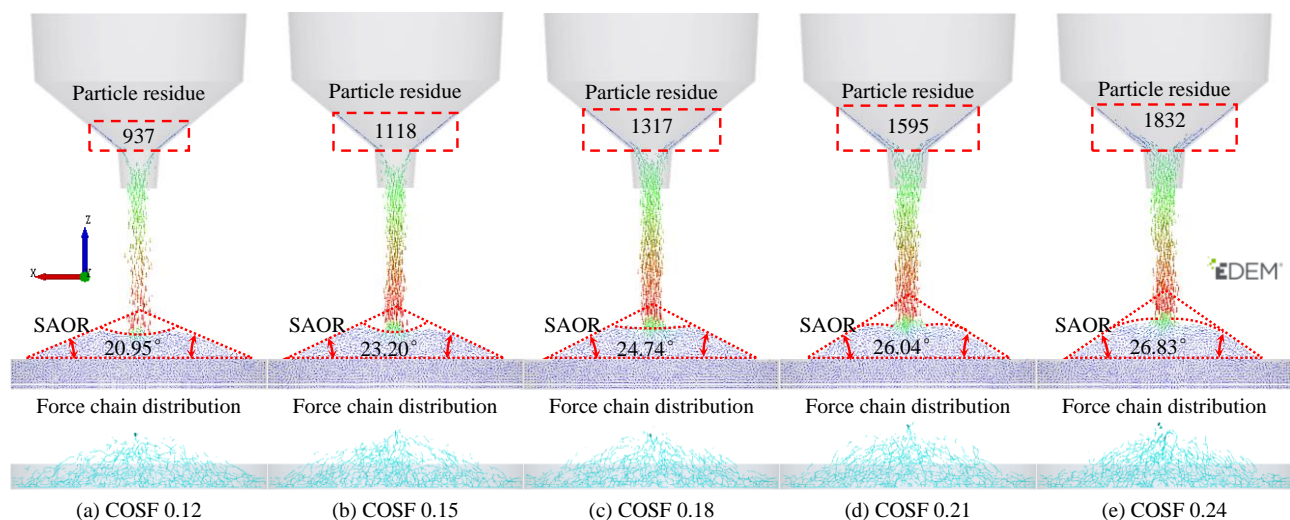
Fig. 6 – Schematic diagram of fertilizer particle retention, bottom particle repose and force chain distribution in the funnel with different inter-particle COSF

It can be seen that the SAOR increases with the increase of the COSF between the particles (Fig.5), and the effect of each factor level on the SAOR is significant, and the COSF corresponding to the actual value of the SAOR is between 0.15 and 0.18. The variation of the force chain distribution strength of the bottom fertilizer particles with the inter-particle COSF is shown in Fig. 5(b).

The smaller the inter-particle COSF is the weaker the strength of the force chain generated by the bottom particles stacking. Combined with Fig. 6, it can be seen that the fertilizer granules flow from the funnel impacts the surface layer of the fertilizer pile, and the weak force chain on the cone surface is easily broken to trigger the slippage of the granules on the surface layer of the fertilizer pile, which in turn leads to a smaller

piling angle. The retention amount of fertilizer particles in the funnel and the accumulation state of the bottom particles at each level at the time of 1.8 s are shown in Fig. 6. The inter-particle COSF has a significant effect on the number of fertilizer particles remaining in the funnel, and the number of fertilizer particles remaining in the funnel increases with the increase of the inter-particle COSF, indicating that the increase of the inter-particle COSF leads to the poor mobility of fertilizer particles; the SAOR of the bottom particles increases with the pile angle at the bottom increased with the increase of inter-granular COSF, and the shape of the intersection of fertilizer pile and fertilizer flow gradually changed from concave to flat and to convex.

Coefficient of rolling friction (CORF)

Set the COR and COSF between fertilizer particles to 0.5 and 0.18, respectively. The CORF between fertilizer particles ranges from 0.025 to 0.045, and the horizontal gradient is 0.005.

The variation of the SAOR of fertilizer particles under each CORF gradient between fertilizer particles is shown in Fig. 7(a). One-way ANOVA was performed using SPSS 25.0, and the homogeneity of the variance test result was significant at 0.875>0.05, the analysis of variance could be performed; ANOVA results showed $P<0.0001$, indicating significant differences in the effects of different inter-granule CORF on the SAOR.

From Fig. 7(a), it can be seen that the SAOR increases with the increase of CORF between particles, and the effect of each factor level on the SAOR is significant, and the CORF corresponding to the true value of the stacking angle is between 0.30 and 0.35.

The variation of the average rotational energy of the particles with the CORF is shown in Fig. 7(b). The average rotational energy of particles decreases with the increase of CORF, and the larger the rotational energy is, the more likely the particles falling on the surface layer of the fertilizer pile will roll, which in turn destroys the stable accumulation state between the particles on the surface layer of the cone and causes the surface particles to roll off and the accumulation angle becomes smaller.

(a) SAOR   (b) Rotational kinetic energy
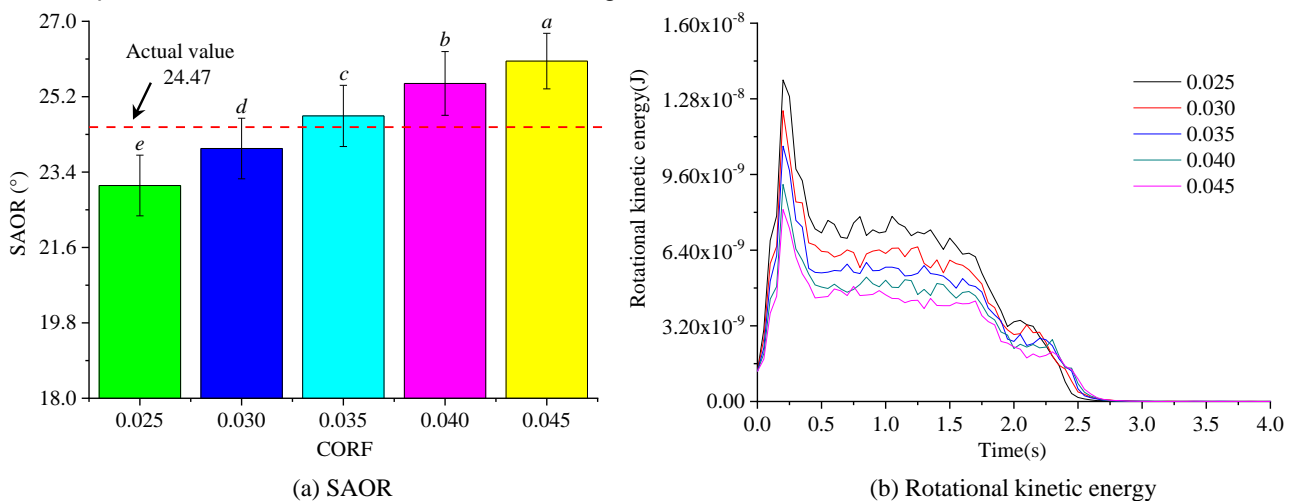
Fig. 7 – Effect of RFC and average rotational energy of granules on repose angle

CCD CALIBRATION TEST

According to the results of pre-experiment and single-factor analysis, the CCD test was carried out on the COR, COSF, and CORF between particles, and the test results are shown in Table 1.

Table 1

CCD test plan and results

Number	COR x_1	COSF x_2	CORF x_3	SAOR y (°)
1	0.40	0.15	0.0300	22.8850
2	0.70	0.15	0.0300	21.9785
3	0.40	0.21	0.0300	25.2489
4	0.70	0.21	0.0300	23.8707
5	0.40	0.15	0.0400	23.5763
5	0.40	0.15	0.0400	23.5763
6	0.70	0.15	0.0400	23.4178
7	0.40	0.21	0.0400	27.0148

Table 1

(continuation)

Number	COR x_1	COSF x_2	CORF x_3	SAOR y (°)
8	0.70	0.21	0.0400	25.6742
9	0.30	0.18	0.0350	24.8131
10	0.80	0.18	0.0350	22.9109
11	0.55	0.13	0.0350	21.7858
12	0.55	0.23	0.0350	26.5836
13	0.55	0.18	0.0266	23.1235
14	0.55	0.18	0.0434	25.6804
15	0.55	0.18	0.0350	24.7499
16	0.55	0.18	0.0350	24.6826
17	0.55	0.18	0.0350	24.5547
18	0.55	0.18	0.0350	24.4386
19	0.55	0.18	0.0350	24.8903
20	0.55	0.18	0.0350	24.7471
21	0.55	0.18	0.0350	25.0695
22	0.55	0.18	0.0350	24.9396
23	0.55	0.18	0.0350	25.1522

Using Design-Expert 10.0 software to perform multiple quadratic regression fitting on the experimental data, a regression model of the SAOR of fertilizer particles and the contact parameters between the particles was established, and the regression equation y was obtained as:

$$y = 1.8853 + 15.5406x_1 + 106.5343x_2 + 198.2651x_3 - 45.9381x_1x_2 + 130.9310x_1x_3 +$$
$$1198.9543x_2x_3 - 13.8756x_1^2 - 220.1364x_2^2 - 4851.9527x_3^2$$

(3)

The significance test of the regression equation is shown in Table 2. It can be seen from the table that the degree of fit of the model is extremely significant ($P<0.0001$), and the lack of fit term is not significant ($P>0.05$), indicating that the equation fits well, and the regression model can be used to express the relationship between response indicators and various experimental factors.

Table 2

Analysis of variance table

Source	Sum of Squares	df	Mean Square	F-Value	P-Value
Model	37.7275	9	4.1919	80.8013	< 0.0001∗∗
x_1	3.5705	1	3.5705	68.8222	< 0.0001∗∗
x_2	23.7769	1	23.7769	458.3093	< 0.0001∗∗
x_3	7.3229	1	7.3229	141.1515	< 0.0001∗∗
$x_1 x_2$	0.3419	1	0.3419	6.5897	0.0234∗
$x_1 x_3$	0.0771	1	0.0771	1.4870	0.2444
$x_2 x_3$	0.2587	1	0.2587	4.9875	0.0437∗
x_1^2	1.5487	1	1.5487	29.8522	0.0001∗∗
x_2^2	0.6237	1	0.6237	12.0221	0.0042∗∗
x_3^2	0.2338	1	0.2338	4.5063	0.0535
Residual	0.6744	13	0.0519		
Lack of Fit	0.2403	5	0.0481	0.8857	0.5322
Pure Error	0.4341	8	0.0543		
Cor Total	38.4019	22			
R^2=0.9824; CV%=0.93					

Note: ∗∗ means extremely significant impact($P<0.01$), ∗ means significant impact($P<0.05$).

It can be seen from Table 2 that the impact COR, COSF, and CORF of fertilizer particles in the first item have a significant impact on the SAOR; in the interaction item, the impact COR-COSF and COSF-CORF have significant effects on the SAOR; Fig. 8 shows the response surface for interactive factors.

a. Interaction diagram between COSF
and COR

b. Interaction diagram between COSF
and CORF
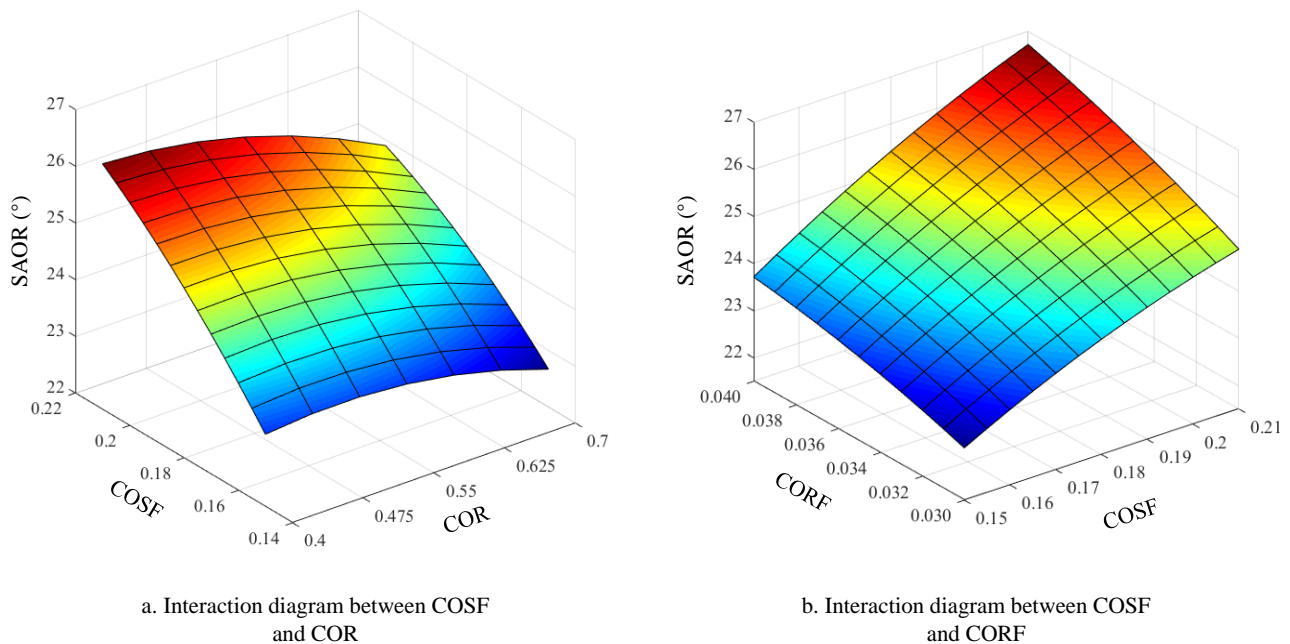
Fig. 8 – Response surface diagram

It can be seen from Fig. 8a that the SAOR increases with the increase of the COSF, and decreases with the increase of the COR, which is consistent with the results of the analysis of variance; The slope of the response surface curve of the crash COR and the COSF at each level is lower than the slope at the interaction level, indicating that the interaction is significant. It can be seen from Fig. 8b that the SAOR increases with the increase of the COSF, and with the increase of the CORF, which is consistent with the results of the analysis of variance; The slope of the response surface curve of the CORF and the COSF at each level is lower than the slope at the interaction level, indicating that the interaction is significant.

Use the optimization module of Design-Expert 10.0 software to solve the optimal parameters of the regression model, and select the constraint condition of the objective function as:

$$
\begin{cases}
y=24.47415 \\
\text{s.t.} \begin{cases} 0.40 \le x_1 \le 0.70 \\ 0.15 \le x_2 \le 0.21 \\ 0.03 \le x_3 \le 0.04 \end{cases}
\end{cases}
\tag{4}
$$

According to the constraints, the objective function is optimized and the combined parameters are obtained: the COR, the COSF, and the CORF are 0.625, 0.175, and 0.037, respectively, and the SAOR is 24.474°. The simulation test is carried out under this parameter, and the SAOR of simulation is 24.173°, and the relative error from the true value is 1.230%. A comparison of the simulation and actual SAOR profiles is shown in Fig. 9.
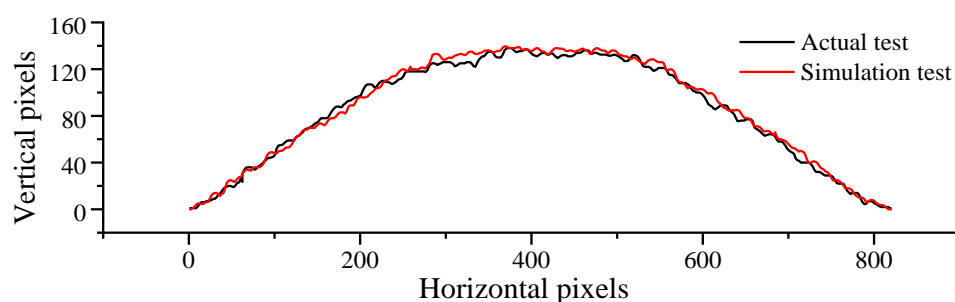
Fig. 9 – Comparison of actual and simulation SAOR profiles

CONCLUSIONS

The COR, COEF and CORF between fertilizer granules and ABS were 0.47, 0.42, and 0.095, respectively, measured and calibrated by the drop test, sliding test, and rolling test of the sloped plate. Through single-factor experiments, it is obtained that the COR, COSF and CORF of fertilizer particles have a direct effect on the total kinetic energy of the particles, the strength of the force chain, and the rotation energy of the particles, respectively, and then change the accumulation state between the particles and cause the SAOR change. The regression model of the SAOR of fertilizer particles and the contact parameters between the particles was established by the CCD test and the optimal parameters were solved. The COR, COSF and CORF were 0.625, 0.175 and 0.037, respectively, and the SAOR is 24.474°. The simulation test is carried out under this parameter, and the SAOR of simulation is 24.173°, and the relative error from the true value is 1.230%.

ACKNOWLEDGEMENT

REFERENCES

[1]   Benvenuti, L., Kloss, C., Pirker, S., (2016). Identification of DEM simulation parameters by Artificial Neural Networks and bulk experiments. *Powder Technology*, 291:456-465.

[2]   Chen, P.Y., (2017). Effects of Microparameters on Macroparameters of Flat-Jointed Bonded-Particle Materials and Suggestions on Trial-and-Error Method. *Geotechnical and Geological Engineering*, 35 (2):663-677.

[3]   Chen, X., Cui, Z., Fan, M., et al, (2014). Producing more grain with lower environmental costs. *Nature*, 514 (7523):486-489.

[4]   Chojnacka, K., Moustakas, K., Witek-Krowiak, A., (2020). Bio-based fertilizers: A practical approach towards circular economy. *Bioresource Technology*, 295:122223.

[5]   Coetzee, C.J., (2017). Review: Calibration of the discrete element method. *Powder Technology*, 310:104-142.

[6]   Cundall, P., Strack, O. (1979). Discrete numerical model for granular assemblies. *International Journal of Rock Mechanics and Mining Sciences & Geomechanics Abstracts*, 16 (4):77.

[7]   Dimkpa, C.O., Fugice, J., Singh, U., et al, (2020). Development of fertilizers for enhanced nitrogen use efficiency – Trends and perspectives. *Science of the Total Environment*, 731:139113.

[8]   Do, H.Q., Aragón, A.M., Schott, D.L., (2018). A calibration framework for discrete element model parameters using genetic algorithms. *Advanced Powder Technology*, 29 (6):1393-1403.

[9]   Gao, F., Stead, D., Elmo, D., (2016). Numerical simulation of microstructure of brittle rock using a grain-breakable distinct element grain-based model. *Computers and Geotechnics*, 78:203-217.

[10]   Han, S., Qi, J., Kan, Z., et al, (2021). Parameters calibration of discrete element for deep application of bulk manure in Xinjiang orchard. (新疆果园深施散体厩肥离散元参数标定研究) *Transactions of the Chinese Society for Agricultural Machinery*, 52 (04):101-108.

[11]   Hanley, K.J., O'Sullivan, C., Oliveira, J.C., et al, (2011). Application of Taguchi methods to DEM calibration of bonded agglomerates. *Powder Technology*, 210 (3):230-240.

[12]   Hvistendahl, M., (2010). China's push to add by subtracting fertilizer. *Science*, 327 (5967):801.

[13]   Kornei, K., (2017). 'Slow-release' fertilizer boosts crop yields, reduces environmental damage. *Science*.

[14]   Landry, H., Laguë, C., Roberge, M., (2006). Discrete element representation of manure products. *Computers and Electronics in Agriculture*, 51 (1-2):17-34.

[15]   Liu, C., Wei, D., Song, J., et al, (2018). Systematic study on boundary parameters of discrete element simulation of granular fertilizer. (颗粒肥料离散元仿真边界参数系统化研究) *Transactions of the Chinese Society for Agricultural Machinery*, 49 (09):82-89.

[16]   Lu, G., Third, J.R., Müller, C.R., (2015). Discrete element models for non-spherical particle systems: From theoretical developments to applications. *Chemical Engineering Science*, 127:425-465.

[17]   Luo, S., Yuan, Q., GOUDA, S., et al, (2018). Parameters calibration of vermicomposting nursery substrate with discrete element method based on JKR contact model. (基于JKR粘结模型的蚯蚓粪基质离散元法参数标定) *Transactions of the Chinese Society for Agricultural Machinery*, 49 (04):343-350.

[18]   Lv, H., Yu, J., Fu, H., (2013). Simulation of the operation of a fertilizer spreader based on an outer groove wheel using a discrete element method. *Mathematical and computer modelling*, 58 (3-4):836-845.

[19]   Myers, R.H., Montgomery, D.C., Anderson-Cook, C.M., (2016). *Response Surface Methodology: Process and Product Optimization Using Designed Experiments*. New York: John Wiley & Sons, Incorporated.

[20]   Rackl, M., Hanley, K.J., (2017). A methodical calibration procedure for discrete element models. *Powder Technology*, 307:73-83.

[21]   Shen, Z., Jiang, M., Thornton, C., (2016). DEM simulation of bonded granular material. Part I: Contact model and application to cemented sand. *Computers and Geotechnics*, 75:192-209.

[22]   Wang, B., Bai, L., Ding, S., et al, (2017). Simulation and experiment study on impact of fluted-roller fertilizer key parameters on fertilizer amount. (外槽轮排肥器关键工作参数对排肥量影响的仿真与试验研究) *Journal of Chinese Agricultural Mechanization*, 38 (10):1-6, 23.

[23]   Wen, X., Yuan, H., Wang, G., et al, (2020). Calibration method of friction coefficient of granular fertilizer by discrete element simulation. (颗粒肥料离散元仿真摩擦因数标定方法研究) *Transactions of the Chinese Society for Agricultural Machinery*, 51 (02):115-122.

[24]   Yuan, Q., Xu, L., Xing, J., et al, (2018). Parameter calibration of discrete element model of organic fertilizer particles for mechanical fertilization. (机施有机肥散体颗粒离散元模型参数标定) *Transactions of the Chinese Society of Agricultural Engineering*, 34 (18):21-27.

[25]   Zhao, G., Dai, B., Ma, C., (2012). Study of effects of microparameters on macroproperties for parallel bonded model. *Yanshilixue Yu Gongcheng Xuebao/Chinese Journal of Rock Mechanics and Engineering*, 31 (7):1491-1498.

[26]   Zhou, H., Hu, Z., Chen, J., et al, (2018). Calibration of DEM models for irregular particles based on experimental design method and bulk experiments. *Powder Technology*, 332:210-223.

[27]   Zhu, Q., Wu, G., Chen, L., et al, (2018). Influences of structure parameters of straight flute wheel on fertilizing performance of fertilizer apparatus. (槽轮结构参数对直槽轮式排肥器排肥性能的影响) *Transactions of the Chinese Society of Agricultural Engineering*, 34 (18):12-20.

DESIGN OF INNER AND OUTER ROLLER BUCKWHEAT THRESHER AND FIELD TEST
/
内外滚筒式荞麦脱粒机设计及田间试验

Jiawei WANG[1), Xiaohong YU* 2), Jianlong ZHANG1), Decong ZHENG1), Zhiwei LI1), Haiyan SONG1)   [1]
[1)] College of Agricultural Engineering, Shanxi Agriculture University, Taigu/China
[2)] Foundation Department, Shanxi Agriculture University, Taigu/China
Tel: +86-0354-6289686; E-mail: wjwzzz@163.com

ABSTRACT

Aiming at the problems of large loss rate and high damage rate during buckwheat threshing, an inner and outer roller buckwheat thresher was designed. The device is mainly composed of an inner roller and an outer roller, the inner roller is a rod-tooth combination roller, and the outer roller is a grid roller, the inner and outer rollers can be rotated independently. The outer roller is supported on the friction wheels and the supporting wheels, and driven to rotate by the friction wheel transmission system. The compression device is installed at the top to prevent the outer roller from slipping during the rotation. During working, the materials enter between the inner and outer rollers and the separation of grains and stems under the brushing and kneading action of the inner and outer rollers takes place. In order to push the materials between the inner and outer rollers smoothly, a double spiral blade type screw feeding device was designed. By establishing a mathematical model of material pushing, the screw feeding device has a material conveying speed of 1.87 m/s and a conveying capacity of 4.29 kg/s. In order to study the threshing performance, the threshing device was installed on the basis of the Kubota 688 tracked type combine to complete a prototype of a tracked buckwheat combination harvester. Field tests show that the grain impurity rate is 6.50%, the grain damage rate is 1.42%, the threshing loss rate is 0.25%, the cleaning loss rate is 1.01%, the direct loss rate of the header is 2.43%, and the total machine harvest loss rate is 3.69% at the working speed of 0.53 m/s and the feeding rate of 0.41 kg/s. The test results provide a basis for the improvement of buckwheat mechanized harvesting machinery.

摘要

针对荞麦脱粒损失率大、破碎率高等问题，设计了内外滚筒式荞麦脱粒机，该装置主要由内滚筒和外滚筒组成，内滚筒为纹杆—钉齿组合式滚筒，外滚筒为栅格滚筒，内外滚筒均可独立旋转。工作时，物料进入内外滚筒间，在内外滚筒的梳刷、揉搓作用下完成籽粒与茎秆的分离。为了将物料顺利推送至内外滚筒之间，设计了双螺旋叶片式螺旋喂入装置，并通过建立物料推送的数学模型，得到螺旋喂入装置物料输送速度为1874mm/s，输送量为 4.29kg/s。为了对该脱粒装置脱粒性能进行研究，在久保田 688 型履带式联合收获机基础上，安装该脱粒装置，完成履带式荞麦联合收获机样机。通过田间试验得到：该样机在作业速度为0.53m/s，喂入量为 0.41kg/s 的条件下，籽粒含杂率为 6.50%，籽粒破碎率为 1.42%，脱粒损失率为 0.25%，清选损失率为 1.01%，割台直接损失率为 2.43%，总损失率为 3.69%，试验测试效果良好，为荞麦机械化收获机械的改进提供依据。

INTRODUCTION

When buckwheat is harvested, the maturity of the grains is inconsistent, the mature grains are easy to fall off, and the stem has high moisture content *(Ren Changzhong et al., 2018)*. It has large damage rate and high impurity content during mechanized harvesting, and it is easy to block the threshing roller, which seriously restricts the mechanized development of the buckwheat industry *(Huang Xiaona et al., 2018; Farooq et al., 2016)*. The existing buckwheat combine harvesters are improved machines based on rice, wheat and other small grain combine harvesters, and there are few specialized buckwheat harvesting machines *(Lu Wentao et al., 2017)*.

---

[1] *Jiawei Wang, As Lec. Ph.D. Eng.; Xiaohong Yu*, Lec. M.S. Eng.; Jianlong Zhang, Lec. M.S. Eng.;*
Decong Zheng, Prof. Ph.D. Eng.; Zhiwei Li Prof. Ph.D. Eng.; Haiyan Song, Prof. Ph.D. Eng.

The main structure of horizontal-flow threshing device of domestic full-feed combine harvester is single horizontal and cross-flow double-roller threshing device. During field harvesting, the threshing device has limited processing capacity and encountered difficulties in stalk and green leaves. When threshing crops, the threshing loss is large and clogging is easy to occur, which reduces the harvesting efficiency *(Lachuga et al., 2020; Maertens et al., 2004; Petkevichius et al., 2008)*. When the combine harvester's axial flow threshing device works, the crops make spiral movements, and the threshing is gentle and the working time is long. Therefore, it is superior to the traditional cutting device in terms of removal rate, damage rate, and separation rate, and can increase productivity without increasing the volume of the body *(Chuan-udom et al., 2011; Barać et al., 2011; Dhananchezhiyan et al., 2013)*. Theoretical research is the basis of threshing device research. Through the establishment of mathematical models and computer simulation, the movement of seeds in the threshing roll provides a lot of theoretical information for the design of threshing device *(Miu et al., 2007; Powar et al., 2019; Govindaraj et al., 2017)*.

In recent years, a large number of scholars have studied the threshing device of combine harvesters. *Liu Zhenghuai et al. (2018)* designed a rotary grid concave plate threshing device to effectively prevent the threshing roller from blocking and improve the threshing effect. *Hou Shouyin et al. (2012)* designed a vertical axial flow soybean breeding threshing machine, and provided a basis for the design of the vertical axial flow soybean breeding thresher. *Di Zhifeng et al. (2018)* designed a combined axial flow threshing roller to provide a theoretical basis for the development of a grain harvester. *Zong Wangyuan et al. (2013)* designed a combined rapeseed threshing device, which can effectively improve the efficiency of threshing and separation of rapeseed and reduce the loss rate.

Based on the axial flow threshing device, this paper designs an independent rotary buckwheat threshing device with inner and outer rollers, and applies it to a track-type combine harvester, which is the basis for the development of buckwheat mechanized harvesting machinery.

MATERIALS AND METHODS
Inner and outer roller buckwheat threshing device
The overall structure

The overall structure of the inner and outer roller buckwheat threshing device is shown in Fig. 1. It is mainly composed of feeding inlet, top cover, screw feeding device, outer roller pressing device, grid roller, tie rod roller, main shaft, nail tooth roller, speed reducer, grass discharge port, frame, friction wheel drive shaft, friction wheel and so on. The spiral feeding device, which is welded by double spiral blades and cone barrels, is connected to the tie rod roller and nail tooth roller through the main shaft to form an inner roller. The grid roller is an outer roller, the two ends of the outer roller are supported by the support wheels and friction wheels, and driven to rotate by the friction wheel. In order to prevent jumping and slipping during the rotation of the outer roller, an elastic pressing device is installed on the top of the outer roller. The inner and outer rollers are eccentrically mounted at 22.5 mm in the vertical direction, the maximum gap at the top is 46 mm, the minimum gap at the bottom is 10 mm, and the gap between other positions is between 10 mm~46 mm. While ensuring threshing, there is enough space for the material to flip and push backwards, which improves the threshing and separation effect. A side cover is installed on the right wall of the box rack, which can be opened for cleaning.
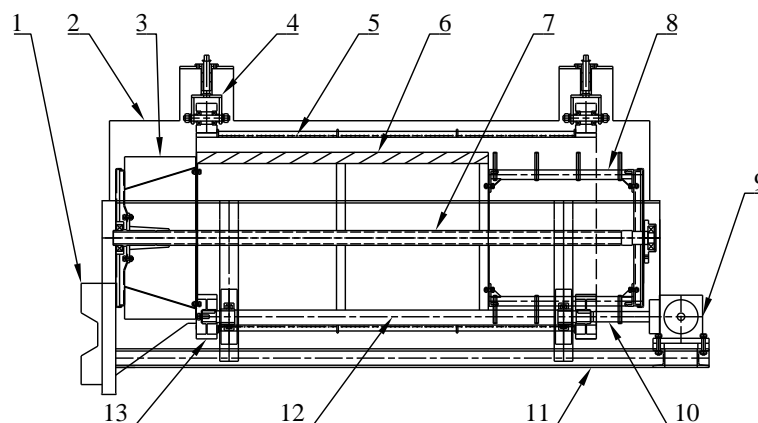
Fig. 1 - Structure of buckwheat threshing device
1- Feeding inlet; 2- Top cover; 3- Screw feeding device; 4- Outer roller pressing device; 5- Grid roller; 6- Tie rod roller; 7- Main shaft; 8- Nail tooth roller; 9- Speed reducer; 10- Grass discharge port; 11- Frame; 12- Friction wheel drive shaft; 13- Friction wheel

Inner roller

The inner roller of this design adopts the rod-tooth combination roller, with the tie rod roller in front, the nail tooth roller behind. Buckwheat completes the separation of the main grains under the action of the tie rod roller, after the hard-to-remove grains enter the nail roller, they are further separated by the impact of the nail tooth roller, and finally the straw is thrown out of the machine.

The structure of the tie rod roller is shown in Fig. 2. The hexagonal star-shaped front panel, hexagonal star-shaped intermediate panel, and hexagonal star-shaped rear panel are welded on the inner roller's main shaft. 6 D-shaped left-handed rods are fixed on the raised portion of the plate by bolts. In order to balance the rotation process, 6 even-numbered rods are used. The thick iron sheet is covered between the rod and the roller to form a closed roller, prevent the straw from intertwining with the main shaft during the threshing process, and reduce the leakage and break of the kernel. The length of the tie rod roller is 988 mm, and the working outer diameter is φ580 mm.
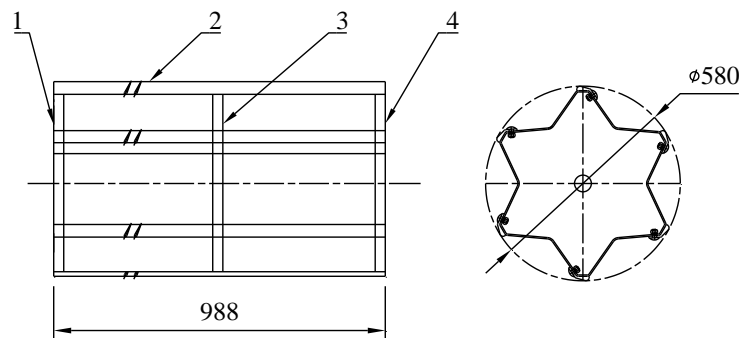
Fig. 2- Structure of tie rod roller

1- Front plate; 2- D-shaped left-handed rod; 3- Middle plate; 4- Rear plate

The structure of the nail tooth roller is shown in Fig. 3. The circular front panel and the circular rear panel are connected into a cylindrical structure by bolts through 6 nail connecting rods. The nails are welded with nail rods distributed in an axial spiral. The diameter of the nails is φ12 mm and the length of the nails is 60 mm. In order to prevent the grass from hanging during the rotation, each nail is installed at an angle of 11° backward in the direction of rotation.
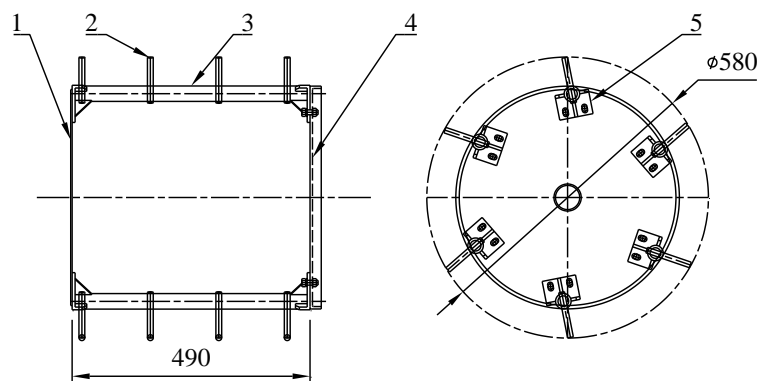
Fig. 3 - Structure of nail tooth roller

1- Front panel; 2- Nail; 3- Nail rod; 4- Rear panel

Outer roller

In order to improve the effect of threshing and separation, the grid concave plate is designed as a round outer roller and can be rotated freely, which effectively solves the problems of common grid concave plate easy to block causing serious wear during the threshing process. The extract passes through the outer roller of the grid, which can be evenly spread on the vibrating screen, and beneficial to the further separation and cleaning of the buckwheat extract. The structure of the outer grid roller is shown in Fig. 4. Equivalently spaced 4 internal ribbed plate fixing slots with internal grooves, 120 holes perforated ribbed plates are evenly fixed in the inner circumferential direction to form a cylindrical grid roller. A circular iron wire is worn every 15 mm in the axial direction of the roller, and the diameter of the iron wire is φ3 mm. In this way, the surface of the roller constitutes a grid of hole length 14 mm and hole width 12 mm. The top surface is higher than the iron wire 5 mm in order to block crops, improve the impact of the roller on the crops, and the brushing effect.
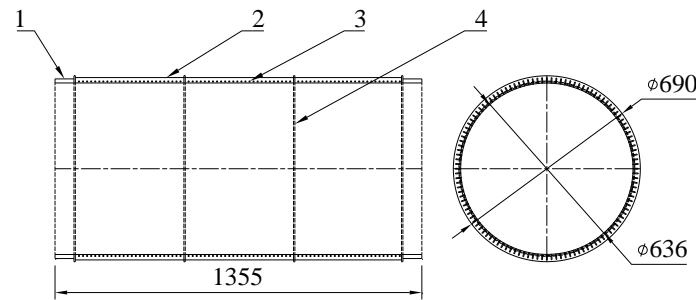
Fig. 4 - Structure of outer roller
1- Support plate; 2- Rib; 3- Iron wire; 4- Rib fixed plate

Screw feeding device

The spiral feeding device is shown in Fig. 5. Its main function is to forcibly squeeze the materials entering the feed inlet between the inner and outer rollers through spiral blades to complete the threshing. Its performance directly affects the feeding amount and threshing performance of the threshing device. The spiral feeding device is welded by the front panel, cone cylinder, rear panel and spiral blades. The diameter of the front panel is φ460 mm, the diameter of the rear panel is φ415 mm, the diameter of the small end of the cone cylinder is φ272mm, the diameter of the large end of the cone cylinder is φ415 mm, and the height of the cone cylinder is 241 mm, the blade rise angle is 48°.
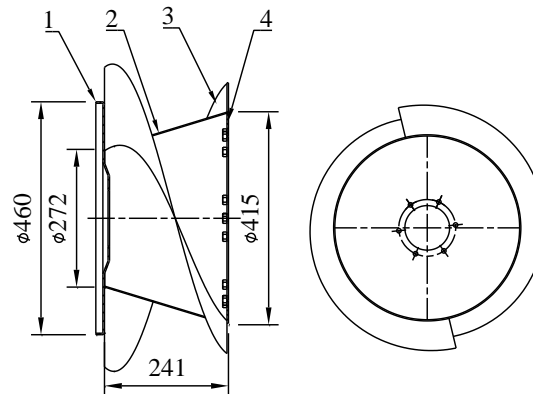
Fig. 5- Structure of screw feeding device
1- Front panel; 2- Cone cylinder; 3- Spiral blade; 4- Rear panel

Friction wheel transmission system

The friction wheel transmission system used in the threshing device is shown in Fig. 6, which is mainly composed of friction wheels, transmission shafts, bearings with vertical seats and coupling. The left friction wheel is connected to the left end of the drive shaft by bolts and flat keys, the right friction wheel is connected to the right end of the drive shaft by a flat key and a snap ring, and the right end of the drive shaft is connected to the outer roller reducer through a coupling to drive the spindle to rotate.
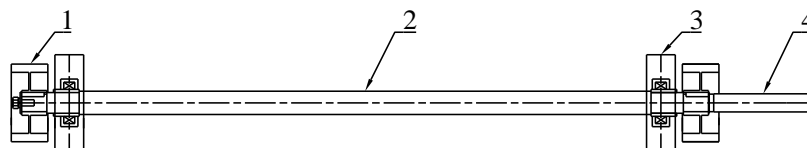
Fig. 6- Structure of friction wheel transmission system
1- Friction wheel; 2- Drive shaft; 3- Bearing with vertical seat; 4- Coupling

Outer roller pressing device

The outer roller pressing device is mainly composed of pressure wheel, pressure wheel shaft, pressure wheel frame, pressure wheel frame fixed shaft, copper sleeve, as shown in Fig. 7. The pressure wheel is mounted on the pressure wheel shaft through bearing. The pressure wheel shaft is connected to the frame, and the top of the frame is welded with a fixed shaft, there is copper sleeve between them so that the wheel frame can slide freely up and down along the sleeve. A spring is installed between the wheel frame and the top cover.
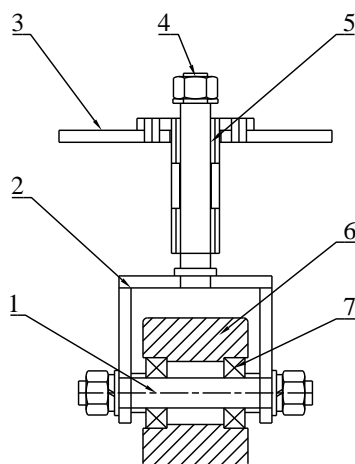
Fig. 7- Structure of outer roller pressing device

1- Pressure wheel shaft; 2- Pressure wheel frame; 3- Top cover; 4- Pressure wheel frame fixed shaft;
5- Copper sleeve; 6- Pressure wheel; 7- Bearing

Test prototype

The prototype of a tracked buckwheat combine harvester is shown in Fig. 8. The main machine and chassis are equipped with a Kubota 688 tracked combine harvester, the threshing device uses an independently designed internal and external roller rotary buckwheat threshing device. The main working parameters are shown in Tab. 1. During work, the reel wheel will turn the cut buckwheat plant to the screw conveyor, and enter the feeding bridge under the action of the screw conveyor, and then enter the internal and external roller rotary thresher through the feeding chain through the bridge. During the rotation of the inner and outer rollers, the buckwheat plants are brushed and rubbed to achieve the separation of buckwheat grains and stalks. The mixture is taken out and thrown out of the outer roller to fall into an air-screen cleaning device, the straw is discharged at the discharge port. The separated mixture fall into the cleaning device and is separated by the fan and the vibrating screen. After the selection, the grains fall into the grain conveyor and are sent to the grain silo, the debris is shaken out of the machine by the shaker.

Fig. 8 - Tracked buckwheat combine harvester prototype

Table 1

Tracked buckwheat combine harvester technical parameters

Project Name		Technical Parameters
Dimensions, [mm]		4950×2440×2800
Quality, [kg]		2790
Matching engine	Model	V2403-M-DI-T-ES04
	Power, [kW]	49.2
	Rotating speed, [r/min]	2700

Table 1
(continuation)

Project Name	Technical Parameters
Header width, [mm]	2000
Minimum stubble height, [mm]	40
Threshing pattern	Internal and external roller rotary
Feed amount, [kg/s]	1.5
Threshing gap, [mm]	10
Speed of inner roller, [r/min]	530
Speed of outer roller, [r/min]	+50
Screen type	Woven screen
Vibration screen frequency, [Hz]	6
Fan speed, [r/min]	1100
Minimum ground clearance, [mm]	275
Working speed, [km/h]	0~4.93

Test material

Field test is in Shouyang Shanxi Province, October 2020. The test buckwheat is "Red Mountain" buckwheat, and its characteristics are shown in Tab. 2.

Table 2

Main properties of buckwheat

Parameter	Value
High of buckwheat, [mm]	1500
Average grain moisture content, [%]	19.9
Stem average moisture content, [%]	82.9
Grain to grass ratio	1:3.57
Thousand weights, [g]	27.2

Test method

The tests are carried out in accordance with GB/T 8097-2008 "Test methods for harvesting machines and combine harvesters" and GB/T 5262-2008 "General rules for the determination of test conditions for agricultural machinery". Three test areas are selected in the test field, the test area is 50 m in length and 2 m in width, and signposts are set up at both ends of the test area *(Li Yaoming et al., 2018; Chen Jin et al., 2018)*. When the header enters the test area, it starts timing and works at normal speed. When it leaves the test area, it stops timing.

The quality of the stalks on the receiving cloth, the quality of the grains mixed in the stalks, the quality of the unsettled grains on the stalks, and the quality of the grains that fell on the ground when the cutting platform passed are collected by artificial methods, and the natural fall of the measurement area is measured before testing. Calculating threshing loss rate, cleaning loss rate, header loss rate, natural fall loss and total loss rate. Three samples are randomly sampled from each of the test areas, 500 g each, and the damage kernels and impurities are manually selected to calculate the damage rate and impurity rate.

$$S_t = \frac{W_t}{W}$$

(1)

$$S_x = \frac{W_x}{W}$$

(2)

$$S_g = \frac{W_g}{W}$$

(3)

$$S_r = \frac{W_r}{W}$$

(4)

$$S = S_t + S_x + S_g + S_r \tag{5}$$

$$W = W_z + W_t + W_x + W_g + W_r \tag{6}$$

where:

S_t is threshing loss rate, [%]; S_x is cleaning loss rate, [%]; S_g is direct header loss rate, [%];
S_r is natural grain loss rate, [%]; S is total loss rate, [%]; W_t is grain quality of threshing loss, [g];
W_x is grain quality of cleaning loss, [g]; W_g is grain quality of direct header loss, [g];
W_r is grain quality of natural loss, [g]; W_z is grain quality of sample, [g].

RESULTS

Analysis of conveying capacity

The material under the action of the spiral blade is simplified into particles M *(Peng Yuxing et al., 2016)*, and the force analysis is performed as shown in Fig. 9. The force exerted by the spiral blade on the material particle M is F. Because the material is affected by the frictional force of the blade, the F direction is offset from the normal direction of the spiral blade by an angle β. The β is determined by the friction angle ρ of the material on the spiral blade and the surface roughness of the spiral blade. For spiral blades made of hot-pressed or cold-rolled steel plates, the effect of surface roughness on β can be ignored, so $\beta=\rho$. F can be decomposed into a normal component force F_1 and a tangential component force F_2, where the angle between F_1 and the axial direction is the helical blade lift angle α, and the projection of F in the axial direction F_t is the axial component force on the material M. Material M performs compound motion in the trough under the action of force F, which moves both axially and tangentially, as shown in Fig. 10, and the axial velocity V_1 and the tangential peripheral velocity V_2, the combined velocity V.
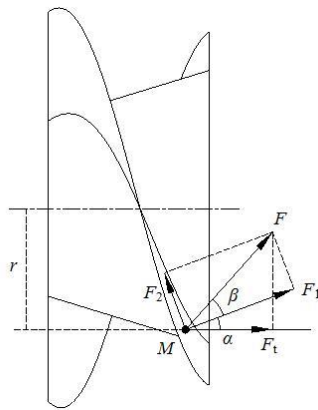
Fig. 9 - Material force analysis   **Fig. 10 - Material moving speed analysis**
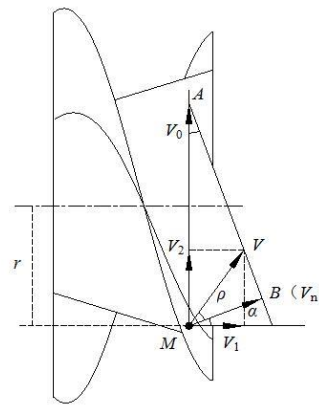
When the spiral blade rotates around the axis at an angular velocity ω, the speed of the material M at the radius r from the axis of the spiral blade can be solved by the speed triangle, as shown in Figure 10. V_0 is the impulsive motion speed of the material M, which is represented by the vector MA, and the direction is along the tangential direction of rotation of the point M, the relative sliding speed of the material M relative to the spiral blade is parallel to the spiral tangent direction of the point M, and is expressed by the vector AB. Regardless of the friction of the spiral blade, the absolute moving speed V_n of the material M should be along the normal direction of the M point on the spiral blade, which is expressed by the vector MB. Because the spiral blade has a friction effect on the material, the moving speed V direction of the material M and the normal direction are offset by the friction angle ρ. By decomposing the speed V, the axial speed V_1 and tangential peripheral speed V_2 of the material M can be obtained, where V_1 is the speed of the material in the material tank in the axial direction, and V_2 is the blocking speed of the material by the spiral blade. According to the analysis of the moving speed of the material M, the axial conveying speed of the material M is:

$$V_1 = V \cos(\alpha + \rho) \tag{7}$$

Because:

$$V = V_n / \cos \rho \,, \quad V_n = V_0 \sin \rho$$

So:

$$V_1 = V_0 \frac{\sin \alpha}{\cos \rho} \cos(\alpha + \rho)$$

(8)

$$V_0 = \omega \cdot r = \frac{2\pi n}{60} \cdot \frac{S}{2\pi \tan \alpha} = \frac{n \cdot S}{60 \tan \alpha}$$

(9)

$$\cos \alpha = \frac{1}{\sqrt{1 + (S/2\pi\, r)^2}}$$

(10)

$$\tan \alpha = \frac{S}{2\pi\, r}$$

(11)

Substituting formula 3, formula 4, and formula 5 into formula 2, the axial conveying speed of material *M* can be obtained:

$$V_1 = \frac{Sn}{60} \cdot \frac{1 - f\, S/2\pi\, r}{1 + (S/2\pi\, r)^2}$$

(12)

Similarly, the circumferential tangential velocity of the material *M* can be obtained:

$$V_2 = \frac{Sn}{60} \cdot \frac{f + S/2\pi r}{1 + (S/2\pi r)^2}$$

(13)

Where:

S is pitch of spiral blade, 241 mm; n is rotating speed of screw conveyor, 430 r/min; f is coefficient of friction between material and spiral blade, $f = tan\ \rho = 0.1$; ρ is friction angle between material and spiral blade, 6°; α is rising angle of spiral blade, 48°;

Calculated from formula 6, the axial conveying speed of material M is 1.87 m/s.

The conveying amount Q is an important index for measuring the conveying capacity of the screw feeding device.

The formula for calculating the conveying amount Q is as follows:

$$Q = A \cdot \lambda \cdot V_1 \cdot \varepsilon$$

(14)

$$A = \phi \cdot D^2 \cdot \pi / 4$$

(15)

Where:

Q is conveying amount of the screw feeding device, [kg/s]; A is cross-sectional area of material in the trough, 36512 mm²; φ is material fill factor, $\varphi = 0.125$; D is spiral blade diameter, 610 mm; λ is buckwheat material density, 0.1×10^{-6} kg/mm³; ε is conveying coefficient of screw conveying device, $\varepsilon = 0.70$;

Comprehensive calculation, the conveying capacity of the spiral feeding device $Q = 4.29$ kg/s.

Field test result

The field test results are shown in Tab. 3. Under the conditions of working speed of 0.53 m/s, feed rate of 0.41 kg/s, the field operation quality indicators of the crawler buckwheat combine harvester are as follows: the grain impurity rate is 6.50%, the grain damage rate is 1.42%, the threshing loss rate is 0.25%, the cleaning loss rate is 1.01%, the direct header loss rate is 2.43%, the natural grain loss rate is 2.98%, and total loss rate is 6.67%. If the natural grain loss rate is not included, the total machine harvest loss rate is 3.69%. The average grain yield of buckwheat in the measurement area is 15.87 kg, the biological yield is 38.53 kg, the average test time is 105.06 s, the average productivity is 3788.72 m²/h, and the average stubble height is 376.56 mm. The test results are good, and basically meet the requirements of the indicators formulated by the national project.

It can be seen from the test results that as the working speed decreases, the feed rate gradually decreases, and the header loss rate gradually increases. The grain damage rate, threshing loss rate, and cleaning loss rate all decrease first and then increase, so is the total loss rate. Therefore, the harvest effect is best when the working speed is at a medium speed.

Table 3

Field test results

Test item	Test result				
	1	2	3	4	average
Test length, [m]	50.00	50.00	50.00	50.00	50.00
Test width, [m]	2.00	2.00	2.00	2.00	2.00
Test time, [s]	59.52	107.50	112.56	140.66	105.06
Working speed, [m/s]	0.84	0.47	0.44	0.36	0.53
Stubble height, [mm]	359.25	376.67	388.33	382.00	376.56
Feed rate, [kg/s]	0.65	0.37	0.37	0.26	0.41
Productivity, [m²/h]	6048.40	3348.84	3198.29	2559.36	3788.72
Biological yield, [kg]	35.84	40.26	41.71	36.32	38.53
Grain yield, [kg]	15.28	17.11	16.69	14.40	15.87
Grain impurity rate, [%]	5.72	4.10	9.30	6.87	6.50
Grain damage rate, [%]	1.84	1.46	1.15	1.22	1.42
Threshing loss rate, [%]	0.4	0.21	0.13	0.27	0.25
Cleaning loss rate, [%]	1.36	1.11	0.74	0.83	1.01
Header loss rate, [%]	2.06	2.40	2.42	2.83	2.43
Natural grain loss rate, [%]	3.09	2.76	2.79	3.26	2.98
Total loss rate, [%]	6.91	6.48	6.08	7.19	6.67

CONCLUSIONS

(1) The inner and outer roller rotary buckwheat threshing device was designed. The device is mainly composed of an inner threshing roller and a grid outer roller. The inner and outer rollers rotate at the same time to knead and squeeze the material to complete the separation of buckwheat grains and stalks. On the basis of the Kubota 688 tracked combine harvester, the threshing device was installed to complete a tracked buckwheat combined harvester prototype.

(2) The screw feeding device was designed, and the mathematical model of the screw feeding device was established. By calculation, the material feeding speed of the screw feeding device was 1.87 m/s, and the conveying capacity was 4.29 kg/s.

(3) The field operation quality indicators of this model were as follows: the average grain impurity rate was 6.50%, the grain damage rate was 1.42%, the threshing loss rate was 0.25%, the cleaning loss rate was 1.01%, the direct header loss rate was 2.43%, the natural grain loss rate was 2.98%, and the total machine harvest loss rate was 3.69%. The test results provided a basis for the improvement of buckwheat mechanized harvesting machinery.

ACKNOWLEDGEMENT

REFERENCES

[1] Barać S.R., Biberdžić M., Đikić A., (2011), Result of testing of seeds and quality losses of harvested mass depending on the drum-underdrum interspace at buckwheat harvest grain combines. *Research Journal of Agricultural Science*, Vol. 43, Issue 1, pp. 283-288, Timisoara/Romania;

[2] Chen Jin, Wang Shuqing, Lian Yi., (2018), Design and test of header parameter keys electric control adjusting device for rice and wheat combined harvester. *Transactions of the Chinese Society of Agricultural Engineering*, Vol. 34, Issue 16, pp. 19-26, Beijing/China;

[3]　Chuan-udom S., Chinsuwan W., (2011), Effects of operating factors of an axial flow rice combine harvester on grain breakage. *Sonklanakarin Journal of Science and Technology*, Vol. 33, Issue 2, pp. 221–225, Hatyai/Thailand;

[4]　Dhananchezhiyan P., Parveen S., Rangasamy K., et al., (2013), Development of a nylon rasp bar threshing cylinder for portable paddy thresher and its performance evaluation, *Madras Agricultural Journal*, Vol. 2013, Issue 100, pp. 623–626, New Delhi/India;

[5]　Di Zhifeng, Cui Zhongkai, Zhang Hua., et al., (2018), Design and experiment of rasp bar and nail tooth combined axial flow corn threshing cylinder. *Transactions of the Chinese Society of Agricultural Engineering*, Vol. 34, Issue 1, pp. 28-34, Beijing/China;

[6]　Farooq S., Rehman R.U., Pirzadah T., et al., (2016), Cultivation agronomic practices and growth performance of buckwheat. Molecular breeding and nutritional aspects of buckwheat, Elsevier, Amsterdam/Netherlands;

[7]　Govindaraj M., Masilamani P., Asokan D., et al., (2017), Effect of different harvesting and threshing methods on seed quality of rice varieties. *International Journal of Current Microbiology and Applied Sciences*, Vol. 2017, Issue 6, pp. 2375–2383, Tamil Nadu/India;

[8]　Hou Shouyin, Chen Haitao., (2012), Parameters optimization of vertical axial flow thresher for soybean breeding. *Transactions of the Chinese Society of Agricultural Engineering*, Vol. 28, Issue 5, pp. 19-25, Beijing/China;

[9]　Huang Xiaona, Zhang Weiguo, Dang Weilong., et al., (2018), Research status and development trend of buckwheat harvesting machinery. *Farm Machinery*, Vol. 2018, Issue 10, pp. 84-90, Beijing/China;

[10]　Lachuga Y.F., Bur'yanov A.I., Pakhomov V.I., et al., (2020), Adaptation of threshing devices to physical and mechanical characteristics of harvested crops. *Russian Agricultural Sciences*, Vol. 46, Issue 2, pp. 198-201, Moscow/Russia;

[11]　Li Yaoming, Wang Jianpeng, Xu Lizhang., et al., (2018), Design and experiment on adjusting mechanism of concave clearance of combine harvester cylinder. *Transactions of the Chinese Society for Agricultural Machinery*, Vol. 49, Issue 8, pp. 68-75, Beijing/China;

[12]　Liu Zhenghuai, Dai Sujiang, Tian Liquan., et al., (2018), Design and experiment on rotary grate concave threshing-separating unit of head-feeding combine harvester. *Transactions of the Chinese Society for Agricultural Machinery*, Vol. 49, Issue 5, pp. 169-178, Beijing/China;

[13]　Lu Wentao, Wang Rongxian, Deng Zhigang., (2017), Development status and prospect of threshing technologies for coarse cereal. *Journal of Chinese Agricultural Mechanization*, Vol. 38, Issue 11, pp. 11-16, Nanjing/China;

[14]　Maertens K., Ramon H., Baerdemaeker J.D., (2004), An on-the-go monitoring algorithm for separation processes in combine harvesters. *Computers and Electronics in Agriculture*, Vol. 43, Issue 3, pp. 197-207, Amsterdam/Netherlands;

[15]　Miu P.I., Kutzbach H.D., (2007), Mathematical model of material kinematics in an axial threshing unit. *Computers and Electronics in Agriculture*, Vol. 58, Issue 2, pp. 93-99, Amsterdam/Netherlands;

[16]　Peng Yuxing, Li Xu, Liu Dawei., et al., (2016), Design and performance experiment of a threshing cylinder with longitudinal single axial flow. *Journal of Hunan Agricultural University*, Vol. 42, Issue 5, pp.554-560, Changsha/China;

[17]　Petkevichius S., Shpokas L., Kutzbach H.D., (2008), Investigation of the maize ear threshing process. *Biosystems Engineeri*ng, Vol. 99, Issue 4, pp. 532-539, London/ England;

[18]　Powar R.V., Aware V.V., Shahare P.U., (2019), Optimizing operational parameters of finger millet threshing drum using RSM. *Journal of Food Science and Technology*, Vol. 56, Issue 7, pp. 93-99, Mysore/India;

[19]　Ren Changzhong, Cui Lin, He Feng., et al., (2018), Construction and development of China oat and buckwheat industrial technology system. *Journal of Jilin Agricultural University*, Vol. 40, Issue 4, pp.524-532, Changchun/China;

[20]　Zong Wangyuan, Liao Qingxi, Huang Peng., et al., (2013), Design of combined rape threshing device and analysis of rape cane movement trail. *Transactions of the Chinese Society for Agricultural Machinery*, Vol. 44, Issue S2, pp. 41-46, Beijing/China.

RESEARCH OF THE CLEANING SYSTEM FOR THIN-WALLED FERMENTER, USED IN THE MANUFACTURING OF MICROBIAL PLANT PROTECTION PRODUCTS
/
ДОСЛІДЖЕННЯ СИСТЕМ ОЧИЩЕННЯ ТОНКОСТІННОГО ФЕРМЕНТЕРУ ПРИ ВИРОБНИЦТВІ МІКРОБІОЛОГІЧНИХ ЗАСОБІВ ЗАХИСТУ РОСЛИН

BESPALOV I.[1)], **YAROSHEVSKY V.**[1)], **BULGAKOV V.**[2)], **IVANOVS S.**[3)]　　[1]
[1)] Engineering and Technological Institute "Biotekhnika", Ukraine;
[2)] National University of Life and Environmental Sciences of Ukraine, Ukraine;
[3)] Latvia University of Life Sciences and Technologies, Latvia

Keywords: thin-walled fermenter, cleaning, pasteurisation, steriliser, heated water.

ABSTRACT
The peculiarities of microbial plant protection products from pests and diseases allow the use of thin-walled fermenters in their production, in which there is no sterilisation under high pressure. The article is devoted to the development of the cleaning in place system for such fermenters. Experimental studies have been carried out to ensure a pasteurising effect when treating the fermenter with heated sterile water and a nutrient medium concentrate obtained from the sterilizer. Its parameters: its volume, temperature, the time delay have been determined. There is proposed a hardware diagram of the fermentation plant, consisting of an industrial steriliser and a thin-walled fermenter. The cleaning procedure is combined with the main technological process and does not require additional equipment. The production tests have confirmed the cleaning efficiency.

АНОТАЦІЯ
Особливості мікробіологічних засобів захисту рослин від шкідників і хвороб дозволяють при їх виробництві використовувати тонкостінні ферментери, в яких відсутня стерилізація під високим тиском. Стаття присвячена розробленню системи очищення на місці для таких ферментерів. Проведено експериментальні дослідження із забезпечення ефекту пастеризації при обробленні ферментеру нагрітою стерильною водою й концентратом поживного середовища, що пройшло стерилізацію. Відзначені її параметри: об'єм, температура, час витримки. Запропоновано апаратурну схему ферментаційної установки, що складається з промислового стерилізатору і тонкостінного ферментеру. Процедура очищення відбувається сумісно з основним технологічним процесом й не потребує додаткового устаткування. Ефективність очищення підтверджено промисловими випробуваннями.

INTRODUCTION

Ecologisation of agriculture as a strategic direction of sustainable development of environmental activities provides for the widespread use of microbial plant protection products from pests and diseases (hereinafter biopesticides) *(Liu et al., 2021; Arshad, 2018; Van Oosten, et al., 2017; Nicolopoulou-Stamati et al., 2016)*. It has historically occurred in Ukraine that their production, despite the presence of the microbiological industry, was carried out mainly in biological laboratories - small enterprises that were part of the agricultural system. This structure is still in effect and is the most promising at the deficiency of investments *(Krutyakova, 2019)*.

Microbiological production, as a branch of industry, has significant and sufficient scientific support *(Panda, 2011; Köhler et al., 2015; Yaroshevsky et al., 2020)*. Its main processes - sterilisation and fermentation - have many hardware and technological implementations *(Lukanin, 2020)*. Yet, as practice shows, most of them have not found application in biological laboratories due to the unacceptable cost of classic high-pressure fermenters, significant costs of thermal sterilisation and, most importantly, the inexpediency of creating microbiological production facilities with full infrastructure at small enterprises.

---

[1] *Bespalov I., Ph.D.; Yaroshevsky V., Ph.D.; Bulgakov V., Prof. Ph.D. Eng.; Ivanovs S., Ph.D. Eng.*

It is known that a necessary condition for the functioning of the fermentation complexes is the presence of two systems (*Lukanin, 2020; Goode et al., 2013; Pettigrew et al., 2015)*. The equipment cleaning by CIP-system (Cleaning-in-Place) for ensuring the required level of equipment cleanliness. The processing is performed in several stages: rinsing with water, rinsing with a detergent reagent, rinsing to neutralise the reagent. The equipment sterilisation by SIP-system (Sterilisation-in-Place) without its preliminary dismantling. Typically, saturated steam is used for sterilisation at a temperature of 120°C and a pressure of 2 bars for about 60–70 minutes. The developed variety of the sterilisation modes testifies mainly to the fact that these modes have a practical basis and are not based on the theoretical foundations of the present-day thermal sterilisation. The existing approach to the assessment of the efficiency of the sterilisation regimes does not allow determination of the efficiency that is really necessary for guaranteed inactivation of the extraneous microflora (*Lukanin, 2020)*.

Usually, these systems are implemented by means of additional equipment as part of a complex with the high-pressure fermenters, being created for the food and pharmaceutical industries. Analysis of the production and use of biopesticides showed that in most cases of conditionally aseptic production is sufficient (*Kotlyarov and Sedinina, 2014; Krutyakova et al., 2017)*. This is primarily due to the marketable form of the preparations and their purpose when the product is a culture liquid from fermenters with a short shelf life, which is used to treat plants or the soil. Therefore, the so-called thin-walled fermentation devices have been developed specifically for the production of biopesticides at the Engineering and Technological Institute "Biotekhnika" (*Starchevsky et al, 2007; Krutyakova et al, 2019)*.

In thin-walled fermenters the metal consumption is significantly reduced in contrast to the industrial fermenters due to their manufacture from thin-sheet corrosion-resistant steel (δ = 0.8...1.5 mm). The pressure inside the fermenter is almost equal to the atmospheric pressure, which automatically eliminates the requirements of the government regulations for pressure vessels.

The disadvantages of the thin-walled reactors were problems with sterilisation of the equipment, which necessitated application of special methods. Treatment with disinfectant solutions, heating of the metal surfaces to high temperatures *(Palabiyik et al., 2015; Wilson et al., 2015)*, and other methods were used for such fermenters sterilization. The purpose of this work was to develop a cleaning system with the sterilisation elements for a modern thin-walled fermenter *(Bespalov and Khodorchuk, 2017)*.

MATERIALS AND METHODS

Long-term operation of the fermentation plants suggested one more method of cleaning and sterilisation "in place" without the use of additional tools or devices. The known methods of pasteurisation of the food products were used *(Bredikhin, 2021)*, which ensure the death of vegetative forms of microorganisms. The efficiency of pasteurization depends on two parameters: the temperature to which the product is heated, and its exposure at this temperature.

Numerous data for the dairy products indicate that at temperatures above 85°C, an exposure of 10 minutes is sufficient. These values were used as a reference in the design of the cleaning system. The experimental equipment (See Fig. 1), on which the research was performed, is a part of the pilot fermentation plant *(Bespalov and Khodorchuk, 2017)* at the Engineering and Technological Institute "Biotekhnika" (See Fig. 2).

The thin-walled fermenter with a 115 litres capacity was made of stainless steel with a thickness of 1...2 mm. It consists of vessel *3*, cover *2*, air jacket *4* through which the ambient air was pumped by fan *5* for cooling. Sterile water was supplied through valve *V1*. Agitation was made by sterile air supplying under pressure through valve *V3* into the liquid volume through the nozzle *1*.

An industrial autoclave VK-75 was used as a sterilizer. The sterilizer had the sterilization chamber *6* with water jacket *8* between which valve V9 is installed. The sterile water is supplied to the chamber through valve *V5*.

Concentrated nutrient medium (CNM) making procedure involved CNM components addition through open lid *7* into water volume, contained in chamber *6*, further homogenization of mixture by pressured air, which was supplied through valve *V8*, and thermal sterilization at 2 bars according to the standard method. The heated steam-water mixture, after reaching the set temperature or sterile CNM with the same temperature, is fed from the sterilizer to the fermenter through a flexible corrugated stainless-steel pipe *10,* with detachable connections.
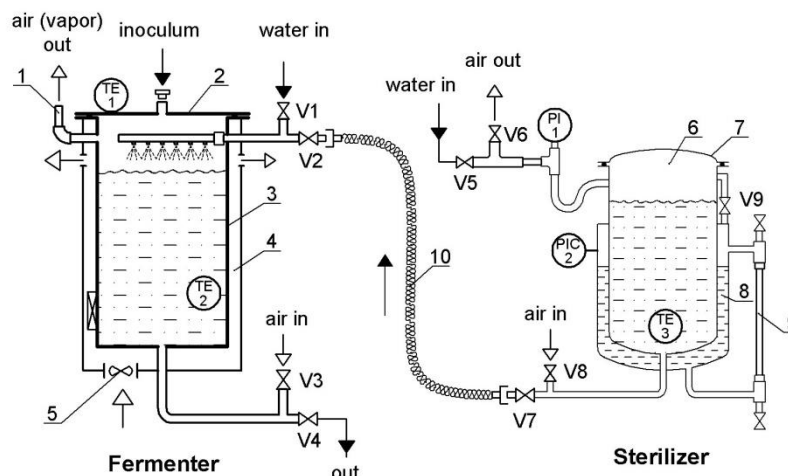
Fig. 1 - The hardware diagram of the experimental fermentation plant

Fig. 2 - The pilot fermentation plant

The bypass is carried out under the action of the sterilisation pressure in chamber *6* by opening valves V7, V2, valve V9 being closed to preserve water in jacket *8*. The measurement of the parameters in the experiment was conducted by a set of instruments with an accuracy class of 0.5, including:

t_C – temperature of the outer surface of cover *2* by the TE in sensor *1*;

t_V – temperature inside the fermenter vessel by TE in sensor *2*;

t_S – the temperature of the liquid in sterilizer chamber *6* by the TE in sensor *3*;

t_a – the ambient air temperature in the room (sensor not shown).

Temperature t_S was controlled using the electrocontact manometer PIG / 2. Statistical processing of the measurements was performed using the MS Excel spreadsheet according to the standard method (Dally, 2008). During data processing there were determined the arithmetic mean values of the measured values, the standard deviation; the relative and absolute measurement errors were calculated for a 95% confidence level.

Cleaning of the fermenter and pipelines was carried out with tap water, which was heated in the sterilizer to an average temperature of t_s = 127.0°C, and then, under surplus pressure in the sterilizer, it was released into the fermenter, the fermenter communicating with the atmosphere through outlet pipe 1 (Fig. 1). The average air temperature in the room was t_a = 20.6°C. In the first experiment there were taken 10 dm³ of water in 4 replicates, which provided the maximum average temperature in the fermenter, equal t_{V1} = 91.8°C. At atmospheric pressure this value cannot exceed 100°C, and the task of the research was maximum approximation to this value. In the second experiment, in 6 replicates, the volume of water was increased to 16 dm³.

In statistical processing *(Nicolopoulou-Stamati et al., 2016)* there was used the criterion of Student's test 2.57 for the significance level of 0.05. When the temperatures were decreasing, ε increased, but this did not change the main result with value t_{V1} = 98.3°C, which was considered sufficient.

RESULTS

The graphs of the arithmetic mean temperatures of the vapour-air medium in the vessel - t_V and the outer surface of the cover - t_C are shown in Fig. 3. The measurements were made at time points 0; 1; 5; 10; 25 minutes. The maximum of heating was reached in 1 minute, and it amounted to:

$$t_{V1} = 98.3 \pm 1.8° \text{ C}, \quad MSD = 1.84 \text{ \%}$$
$$t_{C1} = 95.0 \pm 2.5° \text{ C}, \quad MSD = 2.63 \text{ \%},$$

where MSD is the mean-square deviation.
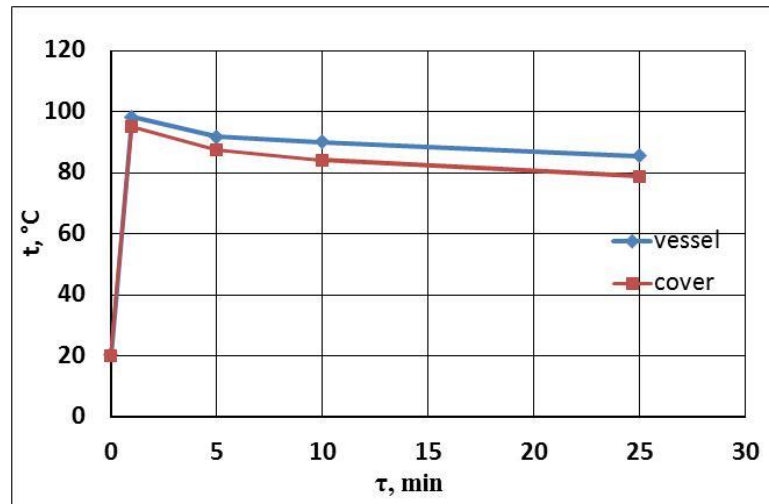
Fig. 3 - The fermenter temperature during pasteurization

Logical analysis shows that the temperature of the internal surfaces of the fermenter for our design must satisfy the ratio:

$$t_c < t_f < t_v \tag{1}$$

where: t_f – average temperature of the inner surface of the fermenter.

The obtained graphs (Fig. 3) show that the temperature t_f > 85°C is maintained for 10 minutes, i.e., the pasteurization mode inside the vessel is ensured. MSD increased when the temperatures were decreasing. However, this did not change the main result with value t_{V1} = 98.3°C, which was considered sufficient.

The water with a temperature of about 85°C is discharged by gravity from the fermenter after the end of the holding time, while opening its outlet pipe with valve V4. Cleaning the bypass line between the sterilizer and the fermenter (outlet and inlet nozzles, valves V2, V7, flexible pipe 10) takes place by boiling water within the first minute at a temperature of at least 100°C. The amount of water for cleaning was selected in accordance with the technological regulations for this fermentation plant. The regulations include the following ratios:

$$\upsilon_u = \upsilon_s + \upsilon_w + \upsilon_i, \tag{2}$$

$\upsilon_s : \upsilon_w$ = 1:4, υ_i = (3-5 %) υ_u,

where:

υ_u = 84 dm^3 – the useful volume of the fermenter;

υ_s = 16 dm^3 – the volume of the CNM;

υ_w = 64 dm^3 – the volume of sterile water;

υ_i = 4 dm^3 – the inoculum volume.

After cleaning is completed, the next technological stage is performed - nutrient medium making in the fermenter. In the sterilizer a concentrated nutrient medium v_s = 16 dm^3 is prepared, being sterilised at t_s = 127.0°C, and then supplied into the fermenter, with its thermal effect proceeding similar to the cleaning process by heated water, and accompanied by the same pasteurizing effect. After cooling the CNM, cold sterile water is added to the fermenter in ratio (1). The cyclogram of the fermenter cleaning processes in the form of temperature changes in the tank t_V at different stages of the technological process is shown in Fig. 4. Sterile water is poured into the sterilizer with volume v_w; at the moment τ_0 = 0, heating is turned on, which ends at t_s = 127.0°C. The sterilizer turns off, valves V2, V7 are opening, the steam-water mixture flows into the fermenter, heating its volume at the moment τ_1 to temperature t_{V1} = 98.3°C. Then the fermenter cools down to temperature t_V = 85°C. Holding at these temperatures determines the high-temperature pasteurisation on the inner surfaces of the fermenter. After that valve V4 opens, and hot water is released into the sewer, cleaning the outlet pipe with a tap.
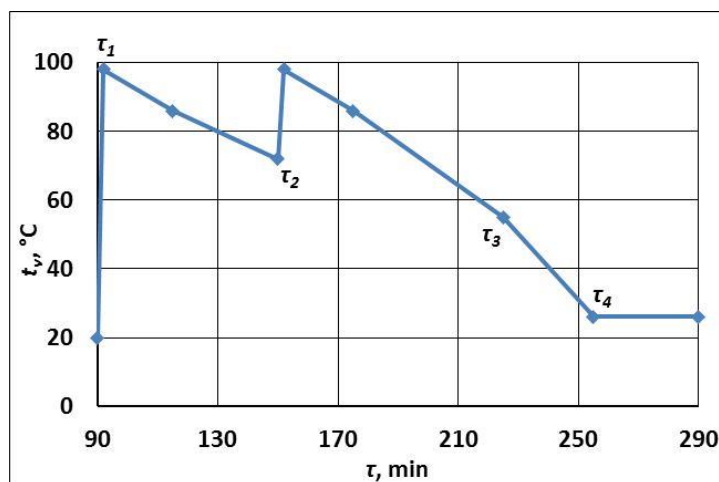
Fig. 4 - Cyclogram of the fermenter cleaning processes

The subsequent stages of cleaning with a pasteurizing effect are already associated with the implementation of the main technological process. After freeing the sterilizer from water at the moment of time τ_1, a concentrated nutrient medium is prepared in it, the sterilisation of which ends at the moment of time τ_2. Next, the bypass of the CNM opens into the fermenter.

The second stage of heating and pasteurization of the fermenter takes place, as it was described earlier. This process ends in 10 minutes, and air cooling of the fermenter is turned on by fan *5* in the jacket. The cleaning process is complete. When temperature t_{V3} drops to 50-55°C at the moment τ_3, sterile water with a volume of v_w at 20-25°C is supplied to the fermenter to dilute the CNM to the required concentration of the nutrient medium. By choosing ratios v_w, v_s, t_{V3} it is possible to regulate the final temperature of the nutrient medium at the end of the dilution at moment τ_4, usually 25...28°C. This indicates the end of the pre-fermentation stage. Inoculation with the seed culture is carried out, and then - the cultivation process starts. The research was carried out under the conditions of real production of biopesticides.

The cyclogram presents maximum values of the stage durations, which were recorded at a particular fermentation plant. For a fermenter with a different volume, it is necessary to select volumes v_s; this will change the duration of the operations. The developed method provided double heating of the inner surfaces of the fermenter to temperatures that guarantee the implementation of the pasteurizing effect. The system for cleaning the fermentation plant from a 75-litre steriliser and a 115-litre fermenter made it possible to implement the cleaning and pre-fermentation stage in 4.0 ... 4.5 hours, that is, one steriliser can serve two fermenters during a working shift. This later determined the optimal composition of the unit *(Krutyakova et al., 2019)*.

The final assessment of the cleaning system was made on the basis of the results of the pilot production of two complex biopesticides "Biohybervit BT" TU U 72.1-00495929-026: 2020 and "Vitastim BT" TU U 72.1-00495929-025: 2020, based on two strains of bacteria *Pseudomonas fluoresens* and two strains of the antagonist fungus *Trichoderma lignorum*. The titre of biopesticides was within (1-4)·10^9 CFU cm^{-3} (colony-forming units). The amount of the extraneous microflora was less than the value of 0.3%, established by the Technical Specifications.

CONCLUSIONS

A CIP-system for a fermentation plant has been developed, which consists of an industrial steriliser and a thin-walled reactor. Cleaning from contamination is combined with a pasteurizing effect, which ensures the death of vegetative forms of microorganisms on the inner surface of the equipment.

Cleaning is performed by water with the initial temperature of 98.3°C without the use of additional devices. The pasteurizing effect is achieved by heating the inner surfaces twice to a temperature of more than 85°C with holding for 10 minutes.

The cleaning procedure is combined with the main technological process and does not require additional equipment. Testing of the system in the production of biopesticides has confirmed its efficiency. The level of contamination by extraneous microflora did not exceed the established standard value 0.3%.

REFERENCES

[1] Arshad A., (2018), *Biopesticides and bioagents: novel tools for pest management*. Boca Raton: Apple Academic Press, Bihar / India, 419 p.

[2] Bespalov I., Khodorchuk V., (2017), Economic fermentation plant for the production of microbiological plant protection products (Економічна ферментаційна установка для виробництва мікробіологічних засобів захисту рослин). *Bulletin of Agricultural Science*, Vol. 95 (1), Kiev / Ukraine, pp. 38–42.

[3] Bredikhin S., (2021), *Technology and techniques of milk processing (Технология и приемы переработки молока)*. Moscow / Russia 443 p.

[4] Dally J.W., (2008), Statistical Analysis of Experimental Data. Springer Handbooks. Boston / USA.

[5] Goode K.R., Asteriadou K., Robbins P.T., Fryer P.J., (2013), Fouling and cleaning studies in the food and beverage industry classified by cleaning type *Comprehensive Reviews in Food Science and Food Safety*, 12 (2), Birmingham / UK, pp. 121-143.

[6] Goode K.R., Asteriadou K., Fryer P.J., Picksley, M., Robbins, P.T., (2010), Characterising the cleaning mechanisms of yeast and the implications for Cleaning in Place (CIP) *Food and Bioproducts Processing*, 88 (4), pp. 365-374, Birmingham / UK.

[7] Kotlyarov V., Sedinina N., (2014), Features of low-tonnage production of microbiological preparations for plant protection and its optimization (Особенности малотоннажного производства микробиологических препаратов для защиты растений и его оптимизация). *Scientific journal KubSAU*, Vol.100 (06), pp. 784–802, Krasnodar / Russia.

[8] Köhler H., Stoye H., Mauermann M., Weyrauch T., Majschak, J.P., (2015), How to assess cleaning? Evaluating the cleaning performance of moving impinging jets *Food and Bioproducts Processing*, 93, pp. 327-332, Amsterdam / Netherlands.

[9] Krutyakova V., (2019), Innovative approaches for creating a system of production of biological plant protection products in Ukraine (Інноваційні підходи до створення системи виробництва біологічних засобів захисту рослин в Україні). *Bulletin of Agricultural Science*. Vol.12, pp. 54–58. Kiev / Ukraine

[10] Krutyakova V., Bespalov I., Molchanova O., Loban L., (2017), *Engineering and technological innovations in the production of entomological and microbiological methods of plant protection (Інженерно-технологічні інновації у виробництві ентомологічних та мікробіологічних методів захисту рослин).* Monograph, 196 p., Odessa / Ukraine.

[11] Krutyakova V., Belousov M., Osipenko T., Burdenko T., Shalova N., (2019), Energy-efficient technologies and equipment for small-scale production of microbiological plant protection products. 104 p., Odessa / Ukraine.

[12] Lukanin A., (2020), Engineering biotechnology: fundamentals of microbiological production technology (Инженерная биотехнология: основы технологии микробиологического производства), 304 p., INFRA-M, Moscow / Russia.

[13] Nicolopoulou-Stamati, P., Maipas, S., Kotampasi, C., Stamatis, P., Hens, L., (2016), Chemical Pesticides and Human Health: The Urgent Need for a New Concept in Agriculture. *Front. Public Health*, 4, 148 p., London / UK.

[14] Liu X., Cao A., Yan D., Ouyang C., Wang Q., Li, Y., (2021), Overview of mechanisms and uses of biopesticides. *International Journal of Pest Management*, 67 (1), pp. 65-72, Delhi / India.

[15] Palabiyik I., Yilmaz M.T., Fryer P.J., Robbins P.T., Toker O.S., (2015), Minimizing the environmental footprint of industrial-scaled cleaning processes by optimisation of a novel clean-in-place system protocol. *Journal of Cleaner Production*, 108, pp. 1009-1018, Amsterdam / Netherlands.

[16] Panda T. (2011). Bioreactors. Analysis and design. New Delhi: Tata McGraw Hill, 514 p., Delhi / India.

[17] Pettigrew L., Blomenhofer V., Hubert S., Groß F., Delgado A., (2015), Optimisation of water usage in a brewery clean-in-place system using reference nets *Journal of Cleaner Production*, 87 (1), pp. 583-593, London / UK.

[18] Starchevsky Y., Kosoy S., Burdenko T., (2007), Production of liquid bio-pesticides using thin-walled fermenters. Bulletin of Agrarian Science of the Southern Region of Ukraine (Series "Agricultural and Biological Sciences"), Issue. 9, pp. 122–126 Odesa / Ukraine.

[19] Yaroshevsky V., Bulgakov V., Ivanovs S., Krutyakova V, Belchenko V., Olt J., (2020), Research on the impact of the air-liquid jet mixer upon ring bioreactor operation. *INMATEH – Agricultural Engineering,* Vol. 60(1), pp.115-122, Bucharest / Romania.

[20] Van Oosten, M.J., Pepe, O., De Pascale, S., Silletti, S., Maggio, A., (2017), The role of biostimulants and bioeffectors as alleviators of abiotic stress in crop plants. *Chemical and Biological Technologies in Agriculture*, 4 (1), art. no. 5, Amsterdam/ Netherlands.

[21] Wilson, D.I., Köhler, H., Cai, L., Majschak, J.-P., Davidson, J.F., (2015), Cleaning of a model food soil from horizontal plates by a moving vertical water jet. *Chemical Engineering Science*, 123, pp. 450-459, Amsterdam / Netherlands.

STUDY ON THE INTERACTION BETWEEN AN AGRICULTURAL TRACTOR AND FIELD TERRAIN PROFILES
/
农用拖拉机与田间地面相互作用的研究

Jianguo YAN, Lijuan WANG*), Shengshi XIE, Chunguang WANG

Inner Mongolia Agricultural University, College of Mechanical and Electrical Engineering, Hohhot, China
(*) Corresponding author: Lijuan Wang; E-mail: wanglijuan_qq @163.com

ABSTRACT

To study the interaction between the tractor and the field terrain on which the tractor operates, the characteristics of tractor vibrations excited by the measured profiles were analyzed by simulations and experiments. The results show that the theoretically calculated values of the tractor vibrations excited by the field road profiles, including the natural frequencies of the tractor's center of gravity, acceleration RMS values of the tractor axles, and the wheel dynamic loads, were close to the measured values, with an error range of 3.5% to 10.9%. Considering the filtering effect of large tractor tires on the measured road profiles, these errors are within an acceptable range. The results confirm the validity of the methodology presented in this paper for investigating the tractor vibrations caused by measured profiles as excitations.

摘要

为了研究拖拉机与田间地面的相互作用，通过仿真分析和实验验证的方法分析了田间地面不平度激励下的拖拉机振动特性。结果表明，拖拉机在田间路面激励下的振动理论计算值包括质心处固有频率、车轴加速度均方根值和车轮动载荷，都与实测值接近，误差范围为 3.5% ~ 10.9%，考虑到大型拖拉机轮胎对实测路面轮廓的滤波作用，这些误差在可接受的范围内。证实了本文提出由实测地面不平度作为激励源研究拖拉机振动特性的方法的有效性。

INTRODUCTION

The dynamic behavior of a tractor is strongly affected by the surface profile of the agricultural terrain upon which the tractor operates. In many cases, only the standard Power Spectral Density (PSD) of the profile is provided, not the actual measured profile *(ISO 8608, 2016)*. Carrying out profiling tests and analyses of some typical agricultural terrains and revealing the surface roughness characteristics of the measured terrains not only lays a foundation for the further study of tractor vibrations excited by different terrain profiles but also provides a realistic representation of the desired terrain for the virtual simulation and optimal design of agricultural machinery. The analysis of profile data should be targeted at an application involving excitation sources that induce dynamic response in agricultural machinery. However, most studies have focused on the acquisition of terrain profiles and modeling, which are relatively independent of the research on the interactions between vehicles and terrain *(Gialamas et al., 2016; Goodin et al., 2017; Botha et al., 2019)*. Additionally, many studies have concentrated on the simulation analysis of vehicle vibrations by using measured terrain profiles *(Kropáč et al., 2009; Wei et al., 2016; Zheng et al., 2016; Sim et al., 2017)*, but it is difficult to verify the vehicle vibrations caused by the measured profiles as excitations.

This study was designed to study the interaction between a tractor and the field terrain on which the tractor operates, the tractor vibration excited by the measured profiles was investigated by theoretical analysis and experimental research.

MATERIALS AND METHODS

As shown in Figure 1, a surface profiling apparatus (profiler) was mounted on the front counterweight of a tractor *(John Deere 904, John Deere Tianjin Co.ltd.)*, which makes it easy to further

analyze the coupling vibration between the tractor and the field terrain because the measured profiles are the sources of excitation that will cause the tractor to vibrate when the tractor wheels roll along the profile path. Previous studies have laid a foundation for the approach proposed in this study. The design and validation of the profiler was presented in detail in a previous study *(Yan et al., 2019)*. Details on the testing and analysis of agricultural terrain profiles can be found in *Wang et al (2020)*, in which the profiling tests were carried out in a harvested potato field, a grass field, a corn stubble field and a field road.

Fig. 1 - Profiling apparatus mounted on the front counterweight of a tractor

Fig. 2 - Terrain profile and tractor vibration test on field road

a) Front axle end   *b) Directly below seat*   *c) Rear axle end*

d) Directly below the front axle   *e) Directly below the rear axle*

Fig. 3 - Sensor installation positions

To investigate the tractor vibration caused by the field terrain upon which the tractor was driven, the terrain profiles were measured on the field road, and the vibration accelerations of the tractor body and axles were measured simultaneously with a forward driving speed of 5.41 km/h. During the test, the width of each surface profiles on the parallel tracks was adjusted to be the same as the width of the tractor wheel tracks, as shown in Figure 2, hence, the measured profiles were the excitation source that caused the tractor to vibrate when the tractor wheels rolled along the profile path. Then, the tractor vibrations excited by the measured profiles were investigated. The tire pressure of the tractor was 170 kPa in the front and 160 kPa in the rear.

Seven single-direction accelerometers (IEPE 1A111E) with a frequency bandwidth of 0.5-10000 Hz and a maximum acceleration of 500 m/s^2 were attached to the tractor to measure the vibration intensity of the tractor body and axles, as shown in Figure 3. The specific arrangement of accelerometers is as follows: four accelerometers were attached to the ends of the axles at the centers of the tractor's four wheels to measure the vertical acceleration of each wheel during the tractor wheel dynamic load calculation; one accelerometer was attached to the tractor cab floor below the driver's seat in the middle of the tractor body to measure the vertical acceleration of the tractor body; and two accelerometers were attached at the midpoints of the front and rear axles to measure the vertical acceleration of each axle. The measured acceleration and profiling signals were collected by the profiler's data acquisition system in tandem during the measurement process with a sample acquisition rate of 256 Hz.

MODEL ANALYSIS OF TRACTOR VIBRATION

To investigate the vibrations in an agricultural tractor produced by the interaction between the tractor and the field terrain, an equivalent model of a wheeled tractor was established, as shown in Figure 4. A John Deere 904 tractor was selected as the prototype. Referring to the relevant Chinese standard, the inherent parameters of the tractor, such as the centroid position, pitch and roll moment of inertia were measured and determined as shown in Table 1. The tractor vibration model includes the vertical displacement of the tractor's center of gravity z_c, pitch angle displacement of the tractor's center of gravity φ_c, roll angle displacement of the tractor's center of gravity θ_c, and road profile excitations q_{f1}, q_{r1}, q_{f2}, and q_{r2}.

Table 1

Some inherent parameters of the John Deere 904 tractor

Parameters	Value	Variable unit
Mass of the tractor body	M_c = 4180	[kg]
Pitch moment of inertia	J_φ = 4529.2	[kg·m^2]
Roll moment of inertia	J_θ = 2184.3	[kg·m^2]
Distance from the tractor center of gravity to the front axle	l_{cf} = 1.31	[m]
Distance from the tractor center of gravity to the rear axle	l_{cr}= 0.99	[m]
Distance from tractor centerline to the front wheel center	l_{df} = 0.82	[m]
Distance from tractor centerline to the rear wheel center	l_{dr} = 0.86	[m]
Stiffness of the front tire with a pressure of 170 kPa	k_f = 357425	[N/m]
Stiffness of the rear tire with a pressure of 160 kPa	k_r = 369840	[N/m]
Damping coefficient of the front tire with a pressure of 170 kPa	c_f = 3253	[N·s/m]
Damping coefficient of the rear tire with pressure of 160 kPa	c_r = 3674	[N·s/m]
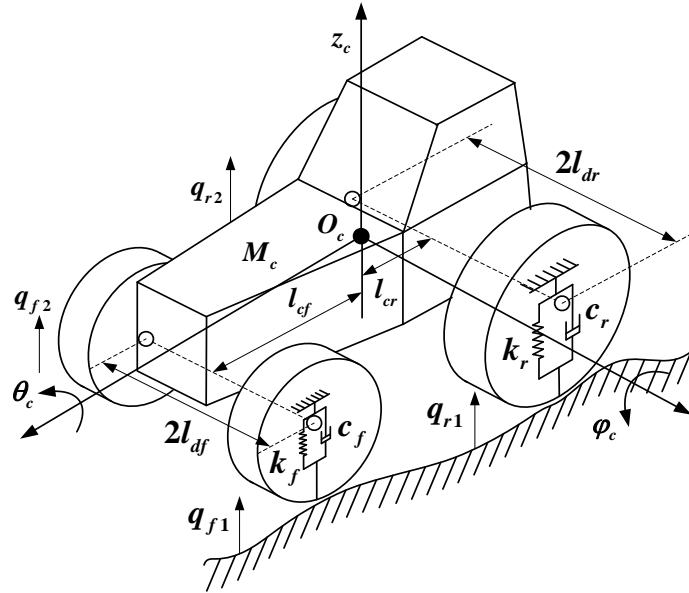
Fig. 4 - Tractor vibration model

The tractor vibration model has three DOFs with the following equations:

$$\begin{cases} M_c \ddot{z}_c + (2c_f + 2c_r)\dot{z}_c + (2k_f + 2k_r)z_c + (-2c_f l_{cf} + 2c_r l_{cr})\dot{\varphi}_c + (-2k_f l_{cf} + 2k_r l_{cr})\varphi_c \\ = c_f(\dot{q}_{f1} + \dot{q}_{f2}) + k_f(q_{f1} + q_{f2}) + c_r(\dot{q}_{r1} + \dot{q}_{r2}) + k_r(q_{r1} + q_{r2}) \\ J_\varphi \ddot{\varphi}_c + (2c_f l_{cf}^2 + 2c_r l_{cr}^2)\dot{\varphi}_c + (2k_f l_{cf}^2 + 2k_r l_{cr}^2)\varphi_c + (-2c_f l_{cf} + 2c_r l_{cr})\dot{z}_c + (-2k_f l_{cf} + 2k_r l_{cr})z_c \\ = -c_f l_{cf}(\dot{q}_{f1} + \dot{q}_{f2}) - k_f l_{cf}(q_{f1} + q_{f2}) + c_r l_{cr}(\dot{q}_{r1} + \dot{q}_{r2}) + k_r l_{cr}(q_{r1} + q_{r2}) \\ J_\theta \ddot{\theta}_c + (2c_f l_{df}^2 + 2c_r l_{dr}^2)\dot{\theta}_c + (2k_f l_{df}^2 + 2k_r l_{dr}^2)\theta_c \\ = c_f l_{df}(\dot{q}_{f1} - \dot{q}_{f2}) + k_f l_{df}(q_{f1} - q_{f2}) + c_r l_{dr}(\dot{q}_{r1} - \dot{q}_{r2}) + k_r l_{dr}(q_{r1} - q_{r2}) \end{cases} \quad (1)$$

The front axle vertical acceleration $\ddot{z}_f$ and rear axle vertical acceleration $\ddot{z}_r$ can be derived from the vertical acceleration of the center of gravity $\ddot{z}_c$ and the pitch angle acceleration of the tractor's center of gravity $\ddot{\varphi}_c$, as shown in Eq (2).

$$\begin{cases} \ddot{z}_f = \ddot{z}_c - l_1 \ddot{\varphi}_c \\ \ddot{z}_r = \ddot{z}_c + l_2 \ddot{\varphi}_c \end{cases} \quad (2)$$

The dynamic loads of the two front wheels in response to the excitations of terrain profiles q_{f1} and q_{f2} are determined as follows:

$$\begin{cases} F_{f1}(t) = k_f(q_{f1} - z_c + \varphi_c l_{cf} - \theta_c l_{df}) + c_f(\dot{q}_{f1} - \dot{z}_c + \dot{\varphi}_c l_{cf} - \dot{\theta}_c l_{df}) \\ F_{f2}(t) = k_f(q_{f2} - z_c + \varphi_c l_{cf} + \theta_c l_{df}) + c_f(\dot{q}_{f2} - \dot{z}_c + \dot{\varphi}_c l_{cf} + \dot{\theta}_c l_{df}) \end{cases} \quad (3)$$

The dynamic loads of the two rear wheels in response to the excitations of terrain profiles q_{r1} and q_{r2} are similarly determined as follows:

$$\begin{cases} F_{r1}(t) = k_r(q_{r1} - z_c - \varphi_c l_{cr} - \theta_c l_{dr}) + c_r(\dot{q}_{r1} - \dot{z}_c - \dot{\varphi}_c l_{cr} - \dot{\theta}_c l_{dr}) \\ F_{r2}(t) = k_r(q_{r2} - z_c - \varphi_c l_{cr} + \theta_c l_{dr}) + c_r(\dot{q}_{r2} - \dot{z}_c - \dot{\varphi}_c l_{cr} + \dot{\theta}_c l_{dr}) \end{cases} \quad (4)$$

The *RMS* values of the dynamic loads of the tractor wheels are as follows:

$$RMS_{F_{f1}} = \sqrt{\sum_{i=1}^{N} F_{f1}^2(t) \Big/ N} \tag{5}$$

$$RMS_{F_{f2}} = \sqrt{\sum_{i=1}^{N} F_{f2}^2(t) \Big/ N} \tag{6}$$

$$RMS_{F_{r1}} = \sqrt{\sum_{i=1}^{N} F_{r1}^2(t) \Big/ N} \tag{7}$$

$$RMS_{F_{r2}} = \sqrt{\sum_{i=1}^{N} F_{r2}^2(t) \Big/ N} \tag{8}$$

Where:

N is the number of sampling points.

Eq.(1) may be rearranged in matrix form as:

$$M\ddot{Z} + C\dot{Z} + KZ = F \tag{9}$$

Where:

$$Z = \begin{bmatrix} z_c \\ \varphi_c \\ \theta_c \end{bmatrix} \quad M = \begin{bmatrix} M_c & 0 & 0 \\ 0 & J_\varphi & 0 \\ 0 & 0 & J_\theta \end{bmatrix}$$

$$C = \begin{bmatrix} 2c_f + 2c_r & -2c_f l_{cf} + 2c_r l_{cr} & 0 \\ -2c_f l_{cf} + 2c_r l_{cr} & 2c_f l_{cf}^2 + 2c_r l_{cr}^2 & 0 \\ 0 & 0 & 2c_f l_{df}^2 + 2c_r l_{dr}^2 \end{bmatrix}$$

$$K = \begin{bmatrix} 2k_f + 2k_r & -2k_f l_{cf} + 2k_r l_{cr} & 0 \\ -2k_f l_{cf} + 2k_r l_{cr} & 2k_f l_{cf}^2 + 2k_r l_{cr}^2 & 0 \\ 0 & 0 & 2k_f l_{df}^2 + 2k_r l_{dr}^2 \end{bmatrix}$$

$$F = \begin{bmatrix} c_f(\dot{q}_{f1} + \dot{q}_{f2}) + k_f(q_{f1} + q_{f2}) + c_r(\dot{q}_{r1} + \dot{q}_{r2}) + k_r(q_{r1} + q_{r2}) \\ -c_f l_{cf}(\dot{q}_{f1} + \dot{q}_{f2}) - k_f l_{cf}(q_{f1} + q_{f2}) + c_r l_{cr}(\dot{q}_{r1} + \dot{q}_{r2}) + k_r l_{cr}(q_{r1} + q_{r2}) \\ c_f l_{df}(\dot{q}_{f1} - \dot{q}_{f2}) + k_f l_{df}(q_{f1} - q_{f2}) + c_r l_{dr}(\dot{q}_{r1} - \dot{q}_{r2}) + k_r l_{dr}(q_{r1} - q_{r2}) \end{bmatrix}$$

The natural frequencies of the tractor's center of gravity, such as the vertical vibration frequency f_z, pitching vibration frequency f_φ and roll vibration frequency f_θ, were determined by the undamped vibration equations, for which the eigenvalues of $H = M^{-1}K$ need to be derived. Then, the natural frequencies were calculated as follows:

$$\begin{cases} f_z \approx 2.88 \text{ Hz} \\ f_\varphi \approx 3.38 \text{ Hz} \\ f_\theta \approx 3.45 \text{ Hz} \end{cases}$$

Simulation of tractor vibration accelerations

To simulate the tractor vibrations caused by the measured profiles as excitations in the MATLAB Simulink environment, Eq (1) can be written in terms of state-space equations:

$$\begin{cases} \dot{X} = AX + BU \\ Y = CX + DU \end{cases} \tag{10}$$

Where:

A is the system matrix, B is the input matrix, C is the output matrix, D is the feed-forward matrix, X is known as the state vector, Y is the output vector, and U is the input vector.

$$A = \begin{bmatrix} -\dfrac{2c_f+2c_r}{M_c} & -\dfrac{-2c_fl_{cf}+2c_rl_{cr}}{M_c} & 0 & -\dfrac{2k_f+2k_r}{M_c} & -\dfrac{-2k_fl_{cf}+2k_rl_{cr}}{M_c} & 0 \\ -\dfrac{-2c_fl_{cf}+2c_rl_{cr}}{J_\varphi} & -\dfrac{2c_fl_{cf}^2+2c_rl_{cr}^2}{J_\varphi} & 0 & -\dfrac{-2k_fl_{cf}+2k_rl_{cr}}{J_\varphi} & -\dfrac{2k_fl_{cf}^2+2k_rl_{cr}^2}{J_\varphi} & 0 \\ 0 & 0 & -\dfrac{2c_fl_{df}^2+2c_rl_{dr}^2}{J_\theta} & 0 & 0 & -\dfrac{2k_fl_{df}^2+2k_rl_{dr}^2}{J_\theta} \\ 1 & 0 & 0 & 0 & 0 & 0 \\ 0 & 1 & 0 & 0 & 0 & 0 \\ 0 & 0 & 1 & 0 & 0 & 0 \end{bmatrix}^{T}$$

$$B = \begin{bmatrix} \dfrac{c_f}{M_c} & \dfrac{c_r}{M_c} & \dfrac{c_f}{M_c} & \dfrac{c_r}{M_c} & \dfrac{k_f}{M_c} & \dfrac{k_r}{M_c} & \dfrac{k_f}{M_c} & \dfrac{k_r}{M_c} \\ -\dfrac{c_fl_{cf}}{J_\varphi} & \dfrac{c_rl_{cr}}{J_\varphi} & -\dfrac{c_fl_{cf}}{J_\varphi} & \dfrac{c_rl_{cr}}{J_\varphi} & -\dfrac{k_fl_{cf}}{J_\varphi} & \dfrac{k_rl_{cr}}{J_\varphi} & -\dfrac{k_fl_{cf}}{J_\varphi} & \dfrac{k_rl_{cr}}{J_\varphi} \\ \dfrac{c_fl_{df}}{J_\theta} & \dfrac{c_rl_{dr}}{J_\theta} & -\dfrac{c_fl_{df}}{J_\theta} & -\dfrac{c_rl_{dr}}{J_\theta} & \dfrac{k_fl_{df}}{J_\theta} & \dfrac{k_rl_{dr}}{J_\theta} & -\dfrac{k_fl_{df}}{J_\theta} & -\dfrac{k_rl_{dr}}{J_\theta} \\ 0 & 0 & 0 & 0 & 0 & 0 & 0 & 0 \\ 0 & 0 & 0 & 0 & 0 & 0 & 0 & 0 \\ 0 & 0 & 0 & 0 & 0 & 0 & 0 & 0 \end{bmatrix} = D$$

$$C = \begin{bmatrix} -\dfrac{2c_f+2c_r}{M_c} & -\dfrac{-2c_fl_{cf}+2c_rl_{cr}}{M_c} & 0 & -\dfrac{2k_f+2k_r}{M_c} & -\dfrac{-2k_fl_{cf}+2k_rl_{cr}}{M_c} & 0 \\ -\dfrac{-2c_fl_{cf}+2c_rl_{cr}}{J_\varphi} & -\dfrac{2c_fl_{cf}^2+2c_rl_{cr}^2}{J_\varphi} & 0 & -\dfrac{-2k_fl_{cf}+2k_rl_{cr}}{J_\varphi} & -\dfrac{2k_fl_{cf}^2+2k_rl_{cr}^2}{J_\varphi} & 0 \\ 0 & 0 & -\dfrac{2c_fl_{df}^2+2c_rl_{dr}^2}{J_\theta} & 0 & 0 & -\dfrac{2k_fl_{df}^2+2k_rl_{dr}^2}{J_\theta} \\ 0 & 0 & 0 & 1 & 0 & 0 \\ 0 & 0 & 0 & 0 & 1 & 0 \\ 0 & 0 & 0 & 0 & 0 & 1 \end{bmatrix}^{T}$$

$$X = \begin{bmatrix} \dot{z}_c & \dot{\varphi}_c & \dot{\theta}_c & z_c & \varphi_c & \theta_c \end{bmatrix}^{T}$$

$$U = \begin{bmatrix} \dot{q}_{f1} & \dot{q}_{r1} & \dot{q}_{f2} & \dot{q}_{r2} & q_{f1} & q_{r1} & q_{lf2} & q_{lr2} \end{bmatrix}^{T}$$

$$Y = \begin{bmatrix} \ddot{z}_c & \ddot{\varphi}_c & \ddot{\theta}_c & z_c & \varphi_c & \theta_c \end{bmatrix}^{T}$$

According to the state-space expression (10), the Simulink model was established as shown in Figure 5 and was to analyze the vertical, pitch and roll vibrations of the tractor's center of gravity, as well as the vibrations of the front and rear axles excited by the terrain profiles.

The values of the elements in matrices *A, B, C* and *D* determined in the state-space expression (10) were calculated according to the parameters in Table 1.
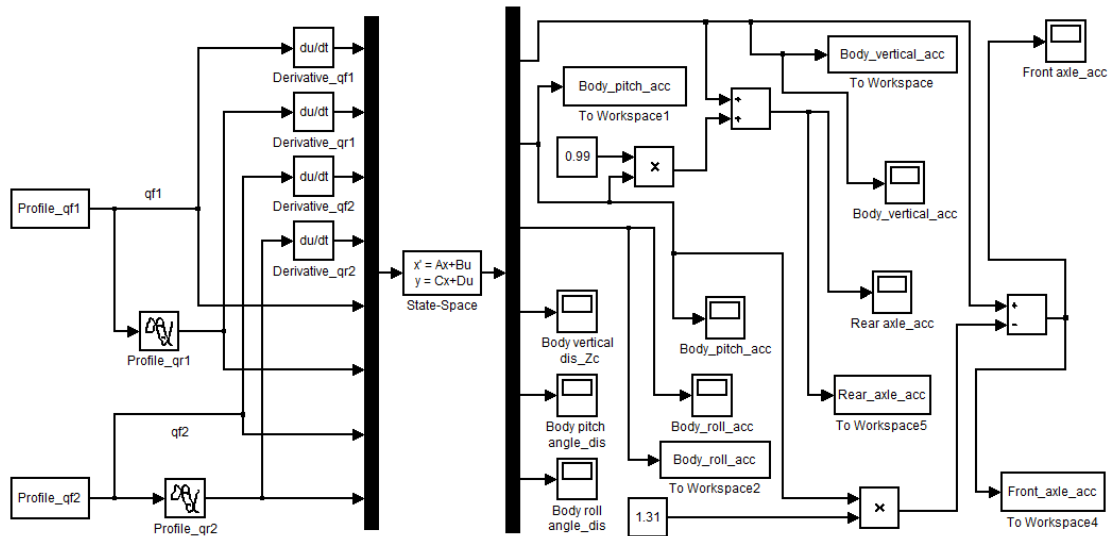
Fig. 5 - Simulink model of the tractor's center of gravity and axle vibrations.

Simulation of tractor wheel dynamic loads was used to analyze the dynamic load of the front wheel in response to the terrain due to excitation of terrain profile q_{f1} and q_{f2} excitation. The analytical model of the dynamic load characteristics of the tractor rear wheels in response to the terrain is similar to that of the dynamic load characteristics of the tractor front wheel.

RESULTS AND DISCUSSION

The field road profiles from the left and right tractor wheel tracks measured by the profiler at a speed of 5.41 km/h are shown in Figure 6.

a) Left track   *b) Right track*
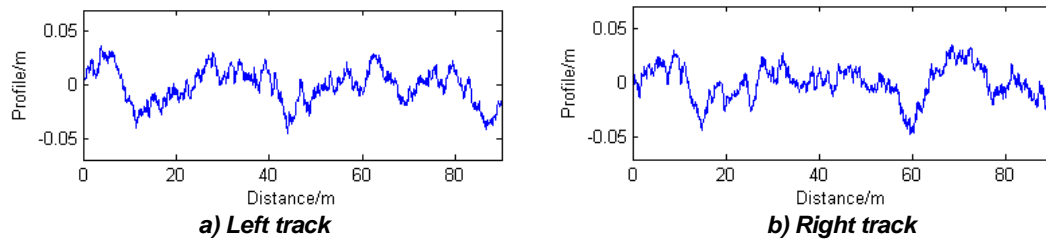
Fig. 6 - Measured field road profiles

According to the geometric relationship between the tractor's center of gravity and the positions of the accelerometers attached to the tractor body, the measured vertical acceleration of the center of gravity $\ddot{z}_c$ can be derived from the vertical acceleration $\ddot{z}_s$ of the accelerometer attached to the tractor body below the driver's seat with the following equation:

$$\ddot{z}_c = \ddot{z}_s - l_{cs}\ddot{\varphi}_c \qquad (11)$$

Where:

l_{cs} is the distance from the tractor's center of gravity to the position of the accelerometer attached to the tractor cab floor below the driver's seat in the middle of the tractor body.

The measured vertical, pitching and rolling vibration accelerations of the tractor's center of gravity in the time domain while the tractor was driving on the field road at a speed of 5.41 km/h are shown in Figures 7-9. These figures show that the amplitude of the vertical vibration of the tractor's center of gravity was larger than the amplitudes of the pitching and rolling vibrations.

The measured vibration accelerations of the front and rear axles in the time domain are shown in Figure 10 and Figure 11, respectively, indicating that the vibration acceleration amplitude of the front axle was larger than that of the rear axle. The dynamic loads of the front and rear wheels are shown in Figure 12 and Figure 13, respectively.
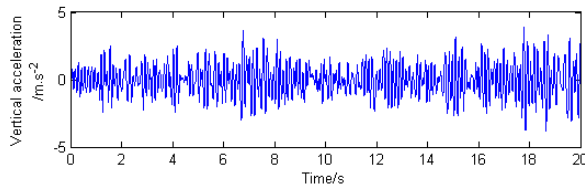
Fig. 7 - Vertical vibration acceleration of the tractor's center of gravity
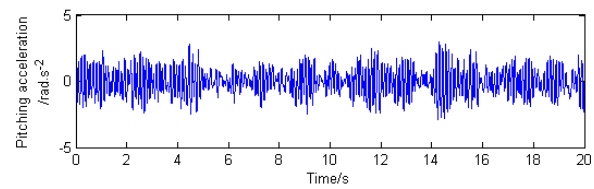
Fig. 8 - Pitching vibration acceleration of the tractor's center of gravity
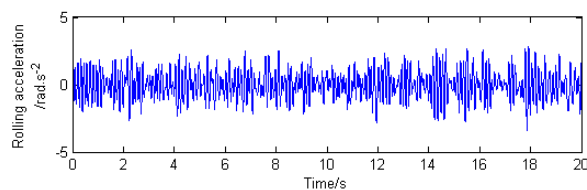
Fig. 9 - Rolling vibration acceleration of the tractor's center of gravity
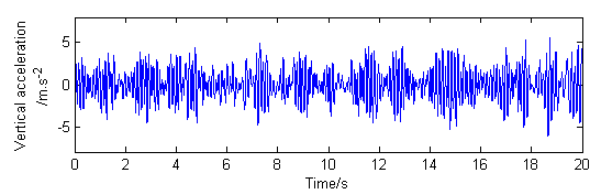
Fig. 10 - Vertical vibration acceleration of the front axle
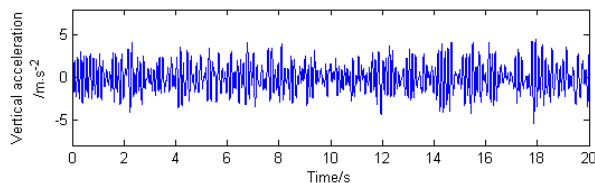
Fig. 11 - Vertical vibration acceleration of the rear axle
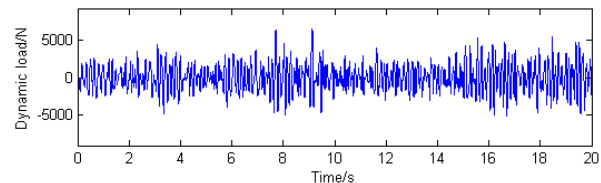
Fig. 12 - Dynamic load of the tractor front wheel
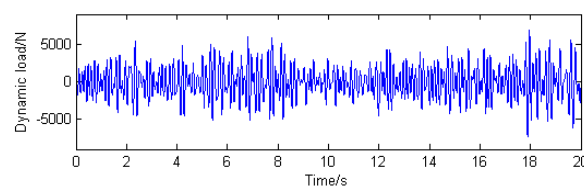
Fig. 13 - Dynamic load of the tractor rear wheel

The *PSD*s of the vertical, pitching and rolling vibration accelerations of the tractor's center of gravity corresponding to Figures 7-9 are shown in Figure 14(a), Figure 15(a) and Figure 16(a), respectively.

These figures display the vibration acceleration *PSD* in the range of 0 ~ 20 Hz, which covers the main frequency range of the tractor's natural frequencies and vibration response energy.

The natural frequencies of the tractor's center of gravity can be obtained from the peak frequencies of the vertical, pitching and rolling vibration acceleration *PSD*s of the tractor body's responses to the wheel excitations *(Zhu et al., 2016)*.

The natural frequencies of the vertical, pitching and rolling vibrations were 2.623 Hz, 3.148 Hz and 3.575 Hz, as shown in Figure 14(a), Figure 15(a) and Figure 16(a), respectively.
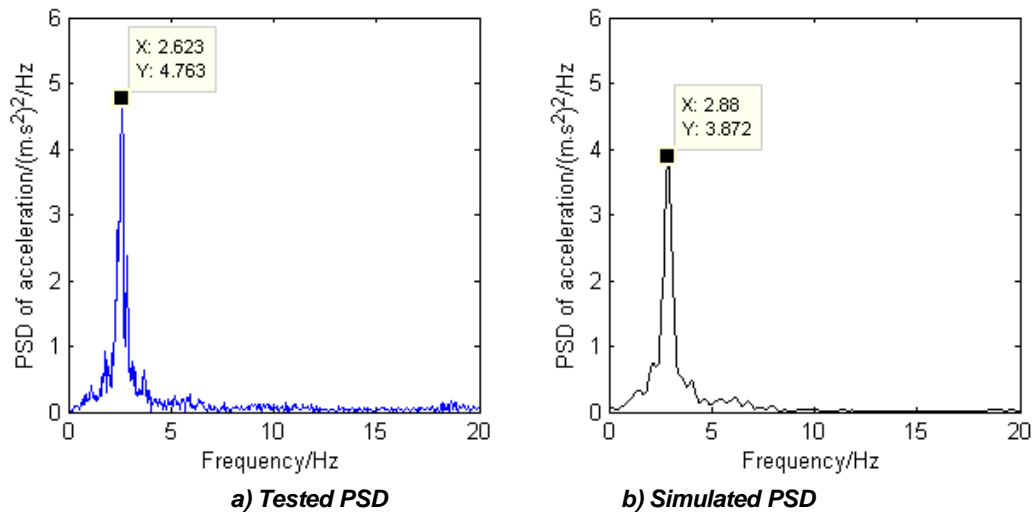
a) Tested PSD

b) Simulated PSD

Fig. 14 - Vertical vibration acceleration PSDs of the tractor's center of gravity

a) Tested PSD

b) Simulated PSD

Fig. 15 - Pitching vibration acceleration PSDs of the tractor's center of gravity

a) Tested PSD
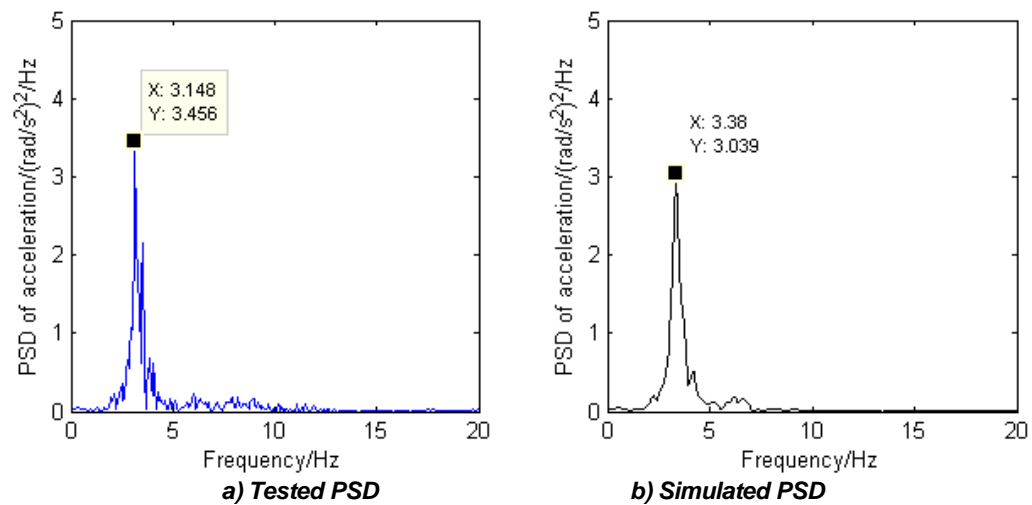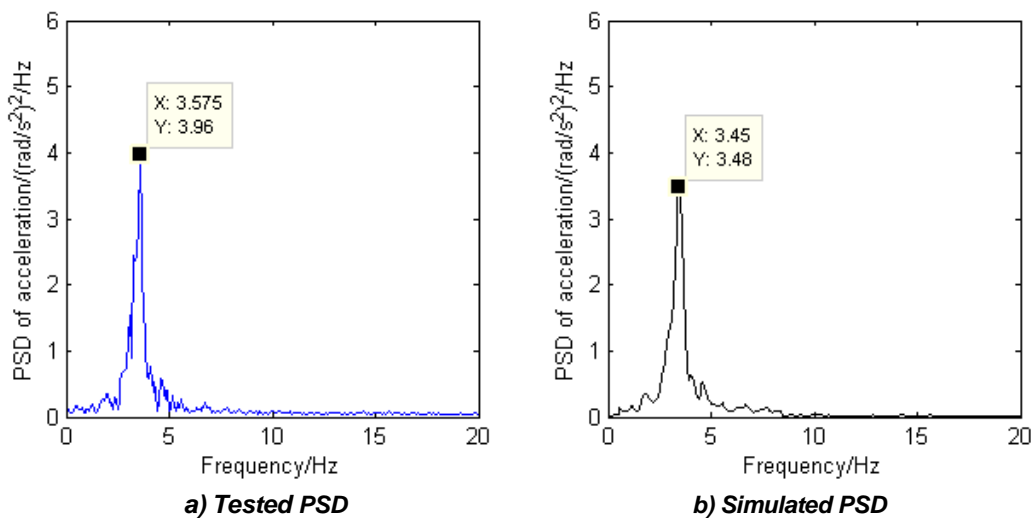
b) Simulated PSD

Fig. 16 - Rolling vibration acceleration PSDs of the tractor's center of gravity

The simulated *PSD*s of the vertical, pitching and rolling vibration accelerations of the tractor's center of gravity excited by the measured field road profiles of the left and right tractor wheel tracks are shown in Figure 14(b), Figure 15(b) and Figure 16(b), respectively.

The measured and theoretically calculated values of tractor vibrations excited by the field road profiles, including the natural frequencies of the tractor's center of gravity, the *RMS* values of the tractor axle accelerations and the wheel dynamic loads, are concluded in Table 2. A comparison between the measured values and the theoretically calculated values of tractor vibrations shows that the theoretical values are close to the measured values with an error range of 3.5% to 10.9%. Considering the filtering effect of large tractor tires on the measured road profiles, these errors are within an acceptable range. This conclusion confirms the validity of the developed tractor vibration model and the proposed methodology for investigating the tractor vibrations caused by measured profiles as excitations.

Table 2

Experimental values and theoretically calculated results of the tractor vibration tests on a field road (test speed: 5.41 km/h)

Value	Measured values	Theoretical values	Error
Natural frequency of the tractor's center of gravity vertical vibration (Hz)	2.623	2.88	9.8%
Natural frequency of the tractor's center of gravity pitching vibration (Hz)	3.148	3.38	7.4%
Natural frequency of the tractor's center of gravity rolling vibration (Hz)	3.575	3.45	3.5%
RMS value of the vertical vibration acceleration of the tractor's center of gravity (m/s^2)	1.18	1.08	8.5%
RMS value of the pitching vibration acceleration of the tractor's center of gravity (rad/s^2)	1.01	0.93	7.9%
RMS value of the rolling vibration acceleration of the tractor's center of gravity (rad/s^2)	1.06	0.97	8.5%
RMS value of the front axle acceleration (m/s^2)	1.88	1.69	10.1%
RMS value of the rear axle acceleration (m/s^2)	1.65	1.55	6.1%
RMS value of the tractor front wheel load (N)	2750	2941	6.9%
RMS value of the tractor rear wheel load (N)	3142	3484	10.9%

CONCLUSIONS

In this paper, a surface profiling apparatus mounted on the front counterweight of a tractor was designed to measure agricultural terrain profiles along parallel tracks. To investigate the interaction between a tractor and the field terrain on which the tractor operates, the terrain profiles were measured on the field road, and the vibration accelerations of the tractor body and axles were measured simultaneously with a forward driving speed of 5.41 km/h. An equivalent model of a wheeled tractor was established. Then, natural frequencies of the tractor's center of gravity, acceleration *RMS* values of the tractor axles, and wheel dynamic loads were investigated by theoretical analysis and experimental research. The results show that the theoretically calculated values of tractor vibrations excited by the field road profiles were close to the measured values, with an error range of 3.5% to 10.9%. This conclusion confirms the validity of the developed tractor vibration model and the proposed methodology for investigating the tractor vibrations caused by measured profiles as excitations.

ACKNOWLEDGEMENT

REFERENCES

[1]   Botha T, Johnson D, Els S, Shoop S (2019) Real time rut profile measurement in varying terrain types using digital image correlation. *Journal of Terramechanics 82*(4):53-61. https://doi.org/10.1016/j.jterra.2018.12.003

[2]   Gialamas T, Gravalos I, Kateris D, et al (2016) Vibration analysis on driver's seat of agricultural tractors during tillage tests. *Spanish Journal of Agricultural Research 14*(4):1-10. https://doi.org/10.5424/sjar/2016144-9664

[3]   Goodin C, Stevens M, Rosa FJV (2017) Calculating fractal parameters from low-resolution terrain profiles. *Journal of Terramechanics 72*(8):21-26. https://doi.org/10.1016/j.jterra.2017.03.002

[4]   ISO 8608 (2016) Mechanical Vibration-Road Surface Profiles-Reporting of Measured Data.

[5]   Kropáč O, Múčka P (2009) Effects of longitudinal road waviness on vehicle vibration response. *Vehicle System Dynamics 47*(2):135-153. https://doi.org/10.1080/00423110701867299

[6]   Sim K, Lee H, Yoon JW, et al (2017) Effectiveness evaluation of hydro-pneumatic and semi-active cab suspension for the improvement of ride comfort of agricultural tractors. *Journal of Terramechanics 69* (2):23-32. https://doi.org/10.1016/j.jterra.2016.10.003

[7]   Wei CF, Olatunbosun OA Behroozi M (2016) Simulation of tyre rolling resistance generated on uneven road. *International Journal of Vehicle Design 70*(2):113-136. https://doi.org/10.1504/IJVD.2016.074415

[8]   Yan JG, Wang CG, Xie SS, Wang LJ (2019) Design and validation of a surface profiling apparatus for agricultural terrain roughness measurements. *INMATEH Agriculture Engineering 59*(3):169-180. https://doi.org/10.35633/INMATEH-59-19

[9]   Zheng E, Fan Y, Zhu R, et al (2016) Prediction of the vibration characteristics for wheeled tractor with suspended driver seat including air spring and MR damper. *Journal of Mechanical Science & Technology 30*(9):4143-4156. https://doi.org/ 10.1007/s12206-016-0826-x

[10]   Zhu SH, Ma JF, Yuan JQ, et al (2016) Vibration characteristics of tractor in condition of paddy operation. *Transactions of the Chinese Society of Agricultural Engineering. 32*(11):31-38. https://doi.org/ 10.11975/j.issn.1002-6819.2016.11.005

[11]   Wang L. J., Yan J. G., Xie S. S., et al, (2020), Testing, analysis and comparison for characteristics of agricultural field and asphalt road roughness, *INMATEH Agriculture Engineering, 62*(3), 147-154. https://doi.org/10.35633/inmateh-62-15

CONSTRUCTION OF IMPACT MECHANICS MODEL AND EXPERIMENTAL STUDY ON IMPACT DAMAGE OF POTATO TUBER
/
马铃薯块茎碰撞物理模型构建和碰撞损伤试验研究

Tianci HUANG [1)], Bei WU [*1,2)], Lucen LI [1)], Tianlin ZUO [1)], Fangping XIE [1,2)] [1]

[1)] Hunan Agricultural University, College of Mechanical and Electrical Engineering, Changsha/China;
[2)] Hunan Key Laboratory of Intelligent Agricultural Machinery and Equipment, Changsha/China.
Tel: +86 15802521582; E-mail: wubei@hunau.edu.cn
Corresponding author: Bei Wu

ABSTRACT

Reducing potato tuber injury rate is responsible for the optimal design of potato harvester, one of the most important goals. To assess the influence of various factors on potato tubers' impact damage, the impact mechanics model of potato tuber was constructed in terms of the deformation and deformation energy analysis during the collision. Secondly, the orthogonal test was conducted. The impact material, potato varieties, potential energy, impact angle were selected as factors. The comprehensive damage index (DI) was taken as the evaluation index. The results showed that the damage degree of potato tuber was decreased with the increasing of coefficient of restitution of impact material, potato yield strength and collision angle, but increased with increasing potato potential energy. When the impact material is a plank, the potential energy is 1.2 J, the type of potato is Lishu No.6, and the collision angle is 15°, the comprehensive damage index is the lowest, 0.0055. According to the result of the orthogonal test, the mathematical regression model was obtained. At the same time, the verification tests were performed. The verification tests showed that the average error between the predicted data of the comprehensive damage index calculated by the mathematical regression model and the experimental data was 5.22%.

摘要

降低马铃薯块茎损伤率是马铃薯收获机优化设计过程中的主要目标之一，为了评估各因素对马铃薯块茎碰撞损伤的影响，本文从马铃薯碰撞变形量和变形能两方面进行分析，构建了马铃薯块茎碰撞物理模型，选取碰撞材料、马铃薯品种、马铃薯重力势能和碰撞角度作为试验因素，以马铃薯损伤综合指数（DI）作为评价指标开展了正交试验，结果表明：随着碰撞恢复系数、马铃薯屈服应力和碰撞角度增大，马铃薯损伤减小，而马铃薯势能越大，马铃薯损伤越大。当碰撞材料为木板、马铃薯种类为丽薯6号、马铃薯势能为1.2J、碰撞角度为15°时，马铃薯损伤综合指数最小为0.0055。根据正交试验结果得到了马铃薯损伤综合指数的回归模型并进行了验证试验，试验结果显示：回归模型对马铃薯损伤综合指数的预测值与实际测量值相比平均误差为5.22%。

INTRODUCTION

The potato is the fourth largest food crop globally after rice, wheat, and maize and has been awarded "underground apple" (*Shi et al., 2010*). The survey outcome showed that about 70% of tuber injury is derived from potato harvesting (*Jian, 2008*). The degree of mechanization in China increased year by year. Therefore, it is of great economic significance to reduce potato damage during the harvesting process to improve the internal quality of potatoes.

At present, the research on the mechanical damage of potato tubers mainly starts from the two aspects of agricultural materials science and damage factors based on harvester analysis. One of the effective strategies to study the damage of mechanized potato harvest is to conduct a collision damage experiment of potatoes under laboratory conditions. Part of the experiments method refers to the collision damage experiment of apples (*Li et al., 2005*) and pears (*Shan et al., 2003; Hui, 2014*). Some scholars analyzed the factors influencing the critical damage rate based on the Hertz model (*Han, 2019; Wei et al., 2020*).

---

[1] *Tianci Huang, Ms. Stud.; Bei Wu, Lect. Ph.D.; Lucen Li, Ms. Stud.; Tianlin Zuo, Ms. Stud.; Fangping Xie, Prof. Ph.D.*

There are also some scholars who analyzed dynamical systems theory (*Parks et al., 1990*). To study the damage degree of potato, a device of potato model was designed (*Ito et al., 1994*). Peters has an assessment of the degree of external damage of potato, based on the appearance of the epidermis (*Peters, 1996*). However, mechanized harvesting also damages the inner structure of potatoes; some investigators studied internal damage changes through mathematical models (*Stephen and McRae, 1998*), the MRI (*Thybo et al., 2004*) and computer-assisted analysis（Mayer et al., 2017）.

Researchers, in turn, carry out a comprehensive and systematic classification of the Internal and external forms of damage (*Baritelle et al., 2000；Arfa, 2007; Mayer et al., 2017*). From the previous research，respiration rate, damage area, damage volume, and damage ratio have all been proposed as indicators of injury assessment to analyze the impact of each factor on the damage degree of potato (*Han, 2019; Mathew and Hyde, 1997; Molema et al., 2000*). There is, however, little isolated information regarding the comprehensive damage index. So, the problem of potato collision damage cannot be comprehensively evaluated. Therefore, this paper aimed to build the mechanistic model of the deformation and deformation energy during the collision process to study the factors affecting the damage of the potato. Then we can analyze the relationship between each factor and the comprehensive damage index, and each factor aligned in order of increasing the comprehensive damage index.

MATERIALS AND METHODS
Deformation analysis
The collision of potato tubers involves two phases, elastic compression phase and elastic-plastic compression phase. Tubers damage begins to occur at critical points between two phases. The collision model of potato tuber and impact material was developed based on Herz-Mindlin contact theory, (*Zhi, 2017; Han, 2019*), which discussed the elastic compression phase up to the critical point during the collision. In the discussion of contact problems, it is generally assumed that:

The potato tuber was simplified to a uniform and isotropic ellipsoid.

The material of the contact body is in an elastic state.

The contact point of the potato tuber and impact material gradually becomes elliptical.

The friction of contact surface and potato falling are not considered.

The potato tuber occurs slight strain during collision. That is: the size of the contact surface is much smaller than the radius of curvature of the elastomers (i.e., potato tubers and impact material) surface.

According to Hertz theory, the relationship between the elastic phase loading and the amount of compressive deformation can be obtained as follows:

$$F = \frac{4}{3} E^* \sqrt{R^*} \delta^{\frac{3}{2}} \tag{1}$$

Where:

F denotes the contact loading, [N]; δ represents the amount of compressive deformation, [mm];

R^* expresses equivalent radius of contact between potato tuber and impact material, [mm]; Since the collision between the potato tuber and the impact material could be simplified as a collision between a sphere and a plane, the equivalent radius equals the curvature radius of potato tuber at collision point.

E^* represents the equivalent modulus of elasticity of potato tuber and impact material, [MPa], which can be obtained as follows:

$$\frac{1}{E^*} = \frac{1 - \mu_1^{\,2}}{E_1} + \frac{1 - \mu_2^{\,2}}{E_2} \tag{2}$$

Where:

E_1 denotes the modulus of elasticity of potato tuber, [MPa];

E_2 denotes the modulus of elasticity of impact material, [MPa];

μ_1 represents the Poisson's ratio of potato tuber;

μ_2 represents the Poisson's ratio of impact material.

As the contact loading increases, the stresses within the contact body also increase. These stresses eventually cause the material within the sphere to yield. The deformation at this initial point of yielding is known as the critical deformation. Jackson and Green (*Jackson and Green, 2005*) derive this critical deformation analytically using the von Mises yield criterion.

The relationship between material yield strength and critical deformation can be written as follows:

$$\begin{cases} \delta' = (C\sigma')^2 \left(\dfrac{\pi\sqrt{R^*}}{2E^*} \right)^2 \\ C = \min\left(1.295e^{0.736\mu_1}, 1.295^{0.736\mu_2}\right) \end{cases} \tag{3}$$

Where:

δ' denotes the critical deformation at the initial point of yielding, [mm];

σ' represents the yield strength of contact material, [MPa];

C is the coefficient.

Substituting equation (3) into equation (1), the critical contact loading was calculated. The resulting critical contact loading at initial yielding is:

$$F = \frac{R^{*2}\left(\pi C\sigma'\right)^3}{6E^{*2}} \tag{4}$$

And then, the maximum elastic energy before tubers damaged (i.e., on the verge of yielding, or plastic deformation) can be expressed as (*Green, 2005*):

$$W_1 = \frac{4}{3}E^*\sqrt{R^*}\int_0^{\delta'}(\delta^{3/2})d\delta = \frac{\left(\pi C\sigma'\right)^5 R^{*3}}{60E^{*4}} \tag{5}$$

Deformation energy analysis

During the collision between potato tuber and impact material, according to the kinetic energy theorem, the following relation is satisfied before the collision.

$$T_0 = mgh = \frac{1}{2}mv_0^2 \tag{6}$$

where:

T_0 is the kinetic energy before the collision, [J];

m denotes the potato tuber mass, [Kg];

g represents the acceleration of gravity, [m/s^2];

h expresses the drop height, [m];

v_0 is the initial impact speed, [m/s].

The velocity satisfies conservation in the tangent and normal direction during the collision, respectively.

$$v_1\sin\lambda = v_0\sin\varphi \tag{7}$$

$$v_1\cos\lambda = ev_0\cos\varphi \tag{8}$$

where:

v_1 denotes the critical velocity after collision, [m/s];

φ represents the angle between the velocity v_0 and the normal of the contact surface, [degree];

λ expresses the angle between the velocity v_1 and the normal of the contact surface, [degree];

e is the coefficient of restitution between potato and impact material.

Then, the kinetic energy after the collision can be expressed as:

$$T_1 = \frac{1}{2}mv_1^2 \tag{9}$$

where:

T_1 is the kinetic energy after the collision, [J];

During the actual collision, if heat generation of the friction between potato tuber and collision material was not considered, all the mechanical energy lost is used to cause tubers damage.

Therefore, the amount of loss with the mechanical energy can be expressed as:

$$E \approx T_0 - T_1 \approx mgh\left(1-e^2\right)\cos^2\varphi \tag{10}$$

Potato tuber drop impact test platform

The drop impact test platform is shown in Fig. 1. The testing device consists of a base, inclination-regulated unit, fixation, column, impact material, and height-adjustable stabilizing apparatus. During the experiment, the potato tuber free-drop onto the platform, which was employed to simulate the collision of potato and harvester. Firstly, the drop impact test platform was placed on the ground stably and away from other object to prevent secondary damage to the potato tuber by other factors. Then, the initial height of the potato tuber is controlled by adjusting the height of the height-adjustable stabilizing apparatus, and the angle between the horizontal plane and impact material could be controlled by adjusting the height of the inclination-regulated unit.

The collision angle can be adjusted precisely to 0°, 15° and 30° through the joint action of the fixing device and the tilting device. Finally, the centers of the height-adjustable stabilizing apparatus and potato tuber were guaranteed at the same height, and the vision is aligned such that potato tuber free-drop in the center of the impact material. The impact materials which were selected include steel Q235, aluminum alloy and plank. The thickness of impact material is no less than 10mm (*Jian et al., 2017*).
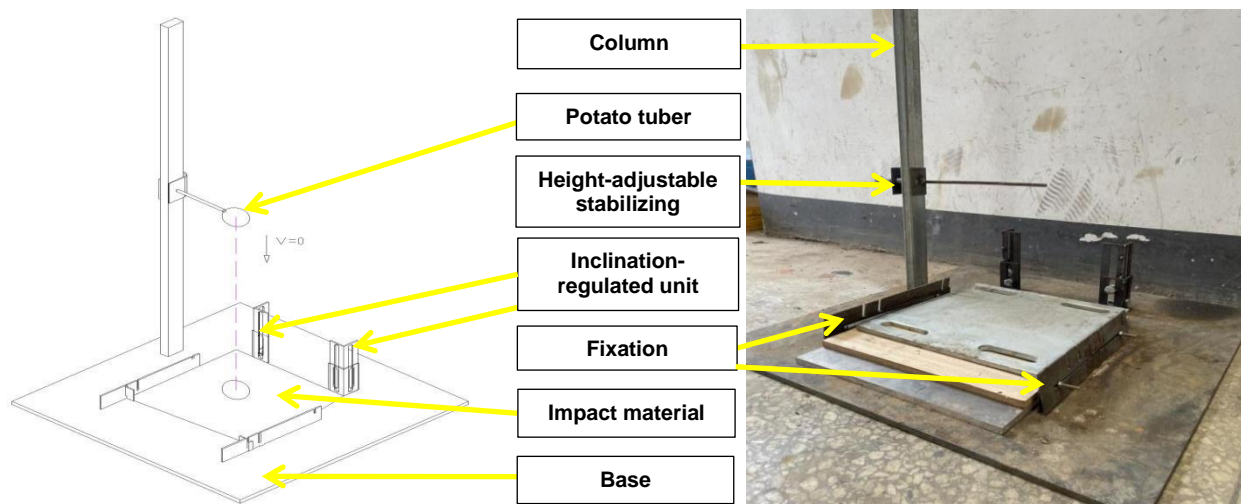
Fig. 1 - Potato tuber drop impact test platform

Orthogonal test scheme

The orthogonal test was conducted to analyze the influence of the various factors on potato tuber damage. According to impact mechanics model in equation (5) and (10): the coefficient of restitution of the impact material (e), the yield stress of the potato (σ'), the modulus of elasticity of potato and impact material (E_1 and E_2), the Poisson's ratio of potato and impact material (μ_1 and μ_2), the curvature radius of potato tuber at collision point (R^*), the potential energy of the potato tuber before collision (mgh) and the collision angle (φ) are all linked to potato damage. In these parameters, e, E_2 and μ_2 cannot be precisely controlled in the experiment, but they all depend on the material type, so the collision material type was selected as one of the test factors. Similarly, potato varieties were selected as another test factor considering the uncontrollable of σ', E_1, μ_1 and R^*. In addition, the potential energy (mgh) and the collision angle (φ) were selected as the third and fourth test factor, which can be precisely controlled during the test.

Steel Q235, aluminum alloy and plank were selected as impact materials. A uniformly steel ball was used to free fall onto the materials at the same height to obtain the coefficients of restitution e between the steel ball and the impact materials, and E_2 and μ_2 were obtain by consulting materials mechanics books. For potato varieties, three varieties (i.e., Atlantic, Longshu NO.7 and Lishu NO.6) commonly grown in China were selected as test material, and their mechanical parameters (i.e., σ', E_1 and μ_1) were measured by a universal testing machine (*Caglayan et al., 2018; Celik et al., 2019*). All of the parameters mentioned above are shown in Table 1 and Table 2.

Table 1

Mechanical parameters of different impact materials

Impact materials	E_2 [MPa]	μ_2	e
Q235 steel	2.14×10^5	0.27	0.55
Aluminum alloy	6.8×10^4	0.321	0.59
Plank	1.35×10^4	0.37	0.72

Table 2

Mechanical parameters of different potato varieties

Potato varieties	E_2 [MPa]	μ_2	$\sigma^{'}$ [MPa]
Atlantic	1.59	0.265	0.76
Lishu NO.6	1.74	0.19	1.10
Longshu NO.7	1.84	0.189	0.99

During the test, the potato tubers of similar shape and maturity were chosen for each variety. In order to set the potential energy to a certain value before collision, the drop height was calculated according to the tuber mass. In the test, the range of tuber mass was 0.10-0.50 kg and the range of drop height was 0.39-2.81 m. Before the test, the original damaged part was marked to avoid confusion with test damage. The test scheme was designed according to the Box–Behnken design method. The tests were performed with five potato tubers per group, and the results were averaged. The test factors and levels were shown in Table 3.

Table 3

Factors and levels

Level	Impact material A	Potato varieties B	Potential energy C [J]	Impact angle D [°]
-1	Q235 steel	Atlantic	1.2	0
0	Aluminum alloy	Lishu NO.6	2.4	15
1	Plank	Longshu NO.7	3.6	30

Evaluation metric

Potato tuber damage during the mechanical harvest is mainly caused by collision, extrusion and friction. The overall extent of damage to the potato can be determined as undamaged, scuffed, peel damage or severe damage (*Arfa, 2007*). According to different performance situations, the damage type can be divided into epidermal abrasions, tissue damage, and tuber fragmentation (*Jian, 2008*). In this experiment, these three types of potato damage were considered and measured separately, and finally a comprehensive damage index (*DI*) was defined. The measurement methods of the three types of damage were as follows.

(1) The measurement method of epidermal abrasions. The degree of epidermal abrasions was determined by calculating the area of the potato tuber damage part. For assessing the area of potato tuber damage part, the area was approximated with an ellipse. As shown in Fig. 2.

$$S = \pi ab \tag{11}$$

where:

S denotes the max epidermal damage area, [m²];

a represents the long-axis of the ellipse, [m];

b expresses the short-axis of the ellipse, [m].

(2) The measurement method of tuber fragmentation. The crack length was measured with a vernier caliper (0.02 mm accuracy). When multiple cracks were noted, the longest crack was measured; when the longest crack had multiple small branches on both sides, the middle crack was selected; when the longest crack had multiple small branches at the end, the most obvious crack was measured. As shown in Fig. 3.
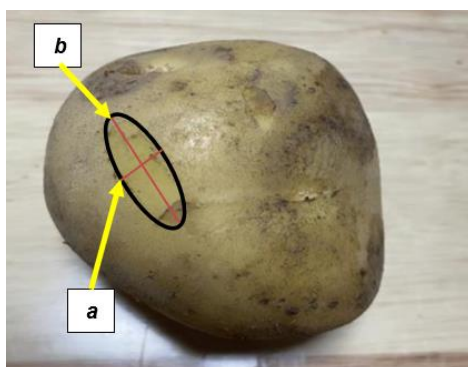
Fig. 2 - Epidermal abrasions
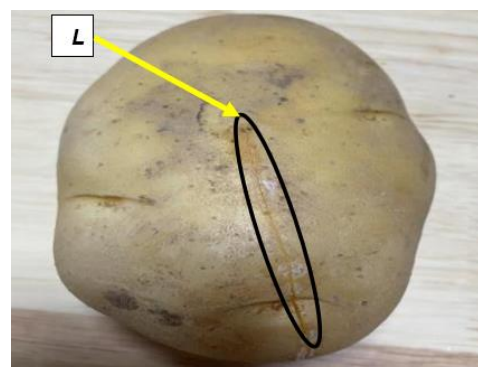
Fig. 3 - Tuber fragmentation

(3) The measurement method of tissue damage. Firstly, potato tubers after the collision were placed on dry ground for five days. Secondly, the potato tubers were cut into slices (1 mm in thickness) (*Jian, 2008*) and then photographed the slices, and the photos were imported to Photoshop software. The original images were converted to gray-scale images by adjusting the RGB mode.

The 3*3 pixels is used as a reference point to check the gray-scale value, and the added value of gray-scale of damaged part can be expressed as:

$$K = K_2 - K_1 \tag{12}$$

where:

K denotes the added value of gray-scale of damaged part;

K_1 represents the gray value of the undamaged part in the potato tuber;

K_2 expresses the gray value of the damaged site in the potato tuber.

Fig. 4 - Slices with a thickness of 1mm
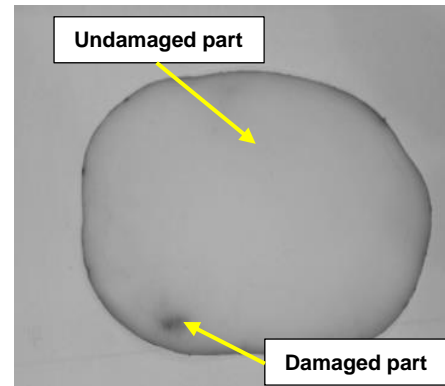
Fig. 5 - Gray-scale image

Before constructing comprehensive damage index (*DI*) by weight distribution of three types of damage, the measured data should be processed without dimensionality as follows:

$$X_{m'(k)} = \frac{\left| X_{m(k)} - \bar{X}_m \right|}{\sigma} \tag{13}$$

where:

$X_{m'(k)}$ represents the dimensionless data;

$X_{m(k)}$ represents the raw data of the kth element derived from the evaluation metrics;

$\bar{X}$ denotes the average values of the same evaluation indices;

σ is the standard deviation of the same evaluation indices.

Then the comprehensive damage index (*DI*) was constructed using three factors, including the epidermal damaged area, the length of the fissure and the added value of gray-scale (*Bin, 2018*), which can be calculated by:

$$DI = 0.25 \cdot X_{S'} + 0.35 \cdot X_{K'} + 0.4 \cdot X_{L'} \tag{14}$$

where:

DI denotes the comprehensive damage index;

$X_{S'}$ is the dimensionless data of epidermal damage area;

$X_{K'}$ is the dimensionless data of added value of gray-scale;

$X_{L'}$ is the dimensionless data of length of the fissure.

RESULTS
Orthogonal test results

The range analysis results are shown in Table 4. The order of influencing factors for the comprehensive damage index is as follows: impact material>potential energy>potato varieties>impact angle. In addition, the results showed that the comprehensive damage index was the lowest when the impact material was a plank, the potential energy was 1.2J, the type of potato was Lishu NO.6, and the impact angle was 15°.

Table 4

Experimental results and range analysis

Test No.	Impact material A	Potato varieties B	Potential energy C [J]	Impact angle D [°]	DI
1	0	-1	1	0	0.5140
2	0	0	0	0	0.2526
3	-1	-1	0	0	0.4917
4	0	-1	0	-1	0.4566
5	-1	0	-1	0	0.3096
6	0	0	1	-1	0.4055
7	1	0	0	1	0.3054
8	0	1	0	1	0.2296
9	0	-1	0	1	0.2972
10	1	0	1	0	0.2576
11	1	1	0	0	0.3841
12	0	0	-1	1	0.2166
13	0	1	1	0	0.4247
14	1	-1	0	0	0.3388
15	1	0	0	-1	0.1412
16	0	0	0	0	0.2526
17	1	0	-1	0	0.0055
18	-1	0	0	1	0.5014
19	0	0	1	1	0.3076
20	0	0	-1	-1	0.1590
21	-1	0	1	0	0.5608
22	0	-1	-1	0	0.2015
23	0	1	-1	0	0.1742
24	-1	1	0	0	0.6598
25	-1	0	0	-1	0.4859
26	0	1	0	-1	0.3079
K_{-1}	0.5015	0.3833	0.1777	0.3260	
K_0	0.3000	0.2872	0.3646	0.3438	
K_1	0.2388	0.3634	0.4117	0.3696	
R	0.2627	0.0961	0.2340	0.0436	

Table 5

Variance analysis of test result of the comprehensive damage index

Source of variation	Sum of squares	Degree of freedom	Mean square	F-Value	P-Value
Mode	0.4872	14	0.0348	5.1	0.0054
A	0.2071	1	0.2071	29.84	0.0002
B	0.0012	1	0.0012	0.1715	0.6868
C	0.1642	1	0.1642	23.66	0.0005
D	0.0008	1	0.0008	0.1160	0.7398
AB	0.0038	1	0.0038	0.5432	0.4766
AC	2.025E-07	1	2.025E-07	0.0000	0.9958
AD	0.0055	1	0.0055	0.7964	0.3913
BC	0.0010	1	0.0010	0.1385	0.7169
BD	0.0016	1	0.0016	0.2369	0.6360
CD	0.0060	1	0.0060	0.8709	0.3707
A^2	0.0353	1	0.0353	5.08	0.0455
B^2	0.0391	1	0.0391	5.64	0.0369
C^2	0.0024	1	0.0024	0.3394	0.5719
D^2	0.0006	1	0.0006	0.0821	0.7798
Residua	0.0763	11	0.0069	—	—
Lack of Fit	0.0763	10	0.0076	—	—
Pure Error	0.0000	1	0.0000	—	—

The variance analysis of test result was shown in Table 5 and the P-Value shows that the test factor B (potato varieties) and D (impact angle) have no significant effect on the comprehensive damage index. On the contrary, factor A (impact material) and C (potential energy) have significant effect on the comprehensive damage index.

Response surface analysis of the comprehensive damage index

Design-Expert software was used to plot the response surface of the comprehensive damage index, the effect of various factors and the interaction between various factors on the comprehensive damage index is shown in Fig. 6.

a) $DI = (A, B, 0, 0)$ b) $DI = (A, 0, C, 0)$

c) $DI = (A, 0, 0, D)$ d) $DI = (0, B, C, 0)$

e) $DI = (0, 0, C, D)$ f) $DI = (0, B, 0, D)$
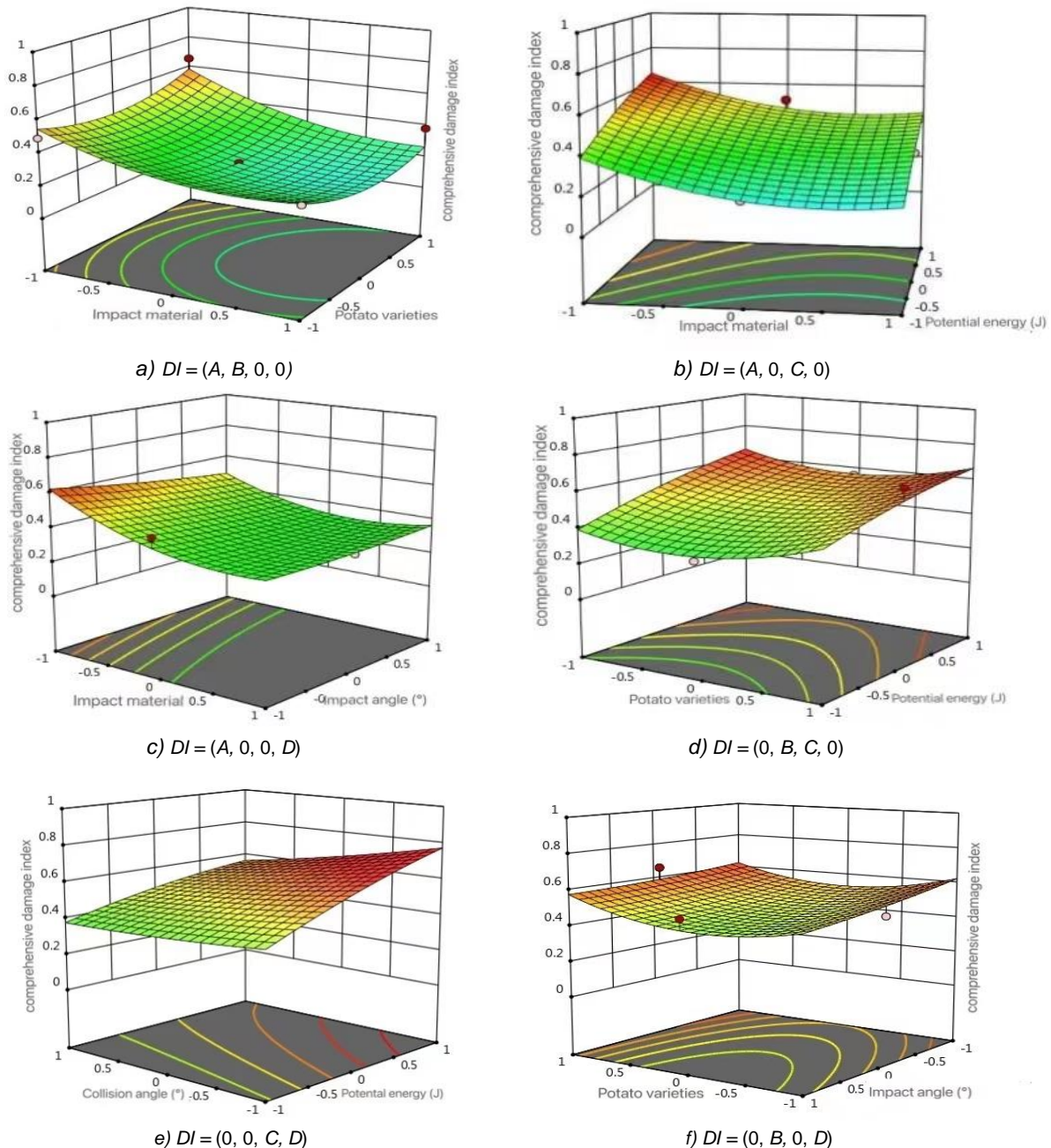
**Fig. 6 - Response surface of the impact material, potato species, potato potential energy
and impact angle to the comprehensive damage**

According to the results of Table 1, Table 2, Table 4, and Fig. 6, the comprehensive damage index (DI), which represents the damage degree of potato tuber in collision decreased with the increasing of coefficient of restitution of impact material (e), potato yield strength (σ') and collision angle (φ), but increased with the increasing of potato potential energy (mgh). The experimental results agreed well with the damage phenomenon explained by the mechanic impact model in equation (5) and (10).

The bigger the coefficient of restitution of the collision material, the less energy lost during the collision and the energy used to damage the potato was less too. Therefore, covering a layer of impact material with a higher coefficient of restitution on the parts of potato harvester to reduce the tuber damage degree should be a feasible method. The higher the potato yield strength, the greater the potato's ability to resist plastic deformation, which means the longer elastic compression phase, and under the premise of no damage, the greater the impact load could bear. These points indicated that potato varieties with high yield strength are more suitable for mechanical harvesting. The larger the potential energy, the greater the initial impact speed, the more mechanical energy lost after a collision, and the greater damage degree.

The larger the collision angle, the greater contact area between the potato tuber and the impact material, which leads to greater damage. Thus, the harvester's operating and structure parameters could be optimized from the perspective of reducing the potential energy of potato tuber being harvested and improving the potato tuber impact angle during harvesting.

Experimental verification

According to Table 3, the two-regression method was applied to analyze the comprehensive damage index and a mathematical regression model was established to explain the relationship between tuber damage degree and the four test factors.

$$DI = 0.2526 - 0.1314 \cdot A - 0.0100 \cdot B + 0.1140 \cdot C - 0.0082 \cdot D - 0.0307 \cdot AB + 0.0002 \cdot AC + 0.0372 \cdot AD$$
$$- 0.0155 \cdot BC + 0.0203 \cdot BD - 0.0389 \cdot CD + 0.0899 \cdot A^2 + 0.0947 \cdot B^2 - 0.0232 \cdot C^2 + 0.0114 \cdot D^2 \tag{15}$$

where:

A denotes the impact material; B expresses the potato varieties; C represents the potato energy; D is the impact angle.

The error value $\triangle$ was obtained by performing five randomized validation trials (five potato tubers per group, and Level factors were randomly selected) and comparing the actual measurement results (DI_1) with the regression model predicted results (DI_2). The predicted results of the comprehensive damage index *were calculated by the* formula (15). The results of validation trials are shown in Table 6.

Table 6

The results of validation trials

Test No.	*A*	*B*	*C*（J）	*D*（°）	*DI₁*	*DI₂*	△（%）
1	-1	0	0	-1	0.5559	0.5307	4.5
2	0	0	0	0	0.2423	0.2526	4.9
3	-1	-1	0	0	0.5182	0.5479	5.7
4	0	0	1	-1	0.4211	0.4049	3.8
5	0	1	1	0	0.3878	0.4156	7.2

Table 6 shows that the error values $\triangle$ in each group are less than 10%, so the quadratic regression model of the comprehensive damage index is hereby able to capture the test situation, the average error between the experimental and predicted data was 5.22%. This model can be used to estimate the damage degree of potato tuber collision.

CONCLUSIONS

(1) The physical model of potato tuber collision was constructed in terms of the deformation and deformation energy analysis during the collision. The model showed that potato damage degree correlates with impact material, potato varieties, potential energy, and impact angle.

(2) The range analysis suggest the order of influencing factors for the comprehensive damage index is as follows: impact material＞potential energy＞potato varieties＞impact angle. The results of the orthogonal test showed that the potato varieties and the impact angle have no significant effect on the comprehensive damage index. On the contrary, impact material and the potential energy have significant effect on the comprehensive damage index. Furthermore, when the impact material is plank, the potential energy is 1.2 J, the potato varieties is Lishu NO.6, and the collision angle is 15 °, the comprehensive damage index is the lowest, 0.0055.

(3) The comprehensive damage index (*DI*) was decreased with the increasing of the coefficient of restitution between impact material and steel (*e*), potato yield strength (*σ'*) and collision angle (*φ*), but increased with the increasing of potato potential energy (mgh).

(4) The quadratic regression model of the comprehensive damage index is obtained by orthogonal test results. The average error between the predicted data of the comprehensive damage index calculated by the mathematical regression model and the experimental data was 5.22%.

ACKNOWLEDGEMENT

REFERENCES

[1] Arfa, G.K. (2007). The effect of harvesting operation on potato crop handling. *Misr Journal of Agricultural Engineering*, Vol. 24, pp. 492-503, Egypt.

[2] Baritelle, A., Hyde, G., Thornton, R., Bajema, R. (2000). A classification system for impact-related defects in potato tubers. *American Journal of Potato Research*, Vol. 77, pp. 143-148, USA.

[3] Thybo, A.K., Jespersen, S.N., Lærke, P.E., Stødkilde-Jørgensen, H.J. (2004). Nondestructive detection of internal bruise and spraing disease symptoms in potatoes using magnetic resonance imaging. *Magnetic resonance imaging*, Vol. 22, pp. 1311-1317, USA.

[4] Bin, F., (2018). *Study on Physical Characteristics and Damage of Potato Tubers at Harvesting Stage* (收获期马铃薯块茎物理特性及损伤机理研究) [Doctoral dissertation, Gansu Agricultural University]. China National Knowledge Infrastructure. https://kns.cnki.net/kns8/defaultresult/index.

[5] Caglayan, N., Oral, O., Celik, H.K., Cinar, R., Rodrigues, L.C.D.A., Rennie, A.E., Akinci, I. (2018). Determination of time dependent stress distribution on a potato tuber during drop case. *Journal of Food Process Engineering*, Vol. 41, pp. e12869, USA.

[6] Celik, H. K., Cinar, R., Yilmaz, D., Ulmeanu, M. E., Rennie, A. E., Akinci, I. (2019). Mechanical collision simulation of potato tubers. *Journal of Food Process Engineering*, Vol. 42, pp. e13078, USA.

[7] Molema, G.J., Bouman, A., Verwijs, B. R., Van Den Berg, J. V., Klooster, J. J. (2000). Subcutaneous tissue discoloration in ware potatoes. 1. A chain analysis in the Netherlands. *Potato research*, Vol. 43, pp. 211-224, Netherlands.

[8] Green, I. (2005). Poisson ratio effects and critical values in spherical and cylindrical Hertzian contacts. *Applied Mechanics and Engineering*, Vol. 10, pp. 451, Netherlands.

[9] Hui S., (2014). *Contact Pressure Analysis of Drop Impact for Korea Pear and Bruising Predication Using Finite Element Analysis* (库尔勒香梨跌落碰撞接触应力分析及损伤预测的研究) [Master's dissertation, Shihezi University]. https://kns.cnki.net/kns8/defaultresult/index.

[10] Han D., (2019). *Mechanical Damage Analysis and Experimental Research on Potato Harvester Elevator* (马铃薯收获机升运过程机械损伤分析与试验) [Master's dissertation, Tohoku University of Agriculture]. https://kns.cnki.net/kns8/defaultresult/index.

[11] Jackson, R.L., Green, I. (2005). A finite element study of elasto-plastic hemispherical contact against a rigid flat. *Journal of Tribology*, Vol.127, pp. 343-354, USA.

[12] Jian Z., (2008). *Assessment Technology and Genetic Analysis for Tuber Browning in Potato (Solanum tuberosum)* (马铃薯块茎损伤评价技术研究及损伤变色性状的遗传分析) [Doctoral dissertation, Chinese Academy of Agricultural Sciences]. China National Knowledge Infrastructure. https://kns.cnki.net/kns8/defaultresult/index.

[13] Jian M., Chun W., Sheng X., Wei D., Shao Q., Jing L., (2017). Measurement test analysis of potato restitution coefficient (马铃薯恢复系数测定试验分析). *Journal of China Agricultural University*, Vol.09, pp.93-100, Beijing/ China.

[14] Li L., Zhi W., (2007). Dropping Impact Mechanical Characteristics of Apple (苹果跌落冲击力学特性研究). *Transactions of the Chinese Society of Agricultural Engineering*, Vol. 02, pp.254-258, Beijing/China.

[15] Ito, M., Sakai, K., Hata, S., Takai, M. (1994). Technical Notes: Damage to the Surface of Potatoes from Collision. *Transactions of the ASAE*, Vol. 37, pp. 1431-1433, USA.

[16] Parks R, Anderson G, Zheng D., (1990). Artificial Potatoes for Damage Research (用于损伤研究的人造马铃薯). *Advances in Mechanics*, Vol. 03, pp. 425-430, Beijing/China.

[17] Peters, R. (1996). Damage of potato tubers, a review. *Potato research*, Vol. 39, pp. 479-484, Netherlands.

[18] Mathew, R., Hyde, G. M. (1997). Potato impact damage thresholds. *Transactions of the ASAE*, Vol. 40, pp. 705-709, USA.

[19] Mayer, V., Vejchar, D., Pastorková, L. (2017). Measurement of potato tubers resistance against mechanical loading. *Research in Agricultural Engineering*, Vol. 1, pp. 22-31, Czech Republic.

[20] Evans, S. D., McRae, D. C. (1998). Quantifying damage as percentage potato tuber volume lost per peeler stroke. *Potato research*, Vol. *41, pp. 277-287,* Netherlands.

[21] Shan C., Yi Z., Jun W., Jian W., (2003). Mechanical parameters of impact occurred due to fruit fall in relation to bruise suffered by fruit (梨的下落碰撞冲击加速度特性研究). *Journal of Zhejiang University (Agriculture and Life Sciences),* Vol. 03, pp. 105-108, Zhejiang/China.

[22] Shi S., Fang W., Hong W., Zheng H., (2010). Study on development of potato harvest machinery in China (我国马铃薯收获机械研制与发展的研究). *Journal of Chinese Agricultural Mechanization*, Vol. 03, pp. 34-39, Jiangsu/China.

[23] Wei D., Chun Wang., Sheng X., (2020). Test research on the impact peak force and damage depth of potato, *INMATEH-Agricultural Engineering*, Vol. 61, pp. 105-114, Bucharest/Romania.

[24] Zhi L., (2017). *Research on Potato Collision Problem and Key Mechanism of Sorting Equipment* (马铃薯碰撞问题及分选装备关键机构研究). [Master's dissertation, Zhejiang University]. China National Knowledge Infrastructure. https://kns.cnki.net/kns8/defaultresult/index.

PERFORMANCE EVALUATION OF AN OBSTACLE AVOIDANCE MOWER ASSEMBLY IN TRUNK TYPE PEAR ORCHARD
/
可避障复合式割草机在主干型梨园中的性能评估

Xiaohui LEI [1)], Jin ZENG [1)], Yannan QI [1)], Tao XYU [1)], Andreas HERBST [2)], Xiaolan LYU [*1)] [1]
[1)] Institute of Agricultural Facilities and Equipment, Jiangsu Academy of Agricultural Sciences / Key Laboratory of Horticultural Equipment (Nanjing), Ministry of Agriculture and Rural Affairs, Nanjing/China;
[2)] Institute for Chemical Application Technology of JKI, Braunschweig Messeweg/Germany;
Tel: +86-025-84390082; E-mail: leixiaohui.2008@163.com
DOI: https://doi.org/10.35633/inmateh-66-15

ABSTRACT

To solve the problem of mechanized weeding in trunk type pear orchard, combined with the technology of stubble elimination and hydraulic obstacle avoidance, the authors designed an obstacle avoidance mower assembly. This paper carried out a field performance evaluation test to verify its usefulness. Six indexes were tested to evaluate its working performance. The results were: inter-row crushing rate of 89.99%, intra-row miss cutting rate of 2.42%, stubble stability coefficient variation of 4.25%, working efficiency of 0.32 hm^2/h, fuel consumption of 16.25 L/hm^2, profitable area of 0.75 hm^2. The study could provide a reference for orchard mechanized weeding.

摘要

为了解决主干型梨园机械化除草问题，结合割茬粉碎和液压避障技术，作者设计了一款可避障复合式割草机。本文采用 6 项指标来对机具进行性能评估试验以证明其实用性。结果显示: 行间碎草率为 89.99%，株间漏割率为 2.42%，割茬稳定性变异系数为 4.25%，工作效率为 0.32 hm^2/h，燃料消耗为 16.25 L/hm^2，盈利面积为 0.75 hm^2。本研究可为果园机械化除草提供参考。

INTRODUCTION

Weeding is a necessary agronomic section in pear orchard management. Herbicide causes droplet drift *(Wang C. et al., 2020)*, since it not only damages fruit tree but also destroys the ecological environment *(Kehayov D. et al., 2020)*. Also, abuse of herbicide promotes weed resistance *(Gaines T. A. et al., 2020)*. With the development of orchard grass planting technology *(Arentoft B. et al., 2013; Bai G. et al., 2018; Martinelli R. et al., 2017)*, chemical weeding has been replaced by mechanized mowing in recent years.

Research on mechanical orchard mower is little and started late in China, mostly focused on intra-row mower with sensor detection. *Li X. et al., (2019)* developed an orchard offset traction type mower, on which the position of cutter can change shape with the ridge surface. *Ma P. et al., (2019)*, developed an orange orchard profile mower, which can adapt to profile work on mountain terrain. *Xu L. et al., (2018)*, developed an intra-row automatic obstacle avoidance mower for trellis grape orchard. The coverage rate of intra-row weeding was 98.1% in the field test. Related research is mature in European and American countries, who concentrated on developing new machines at early age, such as grape intra-row multi-process cultivator produced by Italy Orizzonti, Spraydome series under tree weed mower produced by America Micron Group, and DR series variable width mower produced by Dutch Van Wamel BV. In recent years, the researchers are focused on the effect evaluation of different mechanical weeding methods and new mowing robots. *Mia et al., (2020)*, studied the working performance of integrated weeding in orchards. The indexes include weed species diversity, soil coverage, weed biomass production, soil nitrogen status, and weed abundance. *Muhammad Z. et al., (2021)*, developed a robotic lawnmower for small Japanese pear orchard. It can control the growth of the weed for years automatically.

---

[1] *Xiaohui Lei, Assistant Researcher; Jin Zeng, Research Assistant; Yannan Qi, Research Assistant; Tao Xyu, Research Assistant; Andreas Herbst, Prof.; Xiaolan Lyu, Researcher.*

Trunk type is a mainstream mechanized cultivation pattern for pear orchard. The current weeding method is inter-row rotary tiller combined with intra-row artificial weeding, demonstrating lower efficiency and poor effect. Combined with the technology of stubble elimination and hydraulic obstacle avoidance, the authors designed an obstacle avoidance mower assembly (OACM) that can be used for efficient mechanized weeding *(Lei X. et al., 2020)*. A field performance evaluation test was carried out in trunk type pear orchard. Six indexes were tested to evaluate the working performance, including inter-row crushing rate, intra-row miss cutting rate, stubble stability, working efficiency, fuel consumption and profitable area. The study could provide a reference for mechanized weeding in orchards.

MATERIALS AND METHODS

Structure and working principle of OACM

Planting distances between rows in various orchards are different. For better general use, the mower was designed as unilateral obstacle avoidance type. The whole machine is suspended and driven by a tractor. It is composed by suspension bracket, hydraulic system, mechanical transmission system, inter-row crushing mechanism, intra-row obstacle avoidance cutting mechanism and soil compactor. The inter-row crushing mechanism adopted the roller type stubble cutter, which can crush and return the weed to the field. The intra-row obstacle avoidance cutting mechanism adopted the horizontal rotation obstacle avoidance cutting disc, which can cut weeds without harming the trunk and the root. The structure of the mower is shown in Fig. 1. As shown by the dotted line and arrows in Fig. 2, the mower works in the field along an S-shaped line.
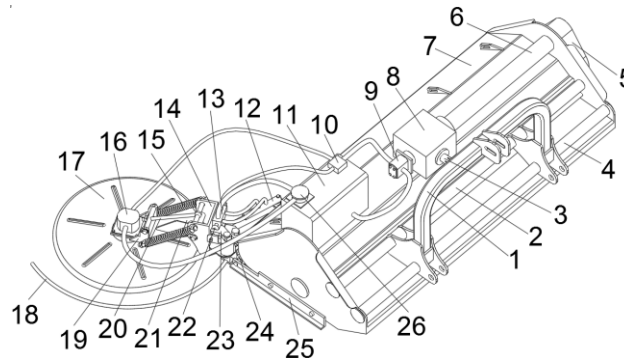
Fig. 1 - Structure of the OACM

1. Suspension bracket; 2. Lateral movement hydraulic cylinder; 3. Power input shaft; 4. Cylindrical rail; 5. Transmission belt shell; 6. Pulley transmission shaft cover; 7. Frame; 8. Bevel gearbox; 9. Gear pump; 10. Hydraulic distribution valve; 11. Hydraulic oil tank; 12. Obstacle avoidance hydraulic cylinder; 13. Hydraulic directional valve; 14. Rotation bracket; 15. Vibration damper; 16. Hydraulic motor; 17. Obstacle avoidance disc; 18. Detection rod; 19. Obstacle avoidance disc bracket; 20. I-shaped profiling bracket; 21. Profiling plate; 22. Plunger; 23. Press block; 24. Soil press roller; 25. Soil press roller bracket; 26. Filter
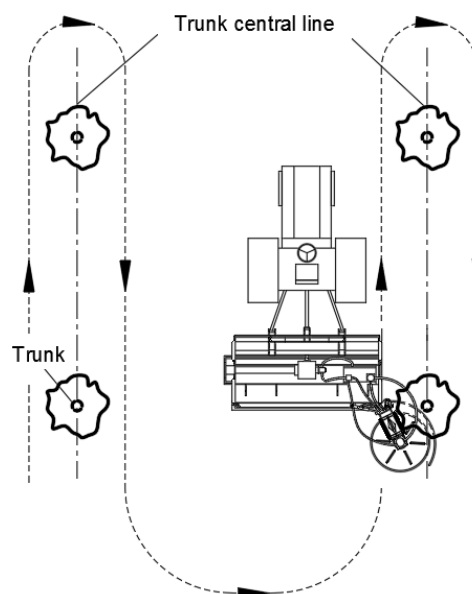
Fig. 2 - Movement path of OACM

The tractor should be equipped with a hydraulic output system to control the position of inter-row crushing mechanism. When the hydraulic cylinder extends, the whole machine moves to the right and the mower approaches the tree. When the hydraulic cylinder shrinks, the whole machine moves to the left and the mower gets far away from the tree. In the working process, tractor PTO drives the power input shaft to rotate through the universal shaft. The tractor transmits power to pulley transmission shaft and gear pump through bevel gearbox. Gear pump supplies hydraulic oil to the hydraulic directional valve and hydraulic motor. Pulley mechanism drives inter-row crushing roller to rotate and hydraulic motor drives intra-row cutting disc to rotate. Hydraulic directional valve drives the obstacle avoidance disc swing around the tree trunk by controlling the obstacle avoidance hydraulic cylinder. A rubber ring is fixed around the obstacle avoidance disc to prevent the steel structure from scraping the trunk. Parallelogram profiling mechanism connects obstacle avoidance disc and rotation bracket. Under the action of vibration damper and profiling slide disc, the longitudinal position of the obstacle avoidance disc can be adjusted according to the terrain around the trunk. The soil pressing roller is installed behind the inter-row crushing roller for soil surface compaction. The main structure and performance parameters of OACM are shown in Tab. 1.

Table 1

Main structure and performance parameters of OACM

Parameters	Values
Tractor power [kW]	44.2
Weight [kg]	427
Size, length×width×height [m]	1.72×2.33×0.89
Largest distance of lateral movement [m]	1
Crushing roller rotation speed [r/min]	2025
Y-shaped blade number	24
Cutting disc rotation speed [r/min]	2531
Blade number of cutting disc	2
Working speed [m/s]	0.44
Inter-row crushing width [m]	1.5
Largest swing distance of obstacle avoidance disc [m]	0.5

Methods of field tests

In April 2021, performance tests were conducted in Yejia pear orchard, Taixing, China. The trees were seven years old (7 a) and planted with row spacing of 4 m and plant spacing of 3 m. The average trunk height was 0.6 m and the average trunk diameter was 8 cm. The road of the orchard was flat and the tractor type was LOVOL M604L-E (Lovol Heavy Industry Co., Ltd., China). Considering that the driver's sight would be affected by the branches and leaves, low speed gear II was chosen (average tractor moving speed was 0.44 m/s) during the test. Test indexes were inter-row crushing rate (*Chinese standard JB/T8401.3*), intra-row miss cutting rate (*Chinese standard GB/T10938*), stubble stability, working efficiency, fuel consumption and profitable area. Three rows 60 m in length were selected for the test on inter-row crushing rate, intra-row miss cutting rate and stubble height. Divide 60 m into six sections with each section 10 m in length. One sample point for inter-row crushing rate and two sample points for intra-row miss cutting rate were selected in one section. One sample point for intra-row miss cutting rate between trunks and one sample point for intra-row miss cutting rate around trunks were selected in one section. After the weed stems were collected, six sample points for inter-row crushing rate and six sample points for intra-row miss cutting rate were selected in each row for stubble height measurement. Ten rows with 100 m in length were selected for tests of working efficiency, fuel consumption and profitable area. The test site of OACM is shown in Fig. 3.

(a) Working site of OACM   (b) Sampling frame   (c) Weighting
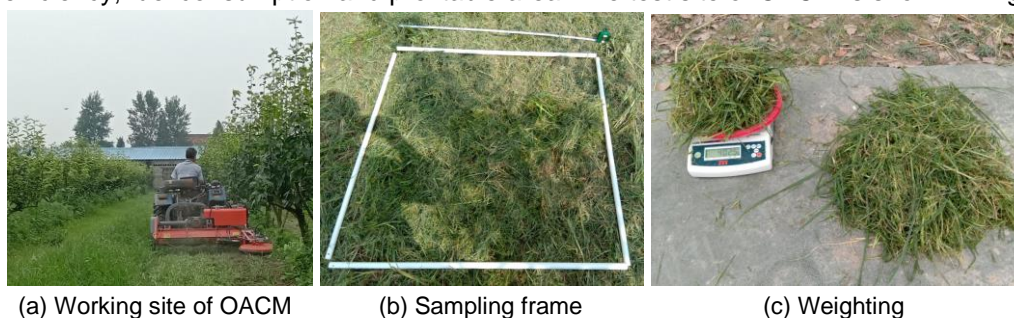
Fig. 3 – Test site

The side length of the sampling frame was 1 m and the sampling area of each point was 1 m². In each inter-row crushing rate sample point, all weed stems were collected and their weight was measured. The stems with length more than 10 cm were taken out, and their weight was measured. The inter-row crushing rate was calculated by Equation (1).

$$C = (1 - \frac{G_{10}}{G_c}) \times 100 \tag{1}$$

where:

C is inter-row crushing rate, [%]; G_{10} is weight of weed stems over 10 cm in length within one sample point, [g]; G_c is weight of crushed weed stems within one sample point, [g].

Miss cutting rate was defined as the miss cutting weight divided by the weight of harvested weeds per unit area. Intra-row miss cutting rate was calculated by Equation (2).

$$M = \frac{G_m}{G_t} \times 100 \tag{2}$$

where:

M is intra-row miss cutting rate, [%]; G_m is the miss cutting weight within one sample point, [g]; G_t is the weight of harvested weeds within one sample point, [g].

For stubble height, five measure points were arranged diagonally within each sample point. Measurements were taken from the ground, and the average height at five measure points was the stubble height of the sample point. The stubble height was calculated by Equation (3).

$$h = \frac{\sum_{i=1}^{n} h_i}{5} \tag{3}$$

where:

h_i is the stubble height at measure point i, [cm]; h is the stubble height of each sample point, [cm].

The working time of OACM was recorded. Working efficiency is the mowing area per hour and was calculated by Equation (4), where working area equals the weeding width multiplied by moving distance.

$$E = \frac{A}{t} \tag{4}$$

where:

E is working efficiency, [hm²/h]; A is working area, [hm²]; t is working time, [h].

Fuel consumption is the fuel volume required for tractor in unit mowing area and was calculated by Equation (5), where fuel volume was measured by graduated cylinder.

$$Q = \frac{V}{A} \tag{5}$$

where:

Q is fuel consumption, [L/hm²]; V is fuel volume consumed, [L].

The profitable area of OACM was calculated based on the working efficiency, so as to guide the orchard manager to choose the optimal operation method. The profitable area is the minimum planting area required by machines to replace labour in management cost. According to Equations (6)-(8), the profitable area was calculated. When the planting area of crops is larger than the profitable area, the machine can bring profits.

$$q = \frac{p}{y} \tag{6}$$

where:

q is the annual depreciation of one OACM, [$];

p is the price of one OACM, [$];

y is the depreciable life, [year].

$$c = \frac{c_0 t}{t_0} \times \eta \tag{7}$$

where:

c is the saved cost of one OACM by replacing labour, [\$/hm^2];

c_0 is the labour cost in an eight-hour day, [\$];

t is the average artificial weeding time of one hectare, [h/hm^2];

t_0 is the working hours of one day, [h];

η is the time-saving proportion of mechanical weeding to artificial weeding.

$$A_p = \frac{q}{c} \tag{8}$$

where:

A_p is the profitable area of one OACM, [hm^2].

RESULTS

Inter-row crushing rate

Weed crushing is the process in which the crushing roller assembly interacts with weeds on the ground. Inter-row crushing rate is used to evaluate the crushing quality between rows. Referring to Chinese national standard JB/T8401.3, the index of crushing rate should be no less than 86%. The higher the crushing rate is, the better the crushing quality becomes. The crushing rate of each sample point is shown in Fig. 4. Coefficient variation of sample points (*Dai N. et al., 2020*) can reflect the individual stability. The calculation formulas of inter-row crushing rate, standard deviation, and coefficient variation are shown in Equations (9), (10) and (11). The results of inter-row crushing rate and coefficient variation are shown in Tab. 2.

Crushing rate is related to the flatness of orchard road, weed species and the design structure of crushing roller assembly. The inter-row crushing rates of three rows were 89.63%, 90.52% and 89.82%, respectively, indicating that the sample points had a higher crushing rate, and all could meet the requirement of stem crushing. Because the working speed and rotation speed of the crushing roller in each sample point were the same, the difference between them is related to the road flatness and weed species. The coefficient variation of three rows was 1.49%, 1.75% and 1.46%, respectively, and the maximum error of coefficient variation was 0.29%. The results showed that there was little difference between the sample points; road flatness and weed species of them were consistent. The average value of inter-row crushing rate and its coefficient variation is 89.99% and 1.57%, respectively. The average value of inter-row crushing rate is 3.99% higher than the index, indicating a better crushing effect. Good working effect benefits from the mechanical structure of inter-row crushing roller assembly: a 1.5 m long crushing roller with 24 Y-shaped stubble blades, which were arranged in a symmetrical double-helix structure with 60° in radial direction. There was no gap between the stubble blades, and the symmetrical double-helix structure of the stubble blades could effectively reduce the vibration caused by the rotation. The inter-row crushing rate of mower met the production requirements.
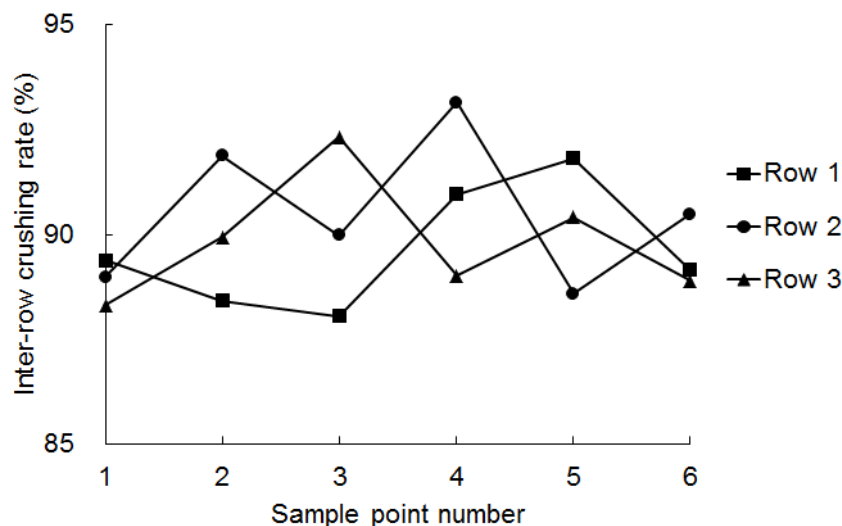
Fig. 4 – Inter-row crushing rate of each sample point

<div align="right">**Table 2**</div>

Inter-row crushing rate C and coefficient variation CV

Row number	Index	Values
1	C [%]	89.63
	CV [%]	1.49
2	C [%]	90.52
	CV [%]	1.75
3	C [%]	89.82
	CV [%]	1.46
Average value	C [%]	89.99
	CV [%]	1.57

$$C = \frac{\sum_{i=1}^{6} C_i}{6} \tag{9}$$

$$S_c = \sqrt{\frac{\sum_{i=1}^{6}(C_i - C)^2}{6}} \tag{10}$$

$$CV = \frac{S_c}{C} \times 100 \tag{11}$$

where:

C_i is the inter-row crushing rate of sample point i, [%];
S_c is the standard deviation of inter-row crushing rate, [%];
CV is the coefficient variation of inter-row crushing rate, [%].

Intra-row miss cutting rate

Intra-row miss cutting rate is used to evaluate the cutting quality within rows. Cutting disc rotation diameter should be a little less than obstacle avoidance disc diameter, so that it will keep the grasses close to trunks from cutting, and the miss cutting weight between and around trunks were different. During sampling, miss cutting rate between and around trunks were measured separately, and the results are shown in Fig. 5. The calculation method of coefficient variation is the same with the inter-row crushing rate. The average value of intra-row miss cutting rate and its coefficient variation are shown in Tab. 3.

The intra-row miss cutting rates of three rows between trunks were 0.22%, 0.23% and 0.22%, respectively. The average value of them is 0.23%, which is almost equal to 0. It shows that OACM had little miss cutting grasses between trunks. The intra-row miss cutting rate of three rows around trunks was 4.38%, 4.66% and 4.76%, respectively. The average value of them is 4.6%, which is higher than that between trunks. Because OACM leaves a certain safe zone around trunks, a few grasses around trunks have not been cut. The average values of coefficient variation between and around trunks were 7.91% and 4.87%, respectively. The coefficient variation around trunks was larger than that between trunks. Because miss cutting weight between trunks was less than that around trunks, the coefficient variation between trunks changed more significantly than that around trunks.

(a) Intra-row miss cutting rate between trunks   (b) Intra-row miss cutting rate around trunks
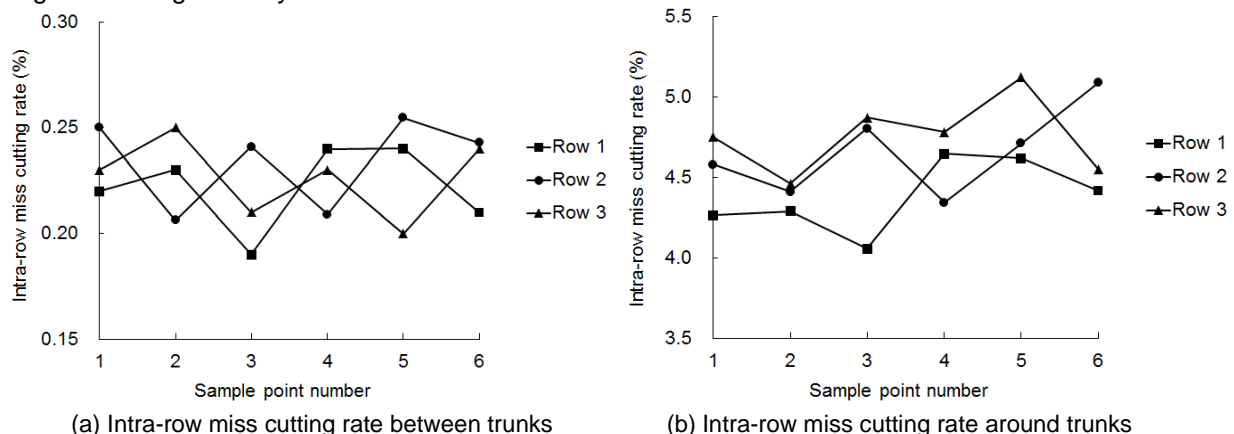
Fig. 5 – Intra-row miss cutting rate of each sample point

Table 3

Intra-row miss cutting rate *M* and coefficient variation CV

Row number	Position	Index	Values
1	Between trunks	M [%]	0.22
		CV [%]	8.01
	Around trunks	M [%]	4.38
		CV [%]	4.71
2	Between trunks	M [%]	0.23
		CV [%]	8.21
	Around trunks	M [%]	4.66
		CV [%]	5.38
3	Between trunks	M [%]	0.23
		CV [%]	7.5
	Around trunks	M [%]	4.76
		CV [%]	4.51
Average value between trunks		M [%]	0.23
		CV [%]	7.91
Average value around trunks		M [%]	4.6
		CV [%]	4.87

Stubble stability

Stubble stability is used to evaluate the working stability of OACM. Stubble height and its coefficient variation in different sample points were calculated. Inter-row and intra-row stubble height of three rows are shown in Fig. 6. The average value of stubble height and its coefficient variation are shown in Tab. 4.

The inter-row stubble height of three rows was 5.05 cm, 4.82 cm and 4.95 cm, respectively. The intra-row stubble height of three rows was 9.68 cm, 9.77 cm and 9.78 cm. The average value of them was 4.94 cm and 9.74 cm, respectively. It was consistent with the design value: inter-row stubble height of 5 cm, intra-row stubble height of 10 cm. The design stubble heights of inter-row and intra-row were different, which was related to the structure of crushing roller and cutting disc. The length of the crushing roller was 1.5 m, and the ground would inevitably have bumps and clods within the operation area. To avoid the mower from touching the soil, the stubble height should be set at 5 cm. The cutting disc was operated under the tree, the slope of the working area was greater, and the height of the stubble was set at 10 cm. The error between inter-row stubble height and the design value was 1.2%. The error between intra-row stubble height and the design value was 2.6%. The error was small because the orchard road was flat and OACM did not bump heavily during the mowing. The difference of two error values lies in the lower flatness of the intra-row than that of the inter-row. The inter-row stubble height coefficient variation of three rows is 4.39%, 4.39% and 3.82%. The intra-row stubble height coefficient variation of three rows was 5.07%, 4.41% and 3.41%, respectively. The average values of them were 4.2% and 4.3%, which are almost the same and reflect high working stability.

(a) Inter-row stubble height
(b) Intra-row stubble height
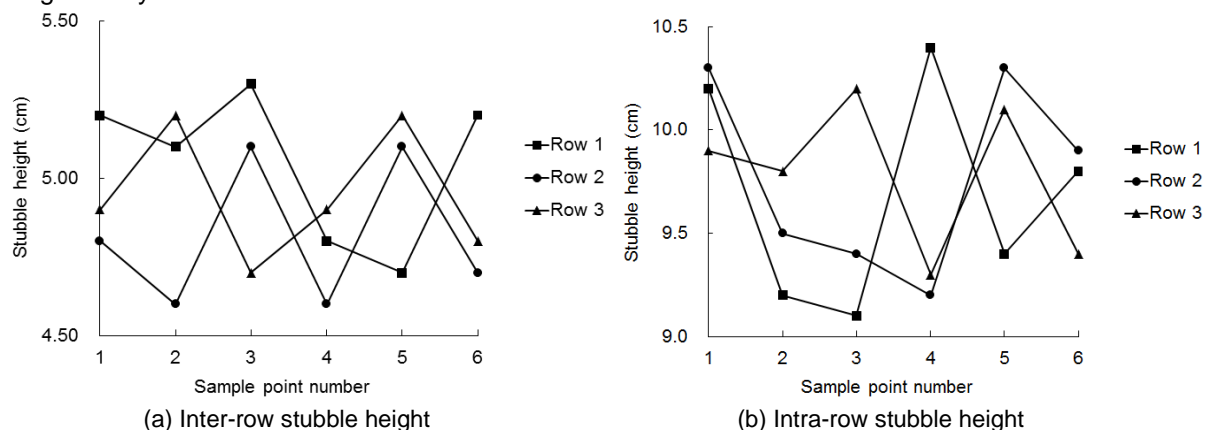
Fig. 6 – Stubble height of each sample point

Table 4

Stubble height h and coefficient variation CV

Row number	Position	Index	Values
1	Inter-row	h [cm]	5.05
		CV [%]	4.39
	Intra-row	h [cm]	9.68
		CV [%]	5.07
2	Inter-row	h [cm]	4.82
		CV [%]	4.39
	Intra-row	h [cm]	9.77
		CV [%]	4.41
3	Inter-row	h [cm]	4.95
		CV [%]	3.82
	Intra-row	h [cm]	9.78
		CV [%]	3.41
Average value inter-row		h [cm]	4.94
		CV [%]	4.2
Average value intra-row		h [cm]	9.74
		CV [%]	4.3

Working efficiency, fuel consumption and profitable area

The average weeding width of the mower was 2 m and the total mowing area of the test was 4000 m². Substitute the value of working time and consumed fuel volume into Equations (4) and (5), and calculate the working efficiency and fuel consumption of OACM. As shown in Tab. 5, working efficiency of OACM was much higher than that of artificial weeding, which is 77 times to artificial weeding (about 0.0042 hm²/h). The mower price was 2333 $, with five years of depreciable life. The labour cost was 19 $ for an eight-hour day. The artificial weeding area was 0.03 hm² per day and weeding time per unit area was 266.67 h/hm². The total time-saving proportion of OACM to artificial weeding was 98.83%. According to Equations (6), (7) and (8), the profitable area of OACM was 0.75 hm². With a large number of farmers working in cities, the small-scale orchard farms have been replaced by modern fruit companies. Manual knapsack mower and artificial weeding, which were suitable for family farms, have become outdated in industry. In this condition, mechanized OACM was especially suitable for the orchard management. Orchard managers can appropriately use a certain amount of OACM according to their orchard planting area and affordable cost range.

Table 5

Working efficiency E and fuel consumption Q

Name	Values
Working time [h]	1.26
Fuel volume [L]	6.5
Working area [hm²]	0.4
E [hm²/h]	0.32
Q [L/hm²]	16.25

CONCLUSIONS

The current mechanized weeding method is inter-row rotary tiller combined with intra-row artificial weeding, which demonstrates lower efficiency and poor effect. Combined with the technology of stubble elimination and hydraulic obstacle avoidance, the authors developed an obstacle avoidance mower assembly that can be used for efficient mechanized weeding in trunk type pear orchard. The roller type stubble cutter was adopted on the inter-row part of the mower, which can crush and return the weed to the field. The horizontal rotation obstacle avoidance cutting disc was adopted on the intra-row part of the mower, which can cut weeds without harming the trunks and roots.

Field performance evaluation test was carried out in trunk type pear orchard. Six kinds of indexes were tested and the results were: inter-row crushing rate of 89.99%, intra-row miss cutting rate of 2.42%, stubble stability coefficient variation of 4.25%, working efficiency of 0.32 hm^2/h, fuel consumption of 16.25 L/hm^2, profitable area of 0.75 hm^2. Inter-row crushing rate, intra-row miss cutting rate and stubble stability coefficient variation reflected a better field test result. The working efficiency, fuel consumption and profitable area can guide the operator to make a reasonable choice for OACM. The study could provide a reference for mechanized weeding in orchards.

ACKNOWLEDGEMENT

REFERENCES

[1] Arentoft B., Ali A., Streibig J., & Andreasen C. (2013). A new method to evaluate the weed-suppressing effect of mulches: a comparison between spruce bark and cocoa husk mulches. *Weed Research*, 53(3), 169-175. https://doi.org/10.1111/wre.12011

[2] Bai G., Zou C., Du S. (2018). Effects of self-sown grass on soil moisture and tree growth in apple orchard on Weibei dry plateau (渭北旱塬果园自然生草对土壤水分及苹果树生长的影响). *Transactions of the Chinese Society of Agricultural Engineering*, 34(3), 151-158.

[3] Dai N., Hou Z., Qiu Y., & Zhang X. (2020). Numerical simulation and experiment of vibration pelletizer based on EDEM. *INMATEH - Agricultural Engineering*, 60(1), 469 – 478, Bucharest / Romania. https://doi.org/10.35633/inmateh-63-48

[4] Gaines T. A., Duke S., Morran S., Rigon C. A. G., Tranel P. J., Küpper A., & Dayan F. (2020). Mechanisms of evolved herbicide resistance. *Journal of Biological Chemistry*, 295(30), 10307–10330. https://doi.org/ 10.1074/jbc.REV120.013572

[5] Kehayov D., Atanasov A. (2019). Modelling herbicide installation for the treatment of peach plantations. *INMATEH - Agricultural Engineering*, 60(1), 303-310. Bucharest / Romania. https://doi.org/10.35633/inmateh-60-34

[6] Lei X., Lv X., Zhang M., Shen Q., Lu D., Ma Z., & Zhong D. (2020). Design and test of orchard unilateral combine mower. *International Agricultural Engineering Journal*, 29(4), 157–167.

[7] Li X., Wang P., Yang X., Li J., Liu H., & Yang X. (2019). Design and test of orchard offset traction type lawn mower (果园垄面割草机设计与试验). *Journal of Chinese Agricultural Mechanization*, 40(5), 47–52.

[8] Ma P., Li S., Zhao C., Zhang Y., Zhang X., & Zhang C. (2019). Design and test of the orange garden profile mower cutter. Journal of Huazhong Agricultural University, 38(6), 156–162.

[9] Martinelli R., Monquero P., Fontanetti A., Conceicao P., & Azevedo F. (2017). Ecological Mowing: An Option for Sustainable Weed Management in Young Citrus Orchards. *Weed Technology*, 31(2), 260-268. https://doi.org/10.1017/wet.2017.3

[10] Mia M., Monaci E., Murri G., Massetani F., Facchi J., & Neri D. (2020). Soil Nitrogen and Weed Biodiversity: An Assessment under Two Orchard Floor Management Practices in a Nitrogen Vulnerable Zone in Italy. *Horticulturae*, 6(4): 96. https://doi.org/10.3390/horticulturae6040096

[11] Muhammad Z., Masakazu K. (2021). Weed Management and Economic Analysis of a Robotic Lawnmower: A Case Study in a Japanese Pear Orchard. *Agriculture-Basel*, 11(2): 113. https://doi.org/10.3390/agriculture11020113

[12] Wang C., Zeng A., He X., Song J., Herbst A., & Gao W. (2020). Spray drift characteristics test of unmanned aerial vehicle spray unit under wind tunnel conditions. *International Journal of Agricultural and Biological Engineering*, 13(3), 13-21. https://doi.org/10.25165/j.ijabe.20201303.5716

[13] Xu L., Yu C., Liu W., Yuan Q., Ma S., Duan Z., & Xing J. (2018). Optimal design on auto obstacle avoidance mechanism of intra-row weeder for trellis cultivated grape (篱架式栽培葡萄株间除草机自动避障机构优化设计). *Transactions of the Chinese Society of Agricultural Engineering*, 34(7), 23–30.

[14] *** China Machinery Industry Federation. (2001). *Smashed root-stubble machine (Standard No. JB/T8401.3-2001).* https://www.mayiwenku.com/p-163589.html

[15] ***Inspection and Quarantine of the People's Republic of China. (2008). *Rotary mowers (Standard No. GB/T 10938-2008).* https://www.doc88.com/p-3784861517639.html

IoT BASED SOIL MOISTURE MANAGEMENT USING CAPACITIVE SENSOR AND USER-FRIENDLY SMARTPHONE APPLICATION
/
ระบบอินเตอร์เน็ตของสรรพสิ่งเพื่อจัดการจัดการความชื้นในดิน

ที่ใช้เซนเซอร์ชนิดเปลี่ยนแปลงค่าความจุไฟฟ้าและแอปพลิเคชันบนสมาร์ทโฟน

Pharunee SARMPHIM [1]), Narongsak SUTTHIPHON [2]), Parimate JAROENSONG [2])
Chitnarong SIRISATHITKUL [3]), Yaowarat SIRISATHITKUL *[4]) [1]
[1]) Faculty of Liberal Arts, Rajamangala University of Technology Srivijaya, Songkhla, 90000, Thailand;
[2]) Faculty of Engineering, Rajamangala University of Technology Srivijaya, Songkhla, 90000, Thailand;
[3]) School of Science, Walailak University, Nakhon Si Thammarat, 80160, Thailand;
[4]) School of Engineering and Technology, Walailak University, Nakhon Si Thammarat, 80160, Thailand
Tel: +66 75 672947; E-mail: kinsywu@gmail.com

ABSTRACT
The Internet of Things (IoT) based system was assembled to monitor the moisture of soils for both indoor and outdoor uses. The SKU:SEN0193 capacitive soil moisture sensor exhibited a linear response to a variation in water volume added to the soil. Microcontroller Arduino NodeMCU was used with ESP8266 Wi-Fi module to transfer the sensing data in real-time, and the soil moisture data was displayed by the Blynk application on a smartphone. When the moisture dropped under the pre-defined threshold, the user was informed via the Line application and able to remotely trigger the irrigation pump.

บทคัดย่อ
ระบบอินเตอร์เน็ตของสรรพสิ่งได้รับการพัฒนาขึ้น เพื่อติดตามค่าความชื้นในดิน สำหรับการใช้งานในร่มและกลางแจ้ง ระบบใช้เซนเซอร์ความชื้นชนิดเปลี่ยนแปลงค่าความจุไฟฟ้ารุ่น SKU:SEN0193 ที่มีการตอบสนองเป็นเชิงเส้นกับปริมาตรของน้ำที่เติมลงในดิน และไมโครคอนโทรลเลอร์ Arduino NodeMCU ร่วมกับ ESP8266 Wi-Fi โมดูล ส่งข้อมูลที่วัดได้แบบเรียลไทม์ ให้สามารถแสดงข้อมูลความชื้นของดินผ่านแอปพลิเคชัน Blynk บนสมาร์ทโฟน ผู้ใช้ระบบจะได้รับการเตือนผ่านแอปพลิเคชัน Line เมื่อความชื้นลดลงต่ำกว่าค่าขีดเริ่มที่ตั้งไว้ เพื่อสามารถสั่งปั๊มให้ทำการรดน้ำ

INTRODUCTION

With the advent of Internet of Things (IoT), smart devices are accessed and connected with others online. Various systems can be remotely monitored by transferring measured data from a wireless sensor network and operated in response to the real-time analysis. There are numerous IoT applications in home automation (*Bheesetti et al., 2021*), industrial automation (*Singholi et al., 2021*), and healthcare (*Indra et al., 2020; Julian et al., 2021*). The applications in precision agriculture have been proposed to increase yields, reduce labour costs and conserve resources. (*Terence and Purushothaman, 2020; Deepa et al., 2021*). The sensing and functioning of devices in such systems are increasingly coordinated by either Raspberry Pi or Arduino UNO board of microcontroller (*Aulin et al., 2019; Barik, 2019; Hashim et al., 2020; Omar et al., 2020; Bheesetti et al., 2021; Ito and Kajisa, 2021*). The Arduino microcontrollers are widely deployed in smart farming because it can be customized for specific uses by opensource programming (*Effendi et al., 2020; Hashim et al., 2020; Omar et al., 2020; Ito and Kajisa, 2021*).

To link the hardware to the Internet, the IoT platform that simplifies the building mobile and web applications is vital. An IOS and Android smartphone application in the cloud platform called "Blynk" has been employed to monitor all devices connected to the Raspberry Pi or Arduino modules. Blynk provides various widgets and user-friendly interface to control the connected devices through smartphones.

---

[1] Pharunee *Sarmphim, Ph.D Physics*; Narongsak *Sutthiphon, B.Eng.;* Parimate *Jaroensong*, B.Eng.;

Chitnarong *Sirisathitkul, Associate Prof. Ph.D. Physics*; Yaowarat *Sirisathitkul, Assistant Prof. M.*SC. *Computer Science.*

Blynk is therefore an automation platform for communicating between different web-based services, applications, and devices. It has been implemented in home automation (*Bheesetti et al., 2021*), street light (*Yusoff et al., 2020*), chicken farming (*Syahrorini et al., 2020*), drainage (*Bhanujyothi et al., 2020*), and water quality monitoring (*Abad et al., 2020*) systems connected to the Internet Wi-Fi. Very recently, the Arduino NodeMCU ESP8266 facilely communicating with a smartphone user via Blynk were used to evaluate the level of waste inside the dustbin (*Maddileti and Kurakula, 2020*).

Of particular relevance to this research is soil moisture monitoring. Accurate and precise measurements of soil moisture are vital to improve crop production and optimize resources. The soil volumetric water content is conventionally measured by means of the gravimetric method and tensiometry. Since the water contents affect the dielectric properties of soils, both resistive and capacitive sensing are viable routes to evaluate the moisture in real-time. Resistive sensors proved effective in low-cost soil moisture monitoring systems, but they are susceptible to systematic errors (*Segundo et al., 2015; Chavanne et al., 2018; Kumar et al., 2021*). Furthermore, commercial capacitive sensors tended to have higher accuracy and precision (*Domínguez-Niño et al., 2019; Adla et al., 2020*). The packed soil between a pair of parallel plates acts the dielectric materials in a capacitor, and the moisture is detected based on changing capacitance and resonant frequency. The SKU:SEN0193 capacitive soil moisture sensor from DFRobot (Shanghai, China) has received much interest recently (*Nagahage et al., 2019; Borah et al., 2020a; Borah et al., 2020b; Placidi et al., 2020; Visconti et al., 2020*). In *Radi et al. (2018)*, it was observed that the moisture reading of this low-cost sensor was not affected by the changes in soil temperature and volume. However, *Nagahage et al. (2019)* suggested that the output from the sensor depended on the soil composition, and soil-specific calibration was demonstrated. In *Placidi et al. (2020)*, the research comprehensively studied the SKU:SEN0193 characteristics and recommended its use in IoT based systems for monitoring a well-defined type of soil.

The objective of this research is to implement the SKU:SEN0193 capacitive sensor in the soil moisture management based on IoT technology. By incorporating Arduino NodeMCU ESP8266 and developing a software platform, sensing data is acquired and viewed remotely on a smartphone. In addition to the soil moisture monitoring, the system also controls an irrigation pump. These automate sensing and remote watering operations are demonstrated for practical uses in agricultural fields, paddies, orchards, as well as urban farming.

MATERIALS AND METHODS

HARDWARE AND SYSTEM DEVELOPMENT

An Arduino microcontroller board (NodeMCU ESP8266) was connected to a capacitive soil moisture sensor (SKU:SEN0193 module v1.2) and a liquid crystal display (LCD). It converted the analog input voltage (0-5 V) from the sensor into digital data. The program was written to adjust the soil moisture percentage from 0 to 100% according to the calibration. The data displayed on the LCD was transferred to a smartphone by linking this moisture sensing system to the Internet Wi-Fi as schematically shown in Fig. 1.
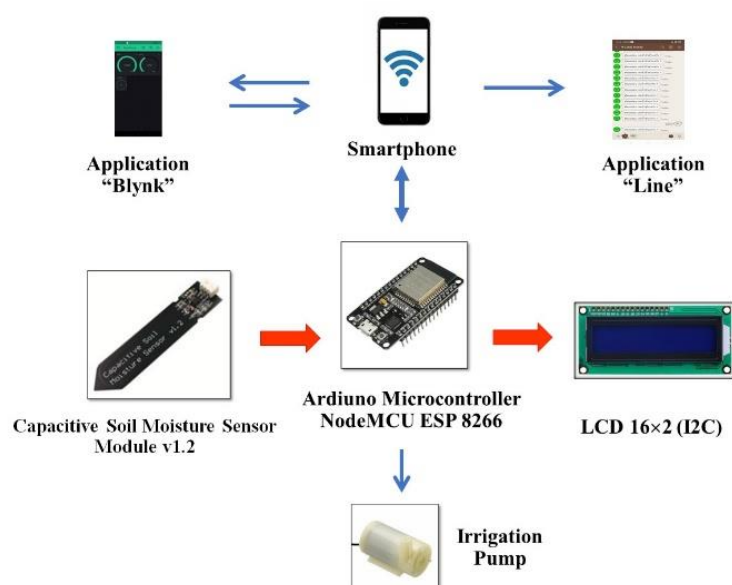
Fig. 1 - Schematic diagram of IoT based soil moisture management system

TEST OF SOIL MOISTURE SENSOR

To demonstrate the sensing operation with packed soils of varying moistures, soils locally acquired from agricultural fields were sieved and then baked in the oven at 150°C for 20 h. In a 100 mL beaker, 65 g of dried soils were filled, and waters of varying volumes up to 32 mL were added. The sensor was installed around the centre of the beaker cross-section at a depth of 3 cm (Fig. 2). The moisture averaged from 5 repeated readings was then plotted as a function of the water content. The beaker was also attached to the water supply from an irrigation pump.
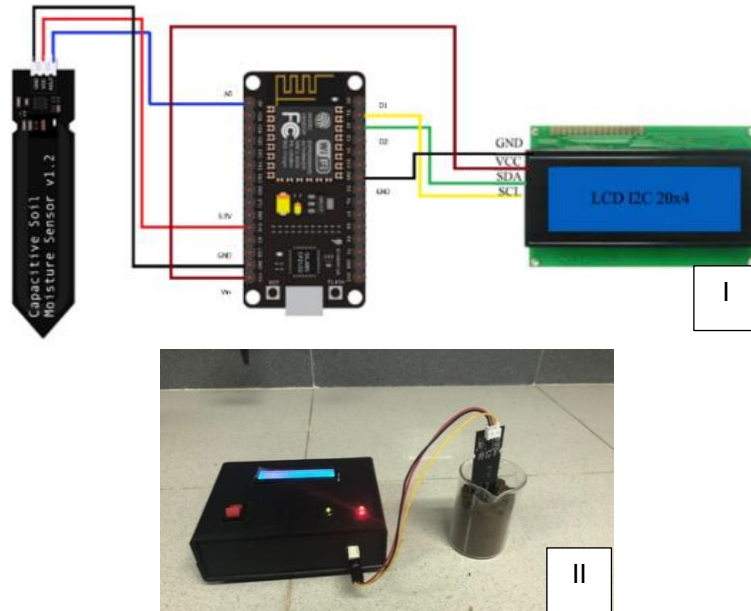
Fig. 2 - Capacitive soil moisture sensor (I) connecting to Arduino board and LCD; (II) probing the packed soil

SOFTWARE DESIGN FOR AUTOMATED MOISTURE MONITORING AND IRRIGATION

The system was developed by taking the electrical signals based on the voltage difference from the SKU:SEN0193 capacitive soil moisture sensor and converted to the moisture level by the Arduino NodeMCU ESP8266. The board was programmed to send the soil moisture to the smartphone and notify the user. Fig. 3 depicts the C programming code to read the soil moisture percentage data and display it on the LCD. The soil moisture data are sent to display on the Blynk application in real-time. The Arduino microcontroller also links the automated irrigation system to a smartphone via the Internet Wi-Fi. If the soil moisture percentage is lower than the pre-defined threshold, the notification message will be sent via the Line application.

The user can execute a command to turn on the irrigation pump via the Blynk application (Fig. 4).

```
//Display moisture level reading from SKU:SEN0193 capacitive sensor
void loop() {
  Serial.print("MOISTURE LEVEL : ");
  value = 1023 - analogRead(sense_Pin);
  lcd.setCursor(10, 0);
  lcd.print(value);
  percent = 1023 - analogRead(sense_Pin);
  percent = (percent / 1023) * 99.89;
  value = value / 10;
  Serial.print(value);
  Serial.print("\t Soil moisture : ");
  Serial.print(percent);
  Serial.println("%");
  delay(3000);
  lcd.setCursor(10, 1);
  lcd.print(percent);
  lcd.setCursor(15,1);
  lcd.print("%");
  delay(100);
}
```

Fig. 3 - The C programming code for collecting the soil moisture data and displaying the reading on the LCD

```
void loop() {
  HumidityValue = 1023 - analogRead (HumiditySensor);
  Serial.print("HumidityValueBlynk :");
  Serial.println (HumidityValueBlynk);
  Serial.println (HumidityValue);
  percent = 1023 - analogRead(HumiditySensor);
  percent = (percent / 1023) * 99.89;
  value = value / 10;
  Blynk.virtualWrite(V0,HumidityValue);
  Blynk.virtualWrite(V3,percent);
. . .
  if (HumidityValue < 350){
    i++;
    HumidityValueBlynk = 0;
    digitalWrite(Pump,ON);
. . .
    Serial.print("PUMP ON");
    Serial.println(i);
    while(i==1){
      Line_Notify(message);
      Serial.println("LINE_Notify");
      i=0;
      delay(10000);
    }
  }
  else {
    i=0;
    HumidityValueBlynk = 1000;
    digitalWrite(Pump, OFF);
    lcd.setCursor(10, 1);
    lcd.print(percent);
    Serial.println("PUMP OFF");
    Serial.println(i);
  }
  …
  Blynk.run();
  …
}
BLYNK_WRITE(V1) {
  int pinValue = param. asInt ();
  Serial.print("V1 Slider value is: ");
  Serial.println(pinValue);
  if (pinValue == 1) {
    digitalWrite (Pump, ON);
    delay(5000);
  }
  else {
    digitalWrite (Pump, OFF);
    delay(5000);
  }
}
```

**Fig. 4 - The C programming code for reading the soil moisture data from Arduino, to display via Blynk
application and notify the user via Line application, and finally controlling the irrigation pump**

RESULTS AND DISCUSSION

From the plot of moisture reading against the variation in water up to 32 ml in Fig. 5, the SKU:SEN0193 capacitive sensor exhibits a linear response to the increase in water content. The linearity obtained in the extended range from 18% to 70% moisture is an advantageous characteristic for practical uses. The standard deviation from 5 repeated measurements, which appeared as error bars in the plot, indicates the precision of the sensing. The largest relative deviation of 4.3% occurs in the case of low water content (5 ml). This precision is comparable to that of a soil moisture meter (Sartorius MA 150) based on the gravimetric method. The performance is consistent with the characterizations of this sensor in the literature (*Borah et al., 2020a; Borah et al., 2020b; Placidi et al., 2020*). From the demonstrations, the SKU:SEN0193 capacitive sensor is fairly robust and applicable for outdoor uses for a period of time. Importantly, the soil-specific calibration is constantly needed to ensure the accuracy of the moisture percentage (*Nagahage et al., 2019*).
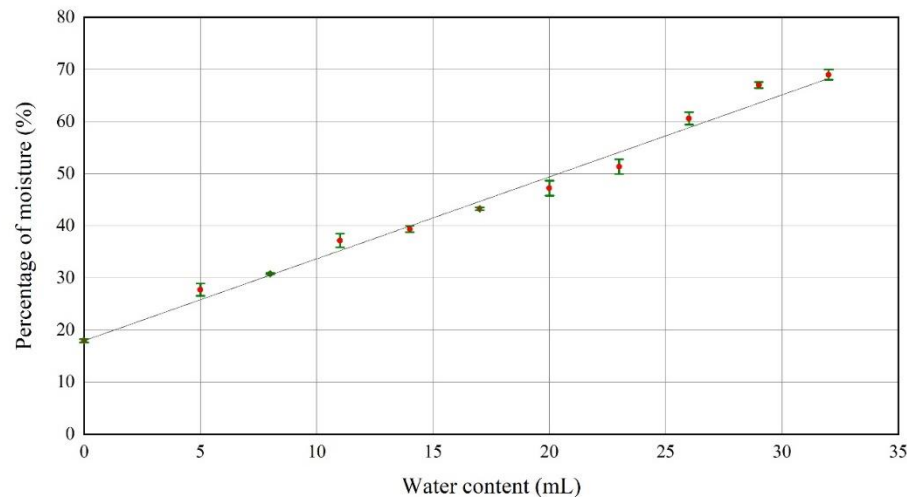
**Fig. 5 - Plot of soil moisture against the water content in the packed soil showing
the linearity of SKU:SEN0193 sensor**

Android applications allow the graphical user interface to receive the data and send commands via the Internet Wi-Fi. Fig. 6(I) shows the smartphone display of soil moisture percentage on the Blynk application, and notifications of the moisture below the threshold of 30% via the Line application are exemplified in Fig. 6(II). As in Fig. 6(III), the irrigation can then be remotely activated by using the Blynk application on any smartphone. Without taking the cost of a smartphone into account, this system costs around 33 USD. The Arduino board constitutes one-third of the cost, whereas the SKU:SEN0193 sensor is available for only a few USD.
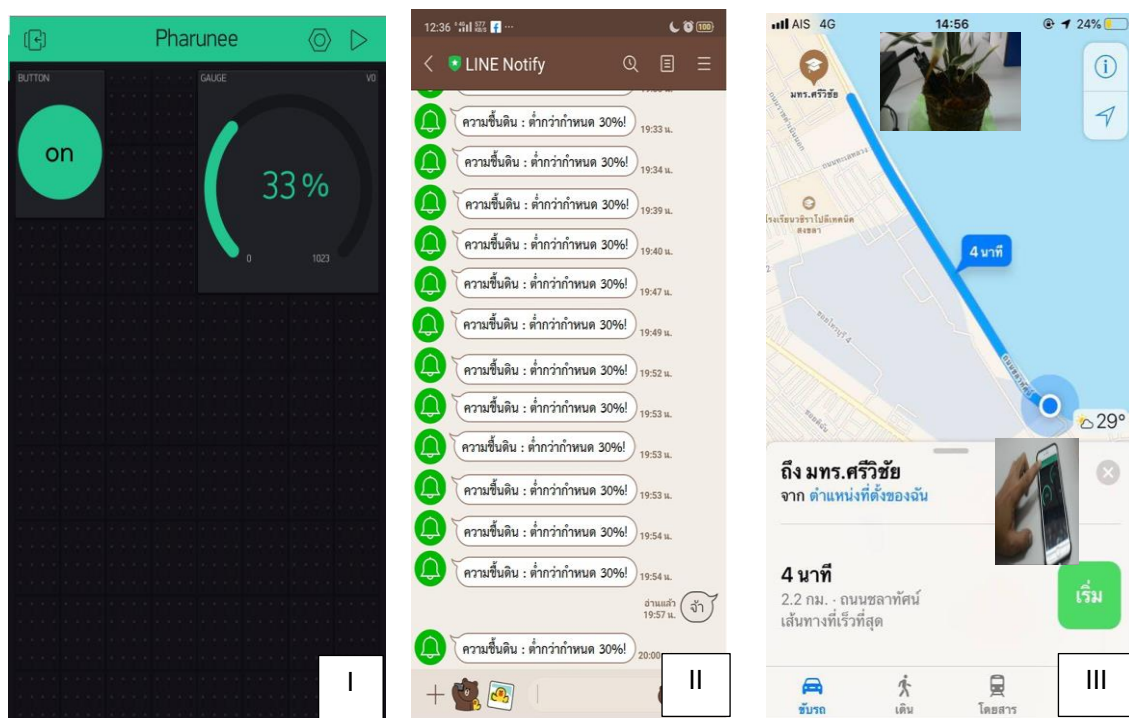
Fig. 6 - Smartphone screenshots of graphical user interface:
*I - soil moisture display on the Blynk application; II - message notifications of the low moisture on the Line application;
III - remote irrigation*

Compared to the earlier systems presented in the literature (*Hashim et al., 2020*), this IoT based system is obviously convenient to be operated by an untrained user because of the exploitation of recent smartphone applications and sensor developments.

As pointed out by (*Omar et al., 2020*), a smartphone platform is user-friendly and advantageous in terms of operational efficiency and productivity in agriculture and farm sectors on any scale (*Effendi et al., 2020*). The Arduino board can be reprogrammable for sensor and feature additions. Multiple sensing nodes are feasible on a limited budget. Other measurements, including temperature and humidity sensing, can be integrated into the system (*Barik, 2019; Kun et al., 2021*), and data can be managed on cloud servers (*Aziz et al., 2019; Hashim et al., 2020*). From the additional information, other operations like automated fertilization were carried out (*Visconti et al., 2020*). This system can be expanded into a soil moisture monitoring station powered by a photovoltaic module (*Ramadan et al., 2018*). Furthermore, it can incorporate weather forecast data and the soil moisture prediction algorithm for irrigation planning (*Goap et al., 2018*).

CONCLUSIONS

By incorporating user-friendly mobile applications and a low-cost capacitive sensor, an IoT based system is demonstrated as a cost-effective and practical route to remotely manage the soil moisture in both agricultural fields and urban farming. A smartphone user is able to monitor the moisture percentage measured by the sensor via the Blynk application and is additionally alerted by the Line application notification whenever the moisture drops below the pre-defined threshold. The irrigation command can then be executed via Internet Wi-Fi. This system can facilely be operated by an untrained user.

ACKNOWLEDGEMENT

REFERENCES

[1]   Abad, B. B., Caranguian, M. M., & Panganiban, E. B. (2020). IoT-based compact-matic drinking water filtration machine. *International Journal of Emerging Trends in Engineering Research*, *8*(7), 3887–3892. https://doi.org/10.30534/ijeter/2020/157872020

[2]   Adla, S., Rai, N. K., Karumanchi, S. H., Tripathi, S., Disse, M., & Pande, S. (2020). Laboratory calibration and performance evaluation of low-cost capacitive and very low-cost resistive soil moisture sensors. *Sensors*, *20*(2), 363. https://doi.org/10.3390/s20020363.

[3]   Aulin V. V., Pankov A. O., Zamota T. M., Lyashuk O. L., Hrynkiv A. V., Tykhyi A. A., & Kuzyk A. V. (2019). Development of mechatronic module for the seeding control system. *INMATEH - Agricultural Engineering, 59*(3), 1–8. https://doi.org/10.35633/INMATEH-59-20

[4]   Aziz, M. A. A., Abas, M. F., Abu Bashri, M. K. A., Saad, N. M., & Ariff, M. H. (2019). Evaluating IoT based passive water catchment monitoring system data acquisition and analysis. *Bulletin of Electrical Engineering and Informatics, 8*(4), 1373–1382. https://doi.org/10.11591/eei.v8i4.1583

[5]   Barik, L. (2019). IoT based temperature and humidity controlling using Arduino and Raspberry Pi. *International Journal of Advanced Computer Science and Applications, 10*(9), 494–502.

[6]   Bhanujyothi, H. C., Jacob, J. I., Vidya, J., Sahana, D. S., & Kumar, P. K. C. (2020). Cloud based smart system for monitoring and managing drainage using IoT. *International Journal of Advanced Trends in Computer Science and Engineering, 9*(5), 7230–7234. https://doi.org/10.30534/ijatcse/2020/50952020

[7]   Bheesetti, D. S. K., Bhogadi, V. N., Kintali, S. K., & Rahman, Z. U. (2021). A complete home automation strategy using Internet of Things. In A. Kumar & S. Mozar (Eds.), ICCCE 2020. *Lecture Notes in Electrical Engineering vol. 698* (pp. 363–373). Singapore: Springer. https://doi.org/10.1007/978-981-15-7961-5_36

[8]   Borah, S., Kumar, R., & Mukherjee, S. (2020a). Low-cost IoT framework for irrigation monitoring and control. *International Journal of Intelligent Unmanned Systems*, *9*(1), 63–79. https://doi.org/10.1108/IJIUS-12-2019-0075.

[9]   Borah, S., Kumar, R., Pakhira, W., & Mukherjee, S. (2020b). Design and analysis of power efficient IoT based capacitive sensor system to measure soil moisture, *Proceedings of 2020 International Conference on Computational Performance Evaluation*, Shillong / India, pp. 771–776.

[10]   Chavanne, X., Bruère, A., & Frangi, J. P. (2018). Comments to: A novel low-cost instrumentation system for measuring the water content and apparent electrical conductivity of soils. *Sensors, 18*(6), 1730. https://doi.org/10.3390/s18061730

[11] Deepa, B., Anusha, C., & Devi, C. P. (2021). Smart agriculture using IOT. In S. Satapathy, V. Bhateja, B. Janakiramaiah & Y. W. Chen (Eds.), *Intelligent System Design. Advances in Intelligent Systems and Computing vol. 1171* (pp. 11–19). Singapore: Springer.

[12] Domínguez-Niño, J. M., Bogena, H. R., Huisman, J. A., Schilling, B., & Casadesús, J. (2019). On the accuracy of factory-calibrated low-cost soil water content sensors. *Sensors, 19*(14), 3101. https://doi.org/10.3390/s19143101

[13] Effendi, M. K. R., Kassim, M., Sulaiman, N. A., & Shahbudin, S. (2020). IoT smart agriculture for aquaponics and maintaining goat stall system. *International Journal of Integrated Engineering*, *12*(8), 240–250. https://doi.org/10.30880/ijie.2020.12.08.023

[14] Goap, A., Sharma, D., Shukla, A. K., & Krishna, R. C. (2018). An IoT based smart irrigation management system using machine learning and open source technologies. *Computers and Electronics in Agriculture, 155*, 41–49. https://doi.org/10.1016/j.compag.2018.09.040

[15] Hashim, N. M. Z., Mazlan, S. R., Abd Aziz, M. Z. A., Salleh, A., Ja'Afar, A. S., & Mohamad, N. R. (2020). Agriculture monitoring system: A study. *Jurnal Teknologi, 77*(1), 53–59. https://doi.org/10.11113/jt.v77.4099

[16] Indra, W. A., & Shariff, M. S. A. M. (2020). Message conveyor by motion for paralyze people powered using RF energy harvesting. *International Journal of Integrated Engineering, 12*(8), 233–239. https://doi.org/10.30880/ijie.2020.12.08.022

[17] Ito R., & Kajisa T. (2021). Development of paddy-field water level gage corresponding to a sensor-network. *INMATEH - Agricultural Engineering, 63*(1), 131–136. https://doi.org/10.35633/inmateh-63-13

[18] Julian, J., Kavitha, R., & Rakesh, J. Y. (2021). An IoT based wearable device for healthcare monitoring. In S. Satapathy, Y. D. Zhang, V. Bhateja & R. Majhi (Eds.), *Intelligent Data Engineering and Analytics. Advances in Intelligent Systems and Computing vol. 1177* (pp. 515–525). Singapore: Springer.

[19] Kumar, S. S., Aithal, G., & Bhat, V. P. (2021). Design, calibration, and experimental study of low-cost resistivity-based soil moisture sensor for detecting moisture at different depths of a soil. In N. Chiplunkar & T. Fukao (Eds.), *Advances in Artificial Intelligence and Data Engineering vol. 1133* (pp. 1383–1397). Singapore: Springer.

[20] Kun, T., Sanmin, S., Liangzong, D., & Shaoliang, Z. (2021). Design of an intelligent irrigation system for a jujube orchard based on IoT. *INMATEH - Agricultural Engineering, 63*(1), 189–198. https://doi.org/10.35633/inmateh-63-19

[21] Maddileti, T., & Kurakula, H. (2020). IoT based smart dustbin. *International Journal of Scientific and Technology Research, 9*(2), 1297–1302.

[22] Nagahage, E. A. A. D., Nagahage, I. S. P., & Fujino, T. (2019). Calibration and validation of a low-cost capacitive moisture sensor to integrate the automated soil moisture monitoring system. *Agriculture, 9*(7), 141. https://doi.org/10.3390/agriculture9070141

[23] Omar, N. B., Zen, H. B., Aldrin, N. N. A., Waluyo, & Hadiatna, F. (2020). Accuracy and reliability of data in IoT system for smart agriculture. *International Journal of Integrated Engineering*, *12*(6), 105–116. https://doi.org/10.30880/ijie.2020.12.06.013

[24] Placidi, P., Gasperini, L., Grassi, A., Cecconi, M., & Scorzoni, A. (2020). Characterization of low-cost capacitive soil moisture sensors for IoT networks. *Sensors, 20*(12), 3585. https://doi.org/10.3390/s20123585

[25] Radi, Murtiningrum, Ngadisih, Muzdrikah, F. S., Nuha, M. S. & Rizqi, F. A. (2018). Calibration of capacitive soil moisture sensor (SKU:SEN0193), *Proceedings of the 4th International Conference on Science and Technology,* Yogyakarta / Indonesia, pp. 1–6.

[26] Ramadan, K. M., Oates, M. J., Molina-Martinez, J. M., & Ruiz-Canales, A. (2018). Design and implementation of a low cost photovoltaic soil moisture monitoring station for irrigation scheduling with different frequency domain analysis probe structures. *Computers and Electronics in Agriculture, 148*, 148–159. https://doi.org/10.1016/j.compag.2017.12.038

[27] Segundo, A. K. R., Martins, J. H., Monteiro, P. M. B., de Oliveira, R. A., & Freitas, G. M. (2015). A novel low-cost instrumentation system for measuring the water content and apparent electrical conductivity of soils. *Sensors, 15*(10), 25546–25563. https://doi.org/10.3390/s151025546

[28] Singholi, A. K. S., Mittal, M., & Bhargava, A. (2021). A review on IoT-based hybrid navigation system for mid-sized autonomous vehicles. In V.C. Pandey, P. M. Pandey & S. K. Garg (Eds.), Advances in Electromechanical Technologies. *Lecture Notes in Mechanical Engineering* (pp. 735–744). Singapore: Springer.

[29]   Syahrorini, S., Rifai, A., Saputra, D. H. R., & Ahfas, A. (2020). Design smart chicken cage based on Internet of Things. *IOP Conference Series: Earth and Environmental Science, 519*, 012014. https://doi.org/10.1088/1755-1315/519/1/012014

[30]   Terence, S., & Purushothaman, G. (2020). Systematic review of Internet of Things in smart farming. *Transactions on Emerging Telecommunications Technologies*, *31*(6), 3958. https://doi.org/10.1002/ett.3958

[31]   Visconti, P., Giannoccaro, N. I., de Fazio, R., Strazzella, S., & Cafagna, D. (2020). IoT-oriented software platform applied to sensors-based farming facility with smartphone farmer app. *Bulletin of Electrical Engineering and Informatics, 9*(3), 1095-1105. https://doi.org/10.11591/eei.v9i3.2177

[32]   Yusoff, Z. M., Muhammad, Z., Razi, M. S. I. M., Razali, N. F., & Hashim, M. H. C. (2020). IOT-based smart street lighting enhances energy conservation. *Indonesian Journal of Electrical Engineering and Computer Science*, *20*(1), 528–536. http://doi.org/10.11591/ijeecs.v20.i1.pp528-536

ANALYSIS AND DESIGN OF SOLID-LIQUID MIXED FERTILIZER DEVICE FOR ORGANIC FERTILIZER ON SOLID-LIQUID TWO-PHASE FLOW
/
基于固液两相流的有机肥固液混合施肥装置分析与设计

Shufeng LIU[1,2), Hanxiang WANG[2), Zhaoqin LV [1,3), Jingwei SUN[1), Xinpeng SHI[1), JinXing WANG[*1,3)   1)
[1) College of Mechanical and Engineering, Shandong Agricultural University, Taian 271000, China;
[2) College of Mechanical Engineering ,China University of Petroleum, Qingdao 266580,China
[3) Shandong Provincial Key Laboratory of Horticultural Machinery and Equipment, Taian 271000, China;
Tel: +86 05388246826; E-mail: jinxingw@163.com

Keywords: Organic fertilizer, Fertilizer device, Agitator, Solid-liquid two-phase flow, Response surface method

ABSTRACT

Organic fertilizer applicator currently has poor versatility toward different properties. A solid-liquid mixed fertilizer device is designed based on the numerical simulation method of solid-liquid two-phase flow. Based on the parameters analysis and viscosity measurement of different organic fertilizer particles, the ribbon-screw type agitator was selected as the basic structure. Using Box-Behnken, three test factors including agitator speed, the mixture ratio of fertilizer and water, agitator height were determined, the agitator was optimized with the test evaluation indexes, the density variation coefficient, and agitator shaft power on 10 mixing planes in the agitator. The result showed that the rotating speed was 80 r/min, the mixing ratio of fertilizer and water was 1.2, and the agitator height was 700 mm, the working parameter combination is optimal. A coarse particle solid-liquid two-phase flow model of the fertilizer discharge pump was established, to obtain the external characteristic curve of the fertilizer pump and analyse the influence of different mixing ratios of fertilizer and rotation speed on the fertilizer pump. In order to prevent the separation of fertilizer and water and achieve better effect, 1140 r/min was comprehensively determined as the working speed of the fertilizer pump. The strength of the agitator meets the working requirements. The solid-liquid deep fertilizer device text bench for organic fertilizer was set up under the optimal working parameters, the result shows that the research results can provide a reference for the design of organic fertilizer solid-liquid mixing fertilizer applicator.

摘要

针对目前有机肥施肥机对不同形态有机肥通用性差，基于固液两相流数值模拟方法，分析并设计一种有机肥固液混合施肥装置。根据多种有机肥颗粒参数分析和黏度测定，通过六种搅拌器固液两相流试验筛选螺带-螺杆式搅拌器型为搅拌装置基本结构。采用 Box-Behnken 试验设计方法进行搅拌器优化，以搅拌器转速、肥水混合比、搅拌器高度 3 个试验因素，肥料桶内 10 个混合平面的密度变异系数和搅拌器轴功率为试验评价指标，转速80r/min、肥水混合比 1.2、搅拌器高度700mm 时效果最优，10 个截面的平均密度为713.16kg/m3，轴功率为24.07kW，变异系数为4.32%。建立排肥泵粗颗粒固液两相流模型，获取排肥泵外特性曲线及排肥泵泵肥影响因素，选取 1140r/min 为排肥泵工作转速。在最优工作参数下搭建有机肥固液混合施肥装置试验台架，台架试验结果表明研究结果可为有机肥固液混合施肥机设计提供参考。

INTRODUCTION

The large amount of fertilizer in agricultural planting increases the risk of environmental pollution (*Han Tang et al, 2019; Hossain Md Zahangir et al, 2021*). The utilization of organic wastes such as livestock manure can greatly reduce the use of chemical fertilizer. Fertilization technology has an important impact on the yield and quality of crops. Reducing fertilizer and increasing efficiency has become an urgent need for sustainable agricultural development (*Rodrigues L.A.T. et al, 2021*). Studies have shown that by applying organic fertilizer instead of chemical fertilizer (*An Siyu et al, 2019*), 70 % of the regions can achieve the goal of chemical fertilizer reduction and reduce the non-point source pollution of nitrogen and phosphorus fertilizers (*Geng Xiuhua et al, 2020; Geng Wei et al, 2013; Sagues William J et al, 2020; Xiaoyong Liu et al, 2018*).

---

[1] *Shufeng Li, Ph.D. Stud. Eng.; Hanxiang Wang, Prof. Ph.D. Eng.; Zhaoqin Lv, Prof. Ph.D. Eng.; Jingwei Sun, M.S. Stud. Eng.; Xinpeng Shi, M.S. Stud. Eng.; JinXing Wang, Prof. Ph.D. Eng.*

The development of organic fertilizer fertilization machinery is also an important means to promote the application of organic fertilizer (*Quiroz et al, 2019*). At present, the application of organic fertilizer mainly stays in the stage of artificial spreading, and the mature organic fertilizer fertilization machinery types are less, mainly concentrated in the spreading machine of solid organic fertilizer and scraper furrow fertilization machine (*Li Jie et al, 2013*). The volume of solid organic fertilizer spreader is large, which can also cause environmental pollution (*Chen Genqiang et al, 2019; Jie Hu et al, 2018; Zhou Yang et al, 2020*); Scraper furrow fertilization machine cannot perform accurately quantitative fertilization according to depth, nor can organic fertilizer be applied to the root part of crops, so fertilizer efficiency is relatively low (*Li Jie et al, 2013*).

There are many kinds of organic fertilizers, which can be divided into solid fertilizers and liquid fertilizers according to the form (*Liu Cailing et al, 2017; Zhou Wenqi et al, 2020; Kang Jianming et al, 2017; Chen Xiongfei et al, 2015; Zeng Shan et al,2020*). Solid fertilizers also include farm compost, stable manure, commercial granular organic fertilizer, and powdery organic fertilizers (*Wang Jinwu et al, 2018; Xu Binxing et al, 2017; Fu Yuchao et al, 2017*). Because farm compost, stable manure, and so on are easy to plug the hole of hole fertilizer applicator, the existing hole fertilizer applicator can only apply commercial granular organic fertilizers (*Bai Youlu et al, 2016*). Liquid organic fertilizer applicator spreads the liquid organic fertilizer directly into the soil or it is applied with drip irrigation, but the production cost is high, fertilization machinery layout is complex, it cannot directly apply manure, crop straw, and other organic fertilizer sources (*Liao Junjie et al, 2021; Chiharu Tokoro et al, 2021*).

According to the fertilization characteristics and technical requirements of organic fertilizer, aiming at the poor universality of organic fertilizer for different physical properties at present, based on the numerical simulation method of solid-liquid two-phase flow, this paper explored the fertilization method of solid-liquid mixed organic fertilizer, studied the effects of different solid-liquid mixing ratios, agitator forms and stirring speeds on the mixing effect, optimized the working parameters of agitator and fertilizer pump, and carried out the bench test, to provide a reference for the design of solid-liquid mixed organic fertilizer applicator.

MATERIAL AND METHOD
Determination of Organic Fertilizer Parameters
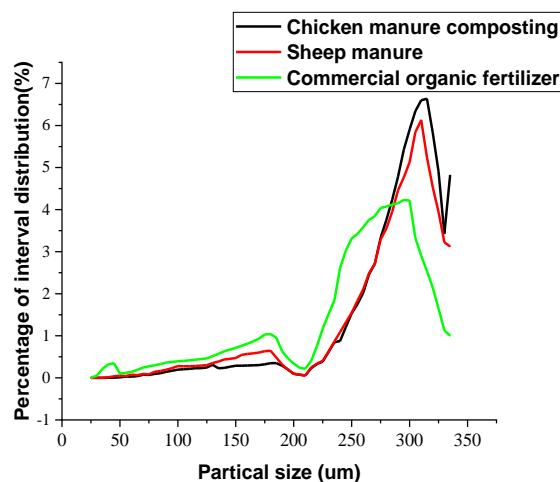
Fig. 1 - Particle size distribution of three kinds of organic fertilizers

Organic fertilizer has a wide variety and complex composition (*Himmelsbach W. et al, 2021*). The mixture of organic fertilizer and water is generally considered a non-Newtonian fluid. According to the design of the fertilizer blender and the needs of flow field analysis, three kinds of organic fertilizers, including chicken manure compost, sheep manure, and commercial powdery organic fertilizer, were selected for crops (*Christwardana M. et al, 2020*). The particle size of organic fertilizer was measured by a laser particle size analyzer (*Foukrach Mohammed et al, 2020*). The measurement results are shown in Fig.1. The particle size of organic fertilizer was mainly distributed between 150-350 um, accounting for more than 85%, and the cumulative proportion between 275-325 um was 48.33%, taking chicken manure composting as an example. The particle size distribution of chicken manure compost was larger than that of sheep manure and commercial powder organic fertilizer, and the particle size of commercial powder organic fertilizer was the smallest and the distribution was the most uniform. The average volume diameter, average area diameter, and average length diameter of chicken manure compost were higher than those of other fertilizers.

According to the needs of practical application and numerical simulation, the viscosity of three kinds of organic fertilizers at different mixing ratios of fertilizer and water mass and stirring speeds was measured by a rotary viscometer. The measurement results are shown in Table 1. The viscosity of organic fertilizer increases with the increase of fertilizer-water ratio; with the increase of stirring speed, the viscosity decreases gradually. Among the three organic fertilizers, chicken manure compost had a wider range of viscosity distribution and the highest viscosity. The viscosity of sheep manure is the lowest.

Table 1

Results of viscosity measurement of organic fertilizer

Mixed ratio of fertilizer and water	Viscometer speed (r/min)	Commercial powder viscosity (Pa·s)	Viscosity of chicken manure compost (Pa·s)	Viscosity of sheep manure (Pa·s)
1:1	40	2.50	0.74	1.21
1:1	60	1.02	0.35	0.66
1:1	80	0.59	0.16	0.31
1.1:1	40	12.55	7.25	3.20
1.1:1	60	3.17	3.28	1.65
1.1:1	80	1.07	1.85	0.70
1.2:1	40	19.67	22.37	4.47
1.2:1	60	7.93	7.16	1.93
1.2:1	80	3.49	4.99	1.10

Design of solid-liquid fertilizer tank

The fertilizer tank mainly includes a tank and other structures installed in the tank. In order to achieve the best mixing effect, the mixer and fertilizer tank need to be well matched. Relevant parameters of fertilizer tanks are designed according to relevant standards and pressure vessel design manuals. The relationship between the diameter of fertilizer tank and the parameters is Eq. (1).

Due to fact that the mixing of materials in the fertilizer tank belongs to the mixing of liquid-solid materials, the length-diameter ratio H/D_i is 1-1.3, the material reaction is gentle in the process of organic fertilizer mixing, there is no boiling state, the foam is less, and the material coefficient η_i is 0.8-0.85. Through calculation and analysis, the fertilizer tank structure is designed as $V_N = 0.4$ m^3, $D_i = 0.8$ m, $H = 0.8$ m, and the flat bottom removable flat cover fertilizer tank is selected. The solid-liquid mixing medium of organic fertilizer has high viscosity. The baffle set in the fertilizer tank will hinder the mixing of organic fertilizer, and the diversion effect of the draft-tube is not obvious, so the fertilizer tank is not set with baffle and draft-tube.

$$H = \frac{V - v_q}{\frac{\pi}{4} D_i^2} = \frac{\frac{V_N}{\eta_i} - v_q}{\frac{\pi}{4} D_i^2} \tag{1}$$

where: D_i – is diameter of fertilizer tank, m; η_i - material coefficient; V_N - nominal volume of fertilizer tank, m^3;

V - full volume of fertilizer tank, m^3; v_q - other structural volumes of fertilizer tank, m^3;

H - height of fertilizer tank, m

Type Selection of Solid-liquid Mixer

Organic fertilizer is a mixture of water-soluble substances, which contains sand, grass, humus, and other substances insoluble in water. Solid-liquid mixing of organic fertilizer and water involves complex solid-liquid two-phase fluid dynamics. According to the traditional design and calculation method, it is impossible to design a reasonable impeller structure shape and size and to calculate the critical speed and shaft power. Based on the above reasons and the measured viscosity of organic fertilizer, the selected stirrer requires that the organic fertilizer and water-solid-liquid mixture are mixed uniformly after mixing, and there is no large amount of deposition medium at the bottom of the fertilizer tank.

To promote the settlement of low-density grass and reduce the deposition of high-density sand, a vertical stirring device was designed. The working environment of an organic fertilizer mixer is a mixture of solid and liquid. According to the particle parameters of organic fertilizer and the viscosity data of solid-liquid mixture with different mixing ratios, the viscosity range of the mixture is 0.31-22.37 Pa•s. Combined with the determination and analysis of organic fertilizer parameters and the design of stirring device, and referring to the design manual, the medium viscosity of the mixer working environment should be less than 100 Pa•s, and the commonly used speed should be 1-100 r/min.

Table 2

Agitator size parameters

Agitator	D_j (mm)	d_j (mm)	S_l (mm)	h (mm)
Inclined vane	380	—	85	—
Push type	380	—	—	400
Box	760	40	300	500
Folded blade turbine	700	250	80	400
Screw belt type	760	—	—	400
Screw-screw type	760	200	200	500

a) Oblique blade type; b) Propelling type; c) Box; d) Folded blade turbine;   e) Screw belt; f) Screw-screw
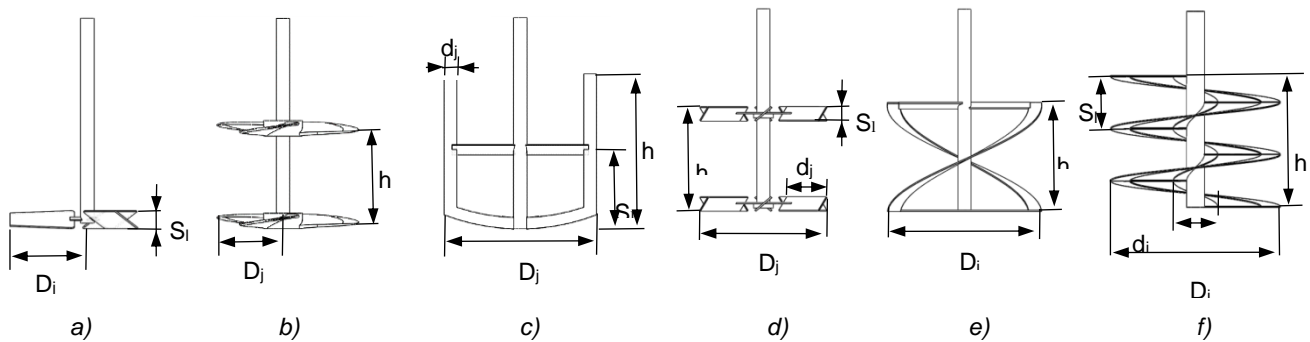
Fig. 2 - Agitator type

According to the requirements of solid-liquid mixing, six types of agitators were selected: inclined blade type, propulsion type, frame type, broken blade turbine type, spiral belt type, and spiral belt-screw type. Mixer types, as shown in Fig. 2. The tank height H and inner diameter D_i are both 800 mm. Referring to the design manual and combined with the actual size requirements of the mixing drum, the size parameters of each mixer are determined as shown in Table 2. At the rotational speed of 60 r/min, organic fertilizer and water were mixed with solid-liquid according to the mass ratio of 1.1: 1. The stirring effect of the agitator was judged by observing the stirring flow pattern and stirring effect evaluation index of different agitators, and the effective agitator was selected.

Establishment of Solid - liquid Mixing Mechanism Model

The particle size of chicken manure compost in organic fertilizer is wider than that of sheep manure and commercial powdery organic fertilizer, and the particle size is large and the viscosity is the highest. The physical parameters of chicken manure compost are selected as the solid particle modeling parameters. The liquid is clear water, and the mixed fertilizer mixer is mainly used for solid-liquid two-phase mixing. In the process of solid suspension, there is a minimum stirring speed that makes the solid suspension, which is called the critical stirring speed of solid suspension. When the solid is completely suspended, the critical speed has the lowest energy loss. The critical stirring speed is calculated by the formula of critical stirring speed, and the speed range of the mixer is determined. The calculation formula of critical stirring speed is Eq. (2).

$$N_c = K D_i^{-2/3} d_p^{1/3} (\frac{\Delta\rho}{\rho})^{2/3} (\frac{\mu}{\rho})^{-1/9} (\frac{V_s}{V_p})^{-0.7} \tag{2}$$

where:

K - is stirring coefficient. The mixing device coefficient is 187-263, which is related to the shape of the fertilizer drum and the form and size of the agitator;

D_i - inner diameter;

d_p - solid particle diameter, mm; $\Delta\rho$ - the density difference between solid particles and liquids, g/m³;

ρ - Fluid density, g/m³; μ - Fluid Viscosity, Pa·s;

V_p - solid true volume, m³; V_s - apparent volume of solids, m³

The stirrer speed range is set as 1-100r/min, d_p is 0.3mm, and after drying the particle density is 580 kg/m³. According to the structural design of the stirring device and the viscosity data measured in Table 1, the liquid density and viscosity under different rotational speeds and fertilizer-water mixing ratios were determined to

calculate the critical stirring speed, respectively. In the numerical simulation, the rotational speeds of the agitator were set as 40 r/min, 60 r/min, and 80 r/min. The volume and volume fraction of water and fertilizer were calculated according to the mass ratios of organic fertilizer and water 1: 1, 1.1: 1 and 1.2: 1.

The model adopts the sliding mesh method. The cylindrical shape of the rotating domain and the static domain is established, and then the static domain and the rotating domain are formed by the Boolean operation to improve the accuracy of numerical simulation. The mesh module is selected for meshing in the model. The mesh correlation coefficient is set to 100, and the density is fine. Ten layers of expansion layer are set in the rotating domain, and the tetrahedral mesh is used for the mesh. The obtained mesh has good quality. RNG k-ε model is used for numerical simulation of flow field

According to the solid-liquid mixing process and the designed rotational speed of the test, the boundary conditions in the fluid simulation module were added, and the wall around the fertilizer bucket was set, and the rest surfaces were automatically generated by the software. The gravity direction y was set as the negative direction, and the rotational speeds of the agitator were 40 r/min, 60 r/min, and 80 r/min, respectively. Organic fertilizer belongs to small particle flow, and solid-liquid mixing adopts the Euler-Euler multiphase flow model, and the two-phase mixture model is set. The first phase is water, and the second phase is organic fertilizer. The relevant parameters of organic fertilizer were obtained through the parameter analysis of organic fertilizer particles and the viscosity test. The turbulence model was RNG k-ε turbulence model, and the constant values of the RNG k-ε model are shown in Table 3. The initialization state parameter settings are shown in Table 4.

Table 3

RNG k-ε model constant

σ_k	σ_ε	$C_{\varepsilon 1}$	$C_{\varepsilon 2}$	C_μ	η_0
0.8311	0.8311	1.44	1.92	0.09	4.36

Table 4

Parameter setting

Parameter	Numerical value
Water density (kg/m^3)	1000
Particle diameter of organic fertilizer (mm)	0.3
Density of organic fertilizer (kg/m^3)	580
Volume fraction of second phase (%)	63.24、65.43、67.37
Rotating shaft speed (r/min)	40、60、80

Mixer screening

Evaluation of the agitator is made mainly from two aspects: mixing effect and energy consumption. There are many ways to determine the mixing effect. The standard deviation of average density is commonly used for non-Newtonian fluid, that is, the standard deviation is calculated by the average density of the uniform section in the vertical direction of the flow field analysis results. The smaller the standard deviation is, the smaller the density difference between the representative sections is, and the better the mixing effect of the mixer is. Because this experiment involves different fertilizer-water mixing ratio test, the density of different test groups is different; in order to eliminate the influence of different densities on the standard deviation measurement scale and dimension of average density, the coefficient of variation is used as the evaluation index of stirring effect. Mixer shaft power is the evaluation index of energy consumption.

The average density of 10 cross-sections of the flow field analysis results was uniformly selected to calculate the standard deviation, and the average density of the whole mixture above the standard deviation ratio was used as the variation coefficient. The greater the coefficient of variation, the better the mixing effect. Select ten sections from bottom to top of mixing zone. The section selection diagram is shown in Fig. 3.

The average density of each section is ρ_i, i=(1,2 10) , the average density is:

$$D_j = \frac{1}{10}\left\{\sum_{i=1}(\rho_i - \bar{\rho})^2\right\}, i = 1,2\cdots 10, j = 1,2\cdots 6 \tag{3}$$

Standard deviation:

$$\sigma_j = \sqrt{D_j}, j = 1,2\cdots 6 \tag{4}$$

Coefficient of variation:

$$C \cdot V_j = \frac{\sigma_j}{D_j} \times 100\%, \ j = 1, 2 \cdots 6 \tag{5}$$

In equations (3), (4), (5): i – is the corresponding 10 section numbers; j - six corresponding mixers.

The torque in the simulation results of flow field analysis is extracted, because the torque and power are positively correlated, and the shaft power of the stirrer is calculated by combining the rotational speed of the stirrer fan blade as the evaluation index of energy consumption. The smaller the shaft power is, the less energy consumption is. The calculation equation of shaft power is:

$$P_j = \frac{M_j \times n}{9550}, \ \ j = 1, 2 \cdots 6 \tag{6}$$

In equation (6): M – is the mixer torque, N•m; n - agitator speed, r/min; P_j - mixer shaft power, kW.
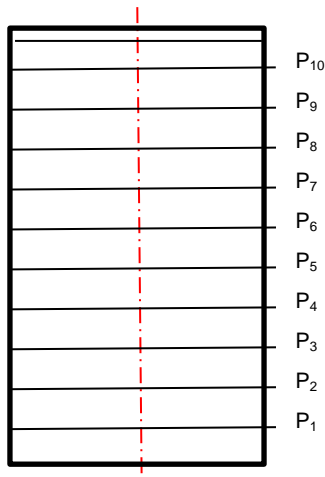
Fig. 3 - Schematic diagram of 10 sections

(a)Oblique blade type (b)Propelling type   (c)Box

(d)Folded blade turbine (e)Screw belt   (f)Screw-screw
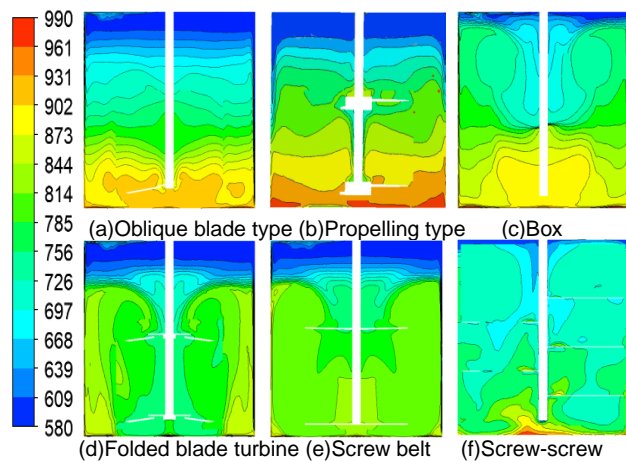
Fig. 4 - Cloud chart of volume concentration distribution in the middle section

According to the design of six kinds of stirrers, the simulation test was carried out to obtain the concentration distribution of solid-liquid mixture after mixing in the mixing drum, and the concentration distribution in the middle section of different stirrers was selected. The test results are shown in Fig. 4. By comparison, it is found that the mixing effect of inclined-leaf mixer and push mixer is poor, and organic fertilizer is still more floating on the surface of the water. The Frame mixer has good laminar mixing at the cross plate, but there is a blind mixing zone at the bottom of the blade, and the effect is not ideal. Blade turbine and spiral belt obtain similar concentration mixing form, with a certain upper and lower circulation capacity, but the effect in the upper and near the wall area of the mixing drum is poor; Screw belt-screw type has good upper and lower circulation ability and can realize the mixing uniformity of full stirred tank.

Ten cross sections (P_1 ($Z = 0$), P_2 ($Z = 85$), P_3 ($Z = 175$), P_4 ($Z = 265$), P_5 ($Z = 355$), P_6 ($Z = 445$), P_7 ($Z = 535$), P_8 ($Z = 625$), P_9 ($Z = 715$), and P_{10} ($Z = 800$)) from the bottom of the tank were taken as shown in Fig.5. The volume concentration distribution and the variation coefficient of average density on the ten sections were used as the evaluation indexes of mixing effect.

At the speed of 60 r/min and fertilizer-water mixing ratio of 1.1: 1, as shown in Fig. 6, the concentration and density of 10 sections of different stirrers increased gradually from top to bottom. Among them, the density difference between the different sections of the propulsion type is the most obvious, and the difference between the upper and lower ten sections of the screw belt screw type is the smallest, which shows that the mixing uniformity of the ten sections is the best.

According to Eq. (3) to Eq. (5), the coefficient of variation of six mixers was calculated. The coefficient of variation of inclined blade type, propulsion type, frame type, broken blade turbine type, screw belt type and screw belt-screw type were 0.85 %, 0.07 %, 1.07 %, 1.09 %, 1.13 % and 1.87 %, respectively. The propulsion minimum indicates the worst mixing uniformity; The coefficient of variation of the belt-screw agitator was 1.87 %, which was the largest among the six agitators, indicating that the belt-screw agitator had the best mixing uniformity.

Making the comprehensive comparison of the volume concentration distribution program of the middle section, the volume concentration distribution program of the ten sections, and the average density

variation analysis of the ten sections of the six mixers, the screw belt-screw mixer structure was determined as the mixing device of the organic fertilizer solid-liquid mixed fertilizer machine in the hilly orchard. The height of the mixer is 500 mm, 600 mm, 700 mm according to the height of the fertilizer tank.
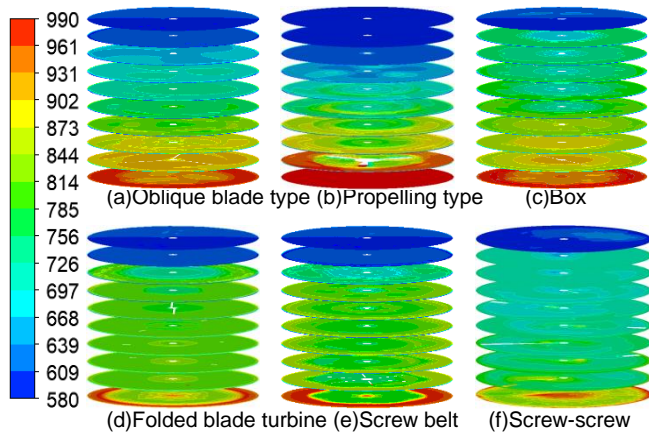
Fig. 5 - Cloud chart of volume concentration distribution on ten sections
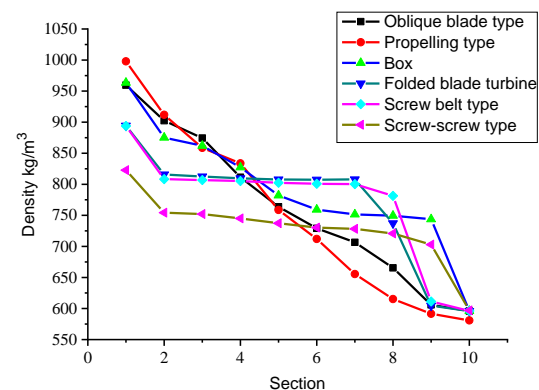
Fig. 6 - Average density distribution on ten sections

Analysis on influencing factors of fertilizer mixing effect of agitator

Based on the fact that there are many structural factors affecting the mixing of agitators, the Box-Behnken design method was adopted. During the experiment, the main factors affecting the stirring effect are the following three: stirrer speed (r/min), fertilizer-water mixing ratio, stirrer height (mm). The stirrer is mainly evaluated from two aspects of stirring effect and energy consumption. The coefficient of variation was used as the evaluation index of the stirring effect. The greater the coefficient of variation, the higher the mixing uniformity, the better the stirring effect. Mixer shaft power is the evaluation index of energy consumption. The torque in the simulation results of flow field analysis was extracted because the torque and power were positively correlated. The power of the agitator shaft was calculated by combining the rotational speed of the agitator as the evaluation index of energy consumption. The smaller the shaft power is, the less energy consumption is. The level and coding of different factors are shown in Table 5.

Table 5

Test factors and codes

Factors	Level		
	-1(Low)	0(Middle)	1(High)
Stirrer speed (r/min)	40	60	80
Fertilizer-water mixing ratio	1	1.1	1.2
Stirrer height (mm)	500	600	700

Table 6

Test design and results

Test serial number	Stirrer speed (r/min)	Fertilizer-water mixing ratio	Stirrer height (mm)	Coefficient of Variation $C \cdot V$ (%)	Shaft power P(kW)
1	-1	-1	0	2.19	30.25
2	0	0	0	1.74	7.6
3	1	0	1	3.83	23.35
4	1	-1	0	2.48	43.44
5	0	0	0	1.74	7.6
6	0	1	1	3.25	14.54
7	-1	1	0	2.47	11.45
8	0	1	-1	2.07	6.53
9	1	0	-1	2.54	78.27
10	0	-1	1	2.1	8.73
11	-1	0	-1	2.34	3.74
12	0	0	0	1.74	7.6
13	0	0	0	1.74	7.6
14	0	0	0	1.74	7.6
15	-1	0	1	2.8	7.28

| 16 | 1 | 1 | 0 | 2.87 | 64.65 |
| 17 | 0 | -1 | -1 | 1.87 | 6.17 |

According to the Box-Behnken experimental principle, the experimental design and results are shown in Table 6. The regression models of stirrer speed, fertilizer-water mixing ratio, and stirrer height on the coefficient of variation and shaft power were established by Design-Expert 11.0 software. The results were shown in Table 7. Fitting model analysis using statistical analysis software to determine the coefficient of variation and shaft power fitting equation, such as Eq. (7) and Eq. (8).

$$C \cdot V = 1.74 + 0.24 x_1 + 0.2525 x_2 + 0.395 x_3 + 0.0275 x_1 x_2 + 0.2075 x_1 x_3 + 0.2375 x_2 x_3$$
$$+ 0.6587 x_1^2 + 0.1037 x_2^2 + 0.4788 x_3^2 \tag{7}$$

$$P = 7.6 + 19.62 x_1 + 1.07 x_2 - 5.1 x_3 + 10 x_1 x_2 - 14.62 x_1 x_3 + 1.36 x_2 x_3$$
$$+ 24.51 x_1^2 + 5.34 x_2^2 - 3.95 x_3^2 \tag{8}$$

Table 7

Variance analysis of regression equation

Evaluating indicator	Source	Sum of Squares	df	Mean Square	f-value	p-value	Signifi-cance
	Model	5.68	9	0.6309	40.63	< 0.0001	**
	x_1	0.4608	1	0.4608	29.67	0.0010	**
	x_2	0.5101	1	0.5101	32.85	0.0007	**
	x_3	1.25	1	1.25	80.38	< 0.0001	**
	x_1^2	1.83	1	1.83	117.66	< 0.0001	**
Coefficient of Variation $C \cdot V$ / %	$x_1 x_2$	0.0030	1	0.0030	0.1948	0.6723	
	$x_1 x_3$	0.1722	1	0.1722	11.09	0.0126	*
	x_2^2	0.0453	1	0.0453	2.92	0.1313	
	$x_2 x_3$	0.2256	1	0.2256	14.53	0.0066	**
	x_3^2	0.9651	1	0.9651	62.15	0.0001	**
	Residual	0.1087	7	0.0155			
	Cor Total	5.79	16				
	Model	7296.84	9	810.76	10.23	0.0029	**
	x_1	3080.73	1	3080.73	38.87	0.0004	**
	x_2	9.20	1	9.20	0.1161	0.7433	
	x_3	208.18	1	208.18	2.63	0.1491	
	x_1^2	2528.92	1	2528.92	31.91	0.0008	**
Shaft power P / kW	$x_1 x_2$	400.20	1	400.20	5.05	0.0594	
	$x_1 x_3$	854.39	1	854.39	10.78	0.0134	*
	x_2^2	120.07	1	120.07	1.52	0.2581	
	$x_2 x_3$	7.43	1	7.43	0.0937	0.7684	
	x_3^2	65.61	1	65.61	0.8279	0.3931	
	Residual	554.76	7	79.25			
	Cor Total	7851.59	16				

*Note: * Indicates significant impact(P＜0.05); ** Indicates a highly significant impact(P＜0.01)*

The analysis shows that the significance P values of the two evaluation index models of coefficient of variation and shaft power are all less than 0.01, indicating that the established regression model is highly significant. The coefficient of variation and the coefficient of determination of the shaft power regression model were 0.9812 and 0.9293, respectively, and the revised coefficient of determination was 0.9571 and 0.8385, respectively.

It shows that the model has a high fitting degree with the corresponding data and small test error. The model can be used to replace the test data for analysis. For coefficient of variation, regression x_1, x_2, x_3, x_1^2,

x_2x_3, x_3^2 were significant (P < 0.01), x_1x_3 were significant (P < 0.05), other effects were not significant, For axial power, regression item x_1, x_1^2 had significant effect (P < 0.01), x_1x_3 had significant effect (P < 0.05), other items had no significant effect. According to the influence significance, for the coefficient of variation, the influence degree is: stirrer height x_3 > stirrer speed x_1 > fertilizer water mixing ratio x_2; For shaft power, the influence degree is: agitator speed x_1 > agitator height x_3 > fertilizer water mixing ratio x_2.

Design-Expert 11.0 was used to draw the response surface diagram of coefficient of variation and shaft power. One of the three factors of stirrer speed, fertilizer-water mixing ratio, and stirrer height was taken as 0. The effects of the other two factors and their interaction on the coefficient of variation and shaft power were analysed, as shown in Fig. 7.

From Fig. 7a, it can be found that the variation coefficient increases with the increase of agitator speed under the same fertilizer-water mixing ratio, and increases with the increase of fertilizer-water mixing ratio under the same agitator speed. From Fig. 7b, it can be found that the variation coefficient decreases first and then increases with the increase of stirrer speed at the same stirrer height, and increases with the increase of stirrer height at the same stirrer speed. Fig. 7c shows that the variation coefficient increases with the increase of fertilizer-water mixing ratio at the same mixer height, and increases with the increase of mixer height at the same fertilizer-water mixing ratio. From Fig. 7d, it can be found that the shaft power increases with the increase of agitator speed under the same fertilizer-water mixing ratio and decreases with the increase of fertilizer-water mixing ratio under the same agitator speed. Fig. 7e shows that the shaft power increases with the increase of stirrer speed at the same stirrer height, increases with the increase of stirrer height at lower stirrer speed, and decreases with the increase of stirrer height at higher stirrer speed. It can be found from Fig. 7f that the influence of fertilizer-water mixing ratio and agitator height on shaft power is not significant, and the influence of size change on shaft power is small.

a. $Y_1 = f(x_1, x_2, 0)$ b. $Y_1 = f(x_1, 0, x_3)$ c. $Y_1 = f(0, x_2, x_3)$

d. $Y_2 = f(x_1, x_2, 0)$ e. $Y_2 = f(x_1, 0, x_3)$ f. $Y_2 = f(0, x_2, x_3)$
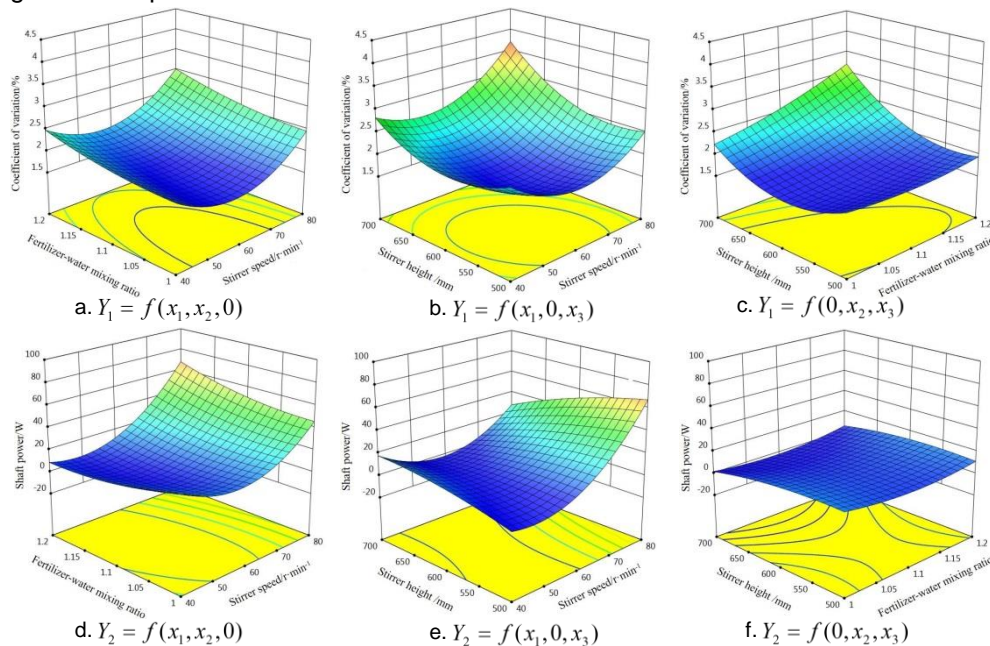
Fig. 7 - Response surfaces of interactive factors influence on test index

Numerical simulation and performance optimization of fertilizer pump

The design of the fertilizer discharge pump is based on the NL vertical sewage mud pump, which is mainly composed of a snail housing, impeller, and pump pad. The effective power formula of the fertilizer pump is as follows:

$$P_1 = \rho \cdot Q \cdot g \cdot H_2 \tag{9}$$

In equation (9): H_2 - lift, m; Q - flow, L/min; ρ - fluid density, kg/m³; g - gravity acceleration, 9.8 m/s²;
P_1 - effective power, kW.

In this design, the fluid in the fertilizer discharge pump belongs to solid-liquid two-phase flow. In practical work, the maximum density is about 750 kg/m³. Therefore, we take ρ=750 kg/m³, H_2=12 m, and Q=500 L/min here, which is obtained by Eq. (9).

Calculation formula of pump shaft power:

$$P_2 = P_1 \cdot \eta_1 \tag{10}$$

In equation (10): η_1 - pump efficiency, $\eta_1 = 0.85$. Calculated $P_2 = 6.25$kW.

A three-dimensional model of fertilizer discharge pump is preliminarily designed and optimized by three-dimensional drawing software. Boolean operations are used to form rotating and stationary domains to improve the accuracy of numerical simulation. After the setup is completed, the mesh is used to divide the grid. Set the unit size to 5 mm and automatically generate the grid as shown in Fig. 8. RNG k-e model is used to simulate the inside of the fertilizer discharge pump. When setting up the fertilizer discharge pump by numerical simulation, the boundary conditions are inlet, outlet, fixed wall, and moving wall. The volume fraction of solid phase must be set when setting the boundary conditions at the inlet boundary, and the external atmospheric pressure must be taken into account to set the inlet pressure; the flow around the fixed wall is the standard wall function method; and the moving wall is the impeller surface, which rotates on the Y-axis in the calculation.

To verify the performance of the drainage pump under different mixing ratios of fertilizer and water, the solid-liquid two-phase flow analysis was carried out with the mixing ratios of 0.6, 0.8, 1.0, and 1.2, corresponding to volume fractions of the second phase 0.5079, 0.5792, 06324 and 0.6737 respectively. The characteristic curves of fertilizer discharge pump with different fertilizer-water mixing ratios were obtained as shown in Fig.9.
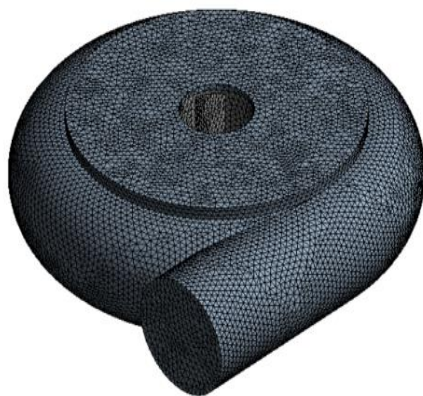
Fig. 8 - **Gridding of fertilizer pump**
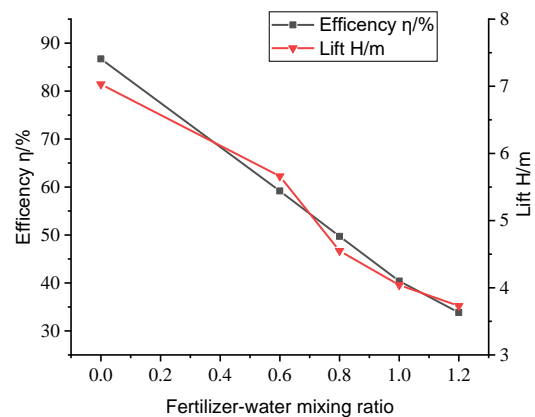
Fig. 9 - **External characteristic curve**

Numerical simulation of external characteristics and particle flow field of fertilizer pump

The fixed flow rate of 500 L/min is set and the speed is rated. The operating efficiency of the fertilizer pump under clean water conditions is 86.7%. With the increase of the proportion of fertilizer to the water, the working efficiency of the fertilizer pump decreases continuously. The main reason is that the higher the mixing ratio of fertilizer and water, the higher the concentration of organic fertilizer particles, the greater the obstruction to the flow path of the fertilizer discharge pump, resulting in increased hydraulic losses. The head of the fertilizer discharge pump under clean water working conditions is 7.03 m, which serves as the design head of the fertilizer discharge pump. With the increase of the proportion of fertilizer to the water, the head of the fertilizer discharge pump keeps decreasing.

At rated operating speed, 500 L/min design flow rate, and 0.3 mm average particle size of organic fertilizer, the solid-liquid two-phase flow numerical simulation of four groups of fertilizer discharge pumps with mixing ratios of 0.6, 0.8, 1.0, and 1.2 were carried out respectively. As shown in Fig. 10, with the increase of the mixing ratio of fertilizer and water, the concentration of particles in the snail housing of the fertilizer pump gradually increases; the concentration of particles at the suction outlet of the lower end of the fertilizer pump and the outer edge of the snail housing is the highest, and the concentration of particles on the working surface of the impeller is lower than that on the back of the impeller; when the mixing ratio of fertilizer and water is greater than 0.8, the distribution of particles near the outlet of the volute tongue is rather uneven; and different fertilizer pumps can suck in the fertilizer-water mixture and complete the organic fertilizer pumping out, which ensures that the organic fertilizer does not accumulate in the snail housing.

The distribution concentration of organic fertilizer particles on the outer edge of snail housing is relatively high, which is mainly due to the concentration of organic fertilizer particles on the outer edge of snail housing under centrifugal force during the process from impeller flow channel to snail housing flow channel. With the increase of mixing ratio, the concentration of organic fertilizer particles on the outer edge is more obvious. The wear of the outer edge of snail housing is easily caused by the long-term operation of the fertilizer discharge pump. Therefore, it is necessary to design the organic fertilizer particles on the outer edge design of strong snail housing.

On the whole working surface of the impeller, the particle distribution is relatively uniform, but due to the high-speed movement of the working surface of the impeller, a pressure difference is generated on the back of the impeller. The fertilizer-water mixture is pumped from the lower suction port of the fertilizer discharge pump. Under different fertilizer-water mixing ratios, the effect of the pump fertilizer is better.

Under the working conditions of 0.3 mm average particle size of organic fertilizer and 1.2 mixing ratio of fertilizer and water, four rotational speeds, 1145 r/min, 572 r/min, 381 r/min, and 286 r/min, are selected for solid-liquid two-phase flow analysis, which correspond to the rated speed, 1/2 rated speed, 1/3 rated speed and 1/4 rated speed of the fertilizer discharge pump respectively. As the speed of the fertilizer pump increases, the cross-flow speed in the impeller flow passage increases on the shaft section of the impeller, but there are obvious vortexes at the edges of both impellers far from the outlet. The vortex area is the largest at 1145 r/min and the smallest at 286 r/min. A jet high-speed area is formed near the pressure surface of the impeller at the fertilizer discharge outlet. The jet area is the largest at 1145r/min and the smallest at 286 r/min. Higher particle flow rate and jet area are conducive to increase the head of the fertilizer pump, the swirl is conducive to the mixing of fertilizer and water, but the generation of swirl will increase the hydraulic loss, resulting in a reduction of hydraulic efficiency of the fertilizer pump, and the bigger jet area, the greater the hydraulic loss will be.
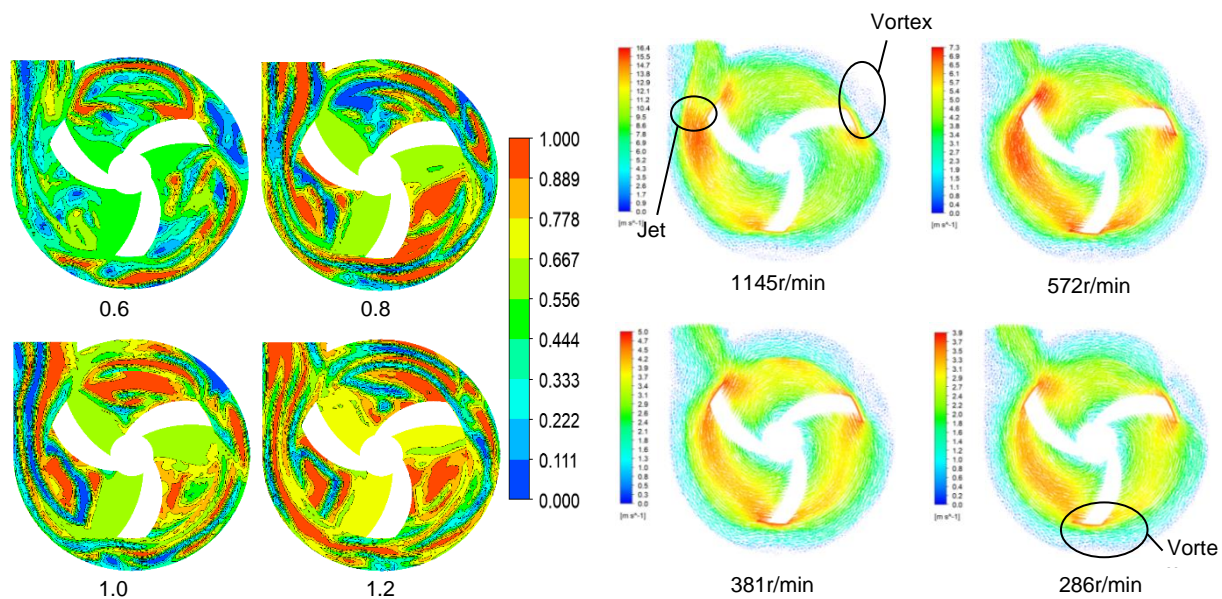
| Fig. 10 - Particle distribution of organic fertilizer with different proportion of fertilizer and water | Fig. 11 - Vector diagram of relative velocity of organic fertilizer particles at different rotational speeds |

Through numerical simulation, it is found that with the increase of rotational speed, the relative speed of organic fertilizer particles in the outlet increases continuously, the jet area increases, the head of the pump increases continuously, the hydraulic loss increases, and the hydraulic efficiency decreases; however, with the increase of rotational speed, the two obvious swirl areas will increase continuously, the hydraulic loss increases and the hydraulic efficiency decreases. Organic fertilizer discharge pump provides power for fertilizer injection and needs higher discharge pressure. To prevent the separation of fertilizer and water, a higher rotation speed should be selected. To increase the hydraulic efficiency of the fertilizer discharge pump, a lower rotation speed should be selected. Therefore, the speed selection of the fertilizer discharge pump needs to select a lower speed according to the specific application and on the premise of satisfying the fertilizer injection requirements.

Test Verification and Analysis

According to the actual working requirements of the agitator, it is required that the agitator mixes well and consumes less power. According to the evaluation index, we hope that the coefficient of variation is large and the shaft power is small. The priority of improving mixing effect is higher than energy consumption. The optimization solution is carried out by software and multi-objective optimization is carried out within the factor control range. It is determined that the target value of variation coefficient optimization is greater than 3.83 of the maximum value of existing tests and the target of shaft power optimization is the minimum value. The optimum solution is obtained with agitator speed $x_1=80$ r/min, fertilizer-water mixing ratio $x_2=1.2$ and agitator height $x_3=700$ mm.

The flow field model of the mixer was established based on the combination of the optimum parameters determined by response surface analysis. The density results of the mixtures with 10 sections after optimization were shown in Fig. 12.

The calculated average density of 10 sections is 713.16 kg/m^3, the shaft power is 24.07 kW and the coefficient of variation is 4.32 %. Compared with the results of the previous 17 groups of simulations, the optimized agitator has the smallest coefficient of variation of the average density of 10 sections and relatively small power, which proves that the optimized agitator is beneficial to improve the effect of mixing fertilizer and reduce energy consumption. The agitator shaft bears the torque of 2873.35 N•m during rotation and the force exerted on the blade surface by the mixture of organic fertilizer materials. The finite element analysis of deformation and stress distribution cloud diagram of the agitator is shown in Fig. 13.
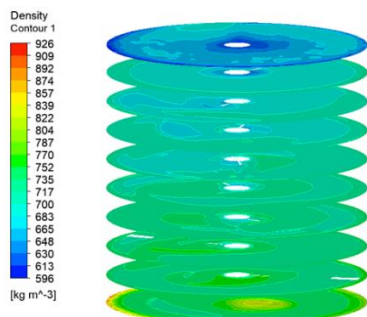
(a) Deformation distribution cloud map   (b) Stress distribution cloud diagram
Fig. 12 - Simulation results after optimization   **Fig. 13 - Finite element analysis of agitator**
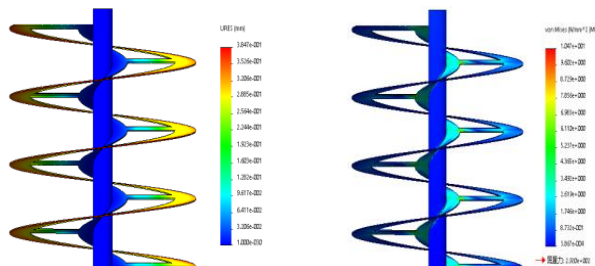
It can be seen from Fig. 13a that the maximum deformation of the agitator occurs at the edge of the screw belt with the maximum deformation of 0.3847 mm. The screw part does not deform. It can be seen that the deformation mainly occurs at the free end. From Fig. 13b, the maximum stress is 10.047 MPa at the weld between the support rod and the edge of the screw blade. At the same time, there are obvious stresses at the weld between the support rod and the screw strip and the screw blade, which are 4 MPa. The stirrer is welded with a JIS 45# steel plate. The yield strength of 45# steel is 355 MPa or more, which is much higher than the maximum stress generated by numerical simulation. The stirrer meets the working requirements.

Bench test

To verify the rationality of the optimized parameters obtained by numerical simulation, the screw-screw agitator is processed according to the optimized simulation results, and the test bench of organic fertilizer solid-liquid mixing fertilizer machine is built (screw drill is not installed), as shown in Fig. 14.
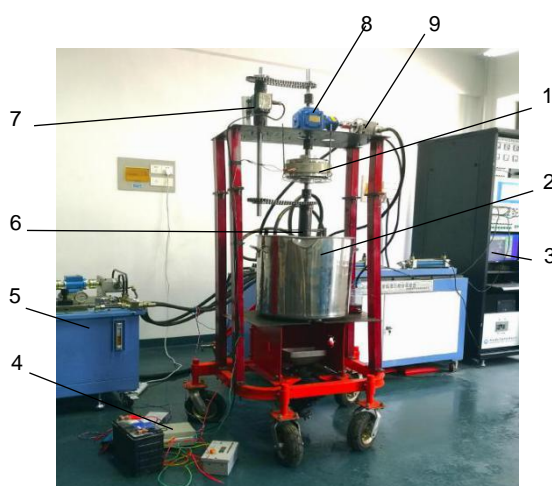
Fig. 14 - Test bench
1. Electromagnetic clutch; 2. Fertilizer drum; 3. Hydraulic comprehensive test stand; 4. Controller; 5. Hydraulic pump station;
6. Stirrer; 7. Torque speed sensor; 8. One input two output gearbox; 9. Hydraulic motor

According to the test parameters of optimization results, the performance of the solid-liquid mixing agitator and fertilizer discharge pump was tested in the laboratory of Shandong Agricultural University on June 5, 2021. The experiment was conducted in the laboratory of Shandong Agricultural University. Chicken manure

composting was set by numerical simulation parameters with the height of agitator 700 mm and added into the fertilizer tank according to the fertilizer-water mixing ratio of 1.2. To prevent the separation of fertilizer and water, the rated speed of the fertilizer discharge pump is selected as the working speed. The hydraulic motor is driven to rotate by the hydraulic control system of a comprehensive hydraulic test stand for agricultural machinery. The speed of the hydraulic motor is controlled at 570 r/min. After transmission of input and output gearbox, the speed of fertilizer discharge pump is 1140 r/min and the speed of agitator is 81.4 r/min after chain wheel deceleration. The torque sensor is mounted on the intermediate shaft between the reducer and the agitator via a coupling and reads the torque directly from the controlled display of the hydraulic comprehensive test stand.

After 5 minutes of the smooth operation of the mixer, open the solenoid butterfly valve at the outlet of the fertilizer pump and engage the electromagnetic clutch 5 times in 5 seconds, T1-T5 respectively. Take 500 ml from the outlet of the fertilizer pump each time. The quality of the sample was measured with an electronic balance and the density of the mixture at the test point was also measured. Three repeated tests were carried out under the same test conditions, the results of which are shown in Fig. 15.
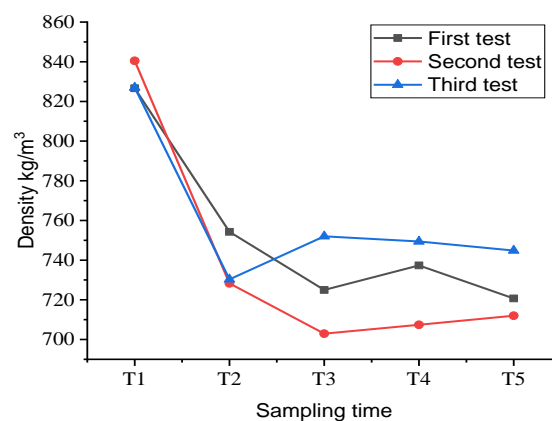
Fig. 15 - Results of three tests on the test bench

In the three tests, the density of mixture taken from T1 is higher, and the density of mixture taken from T2-T4 is consistent with the mass ratio of fertilizer-water mixture added. The possible reason is that the larger density of organic fertilizer-doped sediment is first pumped out by the fertilizer discharge pump in T1, which results in the higher density of the mixture. The results of T2-T4 show that the screw-screw mixer has a good mixing effect and the fertilizer discharge pump can completely pump the fertilizer. The test results show that when the speed of the mixer is 80 r/min, the height of the mixer is 700 mm, the mixing ratio of fertilizer and water is 1.2 and the speed of the discharge pump is 1140 r/min, the organic fertilizer mixed fertilizer is obtained with the best mixing effect, low power consumption and the effect of discharge pump can meet the working requirements of the organic fertilizer solid-liquid mixing and application device.

CONCLUSIONS

(1) A solid-liquid mixing fertilizer device for organic fertilizer in a hilly orchard was designed. According to the analysis of particle parameters and viscosity determination of various organic fertilizers, the basic structure of the screw-screw mixer was screened by numerical simulation of the mixing effect of six mixers, and the size of the fertilizer tank was designed. Through uniform mixing of fertilizer and water, an organic fertilizer applicator could directly apply organic fertilizer with different physical properties.

(2) Through two-phase flow numerical simulation and Box-Behnken design test method, 17 groups of simulation schemes were designed. The mixing effect of organic fertilizer and water during the mixing process of different mixer structures was analysed. Finally, it was determined that when the speed was 80 r/min, the height of the mixer was 700 mm and the mixing ratio of fertilizer and water was 1.2, the average density of 10 sections was 713.16 kg/m^3, the shaft power was 24.07 kW and the coefficient of variation was 4.32 %. Organic fertilizer has the best mixing effect and low power consumption.

(3) According to the optimization results of the agitator and the numerical simulation of the performance of the fertilizer discharge pump, a test bench of the organic fertilizer solid-liquid mixing fertilizer application device is set up for verification test. The test results show that the mixing effect of the test bench is good when the optimum working parameters of the agitator and the fertilizer discharge pump are 1140 r/min. The designed

agitator and the fertilizer discharge pump can meet the working requirements of field organic fertilizer application.

ACKNOWLEDGEMENT

REFERENCES

[1]   An S.Y., Li Y.X., Zhang X.L., Liu X.B., Chen X.C., Tong X., Hu B.Y., Liu K.F., (2019), Potential of Animal Manure in Replacing Chemical Fertilizers for Fruit, Vegetable, and Tea Production in China, *Journal of Agro-Environment Science*, vol.38, issue 8, pp.1712-1722;

[2]   Bai Y.L., (2016), Analysis of the Development and the Demands of Fertilization Machinery, *Soils and Fertilizers Sciences in China*, vol.2016, issue 3, pp.1-4;

[3]   Chen G.Q., Chen L., Wang W., Chen S.Y., Wang H.P., Wei Y., Hong F., (2019), Improved Bacterial Nanocellulose Production from Glucose Without the Loss of Quality by Evaluating Thirteen Agitator Configurations at Low Speed, *Microbial Biotechnology*, vol.12, issue 6, pp.1387-1402;

[4]   Chen X.F., Luo X.W., Wang Z.M., Zhang M.H., Hu L., Yang W.W., Zeng S., Zang Y., Wei H.D., Zheng. L., (2015), Design and experiment of fertilizer distribution apparatus with double-level screws, *Transactions of the Chinese Society of Agricultural Engineering*, vol.31, issue 3, pp.10-16;

[5]   Chiharu T., Yuki I., Yuki T., Jiang X., Kyoko O., Motonori I., Yasuyoshi S., (2021), Optimum Design of Agitator Geometry for a Dry Stirred Media Mill by the Discrete Element Method, *Advanced Powder Technology*, vol.32, issue 3, pp.850-859;

[6]   Christwardana M, Harvianto G.R., Sunandar K, Dwi Novian W., Ramanto R., (2020), Effect of H/D Ratio and Impeller Type on Power Consumption of Agitator in Continuous Stirred Tank Reactor for Nitrocellulose Production From Cotton Linter and Nitric Acid, *International Journal of Chemical Reactor Engineering*, vol.18, issue 12, no.20200109;

[7]   Foukrach M., Bouzit M., Ameur H., Kamla Y., (2020), Effect of Agitator's Types on the Hydrodynamic Flow in an Agitated Tank, *Chinese Journal of Mechanical Engineering*, vol.33, issue 1, no.37;

[8]   Fu Y.C., Yuan W.S., Zhang W.Y., Ji Y., (2017), Present Situation and Problem Analysis of the Technology of Fertilizer Mechanization in China, *Journal of Agricultural Mechanization Research*, vol.39, issue 1, pp.251-255+263;

[9]   Geng W., Sun Y.X., Yuan M.M., Wu G., Wang J.B., (2018), Evaluation of Environmental Carrying Capacity and Manure Organic Fertilizer Instead Chemical Fertilizer Potential of Animal Husbandry in Anhui, *Transactions of the Chinese Society of Agricultural Engineering*, vol.35, issue 1, pp.252-260;

[10]   Geng X.H., Shan Y.J., (2020), Research on Resource Utilization of Livestock Manure, *China Resources Comprehensive Utilization*, vol.38, issue 12, pp.80-82;

[11]   Himmelsbach W., Klaus G., Keller W., Last W., Multner B. (2021), Economies of Scale-Agitator Technology for World-Scale Plants, *Chemic Ingenieur Technik*, vol.93, issue 1-2, pp.71-80;

[12]   Hossain M. Z., Bahar M.M., Sarkar B., Donne S.W., Wade P., Bolan N., (2021), Assessment of the Fertilizer Potential of Biochars Produced from Slow Pyrolysis of Biosolid and Animal Manures, *Journal of Analytical and Applied Pyrolysis*, vol.155, no.105043;

[13]   Hu J., He J.C., Wang Y., Wu Y.P., (2018), Design and Study on Lightweight Organic Fertilizer Distributor, *Computers and Electronics in Agriculture*, vol.92, no.105149;

[14]   Li J., Wu M.L., Tang Y.J., Gong X., (2013), Research Status and Development Trend of Organic Fertilizer Application Machinery, *Journal of Hunan Agricultural University*, vol.39, issue S1, pp.97-100;

[15]   Kang J.M., Li S.J., Yang X.J., Liu L.J., Wang C.W., (2017), Design and Experiment of Ditching Blade Installed in Close Planting Orchard Ditching Machinery Planting Orchard Ditching Machinery, *Transactions of the Chinese Society for Agricultural Machinery*, vol.48, issue 2, pp.68-74;Liu C.L., Li Y.N., Song J.N., Ma T., Wang M.M., (2017), Performance Analysis and Experiment on Fertilizer Spreader with Centrifugal Swing Disk Based on EDEM, *Transactions of the Chinese Society of Agricultural Engineering*, vol.33, issue 14, pp. 32-39;

[16]   Liao J.J., Bai K., Xia Y.M., Li H.Z., Zhao X.Q., Xiao X.M., Wang Y., (2021), Flow Field Characteristics of an Agitator System of a Large Diameter Slurry-Water Shield Machine, *Journal of Mechanical Science and Technology*, vol.35, issue 4, pp.1501-1513; Liu X.Y., Li S.T., (2018), Temporal and Spatial

Distribution of Nutrient Resource from Livestock and Poultry Feces and Its Returning to Cropland, *Transactions of the Chinese Society of Agricultural Engineering*, vol.34, issue 4, pp.1-14;

[17] Quiroz., Flores., (2019), Nitrogen Availability, Maturity and Stability of Bokashi-Type Fertilizers Elaborated with Different Feedstocks of Animal Origin, *Archives of Agronomy and Soil Science*, vol.65, issue 6, pp.867-875;

[18] Rodrigues L.A.T., Giacomini S.J., Aita C., Lourenzi C.R., Brunetto G., Bacca A., Ceretta C.A., (2021), Short- and Long-Term Effects of Animal Manures and Mineral Fertilizer on Carbon Stocks in Subtropical Soil under No-Tillage, *Geoderma*, vol.386, no.114913;

[19] Sagues W.J., Assis C.A., Hah P., Sanchez D.L., Johnson Z., Acharya M., Jameel H., Park S., (2020), Decarbonizing Agriculture Through the Conversion of Animal Manure to Dietary Protein and Ammonia Fertilizer, *Bioresource technology*, vol.297, no.122493;

[20] Tang H., Wang J.W., Xu C.S., Zhou W.Q., Wang J.F., Wang X., (2019), Research Progress Analysis on Key Technology of Chemical Fertilizer Reduction and Efficiency Increase, *Transactions of the Chinese Society for Agricultural Machinery*, vol.50, issue 4, pp. 1-19;

[21] Wang J.W., Zhou W.Q., Bai H.C., Wang J.F., Huang H.N., (2018), Design and Experiment of Differential-Type Bidirectional Distribution Device for Fertilizer Supply for Deep-Fertilizer Liquid Fertilizer Application, *Transactions of the Chinese Society for Agricultural Machinery*, vol.49, issue 6, pp.105-111;

[22] Xu B.X., Ma B., Chen Y.S., Cao W.Q., Gu Z.H., Wu A.B., (2017), Status and Development Trend of Organic Fertilizer Broadcast Application Equipment in Greenhouse Vegetables in China, *Journal of Chinese Agricultural Mechanization*, vol.38, issue 6, pp.40-44;

[23] Yang Z., Ou Z.W., Sun J.F., Duan J.L., Song S.S., (2020), Development of Variable Rate Fertilizer Applicator Based on Distribution Characteristics of Banana Roots, *Transactions of the Chinese Society of Agricultural Engineering*, vol.36, issue 8, pp.1-10;

[24] Zeng S., Tan Y.P., Wang Y., Luo X.W., Yao L.M., Huang D.P., Mo Z.W., (2020), Structural Design and Parameter Determination for Fluted-Roller Fertilizer Applicator, *International Journal of Agriculture and Biology*, vol.13, issue 2, pp.101-110;

[25] Zhou W.Q., Xiao H., Liu Z.M., Wang J.W., Huang H.N., (2018), Design and Test of SYJ-3deep Application-Type Inclined Liquid Fertilizer Hole Applicator, *Transactions of the Chinese Society for Agricultural Machinery*, vol.49, issue 4, pp.105-111.

DESIGN AND EXPERIMENT OF THRESHING AND SEPARATING DEVICE OF CORN GRAIN HARVESTER
/
玉米籽粒收获机脱粒分离装置设计与试验研究

Zhicai SONG, Peisong DIAO*), Huanxiao PANG, Dianbao ZHAO, Hequan MIAO, Xiaowei LI, Duozhen YANG [1]

School of Agricultural and Food Science, Shandong University of Technology, Zibo/China
Tel: +86-13864306142; E-mail: dps2003@163.com
Corresponding author: Diao Peisong
DOI: https://doi.org/10.35633/inmateh-66-18

ABSTRACT

In order to find out the influence rule of threshing system parameters on threshing effect and the optimal parameter combination, the cylinder-concave clearance adjustment device is realized by "Front and back two hydraulic cylinders + Slide rail", the deflector angle adjustment device is realized by "Hydraulic cylinder driving hinge rotation" and the threshing separation device inclination angle adjustment device is realized by "Front adjustable double head pull rod". Multi-objective optimization test was carried out. The experimental results showed that the significant order of the influence of various factors on the grain breakage rate was rotational speed of roller, threshing separation device inclination angle, feeding rate, deflector angle and cylinder-concave clearance. The order of significance of the influence on uncleaned material rate was rotational speed of roller, cylinder-concave clearance, deflector angle, threshing device angle and feeding rate. According to the multi-objective parameter optimization analysis, the optimal operation parameter combination of corn threshing was determined. Under this parameter combination condition, model verification test and field optimization test were carried out. Compared with the field test value after parameter optimization, the grain breakage rate decreased from 4.018% to 3.462%, and the uncleaned material rate decreased from 0.292% to 0.218%.

摘要

为寻求脱粒系统参数对脱粒效果的影响规律及最优参数组合，设计了前后两油缸加滑轨的脱粒间隙调节装置、油缸伸缩带动合页转动的导流板角度调节装置以及前端可调节双头拉杆的脱粒分离装置倾角调节装置。进行多目标优化试验。试验结果表明：各因素对籽粒破碎率影响的显著性大小顺序为滚筒转速、脱粒分离装置倾角、喂入量、导流板角度及脱粒间隙；对未脱净率影响的显著性大小顺序为滚筒转速、脱粒间隙、导流板角度、脱粒分离装置倾角及喂入量。通过多目标参数优化分析，确定装置进行玉米脱粒的最优作业参数组合,在该参数组合条件下进行了模型验证试验以及田间优化试验，参数优化前与参数优化后田间试验值相比，籽粒破碎率由4.018%降为3.462%，未脱净率由0.292%降为0.218%。

INTRODUCTION

The corn grain harvester can complete crop harvesting, threshing, separation and other processes at once *(Chen et al., 2012; Chen et al., 2018)*. The threshing and separating device is the core component of the corn grain harvester, which directly affects the grain breakage rate and the uncleaned material rate during corn harvesting *(Miu et al., 2019; Miu et al., 1997; Kutzbach et al., 2008)*. For the threshing and separation device, scholars have done numerous researches *(Cui et al., 2019; Geng et al., 2019; Yang et al., 2019; Chen et al., 2020, Cujbescu D. et al, 2021, Wang S.S., 2021)*. Although scholars at home and abroad have done a lot of research on the axial flow threshing and separating device, there are still problems of uncleaned material threshing and high crushing rate during harvesting, and when the feeding rate fluctuates, it is easy to block the drum. Therefore, in-depth research is needed for the above issues.

---

[1] *Zhicai Song, Stud.; Peisong Diao, Prof. Ph.D.; Huanxiao Pang, Stud.; Dianbao Zhao, Stud.; Hequan Miao, Stud.; Xiaowei Li, Stud.; Duozhen Yang, Stud.*

This paper is designed to study the rotational speed of roller, feeding rate, threshing separation device inclination, the deflector angle and the cylinder-concave clearance on the operation effect of the device, using the quadratic rotation orthogonal combination design method to carry out multi-objective optimization experiments *(Qian et al., 2017; Liao et al., 2019; Teng et al., 2020; Omid et al., 2010)*, establish the correlation model of each operation index and each influencing factor, analyze the influence of each influencing factor on the operation index laws, and obtain the best combination of operating parameters of the device, in order to provide a reference for improving the operating performance of the longitudinal axial flow threshing device.

MATERIALS AND METHODS
Overall structure and working principle

The overall structure of the longitudinal axial flow corn flexible threshing and separating device is shown in Figure 1. It is composed of a feeding device, a frame, an inclination adjustment device, an upper cover device, a conical threshing drum, a cylinder-concave clearance adjustment device, a control device and a grain collection box. Among them, the feeding device conveys the corn ears from the bottom to the corn threshing and separating device, which can achieve the effect of uniform feeding. The conical threshing drum is equipped with spirally distributed threshing elements. In order to coordinate with the axial conveying of the ears by the threshing elements, there is a uniformly adjustable spiral baffle in the upper cover. The conical flexible threshing drum and the shell are installed above the frame. The threshing and separating device installed in cooperation with the frame and the front end of the threshing and separating device realizes the adjustment of the inclination angle of the threshing and separating device. The crushing and separation effects of grains in different areas are observed.
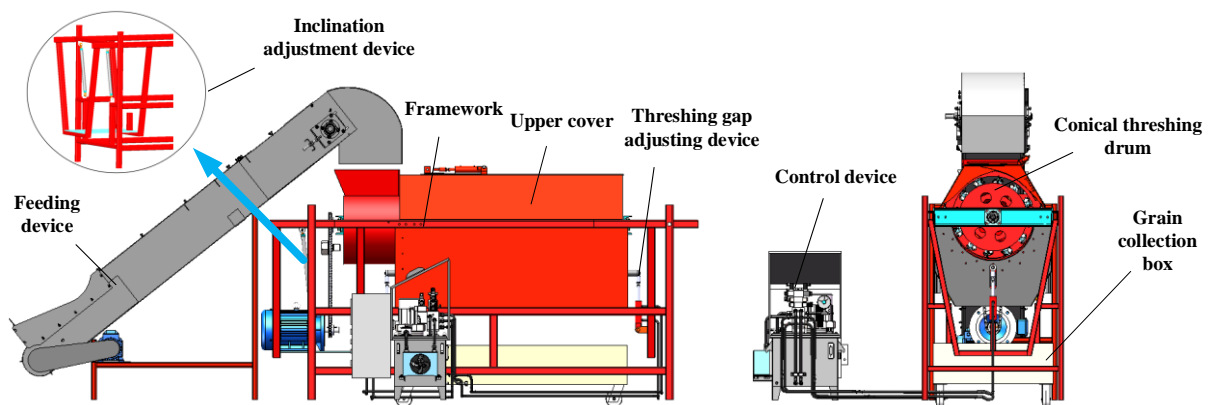
**Fig. 1 - Overall structure of longitudinal axial flow
threshing and separation test rig**

Cylinder-concave clearance adjustment

The cylinder-concave clearance mainly refers to the gap between the threshing drum and the concave screen. The cylinder-concave clearance adjustment device is mainly composed of hydraulic cylinder, support round tube, slide, side panel, inclined board, concave screen. As shown in Figure 3, the cylinder-concave clearance is adjusted by the expansion and contraction of the cylinders on both sides, and the four slide rails on both sides ensure the vertical movement of the segmented concave screen. The side panels on both sides prevent grains from falling from both sides.

Since the designed threshing drum is a cone-shaped threshing drum, the designed cylinder-concave clearance δ is the average gap between the front and rear ends, which can be obtained as follows:

$$\delta = \frac{\delta_1 + \delta_2}{2} \tag{1}$$

where:

δ is the defined cylinder-concave clearance, [mm];

δ_1 is the distance between the rear end of the drum and the concave screen, [mm];

δ_2 is the distance between the front end of the drum and the concave screen, [mm].

The two hydraulic cylinders at the front and rear are the power unit of the concave screen. The designed oil circuit is shown in Figure 4. The adjustment range of the recessed plate gap is 35 mm~60 mm. The speed control valve plays the role of speed control, and the range is 0 mm/s~10 mm/s.
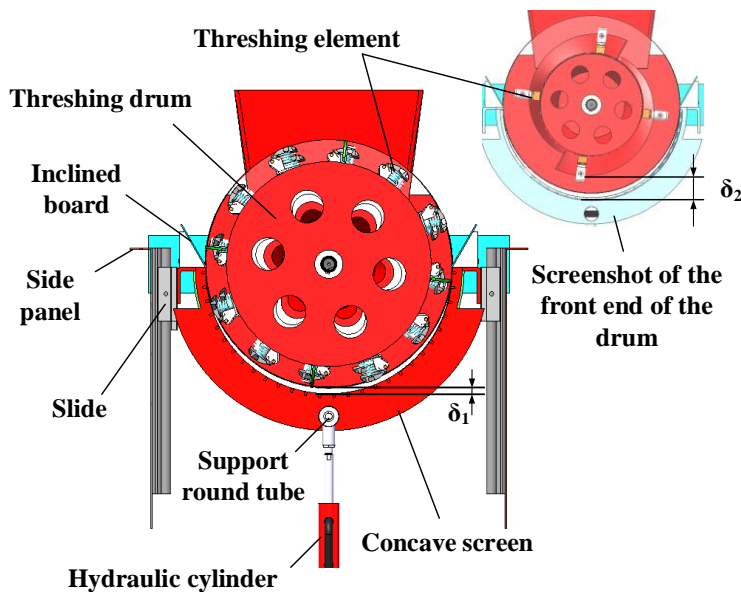
**Fig. 3 - Cylinder-concave clearance adjustment design
Angle adjustment of the deflectors**
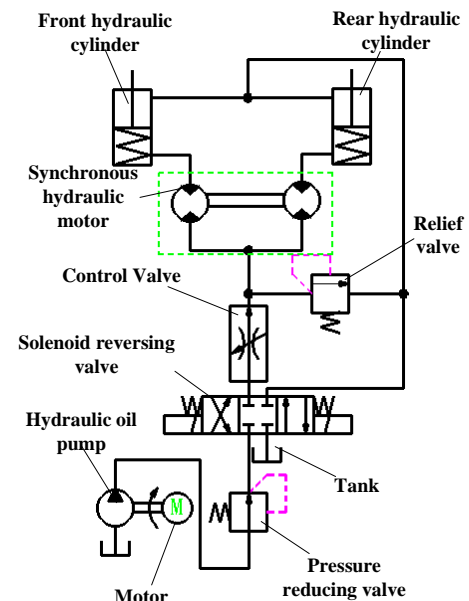
**Fig. 4 - Cylinder-concave clearance
regulation oil circuit**

The upper cover in the threshing and separating device is located above the drum and forms a complete threshing chamber with the concave screen. The inner surface of the top cover is designed with orderly arranged deflectors, and the inclination angle of the deflectors is adjusted by hydraulic cylinders, thereby changing the staying time of the corn ears in the threshing chamber.

The structure of the upper cover is mainly composed of upper cover plate, deflector, hydraulic cylinder, connecting plate, etc., as shown in Figure 5. The angle of the deflector is adjusted by the expansion and contraction of the hydraulic cylinder, as shown in Figure 5.

When the angle of the deflector is too large, the time of the corn ears staying in the threshing and separating device becomes longer, which increases the threshing time of the corn ears, which is beneficial to improve the removal rate, but it is easy to cause the retention, accumulation or blockage of the ears. If the time is too long, the rate of kernel breakage will increase significantly, and the degree of breakage of corn cobs and bracts will also increase, which increases the load of subsequent cleaning and significantly increases the impurity rate. The angle α of the deflector on the top cover is adjustable from 60°to 80°.
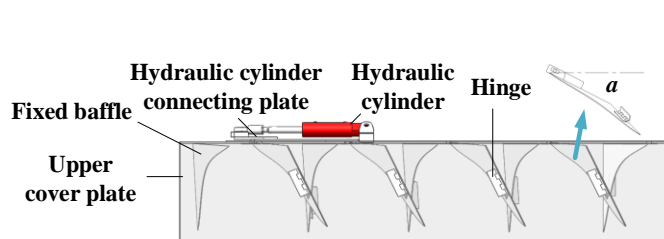
a Three-dimensional drawing of the upper cover structure   *b Schematic diagram of deflector angle adjustment*
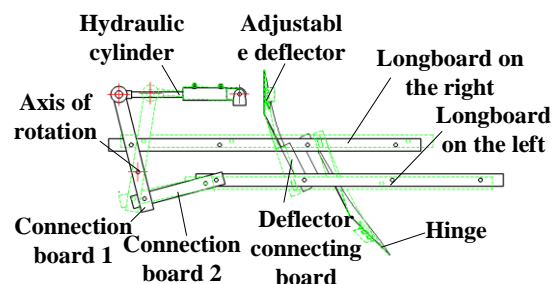
Fig. 5 - Upper cover structure drawing

Angle adjustment of threshing and separating device

Since the working inclination angle of the threshing and separating device affects the subsequent transportation efficiency of corn ears, the working inclination angle of the threshing and separating device is an important factor affecting the efficiency of threshing and separating. It adopts an adjustable double-ended tie rod structure, as shown in Figure 6.

Adjust the height of the front end of the longitudinal axial flow threshing and separating device through the knob of the double-headed reverse screw bolt to realize the inclination adjustment. The adjustable height of the double-headed pull rod is 0 mm~300 mm, which can realize the change adjustment of the inclination angle of the threshing and separating device from 0º ~6º.
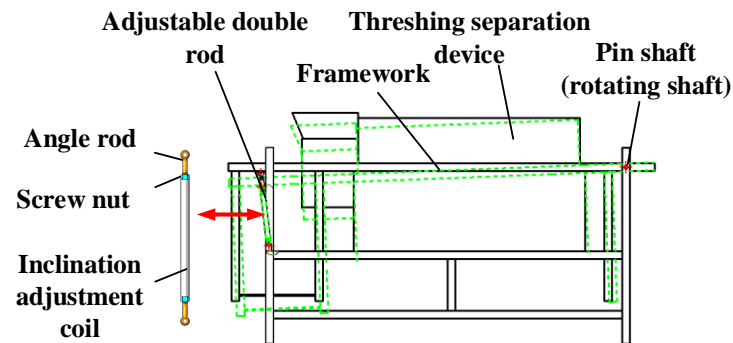
Fig. 6 - Angle adjustment mechanism

RESULTS

Test purpose and materials

In order to explore the influence of various factors in the threshing system on the grain crushing rate and unremoved material rate and the best parameter combination, the corn threshing parameter optimization test was carried out in the Agricultural Machinery Equipment Laboratory of Shandong University of Technology from October 12 to 18, 2021. The test site is shown in Figure 7. The test material is "Liyuan 296". Before the test, the basic characteristic parameters of corn ears are measured randomly using vernier calipers and 101-0BS electric heating blast drying oven.

The basic characteristic parameter values of corn ears are shown in Table 1.

Table 1

Material characteristics of corn

Parameter	Numerical value
Natural plant height	279.7cm
Ear height	104.8cm
Average number of grains per ear	474.1
Average ear length	17.2cm
Average diameter of big end	52.34cm
Average diameter of small end	37.87cm
Average corn kernel moisture content	30.16%

a. Test site   *b. Unbroken kernel*   *c. Broken kernels*

Fig. 7 - Test scene photos

Test results and analysis

According to the Box-Behnken central combination design theory, response surface tests were carried out on the rotational speed of roller *A*, feeding rate *B*, cylinder-concave clearance *C*, deflector angle *D*, and threshing separation device inclination angle *E* with the grain breakage rate Y_1 and the uncleaned material rate Y_2 as response values *(Teng et al., 2012; Chen et al., 2018)*. The optimization test plan and results of the threshing operation parameters of corn ears are shown in Table 2.

Table 2

Experimental design scheme and results

No.	A[a]	B[b]	C[c]	D[d]	E[e]	Y_1[f]	Y_2[g]
1	500	7	5	70	50	5.3	0.32
2	450	7	5	70	45	3.3	0.23
3	400	7	5	80	45	3.08	0.58
4	450	7	5	70	45	3.54	0.25
5	450	7	4	80	45	4.64	0.64

No.	A[a]	B[b]	C[c]	D[d]	E[e]	Y₁[f]	Y₂[g]
6	450	7	5	60	50	4.56	0.34
7	400	7	4	70	45	4.13	0.72
8	500	7	5	70	40	3.86	0.18
9	500	7	4	70	45	5.98	0.43
10	400	6	5	70	45	3.13	0.44
11	450	8	5	70	50	4.41	0.38
12	500	8	5	70	45	5.32	0.26
13	400	7	5	60	45	3.64	0.41
14	450	7	5	70	45	3.14	0.23
15	450	7	5	80	50	4.12	0.51
16	450	6	4	70	45	4.32	0.48
17	450	7	6	70	40	2.85	0.18
18	450	7	6	80	45	3.07	0.4
19	500	7	5	80	45	4.26	0.32
20	450	8	4	70	45	4.03	0.52
21	450	7	5	70	45	3.26	0.21
22	400	7	6	70	45	3.42	0.42
23	400	7	5	70	50	3.43	0.56
24	450	7	4	70	50	5.01	0.58
25	450	8	5	80	45	3.28	0.42
26	450	7	5	70	45	3.08	0.23
27	450	7	4	70	40	4.41	0.41
28	500	7	6	70	45	4.04	0.25
29	450	7	5	70	45	3.43	0.25
30	450	6	5	70	40	2.45	0.15
31	400	7	5	70	40	3.23	0.34
32	450	6	5	80	45	2.54	0.4
33	450	8	5	70	40	3.66	0.19
34	450	7	4	60	45	4.99	0.47
35	450	6	5	70	50	3.07	0.34
36	450	6	6	70	45	2.49	0.25
37	450	7	5	80	40	3.28	0.31
38	450	6	5	60	45	3.08	0.21
39	450	8	6	70	45	3.57	0.24
40	500	6	5	70	45	2.42	0.16
41	450	7	6	70	50	3.42	0.33
42	450	8	5	60	45	4.45	0.26
43	400	8	5	70	45	3.38	0.46
44	450	7	5	60	40	3.62	0.18
45	450	7	6	60	45	3.42	0.24
46	500	7	5	60	45	4.92	0.22

[a] Rotational speed of roller / r/min）;[b]Feeding rate / kg/s）;[c]Threshing separation device inclination angle/°;[d]Deflector angle/°[e]Cylinder-concave clearance / mm;[f]The grain breakage rate/%; [g] The uncleaned material rate/%.

According to the test results in the table, Design-Expert software is used to statistically analyze the test data. The regression equation of grain damage rate Y_1 to the rotational speed of roller A, the feed rate B, threshing separation device inclination angle C, the deflector angle D, and cylinder-concave clearance E was established, and the significance of experimental factors was analyzed.

Multivariate regression fitting of the experimental data, eliminating the insignificance in the model, and obtaining the regression equation of the influence of the grain breakage rate Y_1 and the uncleaned material rate Y_2,

$$Y_1 = 3.29 + 0.54A + 0.54B - 0.7C - 0.28D + 0.37E + 0.66AB - 0.31AC + 0.31AE + 0.34BC$$
$$+ 0.48A^2 - 0.18B^2 + 0.5C^2 + 0.26D^2 + 0.24E^2 \quad (1)$$

$$Y_2 = 0.21 - 0.11A + 0.014B + 0.086C + 0.089D - 0.11E + 0.03AB - 0.028AC - 0.03AD + 0.027AE$$
$$+ 0.099A^2 + 0.017B^2 + 0.033C^2 + 0.093D^2 + 0.11E^2 \quad (2)$$

The grain breakage rate Y_1 and the uncleaned material rate Y_2 variance analysis table is shown in Table 3.

Table 3

Variance analysis of regression equation of grain breakage rate and uncleaned material rate

	Grain breakage rate					Uncleaned material rate			
Source	Sum of squares	D$_f$	F-value	P-value	Source	Sum of squares	D$_f$	F-value	P-value
Model	28.62	14	34.39	< 0.01	Model	0.91	14	108.66	< 0.01
A	4.69	1	78.84	< 0.01	A	0.19	1	323.10	< 0.01
B	4.62	1	77.75	< 0.01	B	3.025×10-3	1	5.05	0.0319

Table 3
(continuation)

	Grain breakage rate					Uncleaned material rate			
Source	**Sum of squares**	**Dɟ**	***F-value***	***P-value***	**Source**	**Sum of squares**	**Dɟ**	***F-value***	***P-value***
C	7.88	1	132.58	< 0.01	**C**	0.12	1	195.77	< 0.01
D	1.22	1	20.44	< 0.01	**D**	0.13	1	213.30	< 0.01
E	2.22	1	37.34	< 0.01	**E**	0.21	1	345.51	< 0.01
AB	1.76	1	29.53	< 0.01	**AB**	$3.600×10^{-3}$	1	6.01	0.0201
AC	0.38	1	6.36	0.0170	**AC**	$3.025×10^{-3}$	1	5.05	0.0319
AE	0.38	1	6.47	0.0162	**AD**	$3.600×10^{-3}$	1	6.01	0.0201
BC	0.47	1	7.89	< 0.01	**AE**	$3.025×10^{-3}$	1	5.05	0.0319
A²	1.98	1	33.35	< 0.01	**A²**	0.085	1	142.63	< 0.01
B²	0.30	1	5.02	0.0323	**B²**	$2.609×10^{-3}$	1	4.35	0.0452
C²	2.16	1	36.33	< 0.01	**C²**	$9.576×10^{-3}$	1	15.98	< 0.01
D²	0.59	1	9.99	< 0.01	**D²**	0.076	1	126.31	< 0.01
E²	0.50	1	8.34	< 0.01	**E²**	0.18	1	294.90	< 0.01
Residual	1.84	31			**Residual**	0.019	31		
Lack of fit	1.69	26	2.18	0.1975	**Lack of fit**	0.016	26	1.03	0.5487
Error	0.15	5			**Error**	$2.933×10^{-3}$	5		
Sum	30.47	45			**Sum**	0.93	45		

Note: P<0.01 (very significant); 0.01≤P<0.05 (significant); P≥0.05 (not significant).

The contribution value K can reflect the degree of influence of a single factor on the established model. The larger the value of K, the greater the degree of influence of the factor on the model. The calculation methods are shown in Eq.3 and Eq.4.

$$K_i = \delta_i + \frac{1}{4}\Sigma\delta_{ij} + \delta_{i2} \tag{3}$$

$$\delta = \begin{cases} 0, & F \leq 1 \\ 1-\frac{1}{F}, & F>1 \end{cases} \tag{4}$$

where is the assessment value, $i,j = A, B, C, D, E$, and $i \neq j$.

According to formula (2) and formula (3), the contribution values of rotational speed of roller, feed rate, inclination angle of threshing separation device, deflector angle and cylinder-concave clearance to the crushing rate are calculated to be 2.621, 2.248, 2.394, 1.851 and 2.065, respectively. Therefore, the significant order of the influence of various factors on the crushing rate is the rotational speed of roller, the inclination angle of the threshing and separating device, the feeding rate, the deflector angle and the cylinder-concave clearance. The contribution of rotational speed of roller, feed rate, inclination angle of the threshing and separating device, deflector angle and cylinder-concave clearance to the uncleaned material rate are calculated to be 2.856, 1.780, 2.133, 2.196 and 2.243 respectively. Therefore, the significant order of the influence of various factors on the uncleaned material rate is the rotational speed of roller, the cylinder-concave clearance, deflector angle, the inclination angle of the threshing and separating device and the feeding rate.

When studying actual problems, it is usually necessary to consider the influence of the interaction of two factors on the test results. Respectively set $C=D=E=0$, $B=D=E=0$, $B=C=D=0$, $A=D=E=0$, and get the interaction factors AB, AC, AE, BC to the grain breakage rate Y_1. The law of influence is shown in Figure 8. Respectively set C=D=E=0, B=D=E=0, B=C=E=0, B=C=D=0, and get the interaction factors AB, AC, AD, AE on the uncleaned material rate Y_2. The law of influence is shown in Figure 9.

a. $Y_1=f$ $(A,B,0,0,0)$　　b. $Y_1=f$ $(A,0,C,0,0)$　　c. $Y_1=f$ $(A,0,0,0,E)$　　d. $Y_1=f$ $(0,B,C,0,0)$
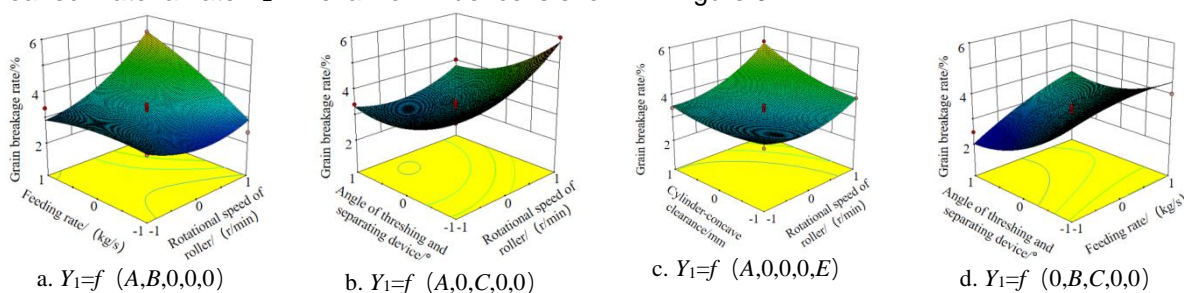
Fig. 8 - Effects of interaction of various factors on the grain breakage rate

a. $Y_2=f$ $(A,B,0,0,0)$ b. $Y_2=f$ $(A,0,C,0,0)$ c. $Y_2=f$ $(A,0,0,D,0)$ d. $Y_1=f$ $(A,0,0,0,E)$
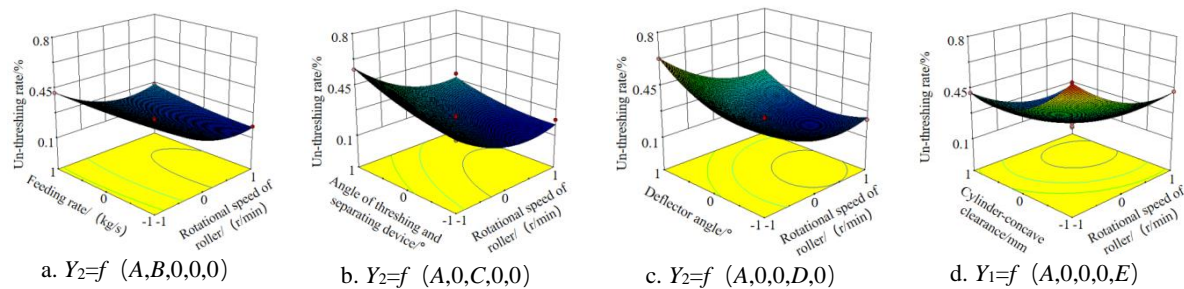
Fig. 9 - The influence of the interaction of various factors on the uncleaned material rate

It can be seen from Figure 8a that in the interaction of the rotational speed of roller A and the feeding rate B on the grain breakage rate Y_1, the rotational speed of roller has a greater influence on the interaction. When the rotational speed of roller is 400 r/min and the feeding rate is 6 kg/s, the grain breakage rate is the smallest. It can be seen from Figure 8b that in the interaction of the rotational speed of roller A and the inclination angle of the threshing and separating device C on the grain breakage rate Y_1, the rotational speed of roller has a greater influence on the interaction. When the rotational speed of roller is 400 r/min and the inclination angle of the threshing and separating device is 6°, the grain breakage rate is the smallest. It can be seen from Figure 8c that in the interaction between the rotational speed of roller A and the cylinder-concave clearance E on the grain breakage rate Y_1, the rotational speed of roller has a greater impact on the interaction. When the rotational speed of roller is 400 r/min and the cylinder-concave clearance is 40 mm, the grain breakage rate is the smallest. It can be seen from Figure 8d that in the interaction between the feeding rate B and the inclination angle of the threshing and separating device C on the grain breakage rate Y_1, the inclination angle of the threshing and separating device has a greater influence on the interaction. When the inclination angle of the threshing and separating device is 6°, the grain breakage rate is the smallest.

It can be seen from Figure 9a that in the interaction of the rotational speed of roller A and the feeding rate B on the uncleaned material rate Y_2, the rotational speed of roller has a greater influence on the interaction. When the rotational speed of roller is 500 r/min and the feeding rate is 6 kg/s, the uncleaned material rate is the smallest. It can be seen from Figure 9b that in the interaction of the rotational speed of roller A and the inclination angle of the threshing and separating device C on the uncleaned material rate Y_2, the rotational speed of roller has a greater influence on the interaction. When the rotational speed of roller is 500 r/min and the inclination angle of the threshing and separating device is 6°, the uncleaned material rate is the smallest. It can be seen from Figure 9c that in the interaction of the rotational speed of roller A and the deflector angle D on the uncleaned material rate Y_2, the rotational speed of roller has a greater influence on the interaction. When the rotational speed of roller is 500 r/min and the deflector angle is 40 mm, the uncleaned material rate is the smallest. It can be seen from Figure 9d that in the interaction between the rotational speed of roller A and the cylinder-concave clearance E on the uncleaned material rate Y_2, the cylinder-concave clearance has a greater impact on the interaction. When the cylinder-concave clearance is 45 mm and the rotational speed of roller is 450 r/min, the uncleaned material rate is the smallest.

Parameter optimization and experimental verification

Use the optimization module in Design-expert to determine the optimal combination of parameters, select test indicators; the range of conditions for test factors is shown in Table 4.

Table 4

Factors limiting condition

Name	A	B	C	D	E	Y_1	Y_2
Target range	in range	in range	in range	in range	in range	minimum	minimum
Lower limit	400	6	4	60	40	2.42	0.16
Upper limit	500	8	6	80	50	5.98	0.71

Note: The importance of kernel damage rate is set to " + + + + +", and the importance of uncleaned material rate is set to " + + + +"

According to the optimization results, the rotational speed of roller is 476.7 r/min, the feed rate is 6 kg/s, the inclination angle of the threshing and separating device is 5.3°, the deflector angle is 68.2°, and the cylinder-concave clearance is 45.6 mm, the grain crushing rate is 2.420% and the uncleaned material rate is 0.178%.

In order to verify the accuracy of the prediction of each index model and the operating effect of the whole machine under the optimal parameter combination of the threshing system, the model prediction test was first carried out in the Agricultural Machinery Equipment Laboratory of Shandong University of Technology. The corn material characteristics during the test were the same as those in Table 1. The parameters of the threshing system were the optimal parameter combination, and 5 sets of parallel experiments were carried out. The test results are shown in Table 5. Under the optimal parameter combination conditions, the model verification test has a grain breakage rate of 2.523% and an uncleaned material rate of 0.186%. The relative errors of each evaluation index and the predicted value of the model are 4.21% and 4.50% respectively, both less than 5%, and the parameter optimization results are reliable. Afterwards, field test verification was carried out in the experimental field of Fenghuang Town, Linzi, Shandong province, China as shown in Figure 10. The test materials and methods were the same as above. Five groups of parallel tests were designed before and after parameter optimization. The test results are shown in Table 8. Before parameter optimization, compared with the field test value after parameter optimization, the grain breakage rate decreased from 4.018% to 3.462%, and the uncleaned material rate decreased from 0.292% to 0.218%.

Table 5

Test results of optimized parameter

Project	Grain breakage rate (%)	Uncleaned material rate (%)
Model prediction	2.421	0.178
Verification test value	2.523	0.186
Relative error	4.21	4.50
Field test value before parameter optimization	4.018	0.292
Field test value after parameter optimization	3.462	0.218

| *a Field test site* | *b Water content measurement* | *c Broken grain selection* | *d Grain weighing* |
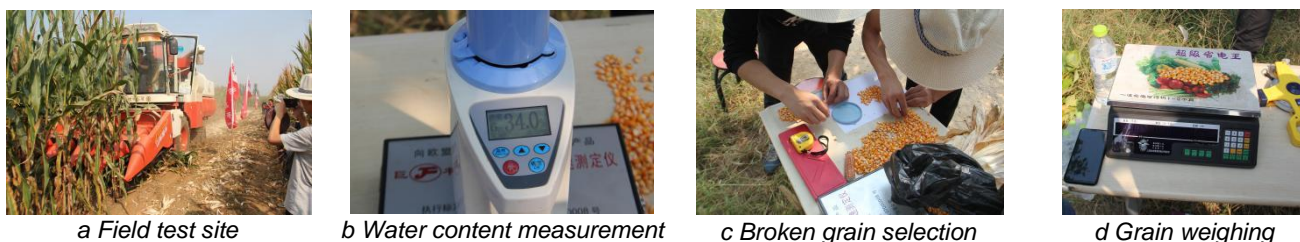
Fig. 10 - Photos of field test scenes

CONCLUSIONS

(1) In order to seek the law and optimal influence of the parameters of the threshing system on the threshing effect combining parameters, a "Front and back two hydraulic cylinders + Slide rail" was designed, the deflector angle adjustment device was *realized by* "Hydraulic cylinder driving hinge rotation" and the threshing separation device inclination angle adjustment device was *realized by* "Front adjustable double head pull rod".

(2) Through multi-objective optimization experiments, a mathematical model of rotational speed of roller, feeding rate, the inclination angle of the threshing and separating device, deflector angle, cylinder-concave clearance, and the rates of corn threshing grain breakage and of uncleaned material were established. Through analysis, it can be seen that the significant order of the influence of various factors on the grain breakage rate model is the rotational speed of roller, the inclination angle of the threshing and separating device, the feeding rate, the deflector angle, and the cylinder-concave clearance. The significant order of the influence of various factors on the uncleaned material rate model is the rotation speed of roller, the cylinder-concave clearance, the deflector angle, the inclination angle of the threshing and separating device, and the feeding rate.

(3) A parameter optimization model of longitudinal axial flow threshing device was established, and the optimal parameters were as follows: roller rotational speed is 476.7 r/min, feeding rate is 6 kg/s, threshing separation device inclination angle is 5.3°, deflector angle is 68.2°, cylinder-concave clearance is 45.6 mm, the grain breakage rate is 2.420%, the uncleaned material rate is 0.178%. Verification test was conducted on this parameter combination, and the verification test results are as follows: The relative errors of each index and the predicted values were all less than 5%, which proved the correctness of the prediction model. The field experiment of parameter optimization was carried out, and the experimental results showed that the grain breakage rate and the uncleaned material rate after parameter optimization were lower than those before optimization.

REFERENCES

[1]   Chen M.Z., Xu G.F., Wei M.J., Song Z.C., Wang W.J., Diao P.S., Teng S.M., (2021), Longitudinal compressing and shearing properties of silage corn stalk in north China plain. *INMATEH – Agricultural Engineering*, vol. 65, no.3, pp. 47-56; DOI: https://doi.org/10.35633/inmateh-65-05

[2]   Chen Z., Hao F.P., Wang D., Su W.F., Cui J.W., (2012). Development of technology and equipment of corn harvester in China (中国玉米收获技术与装备发展研究). *Transactions of the Chinese Society for Agricultural Machinery*, 43 (12): 44-50.

[3]   Craessaerts G., Baerdemaeker J.D., (2010), Fuzzy control of the cleaning process on a combine harvester [J]. *Biosystems Engineering*, 2010, 106(2): 103-111.

[4]   Cui T., Fan C.L., Zhang D.X., Yang L., Li Y.B., Zhao H.H., (2019). Research progress of maize mechanized harvesting technology (玉米机械化收获技术研究进展分析). *Transactions of the Chinese Society for Agricultural Machinery*，50 (12): 1–13.

[5]   Cujbescu D., Găgeanu I., Iosif A., (2021), Mathematical modeling of ear grain separation process depending on the length of the axial flow threshing apparatus. *INMATEH – Agricultural Engineering*, vol. 65, no.3, pp. 101-110. DOI：https://doi.org/10.35633/inmateh-65-11

[6]   Dai F., Song X.F., Zhao W.Y. et al, (2019), Motion simulation and test on threshed grains in tapered threshing and transmission device for plot wheat breeding based on CFD-DEM. *International Journal of Agricultural and Biological Engineering*, 12(1): 66-73.

[7]   Guan Z.H., Zhang Z., Jiang T., Li Y., Wu C.Y., Mu S.L.,（2020），Development and test of speed control system for combine harvester threshing and cleaning device. *INMATEH – Agricultural Engineering*, vol. 61, no.2, pp. 305-314; DOI: https://doi.org/10.35633/inmateh-61-33

[8]   Kutzbach H.D., (2008), Modeling and simulation of grain threshing and separation in threshing units-Part I. *Computer and Electronics in Agriculture*, 2008, 60(1): 96-104.

[9]   Liao Q.X., Xu Y., Jiang Y.J., (2019). Design and experiment on combined tangential and throwing longitudinal axial flow threshing and separating device of rape combine harvester (油菜联合收获机切抛组合式纵轴流脱离装置设计与试验). *Transactions of the CSAM*, 2019; 50(7): 140–150.

[10] Miu P.I., Beck F., Kutzbach H.D., (1997), Mathematical modeling of threshing and separating process in axial threshing units, *ASAE,* 1997: 97-106.

[11] Omid M., Lashgair M., Mobli H., (2010). Design of fuzzy logic control system incorporating human expert knowledge for combine harvester. *Expert Systems with Applications*, 37(10): 7080-7085.

[12] Qian Z.J., Jin C.Q. Zhang D.G., (2017), Multiple frictional impact dynamics of threshing process between flexible tooth and grain kernel. *Computers and Electronics in Agriculture*,114:276-28.

[13] Tang Z., Li Y.M., Xu L.Z., Li H.C., Pang J., (2012). Experiment and evaluating indicators of wheat threshing and separating on test-bed of longitudinal axial-threshing unit (切纵流联合收获机小麦脱粒分离性能评价与试验). *Transactions of the Chinese Society of Agricultural Engineering*, 28(3): 14-19.

[14] Wang S.S., Chen P., Li J. T., Lu M.Q., (2021), Design and experimental study of flexible threshing unit for Chinese cabbage seeds. *INMATEH – Agricultural Engineering*, vol. 65, no. 3, pp. 333-344; DOI: https://doi.org/10.35633/inmateh-65-35

[15] Yang L.Q., Wang W.Z., Zang H.M., Li L.H., Wang M. M., Hou M.T., (2018), Improved design and bench test based on tangential flow-transverse axial flow threshing system (切流-横轴流玉米脱粒系统改进设计及台架试验). *Transactions of the Chinese Society of Agricultural Engineering*, 34(1): 35-43.

[16] Zhu X.L., Chi R. J., Du Y.F., (2020), Experimental study on the key factors of low-loss threshing of high-moisture maize. *International Journal of Agricultural and Biological Engineering*, 2020, 13(5):23-31.

DESIGN AND APPLICATION OF A TEST BENCH FOR ROTATION TYPE ANTI-BLOCKING DEVICE OF NO-MINIMUM TILL SEEDER
/
少免耕播种机旋转类防堵装置性能试验台设计与应用

Hongbo ZHAO[1), Zhiqi ZHENG[1) Weiguo ZHANG[1) Zhengdao LIU[1) Wenzheng LIU[2) Yuxiang HUANG*[1)
[1) College of Mechanical and Electronic Engineering, Northwest A&F University, Yangling 712100, China;
[2) College of Enology, Northwest A&F University, Yangling 712100, China;
Tel:+8610 87092064; E-mail: hyx@nwsuaf.edu.cn

ABSTRACT

Anti-blocking and seedbed cleaning are one of the key processes in no-minimum till seeding in the Northwest arid area in China. Soil tillage performance and straw cutting performance such as tillage depth stability, straw cutting ratio, torque requirement are important indexes that influence anti-blocking and seedbed cleaning performance. In order to investigate the performance of rotation type anti-blocking device of no-minimum till seeder under different operation parameters, this paper designed a rotation type anti-blocking device test bench. It mainly comprises frame, torque sensor, speed sensor, speed-adjustable motor, straw fixture, rotation blades and land wheel, its working width was 1100 mm. The torque requirement could be determined with torque sensor and rotation speed could be determined with proximity speed sensor. The test bench could hitch with test vehicle of soil bin to conduct experiment. With the test vehicle, travel speed could be adjusted; with the speed adjustable motor, rotation speed (0-300 r/min) could be adjusted; besides, operation performance of different rotation type device can be determined by changing the device. Soil bin experiment of idling test, tillage test and straw cutting performance test was conducted taking rotation speed as testing factors and torque and straw cutting performance as response indicators. Results showed that tillage depth stability of the test bench was 87.2%, and it could satisfy the test requirement and operation steadily. Results of the tillage experiment showed that torque requirement of tillage and idling test both increased with the increase rotation speed significantly; results of the straw cutting test preliminarily found that the critical cutting speed under supported cutting was between 100-200 r/min under the given condition. This study could provide reference for the performance research for anti-blocking device of no-minimum till seeder.

摘要

清秸防堵是中国西北旱区少免耕播种作业的重要环节之一。土壤耕作效果及秸秆切割效果如耕深稳定性、秸秆切断率、作业扭矩等是影响清秸防堵效果的重要指标。为了测定不同作业参数下少免耕播种机旋转类防堵装置的作业性能，本文设计了旋转类部件作业性能试验台，其主要由扭矩传感器、转速传感器、转速可调电机、秸秆夹持装置、旋转类刀具、地轮等部件组成，其工作幅宽为1100mm。作业扭矩通过扭矩传感器测定，实时转速通过接近转速传感器测定。其能够通过三点悬挂装置挂接在土槽台车上进行试验作业，通过调整台车前进速度，可实现不同前进速度下作业性能的测定；通过调整电机转速，可实现不同刀具转速作业性能（0-300r/min）的测定；此外通过更换装置还可实现不同结构装置对作业性能影响的测定。以刀轴转速为因素，以作业扭矩和秸秆切断情况为响应指标，应用试验台开展了空转试验、土壤耕作试验及秸秆切割性能试验。试验结果表明所设计试验台耕深稳定性为87.2%。工作稳定可靠，能满足试验需求。空转试验和土壤耕作试验均表明作业扭矩随刀轴转速的增加而增加，秸秆切断试验初步表明支撑条件下秸秆临界切断转速在100-200r/min之间。本文可为少免耕播种清秸防堵装置性能研究提供参考。

INTRODUCTION

Conservation agriculture (CA) has been widely adopted globally, showing great advantage to protect the soil from water and wind erosion, improve soil health and decrease input and make agricultural production systems sustainable *(Ram et al., 2013; He et al., 2018; Friedrich et al., 2012.)*.

Hongbo Zhao, Ph.D.; Zhiqi Zheng, Ph.D.; Weiguo Zhang, associate Prof.; Zhengdao Liu, Ph.D.; Wenzheng Liu, Ph.D.; Yuxiang Huang, Prof.

According to the research of *Cameron et al. (2014)* CA shows more potential in yield increasing in arid area for its capacity of saving water, such as northwest arid area in China.

The major principle of CA includes minimal mechanical soil disturbance by no-minimum till seeding; and maintenance of a permanent soil cover by mulch or growing cover crops *(FAO., 2012; Gao et al., 2003)*. In order to ensure the anti-blocking and seedbed cleaning performance for no-minimum till seeding in Northwest arid area in China, straw cutting and seedbed tillage are often used as one of the key technical processes in the operation *(Gao et al., 2008; Zhao et al., 2020)*. If the long straws are not successfully cut off, it would be likely to cause blockage by tangling in the opener or between two openers; if the seedbed was not tilled well, the seed cannot germinate successfully *(Vaitauskiene et al., 2017; Zhao et al., 2018)*. Therefore, straw cutting and seedbed tillage performance of the relevant parts could directly affect seeding quality of till seeder.

However, it is usually difficult to obtain some straw cutting and seedbed tillage data in field operation, and it is not convenient to conduct comparison experiment on the straw cutting and tillage performance of different working and structure parameters of the rotation blades of no-minimum till seeder in field. To solve this problem, several straw cutting and tillage performance test benches have been developed. *Hou et al., (2014),* designed a reciprocating cutting test bench for wheat straw, the cutting speed, forward speed, cutting angle and blade gap could be adjusted, the cutting force could be determined. Results showed that blade gap, cutting speed and cutting position had significant influence on the cutting performance. *Lu et al., (2014),* designed a pendulum testing device to determine the critical kinetic energy and critical cutting speed of straw cutting, and found that straw diameter, moisture content has influence on critical kinetic energy and critical cutting speed. *Zeng et al., (2020),* designed a tillage performance test bench which could adjust travel speed, torque, rotation speed of the shaft and tillage depth and collect torque and power consumption. *Li et al., (2012),* designed a rotary tillage test device based on the soil bin test bench, which could collect resistance, torque and power consumption under different working parameters. These test benches could complete straw cutting or tillage experiment and obtain relevant data, but straw cutting torque under different working parameters cannot be tested, while it could generate significant difference in straw cutting performance. Besides, the tillage performance cannot be tested simultaneously.

To this end, this paper aims to design a test bench which could mimic straw cutting and soil tillage process. It could operate with the test vehicle of soil bin. The working parameters such as travel speed and rotation speed of the blade could be adjusted and the torque and rotary speed could be determined conveniently, the rotation type blade could be replaced as well, so as to determine the operation performance of rotation type anti-blocking device of till seeder.

MATERIALS AND METHODS
Structure of the test bench

Based on the requirements of straw cutting and soil tillage, the test bench which could mimic straw cutting and soil tillage process was designed. It mainly comprises the frame, torque sensor, speed sensor, speed-adjustable motor, land wheel, and rotation type blades, as shown in Fig. 1. The working width of the test bench was 1100 mm with two rows of rotation blades and the deepest tillage depth was 150 mm. Considering maize row space the distance between two blades was set as 600 mm. The disc blade could be replaced with rotary blade to test the performance of rotary tillage device.
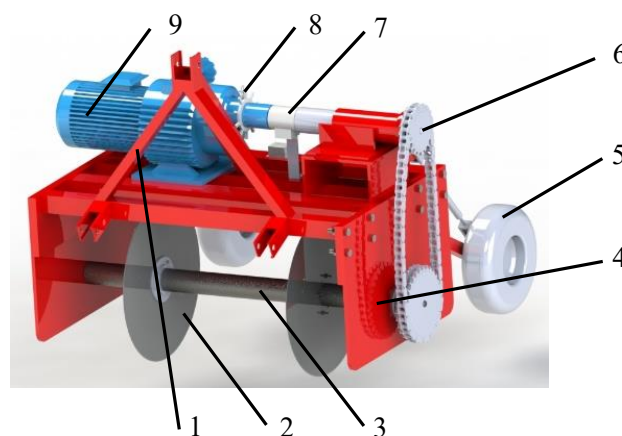
Fig. 1 - Test bench diagram

1. Three-point linkage; 2. Disc blade; 3. Cutter shaft; 4. Side board; 5. Land wheel; 6. Chain drive device

7. Torque sensor 8. Speed sensor 9. Speed-adjustable motor

Operation principle of the test bench

The straw cutting and soil tillage performance test was designed to be conducted as follows. Firstly, the rotation type anti-blocking device to be tested was installed on the shaft; then, the test bench was hitched on the testing vehicle of the soil bin. Secondly, the test bench was started by turning on the motor and the anti-blocking device began to rotate, then the rotation speed was adjusted to the testing value. Thirdly, a certain number of straw was clamped on the straw fixture. At last, the tillage depth was adjusted to the testing value and the testing vehicle of the soil bin could be started to pull the test bench travel forward to tillage or cut off straw samples. At the same time, the rotation speed and torque of the torque sensor was recorded. After one test, the test factors can be changed and the above process can be repeated to conduct the following experiment. The flow chart of the testing process is shown in Fig. 2.
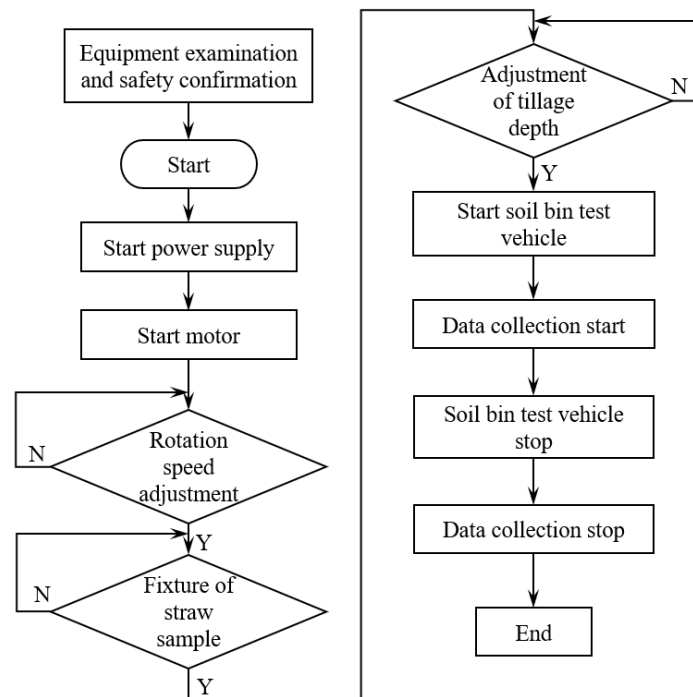
Fig. 2 - Flow chart of the experiment process

Rotation radius of the blade

The rotation radius of the blade is the summation of the shaft radius (38mm), the distance of shaft to soil surface and tillage depth. To avoid straw twining around the shaft, the rotation radius of the blade should not be too small, but with the increase of the rotation radius, arm of force would be longer and the torque requirement would be larger *(Zhang et al., 2009)*. Taking anti-blocking performance and design requirement of the test bench into consideration, the rotation radius of the blade was finally designed as $r =275$ mm.

Tillage depth

Based on the agronomy requirement in northwest arid area, the fertilizing depth of maize and wheat is about 8 cm, so that the tillage depth must be deeper than 8 cm. Apart from that, in the arid area, the moisture of surface soil is generally low and could not satisfy the requirement of seed germination. In order to ensure the quality of the seedbed and offer more moisture to the seeds, the tillage depth of rotation type device of no-minimum till seeder was generally deeper than 12 cm; this test bench was designed for experimental use, so the maximum tillage depth was designed as 15 cm. Tillage depth could be adjusted by adjusting the land wheel or the lifting height of the three-point linkage in the testing vehicle of the soil bin.

Rotation speed

Rotation speed of the anti-blocking device is one of the most important parameters that affect the performance of straw cutting and tillage. In the operation of the test bench, the motion of any point at the edge of the blade curve was the combination of uniform linear motion that travels with the test bench and circular

motion that circles with the shaft axis. The motion finally displays a trochoid motion in the vertical plane, as shown in Fig. 3.
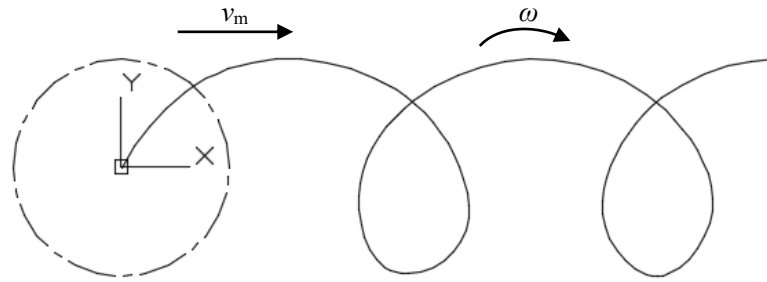
Fig. 3 - Trochoid path of any point at the edge of the blade curve

The kinematic equation of any point at the edge of the blade curve was

$$\begin{cases} x = v_m t + r \cos \omega t \\ y = r \sin \omega t \end{cases} \tag{1}$$

Where, v_m was the travel speed of the test bench; ω was angular velocity of the blade; r was the rotation radius of the blade.

Take the derivative of t, the absolute linear velocity of the blade tip was

$$v = \sqrt{v_x^2 + v_y^2} = \sqrt{v_m^2 + r^2 \omega^2 - 2 v_m r \omega \sin \omega t} \tag{2}$$

And the linear velocity in x and y direction was

$$\begin{cases} v_x = v_m - r \omega \sin \omega t \\ v_y = r \omega \cos \omega t \end{cases} \tag{3}$$

Based on the research of *Ma et al. (2006)*, under the condition that the straw was laying on soil surface (e.g. one side support cutting), the straw cutting ratio was higher than 98% when the linear velocity of disc blade was larger than 7.4 m/s. According to the research of *Lu, (2014)*, under the manner of two side support cutting, the critical straw cutting speed was 2.86~3.46 m/s. In the operation of no-minimum till seeding, travel speed was about 1 m/s so as to avoid straw blockage caused by high travel speed. For experimental purpose, travel speed could be controlled and adjusted by the testing vehicle of soil bin ranging from 0-3 m/s. Take the above data into equation 2. Under one side support cutting manner, the rotation speed should be designed in the range of 222~291 r/min, under two side support cutting manner, the rotation speed should be designed in the range of 65~155 r/min, so the range of rotation speed should be available to be set higher than 291 r/min and lower than 65 r/min. The motor was selected with a speed adjustable motor, rotation speed could be adjusted mechanically from 0-3000 r/min. Chain transmission, which was frequently used in agricultural machinery was adopted in this test bench, the final transmission ratio was 19:30, while the drive sprocket has 19 teeth and the driven sprocket has 30 teeth. With this transmission system, the adjustment of rotation speed in the test range could be easily accomplished.

Straw fixture

According to the literature of agricultural mechanics written by *Geng et al., (2011),* and the research conducted by *Zheng et al., (2016),* supporting manners have vital influence on straw cutting performance and resistance. In order to test the straw cutting performance under different supporting manners, a pair of straw holding device was designed as shown in Fig. 4. It was composed of the top holding part and the bottom holding part, and a supporting pole was weld underneath each bottom holding part to stick into the soil and keep the straw cutting process stable. Before each experiment, the straw was fixed in different ways by the fixture to change the supporting manners of the straw cutting test.

Fig. 4 – Fixture of straw

Experiment description

Experiment was conducted in January 2022 in an indoor soil bin of College of Engineering and Electronics in Northwest A&F University. The soil bin was 60 m long and soil characteristics are shown in Table 1. The straw sample was collected on September after maize harvesting form experiment field of Northwest A&F University in Yangling, Shanxi Province, China. Its characteristics are shown in Table 2.

Table 1

Experiment condition of soil

Soil texture	Soil moisture	Soil compactness/ kPa			
		5 cm	**10 cm**	**15 cm**	**Mean value**
Loam soil	*15.32%*	*1135*	*994*	*1978*	*1369*

Table 2

Experiment condition of maize straw

Average straw diameter	Average straw moisture	Straw variety
15.4 cm	*9.3 %*	*Shandan 650*

During the experiment, the test bench was hitched on the back of the testing vehicle of the soil bin through three point linkage, so it could advance with the testing vehicle. The computer of the torque determination system was placed on the testing vehicle. Data was collected when the testing vehicle travelled with constant speed and the work of the test bench was stable.

a. Hitch on the testing vehicle of soil bin
1. Testing vehicle 2. Designed test bench 3. Soil bin

b. Tillage test   c. Straw cutting test

Fig. 4 - Soil bin experiment

Tillage depth stability

In order to determine the operation performance of the test bench, tillage depth and tillage depth stability were determined after operation. Ten testing points were determined at each row and three rows were determined. Average tillage depth could be obtained easily. Tillage depth stability was calculated as follow:

$$\begin{cases} a_j = \dfrac{\sum_{i=1}^{n_j} a_{ji}}{n_j} \\ S_j = \sqrt{\dfrac{\sum_{i=1}^{n_j} (a_{ji} - a_j)^2}{n_j - 1}} \\ V_j = \dfrac{S_j}{a_j} \times 100 \\ U_j = 100 - V_j \end{cases} \tag{4}$$

Where a_j was the mean value of tillage depth at route j, cm; a_{ji} was the tillage depth of point i at route j, cm; n_j was the determining number of route j; S_j was the standard deviation of route j, cm; V_j was the variable coefficient of tillage depth at route j, %; U_j was the tillage depth stability of route j, %.

Determination of rotation speed

The rotation speed is one of the main factors affecting straw cutting performance, therefore it is important to collect rotation speed data during the experiment. The rotation speed was determined by a proximity speed sensor which could gather data when the distance of the sensor and metal material were closer than a certain value, which was 5 mm. The sensor was produced by Youyide Company in Dongguan, Guangdong Province. In order to improve the accuracy of the collected date, a notch disk was made with 10 teeth, so in each circle, the sensor could collect 10 signals, and the real rotary speed was calculated by the system and displayed on the screen.

Determination of torque requirement

FC-DAQ torque determining system was produced by Shanghai Forcechina Measurement Technology Company in Shanghai, China. The system consisted of a torque sensor, a storage battery and a computer. The torque sensor rotated with the shaft and its power was supplied by the storage battery, the torque data could be collected in real time and recorded by computer. Then the average torque was calculated and torque data could be used for analysis.

RESULTS

As observed during the tillage and straw cutting test, the test bench could rotate smoothly and operate well. Specific results of the tested index are described and discussed as follows.

Tillage depth stability

As shown in Table3, while target tillage depth was 10cm, the average value of actual tillage depth was 9.9, 10.0 ,10.1 cm in three experiment travels, respectively, and the depth stability was 88.4%, 86.8% and 86.5%, respectively, with an average value of 87.2%, which is higher than the requirement of National standard of 85% for rotary tiller. The results indicated that the test bench could operate steady and satisfy the experiment requirement.

Table 3

Tillage depth of three testing rows (cm)

Testing point	Travel 1	Travel 2	Travel 3
1	9.7	10.1	10.2
2	10.0	9.9	10.3
3	10.0	10.0	10.0
4	9.9	10.0	9.9
5	9.8	9.8	10.0
6	9.9	10.1	10.3
7	10.0	9.9	10.1
8	9.9	10.2	10.2
9	10.1	9.8	10.2
10	10.0	10.0	10.2
Mean value	9.9	10.0	10.1
Stability	88.4%	86.8%	86.5%

Torque requirement of tillage test

Real time torque requirement of the tillage test and idling test of the test bench under three different rotation speeds is shown in Fig. 5. As we can see, the torque was relatively steady with a fluctuation in an acceptable range, which may be attributed to the texture of the soil and the vibration of the test bench equipment. Generally, the test bench could operate well.

a) 100 r/min

b)   200 r/min

c) 300 r/min
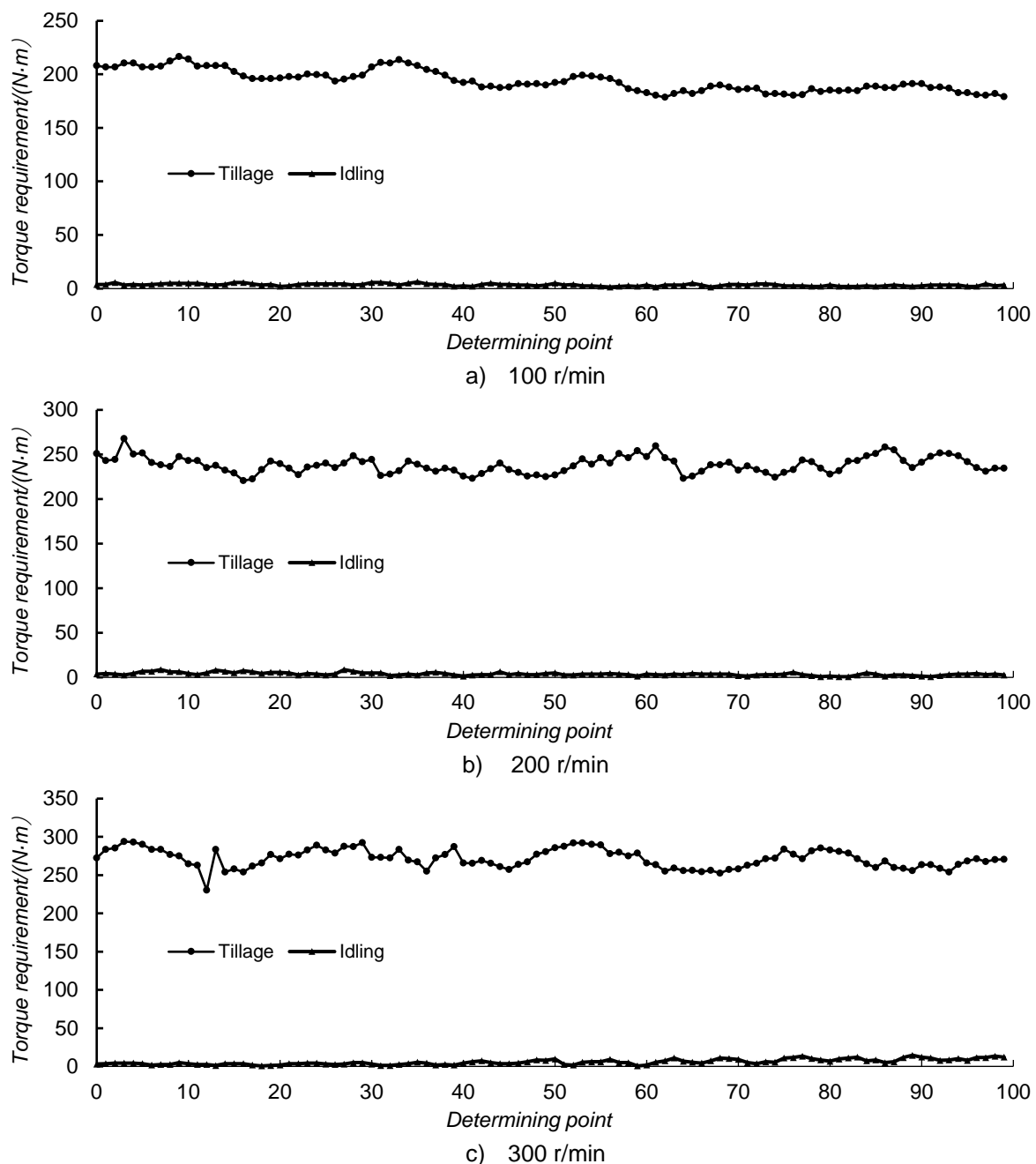
Fig. 5 - Torque requirement of the test bench

The average tillage torque requirement of the tillage test and idling test was calculated and the variance analysis was done, as shown in Fig. 6 and Table 4. The average torque requirement of tillage test was 193.7, 238.2 and 271.7 N·m under the rotation speed of 100, 200 and 300 r/min. The torque requirement increased significantly with the increase of rotation speed for tillage test. The same trend was also found in the average torque requirement of idling test, of which the torque requirement was 3.3, 3.7 and 3.9 N·m under the rotation speed of 100, 200 and 300 r/min. And the differences were highly significant. This phenomenon was also found by *Fang et al., (2016),* and *Xiong et al., (2018),* for the torque requirement of rotary tillage test, and the reason may be that, with the increase of rotation speed, the blade cut and threw more soil at certain period, so the friction and throwing resistance increased.

a) Tillage test   b) Idling test
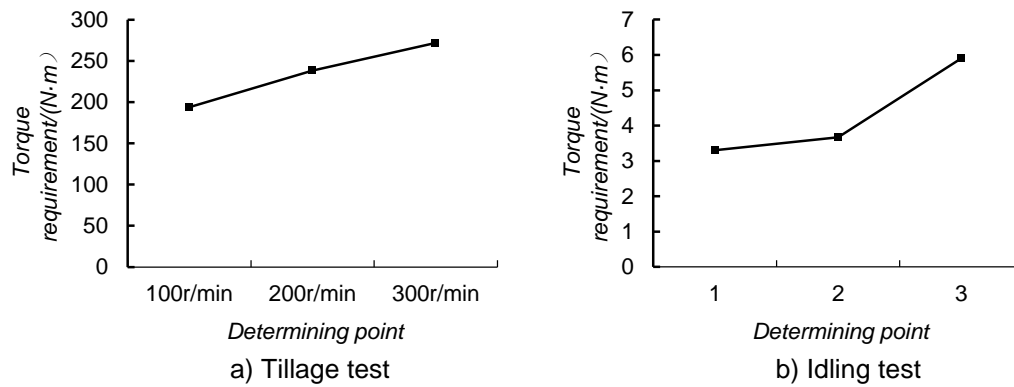
Fig. 6 – Average torque requirement of tillage test

Table 4

Variance analysis of the average torque requirement

	Source of variation	Sum of squares	Degree of freedom	Mean square	F	P-value	Significance
Tillage Test	interclass	309693.3	2	154846.6	1408.01	3.4×10^{-153}	**
	intraclass	32992.65	300	109.9755			
	Total	342685.9	302				
Idling test	interclass	399.9416788	2	199.9708394	36.80	5.1×10^{-15}	**
	intraclass	1630.520695	300	5.435068984			
	Total	2030.462374	302				
Note: ** indicates highly significant, $P < 0.01$; * indicates significant, $P < 0.05$.							

Straw cutting test

With the increase of rotation speed of the blade, straw cutting performance changed. As shown in Fig. 7, the straw could not be cut off at the rotation speed of 50 r/min, and when the speed increased to 100 r/min, the straw sample was ruptured (Fig. 7 a). And when the rotary speed increased as high as 200 r/min, the straw was cut off, as shown in Fig. 7 b. The results indicated that the critical speed when the straw was cut off was between 100-200 r/min for the collected straw samples under supported cutting manners, which was in accordance with the results of study by *Ma et al., (2006),* and *Lu, (2014)*. These results indicate that the test bench was reasonably designed, and the specific critical speed should be investigated further.

a.   100 r/min

b.   200 r/min
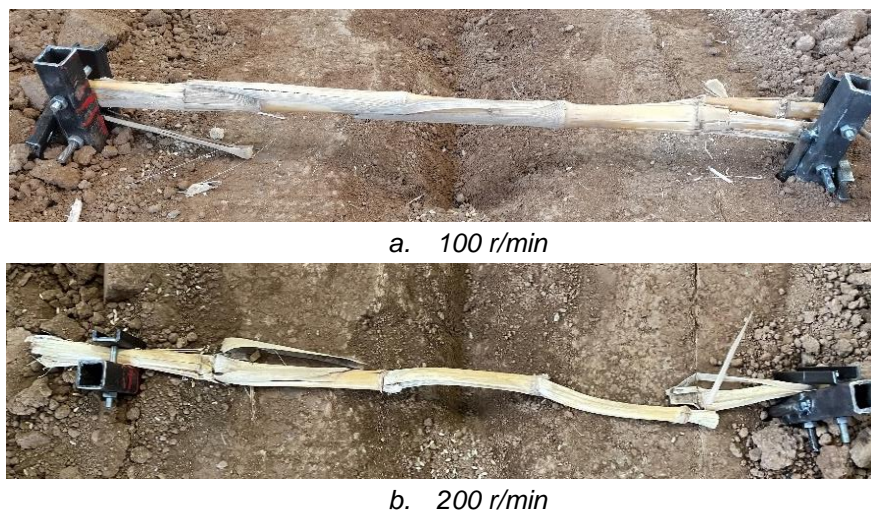
Fig.7 - Results of straw cutting test

CONCLUSIONS

(1) A straw cutting and seedbed tillage performance test bench for rotation type anti-blocking device of no-minimum till seeder was developed. It mainly comprises the frame, torque sensor, speed sensor, speed-adjustable motor, land wheel, and rotation type blades. With this test bench, travel speed, tillage depth, rotation speed of the blade and supporting manner of the straw could be adjusted, torque and rotation speed of the test bench could be collected.

(2) Key structural parameters and working parameters of the test bench were designed. The rotation radius of the blade was 275 mm, the rotation speed was designed to change between 0-300 r/min via the speed-adjustable motor and the transmission ratio was 19:30.

(3) The soil tillage and straw cutting performance test was conducted successfully. The torque was steady and fluctuated in a limited range, and tillage depth stability was 87.2%, higher than the national standard of China. It indicates that the test bench could operate well.

(4) Results of the tillage experiment showed that torque requirement of tillage and idling test both increased with the increase of rotation speed significantly; results of the straw cutting test preliminarily found that the critical cutting speed under supported cutting was between 100-200 r/min under the given condition.

ACKNOWLEDGEMENT

REFERENCES

[1]   Cameron M. P., Liang X. Q., Bruce A. L., Groenigen K. J. V., Lee J., Lundy M. E., Gestel N. V., Six J., Venterea T. R., Kessel C. V. (2014). Productivity limits and potentials of the principles of conservation agriculture [J]. *Nature*, 517:365-368.

[2]   Fang H. M., Ji C. Y., Zhang Q. Y., Guo J. (2016). Force analysis of rotary blade based on distinct element method (基于离散元法的旋耕刀受力分析) [J]. *Transactions of the Chinese Society of Agricultural Engineering*, 32(21): 54-59.

[3]   Friedrich T., Derpsch R. and Kassam A. (2012). Overview of the global spread of conservation agriculture. Field Actions Science Reports, *Special issue 6 (2012) on Reconciling Poverty Eradication and Protection of the Environmen*t. Available at: http://factsreports.revues.org/1941 (accessed 5 December).

[4]   Gao H. W., Li W. Y., Li H. W. (2003). Conservation tillage technology with Chinese characteristics (中国特色保护性耕作技术) [J]. *Transactions of the CSAE*, 19(3):1-4.

[5]   Gao H. W., Li H. W., Yao Z. L. (2008) Study on the Chinese light no-till seeders (我国轻型免耕播种机研究) [J]. *Transactions of the Chinese Society for Agricultural Machinery*, 39(4):78-82.

[6]   Geng D. Y., Zhang D. L., Wang X. Y., Yang Z. D. (2011). *Newly organized agricultural mechanics* [M]. National Defense Industry Press. Beijing.

[7]   He J., Li H. W., Chen H.T., Lu C. Y., Wang Q. J. (2018). Research progress of conservation tillage technology and machine (保护性耕作技术与机具研究进展) [J]. *Transactions of the Chinese Society for Agricultural Machinery*. 49(4): 1-19.

[8]   Hou J. L., Jiang T., Wu Y. Q., Liu L., Lv Z. X., Yang Q.Y. (2014). Design and experiment of wheat straw cutting reciprocating test bench (小麦秸秆往复式切割试验台设计与应用) [J]. *Transactions of the Chinese Society for Agricultural Machinery*. (S1):101-106.

[9]   Li Y. L., Song J. N., Dong X. Q., Zhang J. K., Wang J. C. (2012). Design of test device for rotary tiller components based on soil bin (基于土槽试验的旋转耕作部件试验装置设计) [J]. *Transactions of the Chinese Society of Agricultural Engineering*, 28(17): 38-43.

[10]   Lu C. Y. (2014). *Study on anti-blocking technology and device of rotary cutting with slide plate pressing straw for no-till planter* (免耕播种机滑板压秆旋切式防堵技术与装置研究) [D]. China Agricultural University. Beijing.

[11]   Ma H. L., Gao H. W., Li H. W., Wei S. Y. (2006). Design and experiment of no-till planter with oblique driven disc (斜置驱动圆盘免耕播种机设计与试验) [J]. *Transactions of the Chinese Society for Agricultural Machinery*. 37(5):45-47, 66.

[12]   Ram A. J., Kanwar. L. S., Amir H. K. (2013). *Conservation Agriculture, Global Prospects and Challenges. Printed and bound in the UK by CPI Group* (UK) Ltd, Croydon, CR0 4YY.

[13]   Vaitauskiene K., Arauskis E., Romaneckas K., Jasinskas A. (2017). Design, development and field evaluation of row-cleaners for strip tillage in conservation farming [J]. Soil & Tillage Research, 174(12): 139-146.

[14]   Xiong P. Y., Yang Z., Sun Z. Q., Zhang Q. Q., Huang Y. Q., Zhang Z. W. (2018). Simulation analysis and experiment for three-axis working resistances of rotary blade based on discrete element method (基于离散元法的旋耕刀三向工作阻力仿真分析与试验) [J]. *Transactions of the Chinese Society of Agricultural Engineering*, 34(18): 113-121.

[15]   Zhao H. B., He J., Zheng Z. Q., Zhang Z. G., Liu W. Z. (2020) Strip tillage Inter-row residue side-throwing device of no-minimum-till seeder for anti-blocking and seedbed-cleaning (少免耕播种机条带型行间侧抛清秸防堵装置研究) [J]. *Transactions of the Chinese Society for Agricultural Machinery*, 51(12):25-34.

[16]   Zhao H. B., He J., Li H. W., Wang Q. J., Li W. Y., Liu W. Z. (2018). Effect of straw returning manners on seedbed soil physical properties and winter wheat growth (秸秆还田方式对种床土壤物理性质和小麦生长的影响) [J]. *Transactions of the Chinese Society for Agricultural Machinery*, 49(Supp.):60-67.

[17]   Zhang X.R., He J., Li H. W., Li W. Y., Li H. (2009). Design and experiment on the driving disc of anti-blocking unit for no-tillage planter (免耕播种机驱动圆盘防堵单元体的设计与试验) [J]. *Transactions of the CSAE*, 25(9):117-121.

[18]   Zeng R., Li D. D., Zhu Y. H., Xia J. F. (2020). Design and application of performance test bench for rotary tiller components (旋转耕作部件性能测试试验台设计与应用) [J]. *Transactions of the Chinese Society for Agricultural Machinery*. 51(5):88-97.

[19]   Zheng Z.Q., He J., Li H. W., Diao P. S., Wang Q. J., Zhang X. C. (2016). Design and experiment of straw-chopping device with chopping and fixed knife supported slide cutting (动定刀支撑滑切式秸秆粉碎装置设计与试验) [J]. *Transactions of the Chinese Society for Agricultural Machinery*. 47(S1): 108-116.

[20]   FAO. (2012). *What is Conservation Agriculture*. Available at: http://www.fao.org/ag/ca/1a.html.

PARAMETER CALIBRATION OF DISCRETE ELEMENT SIMULATION MODEL OF WHEAT STRAW-SOIL MIXTURE IN HUANG HUAI HAI PRODUCTION AREA
/
黄淮海产区小麦秸秆-土壤混合物的离散元仿真模型参数标定

Zenghui GAO[1)], Shuqi SHANG[1,2)], Nan XU[3)], Dongwei WANG [2*)]
[1)] Xinjiang Agricultural University, College of Mechanical and Electronic Engineering, Xinjiang, China
[2)] Qingdao Agricultural University, College of Mechanical and Electronic Engineering, Shandong, China
[3)] Shandong Agricultural University, College of Mechanical and Electronic Engineering, Shandong, China
*Tel: 13869881615;   *) Corresponding author E-mail: w88030661@163.com*
DOI: https://doi.org/10.35633/inmateh-66-20

ABSTRACT

At present, there is a lack of accurate discrete element simulation model and parameters in the equipment in Huang Huai Hai double cropping production area, which hinders the optimization and improvement of equipment operation effect. In this paper, the discrete element method is used to study the interaction between soil-touching components and wheat straw-soil mixture to improve the performance of equipment. Firstly, the Hertz-Mindlin with JKR Cohesion contact model is selected for the wheat straw-soil mixture to calibrate the parameters. Then, the method of combining physical test and simulation test is used to calibrate the parameters, the cylinder lifting method is used to determine the buildup angle of wheat straw soil mixture, and the Plackett-Burman screening method and the steepest climbing test are used to determine the optimal combination range of soil-straw static friction coefficient, soil-straw dynamic friction coefficient and soil-soil dynamic friction coefficient contact model parameters. Using Box-Behnken optimization research and development of key components such as soil contact of seedbed preparation test, the regression equation of the stacking angle of wheat straw soil mixture was obtained, and the variance and interaction effect of the regression model were analysed. The regression model was used to find the optimal solution in Design-Expert software with an angle of repose of 41.23°, which yielded a soil-straw static friction factor of 0.072, a soil-straw dynamic friction factor of 0.78, and a soil-soil dynamic friction factor of 0.068, with an angle of repose error of 1.43%, indicating that the contact model parameters are reliable, and the parameters can provide a reference and theoretical basis for the study of the key components of the seedbed preparation equipment such as touching soil in the Yellow and Huaihai Sea two-maturity zone.

摘要

当前我国黄淮海两熟制产区种床制备装备触土等关键部件优化研发过程中缺乏精确的离散元仿真模型与参数，阻碍了装备作业效果的优化提升。本文采用离散元法对触土部件与小麦秸秆-土壤混合物进行互作研究，首先针对小麦秸秆-土壤混合物，选用 Hertz-Mindlin with JKR Cohesion 接触模型，进行参数标定；然后使用圆筒提升法对小麦秸秆-土壤混合物堆积角进行测定，使用 Plackett-Burman 筛选法与最陡爬坡试验，确定了各参数最优组合范围，使用 Box-Behnken 试验，得到了小麦秸秆-土壤混合物堆积角的回归方程，并进行了回归模型方差与交互效应分析；在 Design-Expert 软件中以堆积角为 41.23° 为目标，通过回归模型寻找到了最优解，得出土壤-秸秆静摩擦因数 0.072、土壤-秸秆动摩擦因数 0.78、土壤-土壤动摩擦因数 0.068，堆积角误差为 1.43%，说明接触模型参数较为可靠，参数可以为研究黄淮海两熟制产区种床制备装备触土等关键部件提供参考与理论依据。

INTRODUCTION

The main planting mode in Huang Huai Hai double cropping area is peanut direct seeding in summer after wheat. Wheat straw burying and returning to the field is an important way to deal with straw, which plays an important role in improving soil fertility, storing water and moisture, and realizing high yield of crops in the following season.

---

[1] *Zenghui Gao, Ph.D. Stud. ; Shuqi Shang, Prof. ; Nan Xu, Ph.D. Stud. ; Dongwei Wang, Prof.*

At present, most of the Huang Huai marine production areas use land preparation equipment such as dynamic rake to treat wheat straw, so as to realize the deep burial of straw and the preparation of high-quality summer peanut seedbed. Due to the complex characteristics of wheat straw soil mixture, it is impossible to study the interaction relationship through traditional methods such as field experiment. Therefore, it is of great significance to calibrate the contact parameters of wheat straw soil mixture by discrete element method.

To address the problem of complex straw-soil mixing characteristics, in recent years, experts and scholars in related fields at home and abroad have proposed the use of the discrete element method to calibrate the parameters of simulation models for granular materials such as soil, straw, fertilizer and seeds (*Wang et al., 2019; Zhou et al., 2014*). Joash Bryan Adajar and others studied the macro and micro shear characteristics of five different crop straws (rape, corn, flax, oats and wheat) and their interaction with soil, so as to improve the reliability of the discrete element model simulating the interaction between soil and crop residues in the process of tillage (*Joash et al., 2021*). Zeng Fandi et al. verified the correctness of the duckbill planter-soil discrete element simulation model by using the Hertz-Mindlin with Bonding model to calibrate the parameters of the field soil in the transplanting environment in Inner Mongolia (*Zeng et al., 2021*). In view of the lack of accurate and reliable discrete element simulation parameters in the research on the interaction mechanism between soil and rotary tillage components on the Loess Plateau, Sun Jingbin and others selected the Hertz-Mindlin with JKR coordination contact model in EDEM to calibrate the relevant simulation parameters, and verified the accuracy of the calibration results of discrete element simulation parameters through the field test and simulation test of rotary tillage on the slope (*Sun et al., 2022*). Liu F. et al. used Hertz-Mindlin with JKR Bonding in EDEM to calibrate the parameters of quinoa stacking angle and set up a comparative test for validation using quinoa (*Liu F. et al., 2020*). Aiming at the lack of accurate discrete element simulation model parameters in the design and optimization of key agricultural machinery components in conservation tillage in black soil area, Tian Xinliang and others used the method of combining physical test and EDEM simulation test, and selected Hertz-Mindlin with JKR contact model to calibrate the discrete element simulation contact parameters (*Tian et al., 2021*). In order to improve the accuracy of the parameters required by the discrete element simulation in the process of dense forming of corn straw powder, Wang Weiwei and others took corn straw powder as the research object, and used the Hertz-Mindlin with JKR Bonding contact model in EDEM software to calibrate the parameters of the discrete element simulation model of dense forming of corn straw powder (*Wang et al., 2021*). Jia S.L. et al. calibrated the parameters related to the mid-term of maize dispersal under different conditions by constructing a maize seed disperser model and performing simulation analysis based on EDEM (*Jia S.L. et al., 2021*). In order to obtain the discrete element simulation parameters that can be used for the interaction between viscous black soil and soil contacting parts in Northeast China, Li Junwei and others calibrated the relevant parameters of viscous black soil in Northeast China with different moisture content by using the Hertz- Mindlin with JKR Cohesion contact model in EDEM (*Li et al., 2019*).

From the above information, it can be seen that the current studies by experts and scholars at home and abroad are all aimed at different operating conditions in different regions, and most of them revolve around the types of soils such as north-eastern clay and north-western loam, combined with locally grown crops. There is a lack of research on the calibration of discrete element simulation parameters for wheat straw-soil mixtures in loamy soils of the Yellow Huaihai Sea. Accurate completion of parameter calibration lays a theoretical foundation for further research on the interaction relationship between soil-touching components and is of great importance for improving the quality of seedbed preparation.

In this paper, the Hertz-Mindlin with JKR fusion contact model in EDEM is selected, and the parameters of the discrete element simulation model of wheat straw-soil mixture are calibrated by the combination of physical test and virtual simulation test. Then, the angle of repose simulation test is carried out and compared with the angle of repose results of physical test to verify the accuracy of the calibration results of discrete element simulation parameters (*Liu et al., 2016; Qi et al., 2019*).

MATERIALS AND METHODS
Test material

This paper studies the wheat straw-soil mixture. The selected wheat straw-soil mixture materials are from the experimental base in Taishan District, Tai'an City (36°16′ N, 117°16′ E). The soil of the experimental base is clay loam with pH value of about 7.5, base saturation of 82% and annual precipitation of about 700 mm. Its soil organic matter and nutrient status are suitable for planting wheat, peanut and other crops.

The soil and straw of the selected plot have been subject to the disc harrow operation. After the disc harrow operation, the wheat straw is basically mixed into the soil surface to the depth of 20 cm, so the mixture at the depth of 0-20 cm is selected.

Test Method

The parameters of the wheat straw-soil mixture were calibrated using a combination of the physical test method of cylinder lifting and the EDEM discrete element simulation test method. The parameters with significant effects on the angle of repose of wheat straw-soil were selected using the Plackett-Burman section of the Design-Expert software, and the optimal interval of each parameter was determined by the steepest climbing method, and the optimal combination of parameters was finally determined using the Design-Expert software. The differences between the angles of repose derived from physical tests and those from simulation experiments were compared to verify the accuracy of the parameter calibration (*Zhang et al., 2018*).

Physical experiment on the angle of repose of wheat straw-soil mixture

The cylinder lifting method is applied to build the physical test device for the angle of repose of wheat straw-soil mixture, as shown in the Figure 1, which is mainly composed of Sans cmt4503 universal tester, cylindrical steel pipe and steel plate (*Feng et al., 2015*). The length of steel pipe is 200 mm and the diameter is 50 mm. The initial state is that the steel pipe is erected on the steel plate, the wheat straw-soil mixture is in the steel pipe, the universal tester is used to lift the steel pipe upward at a uniform speed of 0.05 m/s, and the mixture falls on the steel plate until the mixture pile tends to be relatively stable. After that, the high-definition camera is used to take photos vertically with the steel plate to obtain the main view of the mixture pile, and then the gray-scale processing is carried out by MATLAB software, The contour of the mixture pile is linearly fitted, and the angle of repose is obtained. After repeating the test for 10 times, the average value of the results is obtained, and the angle of repose of wheat straw-soil mixture is 41.23°.

Fig. 1 – Physical test of angle of repose by cylinder lifting method

SIMULATION EXPERIMENT ON ANGLE OF REPOSE OF WHEAT STRAW-SOIL MIXTURE

Contact model selection

The selected soil is one of the typical soil types in the Yellow Huaihai region, and it is mostly clay loam, and after research and literature search, it is known that the soil moisture content in this region is generally between 15-20%. Since the main research objective is to investigate the interaction mechanism of wheat straw-soil mixture in the Yellow and Huaihai Sea region, and since there is a certain adhesion phenomenon between the particles of clay loam, the contact model should be chosen to represent the type of adhesion and agglomeration between the particles.

EDEM mainly has three more suitable contact models between soil and straw, namely Hertz-Mindlin, Hertz-Mindlin with bonding and Hertz-Mindlin with JKR Cohesion. Hertz-Mindlin cannot show the influence of the bonding force between granular materials, and cannot accurately simulate the movement and fragmentation of soil after dynamic target operation; Hertz-Mindlin with bonding is suitable for simulating hard objects such as seeds; Hertz-Mindlin with JKR Cohesion is a cohesive contact model based on Hertz-Mindlin and JKR theory. It mainly considers the influence of the bonding force between water particles on the movement and fragmentation of material particles.

It is suitable for studying materials such as soil due to water bonding and agglomeration. Because the moisture content of the selected soil and straw mixture is high, the Hertz-Mindlin with JKR Cohesion model is selected to simulate the wheat straw-soil mixture in the Huang Huai Hai area, and the parameters required by the model are calibrated.

Simulation model building

The virtual three-dimensional model of the physical test device is drawn and established with SolidWorks software, and the size is completely consistent, as shown in Figure 2.
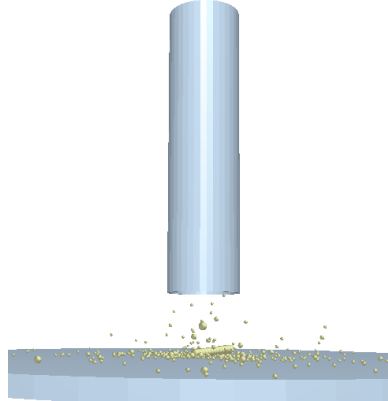
Fig. 2– Simulation test of angle of repose of cylinder lifting method

The ring blade method is used to measure the wet density of soil. The ring knife with a volume of 200 cm³ is mainly used to sample soil, and the electronic balance with a measuring range of 510 g and an accuracy of 0.001 g is used to carry out 10 repeated tests, and the average value of 1280 kg/m³ is obtained. Referring to the literature, the wet density of wheat straw is 241 kg/m³. The Poisson's ratio and shear modulus of soil and straw samples were measured by SMS texture analyser (as shown in Figure 3).

(a)   Cutting Ring   *(b)   SMS Texture Analyzer*

Fig. 3 – Parameter calibration physical test instrument

Soil and straw are homogeneous isotropic materials, and the relationship between shear modulus, Young's modulus and Poisson's ratio is as follows:

$$G = \frac{E}{2(1+v)} \tag{1}$$

According to the material model established by L.H. Han and others for the powder, through the fixed transverse deformation space, it is known that the stress-strain during rebound is related to the Young's modulus and Poisson's ratio of the sample *(L.H. Han et al., 2008)*, and the relation is as follows:

$$S = \frac{E(1-v)}{(1+v)(1-2v)} \tag{2}$$

where: v - Poisson's ratio;

G - shear modulus, MPa;

E - Young's modulus, GPa;

S - Stress strain ratio during rebound.

The ratio of the modulus of resilience to the strain of the soil is calculated by the Young's modulus of resilience and the ratio of the shear modulus to the mass of the soil as shown in the Table 1.

Table 1

Basic properties of test samples

Material	Poisson's ratio	Shear modulus [Pa]	Density [kg/m³]	Source
Soil	0.38	1×10^6	1280	Determination
Straw	0.40	1×10^6	241	Literature *(Guo, 2017)*

According to many field tests, in the range of soil depth 0-20 cm, the length of straw after crushing and returning to the field generally does not exceed 50 mm, and the quality of soil and straw is about 98:2. Other motion and physical parameters are the same as those in physical test.

Using the generic EDEM material model database (GEMM), according to the measured density and angle of repose of soil and straw, combined with the parameter selection range of references, the contact model parameters to be calibrated are obtained, as shown in the Table 2.

Table 2

Contact model parameters

Parameter	Numerical value
Soil-soil recovery coefficient	0.15-0.75
Soil-soil static friction coefficient	0.32-1.16
Soil-soil dynamic friction coefficient	0.05-0.1
Soil-straw recovery coefficient	0.15-0.75
Soil-straw static friction coefficient	0.60-1.00
Soil-straw dynamic friction coefficient	0.05-0.1
Straw-straw recovery coefficient	0.35-0.75
Straw-straw static friction coefficient	0.20-1.16
Straw-straw dynamic friction coefficient	0.15-0.20
Soil JKR surface energy / ($J \cdot m^{-2}$)	4-16
Soil-straw JKR surface energy / ($J \cdot m^{-2}$)	4-14

Significance screening test of contact model parameters

Because there are many parameters in the contact model, the parameters that have a significant impact on the angle of repose should be selected first. The Plackett-Burman section of design expert software is used for screening test design. Taking the angle of repose of soil-wheat straw mixture as the index, the soil-soil recovery coefficient (A), soil-soil static friction coefficient (B), soil-soil dynamic friction coefficient (C), soil-straw recovery coefficient (D), soil-straw static friction coefficient (E), soil-straw dynamic friction coefficient (F), straw-straw recovery coefficient (G) straw-straw static friction coefficient (H), straw-straw dynamic friction coefficient (I), soil JKR surface energy (J) and soil-straw JKR surface energy (K) are the factors. The level is shown in Table 3.

Table 3

Factors and levels

Level	A	B	C	D	E	F	G	H	I	J	K
-1	0.15	0.32	0.05	0.15	0.60	0.05	0.35	0.20	0.15	4	4
0	0.45	0.74	0.075	0.45	0.80	0.075	0.55	0.68	0.175	10	9
1	0.75	1.16	0.10	0.75	1.00	0.10	0.75	1.16	0.20	16	14

RESULTS AND ANALYSIS

Plackett-Burman screening test and significance analysis

The software generates Plackett-Burman test design, and applies EDEM to complete 12 tests to obtain the angle of repose. The test design and results are shown in Table 4. Then, the design expert software is used to analyse and obtain the contribution degree and ranking of various factors, that is, the significance relationship. From Table 5, it can be seen that: soil-straw static friction factor, soil-straw dynamic friction factor and soil-soil dynamic friction factor have the most significant effect on the angle of repose, while the contribution of the remaining factors does not exceed 5%.

Table 4

Test design and results

Serial number	Factor											Angle of repose / (°)
	A	B	C	D	E	F	G	H	I	J	K	
1	1	1	-1	1	1	1	-1	-1	-1	1	-1	42.63
2	1	-1	-1	-1	1	-1	1	1	-1	1	1	40.89
3	1	-1	1	1	1	-1	-1	-1	1	-1	1	41.05
4	1	-1	1	1	-1	1	1	1	-1	-1	-1	41.16
5	-1	-1	-1	-1	-1	-1	-1	-1	-1	-1	-1	38.52
6	-1	1	1	1	-1	-1	-1	1	-1	1	1	39.48
7	1	1	-1	-1	-1	1	-1	1	1	-1	1	41.54
8	-1	-1	-1	1	-1	1	1	-1	1	1	1	40.96
9	-1	1	-1	1	1	-1	1	1	1	-1	-1	39.26
10	1	1	1	-1	-1	-1	1	-1	1	1	-1	40.08
11	-1	1	1	-1	1	1	1	-1	-1	-1	1	43.08
12	-1	-1	1	-1	1	1	-1	1	1	1	-1	43.86

Table 5

Test results analysis

Factors	A	B	C	D	E	F	G	H	I	J	K
Contribution degree /%	1.44	0.041	7.22	3.53	24.43	58.31	0.82	0.005	0.29	3.24	0.67
Sort	6	10	3	4	2	1	7	11	9	5	8

Analysis of the steepest climbing test

Soil-straw static friction coefficient, soil-straw dynamic friction coefficient and soil-soil dynamic friction coefficient have great influence on the size of angle of repose. Therefore, based on the screening test, in order to determine the optimal range of contact model parameters required in the simulation, the steepest climbing test analysis is carried out. For the parameters with insignificant influence, the level 0 values in Table 3 are selected, namely soil-soil recovery coefficient 0.45, soil-soil static friction coefficient 0.74, soil-straw recovery coefficient 0.45, straw-straw recovery coefficient 0.55, straw-straw static friction coefficient 0.68, straw-straw dynamic friction coefficient 0.175, soil JKR surface energy 10 and soil-straw JKR surface energy 9. The steepest climbing test design and result analysis are shown in Table 6.

Table 6

Experimental design and result analysis

Serial number	C	E	F	Angle of repose / (°)	Error / %
1	0.05	0.60	0.05	35.76	13.26
2	0.0625	0.70	0.0625	38.32	7.05
3	0.075	0.80	0.075	42.58	3.27
4	0.0875	0.90	0.0875	44.91	8.92
5	0.10	1.00	0.10	46.19	12.03

It can be seen from the table that the angle of repose error of test 3 is relatively small, so the optimal combination of contact model parameters is near test 3.

Box-Behnken test analysis

In order to reduce the error of each contact model parameter and improve the accuracy of simulation, it is necessary to carry out the optimal parameter combination test for soil-straw static friction coefficient, soil-straw dynamic friction coefficient and soil-soil dynamic friction coefficient. According to the steepest climbing test, it is known that the optimal combination of contact model parameters is near test 3, so the box Behnken test is carried out at the level of test 2, 3 and 4, and the three factor and three-level test is carried out with the angle of repose as the test index. The test design and results are shown in Table 7.

Table7

Experimental design and results

Serial number	Factors			Angle of repose R
	C	**E**	**F**	(°)
1	-1	0	-1	42.03
2	-1	-1	0	42.24
3	-1	0	1	43.92
4	-1	1	0	42.32
5	0	-1	1	43.81
6	0	0	0	42.58
7	1	-1	0	42.40
8	1	0	1	44.06
9	0	1	1	44.38
10	0	0	0	42.58
11	0	-1	-1	41.86
12	0	0	0	42.58
13	1	0	-1	42.10
14	0	0	0	42.58
15	0	1	-1	42.25
16	0	0	0	42.58
17	1	1	0	42.79

It can be seen intuitively from the above table that the three factors of soil-straw static friction coefficient, soil-straw dynamic friction coefficient and soil-soil dynamic friction coefficient are taken as the research objects to explore the relevant conclusions affecting the size of angle of repose. The angle of repose is generally within 41.86 ~ 44.38%.

Through the above test results, the regression coefficient and significance of the angle of repose are analysed. According to the feedback information in the above table, the regression equation of the angle of repose is:

$$R = 42.58 + 0.11C + 0.18E + 0.99F + 0.077CE + 0.018CF$$
$$+0.045EF - 0.095C^2 - 0.048E^2 + 0.54F^2 \tag{3}$$

According to the regression equation, the influence of the three influencing factors on the angle of repose is that the soil-soil dynamic friction coefficient is the largest, the soil-straw dynamic friction coefficient is slightly smaller, and the soil-straw static friction coefficient is the smallest.

Table 8

Analysis of variance of regression model

Source	Sum of squares	Freedom Degrees	Mean Square	F Value	P-value Prob＞F
Model	9.50	9	1.06	125.90	< 0.0001
C	0.088	1	0.088	10.52	0.0142
E	0.26	1	0.26	30.49	0.0009
F	7.86	1	7.86	937.78	< 0.0001
CE	0.024	1	0.024	2.87	0.1343
CF	1.225E-003	1	1.225E-003	0.15	0.7136
EF	8.100E-003	1	8.100E-003	0.97	0.3583
C^2	0.038	1	0.038	4.53	0.0708
E^2	9.500E-003	1	9.500E-003	1.13	0.3224
F^2	1.24	1	1.24	147.84	< 0.0001
Residual	0.059	7	8.382E-003	_	_
Lack of Fit	0.059	3	0.020	_	_
Pure Error	0.000	4	0.000	_	_
Cor Total	9.56	16	_	_	_
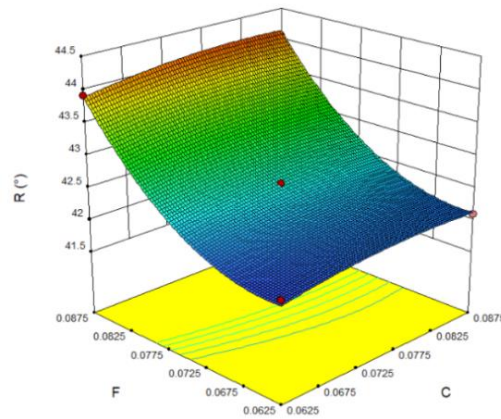
Fig. 4 – Effect of C and F on angle of repose (R) response surface
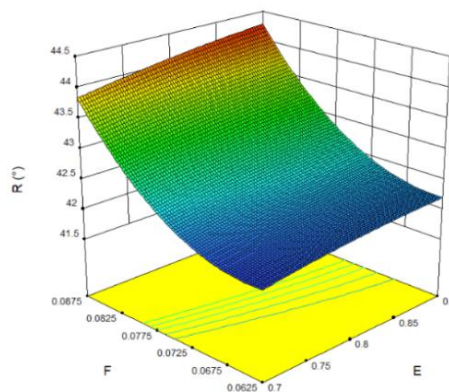
Fig. 5 – Effect of E and F on angle of repose (R) response surface
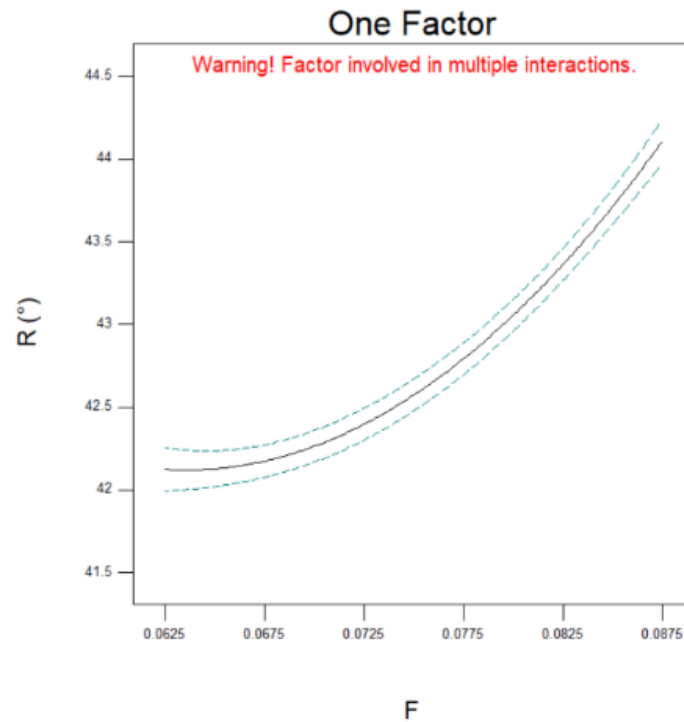
Fig. 6 – Effect of F on angle of repose (R) response curve

It can be seen from Table 8 and figures 4, 5 and 6 that E, F and F^2 have a significant impact on the angle of repose, C has a significant impact on the angle of repose, and CE, CF, EF, C^2 and E^2 have no significant impact on the angle of repose.

Using the parameter optimization module in the design expert software, the optimal solution is found through the regression model with the angle of repose of 41.23°. After several groups of simulation verification, the optimal solutions are soil-straw static friction coefficient 0.072, soil-straw dynamic friction coefficient 0.78 and soil-soil dynamic friction coefficient 0.068. The simulation angle of repose under the optimal solution is 41.82 and the error is 1.43%. The results of physical test and simulation test are shown in Figure 7.
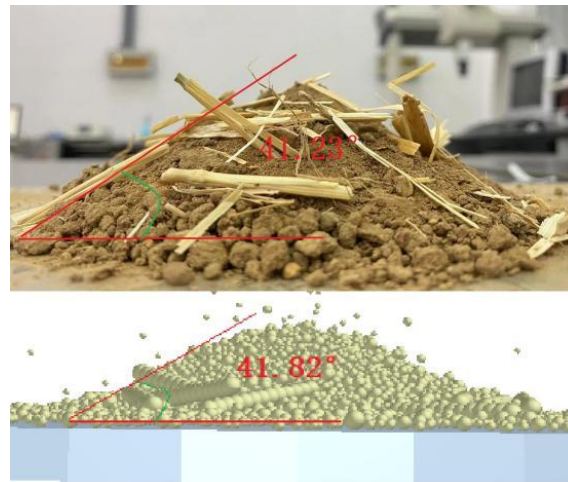
Fig. 7 – Comparison of angle of repose between physical and simulation tests

DISCUSSION

The calibration of discrete element model parameters for straw-soil mixtures had important effects on straw return, seedbed preparation, and optimization of structure and motion parameters of soil-touching components, which is the same as the findings of *Wang et al., (2021), Guo, (2017)*. *Tian et al., (2021)*, when analysing the factors affecting the angle of repose, concluded that the influence of each factor on the angle of repose was caused by as soil-soil dynamic friction factor, soil-straw dynamic friction factor, and soil-straw static friction factor, which is consistent with the results of this study. The results in research done by *Sun et al., (2021), Li et al. (2019)* showed that the errors of 1.7% and 1.52% for the angle of repose simulation experiments and physical tests, respectively, were higher than the 1.43% results obtained in this study, which proved that the contact model used in this study is more reliable.

CONCLUSIONS

1) The discrete element method was used to conduct a study on the interaction between soil-touching components and wheat straw-soil mixtures. For wheat straw-soil mixtures, the EDEM software was applied and the Hertz-Mindlin with JKR Cohesion contact model was selected for parameter calibration to lay the foundation for conducting research on seedbed preparation equipment in the Yellow and Huaihai regions.

2) The parameter calibration adopts the method of combining physical test and simulation test. The cylinder lifting method was used to measure the angle of repose of wheat straw-soil mixture. Using Plackett-Burman screening method and steepest climbing test, the optimal combination range of soil-straw static friction coefficient, soil-straw dynamic friction coefficient and soil-soil dynamic friction coefficient contact model parameters was determined. Using box Behnken test, the regression equation of angle of repose of wheat straw-soil mixture was obtained, and the variance and interaction effect of the regression model were analysed.

3) Using the parameter optimization module in design expert software, aiming at the accumulation angle of 41.23°, the optimal solution is found through the regression model. The soil-straw static friction coefficient is 0.072, the soil-straw dynamic friction coefficient is 0.78, the soil-soil dynamic friction coefficient is 0.068, and the accumulation angle error is 1.43%, indicating that the parameters of the contact model are relatively reliable.

REFERENCES

[1]   Feng J., Lin J., Li S., Zhou J., Zhou Z., (2015), Calibration of discrete element parameters of particle in rotary solid-state fermenter (秸秆固态发酵回转筒内颗粒混合状态离散元参数标定). *Transactions of the Chinese Society of Agricultural Machinery*, Vol. 46, Issue 3, pp. 208-213.

[2]   Guo J., (2017), *Study on operation performance of straw returning machine sawtooth knife and rotary tillage knife (秸秆还田机—锯齿刀和旋耕刀作业性能研究)*, Nanjing Agricultural University.

[3]   Han L.H., Elliott J.A., Bentham A.C., Mills A., Amidon G.E., Hancock B.C., (2008), *A modified Drucker-Prager Cap model for die compaction simulation of pharmaceutical powders*，Vol. 45，pp. 3088-3106.

[4]   Jia S.L., (2021), Simulation analysis and construction of maize seeder model based on EDEM (EM solutions EDEM). *INMATEH - Agricultural Engineering*, Vol. 63, Issue 1, pp. 365-374, Bucharest / Romania.

[5]   Joash B.A., Marolo A., Chen Y., Zeng Zh., (2021), Calibration of discrete element parameters of crop residues and their interfaces with soil. *Computers and Electronics in Agriculture*, 188.

[6]   Li J., Tong J., Hu B., Wang H., Mao Ch., (2019), Ma Yunhai Discrete element simulation parameter calibration of the interaction between clayey black soil with different moisture content and soil contacting parts (不同含水率黏重黑土与触土部件互作的离散元仿真参数标定). *Transactions of the Chinese Society of Agricultural Engineering*, Vol. 35, Issue 6, pp. 130-140.

[7]   Liu F., (2020), Analysis and calibration of quinoa grain parameters used in a discrete element method based on the repose angle of the particle heap. *INMATEH - Agricultural Engineering*, Vol. 61, Issue 2, pp. 77-86, Bucharest/Romania;

[8]   Liu F., Zhang J., Li B., Chen J., (2016), Calibration of parameters of wheat required in discrete element method simulation based on repose angle of particle heap (基于堆积试验的小麦离散元参数分析及标定). *Transactions of the Chinese Society of Agricultural Engineering*, Vol. 32, Issue 12, pp. 247-253.

[9]   Qi L., Chen Y., Mohammad S. (2019), Simulations of soil flow properties using the discrete element method (DEM). *Computers and Electronics in Agriculture*, 2019,157, pp. 254-260.

[10]   Sun J., Liu Q., Yang F., Liu Zh., Wang Zh., (2022), Calibration of Discrete Element Simulation Parameters of Sloping Soil on the Loess Plateau and Its Interaction with Rotary Tillage Components (黄土高原坡地土壤与旋耕部件互作离散元仿真参数标定). *Transactions of the Chinese Society of Agricultural Machinery*, Vol. 53, Issue 1, pp. 63-73.

[11]   Tian X., Cong X., Qi J., Guo H., Li M., Fan X., (2021), Parameter Calibration of Discrete Element Model for Corn Straw－Soil Mixture in Black Soil Areas (黑土区玉米秸秆-土壤混料离散元模型参数标定). *Transactions of the Chinese Society of Agricultural Machinery*, Vol. 52, Issue 10, pp. 100-108+242.

[12]   Wang W., Cai D., Xie J., Zhang Ch., Liu L., Chen L., (2021), Parameters Calibration of Discrete Element Model for Corn Stalk Powder Compression Simulation (玉米秸秆粉料致密成型离散元模型参数标定). *Transactions of the Chinese Society of Agricultural Machinery*, Vol. 52, Issue 3, pp. 127-134.

[13]   Wang X., Zhang S., Pan H., Zheng Zh., Huang Y., Ruixiang Zhu, (2019), Effect of soil particle size on soil-subsoiler interactions using the discrete element method simulations. *Biosystems Engineering*, 182, pp. 138-150.

[14]   Zeng F., Li X., Zhang Y., Zhao Z., Cheng C., (2021), Using the discrete element method to analyse and calibrate a model for the interaction between a planting device and soil particles. *INMATEH - Agricultural Engineering*, Vol. 63, Issue 1, pp. 413-424, Bucharest / Romania.

[15]   Zhang T., Liu F., Zhao M., Ma Q., Wang W., Fan Q., Yan P., (2018), Determination of corn stalk contact parameters and calibration of Discrete Element Method simulation (玉米秸秆接触物理参数测定与离散元仿真标定). *Journal of China Agricultural University*, Vol. 23, Issue 4, pp.120-127.

[16]   Zhou H., Chen Y., Mohammad A. S., (2014), Modelling of soil-seed contact using the Discrete Element Method (DEM). *Biosystems Engineering*, 121, pp. 56-66.

RESEARCH ON THE VALIDATION OF MATHEMATICAL MODELS FOR BIOMASS POWDER COMPACTION USING A RING DIE PELLETING EQUIPMENT
/
CERCETĂRI PRIVIND VALIDAREA MODELELOR MATEMATICE PENTRU COMPACTAREA PULBERILOR DE BIOMASĂ UTILIZÂND UN ECHIPAMENT DE PELETIZARE CU MATRIȚĂ INELARĂ

Iuliana GĂGEANU, Dan CUJBESCU *), Cătălin PERSU, Gabriel GHEORGHE
National Institute of Research – Development for Machines and Installations Designed
for Agriculture and Food Industry – INMA Bucharest / Romania
E-mail: dcujbescu@yahoo.com
DOI: https://doi.org/10.35633/inmateh-66-21

ABSTRACT

The paper presents the experimental validation of two mathematical models describing biomass powders compaction (a model that expresses the final density of pellets as determined by the final pressure applied during the process, the initial material moisture and the initial density of the material, but also a mathematical model obtained through dimensional analysis, using Π theorem, expressing the density of pellets as determined by pressure, heat, the initial density of the material, the pelleting speed of and the initial volume of the material), through experimental researches using a ring die pelleting equipment. The results showed a strong correlation between the data estimated theoretically and the experimental data, but also a strong influence of biomass material initial moisture on the density of the pellets obtained.

REZUMAT

Articolul prezintă validarea experimentală a două modele matematice care descriu compactarea pulberilor de biomasă, (un model matematic ce exprimă densitatea finală a peletelor ca fiind determinată de către presiunea finală aplicată în timpul procesului, umiditatea inițială a materialului și densitatea inițială a materialului, dar și un model matematic obținut prin analiză dimensională, utilizând teorema Π, care exprimă densitatea peletelor ca fiind determinată de presiune, căldură, densitatea inițială a materialului, viteza de peletizare și volumul inițial al materialului), prin cercetări experimentale pe un echipament de peletizat cu matriță inelară. Rezultatele au arătat o corelare foarte bună a datelor estimate teoretic cu cele experimentale, dar și o puternică influență a umidității inițiale a materialului din biomasă asupra densității peletelor obținute.

INTRODUCTION

Currently, researches in the field of obtaining solid biofuels is a major concern in the field of mechanical engineering, whose main aim is to optimize the densification processes, improve the quality of biomass products, minimize costs, increase the yields of compression equipment, as well as contribute to the protection of the environment (*Anukam et al., 2021; Gilvari et al., 2021, Golub et al., 2020*).

In order to obtain solid biofuels with adequate density and durability, there must be a very good correlation between the physical-chemical properties of the biomass used as raw material (particle size, material moisture) and the characteristics of the pelleting equipment (type of die, size of orifices, type of material drive, pelleting speed, etc.). Pellets can be formed by compacting particles by force using pressure, when the particles join together with or without the use of binders (*Celik, 2016; Lisowski et al., 2020; Serrano et al., 2011*).

Agricultural and lignocellulosic biomass compaction or densification in the form of pellets is an essential process for obtaining biofuels. It was found by various researchers that grinded biomass particles behave in a different manner when various forces are applied (*Agar et al., 2018; Andreiko and Grochowicz, 2007).* Therefore, it is important to investigate the changes in the density and volume of the material when applying pressure. Theoretical and experimental researches in the field of biomass pelleting aim to increase the quality of the finished products, correlated with the decrease of the costs and the impact on the environment (*Garcia-Maraver et al., 2015; Lisowski et al., 2019; Welker et al., 2015*).

It was found (*Ndiema et al., 2002*) that by applying high pressures and temperatures during densification, solid bridges can develop by diffusing molecules from one particle to another at points of contact, thus increasing the density.

Related to the influence of biomass on the pelleting process, researchers (*Frodeson et al., 2019*) have found that pellets have poor quality in terms of both density and durability when using biomass with a very low initial moisture (2%, 4 %) but also in the case of high initial moisture (14 %, 16%). Demirbas A. and Dermibas A.S. (*Demirbas and Dermibas, 2004*) found that by increasing the moisture content from 7 to 15% in spruce sawdust, the durability of compressed biomass increased significantly. Mani, Tabil and Sokhansanj (*Mani et al. 2006*), in their paper on the densification of corn stalks, found that low material moisture (5-10%) led to more stable, denser, but also more durable briquettes.

Studying the effect compaction force on pellet density, using forces of 6kN, 12 kN, 16 kN and 20 kN, authors of paper (*Poddar et al., 2014*) determined that pellet density gradually increased for samples obtained increasing compaction force.

One of the most important reasons for putting the experimental data into a compression model (equation) is to generate diagrams that make their comparison easier. Compression models help show the behaviour of powder biomass particles during the compression (pelleting) process and can help optimize the parameters needed to obtain good quality pellet (*Comoglu, T., 2007*).

In order to be able to determine the influence of the disturbing factors on the pelleting process, which ultimately lead to decreases in the quality of the obtained products or even to the blocking of the equipment, a series of experimental determinations must be made with the variation of these disturbing factors.

The paper presents the validation of two mathematical models for the densification of powder biomass with experimental data obtained using ring die pelleting equipment.

MATERIALS AND METHODS

Taking into account the parameters that have influence on the pelleting process (Table 1) on ring die pelleting equipment, two mathematical models are proposed to express the density of pellets.

Table 1

Parameters of the pelleting process taken into account in the analysis

Parameter	Name	Notation	Measurement unit	Physical dimension
1	Quantity of heat	Q	kg m^2/s^2	ML^2T^{-2}
2	Compression pressure	p	N/m^2	$ML^{-1}T^{-2}$
3	Initial material moisture	U_i	%	-
4	Pellet density	ρ_p	kg/m^3	ML^{-3}
6	Volumetric mass of raw material	ρ_0	kg/m^3	ML^{-3}
7	Initial volume of the raw material	V_0	m^3	L^3
8	Pelleting speed	v	m/s	LT^{-1}

The first model used for experimental validation is based on the determination of pellet density as a function of the pressure applied to the biomass, but takes into account the correction factor that takes into consideration the moisture of the raw material.

The proposed formula is presented in relation (1).

$$\rho_p(\rho_0, p, U_i) = a \times \rho_0 \left(\frac{p}{p_0}\right)^b \times U_i^{\,c} \tag{1}$$

where: a, b and c are model parameters, [dimensionless];

p_0 is the atmospheric pressure, [MPa];

p - compression pressure, [kPa];

$$p = \frac{4F_{max}}{\pi d^2} \tag{2}$$

F_{max} – force applied to the raw material, [kN];

d - diameter of the die, [m].

The second model represents a more complex version, taking into account both the moisture of the raw material and the temperature of the die during the pelleting process, and it was obtained using the Buckingham theory (*Buckingham, 1914*). The model obtained is given in formula (3):

$$\rho_p(\rho_0, p, U_i) = \rho_0 \left(\frac{Q}{\rho_0 \cdot v^2 \cdot V_0}\right)^a \left(\frac{p}{p_0}\right)^b \times U_i^c. \tag{3}$$

In the model in relation (3), the control parameter represented by the temperature of the die was introduced in a dimensionless factor considering the temperature as having an energetic nature (quantity of heat), in the second factor of the right member, which rises to the power of *a*.

In order to validate the proposed mathematical models, experimental tests were conducted for pelletizing fir sawdust using a pelletizing press with a fixed ring (cylindrical) die with 8 mm pelleting orifices and two pressing rollers (fig. 1), in which biomass was introduced at the top, the actual pelleting process being performed at the point of contact between the pressing rollers and the die.

The pelleting equipment with fixed ring die (having compression orifices with a diameter of 8 mm) and press rollers driven by a rotor shaft is an equipment designed to obtain pellets that can be used in installations for the production of heat and domestic hot water, for small and medium-sized farms, as well as for households, with the aim of ensuring energy independence.

The mass of material (sawdust) from grinded solid biomass is introduced into the hopper of the equipment, from there being transported inside the press by an auger. The pellets are discharged at the bottom of the equipment, just below the die.

Fig. 1 - Ring die pelleting equipment used for experiments
1. material hopper; 2. pellet cutting blade motor; pelleting equipment casing;
4. feed hopper motor; 5. control panel; 6. pelleting equipment main motor

The material used for experiments was represented by fir tree sawdust. To ensure an even distribution of particles, the sawdust was sieved using a Retsch AS 200 sieving equipment, and only sawdust with sizes smaller than 2 mm was used.

Using the pelleting equipment, the pellets from fir sawdust were obtained using the following methodology:

1. The initial moisture of the raw material was determined using the thermal balance.

2. The required quantity (10 kg for each sample) to be introduced into the pelleting equipment was measured using a balance.

3. The pellet casing and blade for cutting the pellets were demounted to allow the force measurement dose to be mounted on the ring die and a material feed funnel was fitted;

4. The force gauge was mounted on the cylindrical die in order to measure the compressive force and then to calculate the pelletizing pressure by reference to the diameter of the die.

5. the dose was connected to a data acquisition system (MGCPlus – HBM, Germany), that in turn was connected to a computer in order to record the data;

6. The actual pelleting process was conducted using the pelleting equipment;

7. The size of 40 pellets in each pellet sample was measured.

8. Those 40 pellets from each sample were weighed for further determination of density.
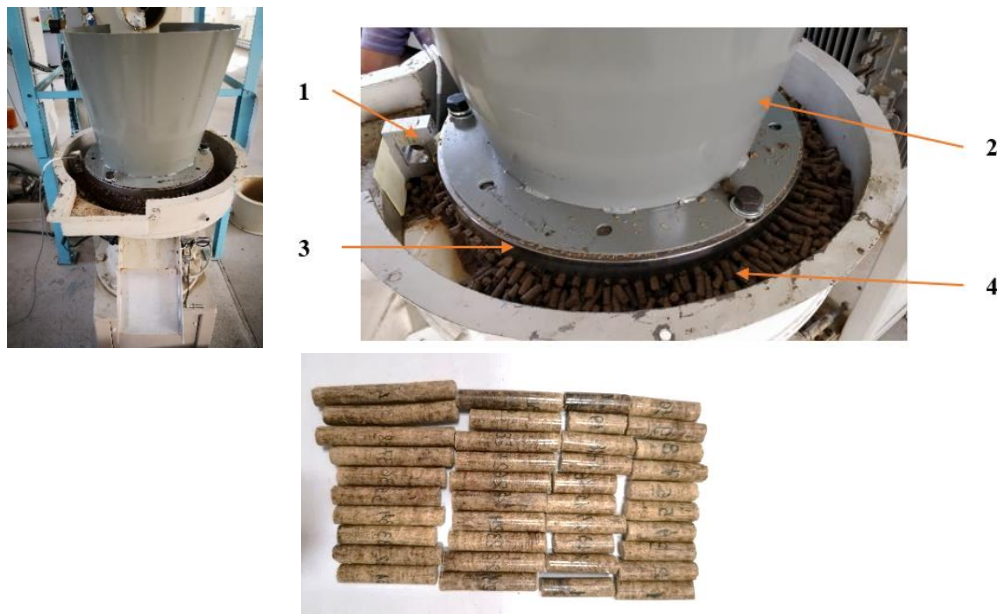
Fig. 2 - Aspects during the experiments using the ring die equipment
1. force gauge; 2. material feed funnel; 3. pelleting die; 4. Pellets

A number of 6 samples (2 samples for the three raw material moistures used: 10%, 13% and 16%) were obtained from fir tree sawdust. The three moistures were obtained by either drying the biomass sawdust in the oven or watering and thoroughly mixing the material.

RESULTS

During the experiments, the following compression pressures were recorded: 107 MPa for experiments conducted using biomass material with 10% and 13% initial moisture and 105 MPa for experiments conducted using material with 16% initial moisture.

Following the experimental researches on the pelleting equipment with fixed ring die and the measurements and density calculations, the following results were obtained, presented in tables 2 - 4.

Table 2

Results obtained after conducting the experimental researches for the initial moisture of 10%

Sample	ρ_p kg/m^3	Sample	ρ_p kg/m^3	Sample	ρ_p kg/m^3	Sample	ρ_p kg/m^3
1	1074.38	11	1145.12	21	1178.37	31	1152.13
2	1123.98	12	1121.47	22	1147.93	32	1198.78
3	1184.52	13	1152.32	23	1109.74	33	1138.29
4	1147.48	14	1147.81	24	1142.11	34	1183.09
5	1082.13	15	1141.16	25	1098.00	35	1149.33
6	1063.95	16	1083.19	26	1148.54	36	1161.95
7	1104.84	17	1142.30	27	1139.52	37	1150.21
8	1081.56	18	1108.22	28	1110.12	38	1123.18
9	1112.74	19	1074.85	29	1097.44	39	1141.04
10	1142.89	20	1156.08	30	1189.91	40	1139.90

Table 3
(continuation)

Sample	ρ_p kg/m³	Sample	ρ_p kg/m³	Sample	ρ_p kg/m³	Sample	ρ_p kg/m³
1	1054.36	11	1076.42	21	1050.85	31	1087.29
2	1081.22	12	1055.38	22	1071.35	32	1127.86
3	1131.65	13	1061.23	23	1058.52	33	1084.18
4	1115.34	14	1065.50	24	1088.11	34	1116.16
5	1026.61	15	1068.50	25	1022.91	35	1084.29
6	995.69	16	1035.08	26	1079.73	36	1086.56
7	1054.88	17	1073.84	27	1072.83	37	1057.42
8	1025.51	18	1042.62	28	1037.97	38	1046.16
9	1050.76	19	954.70	29	1035.55	39	1069.40
10	1085.66	20	1080.52	30	1127.15	40	1060.46

Table 4

Results obtained after conducting the experimental researches for the initial moisture of 16%

Sample	ρ_p kg/m³	Sample	ρ_p kg/m³	Sample	ρ_p kg/m³	Sample	ρ_p kg/m³
1	877.31	11	883.94	21	888.93	31	904.33
2	878.85	12	914.85	22	907.83	32	903.63
3	901.85	13	878.48	23	898.29	33	893.84
4	901.20	14	875.92	24	900.47	34	889.25
5	902.85	15	884.28	25	910.78	35	897.43
6	910.72	16	901.87	26	886.71	36	901.72
7	904.28	17	907.20	27	917.24	37	884.62
8	909.75	18	889.84	28	879.39	38	871.59
9	891.28	19	885.40	29	888.86	39	893.74
10	907.28	20	864.96	30	894.62	40	905.70

From tables 2-4, it can be noted that pellet density decreases as the moisture of the raw material increases, from an average density of 1132.26 kg/m³ for a 10% material moisture, to 1065.01 kg/m³ for the 13% material moisture and dropping down to 894.78 for the 16% material moisture.

Following the experimental research, the theoretical data resulting from the models described in relations (1) and (3) were calculated for the input and control parameters of the pelleting process on the ring die equipment. Figure 3 shows a graphical comparison between the experimental data and the data calculated using relation (1).
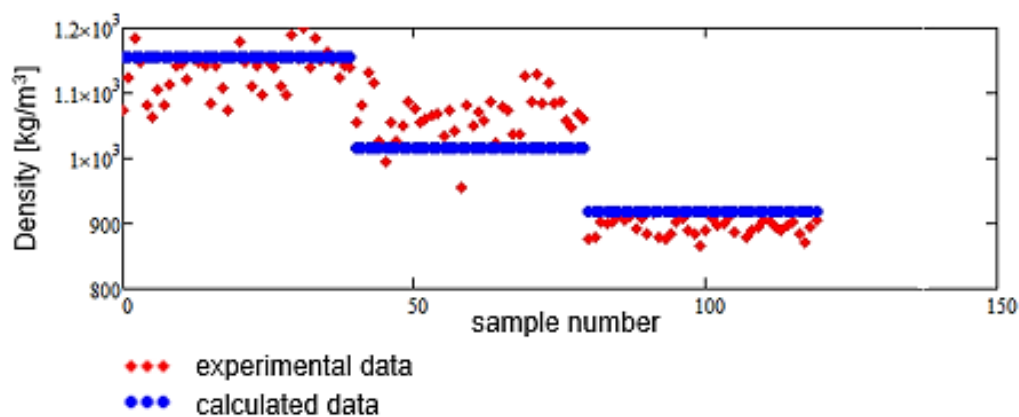
Fig. 3 – Comparative graphical representation of the experimental data obtained with the pelleting equipment and of the data calculated using relation (1)

From figure 3, a strong correlation can be observed between the data calculated using relation (1) and the experimental data.

Figure 4 shows the dependence of the pellet density on the input and control parameters for the model in relation (1).
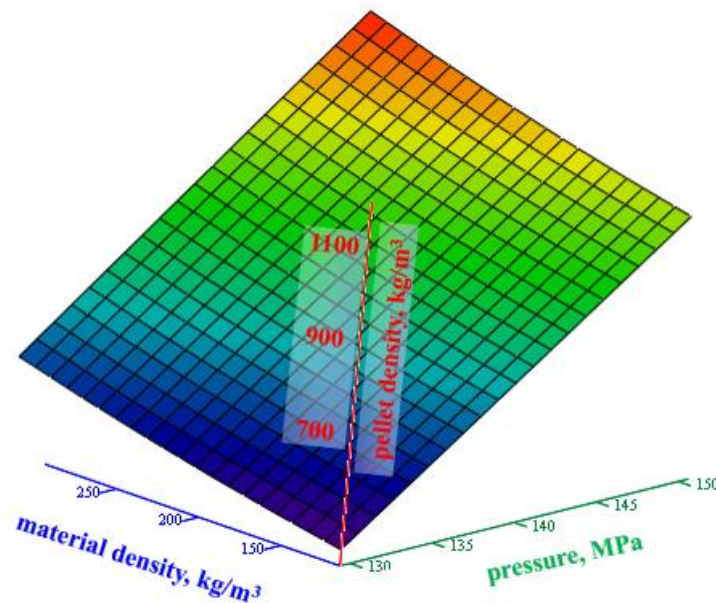
Fig. 4 - Dependence of pellet density on the maximum pressure and the density of the sawdust for the samples obtained using the ring die pelleting equipment for model (1)

The diagram shows that as the density increases (the initial moisture of the material increases), the density of the pellets decreases regardless of the value of the compression pressure.

Figure 5 shows a graphical comparison between the experimental data and the data calculated using relation (3).
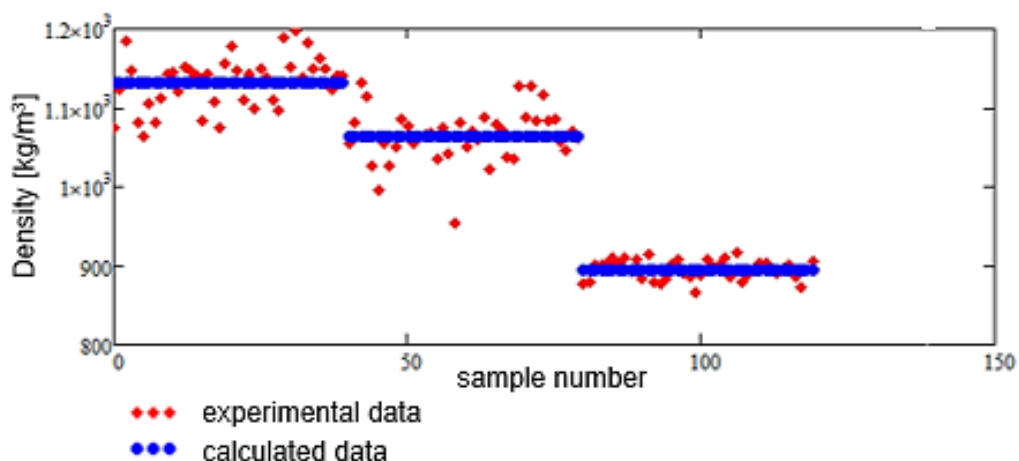
Fig. 5 - Comparative graphical representation of the experimental data obtained with the pelleting equipment and of the data calculated using relation (3)

From figure 5, an even stronger correlation can be observed between the data calculated using relation (3) and the experimental data, compared to results obtained for relation (1).

Figure 6 shows the dependence of the density of pellets on the compression pressure and the density of the raw material, for relation (3).
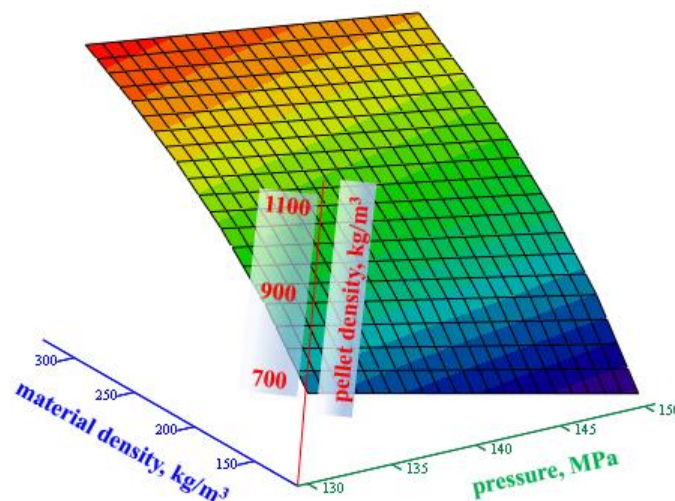
Fig. 6 - Dependence of pellet density on the maximum pressure and the density of the sawdust for the samples obtained using the ring die pelleting equipment for model (3)

The diagram shows, as in the case of the first model, that when the density increases, the density of the pellets decreases even at higher values of the compression pressure.

CONCLUSIONS

The densification of biomass depends on the complex interaction between the material properties and the parameters characteristic to the equipment used for densification. The mathematical models developed for the compaction process help to present the behaviour of the particles during the compaction process and can help optimize the parameters to obtain good quality products.

After conducting the experimental research and validating the two proposed mathematical models for the data obtained using the pelleting equipment with the fixed ring die, a strong correlation was found between the experimental data and the data estimated theoretically, $R = 0.911$ for model 1 and $R = 0.935$ for model 2.

An important conclusion found after conducting the experiments is that material moisture greatly influences pellet quality. Density decreased on average by 6 % for pellets obtained using material with 13% initial moisture compared to those obtained with material having 10% initial moisture and by almost 21% for pellets obtained from material with 16% initial moisture compared to the 10% initial moisture ones.

REFERENCES

[1]   Agar, D. A., Rudolfsson, M., Kaĺen, G., Campargue, M. (2018). A systematic study of ring-die pellet production from forest and agricultural biomass. *Fuel Process Technology 180*, 47–55

[2]   Andreiko, D., Grochowicz, J. (2007). Effect of moisture content on compression energy and strength characteristics of lupine briquettes. *Journal of Food Engineering*, *83*(1), 116-120

[3]   Anukam, A., Berghel, J., Henrikson, G., Frodeson, S., Stahl, M. (2021). A review of the mechanism of bonding in densified biomass pellets, *Renewable and Sustainable Energy Reviews 148*, 111249, https://doi.org/10.1016/j.rser.2021.111249

[4]   Buckingham, E. (1914). On physically similar systems. Illustrations of the use of dimensional equations. *Physical Review, 4*, 345 – 376

[5]   Celik, M. (2016), Pharmaceutical Powder Compaction Technology, *Drugs and Pharmaceutical Sciences, vol. 197*, ISBN-13: 978-1420089172

[6]   Çomoğlu, T. (2007). An Overview of Compaction Equations, *Journal of the Faculty of Pharmacy 36*(2), Ankara, 123-133

[7]   Demirbas, A., Demirbas, A.S. (200). Briquetting properties of biomass waste materials, *Energy Sources, 26*, 83–91

[8]   Frodeson, S., Henrikssonb, G., Berghela, J. (2019). Effects of moisture content during densification of biomass pellets, focusing on polysaccharide substances, *Biomass and Bioenergy, 122*, 322–330

[9]   Garcia-Maraver, A., Rodriguez, M.L., Serrano-Bernardo, F., Diaz, L.F., Zamorano, M. (2015). Factors affecting the quality of pellets made from residual biomass of olive trees. *Fuel Process. Technol. 129*, 1–7, http://dx.doi.org/10.1016/j.fuproc.2014.08.018

[10]   Gilvari, H., van Battum, C., van Dijk, S.A., de Jong, W., Schott, D.L. (2021). Large-scale transportation and storage of wood pellets: Investigation of the change in physical properties. *Particuology 57*, 146-156, https://doi.org/10.1016/j.partic.2020.12.006

[11]   Golub, G., Kukharets, S., Cesna, J., Yaroch, Y., Kukharets, M. (2020). Research on changes in biomass during gasification, *INMATEH–Agricultural Engineering Journal, Vol. 61*, No. 2/2020, 17-24, DOI: https://doi.org/10.35633/inmateh-61-02

[12]   Lisowski, A., Pajor, M., Świętochowski, A., Dabrowska, M., Klonowski, J., Mieszkalski, L., Ekielski, A., Stasiak, M., Piatek, M. (2019). Effect of moisture content, temperature, and die thickness on the compaction process and the density and strength of walnut shell pellets. *Renewable Energy, 141*, 770–781, https://doi.org/10.1016/j.renene.2019.04.050

[13]   Lisowski, A., Matkowski, P., Dąbrowska, M., Piątek, M.., Świętochowski, A., Klonowski, J., Mieszkalski, L., Reshetiuk, V. (2020). Particle Size Distribution and Physicochemical Properties of Pellets Made of Straw, Hay, and Their Blends. *Waste Biomass Valorisation, 11*, 63–75. https://doi.org/10.1007/s12649-018-0458-8

[14]   Mani, S., Tabil, L. G., Sokhansanj, S. (2006) Specific Energy Requirement for Compacting Corn Stover, *Bioresource Technology, 97*, 1420–1426

[15]   Ndiema, C.K.W., Manga, P.N., Ruttoh C.R. (2002). Influence of Die Pressure on Relaxation Characteristics of Briquetted Biomass, *Energy Conversion and Management, 43*, pp. 2157–2161

[16]   Poddar, S., Kamruzzaman, M., Sujan, S.M.A., Hossain, M., Jamal, M.S., Gafur, M.A., Khanam, M. (2014). Effect of compression pressure on lignocellulosic biomass pellet to improve fuel properties: Higher heating value, *Fuel 131*, 43–48

[17]   Serrano, C., Monedero E., Lapuerta M., Poertero H. (2011). Effect of moisture content, particle size and pine addition on quality of barley straw pellets. *Fuel Processing Technology 92*(3), 699-706

[18]   Welker, C.M., Balasubramanian, V.K., Petti, C., Rai, K. M., DeBolt, S., Mendu, V. (2015). Engineering Plant Biomass Lignin Content and Composition for Biofuels and Bioproducts, *Energies, 8*(8), 7654-7676, https://doi.org/10.3390/en8087654

OPTIMUM DESIGN OF SEED HOLDING RING OF VERTICAL DISC SEED-METERING DEVICE
/
垂直圆盘排种器护种环的优化设计

Yajun ZHUANG[1]); Jie HAN[1]); Zeqi LIU[1]); Meng ZHANG[1]); Zheng ZHANG[1]); Yubin LAN[1,2]); Yulong CHEN [*1,3) 1]
[1]) School of Agricultural Engineering and Food Science, Shandong University of Technology, Zibo 255000, China;
[2]) Shandong Provincial Collaborative Innovation Center of Dry-farming Intelligent Agricultural Equipment, Zibo, China;
[3]) Research of Institute of Ecological Unmanned Farm, Shandong University of Technology, Zibo 255000, China
Tel: +86 15315206471; E-mail: 1097402292 @qq.com

Keywords: seed metering device, vertical disc, seed holding ring, filling performance

ABSTRACT

In this paper, the vertical disk mechanical seed-metering device is taken as the object to optimize the design of seed holding ring. The laboratory test is carried out with seed-metering test bench and high-speed camera system; and the influence law of starting and ending angle, front inclination angle and flexible buffer of seed holding ring on the seed filling performance is studied. The ending angle of seed holding ring shall be consistent with seed throwing angle of seed-metering device, and the starting angle of seed holding ring has a significant effect on seed filling performance. The quality of fill index will first increase and then decrease, reaching the maximum at 35.7°; while miss fill index will first decrease and then increase, and the multiple fill index will be 0% when the starting angle is greater than 50°; and seed damage index will first decrease and then increase. In order to improve seed filling performance, the front end of seed holding ring is treated with inner chamfering. The larger the angle is, the lower the quality of fill index, the higher the multiple fill index and the lower the miss fill index, but the seed damage index will also increase. By setting a flexible buffer in the front end of seed holding ring, the seed damage index can be effectively reduced. When the buffer is 60 mm, the seed can be cleaned smoothingly, and the seed damage index will be 0%.

摘要

本文以垂直圆盘机械式排种器为对象，对护种环进行优化设计。利用排种试验台和高速摄像系统进行室内试验；研究护种环的起止角度、前端倾斜角度、柔性缓冲区对充种性能的影响规律。护种环的终止角与排种器的投种角保持一致，护种环的起始角对充种性能具有显著影响，充种合格率先增大后减小，在35.7°时达到最大，漏充率先减小后增大，当起始角大于50°时重充率为0%，破碎率先减小后增大。为了提高充种性能，对护种环前端进行内倒角处理，角度越大，充种合格率越低、重充率越高、漏充率越低，但是破碎率也会增高。通过在护种环前部设置柔性缓冲区，可以有效降低破碎率，缓冲区60mm 时，能够顺利清种，且种子破碎率为0%。

INTRODUCTION

Seed-metering device is the core component of seeder, and its performance has an important effect on seeding effect. At present, the pneumatic seed-metering device is adopted in the developed countries (*Cujbescu et al., 2019; St Jack et al., 2013*), including air suction type (*Yazgi et al., 2007*), air pressure type (*Yu et al., 2014*), air delivery type and other forms (*Correia et al., 2016; Dylan et al., 2013; Lei et al., 2021*). The pneumatic seed-metering device can adapt to high-speed operation with excellent performance and small seed damage (*Liao et al., 2018*), but the cost will be high; therefore, a large number of mechanical seed-metering devices is still used in some developing countries (*Ding et al., 2021; Shen et al., 2021; Yang et al., 2016*). The mechanical seed-metering device is low in cost, but high in the seed damage, and it is difficult to adapt to high-speed operation (*Yang et al., 2016*). According to the installation mode of planter plate and the seed filling direction, the mechanical seed-metering device can be divided into horizontal disc type (*Vianna et al., 2014*), inclined disc type, vertical disc type (*Liu et al., 2015*), spoon type, and other types of seed-metering device (*Wang et al., 2017*), among which the seeding operation of the spoon type and clamping type are mainly for corn, and the disc type is mainly for beans.

---

[1] *Yajun Zhuang, M.S. Stud. Eng.; Jie Han, M.S. Stud. Eng.; Zeqi Liu, M.S. Stud. Eng.; Meng Zhang, M.S. Stud. Eng.;*
Zheng Zhang, B.S. Stud. Eng.; Yubin Lan, Prof. Ph.D. Eng.; Yulong Chen, Lecture Ph.D. Eng.

The vertical disk seed-metering device is a mechanical seed-metering device used for sowing beans (*Chen et al., 2021; Liu et al., 2015*). A number of seed collection holes open to the side is distributed in the circumferential direction of planter plate. When the planter plate passes through the population in the rotation process, the seed collection operation is completed with the seed collection holes. However, when seeds are taken from population by seed collection hole, they cannot be guaranteed to stay in the seed collection hole under the action of its own gravity and external vibration; therefore, the seed holding ring needs to be provided, so that a closed space will be composed of seed holding ring and seed collection hole and the seeds can be kept in the seed collection hole. The seed holding ring plays an important role in the operation process of seed-metering device. In this paper, the optimal design will be conducted for its structure.

MATERIALS AND METHODS
Vertical disc metering device

The vertical disc seed-metering device consists of shell, disk, shaft, bearing, flange and seed holding ring which is installed inside the shell (Fig.1).

a. Structure of seed metering device   *b. Principle of seed metering device*
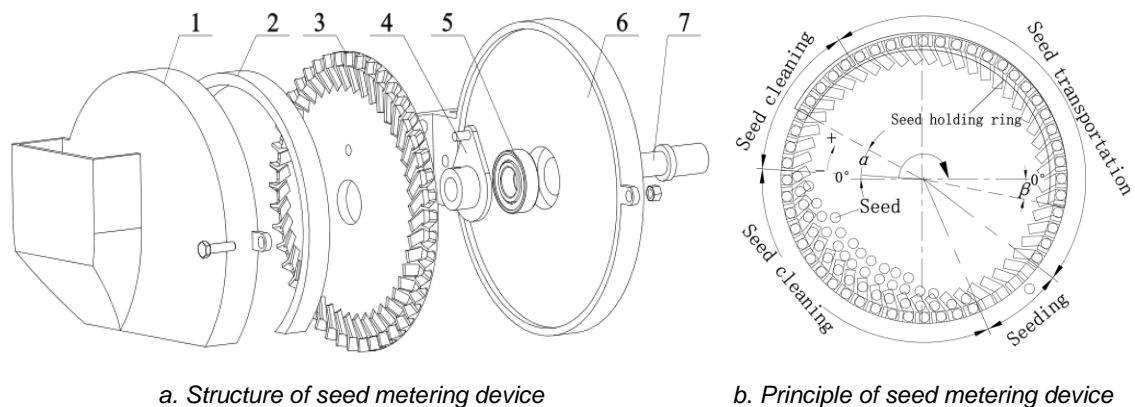
Fig. 1 - Structure and principle of vertical disc metering device
1. Shell; 2. Seed holding ring; 3. Disk; 4. Flange; 5. Bearing; 6. Base; 7. Shaft

The operation process of vertical-plate seed-metering device consists of four stages, i.e., seed filling stage, seed clearing stage, seed transportation stage and seed throwing stage. In the seed filling stage, the seeds will enter the seed collection hole by filling the space under the action of gravity and population internal force. In the seed clearing stage, the excess seeds will be removed by gravity before the seed collection hole reaches the seed holding ring. If there are still excess seeds in contact with the seed holding ring, the excess seeds will be removed continuously in the front end of the seed holding ring, but only one seed will be kept in the seed collection hole at last and it will enter into the coverage area of the seed holding ring. And then in the seed transportation stage, the seeds will move circularly after being kept in the seed collection hole under the protection of seed holding ring. At the seed throwing position, the seed holding ring disappears, so that the seed is no longer protected by the seed holding ring and will be thrown out under the action of gravity.
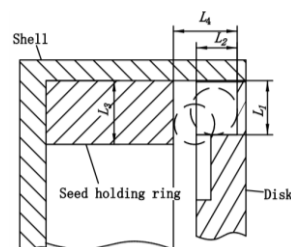
Fig. 2 - Schematic diagram of seed holding ring

In the previous study (*Chen et al., 2021; Jia et al., 2018*), the optimal experiment was carried out for the structural size of the seed collection hole, and the optimal length L_1 and thickness L_2 were 10.2 and 6.3 mm respectively. In order to ensure that the seeds would not fall off during seed transportation, the radial thickness L_3 of the seed holding ring should be larger than L_1, which is 12.0 mm in this paper, and the distance L_4 from the inner side of the seed holding ring to the bottom of seed collection hole should be within the range of d_{max} to $L_2+0.5d_{min}$, with L_4 of 10.0 mm in this paper.

The seed holding ring adopts PMMA processing and plays a role of seed holding and seed clearing at the same time, so that the starting angle of the seed holding ring has an important influence on the seed collection effect. The starting angle of seed holding ring is α, the horizontal negative direction is defined as 0°, and the clockwise direction is positive (Fig. 2); while the ending angle of seed holding ring is β, the horizontal positive direction is defined as 0°, and the clockwise direction is positive direction. The ending angle of the seed holding ring should cover the seed throwing position of the seed-metering device and be adjusted according to the seed throwing angle. After the previous test (*Chen et al., 2021; Jia et al., 2018*), the optimal seed throwing angle will be 39.5°, so that the ending angle of the seed holding ring is also 39.5°. In order to ensure that the seed clearing is smooth under the action of gravity and will not be slipped from the seed collection hole, the starting angle of seed holding ring should be as close as possible to the upper surface of the population, but space should be left for seed clearing under gravity at the same time. The starting angle of seed holding ring will be determined through experiments.

Prototype experiment

Laboratory bench test is a commonly used test method in the research process of seed-metering device (*Karayel et al., 2006; Zhang et al., 2015*). JPS-12 test bench for operation and performance of seed-metering device is used for laboratory test, and such test bench consists of the fixed device of seed-metering device, rotary conveyor belt and oil injection mechanism. During the test, the seed-metering device is fixed, but the conveyor belt moves, thus simulating the relative movement between the seed-metering device and the soil; meanwhile, oil is constantly sprayed to the conveyor belt to reduce the bouncing and displacement of seeds falling on the conveyor belt, so as to accurately detect the performance of the seed-metering device.
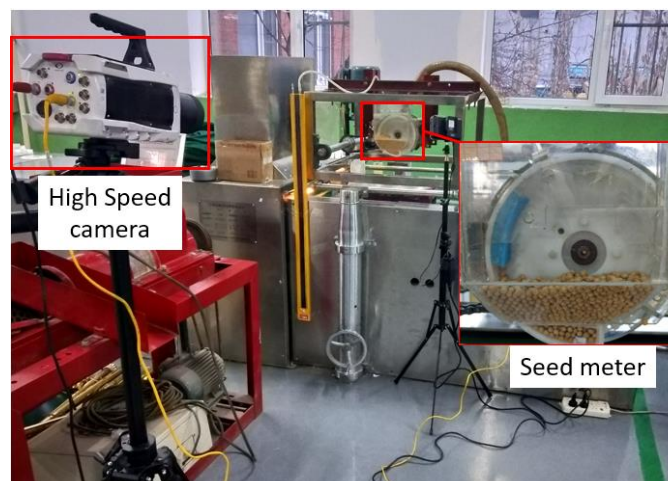
Fig. 3 - Physical prototype

In order to observe the instantaneous movement of seeds in the process of seed collection, a snapshot shall be made with a high-speed camera (Phantom V711) (*Karayel et al., 2006; Shen et al., 2021*), and the shooting frequency shall be set at 100 fps (Fig.3).

a. Front inclination of seed holding ring   *b. Flexible buffer zone of seed holding ring*
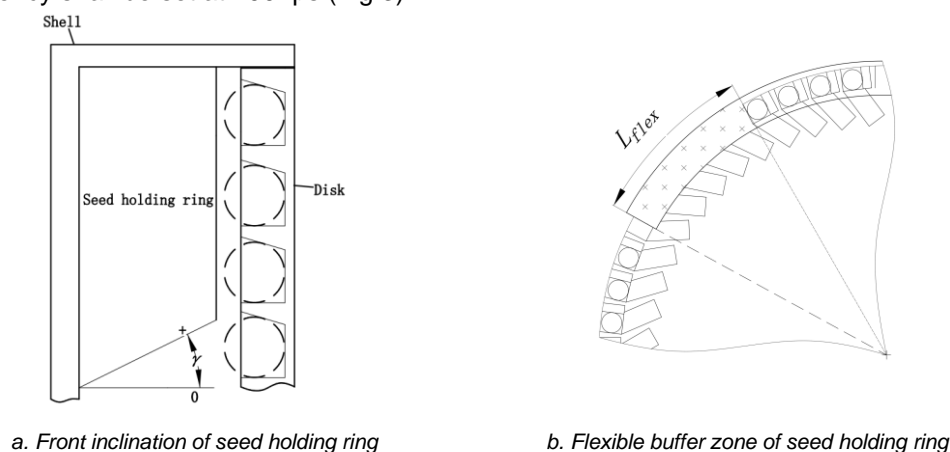
Fig. 4 - Experimental factors of seed holding ring

The experimental study shall be conducted for the starting angle α, the front inclination angle γ and the length L_{flex} of the flexible buffer of seed holding ring through bench test (Fig.4), and different test levels shall be designed respectively (Table 1).

Table 1

Factors and codes of orthogonal rotation combination test

Level	Factors		
	α [°]	γ [°]	L_{soft} [mm]
1	0	30	5
2	10	45	10
3	20	60	15
4	30	75	20
.	…		…
.	90		40

Evaluating indicator

According to GB/T 6973-2005 test methods for single seed (precision) planter, and JB/T10293-2001 Specification for single grain (precision) planter, 250 seeds were collected for statistics in each group of experiments, and the test was repeated for 3 times, and the seed metering performance evaluation indexes were *FA*, *FD*, *FM* and *P* (*Chen et al., 2021; Lei et al., 2021*).

$$FA = n_1 / N \times 100\% \tag{1}$$

$$FD = n_2 / N \times 100\% \tag{2}$$

$$FM = 100\% - FA - FD \tag{3}$$

$$P = m_1 / m_2 \times 100\% \tag{4}$$

Where：

n_1 is the number of seed holes containing only one seed in the test; n_2 is the number of seed holes containing more than one seed in the test; N is the total number of seed holes recorded in the test; m_1 is the weight of broken seeds; m_2 is the total mass of seeds discharged by seed metering device.

RESULTS AND ANALYSIS
Effect of initial angle of seed holding ring on seed filling performance

In order to make clear the effect of α on seed filling performance, α shall be set as 0°, 10°, 20°... 90°, and seed filling test shall be carried out at the forward speed of 4 km/h (Table 2).

Table 2

Effect of initial angle on seed filling performance

α [°]	Seed filling performance			
	FA [%]	*FD* [%]	*FM* [%]	*P* [%]
0	85.64	5.62	8.74	3.24
10	86.32	4.83	8.85	2.86
20	87.45	5.14	7.41	1.52
30	91.74	2.15	6.11	0.93
40	92.68	1.04	6.28	0.86
50	90.52	0	9.48	1.85
60	82.63	0	17.37	2.43
70	56.84	0	43.16	3.68
80	34.65	0	65.35	3.24
90	16.83	0	83.17	3.43

α has a significant effect on *FA*, and the change of *FA* is less obvious when the starting angle is from 0° to 20° When α is greater than 20°, *FA* increases gradually and reaches the maximum value, 92.68%, at 40°. When α is greater than 50°, *FA* decreases sharply, only 16.83% at 90°.

α has a significant effect on *FD*. With the increase of α, *FD* decreases gradually, and the maximum value of *FD* is 5.62% at 0°. When α is greater than 50°, multiple *FD* is 0.

α has a significant effect on *FM*. *FM* decreases gradually from 0° to 40°, reaching the minimum value, 6.11%, at 30°. When α is greater than 50°, *FM* increases greatly, reaching 83.17% at 90°.

α has a significant effect on *P*. With the increase of angle, *P* decreases first and then increases, and the minimum value is 0.86% at 40°. At 0° and 90°, *P* remains maximum value, 3.24% and 3.43%, respectively.

The high-speed camera shall be used to observe the process of seed damage. It is found that seed damage mainly occurs at the moment when seeds enter the seed holding ring, and the seeds are damaged under the extrusion between the seed collection hole and the front face of the seed holding ring; meanwhile, the enormous energy will be released, thus leading to the impact on the population and causing the failure of subsequent one or more seed collection holes to fill seeds successfully. Therefore, seed damage is often accompanied by miss fill (Fig.5).

a. Seed breaking   *b. Seed group impact diffusion*
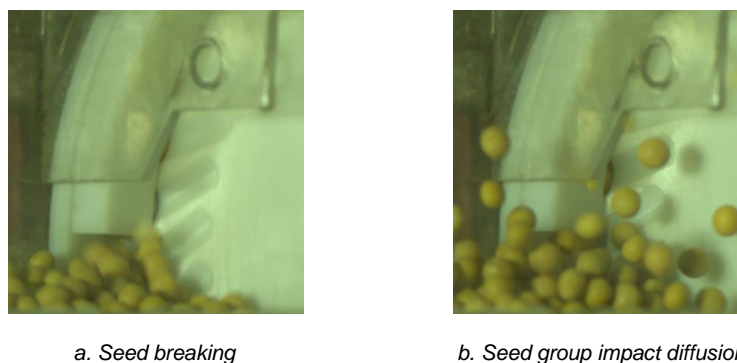
Fig. 5 - High speed camera picture of seed filling process

After excluding the data when α is 0° and 10°, regression analysis on the remaining data shows that the regression equation between *FA* and *α* is:

$$y = -0.027x^2 + 1.95x + 59.51, R^2 = 0.98 \qquad (5)$$

Derivation of equation (5) shows that *α* at the maximum of *FA* is 35.7°. For convenience of design, *α* is set to 36° thereafter.

Effect of front-end inclination on seed filling performance

In order to reduce *P*, the front face of the seed holding ring is treated with inner chamfering, and the front inclination angle *γ* is set as 30°, 45°, 60° and 75° respectively. When the starting angle of seed filling is 36° and other conditions remain unchanged, the experiment shall be carried out again.

Table 3

Effect of front-end inclination on seed filling performance

γ [°]	Seed filling performance			
	FA [%]	*FD* [%]	*FM* [%]	*P* [%]
30	93.52	1.66	4.82	0.91
45	86.32	12.28	1.40	1.88
60	84.65	14.03	1.32	2.25
75	82.73	16.64	0.63	3.05

The test results (Table 3) shows that *FA* is not improved in the design of inner chamfering at the front end of seed holding ring. When *γ* is 30°, *FA* is only 89.62% at maximum, which is smaller than that without inner chamfering. Meanwhile, the size of *γ* has a significant effect on seed filling performance. With the increase of *γ*, the lower *FA*, the higher *FD*, the lower *FM*, and the higher *P* are.

a. Successful seed filling   a. Seed crushing
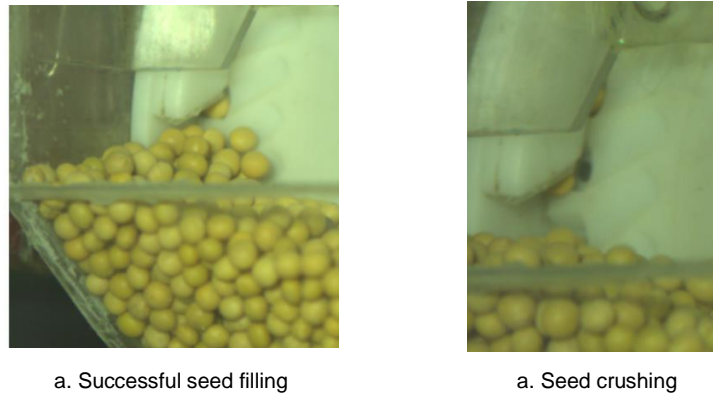
Fig. 6 - High speed photography of seed filling process when the front was tilted

After observation for seed filling process after chamfering on the front face of the seed holding ring through high-speed camera, it is found that the fill index is improved after chamfering treatment, and some cases of seed damage or miss fill under the original conditions are alleviated. Some seeds have been separated from the seed collection hole before contact with the seed holding ring, but with the help of the inclination angle, the seeds return to the seed collection hole, and the seed filling is successfully completed.

However, at high speed, there are still more damage phenomena. Through high-speed camera observation, it is found that when half or bigger part of a seed is separated from seed collection hole, seed extrusion will still occur during the contact between the seed and seed holding ring, and even deformation of seed-metering device will be caused.

In conclusion, it is impossible to improve seed filling performance by changing the front inclination angle of seed holding ring.

Effect of flexible buffer length on seed filling performance

Through high-speed camera observation, it is found that the seed damage index is increased by seed holding ring. The main reason for seed damage is that both planter plate and seed holding ring are rigid materials. When the seeds contact with the seed holding ring, extrusion can be easily occurred, so that seeds will be damaged. Therefore, the seed holding ring shall be replaced with flexible material, and polyester sponge shall be chosen as the replacement material.

Table 4

Effect of the length of flexible buffer on seed filling performance

L_{flex} [mm]	Seed filling performance			
	FA [%]	*FD* [%]	*FM* [%]	*P* [%]
5	88.45	7.82	3.73	1.54
10	91.65	5.07	3.28	0.96
15	94.24	1.25	4.51	0.51
20	95.88	0	4.12	0
25	96.56	0	3.44	0
30	97.02	0	2.98	0
35	96.68	0	3.32	0
40	96.88	0	3.12	0

Polyester sponge belongs to vulnerable and consumable material and should be used as less as possible. The extrusion collision between seed and seed holding ring mainly occurs at the edge of seed holding ring; therefore, polyester sponge shall only be set at the front end of seed holding ring as a buffer. The length of flexible buffer is L_{flex}, and the rest of seed holding ring shall still adopt PMMA material.

When the flexible material contacts with the seed, it will tilt and the effective thickness will decrease; therefore, the buffer thickness will increase by 4 mm compared with that of the original seed holding ring.

In order to study the influence of L_{flex} on seed filling performance, the test shall be carried out (Table 4) when the forward speed is 4 km/h, and L_{flex} is 5, 10, 15... 40 mm respectively.

The test results (Table 4) show that L_{flex} has a significant effect on FA. With the increase of L_{flex}, FA gradually increases. When L_{flex} is larger than 25 mm, *FA* gradually remains at about 96%.

L_{flex} has a significant effect on *FD*, and as L_{flex} increases, *FD* decreases gradually, reaching 0% after length is 20 mm.

L_{flex} has no significant effect on *FM* because *FM* has a little change when L_{flex} increases. By observing the seed filling process with high-speed camera, it is found that the miss fill occurs at the moment when the seed contacts with the buffer. No matter how L_{flex} changes, there is no change in contact state between the seed and buffer; therefore, there is no significant change in miss fill.

It is found through high-speed camera observation that seed clearing operation under gravity cannot be completed due to the participation of seed holding ring and buffer, and the buffer plays a role of seed clearing. Most of the excess seeds are removed at the moment when the seed contacts with the buffer, and a small portion of seeds enter the buffer and move forward with the seed collection hole. In this process, some of the excess seeds are separated from the side of buffer to complete seed clearing. The effect of seed clearing will be determined by the length of buffer. When L_{flex} is less than 20 mm, partial seeds cannot be separated from the side and move to the position of seed holding ring. At this time, two situations will occur; first, when the size of seed and excess seed in the seed collection hole is small, the two seeds enter the seed holding ring at the same time; second, when the size of the two seeds is large, the fierce collision will occur between excess seeds and the seed holding ring, resulting in seed damage. Therefore, L_{flex} has a significant effect on *FD* and *P*.

Table 5

Effect of speed on seeding performance with flexible buffer

Forward speed [km·h⁻¹]	Seed filling performance			
	FA [%]	*FD* [%]	*FM* [%]	*P* [%]
1	96.83	0	3.17	0
2	95.52	0	4.48	0
3	96.33	0	3.67	0
4	96.88	0	3.12	0
5	96.22	0	3.78	0
6	94.61	0	5.39	0
7	93.66	0	6.34	0
8	92.75	0	7.25	0
9	91.33	0	8.67	0
10	90.25	0.51	9.24	0.86
11	87.64	0.83	11.53	1.25
12	85.32	1.25	13.43	1.68

When α is 36° (including buffer) and L_{flex} is 40 mm, seed filling performance tests shall be carried out at speeds ranging from 1 to 12 km/h (Table 5).

The test results (Table 5) show that the forward speed has a significant effect on seed filling performance. When the forward speed is less than 4 km/h, the seed filling performance is not sensitive to the forward speed. When the forward speed is greater than 4 km/h, with the increase of speed, *FA* gradually decreases and *FM* gradually increases.

When the forward speed is less than 9 km/h, both FD and P are 0. When the forward speed is more than 10 km/h, FD and P gradually increase. It is found through high-speed camera observation that the clearing distance of seeds into the buffer increases with the increase of speed (Fig. 7). When the speed is greater than 10 km/h, the clearing distance is greater than 40 mm; therefore, the seeds cannot successfully escape from the buffer, thus leading to the multiple fill and damage phenomenon.
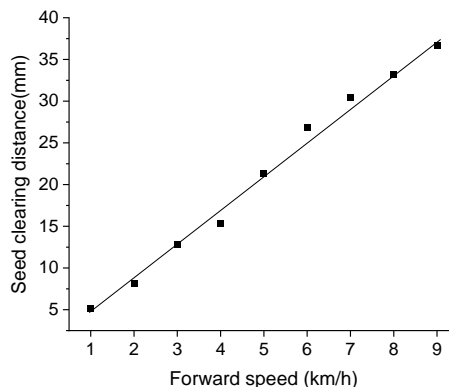
Fig. 7 - Effect of forward speed on seed clearing distance

Regression analysis is conducted on the forward speed and the distance of seed clearing, and the regression equation is obtained as,

$$y = 4.14x + 0.43, R^2 = 0.99 \tag{6}$$

According to the calculation of regression equation (6), when the forward speed is 12 km/h, the seed clearing distance is 50.1 mm. In order to ensure that the seed clearing can be completed, the buffer length is set to 60 mm for the verification test of seed filling performance.
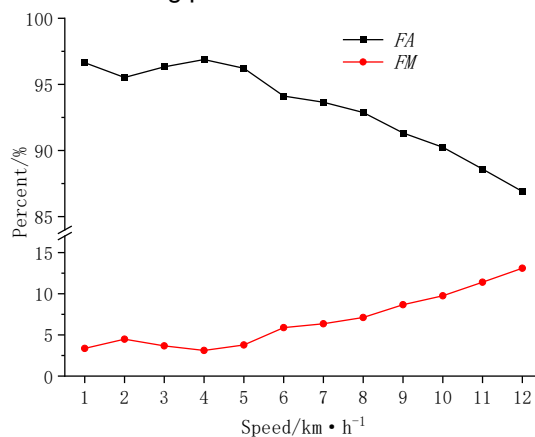
Fig. 8 – The result of verification experiment

The verification test results (Fig.8) show that the seed clearing effect is good when FD and P are reduced to zero after extending buffer. FA is further improved and FM is slightly decreased.

CONCLUSIONS

In this paper, the indoor seed-metering test bench and high-speed camera system are used to optimize the design of the seed holding ring of vertical-plate seed-metering device. With the seed filling performance as the evaluation index, the study on starting and ending angle, the front inclination angle and the flexible buffer is carried out.

(1) The starting angle of seed holding ring has a significant effect on seed filling performance. The regression equation shows that the best filling performance can be achieved when the starting angle is 35.7°, but the problem of high P always exists. The seeds are damaged under the extrusion between the seed collection hole and the front face of the seed holding ring, accompanied by the miss fill phenomenon.

(2) By setting the inner chamfer in the front section of seed holding ring, the seed filling performance is significantly affected. The higher γ is, the lower FA, higher FD and lower FM are. Although P is alleviated to a certain extent, it still fails to meet the qualified standard.

(3) In order to further reduce P, flexible buffer is added in the front section of seed holding ring. When L_{flex} is 60 mm, seed filling performance is better, and FD and P are 0%, which meets the requirements of precision seeding.

ACKNOWLEDGEMENT

REFERENCES

[1]   Chen, Y. L., Zhang, M., Liu, Z. Q., Lan Y. B., Yi, L. L., Peng, Q. J., & Yin, X. (2021), Design and experiment of seed agitator for vertical disk seed metering device, *INMATEH - Agricultural Engineering*, vol. 63, issue 1, pp. 179-188.

[2]   Correia, T., Sousa, S., Silva, P. & Patricia, P. (2016), Sowing performance by a metering mechanism of continuous flow in different slope conditions, *Engenharia Agrícola*, vol. 36, issue 5, pp. 839-845; 10.1590/1809-4430-Eng.Agric.v36n5p839-845/2016

[3]   Cujbescu, D., Matache, M., & Voicu, G. (2019), Mathematical model for sowing precision estimation of vacuum seed metering device, *UPB Scientific Bulletin, Series D: Mechanical Engineering*, vol. 81, issue 3, pp. 225-234.

[4]   Ding, Y., Wang, K., Liu, X., Liu, W., Chen, L., Liu, B. & Du, C. (2021), Research progress of seeding detection technology for medium and small size seeds, *Transactions of the CSAE,* vol. 37, issue 8, pp. 30-41;

[5]   Dylan, S. J., Hesterman, D. C., & Guzzomi, A. L. (2013) Precision metering of Santalum spicatum (Australian Sandalwood) seeds, *Biosystems Engineering*, vol. 115, issue 2, pp. 171-183; https://doi.org/10.1016/j.biosystemseng.2013.03.004

[6]   Jia, H. L., Chen, Y. L., Zhao, J. L., Wang, J. X., Guo, M. Z., & Zhuang, J. (2018), Design and Experiment of Pneumatic-mechanical Combined Precision Metering Device for Soybean, *Transactions of the CSAM*, vol. 49, issue 4, pp. 75-86+139.

[7]   Karayel, D., Wiesehoff, M., Ozmerzi, A., & Muller, J. (2006), Laboratory measurement of seed drill seed spacing and velocity of fall of seeds using high-speed camera system, *Computers and Electronics in Agriculture*, vol. 50, issue. 2, pp. 89-96; https://doi.org/10.1016/j.compag.2005.05.005

[8]   Lei, X. L., Hu, H. J., Wu W. C., Liu, H. N., Liu, L. Y., Yang, W. H., Zhou, Z. L., Ren, W. J., (2021), Seed motion characteristics and seeding performance of a centralized seed metering system for rapeseed investigated by DEM simulation and bench testing, *Biosystems Engineering*, vol. 203, pp. 22-33; https://doi.org/10.1016/j.biosystemseng. 2020.12.017.

[9]   Liao, Y. T., Liao, Q. X., Wang, L., Zheng, J., & Gao, L. P. (2018), Investigation on vacuum singulating effect influencing factors of pneumatic precision seed metering device for small particle size of seeds, *Transactions of the Chinese Society of Agricultural Engineering*, vol.34, issue 24, pp. 10-17; https://doi.org/ 10.11975/j.issn.1002-6819.2018.24.002

[10]   Liu, H. X., Guo, L. F., Fu, L. L., & Tang, S. F. (2015), Study on multi-size seed-metering device for vertical plate soybean precision planter, *International Journal of Agricultural and Biological Engineering*, vol. 8, issue 1, pp. 1-8; https://doi.org/10.3965/j.ijabe.20150801.001

[11]   Shen, H., Zhang, J. J., Chen, X. H., Dong, J. X., Huang, Y. X., Shi, J. T. (2021), Development of a guiding-groove precision metering device for high-speed planting of soybean, *Transactions of the ASABE*. vol. 64, issue 3, pp. 1113-1122. (doi: 10.13031/trans.14307)

[12]   Singh, R., Singh, G., & Saraswat, D. (2007), Design and operational parameters of a pneumatic seed metering device for planting of groundnut (Arachis hypogaea) seeds, *Indian Journal of Agricultural Sciences*, vol. 77, issue 1, pp. 40-42

[13]   St Jack, D., Hesterman, D. & Guzzomi, A. (2013) Precision metering of Santalum spicatum (Australian Sandalwood) seeds, *Biosystems Engineering*, vol. 115, issue 2, pp. 171-183; 10.1016/j.biosystemseng.2013.03.004

[14]   Vianna, L., Reis, A., & Machado, A. (2014), Development of a horizontal plate meter with double seed outlets, *Revista Brasileira de Engenharia Agricola e Ambiental-Agriambi*, vol. 18, issue 10, pp. 1086-1091; https://doi.org/10.1590/1807-1929/agriambi.v18n10p1086-1091

[15]   Wang, J. W., Tang, H., Wang, J. F., Li, X., & Huang, H. N. (2017), Optimization design and experiment on ripple surface type pickup finger of precision maize seed metering device, *International Journal of Agricultural and Biological Engineering*, vol. 10, issue 1, pp. 61-71; https://doi.org/10.3965/j.ijabe.20171001.2050

[16]   Yang, L., Yan, B., Yu, Y., He, X., Liu, Q., Liang, Zh., Yin, X., Cui, T., & Zhang, D. (2016), Global overview of research progress and development of precision maize planters, *International Journal of Agricultural and Biological Engineering*, vol. 9, issue 1, pp. 9-26

[17]   Yazgi, A., & Degirmencioglu, A. (2007), Optimization of the seed spacing uniformity performance of a vacuum-type precision seeder using response surface methodology, *Biosystems Engineering*, vol. 97, issue 3, pp. 347-356; https://doi.org/10.1016/j.biosystemseng.2007.03.013

[18]   Yu, J. J., Liao, Y. T., Cong, J. L., Yang, S., & Liao, Q. X. (2014), Simulation analysis and match experiment on negative and positive pressures of pneumatic precision metering device for rapeseed, *International Journal of Agricultural and Biological Engineering*, vol. 7, issue 3, pp. 1-12.

[19]   Zhang, G. Z., Zang, Y., Luo, X. W., Wang, Z. M., Zhang, Q., & Zhang, S. S. (2015), Design and indoor simulated experiment of pneumatic rice seed metering device), *International Journal of Agricultural and Biological Engineering*, vol. 8, issue 4, pp. 10-18; https://doi.org/10.3965/j.ijabe.20150804.1626

[20]   Zhao, Z., Li, Y., Chen, J., & Xu, L. (2010), Numerical analysis and laboratory testing of seed spacing uniformity performance for vacuum-cylinder precision seeder, *Biosystems Engineering*, vol. 106, issue 4, pp. 344-351; https://doi.org/10.1016/j.biosystemseng.2010.02.012

DESIGN, ANALYSIS AND TEST OF CLEANING MACHINE FOR GRAPEVINE COLD-PROOF SOIL

/

葡萄藤防寒土清土机设计、分析与试验

JiaXi ZHANG[*)], JinMing LI, YiChao WANG, MaoBo WANG, Peng ZHANG, ZhaoSen DONG, YunLong MA [1]

Xinjiang Agricultural University, School of Mechanical and Electrical Engineering, Urumqi/China;
Tel: 8613899961137; E-mail: 563810112 @qq.com

ABSTRACT

In order to address the problems of low efficiency and low degree of mechanization of artificial soil clearing of the grapevines in spring in Xinjiang grape growing regions, a grapevine cold-proof soil clearing machine was designed. The machine is mainly composed of a frame, gearbox, suspension device, soil clearing parts, hydraulic system and mechanical transmission system, etc. The motion track of the soil clearing parts was analyzed to obtain the key factors affecting the performance of the grapevine cold-proof soil clearing machine that were determined. The three-factor, three-level quadratic regression orthogonal experiment was carried out with the forward speed, soil clearing parts' diameter and rotation rate of soil clearing parts as factors and the soil clearing distance was used as evaluation index. The results showed that the order of influence on the soil clearing distance was rotation rate of soil clearing parts > forward speed> soil clearing parts diameter. The parameters were optimized based on response surface method with the following results: the rotation rate of soil clearing parts speed was 277.7 r/min, the forward speed was 3.5 km/h, and the soil clearing parts diameter was 681.7 mm. The validation experiment was carried out with the optimal parameters' combination. The soil clearing distance was 85.44 cm, which was consistent with the predicted results of the model. This research results can provide reference for the development of other types of grapevine soil clearing machine.

摘要

为了解决目前新疆葡萄种植区春季人工进行葡萄藤清土作业效率低、机械化程度低的问题。本文设计了葡萄防寒土清土机，主要由机架、齿轮箱、清土部件、液压系统、传动系统等组成。分析了清土部件运动轨迹，确定了影响葡萄防寒土清土机性能的关键因素。为确定葡萄防寒土清土机最佳工作参数组合，以前进速度、刷片直径、清土刷转速为试验因素，以清土距离为评价指标，开展了三因素三水平二次回归正交试验。结果表明，影响清土距离的主次顺序为：清土部件转速>前进速度>清土部件直径。基于响应面法进行参数优化，优化结果为：清土部件直径为 681.7mm，前进速度为 3.5km/h，清土部件转速为 277.7r/min。以优化后参数组合进行试验验证，结果为：清土距离为 85.77cm，与模型预测结果一致。本研究结果可为其他类型葡萄藤清土机的研制提供参考。

INTRODUCTION

Xinjiang is located in the northwestern part of China, there is plentiful of heat that benefits the growth of grape. Xinjiang is one of the largest grape planting areas in the China, and the grape growing areas cover a total of 146700 hm². Grape is mainly planted in Changji, Turpan, Tacheng. The grape industry has become an essential pillar for the economic development in Xinjiang *(Xu L.M. et al, 2019)*. Grapevines are vulnerable to damage at low temperatures. They will cause the grapevines to dry out and frostbite, affecting the growth and yield for the next year. There are some very good management measures that can help reducing the risk of incurring cold damage during the winter. Examples of such measures include: planting cold hardy cultivars in the respective cold hardiness adapted zones; delayed pruning; burying grapevines in soil etc. *(Yuan Q.C. et al, 2017; Wisniewski and Gusta, 2014)*.

The most commonly used method for protecting grapevines in Xinjiang is burying vines in soil, which is an efficient and environmentally friendly method, completely harmless to grapevines.

[1)]*Jiaxi Zhang,Prof.Ph.D.Eng.; Jinming Li, M.S.Stud. Eng.; Maobo Wang, M.S.Stud.Eng.; Yichao Wang, Ph.D. Stud. Eng.; Peng Zhang, M.S.Stud. Eng ; Zhaosen, Dong, M.S.Stud. Eng ; Yunlong Ma, M.S.Stud. Eng.*

Every winter, the grapevines need to be removed from the trellis and laid on the ground to be covered with soil, and soil must be cleared in spring *(Dami, Ennahli and Zhang, 2012)*. However, clearing grapevines cold-proof soil is an extremely labor-intensive and time-consuming operation, as most grapevines need to be cleared in time and it is necessary to avoid damaging grapevines during clearing. At present, the grapevines cold-proof soil clearing mainly depends on manual clearing, which costs a large amount of labor and has low efficiency. Therefore, it is necessary to develop a grapevine cold-proof soil clearing machine characterized by a compact structure, flexible operation, transfer convenience, low price, etc. thus being able to adapt to the trellis-type planting mode, and conform to the demands of farmers and the market. *(Xu L.M. et al, 2012; Bucur and Dejeu, 2016)*. Overseas, due to the mild and humid climate in winter, in foreign grape producing areas *(Molitor, Caffarra, Sinigoj. Etal, 2014)*, there is no need to perform cold-proof soil burying operation in winter and soil removing in spring *(Zabadal, Dami, Goffinet and Martinson, 2007)*. There are few references on grapevine cold-proof soil clearing in foreign countries *(Zhou W.B. et al, 2017)*. In order to improve the soil clearing efficiency, domestic scholars have done a lot of meaningful exploration and research on cold-proof soil clearing machine, which is a promising solution. For example, the rigid structure winter protection soil clearing machine was developed, the machine structure design is reasonable, the layout is compact, supposes low cost, easy operation and maintenance *(Zeng B.N. et al, 2013; Wang Z.Q et al, 2015)*. The grapevine soil clearing machine was designed, which realized semi-mechanized cleaning of cold-proof soils *(Zhang J.J. et al, 2015)*. The combined grapevine soil clearing machine was designed *(Xie D. et al, 2016; Liu S. et al, 2014; Xu L.M. et al, 2018)*. The layered-staggered structure was adopted in the form of a cross arrangement *(Ma S. et al, 2018)*; it can complete multiple operations simultaneously. The trellis-type grape winter buried soil clearing and cold-proof cloth recycling machine was developed *(Niu C. et al, 2019)*, which showed that operation efficiency of the machine was more than 10 times of the manual soil clearing efficiency. The automatic obstacle-avoiding grapevine cold-proof soil cleaner was designed *(Ma S. et al, 2020)*, which showed that the effects of the operation meet the requirements of automatic obstacle-avoiding grapevine cold-proof soil clearing. An automatic obstacle-avoid digging machine for grapevine was designed *(Liu F.J. et al, 2018)*, which showed that the volume of the cold-proof soil clearing was sufficient and the obstacle-avoiding effect was excellent.

In this paper, based on the research of the self-developed grapevine cold-proof soil clearing machine, the relationship between operating parameters of soil clearing parts and soil clearing quality is studied by taking soil clearing distance as the target and combining it with field trial. Firstly, the factors that have great impact on the soil clearing quality are find out: the forward speed, the rotation rate of soil clearing parts and the soil clearing parts' diameter. Then the response surface of soil clearing distance is established by three-factor three-level response surface test, and the response surface is analyzed to fit the quadratic regression curve and get the regression equation. The influence of each factor on the soil clearing quality evaluation index, as well as the best combination of parameters are researched in order to guide the field operation of grapevine cold-proof soil clearing machine and provide a reference for the design of grapevine cold-proof soil clearing machine.

MATERIALS AND METHODS
Overall structure

Aiming at the grape trellis-type planting mode in Xinjiang regions and meeting the design principles of a machine, a grapevine cold-proof soil clearing machine is studied and designed; it mainly consists of a frame, gearbox, soil clearing parts, suspension device, hydraulic system and mechanical transmission system, etc. The overall structure is shown in Figure 1, while the main performance indexes and technical parameters of the machine are shown in Table 1.

Table 1

Main technical parameters

Parameter	Value	Units
Overall dimension (length × width ×height)	1850×1200×750	mm
Tractor power	≥60	kW
Operation speed	3~5	Km/h
Operating width	800	mm
Driving form	Gearbox drive	-
Structure form	Three-point suspension	-
Number of working rows	1	-
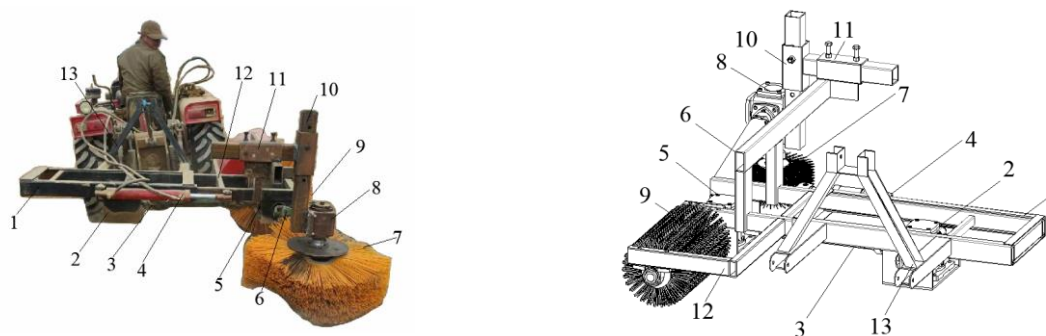
Fig. 1 - Schematic diagram of grapevine cold-proof soil clearing machine
1 – Fixed frame; 2 – Gearbox Ⅰ; 3 – Universal joint drive shaft Ⅰ; 4 – Hydraulic cylinder; 5 – Gearbox Ⅱ;
6 – Universal joint drive shaft Ⅱ; 7 – Soil clearing parts Ⅰ; 8 – Gearbox Ⅲ; 9 – Soil clearing parts Ⅱ;
10 – Longitudinal adjustment frame; 11 – Transverse regulating frame 12 – Mobile frame; 13 – Suspension device

Working principle

During the field operation, the power from the tractor power output shafts is transmitted to the soil clearing parts through the mechanical transmission system, to drive all working devices to finish the clearing of soil. Firstly, the height of the soil clearing device is adjusted by a hydraulic cylinder, as to make the machine height meet the operation requirements; then the clearing machine moves forward; the mechanical transmission system will drive the soil clearing parts to take rotation motion under the joint action of the forward speed and rotation rate of soil clearing parts; the soil clearing parts entered into the soil convey the soil to one side of the machine. After clearing, the clearing devices are raised off the ground, so that the mechanized soil clearing operation is completed.

Analyzing the movement of soil clearing parts, it was found out that there were three factors that affected the soil clearing of the grapevine cold-proof soil clearing machine: the mechanical structure parameters of the machine, the characteristics of the soil itself and the environmental factors. Under the influence of irresistible environmental factors and the mechanical properties of soil itself, this paper mainly studies the influence of the structural parameters of the machine on the law of cold-proof soil clearing to solve the problems appeared during practical work.

Trajectories analysis of front soil clearing brush

During the process of soil clearing, the machine moves forward at a certain speed under the tractor's traction. The movement of the soil clearing device is the combined motion of a uniform linear motion and uniform circular motion around the axis. The soil clearing velocity can also be schematically plotted as combination of forward speed and rotational speed, and the trajectories of soil clearing parts is shown in Figure 2(a). The soil is removed under the joint action of the forward speed v_0 and the soil clearing device linear speed v_t, forming the movement trajectories on the ground that are shown in Figure 2(b).
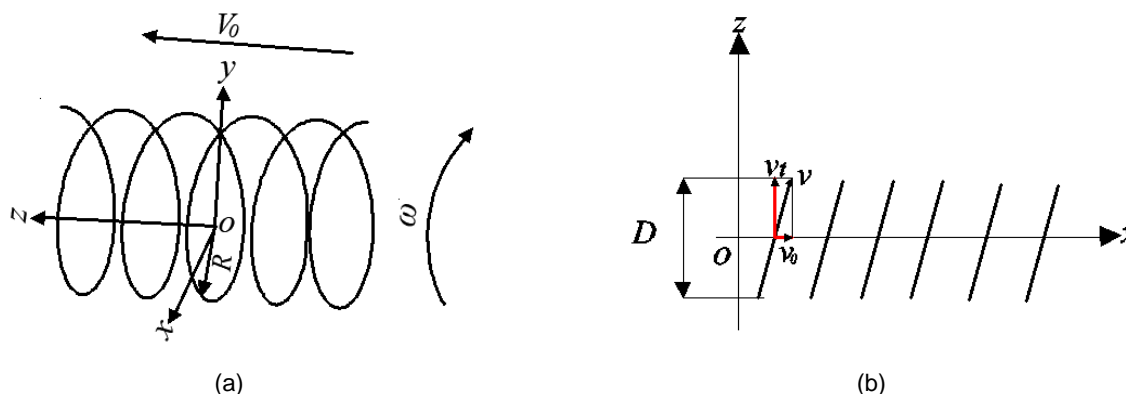
(a)   (b)
Fig. 2 - Analysis diagram of movement track of soil clearing parts

The Cartesian coordinate system was established with the center of the soil clearing parts as the origin and the left side of the x-axis as positive direction. The positive direction of the y-axis is vertical and the positive direction of the *z-axis* is the forward direction of the machine.

The trajectories of the soil clearing parts were plotted, as shown in Fig. 2(a). The motion of soil clearing device is a combined linear and circular motion; thus, the equation for the motion trajectory of soil clearing device can be represented as follows:

$$\begin{cases} x = R\cos(\omega \cdot t) \\ y = R\sin(\omega \cdot t) \\ z = v_0 \cdot t \end{cases} \tag{1}$$

The trajectories formed by the soil clearing parts on the ground is an equidistant curve, and it's clearing width D is related to the soil clearing parts' diameter, as shown in Figure 2. The projection of this trajectories on the *xoz* plane is:

$$x_k = R\cos\left(\frac{\omega}{v_0}x + k\phi\right) = R\cos\left(\frac{\pi n}{30 v_0} + \frac{2k\pi}{m}\right) \tag{2}$$

$$\phi = \frac{2\pi}{m} \tag{3}$$

Where:

   V_0 - forward speed of grapevine cold-proof soil clearing machine, km/h;

   ω - soil clearing parts angular velocity, rad/s;

   t - time, s;

   R - radius of soil clearing parts, mm;

   n - soil clearing parts rotation speed, r/min;

   m - total number of brushes;

   k - brush serial number;

   Φ - phase difference between adjacent brushes.

Main factors impacting the clearing performance of the grapevine cold-proof soil clearing machine include the number of brushes, rotation rate of the clearing parts, diameter of the soil clearing parts, forward speed, soil moisture content. According to the analysis results in formula 2 and the previous field trials, the number of brushes is $m = 17$. This test mainly selects the rotation rate of clearing parts, diameter of the soil clearing parts and forward speed. If the rotation rate of the soil clearing parts is too high, it would lead to high power consumption, but if it is too low, the clearing failure would increase. According to the previous field trials, the rotation rate of the soil clearing parts is designed and calculated to be 200 ~ 300 r/min. If the diameter is too large, it would cause a waste of power, but if it is too small, it may lead to the incomplete soil clearing. As a result, the diameter of the soil clearing parts is designed to be 550 ~ 750 mm. If the forward speed is too high, it would also increase the soil clearing failure, but if it is too low, it may influence the soil clearing efficiency, thus being unable to meet the soil clearing requirements. The forward speed is designed to be 3 ~ 5 km/h.

Test conditions

To verify the soil clearing performances of the grapevine cold-proof soil clearing machine designed in this study, the experiment was conducted in Daxiqu Town, Changji City from November 1 to 5, 2021. The weather was sunny, the temperature was 3~15°C, and the filed test ground was relatively flat, with an area of about 150 m². The grape planting mode was trellis-type, the row spacing was 3 ~ 4 m, and the plant spacing was between 1 ~ 1.5 m, the soil moisture content was 4.4% ~ 12.5%, the soil hardness was 3.8kg ~ 6 kg/cm².

The matching power of the tractor used in the test was greater than 60 kw. The main instruments and equipment used in the field test are grapevine cold-proof soil clearing machine, TYD-2 soil hardness tester, QS-WT soil moisture tester, speed tester, electronic balance, tape measure, adjustable wrench, etc. Before the test, the machine should be strictly inspected to ensure that the rotating parts and the adjusting device are flexible and reliable. The machine should be installed stably and reliably. There should be no abnormal noise, so as not to affect the test results due to poor machine adjustment. In order to ensure that the test results are precise and reliable, the machine needs to be adjusted to the specified speed and the speed is stable before the test. The results showed that performance of the grapevine cold-proof soil clearing machine met the agronomic requirements of grape plantation. Figure 3 shows the field testing of grapevine cold-proof soil clearing machine.

Fig. 3 - Testing of grapevine cold-proof soil clearing machine

Evaluation of soil clearing effect

The soil clearing operation schedule of the grapevine cold-proof soil clearing machine was tested, and the soil clearing operation length of a single row is 55 m for each single-row operation, of which the length of the measuring area is 45 m and the length of the reserve area at both ends is 10 m. Each row along the advance direction was divided into 30 sections as the measuring area according to the successive length of 1.5 m, and a total of 30 sections were tested. During the test, the soil clearing device was raised in the preparation area, and the grapevine cold-proof soil clearing machine entered the working state. After that, the measuring area was passed at the normal working speed.

Due to the difference in planting patterns and varieties in different grapevine areas, and considering that there are no unified and clear requirements for the quality of cold-proof soil clearing, most of the performance evaluation of the soil clearing machine is based on the completion of the soil clearing operation, and there is no unified and clear quantitative index. In this paper, the distance between the original soil ridge center line and the new soil ridge center line was defined as the soil clearing distance L, the maximum value of distance between the original soil ridge center line and the new soil ridge center line was used as the optimal index, during the process of cold-proof soil clearing operation, the greater the distance L, the bigger the soil clearing ability of the machine. The soil clearing distance is shown in Figure 4.
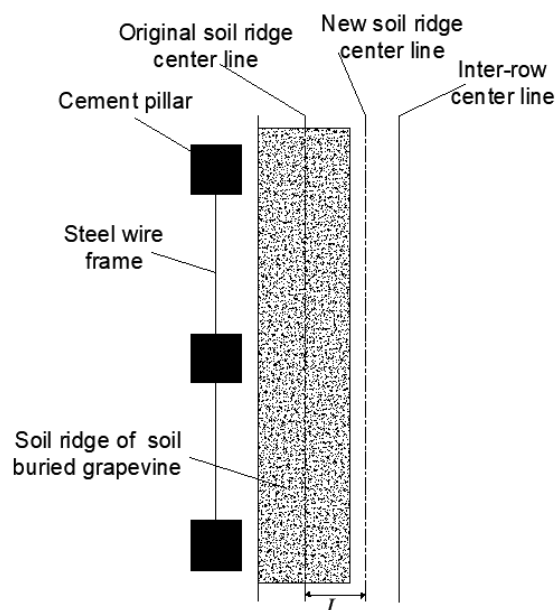
Fig. 4 - Schematic diagram of clearing distance

Test design

Based on the observation and theoretical analysis of previous field experiment, the rotation rate of soil clearing parts *A*, the soil clearing parts diameter *B*, the forward speed *C*, which have a great impact on the soil clearing performance, are selected as the experimental factors, for the response surface test research. Quadratic polynomial regression analysis is conducted for the test data using Design-Expert software *(Chen K. 2005)*, to fit the regression model equations respectively for the soil clearing distance *L*, so as to analyze the influence of factors on the evaluation indexes and the effect law of their interactions. The level of each factor was determined as shown in Table 2.

Table 2

Experimental factors and levels

Levels	Rotation rate of soil clearing parts A	Soil clearing parts diameter B	Forward speed C
	[r/min]	[mm]	[km/h]
-1	200	550	3
0	250	650	4
1	300	750	5

In Design-Expert.8.0, according to the Box-Behnken test scheme, the test results are shown in Table 3. There are 17 groups of data, and the test is repeated five times at the center point.

Table 3

Box-Behnken design scheme and response value of soil cleaning distance

Test number	Rotation rate of soil clearing parts A	Soil clearing parts' diameter B	Forward speed C	Soil clearing distance
	[r/min]	[mm]	[km/h]	[cm]
1	0	0	0	84.23
2	1	-1	0	85.18
3	0	0	0	83.71
4	-1	-1	0	78.95
5	0	0	0	84.04
6	0	1	1	79.28
7	1	0	-1	85.57
8	0	0	0	83.48
9	1	0	1	82.07
10	0	-1	-1	81.38
11	-1	1	0	82.28
12	-1	0	-1	80.8
13	1	1	0	85.76
14	-1	0	1	77.7
15	0	-1	1	76.84
16	0	0	0	83.54
17	0	1	-1	84.64

RESULTS AND ANALYSIS

Test analysis results

According to the data of the test, multiple regression fitting analysis is conducted using Design-Expert software. Furthermore, mathematical regression models are built for the clearing performance indexes of the soil clearing distance *L*, and rotation rate of soil clearing parts *A*, soil clearing parts' diameter *B* and forward speed *C* of the grapevine cold-proof soil clearing machine. The regression model of soil clearing distance was obtained:

$$L = 83.80 + 2.36A + 1.2B - 2.06C - 0.69AB - 0.10AC - 0.21BC + 0.12A^2 - 0.88B^2 - 2.39C^2 \quad (4)$$

where: *A* is rotation rate of soil clearing parts (r/min); *B* is soil clearing parts diameter (mm); *C* is the forward speed (km/h).

The above equations are further analyzed, and the significance test of regression coefficients is carried out at the same time. The analysis results are shown in Table 4.

According to the analysis results in Table 4, the response surface model P of the soil clearing distance L is 0.0001, which is smaller than 0.01, meaning that the significance of models conforms to the requirement. The lack of fit of indexes is 0.0627, greater than 0.05, meaning that the models are of high fitting degree, also meeting the requirement. The determination coefficient R^2 of models is 0.9819, suggesting a high degree of fitting. Besides, the response surface analysis results are of high reliability. Therefore, this model can predict and analyze the changes in the soil clearing performance of the machine.

Table 4

Variance analysis results

Source	Soil clearing distance				
	Squares	DF	MS	F Value	P Value
Model	120.34	9	13.37	42.10	0.0001
A	44.42	1	44.42	139.86	0.0001
B	11.54	1	11.54	36.35	0.0005
C	34.03	1	34.03	107.16	0.0001
AB	1.89	1	1.89	5.95	0.0448
AC	0.040	1	0.040	0.13	0.7331
BC	0.17	1	0.17	0.53	0.4905
A²	0.062	1	0.062	0.19	0.6722
B²	3.25	1	3.25	10.24	0.0151
C²	23.98	1	23.98	75.50	0.0001
Lack of Fit	1.80	3	0.60	5.71	0.0627
Pure Error	0.42	4	0.11		
CorTotal	122.56	16			

The above stated significance analysis shows that A, B, C and C^2 in the soil clearing distance L response model would impact the model very significantly, AB and B^2 also have a significant impact on this model. The items that exert no significant influence on the regression model in the before-mentioned model are removed. Meanwhile, on the basis of guaranteeing that the model $P<0.01$ and lack of fit $P>0.05$, the simplified regression model is shown as follows:

$$L = 83.80 + 2.36A + 1.2B - 2.06C - 0.69AB - 0.88B^2 - 2.39C^2 \tag{4}$$

The analysis shows that the impact of three factors on the soil clearing distance rank as $A>C>B$.

Response surface analysis of clearing distance

In Figure 5a, the forward speed remains at the middle level, that is C=4 km/h. It can be seen Figure 5a that the interactive effects between the two factors are significant. In case of the same soil clearing parts diameter, the soil clearing distance increases with rotation rate of soil clearing parts. In case of the same rotation rate of soil clearing parts, the soil clearing distance increases with the soil clearing parts' diameter. The influence of the soil clearing parts diameter is smaller than that of the rotation rate of soil clearing parts.

In Figure 5b, soil clearing parts diameter is in the middle level, namely, B=650 mm, and it is clear that the interactive effect of the two factors is not significant. Under the same forward speed, the soil clearing distance increases with rotation rate of the clearing parts. Under the same rotation rate of soil clearing parts, the soil clearing distance increases first and decreases afterward as the forward speed increases. The influence of forward speed is not as significant as that of rotation rate of soil clearing parts on soil clearing distance. When the forward speed is too high, it doesn't facilitate the entry of cold-proof soils into the clearing device and lowers the soil clearing distance.

As shown in Figure 5c, the rotation rate of soil clearing parts remains at the middle level, that is, A=250 r/min. It can be seen from Figure 5c that the interactive effects between the two factors are not significant. Under the same rotation rate of soil clearing parts, the soil clearing distance, increases first and decreases afterward as the forward speed increases. A too high forward speed can lead to irregular soil clearing, missed clearing, and lowers the soil clearing distance. Under the same forward speed, the soil clearing distance increases as the forward speed increases because improving rotation rate soil clearing parts can facilitate clearing the soil and reduce soil obstruction of clearing channels.

a. L=(A,B,0)

b. L=(A,0,C)

b. L=(0,B,C)
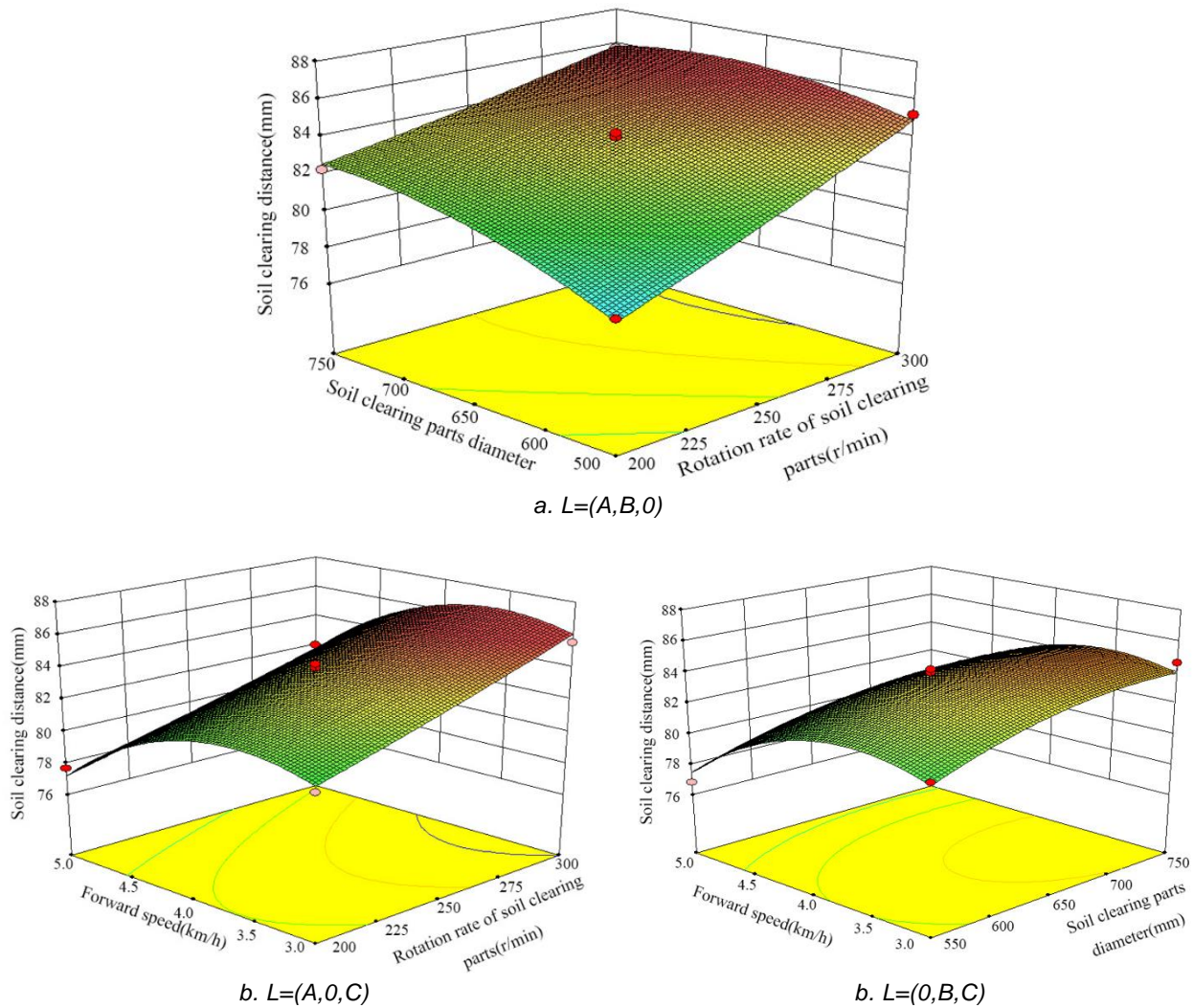
Fig. 5 – Response surface of different experimental factors to soil clearing distance effect

Parameter optimization and validation

To improve the soil clearing performance of the machine, it is required to maximize the soil clearing distance. In order to seek the optimal parameter combination, it is required to conduct the parameter optimization on multiple targets. According to the actual production and design requirements and referring to other relevant standards, the soil clearing distance is required to be more than 80 cm. Hence, the constraint conditions are listed below:

$$\begin{cases} MaxL \\ A \in [200-300\text{r/min}] \\ B \in [550-750\text{mm}] \\ C \in [3-5km/h] \end{cases} \tag{5}$$

After optimization calculation, the optimal working parameters were obtained as follows: forward speed was 3.5 km/h, the rotation rate of soil clearing parts was 277.7 r/min, the soil clearing parts' diameter was 681.7 mm. The predicted value of soil clearing distance was 85.77cm. The validation tests were carried out using the above optimization parameters. The results show that the soil clearing distance was 83 cm, which was consistent with the prediction result of the model, and the prediction errors is less than 4%.

CONCLUSIONS

(1) A grapevine cold-proof soil clearing machine suitable for grape planting areas in the Xinjiang was developed and tested in this paper. It mainly consists of frame, gearbox, suspension device, soil clearing parts, hydraulic system and mechanical transmission system, which effectively solves the difficulties, such as low efficiency and low degree of mechanization, in soil removing by grapevine cold-proof soil clearing machine.

(2) By analyzing the movement trajectories of the soil clearing parts, the key factors affecting the performance of grapevine cold-proof soil clearing machine were determined: forward speed, rotation rate of soil clearing parts and clearing parts' diameter.

(3) The Variance analysis showed that the order of influence on soil clearing distance was rotation of soil clearing parts > forward speed > soil clearing parts' diameter.

(4) There are optimal values for the technical parameters of the grapevine cold-proof soil clearing machine. The structural parameters of the soil clearing device have a significant effect on the soil clearing distance. When the forward speed was 3.5km/h, the rotation rate of soil clearing parts was 277.7 r/min, and the soil clearing parts' diameter was 681.7mm, the soil clearing distance was optimal, Verification test results showed that the soil clearing distance was 83 cm, which was consistent with model prediction.

ACKNOWLEDGEMENT

REFERENCES

[1] Chen, K., (2005), *Experimental Design and Analysis. Beijing*: Tsinghua University Press.
[2] Dami I. E, Ennahli S, Zhang Y., (2012), Assessment of winter injury in grape cultivars and pruning strategies following a freezing stress event. *American Journal of Enology and Viticulture*; 63(1): 106–111.
[3] Liu, S., (2014), *Design and Experimental Study of Conical Spiral Vine Digger in Spring*. Xinjiang Agricultural University.
[4] Liu, F.J., Liu, Z. J., Wang, J. J., Mi, Y., Liu, H. K., Liu, X.Q., (2018), Design and experimental study of automatic obstacle-avoid digging machine for grapevine. *Journal of agricultural mechanization research*, vol. 40, issue 4, pp. 87-90.
[5] Ma, S., Xu, L.M., Xing, J. J, Yuan, Q. C, Yu, C. C, Duan, Z. Z, Chen, C., Zeng, J., (2018), Development of unilateral cleaning machine for grapevine buried by soil with rotary impeller. *Transactions of the Chinese society of agricultural engineering*, vol. 34, issue 23, pp. 1-10.
[6] Ma, S., Xu, L. M., Yuan, Q. C., Niu, C., Wang, S. S., Yuan, X. T., (2020), Development of automatic obstacle avoidance grape vine cold proof soil cleaner. *Journal of agricultural engineering*, vol. 36, issue 7, pp. 1-10.
[7] Niu, C., Xu, L. M., Duan, Z. Z., Liu, X. X., Ma, S., Yuan, Q. C., Wang, S. S., Yuan, X. T., Zeng, J., Chen, C., (2020), Development of hedgerow type soil removal and cold-proof cloth recovery machine for grapevine in winter. *Transactions of the Chinese society of agricultural engineering*, vol. 36, issue 2, pp. 50-58.
[8] Xu, L. M., Duan, Z. Z., Yuan, Q. C. et al. (2018), *A kind of cold-proof cloth clearing machine for grapevine buried soil:*108243638A[P].
[9] Xu, L. M., Li, C., Wang, W. B., et al. (2015) Mechanization Technology and Equipment of grape Production. *Xinjiang Agricultural Mechanization*, issue 5, pp. 24-27.
[10] Xu, L. M., Ma, S., Liu, X. X., Wu, G., Niu, C., Yuan, Q. C., (2019), Present Situation and Development Trend of Grape Production Mechanization in Xinjiang. *Agricultural Mechanization*, issue 3, pp. 10-13.
[11] Wang, Z.Q., Wang, H.B., Liu, F. Z., et al., (2015), Development and experiment of front located winter protection soil cleaning machine. *Journal of Chinese Agricultural Mechanization*, vol. 36, issue 6, pp. 88-91+107.
[12] Bucur, G. M., Dejeu, L., (2016), Research on frost injury of new Romanian grapevine cultivars in the winter 2014-2015. *Agriculture and Agricultural Science Procedia*, vol. 10, pp.233–237.

[13] Xie, D., Zhang, F. W., Zhang, T., Xie, J.H., Zhang, X. K., Dai, F., Zhang, K. Y., (2016), Design and test of a grape cleaner suitable for Hexi area. *Agricultural equipment and vehicle engineering*, vol. 54, issue 9, pp. 56-58+65.

[14] Yuan, Q. C., Xu, L.M., Ma S., Yu, C.C., Duan, Z. Z., Xing J.J., (2017) Current Situation and Thinking of mechanization of grapevine burying in winter and cleaning in spring in Northern China. *Chinese and Foreign Grape & Wine*, issue 6, pp. 66-67.

[15] Wisniewski, M., Gusta, L.V., (2014) The biology of cold hardiness: Adaptive strategies. *Environmental and Experimental Botany*, vol. 106, pp.1–3

[16] Molitor, D., Caffarra, A., Sinigoj, P., Pertot, I., Hoffmann, L., Junk, J., (2014), Late frost damage risk for viticulture under future climate conditions: a case study for the Luxembourgish winegrowing region. *Australian Journal of Grape and Wine Research*, vol. 20, issue 1, pp. 160–168.

[17] Dami, I. E., Ennahli, S., Zhang, Y., (2012) Assessment of winter injury in grape cultivars and pruning strategies following a freezing stress event. *American journal of enology and viticulture*, vol. 63, issue 1, pp. 106–111.

[18] Zabadal, T.J., Dami, I.E., Goffinet, M.C., Martinson, T.E., (2007) Winter injury to grapevines and methods of protection. *Chien M L: Michigan State University Extension*.

[19] Zhou, W.B., (2017), *Design of Grape Vine Lifting Machine*. Ningxia University.

[20] Zhang, J.J., Gou, J., Yan, W.B., Zhao, G.H., Wang, J., (2016), Technology of grape color striped cloth mechanical soil embedding, cold protection and excavation in Shacheng production area. *Chinese and foreign grapes and wine*, issue 4, pp. 32-34.

[21] Zeng, B. N., Tian, Z.D., Zhao, R. L., (2013), Design and development of grape vine machine. *Journal of Chinese agricultural mechanization*, vol. 34, issue 6, pp. 230-232+219.

STUDY ON HULLING CHARACTERISTICS OF BUCKWHEAT HULLER
/
荞麦剥壳机剥壳性能影响因素试验研究

Jixia ZHEN[1], Wei CHEN[2], Hongwei GAO[*3]
[1] Inner Mongolia Technical College of Mechanics and Electrics, Huhhot / China;
[2] Shanxi Polytechnic Institute, Xianyang/China;
[3] Vocational and Technical College of Inner Mongolia Agricultural University, Huhhot / China
Tel: +86-472-8886256;   E-mail: nmghw@163.com
DOI: https://doi.org/10.35633/inmateh-66-24

ABSTRACT

Buckwheat huller is the key equipment of the buckwheat rice processing and its performance is directly related to the quality and yield of buckwheat rice. The key working parts of the sand disc sheller are a pair of parallel sand discs. The structure and the working parameters of the sand discs are the key factors affecting the shelling performance. In this paper, the effect of rotating speed of sand disc, shelling clearance, grain size of sand disc and width of the working face on the shelling performance are experimentally investigated. The results show that the rice yield and relative broken rice rate increase with the increase of the rotating speed of the lower sand disc, and the relative broken rice rate increases sharply when the speed reaches a certain value. With the linear increase of the shelling clearance, the rice yield and the relative broken rice rate are first decreased rapidly, and then decrease slowly. The smaller the particle size of the sand disc is, the higher the rice yield and the relative broken rice rate are, and the influence of the lower sand disc is obviously greater than that of the upper one. Properly widening the width of working face will increase the rice yield but the width tends to have little influence on the rice yield when it increases to a certain extent, and its change has a small impact on the relative broken rice rate. According to the results of single factor test and orthogonal test, the sheller can achieve a better shelling performance and work efficiency when the grain size of the upper sand disc is F24, the grain size of the lower sand disc is F36, the shelling clearance is 5 mm, the rotating speed of the sand disc is 950 r/min, and the width of the working face is 2 cm.

摘要

荞麦剥壳机是荞麦米加工的关键设备,其性能的优劣直接关系着荞麦米的质量和产量。砂盘式剥壳机其关键工作部件为一对平行放置的砂盘,砂盘的结构和工作参数是影响剥壳效果的关键因素。文中以砂盘转速、剥壳间隙、砂盘的粒度及工作面宽度为试验因素对剥壳效果进行了试验研究。试验结果表明:随着下砂盘转速的增加,出米率和相对碎米率随之上升,当速度到达一定数值后相对碎米率急剧上升;随着剥壳间隙的线性增大,出米率和相对碎米率先出现快速下降,随后缓慢下降;砂盘粒度越小出米率和相对碎米率越高,且下砂盘的影响程度明显大于上砂盘;工作面宽度的适当增加会造成出米率的增加,当增大到一定程度后对出米率影响趋于平缓,其对相对碎米率影响较小。综合单因素试验和正交试验结果可知,上砂盘粒度24目、下砂盘粒度36目,剥壳间隙5㎜、砂盘转速950r/min、工作面宽度2cm时,剥壳机能够取得较好的剥壳效果和工作效率。

INTRODUCTION

Buckwheat as a traditional nutritious coarse cereal is rich in biological flavonoids and other high active medicinal ingredients and has the function of lowering blood fat, blood sugar and cholesterol. Buckwheat rice is the primary product of buckwheat processing which can be directly used for cooking and eating and as raw materials for processing buckwheat powder or other foods, and its key production equipment is the buckwheat huller.

---

[1] *Jixia Zhen, Lecturer M.S. Eng.; Wei Chen, Lecturer Ph.D. Eng.; Hongwei Gao, A/Prof M.S. Eng.*

At present, the sand plate buckwheat huller is widely used in the market for its good shelling performance, but it has a low working efficiency. The main working parts of the buckwheat huller are a pair of sand discs which are placed in parallel. The lower sand disc rotates at a high speed and the upper sand disc is stationary. *Campbell et al., (1985),* carried out the buckwheat hulling experiments and achieved good results by using the self-designed sand disc huller. *Ji et al., (1999),* carried out experiments on the sea buckthorn shelling and summarized the influence rules of the moisture content, the rotating speed, the clearance and other factors on the shelling performance by utilizing the double disc structure. Then, the application of the sand disc sheller was reported as developed by Inner Mongolia Agriculture University and the relationship between the buckwheat grading and the shelling clearance was discussed (*Chen et al, 1999; Yu et al, 2002*). *Chen et al., (2001),* made a theoretical analysis of the stress on spherical nuts in the process of shelling and established the relationship between the bending moment on the dangerous section and the distance between grinding plates. *Tian et al., (2002),* carried out the theoretical analysis and numerical simulation on the movement track of grains in the sand disc shelling equipment by using sea buckthorn as raw material. *Sun et al., (2007),* introduced the rubber disc and the soaking technology into the buckwheat hulling process which improved the performance of hulling. In order to improve the separation rate of the traditional buckwheat shell, the air-suction separator of the shell was improved. Further experiments showed that the separation rate of the improved air-suction separator reached up to 99.3% *(Wu et al, 2010)*. The vibration analysis method was introduced into the buckwheat sheller and the test results showed that it had a promoting effect on the buckwheat shelling (*Denisko et al, 2011*). The research showed that the curing process can effectively improve the mechanical properties of Tartary buckwheat and increase the shelling rate (*Liu, 2012*). Base on the principle of rolling-cut, *Ye et al., (2021),* designed a new type of lotus seed shelling. They investigated the effects of the rotational speed of hinge pin, the rubbing roller speed and the tool speed on the shelling rate and the damage rate and found the optimal combined working conditions of the lotus seed shelling. *Diao, (2013),* conducted an experimental analysis of the relationship between the shelling clearance and the whole half kernel rate. *Chen et al., (2018),* conducted an experimental study on the power consumption per ton-meter of the buckwheat hulling unit. *Lü et al., (2019),* presented an on-line measuring method based on machine vision to measure the efficiency parameters of buckwheat hulling and the results showed that the rate of unbroken buckwheat rice measured by this method can effectively reflect the hulling efficiency of the buckwheat huller. Combining the experiment with the EDEM simulation calibration, *Xu et al., (2021),* analysed the contact parameters required for the discrete element simulation of buckwheat rice sieving. The result of the mean error value of discrete element simulation calibration is less than 7.90% which showed that the discrete element method simulation of buckwheat rice screening is feasible. To find out the influence of the flow control on the hulling effect of the buckwheat huller, *Cheng et al., (2020),* selected rotational speed of sand disc, hulling gap, width of working face and size of sand disc as the influence factors to analyse the limited flow on the hulling effect. Results indicated that the influence of hulling gap and working face width has potential value to optimize the limited flow. *Fan et al., (2021),* studied on the processing parameters of different buckwheat varieties including particle size distribution ratio, total ratio of skin and rice and triaxial size. They found that these physical parameters have an important influence on the research of buckwheat shelling. *Qing et al., (2021),* designed a kind of longan flexible counter roll sheller and found that the shelling device had good adaptability to longan with different fruit sizes. According to the physical properties of the coconuts, *Varghese et al., (2021),* designed a prototype of an auger-assisted semi-automatic coconut husking machine and evaluated husking rate, husking effectiveness, husking efficiency, percent of nut breaking, and capacity of the machine.

Few researches have been reported about the influence of the roughness of sand disc and the width of the working face on the buckwheat hulling. In this paper, through the experimental study of sand disc with different particle size and working face width, we can find out its working rules and lay a foundation for the reasonable use of equipment and the improvement of structural parameters.

MATERIALS AND METHODS
Composition of the buckwheat sheller

Buckwheat huller machine is the main test equipment which is mainly composed of hopper, adjusting wheel, upper cover, upper and lower sand disc, material outlet and locking ring. Its main working parts are a pair of parallel sand disc in which the lower sand disc rotates at a high speed and the upper sand disc is stationary. When the graded materials enter the huller and flow through the gap between the upper and lower sand discs, they are shelled under the friction, collision and extrusion of the sand discs, and finally the mixture

of buckwheat, buckwheat rice, buckwheat skin and dust is obtained. The mixture materials at the outlet are screened to get clean buckwheat rice, broken rice and the buckwheat without hulling. The structure is as follows:
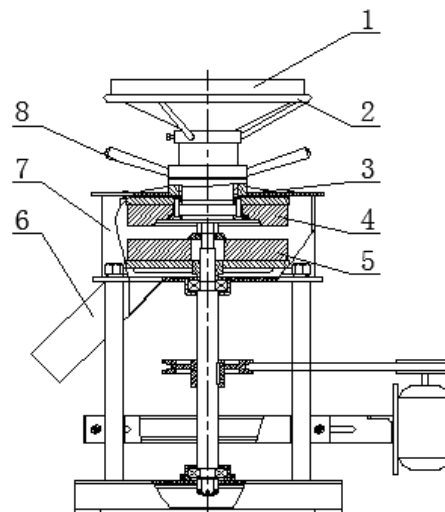
Fig.1 - Structure of buckwheat huller
1. hopper; 2. adjusting wheel; 3. upper cover; 4. upper sand disc; 5. lower sand disc;
6. outlet; 7. outer ring; 8. locking wall

Test materials

In this study, the buckwheat variety selected Windsor which is produced in Wuchuan County of Inner Mongolia Autonomous Region. It was harvested artificially in autumn 2020, and then dried and stored naturally after harvest. The moisture content is 10%-14%.

The raw grains were cleaned using the combined cleaning screen before the experiment, and the cleaned buckwheat was graded by the plane rotary screen, and the graded buckwheat was stored separately. The buckwheat with particle size of 4.6-4.8 mm was selected as the test sample.

Test index

In the process of the buckwheat rice processing, we should not only pursue the quality of buckwheat rice, but also ensure enough productivity, specifically in the shelling performance and the work efficiency. The shelling performance is mainly reflected in the rice yield and the relative broken rice rate. We can get a better shelling performance when the rice yield is higher and the relative broken rice rate is lower. Work efficiency refers to the rice yield per unit time, which is not only related to the rice yield, but also related to the work flow. Higher rice yield and greater working flow correspond to greater rice yield per unit time (*rice yield per unit time = working flow × rice yield*) and thus indicate higher working efficiency of the huller.

Therefore, we should firstly investigate the effects of the particle size of sand disc, the width of the sand disc working face, the working speed and the hulling clearance on the rice yield and the relative broken rice rate in the process of the experiment.

1) Rice yield A

$$A = \frac{M_1}{M} \times 100\% \tag{1}$$

2) Relative broken rice rate B

$$B = \frac{M_2}{M} \times 100\% \tag{2}$$

3) Rice yield per unit time C

$$C = Q \times A \times 100\% \tag{3}$$

Where:

M is the total mass of test sample before hulling, [g];

M_1—Mass of all buckwheat rice obtained after hulling, [g];

M_2—Mass of all broken rice obtained after hulling (undersize materials in diameter of 3 mm), [g];

Q—Feeding flow of huller, [g].

Test method

The single factor hulling tests were carried out with different sand disc rotation speed, hulling clearance, sand disc particle sizes and width of working face L (see Fig. 2), and the influence of various factors on the hulling effect and efficiency were obtained. Before the test, the residual materials inside the equipment were cleaned by using a brush and the hulling clearance is preliminarily adjusted. Then the clearance of the sand disc with a needle gauge was measured and the required clearance was repeatedly adjusted, and the periphery was wrapped with cloth. No load operation for about 15 seconds before and after hulling to ensure that the equipment is in normal working condition. The test process of measuring the rice yield rate and the broken rice rate are as follows: *raw materials→classification→sampling→hulling→powder removing→peeling→separation→weighing.*
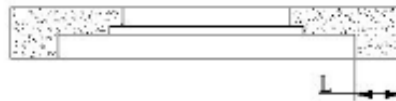
Fig. 2 - Structure of the upper sand disc

The single factor test mainly measured the clearance, the rotating speed of sand disc, the particle size of sand disc and the working face width impacted on the rice yield rate and the relative broken rice rate. All the tests are single factor tests, the selection of factors and levels are shown in table 1. Some test factor levels of the selection are special and one should see the test data for details. The single factor test was repeated three times, and the averaged value was taken as the test result. Material consumption: except for flow measurement, single sample of 500 g is fed into huller at one time.

Table 1

Factor level table

level	Factors			
	hulling clearance /(mm)	sand disc rotating speed /(r/min)	particle size of sand disc /(mesh)	working face width /(mm)
1	4.6	1050	24	10
2	4.8	1000	36	20
3	5.0	950	46	30
4	5.2	900	-	-
5	5.4	850	-	-

RESULTS

Influence of hulling clearance on hulling effect

In the process of the clearance adjustment, after the initial uniform adjustment the gap is gradually adjusted from large gap to small gap, and the test is carried out in turn. The test results are shown in Fig. 3. The results showed that the rice yield of buckwheat decreases with the increase of the hulling clearance. When the clearance increased to a certain value, the rice yields decrease slowly. The relative broken rice rate decreases rapidly firstly and then increases slightly with the increase of hulling clearance. The inflection point of rice yield and relative broken rice yield is about 5.0 mm, and the optimal hulling clearance should be selected near this point. At this time, the value of hulling clearance is larger than the grain size, which is between the length of buckwheat rice and the length of buckwheat. The larger clearance makes buckwheat grains inclined and vertical keep contact with the upper and the lower part of sand disc at the same time. The extrusion deformation is mainly concentrated on the buckwheat shell, and the buckwheat rice suffered little stress, so it is not easy to cause damage to buckwheat rice and enough rice yield can be ensured. It can be seen from the figure that when the hulling clearance is 5 mm, the broken rice rate is only 3.8%, while the rice yield can reach 38.7%, which is much higher than 10%-25% in production. The reason for this phenomenon is that the buckwheat hulling requires high precision of the clearance adjustment. Because the clearance cannot be directly measured in the working process and the clearance adjustment completely depends on the experience of operators, it is difficult to achieve the optimal state.

The optimal hulling clearance in this test is larger than that in the previous studies. The reason may lie in the way of the clearance measurement. Because the working cavity structure of hulling machine is closed, people often use indirect measurement method to measure the clearance previously. It is difficult to observe

and control the adjustment and the measurement error. The direct measurement method in this experiment can effectively reduce the measurement error and the measured data is more accurate.

a) Husked rice yield   b) Relative broken rice yield
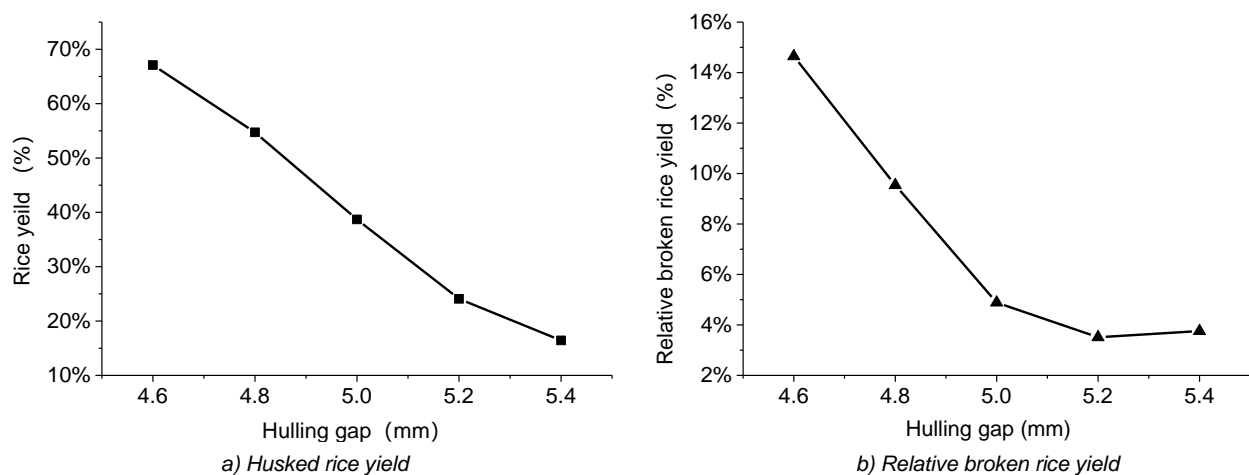
Fig. 3 - Curve of hulling gap

Influence of working face width on hulling performance

During the test, the working speed is 950 r/min, the hulling clearance is 5.0 mm and the relationship between the working face width and the rice yield and the relative broken rice rate is shown in Fig. 4.The test results show that the narrow working face width can reduce the rice yield, but the increase of width cannot significantly improve the rice yield. It can be seen that the width of the working face has a certain decline space. Considering that the decrease of the width of the working face will lead to the increase of the flow, and then increase the yield of buckwheat rice, the width of the working face can be further reduced from 3 cm to 2 cm.

The reason why the linear increase of working face width does not cause the linear increase of rice yield may be that the shelled grains can be shelled within a certain moving distance, while the remaining grains are not shelled because of the close combination of the shell and the rice. The specific hulling process and mechanism need to be further studied.

a) Husked rice yield   b) Relative broken rice yield
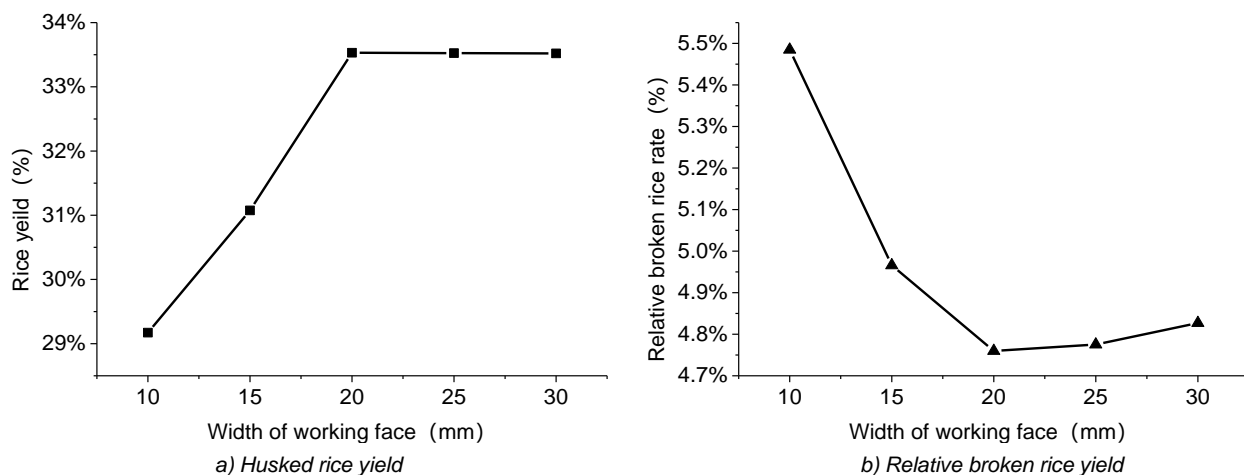
Fig. 4 - Curve of working width

Effect of sand disc mesh size on hulling performance

The surface roughness of the sand disc will directly affect the grinding degree of buckwheat and the friction force, which is mainly determined by the mesh size of the sand disc. The rougher the surface is, the easier it is to produce the dust and the broken rice. The smoother the surface is, the more disadvantageous it is for the grains to stay in the sand disc, resulting in the decrease of the rice yield. In the production, the 24 mesh sand disc is commonly used on the market as the lower sand disc. Due to the special shape of the upper sand disc, it is a special sand disc with the same particle size of 24 mesh. According to the mesh size series table of the sand disc, the upper and lower sand disc of 24, 36 and 46 mesh were selected to test and observe the influence of mesh size on the hulling performance. When the upper sand disc is tested, the lower sand disc is 24 mesh size; otherwise, when the lower sand disc is tested, the upper sand disc is 24 mesh size.

a) Husked rice yield   b) Relative broken rice yield
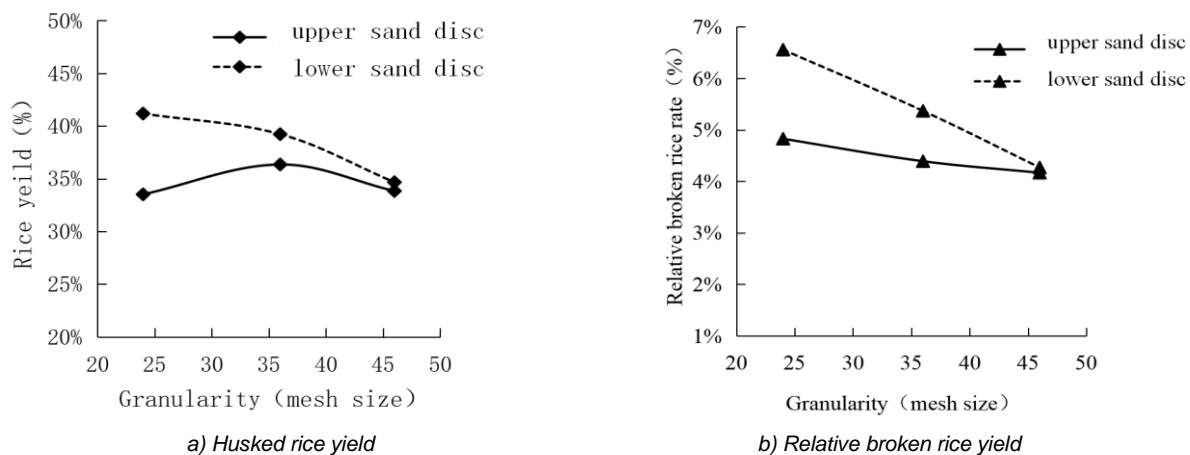
Fig. 5 - Curve of granularity

It can be seen from Fig. 5 that the mesh size of the upper sand disc has little effect on the rice yield and the relative broken rice rate, while the effect of the lower sand disc on the rice yield and the relative broken rice rate is higher than that of the upper one, especially on the relative broken rice rate. The reason is that the impact and grinding effect on buckwheat is more intense in the process of high-speed movement of the lower sand disc, while the upper sand disc is static, so the impact and grinding effect is relatively small. When selecting the mesh size of sand disc, the upper sand disc can be selected with 24 mesh, while the lower sand disc can be selected according to the requirements of the broken rice rate. If the requirement of the relative broken rice rate is not high, 16 mesh or 24 mesh can be selected to increase the rice yield; If the requirement of relative broken rice is high, 36 mesh or 46 mesh can be selected.

Orthogonal test and results

The above single factor test shows the influence of each factor on the test index, without considering the interaction between factors. The following is to analyse the primary and secondary order and significance of each factor through orthogonal test, and select a better parameter combination according to the actual production needs. During the working process, the rotating speed of sand disc is generally a fixed value, which is not taken as a test factor, and its value is 950 r/min. L9 (34) table was used for orthogonal test, and the factors were the hulling clearance, the working face width and the sand disc size.

Table 2

Factor level table for orthogonal test

Level	Experimental factors		
	Hulling gap A (mm)	Width of working face B (mm)	Granularity of sand disc C (mesh size)
1	4.8	10	24
2	5.0	20	36
3	5.2	30	46

Table 3

Result of orthogonal test

Number	Factors			Experimental index	
	A	B	C	Rice yield rate / (%)	Relative broken rice yield rate / (%)
1	1	1	1	29.9	9.5
2	1	2	2	35.5	8.1
3	1	3	3	35.3	7.3
4	2	1	2	17.3	3.9
5	2	2	3	23.5	4.8
6	2	3	1	22.2	4.2
7	3	1	1	10.9	2.9
8	3	2	2	15.1	2.2
9	3	3	2	17.8	3.6

According to the result analysis in Table 3, when the rotation speed of sand disc is fixed, the shelling clearance has the greatest influence on the rice yield and the relative broken rice rate, followed by the working face width and the sand disc particle size. The width of the working face has a significant effect on the rice yield, but it has no significant effect on the relative broken rice yield. Grain size has no significant effect on the rice yield, but it has significant effect on the relative broken rice rate. When selecting the optimal parameters, the comprehensive balance method should be adopted. Taking the relative broken rice rate less than 6% as the main reference and combining the rice yield and the limit working flow, the optimal combination of A2B2C2 is adopted.

Table 4

Result analysis of orthogonal test

Analysis item	Rice yield rate			Relative broken rice yield rate		
	A	B	C	A	B	C
K1	100.7	58.1	71.2	24.9	16.3	17.9
K2	63	74.1	68.6	12.9	15.1	15.2
K3	43.8	75.3	67.7	8.7	15.1	13.4
R	56.9	17.2	3.5	16.2	1.2	4.5
Primary and secondary factors	A>B>C			A>C>B		
Optimal combination	A1>B3>C1			A3>B3>C3		
SS	558.6	61.5	2.2	47.1	0.3	3.4
df	2	2	2	2	2	2
MS	279.3	30.7	1.1	23.6	0.2	1.7
F	270.0	29.7	1.1	336.6	2.3	24.4
Significance	**	*		**		*

CONCLUSIONS

From the above test results, the following conclusions can be drawn:

1) It is helpful to reduce the broken rice rate by appropriately reducing the working speed, but at the same time, it will reduce the rice yield and thus affect the working efficiency. Therefore, 950 r/min is a reasonable choice. The hulling clearance has a great influence on the rice yield and the relative broken rice rate. The optimal hulling clearance is located at the inflection point of the curve of the rice yield and the relative broken rice rate, which is about 5 mm.

2) The width of the working face of sand disc has little influence on the rice yield within a certain range. If it is too small, the rice yield will be reduced. But it can increase the limit flow and thus to improve the output per unit time. So it should be selected slightly larger than 2cm.

3) In the structure of the sand disc huller, only the width of working face has potential value to improve the limit working flow, and other factors can be ignored.

4) The optimal combination of parameters in the working process are the working speed (950 r/min), the hulling clearance (5 mm), the working face width of the sand disc (2 cm), the mesh size of upper sand disc (24 mesh), mesh size of the lower sand disc (36 mesh).

In conclusion, It is difficult to increase the rice yield by greatly increasing the limit flow under the existing structure. The most important factor affecting the shelling performance and the work efficiency is the hulling clearance. According to different varieties and grain sizes of buckwheat, how to adjust the clearance timely and accurately is the key factor to improve the equipment.

ACKNOWLEDGEMENTS

REFERENCES

[1] Abi Varghese, Jippu Jacob, Abraham Iype Rajan, (2021), Design, development and testing of an auger-assisted semi-automatic coconut husking machine. *Journal of Food Process Engineering*, 44(3):1-9.

[2] Campbell C.G., Chubey B B., (1985), A dehuller for buckwheat samples. *Canadian Journal of Plant Science*, 65(3): 771-773;

[3]   Chen Kuifu, Wang Fengzhu, Zhang Ping., (2001), Optimization of disc spacing for peeling spherical nuts(用于剥裂球形坚果的碾磨盘间距优化). *Mechanics and Practice*, 06: 31-33;

[4]   Chen Weizhang, (1999), Processing of buckwheat rice（荞麦米的加工）. *Practical engineering technology in rural areas*, 10:35;

[5]   Bing Xu, Yanqing Zhang, Qingliang Cui et al., (2021), Construction of a discrete element model of buckwheat grain and calibration of parameters（荞麦籽粒离散元模型构建及参数标定）. *INMATEH Agricultural Engineering*, 2021, 64(2):175-184.

[6]   Diao Siqin, Du Wenliang et al., (2013), Effect of shelling gap on whole half kernel rate of Buckwheat (剥壳间隙对荞麦整半仁率的影响规律). *Food and Machinery*, 29(03):191-193+221;

[7]   Denisko O.A., Tkachuk A.I., (2010), Experimental Study of Technological Efficiency Vibrating Peeling Grain, *Scientific Bulletin of NUBiP Ukraine*, (3): 274-280;

[8]   Ji Ping, Chen Jie, Wu Hua et al., (1999), Experimental study on shelling method and device of sea buckthorn seed (沙棘籽脱壳方法及装置的试验研究). *Journal of Agricultural Engineering*, 04: 258-263;

[9]   Liu Caixia, (2012), *Effect of mechanical properties of Tartary Buckwheat before and after ripening on its shelling efficiency (苦荞麦熟化前后的机械特性对其剥壳效率的影响).* Inner Mongolia Agricultural University;

[10]   Shaozhong lü, Wenliang Du, Zhen Chen, Wei Chen, Su Rigalatu, (2019), On-line Measuring Method of Buckwheat Hulling Efficiency Parameters Based on Machine Vision (基于机器视觉的荞麦剥壳性能参数在线检测方法). *Transactions of the Chinese Society for Agricultural Machinery*, 50(10): 35-43;

[11]   Sun Xiaojing, Du Wengliang et.al, (2002), Experiment on hulling method of Tartary Buckwheat (苦荞麦脱壳方法的试验), *Journal of agricultural machinery*, 12: 220-222;

[12]   Tian Zhongxu, Tian Zhongjing, (2002), Trajectory calculation of seed shelling device with flat grinding method (平磨法种子去壳装置中的轨迹计算). *Mechanical design and manufacturing*, 05: 56-57;

[13]   Wei Chen, Wenliang Du et al., (2018), Energy consumption detection of buckwheat hulling unit under different working conditions (荞麦剥壳机组不同工况下能耗检测). *Journal of Agricultural Mechanization Research*, 40(07):190-194+205;

[14]   Shaobo Ye, Decong Zheng, Wei Li et al., (2021), Design and test of negative pressure chamber rotary buckwheat seed metering device (气室旋转式荞麦精密排种器的设计与试验). *INMATEH Agricultural Engineering*, 64(02): 185-194.

[15]   Jinxin Sun, Liqin Yang, Baohui Xu, Yuming Guo, Qingliang Cui, Yanqing Zhang, (2021), Design and experiment of centrifugal collision test device for millet and sweet buckwheat grain (谷子、荞麦籽粒离心式碰撞试验装置设计及试验). *INMATEH Agricultural Engineering*, 65(03): 193-202.

[16]   Yanmen Qing, Changyou Li, Shan Zeng, (2021), Design and experiment of lon gan flexible counter roll shell (龙眼柔性对辊剥壳机的设计与试验). *Journal of South China Agricultural University*, 42(03):126-132;

[17]   Yingsi Wu, Wenliang Du, Fei Liu, Junlan Wang, Wei Chen, (2010), Improvement experiments on the separating device of buckwheat shucker (荞麦剥壳机分离装置的改进试验*). Transactions of the Chinese Society of Agricultural Engineering*, 26(05): 127-131;

[18]   Yu Liping, (2002), Processing of buckwheat rice (荞麦米的加工), *Western grain and oil technology*, 05: 43-44;

[19]   Tuya Cheng, Wei Chen, Wenliang Du, (2020), The Influence of Flow Control on Hulling Effect of Buckwheat Huller (荞麦剥壳机流量控制对剥壳效果的影响). *Journal of HeNan Agricultural Sciences*, 49(01): 174-179;

[20]   Rong Fan, Qingliang Cui, Yanqing Zhang, Qi Lu, (2021), Analysis and calibration of parameters of buckwheat grain based on the stacking experiment (基于堆积试验的荞麦籽粒离散元参数分析及标定). *INMATEH Agricultural Engineering*, 64(02): 467-476.

DETERMINATION AND TESTING OF PELLETIZED COATED PARTICLES
/
丸化包衣颗粒的测定与试验

Min LIU, Zhanfeng HOU*, Xuejie MA, Xiwen ZHANG, Nianzu DAI
Inner Mongolia Agricultural University, College of Mechanical and Electrical Engineering, Inner Mongolia, China
Tel: +86 04714309215; *)Corresponding author E-mail: njauhzf@163.com
DOI: https://doi.org/10.35633/inmateh-66-25

ABSTRACT

The calibration of the powder simulation parameters could improve the accuracy of the pelletizing and coating simulation process. In this paper, we take coated powder (after this referred to as powder) as the research object, based on particle amplification theory, combined with physical tests to calibrate the contact parameters of powder and seeds (after this referred to as seeds), conduct the angle of repose simulation tests of powder, carry out Plackett-Burman test, steepest climb test, and Box-Behnken test in turn, and establish quadratic regression equation to obtain the best combination of powder simulation parameters. The difference between the contact parameter combinations obtained from the simulation tests and the physical test results is less than 1%, providing some reference for calibrating similar powder material parameters.

摘要

为对粉料仿真参数进行标定，可提高丸化包衣仿真过程的准确性。本文以包衣粉料（以下简称粉料）作为研究对象，基于颗粒放大理论，结合物理试验标定紫花苜蓿种子（以下简称种子）与粉料间的接触参数；进行粉料休止角仿真试验，依次开展 Plackett-Burman 试验、最陡爬坡试验与 Box-Behnken 试验，建立二次回归方程，得到粉料最佳仿真参数组合。仿真试验得到接触参数组合与物理试验结果相差均小于 1%，为相似粉体物料参数标定提供一定参考。

INTRODUCTION

Seed pellet coating technology is a processing technology in which seeds, seed coating agents, coating powders, and additives with other active ingredients are mixed in a specific ratio, wrapped evenly and effectively on the surface of the seeds using seed coating equipment as a carrier to protect the seeds from external biotic or abiotic attack and thus improve the seed viability and germination rate (*Zhao, 2009; Afzal, 2020*). By using the discrete element method to analyse the seed pellet coating process, the forces of the particles, of the particles and the working parts can be taken into account, which improves the accuracy of the application of the discrete element method when analysing the seed pellet coating process (*Zeng, 2021*). The powder is a typical bulk material with complex physical properties (*Jaeger, 1997; Liu, 2017*). Considering that the powder is prone to bonding during the test, we chose the JKR (Johnson-Kendall-Roberts) model as the contact model. The JKR model introduces the concept of particle surface energy, which is more suitable for studying small particle powder materials, crops, soil, and other wet materials and could simulate the bonding agglomeration between particles (*Luo, 2018; Johnsonkl, 1971*).

Domestic and foreign scholars have conducted much research on agricultural materials based on the discrete element method. *Boac, (2009),* summarized the crop material and contact parameters to verify the accuracy of the simulation test using soybean as an example and obtained the best combination of parameters for the simulation test on soybean. *John, (2019),* scaled up the cellulose using a coarse-grained approach and calibrated the model using a genetic algorithm. *LaTosha, (2013),* determined the collision recovery coefficient of coal particles and found that the bounce angle has a significant effect on the collision recovery coefficient of particles. *Zeebroeck, (2006),* applied the discrete element method to apple abrasion experiments for the first time, using a single sphere model in EDM to simulate apples, and selected the Kuwabara-and-Kon contact model to carry out simulation tests. *Ma, (2020),* conducted resting angle tests on compressed alfalfa straw powder and established a second-order regression model to obtain the best combination of simulation parameters for alfalfa straw. *Thomas, (2016),* analyses the effect of coarse grain size on the accuracy of simulation tests within a silo flow model based on EDEM.

Mukherjee, (2018), proposes a discrete element model to predict the effect of humidity on drug powder flow by varying the cohesion between particles in a simple hopper geometry. *ASAF, (2007),* established a two-dimensional model of soil particles and sought the optimal soil contact parameters by the Nelder-Mead algorithm. *Alexandros*, *(2020)*, simulated the mobility of the powder at low pressure by DEM and found that the coefficient of friction between the particles affects the confinement factor. *Mohammadreza, (2018),* used the discrete element method to analyse the effect of inter-particle adhesion force on simulation accuracy during powder mixing. *Xing, (2020),* used the JKR model to calibrate soil contact parameters using soil in the hot zone of Hainan. *Li, (2019),* based on particle scaling theory, uses the discrete element method to obtain the optimum combination of contact parameters for wheat flour. *Tamas, (2018),* developed a discrete element simulation model of the soil sweeper and calibrated the soil under different moisture content conditions. Comprehensive domestic and international research status: few studies on the calibration of powder material parameters, and no discrete element simulation parameter calibration for coated powder has been seen.

In this paper, we measure the basic physical parameters of powders by physical experiments combined with simulation tests, and the rest angle is used as the response value for simulation tests to establish the regression equation and obtain the optimal combination of simulation contact parameters for powders, in order to provide a reference for the calibration of discrete element parameters of other powder materials.

MATERIALS AND METHODS
Test material and parameter determination

The experiment uses the seeds and the powder which made up of soybean meal and diatomaceous earth as the radio of 1:1 as the material, and the seed simulation parameters were measured by physical tests (*Hao, 2017*), combining the domestic and international literature and referring to the built-in database of EDEM software (*Zhou, 2017*), the powder simulation parameters were obtained, as shown in Table 1.

Table 1

Discrete element simulation test parameters

Simulation parameters	Values
Poisson's ratio of seed	0.4
Seed shear modulus / Pa	1.02×10^7
Seed density / kg·m^{-3}	1250 ± 0.016
Poisson's ratio of powder	0.296
Powder shear modulus / Pa	3×107
Powder density / kg·m^{-3}	1833 ± 0.1

Simulation Model

The powder and seed simulation models were established in the discrete element simulation software, and the powder particles used a single spherical model, as shown in Figure 1a, and the particle size was enlarged by 6 times based on the particle amplification theory (*Feng, 2009; Thakur, 2016; Sakai, 2014*). The seeds used a multi-sphere aggregation to establish the discrete element simulation model, as shown in Figure 1b. We chose the Hertz-Mindlin no-slip contact model to conduct the contact parameter calibration test between seed and powder (*Wu, 2019*) and chose the Hertz-Mindlin with JKR contact model for conducting the powder rest angle simulation test. We used the fixed-size particles for the simulation, with a Rayleigh Time Step of 6.87×10^{-6}s and a grid size of $3R_{min}$ (*Hu, 2010*).

a. Powder particle																		b. Alfalfa seed
Fig. 1 - Simulation model of alfalfa seeds and powder

PARAMETER CALIBRATION PROCESS
Powder to seed contact parameter calibration
Crash recovery factor

This paper used the collision bounce test to calibrate the collision recovery coefficient of seeds and powder, as shown in Figure 2.

Since the static friction coefficient a_2 and rolling friction coefficient a_3 between seed and powder, the collision recovery coefficient a_4, static friction coefficient a_5, and rolling friction coefficient a_6 between powders do not affect the seed rebound height, they are all set to 0. Take the range of collision recovery coefficient of seed and powder a_1 is 0.1~0.3, the step size is 0.05 for 6 sets of tests, and get the rebound height of seed b_1, the test design and results are shown in Table 3, and the fitting equation is shown in Eq. 1.

| a. Physical tests | b. Simulation test |

Fig. 2 - Collision recovery coefficient test

Table 3

Collision recovery coefficient test design and results

No.	a_1	b_1 / mm
1	0.10	2.499
2	0.15	4.615
3	0.20	6.09
4	0.25	8.502
5	0.30	9.809
6	0.35	13.39

$$b_1 = 20.01479\,a_1 + 47.52143\,a_1^{2} + 0.22856 \qquad (1)$$
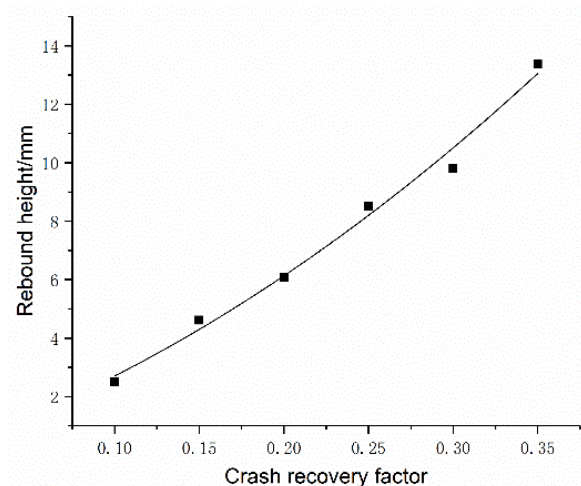
Fig. 3 - Collision recovery coefficient and rebound height fitting curve

The coefficient of determination of the fitted equation $R^2=0.98904$ indicates that the equation fits reliably, and the rebound height of 8.01 mm measured by the physical experiment is brought into the equation, and the solution of a_1 is 0.246. The solution result is input into EDEM for the simulation test, and the rebound height is 8.07, and the relative error is only 0.75%.

Static friction coefficient

In this paper, we use the slope method to determine the static friction coefficient of seed and powder, and the test is shown in Figure 4. When conducting the slope slip simulation test, set a_1 as 0.246, set a_3, a_4, a_5, and a_6 to 0. Take the range of static friction coefficient between seed and powder a_2 from 0.6 to 0.85, set the step size to 0.02 for 6 sets of tests and obtain the rotation angle b_2 of the inclinometer. The test design and results are shown in Table 4, and the fitting equation is shown in Eq.2.

a. Physical tests   b. Simulation test
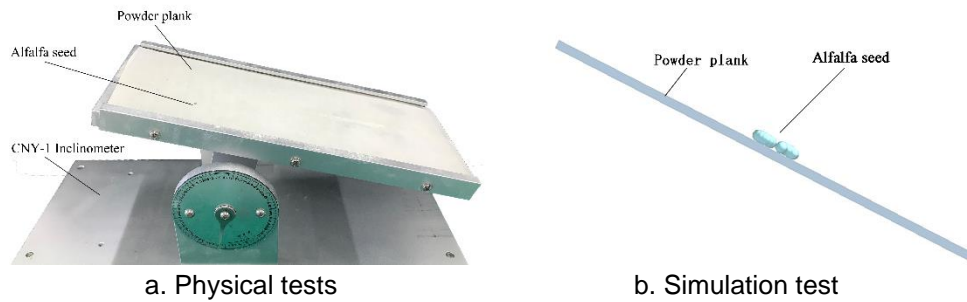
Fig. 4 - Slope slip test

Table 4

Design and results of slope sliding test

No.	a_2	b_2 / mm
1	0.7	20.4
2	0.72	22.86
3	0.74	24.12
4	0.76	29.04
5	0.78	32.76
6	0.8	37.8

$$b_2 = -1349.025\,a_2 + 1015.17857\,a_2^{\,2} + 467.37643 \qquad (2)$$
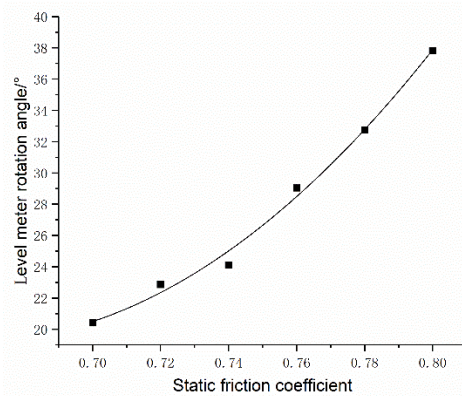
Fig. 5 - Fitting curve of static friction coefficient and rotation angle of inclinometer

The coefficient of determination of the fitted equation R^2=0.98904, the physical test result of 31.85° was brought into the equation, and the solution of a_2 was 0.776. The solution result was input into EDEM for the simulation test, and the rotation angle was 32.06°, and the relative error with the physical test was 0.66%.

Rolling friction coefficient

This paper determined the rolling friction coefficient between seeds and powders by an inclined rolling test, shown in Figure 6. When conducting the inclined rolling simulation test, set a_1 as 0.246, set a_2 as 0.776, set a_4, a_5, and a_6 to 0. The rolling friction coefficient of seed and powder a_3 was taken to be in the range of 0.2-0.3, set a step size of 0.02 for six sets of simulation tests. b_3 was the horizontal rolling distance of seeds, and the experimental design and results are shown in Table 5, and the fitting equation is shown in Eq.3.

a. Physical tests   b. Simulation test
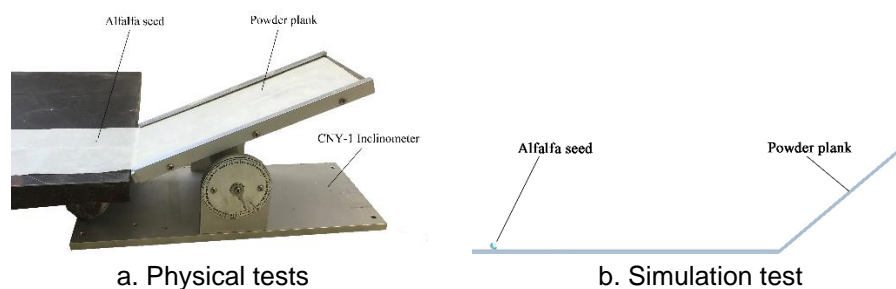
Fig. 6 - Inclined rolling test

Inclined rolling test design and results

No.	a_3	b_3 / mm
1	0.2	114.6
2	0.22	93.12
3	0.24	81.51
4	0.26	63.08
5	0.28	56.00
6	0.3	39.88

$$b_3 = -1721.80714\, a_3 + 2005.35714\, a_3^2 + 377.47571 \tag{3}$$
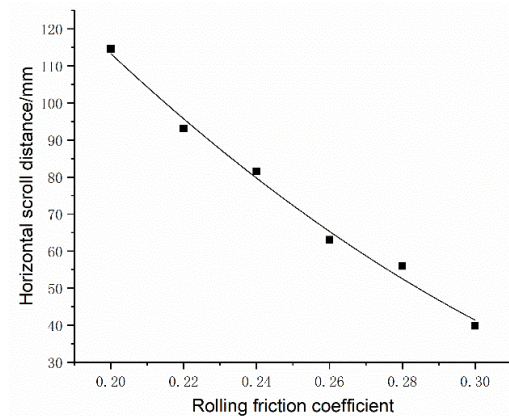
Fig. 7 - Fitting curve of rolling friction coefficient and horizontal rolling distance

The coefficient of determination of the fitted equation R^2=0.99102, the physical test result of 69.2mm was brought into the equation and solved to obtain a_3 of 0.255. The solution result was input into EDEM for the simulation test, and the seed horizontal rolling length was 68.74mm, with a relative error of 0.66% from the physical test.

Contact parameter calibration test of the powder

The angle of the repose test

Using FT-104B resting angle tester for powder resting angle test, as in Figure 8a, the profile curve is extracted by image processing and linearly fitted to obtain the simulation test rest angle, as shown in Figure 9, the average value was obtained as 41.69°±0.79.

a. FT-104B resting angle tester   b. Resting angle simulation model

Fig. 8 - Angle of Repose Test

a. Original image   b. Binarization   c. Boundary extraction   d. Linear fitting
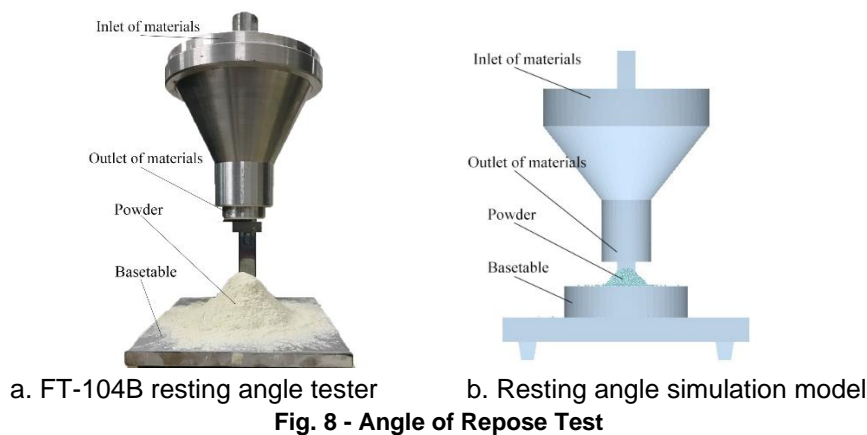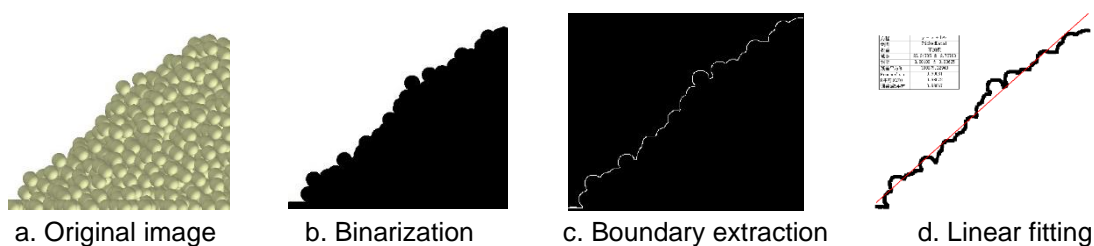
Fig. 9 - Image processing

The Plackett-Burman test

The Plackett-Burman test was conducted with the rest angle as the response value, and the test parameters are shown in Table 6, and the test design and results are shown in Table 7.

Table 6

Plackett-Burman test parameters range table

Simulation test parameters	Low level (-1)	High level (+1)
Powder - powder restitution coefficient *A*	0.05	0.25
Powder - powder static friction coefficient *B*	0.7	0.9
Powder - powder rolling friction coefficient *C*	0.25	0.45
Powder - steel plate restitution coefficient *D*	0.05	0.25
Powder - steel plate static friction coefficient *E*	0.62	0.82
Powder - steel plate rolling friction coefficient *F*	0.19	0.39
JKR surface energy *G*	0.1	0.3

Table 7

Plackett-Burman test protocol and results No.	*A*	*B*	*C*	*D*	*E*	*F*	*G*	Repose angle θ / °
1	1	1	-1	1	1	1	-1	30.86
2	-1	1	1	-1	1	1	1	48.00
3	1	-1	1	1	-1	1	1	49.16
4	-1	1	-1	1	1	-1	1	39.11
5	-1	-1	1	-1	1	1	-1	42.73
6	-1	-1	-1	1	-1	1	1	41.45
7	1	-1	-1	-1	1	-1	1	44.82
8	1	1	-1	-1	-1	1	-1	33.91
9	1	1	1	-1	-1	-1	1	44.41
10	-1	1	1	1	-1	-1	-1	38.53
11	1	-1	1	1	1	-1	-1	43.24
12	-1	-1	-1	-1	-1	-1	-1	32.78
13	0	0	0	0	0	0	0	43.74

Table 8

Plackett-Burman test parameter contribution analysis

Parameters	Stdized effects	Sum of squares	Contribution degree / %
A	0.63	1.20	0.31
B	-3.23	31.23	8.05
C	7.19	155.09	39.99
D	-0.72	1.54	0.40
E	1.42	6.05	1.56
F	0.54	0.86	0.22
G	7.48	168.00	43.32

Table9

Significance analysis of Plackett-Burman test parameters

Parameters	Degree of freedom	Sum of squares	F-value	P-value
Model	7	363.98	13.32	0.0124
A	1	1.20	0.31	0.6084
B	1	31.23	8.00	0.0474*
C	1	155.09	39.72	0.0032**
D	1	1.54	0.39	0.5640
E	1	6.05	1.55	0.2812
F	1	0.86	0.22	0.6626
G	1	168.00	43.03	0.0028**

*Note: ** indicates an extremely significant effect (p<0.01),* indicates a significant effect (p<0.05). Same as below*

From Table 8 we can obtain the effect of each parameter on the rest angle and the contribution rate, where *A*, *C*, *E*, *F*, and *G* have a positive effect on the powder rest angle, the rest angle will increase with the increase of this parameter, and *B* and *D* harm the powder rest angle, the rest angle will decrease with the increase of this parameter (*Peng, 2020*). The contribution of each parameter to the resting angle of the powder is analysed, and the top 3 contributing parameters are *G*, *C*, and *B*, and combined with the significance analysis of the test parameters in Table 9, it was obtained that *G* has a highly significant effect on the resting angle, C and *B* have a significant effect on the resting angle.

The Steepest climb test

Design the steepest climb test according to the parameter effect on the three screened significant parameters; the test design and results are shown in Table 10.

Table 10

Steepest climb test design scheme and results

No.	Powder-powder static friction coefficient, B	Powder-powder rolling friction coefficient, C	JKR surface energy, / J·m⁻², G	Relative error / %
1	0.9	0.25	0.1	22.91
2	0.86	0.29	0.14	0.50
3	0.82	0.33	0.18	2.64
4	0.78	0.37	0.22	4.41
5	0.74	0.41	0.26	6.86
6	0.7	0.45	0.30	31.66

The Box-Behnken test

Based on the steepest climb test results, the screened significant parameters were ranked as low, medium, and high levels then the Box-Behnken test was conducted. The test parameter levels are shown in Table 11; the test design scheme and results are shown in Table 12.

Table 11

Parameter level coding table

Levels	Powder-powder static friction coefficient B	Powder-powder rolling friction coefficient C	JKR surface energy / J·m⁻², G
-1	0.9	0.25	0.1
0	0.86	0.29	0.14
+1	0.82	0.33	0.18

Table 12

Box-Behnken test protocol and results

No.	Powder-powder static friction coefficient B	Powder-powder rolling friction coefficient C	JKR surface energy G	Repose angle θ / °
1	-1	-1	0	36.41
2	1	-1	0	36.96
3	-1	1	0	42.25
4	1	1	0	42.33
5	-1	0	-1	32.76
6	1	0	-1	37.86
7	-1	0	1	38.91
8	1	0	1	38.43
9	0	-1	-1	30.62
10	0	1	-1	38.69
11	0	-1	1	37.21
12	0	1	1	39.96
13	0	0	0	40.55
14	0	0	0	41.17
15	0	0	0	41.53
16	0	0	0	41.31
17	0	0	0	41.7

Box-Behnken test regression model analysis of variance

Source	Mean square	Degree of freedom	Sum of square	P-value
Model	18.85	9	169.61	<0.0001**
B	3.45	1	3.45	0.0244*
C	60.67	1	60.67	<0.0001**
G	26.57	1	26.57	<0.0001**
BC	0.0552	1	0.0552	0.7281
BG	7.78	1	7.78	0.0036**
CG	7.08	1	7.08	0.0046**
B^2	2.05	1	2.05	0.0634
C^2	4.80	1	4.80	0.0119*
G^2	53.51	1	53.51	<0.0001**
Residual	0.4218	7	2.95	
Lack of fit	0.7238	3	2.17	0.1190
Pure error	0.1952	4	0.7809	
Sum		16	172.56	

Using Design-Expert 11.0 software to perform multiple regression analysis on the experimental data, the second-order regression equation for the relative error of the rest angle was obtained as follows:

$$41.25 + 0.6563B + 2.75C + 1.82G$$
$$- 0.1175BC - 1.40BG - 1.33CG \tag{4}$$
$$- 0.6973B^2 - 1.07C^2 - 3.56G^2$$

The results of Box-Behnken test ANOVA are shown in Table 13, where *C*, *G*, *BG*, *CG*, and *G²* have highly significant effects on powder rest angle, *B*, *C²* have significant effects on powder rest angle, while the rest parameters have insignificant effects on powder rest angle. The quadratic regression model has a model P<0.001, a coefficient of determination R^2=0.9829, and a calibrated coefficient of determination adjusted R^2=0.9609, both close to 1 and a coefficient of variation C.V.=1.68%. In summary, the regression model is exceptionally significant and can be further analysed for the rest angle prediction.

Simulation parameter calibration and test verification

Design-Expert 11.0 software was used to find the best combination of parameters for the powder simulation by using the physical test rest angle as the target value for the second-order regression equation: powder-powder static friction coefficient of 0.887, the powder-powder rolling friction coefficient of 0.319, and JKR surface energy of 0.162.

To verify the accuracy and reliability of the powder simulation calibration, the rest angle simulation test was conducted with the combination of the above parameters as EDEM simulation parameters. The mean rest angle obtained is 41.27°, with a relative error of 0.991% from the physical test value of 41.69°. The T-test was performed and P=0.942>0.05, indicating no significant difference between the simulation rest angle and the physical test rest angle. The experimental comparison is shown in Figure 10.

a. Simulation test   b. Physical tests
Fig. 10 - Test comparison of the angle of repose of powder

CONCLUSIONS

1) Physical tests measured the basic physical parameters of seeds and powder; the contact parameters between seeds and powder were obtained by applying an inclinometer and high-speed camera, the resting angle of powder was measured as 41.69±0.79 by using a resting angle instrument.

2) Based on particle amplification theory, the powder particles were amplified 6 times for simulation tests. The contact parameters between seeds and powder were calibrated by collision bounce test, ramp slip test, and ramp roll test.

3) The rest angle simulation test was conducted using the range of contact parameters obtained from the physical test as the basis for selecting the simulation test parameters. The Plackett-Burman test, the steepest climb test, and the Box-Behnken test were conducted in turn to establish and optimize the second-order regression equation of the significant parameters and the rest angle, and the best combination of simulation parameters was obtained: the powder-powder static friction coefficient was 0.887, the powder-powder rolling friction coefficient was 0.319, and the JKR surface energy was 0.162.

4) The calibrated contact parameters were used to conduct the simulation test again; the T-test of the result data was obtained as P=0.942>0.05, indicating that there was no significant difference between the simulation test results and the physical test results, further verifying the reliability of the simulation parameter combination.

ACKNOWLEDGEMENTS

REFERENCES

[1]   Afzal I., (2020), Modern Seed Technology: Seed Coating Delivery Systems for Enhancing Seed and Crop Performance. *Agriculture*, Vol. 10, issue 11;

[2]   Asaf Z., (2007), Determination of discrete element model parameters required for soil tillage. *Soil and Tillage Research*, Vol 92, issue 1-2, pp. 227-242;

[3]   Boac J M., (2010), Material and Interaction Properties of Selected Grains and Oilseeds for Modelling Discrete Particles[J]. *Transactions of the Asabe*, Vol. 53, issue 4, pp.1201-1216;

[4]   Feng Y.T., (2009), On upscaling of discrete element models: similarity principles. *Engineering Computations: International Journal for Computer-Aided Engineering and Software*, Vol. 26, issue 6;

[5]   Hao Y.L., (2017), Research on Spiral Dense Conveying of Powder Packaging. *Jiangnan University*;

[6]   Hu G.M., (2010), *Discrete Element Method Analysis and Simulation of Particle System——Introduction to Industrial Application of Discrete Element Method and EDEM Software*. Wuhan University of Technology Press;

[7]   Johnsonkl, (1971), Surface energy and the contact of elastic solids. *Proceedings of the Royal Society of London Series A, Mathematical and Physical Sciences*, Vol. 324, issue 1558, pp. 301-313;

[8]   Jaeger H.M., (1996), The physics of granular materials. *Physics Today*, Vol 49, issue 2, pp. 32-38;

[9]   Liu Y., (2017), *Study on the relationship between the accumulation and flow characteristics of powder system and the force between particles*. East China University of Science and Technology;

[10]   Li Y.X., (2019), Discrete element parameter calibration of wheat flour-based on grain scaling. *Transactions of the Chinese Society of Agricultural Engineering*, Vol 35, issue 16, pp. 320-327;

[11]   Luo S., (2018), Vermicompost matrix discrete element method parameter calibration based on the JKR bonding model. *Transactions of the Chinese Society of Agricultural Machinery*, Vol. 49, issue 04, pp.343-350;

[12]   LaTosha M. Gibson., (2013), Image analysis measurements of particle coefficient of restitution for coal gasification applications [J] . *Powder Technology*, Vol. 247, pp. 30-43;

[13]   M. Van Zeebroeck, E., (2006), The discrete element method (DEM) to simulate fruit impact damage during transport and handling: Model building and validation of DEM to predict bruise damage of apples [J]. *Postharvest Biology and Technology*, Vol. 41, issue 1;

[14]   Ma Y.H., (2020), Parameter calibration of discrete element model for alfalfa straw compression simulation. *Transactions of the Chinese Society of Agricultural Engineering*, Vol. 36, issue 11, pp. 22-30;

[15]   Mohammadreza A., (2018), A methodology for calibration of DEM input parameters in the simulation of segregation of powder mixtures, a special focus on adhesion. *Powder Technology*;

[16]   Mukherjee R., (2018), DEM based computational model to predict moisture induced cohesion in pharmaceutical powders[J]. *International Journal of Pharmaceutics*, Vol 536, issue 1, pp. 301;

[17]   Peng C.W., (2020) Parameter calibration of the discrete element simulation model for pig manure organic fertilizer treated by Heishui Fly. *Transactions of the Chinese Society of Agricultural Engineering*, Vol. 36, issue 17, pp. 212-218;

[18]   Pachón-Morales, (2019), DEM modelling for flow of cohesive lignocellulosic biomass powders: Model calibration using bulk tests [J]. *Advanced Powder Technology. https://hal.archives-ouvertes.fr/hal-02294258/document*;

[19]   Stavrou Alexandros Georgios, (2020), Investigation of Powder Flowability at Low Stresses by DEM Modelling[J]. *Chemical Engineering Science*, Vol. 211;

[20]   Sakai M., Abe M., Shigeto Y., et al. (2014), Verification and validation of a coarse grain model of the DEM in a bubbling fluidized bed[J]. *Chemical Engineering Journal*, Vol. 244, pp.33-43;

[21]   Thakur S.C, Ooi JY, Ahmadian H. (2016), Scaling of discrete element model parameters for cohesionless and cohesive solid[J].*Powder Technology*, Vol. 293, pp.130-137;

[22]   Tamas K., (2018), The role of bond and damping in the discrete element model of soil-sweep interaction[J]. Biosystems Engineering，Vol. 169, pp. 57-70;

[23]   Weinhart, Thomas, Labra, et al. (2016), Influence of coarse-graining parameters on the analysis of DEM simulations of silo flow.[J]. *Powder Technology*;

[24]   Wu J.S., (2019), Peucedanum praeruptorum seed physical parameters determination and discrete element simulation model parameter calibration. *Journal of Gansu Agricultural University*, Vol. 54, issue 4, pp. 180-189;

[25]   Xing J.J., (2020), Parameter calibration of the discrete element simulation model for the granular red soil in Hainan hot area. *Transactions of the Chinese Society of Agricultural Engineering*, Vol. 36, issue 05, pp. 158- 166;

[26]   Zhao L.L., (2009), Seed coating and its application in China. *Chinese Agricultural Science Bulletin*, Vol. 25, issue 23, pp. 126-131;

[27]   Zeng Z.W., (2021), Application status and the prospect of discrete element method in agricultural engineering research. *Transactions of the Chinese Society of Agricultural Machinery*, Vol 52, issue 04, pp. 1-20;

[28]   Zhou L.H., (2017), EDEM simulation and experimental study of vertical screw conveying. *Zhejiang University of Technology*;

EXPERIMENTAL STUDY OF AERODYNAMIC CHARACTERISTICS AND EVALUATION OF WIND FLOW CONCENTRATOR EFFICIENCY
/
ЕКСПЕРИМЕНТАЛЬНЕ ДОСЛІДЖЕННЯ АЕРОДИНАМІЧНИХ ХАРАКТЕРИСТИК ТА ОЦІНКА ЕФЕКТИВНОСТІ КОНЦЕНТРАТОРА ВІТРОВИХ ПОТОКІВ

**GOROBETS V.G.[1]), TROKHANIAK V.I.[*1]), MASIUK M.Yu.[1]), SPODYNIUK N.A.[1]),
SHEREMETYNSKA O.V.[2]), SHELIMANOVA O.V.[1])**
[1]) National University of Life and Environmental Sciences of Ukraine / Ukraine;
[2]) National University of Food Technologies / Ukraine;
Tel: +380673513082; E-mail: Trohaniak.v@gmail.com
DOI: https://doi.org/10.35633/inmateh-66-26

ABSTRACT
An experimental study of the wind flow concentrator of a new design using the wind tunnel of subsonic speeds was carried out. Experimental studies in the wind tunnel were performed at an air flow velocity of 1 m/s. The fields of velocity and pressure distribution in the areas in front of the wind flow concentrator and in its central part are obtained. Based on the obtained data in the Mathcad, contour graphs are constructed, which show the distribution of wind flow velocities and pressures in the investigated part of the wind flow concentrator. As a result, it was obtained that in the area of the wind turbine blades there is an increase in the velocity of air masses by 4 times compared to the air velocity at the entrance to the wind flow concentrator. The proposed design of the wind flow concentrator makes it possible to increase the efficiency of the wind turbine and receive electric energy at low wind speeds, when the bladed wind turbines do not generate electricity. Verification of experimental data with data of numerical modeling of hydrodynamics in the wind flow concentrator is carried out. The evaluation of the use of wind flow concentrator to increase the efficiency of wind turbines with a vertical axis of rotation is carried out.

РЕЗЮМЕ
Проведено експериментальне дослідження концентратора вітрових потоків нової конструкції з використанням аеродинамічної труби до звукових швидкостей. Експериментальні дослідження в аеродинамічній трубі проводилися при швидкості повітряного потоку 1 м/с. Отримано поля розподілу швидкостей і тисків на ділянках перед концентратором вітрових потоків та в центральній його частині. На основі отриманих даних в середовищі MathCAD побудовано контурні графіки, які показують розподіл швидкостей та тисків вітрового потоку в досліджуваній частині концентратора вітрових потоків. В результаті отримано, що в зоні знаходження лопатей вітротурбіни має місце збільшення швидкості руху повітряних мас в 4 рази в порівнянні з швидкістю руху повітря на вході в концентратор вітрових потоків. Запропонована конструкція концентратора вітрових потоків дає можливість підвищити ефективність вітротурбіни і отримувати електричну енергію при малих швидкостях вітру, коли лопатеві вітротурбіни не генерують електричну енергію. Проведено верифікацію експериментальних даних з даними чисельного моделювання гідродинаміки в концентраторі вітрових потоків. Проведена оцінка використання концентатора вітрових потоків для підвищення ефективності вітрогенераторів з вертикальною віссю обертання.

INTRODUCTION
The efficiency of modern blade type wind turbines (WT) has approached the maximum values of generated power. In contrast to blade type wind turbines, vertical-axis wind turbines can have much higher theoretical values of the wind flow energy utilization factor. Therefore, the development of new designs of vertical-axis wind turbines (VAWT) is of perspective. In this regard, in the field of small and medium capacities, it is advisable to use vertical-axis, orthogonal wind turbines. There are number of theoretical works in which the prospects of development of new designs of vertical axis wind turbines are shown (*Colin Walsh, 2019*).

---

[1] *Gorobets V.G., Head of Dep. DSc. Eng.; Trokhaniak V.I., Assoc. Prof. Ph.D. Eng.; Masiuk M.Yu., Ph.D. Student; Spodyniuk N.A., Assoc. Prof. Ph.D. Eng.; Sheremetynska O.V., Assoc. Prof. Ph.D. Economics; Shelimanova O.V. Assoc. Prof. Ph.D. Eng.*

In recent years, researchers have conducted in-depth studies of the aerodynamic characteristics of vertical-axis wind turbines in different conditions, including their use in terms of urban development (*Balduzzi F. et al., 2012*). Various methods were used to study the conditions of wind flow around the vertical-axis wind turbines, including an analytical model based on the method of double multiple flow pipes, to calculate the characteristics of the rotor for vertical-axis wind turbines with straight variable pitch blades (*Soraghan C.E, et al., 2013*), the method of discrete-vortex modeling (*Wang L. and Yeung R.W., 2016*), cascade model (*Mandal A. and Burton J., 1994*) and 2D and 3D flow modeling around the turbine (CFD modeling) (*Franchina N. et al., 2019*). Among these methods, CFD modeling is considered as a method of high accuracy, which can give a detailed picture of the field of velocities and pressures in the air flow (*Rezaeiha A. et al., 2017*), and also make it possible to detect the interaction of the oncoming flow with the blades and to obtain the existing dynamic effects in the studied wind generation systems (*Ghasemian M. et al., 2017*). An important role in the study of the conditions of hydrodynamic flow when flowing around the vertical-axis wind turbine is played by studies in the wind tunnel, which allows to obtain local characteristics of the flow and to suggest methods to increase their efficiency (*Battisti L. et al., 2018*). All these methods were used to evaluate the influence of various geometric parameters, including the function of the optimal pitch of the blades, based on the optimal angles of the blades (*Xu Y.L. et al., 2019*), symmetrical and curved blades (*Bausas M.D. and Danao L.A.M., 2015*), the influence of strength and aerodynamic profile of the blades on the characteristics of vertical-axis wind turbines (*Subramanian A. et al., 2017*) and the effect of rotor elongation on power characteristics in three-dimensional analysis using the panel method (*Li Q. et al., 2017*).

The aerodynamic parameters of the hybrid-shaped vertical-axis wind turbine in different operating conditions were also studied, which include different speed coefficients of the blade tip (tip speed ratios), torque factor, power factor, (*Ashwindran S. et al., 2019*), Reynolds numbers (*Hand B. et al., 2017*), turbulence intensity (*Su J. et al., 2*019), and also instability of a wind flow (*Danao L.A. et al., 2013*). In addition to the above studies, some new configurations of vertical-axis wind turbine and blade profiles have recently been suggested. *Xu Z. et al. (2018)* conducted an experimental and numerical study on a series of new disk wind rotors used in a small-scale wind turbine. The influence of the blade velocity coefficient, inclination angle and opening angle is estimated and a higher wind rotor power factor is obtained.

Perez-Torro R. and Kim J.W. (2017) investigated the flow characteristics of the NACA0021 wing with sinusoidal corrugated blades using the large vortex simulation technique (LVS). The results showed that the increased lifting force and the reduced traction force are achieved by using the wavy front of the blade instead of the straight front of the blade. Subsequently, *Wang Z. and Zhuang M. (2017)*, studied the conditions for improving the energy performance of the traditional model of H-type vertical-axis wind turbine by using sinusoidal teeth on the leading edge of the turbine blades to control the dynamic flow distribution at low blades` speed coefficient. The output power results showed that the improved configuration has reduced the impact of the dynamic delay effect and increased the generator torque. *Arpino F. et al., (2018)*, suggested a new vertical-axis wind turbines, which use a Darier rotor with three pairs of blades, each of which consists of a main and auxiliary wing. It is proved that the new configuration has a higher power factor at a lower speed coefficient of the tip compared to the classic straight blade of vertical-axis wind turbine, which is the most adaptive for use in urban development. *Chong W.T. et al., (2017),* suggested a wind turbine with transverse blades, consisting of three vertical blades and six horizontal blades, located in the direction of the transverse axis.

In addition to improving the power factor of the wind turbine, a number of authors have suggested the use of auxiliary devices to increase the energy of wind flow, in particular deflectors (*Takao M. et al., 2009; Wong K.H. et al., 2018*) and diffusers (*Zanforlin S. and Letizia S., 2015*). Watanabe and others (*Watanabe K. et al., 2016*) used the structure of the diffuser in the directing channels, utilized in the wind turbine, to increase its power factor. In their research, they also optimized the geometry of this diffuser.

Another way to increase efficiency is to use a device for concentrating the wind flow with curved contours (*Yan Li, et al., 2019*), which are installed in the upper and lower part of the rotor, to increase the wind flow energy.

Installation of wind prefabricated device on the rotor is one of the most perspective researches in recent years, which makes it possible to increase the speed of self-starting of the rotor. *Ji J.F. et al., (2012)*, suggested one of the designs of wind turbine with wind shields, installed around the wind turbine along the inlet flow direction, which can control the inlet flow and increase the wind speed when the wind blows on the rotor. The results showed that the suggested designs to increase the wind speed improved starting and energy indicators of the wind turbine.

Huang J. et al., (2013), studied the design of wind turbines with directing blades, the directing blades of which were installed around the rotor along the inlet flow direction. Results of the study showed that the directing blades improved the starting performance of wind turbine. Similarly, *Xiaohang Wang et al. (2018),* introduced a patented V-shaped directing blade with a solar and wind energy generation system, mounted on an eco-roofing system. As a result of experimental studies, it was found that the speed of self-starting and the speed of rotation of the wind turbine installed over the roof with a V-shaped blade, were significantly increased compared to the wind turbine designs without this type of blade. *Wong Kok Hoe et al., (2018),* using laboratory tests and computer simulations investigated the aerodynamic effects of the flow conditions of the flat deflector and the velocity fields. This deflector was placed in the lower part in front of the micro-rotor of the wind turbine and used to increase the wind flow velocity. Analysis of the simulation results shows that the deflector increases the wind flow velocity in areas located near the wind turbine blades.

Li Yan et al., (2018), suggested an innovative device for the wind flow concentration that have a shortened conical shape, which is installed in the upper and lower part of the rotor. This type of location increases the velocity of the input flow and increases the efficiency of wind turbines.

The main idea of the study (*Abdul Latif Manganhar et al., 2019*) is to use special deflectors that increase the wind flows velocity of the wind power turbine. The suggested rotor design consists of four equidistant vertical walls, which are rotated at an angle of 45 degrees relative to the wind flow direction. The rotated wall deflects the wind flow directing it normally to the surface of the blade. The suggested design has two advantages over the known ones - it prevents the reduction of the negative impact of turbulent flows on the turbine blade and increases the torque.

Vergaerde A. et al., (2020), investigated the influence of the close location of two VAWT on the generated power in the wind tunnel. The increase in power depends on the distance between them, the speed coefficients of the blade tip and the direction of rotation of the two wind turbines. *Kim D. and Gharib M. (2013),* used a flat plate in front of a pair of vertical-axis wind turbines to test its effect on the produced capacity of wind turbines. The effect of accelerating wind flow around the deflector was later confirmed by measuring velocities by visualizing wind flow (*Kim D. and Gharib M., 2014*). *Jin X. et al., (2018),* studied the efficiency of VAWT with a deflector, installed in front of two wind turbines, using three-dimensional (3D) CFD simulations. Based on the obtained results wind generation system (*Yichen Jianga et al., 2020*) was developed. This system consists of two counter-rotating wind turbine rotors and a deflector, which is located between these rotors.

MATERIALS AND METHODS

Development of wind flow concentrator. One of the promising designs of the wind flow concentrator (WFC) is the shape of a truncated cone with directing channels, which is shown in Fig. 1. The suggested concentrator of wind flow consists of a system of narrowing channels of the confuser type (*Gorobets V.G. and Masiuk M.Yu., 2021*). The upper and lower part of these channels are closed by conical surfaces, which makes it possible to concentrate the wind flow towards the rotor.
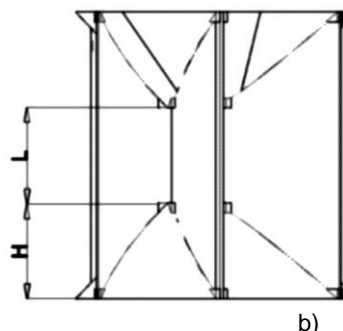
a)   b)
Fig. 1 - Appearance of the wind flow concentrator
a) side view, b) sectional view (top).

According to the equation of continuity of flow in an incompressible liquid (gas), the use of confuser-type narrowing channels increases the flow velocity and contributes to the energy concentration of the wind flow in the direction of the rotor. The geometry of the directing blades of the channels is chosen to direct the wind flow at the optimal angle of attack on the turbine blades.

The suggested design of the wind flow concentrator is universal and works regardless of the wind direction, which flows through the directing channels of the confuser type, where its speed increases due to the Venturi effect.

As a result of using this type of device, can be obtained a greater power of wind flow per unit of area for any wind direction, which increases the performance of the wind turbine. Given the fact that the electromagnetic moment and power of the wind turbine are proportional to the square and the cube of wind speed, respectively, the use of a wind flow concentrator will improve the aerodynamic characteristics of the VAWT.

Design of an experimental sample of wind flow concentrator

Experimental studies of wind flow concentrator are carried out in a wind tunnel, which has the following characteristics: the transverse dimensions of the working area 0.3×0.3 m, the range of changes in wind flow velocity in the working area from 0 to 18 m/s. Based on these characteristics an experimental sample of wind flow concentrator with the following parameters, which are given in Table 1 was developed and designed. The suggested design of the wind flow concentrator contains 6 channels, for which the area of the input and output cross-section of a separate channel is S1 and S2, respectively (Fig. 2).
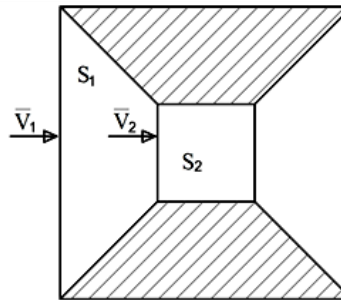
Fig. 2 – Transverse profile of the wind flow concentrator
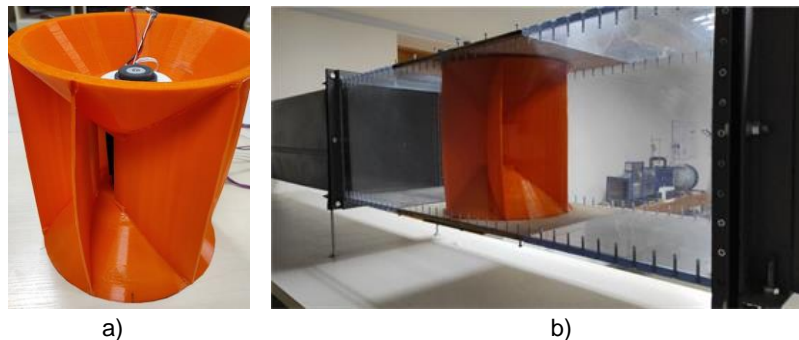
a)   b)
Fig. 3 – General view of the experimental sample
a) wind flow concentrator, b) working area of the wind tunnel with wind flow concentrator and turbine rotor.

Table 1

Structural parameters of the wind flow concentrator

Name	Dimensionality	Size
Cone height H	m	0.1
The height of the working area L	m	0.1
Blade thickness l	m	0.002
The size of the working area LxR	m	0.1x0.1
The area of the inlet of the channel S_1	m^2	0.0471
The area of the outlet of the channel S_2	m^2	0.0052

Research method. The general concept of the WFC is to increase the energy of the wind flow per unit area, increase the torque over the entire area of the blades, reduce the turbulence of the oncoming flow and stabilize the rotor rotation speed. The characteristics of the wind flow concentrator were found by modeling the aerodynamic flows using CFD modeling of commercial package ANSYS FLUENT for both a single channel and for the entire structure (*Gorobets V.G. et al., 2021*). The geometric shape of a single channel was selected from the conditions of minimum hydraulic losses during the passage of wind flow through each channel and the maximum value of the pressure force of this flow on the rotor blades. Experimental study of the vertical-axis wind turbine was conducted in the problem-scientific laboratory "Heat-mass transfer processes and alternative energy sources" at the Department of Heat and Power Engineering of the National University of Life and Environmental Sciences of Ukraine.

During the test, a 10-bladed H-rotor turbine with a rotor diameter of 0.1 m and a height of 0.1 m was used. The general view of the experimental sample of the wind flow concentrator and the turbine rotor is shown in Fig. 3.

Given that the wind flow concentrator is not a symmetrical structure, before the study in the wind tunnel, an initial experiment was conducted for wind flow in its different directions. These studies make it possible to evaluate the efficiency of the wind flow concentrator in comparison with the known designs of vertical-axis wind turbines. The experiment was performed for two positions of the WFC relative to the wind flow direction (Fig. 4). For the first position, the flow direction coincided with the central axis of the inlet channel of the wind flow concentrator, and the accepted position of the concentrator corresponded to 0° (Fig. 4a). For the second position, the wind flow concentrator was shifted by 30°, at which the direction of wind flow was addressed to the edge of one of the walls of the directing channels (Fig. 4b).

During the experimental studies, the WFC was placed in the working area of the wind tunnel. Within the working section of the wind tunnel, a system of measurements of hydrodynamic values of wind flow was developed, namely the fields of velocities and pressures in the vertical section of the working area of the wind tunnel. The air velocity was measured with an AM-70 anemometer, and the pressure values were obtained using a Testo 510 differential manometer and a Pitot-Prantl tube. The measuring parts in the cross section of the working area of the wind tunnel were divided into 15 equal parts, in which measurements to obtain the fields of velocities and pressures in the air flow were made.

The measurement was performed directly in front of the wind flow concentrator and in its central part, where the rotor shaft with blades is located. The WFC was placed in the wind tunnel in accordance with the first position (Fig. 4a). The measurement areas were located directly in front of the wind flow concentrator and in its central part. (Fig. 4a).

a)

b)
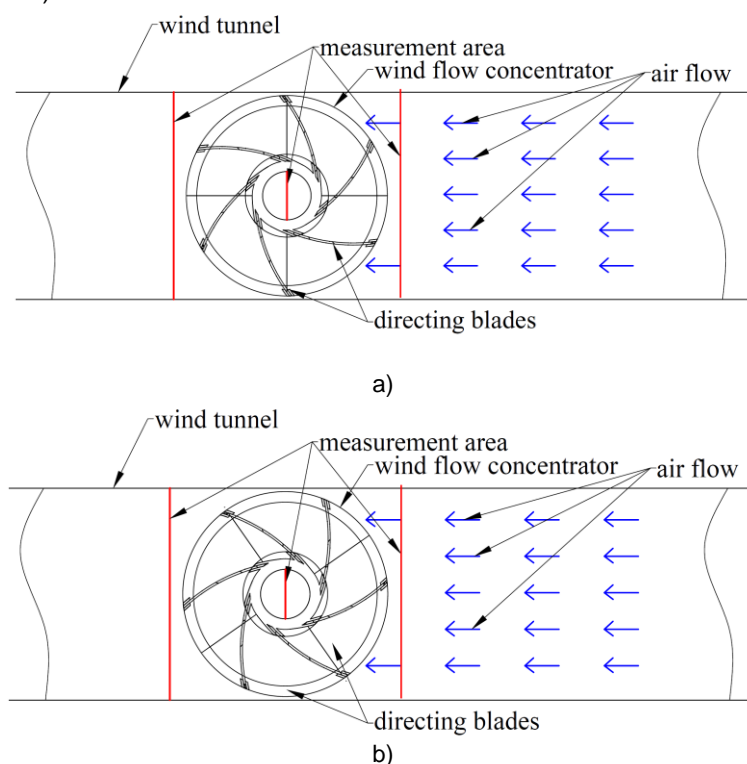
Fig. 4 – Measurement areas for oncoming air flows in position
a) 0 ° to the wind flow concentrator; b) 30 ° to the wind flow concentrator.

RESULTS

Based on the obtained experimental data, contour graphs were constructed, which show the distribution of velocities and pressures in the wind flow in front of the wind flow concentrator (Fig. 5).

Analysis of the obtained graph of wind flow velocity distribution (Fig. 5a) shows that the air velocity increases near the side walls, while in the central part the velocity decreases due to the presence in the working area of the wind tunnel structure that creates aerodynamic resistance. The graph of pressure distribution (Fig. 5b) in the wind flow shows that the highest pressure values are observed in the central part of the vertical section of the wind tunnel, while the pressure drops near the side surfaces.

a) b)
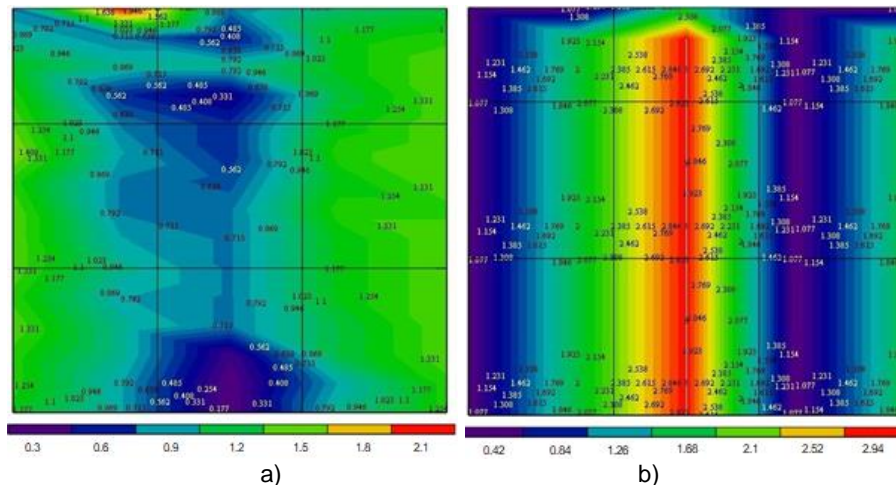
Fig. 5 – Distribution of velocities (a) m/s and pressures (b) Pa of the wind flow in front of the WFC

The next measurement was performed within the central part of the WFC (Fig. 6). According to the internal dimensions of the wind flow concentrator, the number of measurements was less, namely 5 horizontally and 7 vertically. The bold line shows the profile of the blades in the central part of the WFC. Based on the obtained data, contour graphs in the MathCAD software are constructed, which show the distribution of wind flow velocities (Fig. 6a) and pressures (Fig. 6b) in the central part of the wind flow concentrator.

From the graph (Fig. 6a) it follows that there is a significant increase in the velocity of air masses in the area of the wind turbine blades. The average air velocity in the central part of the wind flow concentrator in the area of the wind turbine blades is about 4.5 m/s, at the inlet wind flow velocity in the channels of the wind flow concentrator of 1 m/s.

Analysis of the obtained pressure field in Fig. 6b shows a significant increase in pressure in the area of the wind turbine blades. The average air pressure in the central part of the wind flow concentrator in the area of the wind turbine blades is about 13.3 Pa.

a) b)
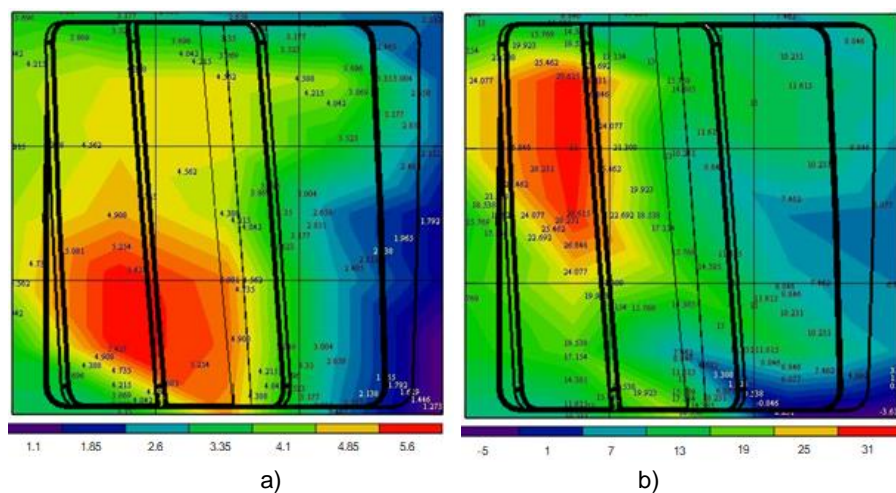
Fig. 6 – Distribution of velocities (a) m/s and pressures (b) Pa of wind flow in the central part of the WFC

Thus, when using the developed design of the WFC in its central part there is a significant increase in air flow velocity in the blades area of the wind turbine rotor. The average air velocity in the central part of the wind flow concentrator in the area of the wind turbine blades is 4 m/s, at an inlet velocity of 1 m/s. As a result of using the design of the wind flow concentrator, when flowing on the rotor of the wind turbine, makes it possible to increase the air flow velocity more than 4 times.

Similar measurements of velocity and pressure fields were performed at the second position of the wind flow concentrator, at its displacement by 30° (Fig. 4b). The measurement results are shown in Fig. 7-10.

The obtained results of experimental studies of the velocity distribution for the position of the WFC at 30° generally correlate with the position of the WFC at 0° (see Fig. 5-6).

The difference lies in the larger values of velocity in the central part of the wind flow concentrator, the average value of which is 4.7 m/s (Fig. 8-9) and a more uniform distribution of air flow velocities in the horizontal section of the working area of the wind tunnel. In addition, for the position of the wind flow concentrator at 30°, the pressure in the central part of the structure is slightly reduced compared to the previous position, and its average value is 8.2 Pa (Fig. 7).

a)   b)
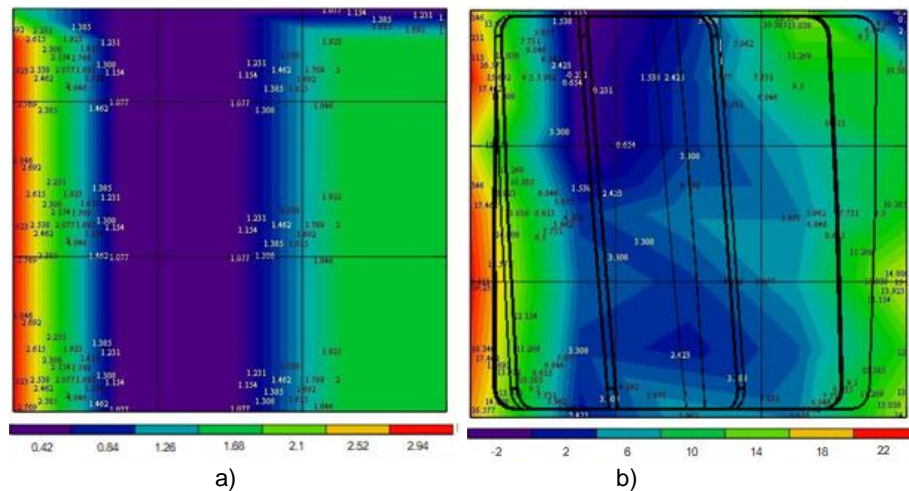
Fig. 7 – Pressure distribution (Pa) of wind flow in front of the WFC (a) and in the central part of the WFC (b)

A comparison of the results of numerical simulations (CFD simulation) (*Gorobets V.G. et al., 2021*) of aerodynamic flow in wind turbine with a vertical axis of rotation and a wind flow concentrator at the second position of the concentrator, which corresponds to its displacement by 30° was performed (see Fig. 4b). The results of the comparison for the distribution of air flow velocities when flowing around the wind flow concentrator are shown in Fig. 17-19.

Fig. 8 shows the results of CFD modeling (*Gorobets V.G. et al., 2021*) and experimental data for local velocity distributions in the air flow in front of the WFC. Fig. 9 shows the same results in its central part. Fig. 10 shows the average values of velocities in the cross section of the working area of the wind tunnel obtained by experimental and numerical study. The comparison shows that the air velocity in front of the WFC in numerical calculation is close to 1.09 m/s, at the same time in the experimental data, the average air velocity is 1.03 m/s (Fig. 10). In the central part of the wind flow concentrator the average values of air velocity in numerical simulation are 5.45 m/s, and in experimental studies the air velocity is close to 4.85 m/s (Fig. 10). Estimates show that the error of CFD modeling results in front of the wind flow concentrator does not exceed 5%, and in its central part – 12.3%. Higher values of errors in numerical simulations within the wind flow concentrator are explained by the more difficult nature of the hydrodynamic flow in this area. In general, the obtained results of experimental studies and numerical calculations (*Gorobets V.G. et al., 2021*) are satisfactorily correlated with each other.

a)   b)
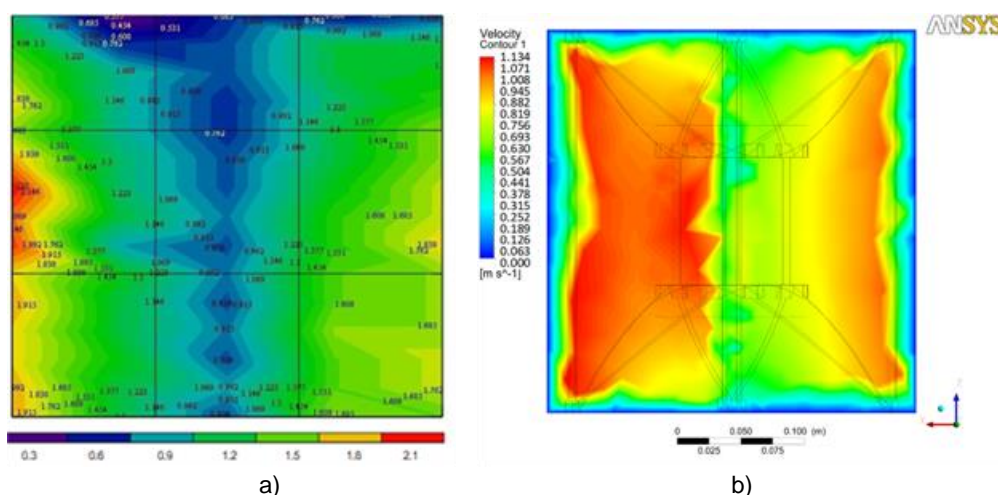
Fig. 8 – Distribution of wind flow velocity (m/s) in front of the WFC
a) experiment, b) CFD modeling (Gorobets V.G. et al., 2021)

a)   b)
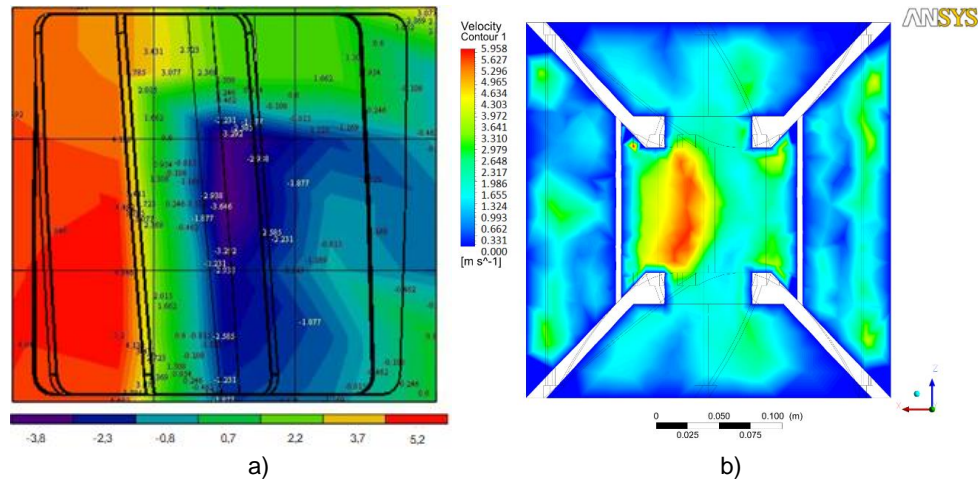
Fig. 9 – Distribution of wind flow velocity (m/s) in the central part of the WFC
a) experiment, b) CFD modeling (Gorobets V.G. et al., 2021)
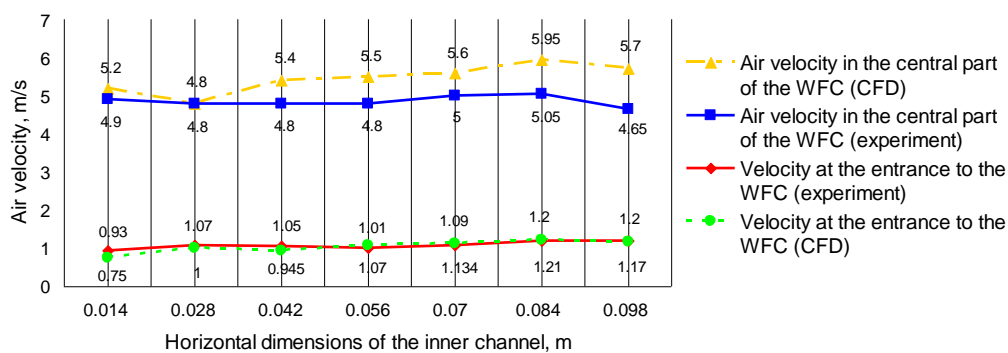
Fig. 10 – Comparison of experimental air velocity data with CFD modeling data *(Gorobets V.G. et al., 2021)*

The results of experimental studies and numerical calculations of hydrodynamics when flowing around the wind flow concentrator of wind turbine with a horizontal axis of rotation make it possible to assess the effectiveness of the suggested device to improve the characteristics of wind turbines. It is known that the efficiency of wind turbines depends on the air flow velocity that flows on the turbine blade:

$$N = C_N N_f \equiv C_N V_{wind}^3 S / 2 \tag{1}$$

Where: N - useful power of the wind turbine, N_f - power of the wind flow, V_{wind} - the air flow velocity flowing on the turbine blade, S - the cross-sectional area of the wind turbine wheel.

Thus, even a small increase in air velocity significantly affects the efficiency of the wind turbine. The use of wind flow concentrator makes it possible to significantly increase the velocity V_{wind} as well as the total power of the wind turbine. In the future efficiency assessments and economic calculations of the suggested systems will be carried out. This will achieve an increase in the efficiency of specific structures of vertical-axis wind turbine.

CONCLUSIONS

1. A new design of the wind flow concentrator is proposed, which makes it possible to significantly increase the air flows velocity, flowing on the blades of wind turbines with a vertical axis of rotation.

2. Experimental studies of the hydrodynamic characteristics of the air flow during the flowing around the wind flow concentrator at different positions relative to the flow direction using a wind tunnel were conducted. The fields of velocities, pressures in front of the concentrator and in its central part were found.

3. It is shown that at wind flow velocities of 1 m/s in the central part of the wind flow concentrator the flow velocity when flowing on the wind turbine blade can exceed 4 m/s, which increases the efficiency of wind turbines especially at low air velocities in the environment.

4. The experimental data are compared with the data of numerical modeling of hydrodynamics in the wind flow concentrator and their satisfactory coincidence is obtained.

5. The prospects of using a wind flow concentrator for vertical-axis wind turbines to increase its efficiency and economic profitability are shown.

REFERENCES

[1]   Abdul Latif Manganhar, Altaf Hussain Rajpar, Muhammad Ramzan Luhur, Saleem Raza Samo, Mehtab Manganhar, (2019), Performance analysis of a Savonius vertical axis wind turbine integrated with wind accelerating and guiding rotor house, *Renewable Energy*, Vol. 136, pp. 512-520, United Kingdom;

[2]   Arpino F., Scungio M., Cortellessa G., (2018), Numerical performance assessment of an innovative Darrieus-style vertical axis wind turbine with auxiliary straight blades, *Energy Conversion and Management,* Vol. 171, pp.769-777. http://dx.doi.org/10.1016/j.enconman.2018.06.028, United Kingdom;

[3]   Ashwindran S., Aziz A.A., Oumer A., (2019), Unsteady computational study of novel biologically inspired offshore vertical axis wind turbine at different tip speed ratios: A two-dimensional study. International, *Journal of Automotive and Mechanical Engineering*, Vol. 16, pp. 6753-6572, Pahang/Malaysia;

[4]   Balduzzi F., Bianchini A., Carnevale E.A., Ferrari L., Magnani S., (2012), Feasibility analysis of a Darrieus vertical-axis wind turbine installation in the rooftop of a building, *Applied Energy,* Vol. 97, pp 921-929, https://doi.org/10.1016/j.apenergy.2011.12.008, Florence/Italy;

[5]   Battisti L., Persico G., Dossena V., Paradiso B., Castelli M.R., Brighenti A., et al., (2018), Experimental benchmark data for h-shaped and troposkien VAWT architectures, *Renewable Energy*, Vol. 125, pp. 425-444, https://doi.org/10.1016/j.renene.2018.02.098, United Kingdom;

[6]   Bausas M.D., Danao L.A.M., (2015), The aerodynamics of a camber-bladed vertical axis wind turbine in unsteady wind, *Energy*, Vol.93 pp.1155-1164, United Kingdom;

[7]   Chong W.T., Muzammil W.K., Wong K.H., Wang C.T., Gwani M., Chu Y.J., et al., (2017), Cross axis wind turbine: Pushing the limit of wind turbine technology with complementary design, *Applied Energy*, Vol.207, pp.78-95, https://doi.org/10.1016/j.apenergy.2017.06.099, United Kingdom;

[8]   Colin Walsh, (2019), Offshore Wind in Europe Key trends and statistics 2018. *WindEurope*; 2019. Brussels/Belgium;

[9]   Danao L.A., Eboibi O., Howell R., (2013), An experimental investigation into the influence of unsteady wind on the performance of a vertical axis wind turbine, *Applied Energy*, 107, 403-411. U.K.;

[10] Franchina N., Persico G., Savini M., (2019), 2D–3D computations of a vertical axis wind turbine flow field: Modeling issues and physical interpretations, *Renewable Energy*, Vol. 136, pp. 1170-1189, https://doi.org/10.1016/j.renene.2018.09.086, United Kingdom;

[11] Ghasemian M., Ashrafi Z.N., Sedaghat A., (2017), A review on computational fluid dynamic simulation techniques for Darrieus vertical axis wind turbines, *Energy Conversion and Management*, Vol. 149, pp. 87-100, https://doi.org/10.1016/j.enconman.2017.07.016 , Riverside/USA;

[12] Gorobets V.G., Masiuk M.Yu., (2021), Patent No 148161 Wind turbine with a vertical axis of rotation and a concentrator of wind flow, Kyiv/Ukraine;

[13] Gorobets V.G., Trokhaniak V.I., Masiuk M.Yu., Spodyniuk N.A., Blesnyuk O.V., Marchishina Ye.I., (2021), CFD modeling of aerodynamic flow in a wind turbine with vertical rotational axis and wind flow concentrator, INMATEH - Agricultural Engineering, Vol. 64, no. 2, 159-166, https://doi.org/10.35633/INMATEH-64-15, Bucharest/Romania;

[14] Hand B., Kelly G., Cashman A., (2017), Numerical simulation of a vertical axis wind turbine airfoil experiencing dynamic stall at high Reynolds numbers, Computers & Fluids, Vol. 149, pp. 12-30. United Kingdom;

[15] Huang J., Zhao Z.Z., Ye F., (2013), Numerical investigation on lift-type vertical axis wind turbine with guide vanes, *Renewable Energy Resources*, Vol. 3, pp. 53-56, Baghdad/Iraq;

[16] Ji J.F., Deng Z.Y., Jiang L., (2012), Optimization design of a 5 kW lift type vertical axis wind turbine with wind shield-growth patterns, *Journal of Thermal Science*, Vol. 33, pp. 560-564, Beijing/China;

[17] Jin X., Wang Y., Ju W., He J., Xie S., (2018), Investigation into parameter influence of upstream deflector on vertical axis wind turbines output power via three-dimensional CFD simulation, *Renewable Energy*, Vol. 115, pp. 41-53, https://doi.org/10.1016/j.renene.2017.08.012, United Kingdom;

[18] Kim D., Gharib M., (2013), Efficiency improvement of straight-bladed vertical-axis wind turbines with an upstream deflector, *Journal of Wind Engineering and Industrial Aerodynamics*, Vol. 115, pp.48-52, Netherlands;

[19] Kim D., Gharib M., (2014), Unsteady loading of a vertical-axis turbine in the interaction with an upstream deflector, *Experiments in Fluids*, Vol. 55, 1658, Germany;

[20] Li Q., Maeda T., Kamada Y., Shimizu K., Ogasawara T., Nakai A., et al., (2017), Effect of rotor aspect ratio and solidity on a straight-bladed vertical axis wind turbine in three dimensional analysis by the panel method, *Energy*, Vol. 121, pp. 1-9, https://doi.org/10.1016/j.energy.2016.12.112, United Kingdom;

[21] Li Yan, Zhao Shouyang, Tagawa Kotaro., (2018), Starting performance effect of a truncated cone-shaped wind gathering device on small-scale straight-bladed vertical axis wind turbine, *Energy Conversion and Management*, Vol. 167, pp.70-80, United Kingdom;

[22] Mandal A., Burton J., (1994), The effects of dynamic stall and flow curvature on the aerodynamics of Darrieus turbines Applying the cascade model, *Wind Engineering,* Vol. 18, pp. 267-282. New York/USA;

[23] Pérez-Torró R., Kim J.W., (2017), A large-eddy simulation on a deep-stalled aerofoil with a wavy leading edge, *Journal of Fluid Mechanics*; Vol. 813, pp. 23-52. Hampshire/United Kingdom;

[24] Rezaeiha A., Kalkman I., Blocken B., (2017), Effect of pitch angle on power performance and aerodynamics of a vertical axis wind turbine, *Applied Energy*, Vol. 197, pp. 132-150, United Kingdom;

[25] Soraghan C.E., Leithead W.E., Feuchtwang J., Yue H., (2013), Double multiple streamtube model for variable pitch vertical axis wind turbines. *In: 31st AIAA Applied aerodynamics conference*, http://dx.doi.org/10.2514/6.2013-2802, Glasgow/United Kingdom;

[26] Su J., Lei H., Zhou D., Han Z., Bao Y., Zhu H., et al., (2019), Aerodynamic noise assessment for a vertical axis wind turbine using improved delayed detached eddy simulation, *Renewable Energy*, Vol. 141, pp. 559-569. https://doi.org/10.1016/j.renene.2019.04.038, United Kingdom;

[27] Subramanian A., Yogesh S.A., Sivanandan H., Giri A., Vasudevan M., Mugundhan V., et al., (2017), Effect of airfoil and solidity on performance of small scale vertical axis wind turbine using three dimensional CFD model, *Energy*, Vol.133, pp. 179-190, United Kingdom;

[28] Takao M., Kuma H., Maeda T., Kamada Y., Oki M., Minoda A., (2009), A straight-bladed vertical axis wind turbine with a directed guide vane row – effect of guide vane geometry on the performance, *Journal of Thermal Science*, Vol.18, pp. 54-57, Beijing/China;

[29] Vergaerde A., De Troyer T., Standaert L., Kluczewska-Bordier J., Pitance D., Immas A., et al., (2020), Experimental validation of the power enhancement of a pair of vertical-axis wind turbines, *Renewable Energy* Vol.146, pp.181-187, https://doi.org/10.1016/j.renene.2019.06.115, United Kingdom;

[30] Wang L., Yeung R.W., (2016), On the performance of a micro-scale Bach-type turbine as predicted by discrete-vortex simulations, *Applied Energy,* Vol. 183, pp. 823-836, United Kingdom;

[31] Wang Z., Zhuang M., (2017), Leading-edge serrations for performance improvement on a vertical-axis wind turbine at low tip-speed-ratios, *Applied Energy*, Vol. 208, pp. 1184–1197, Columbus/USA;

[32] Watanabe K., Takahashi S., Ohya Y., (2016), Application of a diffuser structure to vertical-axis wind turbines, *Energies*, Vol. 9, pp. 406, https://doi.org/10.3390/en9060406, Basel/Switzerland;

[33] Wong K.H., Chong W.T., Sukiman N.L., Shiah Y., Poh S.C., Sopian K., et al., (2018), Experimental and simulation investigation into the effects of a flat plate deflector on vertical axis wind turbine, *Energy Conversion and Management*, Vol. 160, pp. 109-125, United Kingdom;

[34] Wong Kok Hoe, Chong Wen Tong, Sukiman Nazatul Liana., (2018), Experimental and simulation investigation into the effects of a flat plate deflector on vertical axis wind turbine, *Energy Conversion and Management*, Vol. 160, pp. 109-125, United Kingdom;

[35] Xiaohang Wang, Wentong Chong, Kokhoe Wong, et al., (2018), Preliminary Performance Tests and Simulation of a V-Shape Roof Guide Vane Mounted on an Eco-Roof System, *Energies*, Vol. 11, https://doi.org/10.3390/en11102846, Basel/Switzerland;

[36] Xu Y.L., Peng Y.X., Zhan S., (2019), Optimal blade pitch function and control device for high solidity straight-bladed vertical axis wind turbines, *Applied Energy*, Vol. 242, pp. 1613–1625, United Kingdom;

[37] Xu Z., Feng Y.H., Zhao C.Y., Huo Y.L., Li S., Hu X.J., et al., (2018), Experimental and numerical investigation on aerodynamic performance of a novel disc-shaped wind rotor for the small-scale wind turbine, *Energy Conversion and Management,* Vol. 175, pp. 173-91, United Kingdom;

[38] Yan Li,, Shouyang Zhao, Chunming Qu., Guoqiang Tong, Fang Feng, Bin Zhao, Tagawa Kotaro., (2019), Aerodynamic characteristics of Straight-bladed Vertical Axis Wind Turbine with a curved-outline wind gathering device, *Energy Conversion and Management*, Vol. 203, 112249, United Kingdom;

[39] Yichen Jianga, Peidong Zhaoa, Thorsten Stoesserb, Kun Wanga, Li Zou., (2020), Experimental and numerical investigation of twin vertical axis wind turbines with a deflector, *Energy Conversion and Management*, Vol. 209, 112588, https://doi.org/10.1016/j.enconman.2020.112588, United Kingdom;

[40] Zanforlin S., Letizia S., (2015), Improving the performance of wind turbines in urban environment by integrating the action of a diffuser with the aerodynamics of the rooftops, *Energy Procedia*, Vol. 82, pp. 774-781, https://doi.org/10.1016/j.egypro. 2015.11.810, United Kingdom.

PHENOTYPIC PARAMETER EXTRACTION FOR WHEAT EARS BASED ON AN IMPROVED MASK-RCNN ALGORITHM
/
基于改进 Mask-RCNN 算法的麦穗表型参数提取

Ruyi ZHANG [1]), Zongwei JIA *[1]), Ruibin WANG[1]), Simin YAO[1]), Ju ZHANG[1])
[1]) College of Information Science and Engineering, Shanxi Agricultural University, Taigu / China
Correspondence: Tel:+86-13835441286; E-mail: jiazw@sxau.edu.cn

ABSTRACT

The acquisition of traditional wheat ear phenotypic parameters is labour intensive and subjective, and some trait parameters are difficult to measure, which greatly limits the progress of wheat ear research. To obtain the phenotypic parameters of wheat ears in batches at a low cost, this paper proposed a convenient and accurate method for extracting phenotypic parameters of wheat ears. First, three improvement directions were proposed based on the Mask Region-Convolutional Neural Network (Mask-RCNN) model. 1) To extract the multiscale features of wheat ears, a hierarchical residual link was constructed in a single residual block of the backbone network ResNet101 to obtain information on different sizes of receptive fields. 2) The feature pyramid network (FPN) was improved to increase the recognition accuracy of wheat ear edges through multiple two-way information flow sampling. 3) The mask evaluation mechanism was improved, specific network blocks were used to learn and predict the quality of the mask, and the detection of wheat ears and grains was performed by precise segmentation; an automatic extraction algorithm was designed for wheat ear phenotypic parameters based on the segmentation results to extract 22 phenotypic parameters. The experiments showed that the improved Mask-RCNN was superior to the existing model in the segmentation accuracy of wheat ears and grains; the parameters of wheat ear length, width, and number of grains extracted by the automatic extraction algorithm were close to the manual measurement values. This research meets the demand for automatic extraction of wheat ear phenotype data for large-scale quality testing and commercial breeding and has strong practicability.

摘要

传统麦穗表型参数获取劳动强度大，主观性强，且部分性状参数难以测量，很大程度上限制了麦穗研究的进展。为了能用低成本批量获取麦穗的表型参数，本文提出一种便捷且精准的麦穗表型特征参数提取方案。首先基于 Mask-RCNN 模型提出三种改进方向，1）为了提取麦穗多尺度特征，在主干网络 ResNet101 的单个残差块内构建分层残差类链接以获取不同大小感受野的信息；2）改进 FPN 金字塔网络，通过多次双向信息流采样提高麦穗边缘的识别精度；3）增加掩码评价机制，采用特定的网络块来学习和预测掩码的质量，最终实现对麦穗和籽粒的精准分割。然后针对分割结果设计一种麦穗表型参数自动提取算法，提取包含麦穗的成熟度信息、颜色、形状、空间等 22 个表型特征的参数。实验证明本文改进后的 Mask-RCNN 在麦穗与籽粒的分割精度上优于现有模型；麦穗表型参数自动提取算法提取的麦穗长、宽、籽粒个数的参数接近人工测量值，满足大规模质量检测和商业化育种对麦穗表型数据自动化提取的需求，具有较强的实用性。

INTRODUCTION

Cultivate adaptable wheat varieties to increase yield and the sustainability of crop production, and it is inseparable from the extraction of refined wheat phenotyping parameters. As the key to wheat yield, the phenotypic parameters of wheat ears are particularly important. They are the main focus of agricultural researchers. Ear feature extraction helps distinguish wheat varieties *(He et al., 2005; Panfilova et al., 2019)*, evaluate wheat ear quality *(Vavilova et al., 2017; Khan et al., 2020)*, research wheat resistance *(Li et al., 2017; Li et al., 2020)* and Forecast wheat yield *(Khan et al., 2021; Würschum et al., 2018)*. However, we currently rely on the visual inspection of field crops by experts to quantify the characteristics of wheat ear shape under nondestructive conditions. During this task, a large amount of work depends on the judgment of external characteristics such as shape, colour, and spatial layout.

---

[1] Ruyi, Zhang, As. M.Agr. Stud.; Zongwei, Jia, Prof. MCS.; Ruibin, Wang, As. M.Agr. Stud.;
Simin, Yao, As. M.Agr. Stud.; Ju, Zhang, As. M.Agr. Stud.;

These characteristic values are difficult to directly quantify and describe. This has severely restricted the progress of scientific wheat research and the promotion of advanced production technology. Therefore, it is of great significance to quickly extract the phenotypic parameters of wheat ears in batches.

Image processing data acquisition technology, because of its low cost and low difficulty, has been widely used in wheat research *(Sadeghi et al., 2019; Alkhudaydi et al., 2019)*. Bi et al. *(2010)* calculated ear length by finding the main axis direction angle and rotation to calculate the length of the circumscribed rectangle and used corner detection to calculate the wheat awn feature parameters. Wang et al. *(2017)* selected an appropriate threshold to segment wheat based on the pixel characteristics of the ear image and then used the column data waveform characteristics of the corrected image to calculate the number of wheat ears. Lu et al. *(2016)* used the method of fitting the central curve of the main part of the wheat ear to calculate the length of the wheat ear and calculated the number of spikelets by passing the curve through the spikelet area and calculating the grey difference. However, the accuracy of these methods for wheat ear image extraction is not high, and this affects the acquisition of wheat ear phenotypic parameters. In recent years, due to its powerful data extraction capabilities, deep learning has become a promising tool for phenotypic data acquisition *(Tsaftaris et al., 2016; Eliceiri et al., 2016; King., 2007)*. Pound *(2017)* et al. marked the spikelets and the skeleton of potted wheat, constructed a network based on the hourglass model, and used heatmap regression to locate and count the spikelets, and the counting accuracy reached 99.66%. Wang *(2017)* et al. used the improved and efficient Det-D0 model to detect, count and analyse wheat ears, and the counting accuracy reached 94%.

In summary, current scholars have acquired some parameters of wheat ears, such as ear length, width, and number of spikelets *(Du et al., 2018; Wang et al., 2020)*. However, each method is limited in obtaining characteristics, and they cannot meet the various needs of agricultural researchers regarding the phenotypic characteristics of wheat ears.

This paper collects and compares a large number of wheat ears and finds that wheat ears of different varieties or the same variety in different environments have differences in the grain gap, the number of grains per unit area, and the distribution of grains. These characteristics are difficult to measure directly. They cannot be effectively used in wheat ear variety identification and quality inspection. In terms of ear appearance and morphology, researchers mainly focus on the detection of wheat ear problems such as pest prediction and morphological diagnosis *(Huang et al., 2014; Goyal et al., 2021)*. In large-scale planting, the effects of climate and moisture impact the grouting duration, and the impact on the yield of wheat if these effects are not treated in time is extensive *(Verman et al., 2015)*. The identification of the wheat ear growth period can help farmland managers irrigate and fertilize at the correct times, which is helpful for the planning of field management activities *(Yang et al., 2018; Kiss et al., 2014)*.

To achieve batched, accurate, and automatic acquisition of wheat ear maturity information and refined multiangle phenotypic indicators, this paper improves the Mask-RCNN model and designs an automatic extraction algorithm to determine wheat ear phenotype parameters. This precise extraction aims to meet the needs of large-scale selection and breeding.

MATERIALS AND METHODS
Experimental data

To ensure the diversity of the data and improve the applicability of the model, this paper uses data gathered from the wheat filling stage to just before the wheat ears are cut in the mature stage, that is, from 2021-05-12 to 2021-06-08; the data were collected randomly every 3 days for Shanxi Wheat ears in the experimental field outside the University of Agriculture, Dingxiang Fine Seed Field in Xinzhou City, and in Mengjiazhuang Village, Taigu District. During this period, 51 varieties of wheat and 578 wheat ears were collected. The wheat ears picked are sealed each time to prevent the grains from being lost during transportation. During imaging, a clip was used to hold the wheat so that the wheat was in a natural drooping state. A fixed-position Sony camera FDR-AX45 (with a resolution of 5044×3056 pixels) was used. One photo was taken from each of the four angles, and a total of 1064 pictures were taken.

The collected images were processed to meet the data requirements of the model. The data production process is as follows:

1) Labelme 's point annotation (CreatePolygons) was used to circle the overall outline of the ear and the side grain outline and generate a mask image.

2) To increase the training speed, the original image was trimmed and zoomed, and the image was adaptively zoomed to 512 × 512 pixels.

3) Data enhancement operations such as noise interference, colour jitter, contrast transformation, and random rotation were used for data augmentation. 4) According to the ratio of 7:2:1, the data set was randomly divided into a training set, validation set and test set.

Wheat ear segmentation model design based on Mask-RCNN
Basic network architecture

The premise of the accurate extraction of wheat ear phenotypic parameters is to achieve accurate pixel-level segmentation of wheat ears. For this reason, this article aims to address the problems of small wheat ears, high density, and serious awn occlusion. Based on these three goals, the Mask-RCNN model is improved. The overall block diagram of the network is shown in Figure 1. First, the backbone feature extraction network Res2Net101 and the feature pyramid network BFPN are used to obtain the feature layer, and then ROIAlign uses the feature layer to map the candidate frame ROI recommended by the Region Proposal Network，Region (RPN) into a fixed size feature map, and finally, the obtained feature map is classified and detected by branch and bound The box returns. Mask IoU Head optimizes the segmentation branch and obtains the segmentation map.
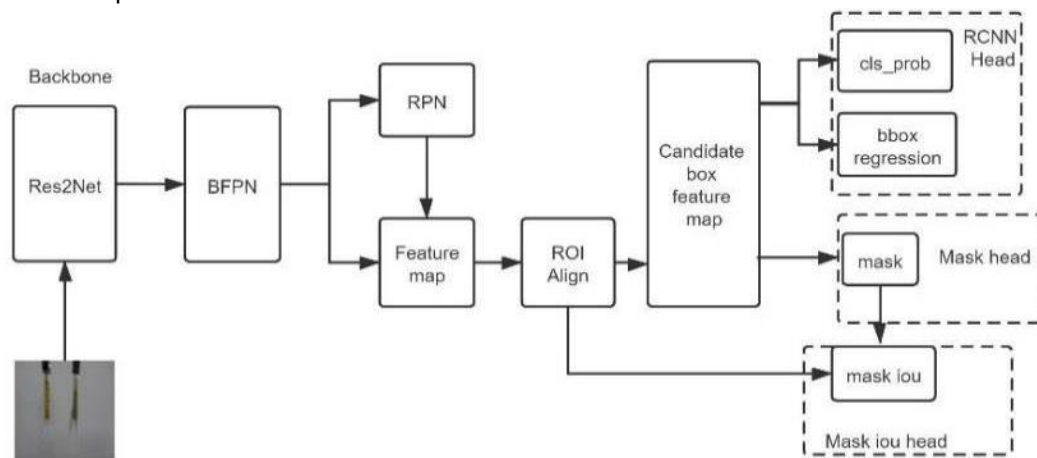
Fig. 1 - The overall block diagram of the improved algorithm based on Mask-RCNN

Feature extraction network design

The extraction of multiscale features is of great significance in computer vision, and designing a more effective structure can improve the ability of the network to extract features. In the process of identifying wheat ears and grains, due to the small grains and serious occlusion of wheat awns, missed inspections and faulty inspections can easily occur. More information is needed to express the characteristics of wheat ears. To improve the feature extraction capabilities of the network, this paper optimizes the backbone feature extraction network ResNet101 of Mask-RCNN and builds a hierarchical residual class link Res2Net module *(Gao et al., 2019)* in a single residual block in the residual network. Thereby improving the multi-scale representation ability at a more granular level, stronger multiscale characterization information under the same computing power is obtained. The structure is shown in Figure 2, and the network output can be expressed by equation (1).
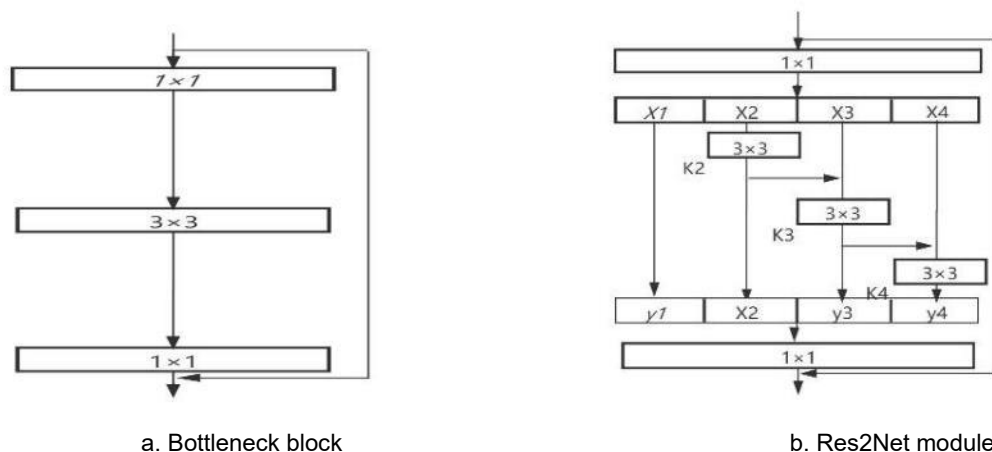
a. Bottleneck block   b. Res2Net module
Fig. 2 - Res2Net structure

$$y_i = \begin{cases} x_i & \text{i=1} \\ k_i \left(x_i + y_i - 1 \right) & 1 < i \leq s \end{cases} \tag{1}$$

The Res2Net module replaces the bottleneck block core of the residual block with multiple 3×3 filters and connects different filters in a hierarchical residual style. The connection form inside the module is similar to that of the residual network, and this helps to obtain different receptive field sizes. For example, y_2 will have a 3×3 receptive field, y_3 will have a 5×5 receptive field, and y_4 will have a larger size such as a 7×7 receptive field. In this way, the multiscale features of the granularity level are expressed, and the range of the receptive field of each network layer is increased. To increase the receptive field while reducing the computation as much as possible, omit the 3 × 3 convolutions, which can also be seen as the repeated use of a feature. In the replacement process, the hierarchical residual link does not increase the number of parameters, so it does not increase the burden on the network.

Design of the feature pyramid network (FPN)

In deep neural networks, shallow features pay more attention to detailed information, while high-level features pay more attention to semantic information. A traditional FPN combines high-level information upsampling with low-level features, which is essentially limited by one-way information flow. Only the high-level semantic information is enhanced, and the shallow semantic information of the neural network is highly correlated with detailed features such as edge shapes. The wheat ears and grains in this paper have serious adhesion, and the extraction of their characteristic parameters requires high edge accuracy. To fuse more features, this paper designs a multi-overlapped BFPN. Based on the unidirectional information flow of the original FPN, reverse downsampling information flow is added to fuse low-level edge features with high-level features to strengthen the extraction of the edge features of the wheat ears. The BFPN is shown in Figure 3.
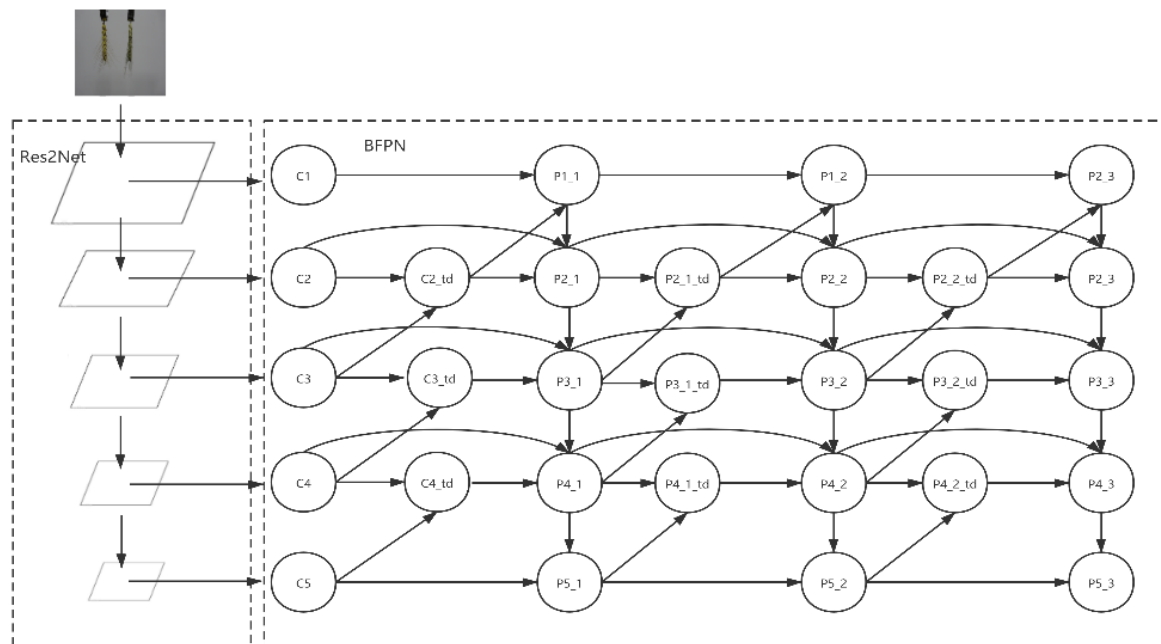
Note: The downward arrow indicates that convolution with a step size of 2 is used for downsampling, and the upward arrow indicates upsampling.

Fig. 3 - BFPN structure

To improve the fusion efficiency, this paper proposes several optimization methods for cross-scale connections. First, we remove the nodes that have only one input edge without feature fusion in the process of original FPN upsampling and shallow feature fusion to reduce the contribution of these nodes to feature fusion. The consumption of resources by small nodes is addressed. Second, when the shallow features are merged with the high-level features through downsampling, an extra edge (the feature layer ending with td in the figure) that is at the same level as the output node and has high-level information is added to fuse more features. Finally, each two-way path is regarded as a layer of the feature network, and the same feature network is stacked three times to obtain a higher level of scale fusion.

Improving the mask evaluation mechanism

In Mask-RCNN, the score of the mask branch is obtained based on the confidence of the classification branch. However, the mask quality usually does not have a high correlation with the classification score. If the score of the mask branch is used to evaluate the mask quality, there will be deviations. In this experiment, the segmentation mask determined based on the target detection classification frame of wheat ears is not the best segmentation structure, and it results in the low accuracy of the score for measuring the quality of wheat segmentation; the accuracy of the score will affect the performance of segmentation. To solve this mismatch problem, this paper adds a mask evaluation strategy, the Mask Scoring RCNN (*Huang et al., 2019*). Mask IoU Head is used to train the evaluation; it takes the features of the RoIAlign layer and the prediction mask together as input, completes the correct classification of the mask, and compares the prediction mask and the ground truth mask. The intersection over union (IoU) between the prediction mask and Mask IoU is used for regression to correct the deviation between the mask quality and mask score. The model in this paper also adds this part of the loss function to the model training. The structure is shown in the figure below, and the mask evaluation strategy is represented by:

$$Smask = Scls \cdot SIoU \tag{2}$$

$Scls$ represents the classification score, which focuses on the classification of the proposal, and represents the score of submission. $SIoU$ Focus on MaskIoU's regression.
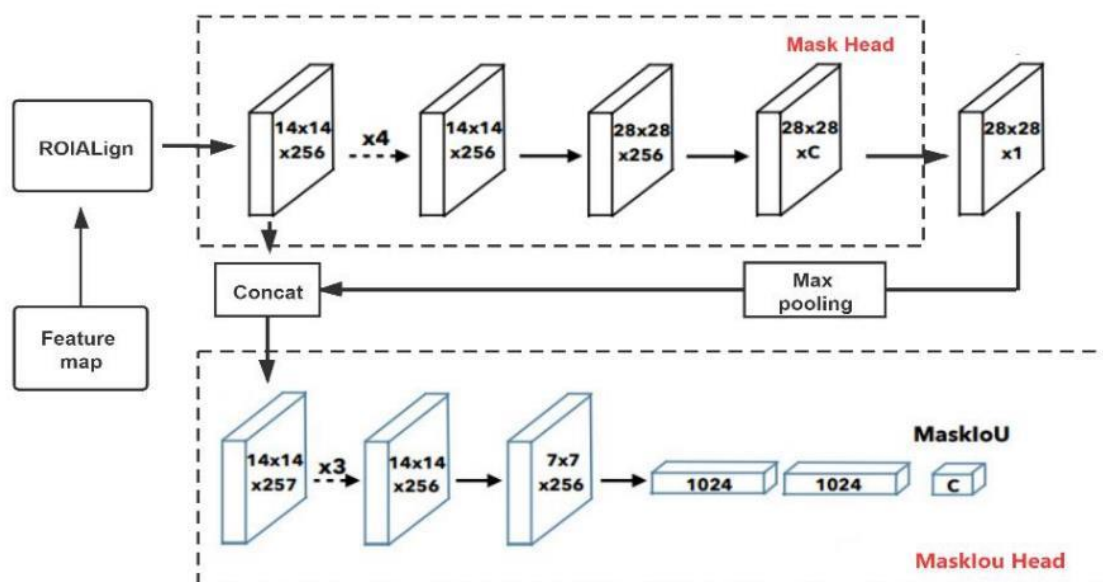
Fig. 4 - Structure diagram of the mask evaluation strategy

Design of the automatic extraction algorithm for wheat ear phenotypic parameters

Five kinds of mature wheat that do not exist in the training set or validation set, Jintai 188, Jintai 182, Zhongmai 175, Jingdong 22, and Chang 4738, were chosen as the test set, 3 plants of each wheat ear were selected, and images were taken from four angles. Finally, the improved Mask-RCNN model was used to segment the test set in real time, and the wheat ear phenotype parameters were obtained through the wheat ear phenotypic feature parameter extraction algorithm (as shown in Figure 5).

Table 1 describes the phenotypic characteristics of wheat ears. The feature extraction design is as follows:

1) Extraction of colour parameters. The wheat ear segmentation result is superimposed with the original image to separate the wheat ear, and the parameter values of the separated wheat ear are selected in the RGB three-colour space to represent the colour characteristics of the wheat ear.

2) Extraction of shape feature parameters. The camera calibration method is used to obtain the unit pixel length $\Delta\omega$, and the ear width and ear length are calculated by multiplying the unit pixel length by the maximum pixels in the vertical and horizontal directions of the wheat ear segmentation image. L is the ear length, W is the ear width, i is the i-th wheat ear, and n is the total number of wheat ears. Then, the average length and width of each ear are:

$$AvL = \frac{1}{n}\sum_{i=1}^{n} L_i \tag{3}$$

$$AvW = \frac{1}{n}\sum_{i=1}^{n} W_i \tag{4}$$

The average area is:

$$AVArea = \frac{1}{n}\sum_{i=1}^{n} CountAreamax \times \Delta\omega^2 \tag{5}$$

The absolute error between the predicted value and true value is:

$$MAE = \frac{1}{n}\sum_{i=1}^{n} |GTi - Prei| \tag{6}$$

Through the results of grain segmentation, each grain on a single wheat ear can be separated, the phenotypic parameters of each grain can be extracted, and then the average value of the kernel parameters on a single wheat ear can be calculated. The number of grains is obtained by the return value of the mask, and the average area of all grains is $\overline{Areas}$:

$$\overline{Areas} = \frac{1}{r}\sum_{i=1}^{r} Areas_i \tag{7}$$

The average perimeter of the grain can be obtained in the same way. If the average value $\overline{x}$ is used, the standard deviation is:

$$\sigma = \sqrt{\frac{1}{r}\sum_{i=1}^{r}(x_i - \overline{x})} \tag{8}$$
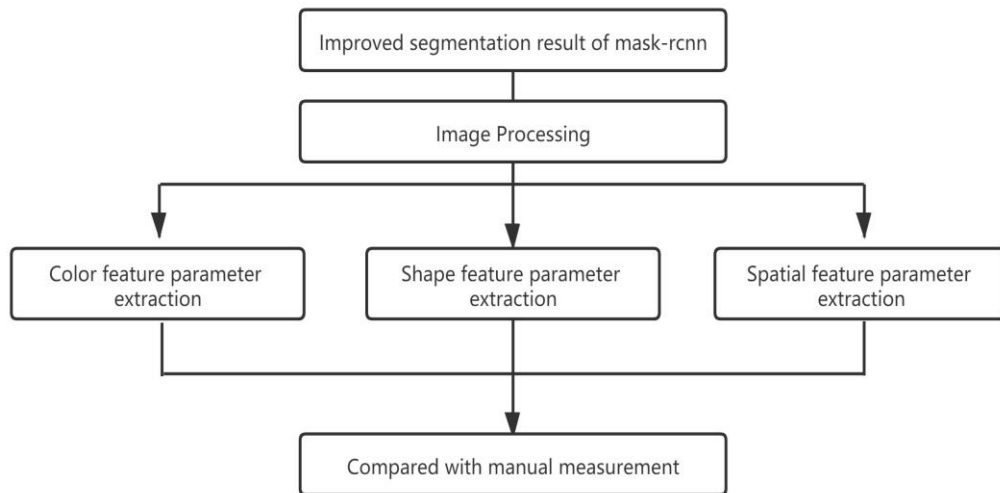
Fig. 5 - Flow chart of automatic extraction algorithm for wheat ear phenotypic parameters

3) Spatial parameter extraction. Spatial parameter extraction is performed jointly by the segmentation results of wheat ears and grains. The ear gap ratio is the ratio of the non-grain area to the entire wheat ear. The average grain angle calculation first derives the normal vector of the wheat ear according to the minimum circumscribed rectangle of the wheat ear mask and then calculates the angle of the grain through the wheat ear normal vector, as shown in Figure 6.

The gap distance between every two crystal grains in the same direction is obtained by the distance of the centre point of the smallest circumscribed rectangle of each crystal grain; then, the average gap distance $\overline{y}$ is:

$$\overline{y} = \frac{y}{r-2} \tag{9}$$

The grain density is closely related to the quantitative trait loci (QTL) mapping in wheat ρ (*Zhang et al., 2009*), and the number of grains per square metre is used to represent the grain density ρ:

$$\rho = \frac{r}{Area} \tag{10}$$

Fig. 6 - The diagram of Angle between grains

Table 1

Description of the wheat ear phenotype index

Types	Phenotyping indices	Description
period	maturity	The period in which wheat is grown or grated
Colour feature	R-channel mean	The red mean of RGB channels
	G-channel mean	The green mean of RGB channels
	B-channel mean	Average blue of RGB channels
Shape feature	Number of wheat ears/unit	The number of ears of wheat in the image
	spike length /cm	Maximum pixel length of the wheat ear in high direction
	ear width /cm	Maximum pixel length of the wheat ear in the broad direction
	panicle area /cm^2	The sum of the areas of the pixels occupied by wheat ears
	ear circumference /cm	Sum of pixel lengths of wheat fringe contour
	number of grains /pieces	The number of grains per ear on the image
	total grain area /cm2	Sum of pixel areas of all grains of a single wheat ear on the image
	Average grain area /cm2	Average pixel area of all grains of a single wheat ear on the image
	Standard deviation of grain area /cm	The standard deviation of a pixel area of all grains on a single ear of wheat on the image
	Average grain circumference /cm	Average pixel length of peripheral contour of all grains on a single wheat ear
	Standard deviation of grain circumference /cm	The standard deviation of pixel length of peripheral contour of all grains on a single wheat ear
Spatial feature	The proportion of ear gap /%	The ratio of non-grain pixel area of a single ear to the pixel area of the whole ear
	Kernel distance /cm	The mean pixel distance between the centre points of each pair of grains facing the same direction in a single ear
	Ear kernel distance standard deviation /cm	The standard deviation of gap length of a single ear
	Grain density /piece/cm2	The number of grains per square centimetre ear of wheat
	Grain density of the upper part /cm	The grain density of the upper part of the line is 1/2 the length of the ear
	Lower part grain density /cm	The grain density of the lower half of the line is 1/2 of the length of the ear
	Average ear grain Angle/º	Taking the centreline of the wheat ear as the normal, the average Angle between the enclosing rectangle and the normal of all grains

RESULTS
Model comparison and analysis

To prove the effectiveness of the improvement, the Mask-RCNN model with a single improvement point was trained and tested in the same experimental environment. Improvement points 1-3 were adding the Res2Net module to the backbone network, improving the FPN, and adding the mask evaluation mechanism. The precision of the model after adding these improvement points is shown in the table 2 and 3. Each improvement point significantly improves the accuracy of wheat ear segmentation. The addition of the mask evaluation mechanism yields the most obvious improvement in accuracy, and the replacement of the backbone network has the least impact on the results. Compared with the original Mask-RCNN, the complete improved model increases 4.65 and 7.26 in the intersection ratios of wheat ear and grain segmentation, respectively; F1 increases 5.42 and 6.22, respectively.

Table 2

Mask-RCNN replacement of wheat ear segmentation accuracy comparison of different modules

Improvement Points of replacement	F1	Miou	Recall	Precision
No improvement	90.92	92.90	92.96	89.75
Improve the point 1	92.53	94.27	93.87	91.23
Improve the point 2	92.79	94.76	94.04	91.58
Improve the point 3	93.54	95.23	94.76	92.35
Improvement points 1, 2 and 3	96.34	96.74	97.21	95.48

Table 3

Mask-RCNN replacement of grain segmentation accuracy comparison of different modules

Improvement Points of replacement	F1	Miou	Recall	Precision
No improvement	90.92	92.90	92.96	89.75
Improve the point 1	92.53	94.27	93.87	91.23
Improve the point 2	92.79	94.76	94.04	91.58
Improve the point 3	93.54	95.23	94.76	92.35
Improvement points 1, 2 and 3	96.34	96.74	97.21	95.48

Figure 7 shows the same experimental environment; for UNet, DeepLabV3+, and Mask-RCNN, the network training process loss change map is displayed. For example, for the accuracy shown in Tables 4 and 5, the network loss value is lower than those of the existing models, reaching approximately 0.1. Mask-RCNN, UNet, and DeepLabV3+ are compared, and the recall, accuracy, F1 and mean IoU (miou) indicators of the proposed model are higher than those of the existing models.
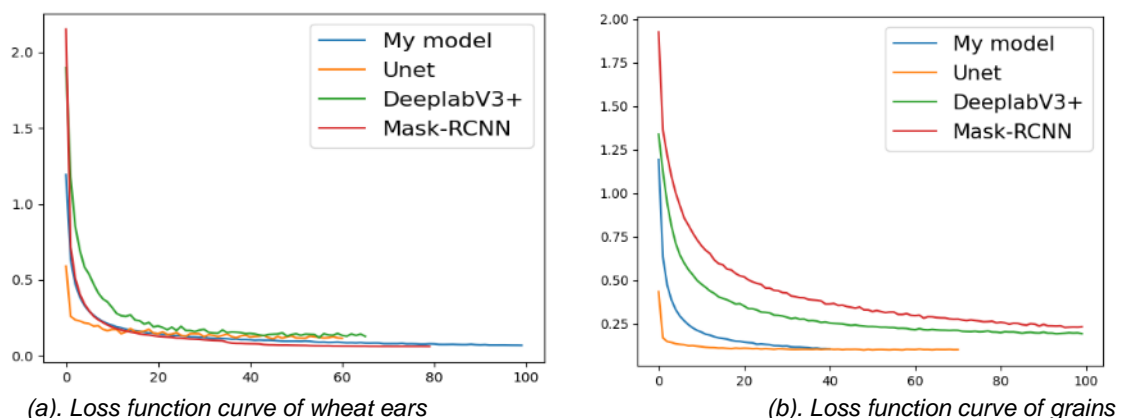
(a). Loss function curve of wheat ears   *(b). Loss function curve of grains*
Fig. 7 - Training loss function curves of different models

Table 4

Comparison of wheat ear segmentation accuracy

Evaluation index	UNet	DeepLabV3+	Mask-RCNN	This model
Recall	91.35	90.15	92.96	97.21
Miou	90.31	89.98	92.90	96.74
Precision	90.21	88.67	89.75	95.48
F1	90.77	89.40	90.20	96.34

Table 5

Comparison of grains Segmentation Accuracy

Evaluation index	UNet	DeepLabV3+	Mask-RCNN	This model
Recall	81.60	76.31	79.64	85.09
Miou	81.40	73.25	81.41	88.67
Precision	74.30	65.45	80.31	87.34
F1	77.41	70.16	79.98	86.20

The segmentation results are shown in Figure 8. In the recognition of wheat, the UNet and DeepLabV3+ segmentation of the edge is rough, and the improved model can clearly recognize the edge details of wheat grains in identification. Since the target is a small grain that is densely distributed, UNet and DeepLabV3+ show inferior segmentation effects and multigrain adhesion. Mask-RCNN can identify each grain well, but the recognition of grain edge features is not sufficiently fine. Compared with the original model, the improved model can segment the grain more accurately.
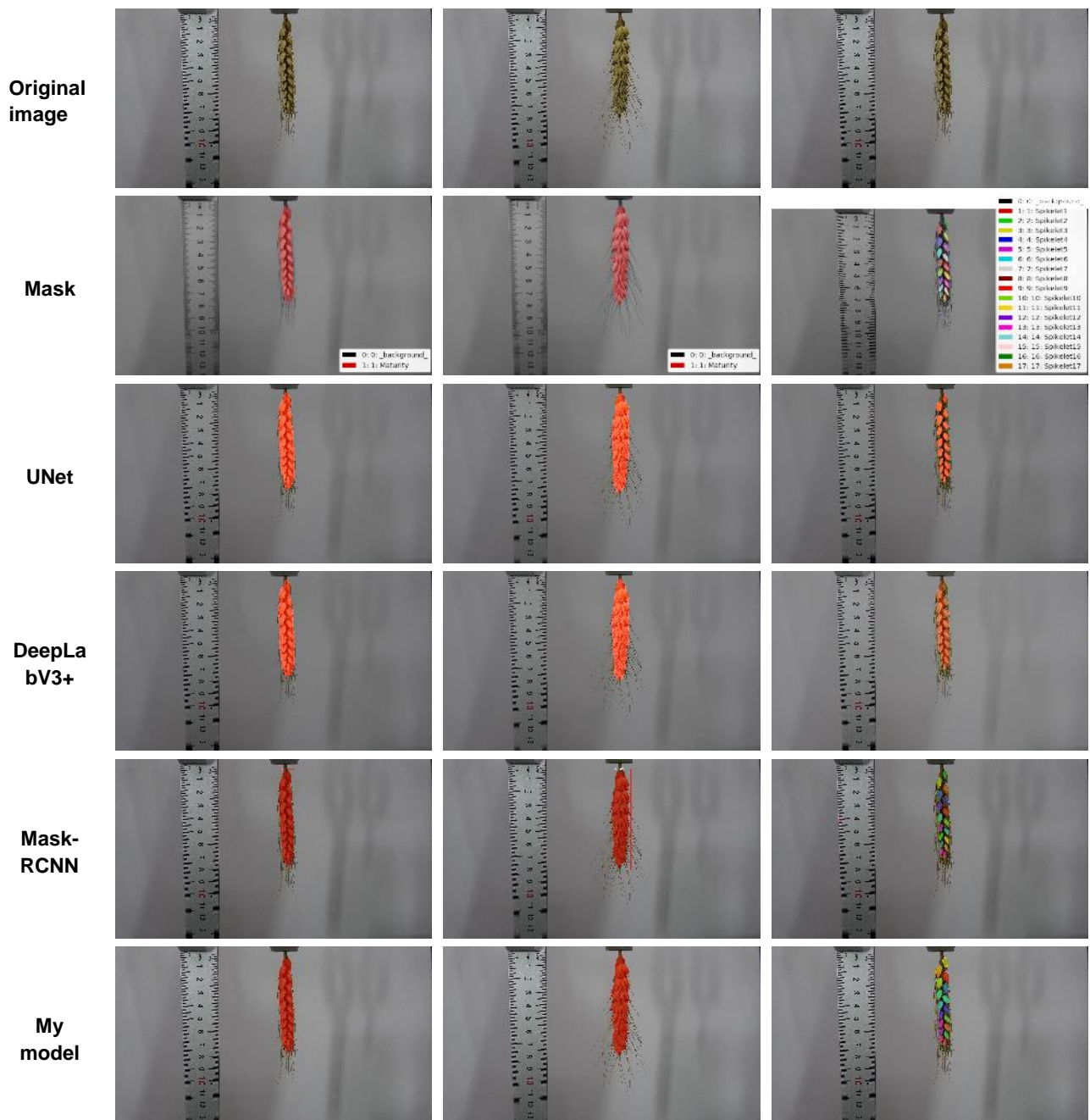
Fig. 8 - Prediction results of different models

Extraction of phenotypic parameters

The phenotypic parameters of wheat ears extracted using the scheme in this paper are shown in Table 6. The prediction of wheat ear maturity and the grains filling period in this scheme is consistent with the actual situation and has very high credibility. There are more or fewer differences in the phenotypic characteristics of different wheat varieties extracted by this scheme, which can provide technical support for the differentiation of wheat varieties and research on insect resistance. The Jintai188 and Zhongmai175 wheat grain density in the upper half are lower than that of the lower half of the grain density, and for Jintai188, the average grain angle is large, with more dispersed grain; for the Zhongmai175 wheat voids, the proportion is larger. Jintai182 is at a relatively high level in terms of length, width, and average grain size, while Jingdong22 is the opposite, with the smallest length, width, and average grain size.

Table 6

Wheat ear phenotypic parameters

Type	Phenotype	Jintai 188	Jintai 182	Zhongmai175	Jingdong22	Length 4738
period	maturity	mature stage	mature stage	mature stage	mature stage	mature stage
Colour feature	R-channel mean	2.01	3.52	2.41	1.97	2.71
	G-channel mean	1.73	3.11	2.07	1.69	2.37
	B-channel mean	0.92	1.58	1.17	1.01	1.36
Shape feature	Number of wheat ears /pieces	1	1	1	1	1
	Average spike length /cm	6.45	7.90	7.53	6.15	8.02
	Average ear width /cm	1.51	1.81	1.51	1.44	1.56
	Average panicle area /cm^2	5.62	8.75	7.26	5.23	7.8
	Average ear circumference /cm	14.60	18.27	14.14	14.18	18.02
	Average number of grains per seed/ pieces	17	17	17	15	17
	Average total grain area of a single ear /cm2	2.15	2.77	2.64	1.56	2.22
	Average grain area /cm2	0.13	0.16	0.156	0.10	0.13
	Standard deviation of grain area /cm	0.03	0.04	0.05	0.02	0.03
	Average grain circumference /cm	1.41	1.66	1.63	1.33	1.53
	Standard deviation of grain circumference /cm	0.21	0.19	0.26	0.19	0.19
Spatial feature	Average ratio of gap between ears /%	40.65	34.14	44.29	37.26	38.04
	Kernel distance /cm	1.65	2.49	1.61	1.54	2.00
	Ear kernel distance standard deviation /cm	1.01	1.96	1.29	1.19	1.57
	Grain density /cm2	3.21	2.09	2.84	3.57	2.93
	Grain density of the upper part /cm	3.02	2.22	2.68	3.80	3.10
	Lower part grain density /cm	3.40	1.96	3.02	3.22	2.74
	Average ear grain Angle /º	25.59	24.82	20.29	17.67	18.94

Table 7

The error between prediction results and manual measurement

Wheat types	Phenotype	Predicted mean	Measured mean	Error value
Jintai188	Length/cm	6.45	6.35	0.10
	Width/cm	1.51	1.45	0.06
	Number of grains/pieces	17	17	0
Jintai182	Length/cm	7.90	9.15	0.18
	Width/cm	1.81	1.90	0.09
	Number of grains/pieces	17	18	1
Zhongmai175	Length/cm	7.53	8.1	0.57
	Width/cm	1.51	1.40	0.11
	Number of grains/pieces	17	17	0
Jingdong22	Length/cm	6.15	6.45	0.30
	Width/cm	1.44	1.30	0.14
	Number of grains/pieces	15	15	0
Long4738	Length/cm	8.02	8.24	0.22
	Width/cm	1.56	1.40	0.16
	Number of grains/pieces	17	17	0

This model can quickly and concisely obtain the corresponding indicators of wheat ear colour, space and shape, but it is difficult to directly measure its parameters manually. The results for the features that can be manually measured by comparing them with the phenotypic parameters returned by the model in this paper are shown in Table 7. The model predicted values and measured values that are artificially strongly correlated by formula (6) can be obtained; the average length of all the wheat errors is 0.274 cm, the average width error is 0.112 cm, and the average error of the grain number is 0.2. The predicted value of the number of grains is basically the same as the actual value. Only one set of pictures has errors. The minimum measurement error of ear width is 0.06 cm, and the minimum error of ear length is 0.10 cm, which is close to the manual measurement value. The experimental results show that the method proposed in this paper has less error than manual measurement, and it can extract some indicators that cannot be directly measured manually while performing automatic extraction in batches.

CONCLUSIONS

In this paper, an automatic extraction scheme for wheat ear phenotypic characteristic parameters was designed to address the time consumption, limited extraction features, and low accuracy of the existing methods for obtaining wheat ear phenotypic characteristic parameters.

1) Aiming at the problems of awn of wheat severely occluded and grains adhesion in wheat ears, an improved Mask-RCNN model was used to segment wheat ears and grains; the Res2Net module was added to the backbone network of the original model to improve the multiscale feature extraction ability. Design a BFPN with 3 times superimposed two-way information flow instead of FPN network to enhance the edge recognition effect. Add the Mask IoU Head network, and improve the mask grading strategy. Finally, the contour of wheat ear segmentation is close to that of labelling, and the grain has clear edges with no adhesion.

2) Wheat ear phenotypic parameters were extracted based on the segmentation results. Aiming at the problem of limited extraction of wheat ear features by existing methods, an automatic extraction algorithm was designed for wheat ear phenotypic parameters. Extract 22 characteristics of wheat ears such as colour, shape, space, and maturity, including the length of the wheat ear, Among them, the index of ear length, width, and grain number are close to the artificial measurement values; other phenotypic index extraction methods can provide important technical support for research on wheat ear.

3) The proposed method can only be used to segment and extract characteristics of wheat ears and grains. The next step will be to study phenotypic extraction based on the number and length of wheat awns to improve the extraction of the phenotypic characteristic parameters of wheat ears.

ACKNOWLEDGEMENT

REFERENCES

[1] Alkhudaydi, T., Reynolds, D., Griffiths, S., Zhou, J., Iglesia, B. I. (2019). An exploration of deep-learning based phenotypic analysis to detect spike regions in field conditions for UK bread wheat. *Plant Phenomics*.

[2] Bi K., Jiang P., Li L., Shi B., Wang C., (2010). Non-destructive measurement of wheat spike characteristics based on morphological image processing. *Transactions of the CSAE*, 26 (12), 212-216.

[3] Du S., Li Y., Yao M., Li L., Ding S & He R., (2018). Grain counting method based on image segmentation of wheat spikes. *Journal of Nanjing Agricultural University*, 41(04), 742-751.

[4] Eliceiri, K.W., Berthold, M.R., Goldberg, I.G., Ibáñez, L., Manjunath, B. S., Martone, M. E., ... & Carpenter, A. E. (2012). Biological imaging software tools. *Nature methods*, *9*(7), 697-710.

[5] Goyal, L., Sharma, C. M., Singh, A., & Singh, P. K. (2021). Leaf and spike wheat disease detection & classification using an improved deep convolutional architecture. *Informatics in Medicine Unlocked*, 100642.

[6] Gao, S., Cheng, M. M., Zhao, K., Zhang, X. Y., Yang, M. H., & Torr, P. H. (2019). Res2net: A new multi-scale backbone architecture. *IEEE transactions on pattern analysis and machine intelligence*.

[7] He S., Li Z., He Z., (2005). Classification of wheat cultivar by digital image analysis. *Chinese Agricultural Sciences*, 38(09),1869-1875.

[8] Huang, Z., Huang, L., Gong, Y., Huang, C., & Wang, X. (2019). Mask scoring R-CNN. In *Proceedings of the IEEE/CVF Conference on Computer Vision and Pattern Recognition* , pp. 6409-6418.

[9] Khan, A. Q., Robe, B. L., & Girma, A. (2020). Evaluation of wheat genotypes (*Triticum aestivum L.*) for yield and yield characteristics under low land area at Arba Minch, Southern Ethiopia. *African Journal of Plant Science*, 14(12), 461-469.

[10] King, A. (2017). Technology: The future of agriculture. *Nature*, *544*(7651), S21-S23.

[11] Kiss, T., Balla, K., Bányai, J., Veisz, O., & Karsai, I. (2014). Effect of different sowing times on the plant developmental parameters of wheat (*Triticum aestivum L.*). *Cereal Research Communications*, *42*(2), 239-251.

[12] Li, Y., Li, H., Li, Y., & Zhang, S. (2017). Improving water-use efficiency by decreasing stomatal conductance and transpiration rate to maintain higher ear photosynthetic rate in drought-resistant wheat. *The Crop Journal*, 5(3), 231-239.

[13] Li, Y., Ma, L., Wu, P., Zhao, X., Chen, X., & Gao, X. (2020). Yield, yield attributes, and photosynthetic physiological characteristics of dryland wheat (*Triticum aestivum L.*)/maize *(Zea mays L.*) strip intercropping. *Field Crops Research*, 248, 107656.

[14] Lu Wenchao, Luo Bin, Pan Dayu, Zhao Yong & Wang C (2016). Synchronous measurement of wheat ear length and spikelets number based on image processing. *Journal of Chinese Agricultural Mechanization* (06), 210-215.

[15] Panfilova, A., Korkhova, M., Gamayunova, V., Drobitko, A., Nikonchuk, N., & Markova, N. (2019). *Formation of photosynthetic and grain yield of soft winter wheat (Triticum aestivum L.) depending on varietal characteristics and optimization of nutrition*.

[16] Pound, M. P., Atkinson, J. A., Wells, D. M., Pridmore, T. P., & French, A. P. (2017). Deep learning for multi-task plant phenotyping. In *Proceedings of the IEEE International Conference on Computer Vision Workshops* (pp. 2055-2063).

[17] Sadeghi-Tehran P., Virlet N., Ampe E. M. et al. DeepCount: in-field automatic quantification of wheat spikes using simple linear iterative clustering and deep convolutional neural networks [J]. *Frontiers in plant science*, 2019, 10: 1176.

[18] Tsaftaris, S. A., Minervini, M., & Scharr, H. (2016). Machine learning for plant phenotyping needs image processing. *Trends in plant science*, *21*(12), 989-991.

[19] Vavilova, V., Konopatskaia, I., Kuznetsova, A. E., Blinov, A., & Goncharov, N. P. (2017). DEP1 gene in wheat species with normal, compactoid and compact spikes. *BMC Genetics*, 18(1), 61-70.

[20] Verman, M. A. H. E. S. H., Jatav, S. K., & Gautam, A. (2015). Phenotypic stability analysis over different sowing times in wheat. *Annals of Plant and Soil Research*, *17*(3), 292-295.

[21] Wang, B., Lin, C., & Xiong, S. (2020). Wheat Phenotype Extraction via Adaptive Supervoxel Segmentation. In *2020 IEEE International Conference on Bioinformatics and Biomedicine (BIBM)*. pp. 807-814. IEEE.

[22] Wang N., Kong B., Wang C., Li W. & Xu H. (2017). Counting grains per wheat spike base in fractal segmentation of image. *Computer System& Applications* (10), 219-224.

[23] Wang, Y., Qin, Y., & Cui, J. (2021). Occlusion Robust Wheat Ear Counting Algorithm Based on Deep Learning. *Frontiers in Plant Science*, 12, 1139.

[24] Würschum T., Leiser W.L., Langer, S. M., Tucker, M. R., & Longin C.F.H. (2018). Phenotypic and genetic analysis of spike and kernel characteristics in wheat reveals long-term genetic trends of grain yield components. *Theoretical and Applied Genetics*, 131(10), 2071-2084.

[25] Yang, Y., Ding, J., Zhang, Y., Wu, J., Zhang, J., Pan, X., ... & He, F. (2018). Effects of tillage and mulching measures on soil moisture and temperature, photosynthetic characteristics and yield of winter wheat. *Agricultural Water Management*, *201*, 299-308.

VIBRATION CHARACTERISTICS TEST AND ANALYSIS OF HANGING CUP TRANSPLANTER
/
吊杯式移栽机振动特性测试与分析

Qiang SU[1], Xuying LI*[1], Fandi ZENG[1], Junyue WANG[1,2], Yongzhi ZHANG[1], Hongbin BAI[1], Lei WU[1], Jie WANG[1]
[1] Inner Mongolia Agricultural University, College of Mechanical and Electrical Engineering, Hohhot/China;
[2] Hohhot Branch of Chinese Academy of Agricultural Mechanization Science Co., Ltd, Hohhot/China
Tel: +86-0471-4309215; E-mail: suqi5199@163.com

ABSTRACT

The vibration of the hanging cup transplanter affected the hole size and tray seedling quality. This paper takes the 2ZP-2 hanging cup transplanter as the research object, studies the vibration characteristics of the transplanter when it works, deduces the mathematical model of the transplanter-soil vibration characteristics, and solves the steady-state vibration response. The Danish B&K vibration test system carried out the vibration test. Studies have shown that the vertical vibration of the transplanter is greater than that of the lateral vibration and the forward vibration. The main factors affecting the vertical vibration of the transplanter are the forward speed of the transplanter, the soil compaction, and the planting depth. When the forward momentum of the transplanter is in the range of 0.8~2.4 km/h, the vertical vibration acceleration increases with increasing forward speed of the transplanter. According to the power, spectral density curve, and spectral curve, the spectrum range of the vertical vibration energy peak is 0~10 Hz, the vibration frequency is between 4.5~5.5 Hz, and the corresponding vibration acceleration amplitude is 0.03~0.33 m/s². The research results can provide a reference for improving the operating speed, comfort, and structural optimization.

摘要

针对吊杯式移栽机受复杂激励产生振动影响栽植孔穴参数、穴盘苗栽植质量的问题，本文以 2ZP-2 型吊杯式移栽机为研究对象，对移栽机工作时的振动特性进行研究，推导了移栽机-土壤振动特性数学模型，求解了稳态振动响应；利用丹麦 B&K 振动测试系统进行了振动测试试验。研究表明移栽机垂直振动大于横向振动和前进方向振动，影响移栽机垂直振动的主要因素是移栽机前进速度、地表坚实度和栽植深度；当移栽机前进速度在 0.8~2.4 km/h 范围内时，随移栽机前进速度增加，垂直振动加速度也增加，由功率谱密度曲线和频谱曲线可知，垂直振动能量峰值出现的频谱区间为 0~10 Hz，振动主频位于 4.5~5.5 Hz 之间，所对应的振动加速度幅值范围为 0.03~0.33 m/s²。研究结果可以为提高移栽机作业速度、舒适性和结构优化提供参考。

INTRODUCTION

Seedling transplanting technology carried out in the Bayannaoer area of Inner Mongolia can avoid natural disasters in spring, prevent pests and weeds, and improve the survival rate of seedlings. Seedling transplanting plays an essential role in warming, heat preservation, soil moisture conservation, and increased crop yield *(Hu et al., 2021)*. At present, hanging cup transplanters are the leading equipment suitable for transplanting on the film *(Wang et al., 2016)*, duckbill-type transplanting machines *(Zhao et al., 2017)*, and water wheel film transplanters *(Xu et al., 2021)*. The hanging cup transplanter can complete the punching, planting, covering soil, and pressing operations all at once. It has high transplanting efficiency, significantly saves the labor force, and reduces the impact on a farmland's ecological environment. Therefore, in the Inner Mongolia Bayannaoer region hanging cup transplanter is widely used. During the field transplanting operation, the transplanting machine had random vibrations due to the complex field conditions. The random vibration affected the planting performance of the transplanter. It reduced the riding comfort of the seedling feeders, which was one of the crucial factors inhibiting the large-scale promotion of the transplanter.

In recent years, scholars at home and abroad have improved planting efficiency and planting qualification rates. Research on the hanging cup transplanters mainly aims to optimize the structure of the transplanter *(Zhang et al., 2015)*, perform planting performance tests *(Jin Seok Jo. et al., 2018)*, explore the law of seedling throwing *(Liu et al., 2018)*, and transplant trajectory *(Liu et al., 2019)*.

Finite element analysis software was used to conduct the modal test on the transplanter (*Wout W et al., 2014*). Lingxin Geng carried out vibration characteristics tests on the seedling picking device of the transplanter (*Geng et al., 2021*). Scholars in China and abroad have performed many studies on the relationship between the vibration caused by soil surface roughness and the operation performance of agricultural machinery. For example, Hildebrand studied the vibration of vehicles passing through rough or undulating dry and soft road surfaces and established a vehicle-soil system vibration model (*Hildebrand R., 2008, G.V.P. Kumara et al., 2011*). Rabbani MA predicted the vibration characteristics of a semi-crawler tractor by establishing a vibration model (*Rabbani M A. et al., 2002*). Xiaodong Zhang studied the relationship between vibrations caused by uneven farmland excitation, the shovel corn precision seeder and the sowing performance, deducing the steady-state response mathematical model (*Zhang et al., 2014*). Based on the above literature, we can see that there have been achievements in the study of vibration caused by agricultural machinery field roughness and in the research of agrarian machinery structure and operation performance. Nevertheless, research on the combination of soil surface roughness excitation and vibration characteristics of transplanting machines is limited.

This study intends to conduct theoretical analysis and vibration tests on the vibration generated by the bucket transplanter under different working conditions. The test determines what factors affect the vibration characteristics of the transplanter. This study provides a reference for selecting the working parameters of hanging cup transplanters and improving the design of planting mechanisms.

MATERIALS AND METHODS

• Structure and working principle of hanging cup transplanter

The 2ZP-2 hanging cup transplanter is mainly composed of a three-point suspension frame, a planting assembly, a covering soil pressing mechanism, a chain feeding seedling assembly, and a ground wheel transmission mechanism, as shown in Figure 1. The planting assembly is fixed on the three-point suspension frame by two parallel support frames; two driving wheels drive the power to the seedling cup and the hanging cup planting device by chain transmission. When the transplanter operates, it is necessary to put the plug seedlings into the seedling feeding cup, given the chain drives the seedling feeding cup to throw the plug seedlings into the planter. The planter rotates around the transplanting spindle at the same time as the transplanter moves horizontally. The transplanter is always perpendicular to the ground and is punched when it comes into contact with the soil.
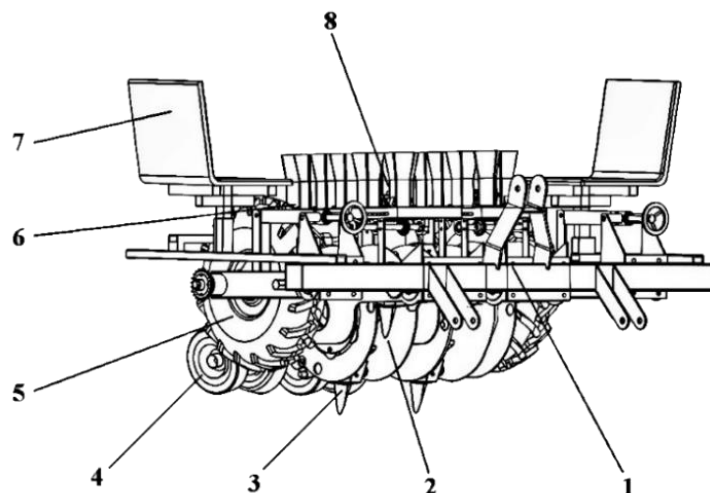
Fig.1 - Structure diagram of hanging cup type transplanter
1.- Three-point hanging mechanism; 2.- Planting mechanism; 3.- Driving wheel;
6.- Planting depth adjustment mechanism; 7.- Seat; 8.- Chain feeding mechanism

• Establishment of a Vibration Characteristic Model of Transplanters

Vibration is common in mechanical structures. Because the working environment of the transplanter is complex, the vibration caused by surface roughness and mechanical design is complex. Vibration affects the ride comfort of seedling feeders and the planting quality of plug seedlings, quickly leadings to structural damage due to resonance. Our research group measured and analyzed the surface roughness (*Liu et al., 2019*).

The surface morphology of the hanging cup transplanter working ground simplifies into a sine curve as shown in Figure 2. The longitudinal ground curve is the height of the ground relative to reference level H. The distance viewed between the two peaks is the soil roughness function (length L of the transplanter walking along the forward direction). Taking into account the influence of the speed of the transplanter on the vibration of the system, the variation of the road height with the road length is used to describe the soil roughness excitation. In the analysis, considering the influence of the transplanter speed on the system vibration, the soil roughness excitation is described by the change of the road height with the road length. When studying the vibration characteristics of the transplanter, considering the influence of the transplanter speed on the system vibration, the soil roughness excitation is described by the change in the road height with the road length (*Zhang et al., 2014*). To better analyze the vibration characteristics of the transplanter, the transplanter model is simplified, so that the whole system is a continuous linear system. Before establishing the model, we make the following assumptions: (1) The transplanter framework, planting assembly, and chain-row seedling feeding assembly are all rigid bodies. (2) The stiffness of the transplanter planting assembly and the stiffness of the ground wheel are linear functions of displacement. (3) The damping caused by the interaction between the planter, the ground wheel, and the soil is a linear function of speed. (4) The ground wheel keeps in contact with the soil without bouncing. The established model is the vertical vibration model of the transplanter without considering the lateral vibration (*Wang et al., 2019, Liu, 2016*). The mathematical model for transplanter-soil vibration based on soil roughness is as follows:
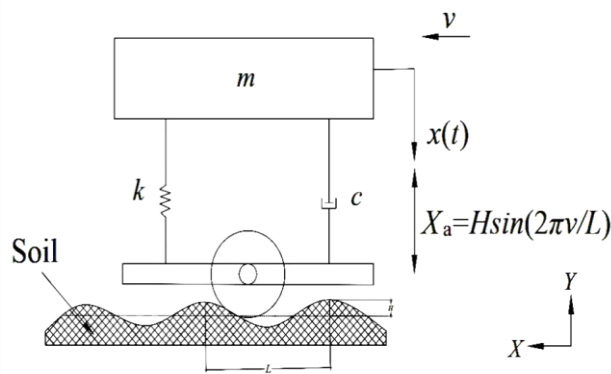
Fig. 2 - Hanging cup transplanter-soil system vibration model

Based on the soil surface roughness, the transplanter is excited by a $\omega=2\pi\frac{vt}{L}$ harmonic.

$$X_a = H \sin\left(\frac{2\pi vt}{L}\right) \tag{1}$$

where: v—advance speed of transplanter, [m/s],
         t—working time of transplanter, [s].

The absolute displacement of transplanter is $x(t)$, so the vibration balance equation is:

$$\mathrm{m}\ddot{x}(t) + \mathrm{c}\left[\dot{x}(t) - \dot{X}_a(t)\right] + \mathrm{k}[x(t) - X_a(t)] = 0 \tag{2}$$

Substituting Formula (1) into Formula (2):

$$\mathrm{m}\ddot{x}(t) + \mathrm{c}\dot{x}(t) + \mathrm{k}x(t) = \mathrm{c}\dot{X}_a(t) + \mathrm{k}X_a(t) = \mathrm{k}X_a \cos\omega t - \mathrm{c}\omega X_a \sin\omega t \tag{3}$$

Equation (3) is simplified, and the motion equation for the vibration system under the operating conditions is:

$$\mathrm{m}\ddot{x}(t) + \mathrm{c}\dot{x}(t) + \mathrm{k}x(t) = X_a\sqrt{\mathrm{k}^2 + (\mathrm{c}\omega)^2}\ \sin\left[\omega t + \tan^{-1}\left(\frac{\mathrm{c}\omega}{\mathrm{k}}\right)\right] \tag{4}$$

The letter in Formula (4) gives the following meanings:

$$\begin{cases} Y_d = X_a\sqrt{\mathrm{k}^2 + (\mathrm{c}\omega)^2} \\ \alpha = tan^{-1}\left(\frac{c\omega}{k}\right) \end{cases} \tag{5}$$

Arrange Formula (4) into the following formula:

$$m\ddot{x}(t)+c\dot{x}(t)+kx(t)=Y_d \sin(\omega t+\alpha) \tag{6}$$

Dividing both sides of the formula by m, where:

$$\begin{cases} 2\xi\omega_n=\dfrac{c}{m} \\[2mm] \omega_n^2=\sqrt{\dfrac{k}{m}} \\[2mm] \delta=\dfrac{Y_d}{m} \end{cases} \tag{7}$$

The above vibration equation can simplify the following equation:

$$\ddot{x}(t)+2\xi\omega_n\dot{x}(t)+\omega_n^2 x(t)=\delta \sin(\omega t+\alpha) \tag{8}$$

- **Steady-state response of transplanter under harmonic excitation**

The steady-state response equation of the bucket transplanter is as follows:

$$X(t)=X\sin(\omega t-\varphi) \tag{9}$$

where: φ——initial phase,

X——amplitude.

Substitute Formula (7) into Formula (6) to obtain the following procedure.

$$X[(\omega_n^2-\omega^2)\cos(\omega t+\alpha-\varphi)-2\xi\omega_n\omega(\omega t+\alpha-\varphi)]=\delta\sin(\omega t+\alpha) \tag{10}$$

Combine trigonometric functions in Formula (8) and obtain the following:

$$\begin{cases} X=\dfrac{X_a\sqrt{1+(2\xi\lambda)^2}}{\sqrt{\left(1-\lambda^2\right)^2+(2\xi\lambda)^2}} \\[4mm] \varphi=\tan^{-1}\dfrac{2\xi\lambda}{1-\lambda^2} \end{cases} \tag{11}$$

In the formula, λ is the ratio of the excitation force-frequency ω to the natural frequency ω_n of the system without damping. Therefore, the steady-state solution of the transplanter vibration system is as follows:

$$X(t)=\frac{X_a\sqrt{(2\xi\lambda)^2}}{\sqrt{(1-\lambda^2)^2+(2\xi\lambda)^2}}\sin\left[\omega t+\tan^{-1}\frac{c\omega}{k}-\tan^{-1}\frac{2\xi\lambda}{1-\lambda^2}\right] \tag{12}$$

Therefore, we can derive the influencing factors from the vibration characteristics and steady-state response of the transplanter. The main factors affecting the vibration of the cup transplanter are forward speed, external excitation, soil surface condition, and structural characteristics of the whole machine.

- **Vibration Test on Transplanter**

The orthogonal vibration test on the hanging cup transplanter explores the main factors influencing the vibration characteristics of the hanging cup transplanter.

The experiment was performed in the intelligent soil-machine-plant laboratory of Inner Mongolia Agricultural University.

We used a 2ZP-2 hanging cup transplanter as the research object to transplant tomato plug seedlings. The test methods refer to JB-T 10291-2013 "Dryland Planting Machinery" and GB/T 5667-2008 "Agricultural Machinery Production Test Method" to ensure the planting performance of the transplanter. Before each test, the soil was subjected to rotary tillage, leveling, compaction, and other operations. The test machine and soil-related physical parameters are shown in Table 1.

Table 1

Test equipment and soil parameters

Item		Data
Intelligent Soil-Machine-Plant Laboratory System Technology Platform	**Rated speed [km/h]**	0.5~10
	Tractive force [t]	1.5
	Maximum traction speed [km/h]	4
Soil physical characteristics	**Soil type**	Clay loam
	Averaging of water saturation [%]	13.6
	Averaging of volumetric weight [g/cm³]	1.2

The test equipment for the vibration signal acquisition of a hanging cup transplanter includes Pulse software of B&K Company of Denmark, a 4506B series triaxial acceleration sensor, and a 3050-B-060 six-channel Pulse LAN-XI data acquisition card. The three-axis acceleration sensor is in the spindle position of the planting mechanism. The *X*-axis direction is the forward direction of the transplanter, the *Y*-axis direction is the horizontal direction of the transplanter, and the *Z*-axis direction is the vertical direction of the transplanter. The sensor connects the data acquisition instrument. The data acquisition instrument processes the analog-to-digital conversion, amplification, filtering and so on, and the voltage signal is transformed the analog signal using analog-to-digital conversion, amplification, and filtering, the voltage signal is converted into a digital signal (*Wang et al., 2021*). After the transplanter runs smoothly, the vibration signal is collected for 8 s in each group of experiments and repeated for three times to take the average value which is taken for analysis.

a) Vibration data acquisition system   *b) Sensor installation position*
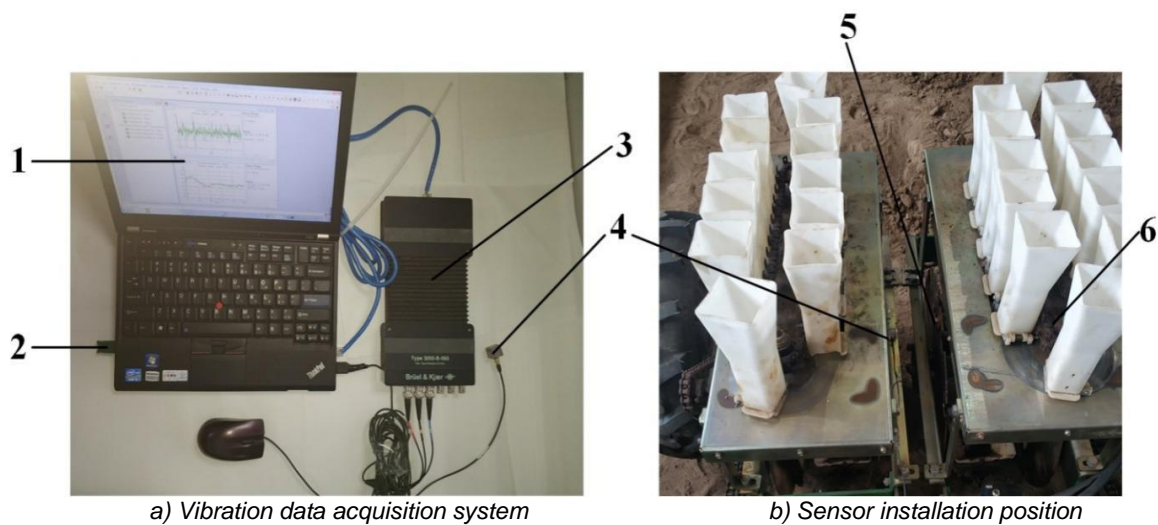
Fig. 3 - Field vibration data collection of transplanter
1.- Electronic key; 2.- Computer; 3.- Data acquisition card of type 3050-B-060; 4.- Sensor;
5.- Planting mechanism; 6.- Feeding mechanism

This experiment used a soil tanker instead of a tractor-drawn cup transplanter for orthogonal vibration experiments. Vibration signal processing and statistical functions are often used to describe its essential characteristics. The root mean square (*RMS*) can explain the strength of vibration signals.

$$\Psi_x^2 = \lim_{T \to \infty} \frac{1}{T} \int_0^T X^2(t) dt \tag{13}$$

The expression is expressed by finite discrete variables as follows.

$$\Psi_x^2 = \lim_{n \to \infty} \frac{1}{n} \sum_{k=1}^{n} X_k(t_i)^2 \tag{14}$$

According to the Box-Behnken experimental principle, three factors and three levels orthogonal experiments were designed.

A total of 17 practical points were included, including 5 zero estimation errors, and each experiment was repeated three times. The root means square used a fair value for the vibration acceleration, given the evaluation index for the vibration amplitude of the transplanting machine. The effects of forward speed, planting depth, and soil solidity on the vibration characteristics of the transplanting machine were analyzed. This experiment does not consider the structural parameters of the cup-type transplanter and the transplanting plug seedlings. Each experimental factors and the levels of each facet are shown in Table 2.

Table 2

Experimental factors and levels

Levels	Forward speed A	Depth of planting B	Soil compaction C
	[Km/h]	[mm]	[N/cm^2]
-1	0.8	50	50~70
0	1.4	70	90~110
1	2.0	90	130~150

a) Developing direction   b) Vertical orientation   c) Horizontal direction
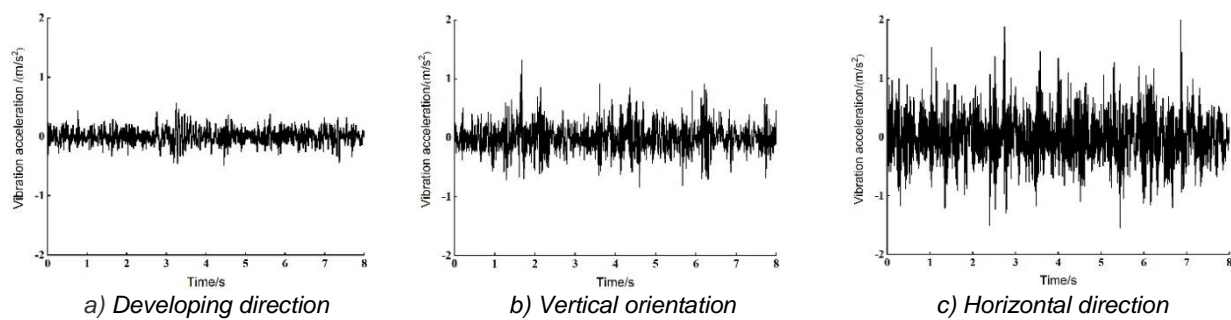
Fig. 4 - Time domain signal with advance speed of 1.2 km/h and planting depth of 70 mm

The Z-axis acceleration amplitude is much larger than the amplitudes for the X-axis and Y-axis. The test data of different acceleration sensor channels are analyzed. Figure 4 shows the time domain signal of the acceleration sensor in the *X*, *Y*, and *Z* directions when the planting depth is 70 mm and the speed is 1.2 km/h. It shows that the vertical vibration of the hanging cup transplanter is the most intense. The root suggests a square value for the vibration acceleration for a short pulse on the transplanter should be emphatically analyzed.

RESULTS

The test results are shown in table 3, in which *A*, *B* and *C* are the factor coding values for the transplanting machine planting depth, forward speed, and surface firmness respectively.

Table 3

Vibration test scheme and results

Test serial number	A	B	C	RMS
	[Km/h]	[mm]	[N/cm^2]	[m/s^2]
1	0	1	1	1.23
2	1	1	0	0.95
3	0	1	-1	0.82
4	0	-1	-1	0.43
5	1	-1	0	0.46
6	-1	-1	0	0.36
7	0	0	0	0.67

Vibration test scheme and results

Test serial number	A	B	C	RMS
	[Km/h]	[mm]	[N/cm²]	[m/s²]
8	0	0	0	0.69
9	0	0	0	0.72
10	-1	0	1	0.98
11	1	0	1	0.82
12	1	0	-1	0.53
13	-1	0	-1	0.63
14	0	-1	1	0.69
15	0	0	0	0.51
16	-1	1	0	0.84
17	0	0	0	0.85

Table 4 shows the variance analysis results. It shows that the overall *P value* of the model was less than 0.05, indicating the model was significantly different. In addition, $R^2 = 0.83$, indicating that the fitting was good. The unremarkable missing fitting term (P=0.7584>0.05) suggests that the model can analyze and predict the change in *RMS*. Since the forward velocity (P<0.0001) and the surface solidity (P=0.0006) have P values less than 0.01, the influence of forwarding velocity and soil solidity on the vertical vibration of the transplanter is significantly different. However, the effect of planting depth on the vertical vibration of the transplanter is not entirely different. Therefore, the factors that affect the size of the *RMS* are the transplanter forward speed, the surface firmness, and the planting depth. When the bold speed changes, the vibration of the transplanter will be more prominent due to the excitation of the soil surface roughness.

Table 4

Analysis of variance of regression equation

Source	Quadratic sum	DF	MS	FValue	PValue
Model	0.6661	3	0.222	20.69	<0.0001
A	0.0003	1	0.0003	0.0291	0.8670
B	0.4513	1	0.4513	42.05	<0.0001
C	0.2145	1	0.2145	19.99	0.0006
Residual error	0.1395	13	0.0107		
Misfit term	0.0802	9	0.0089	0.6015	0.7584
Pure error	0.0593	4	0.0148		
Summation	0.8056	16			

According to the orthogonal test, the main factor affecting the vibration characteristics of the transplanter is the forward speed. To determine the vibration characteristics of the transplanter, a comparative test was conducted at different speeds on the transplanter. The test allowed for time-frequency domain analysis and power spectral density analysis of the measured vibration signals. Figure 5 shows that in the range of 0.8~2.4 km/h, the forward velocity and the vibration acceleration increase.

a) v=0.8 **km/h**   *b) v=1.2* **km/h**

c) v=1.6 **km/h**   *d) v=2.0* **km/h**
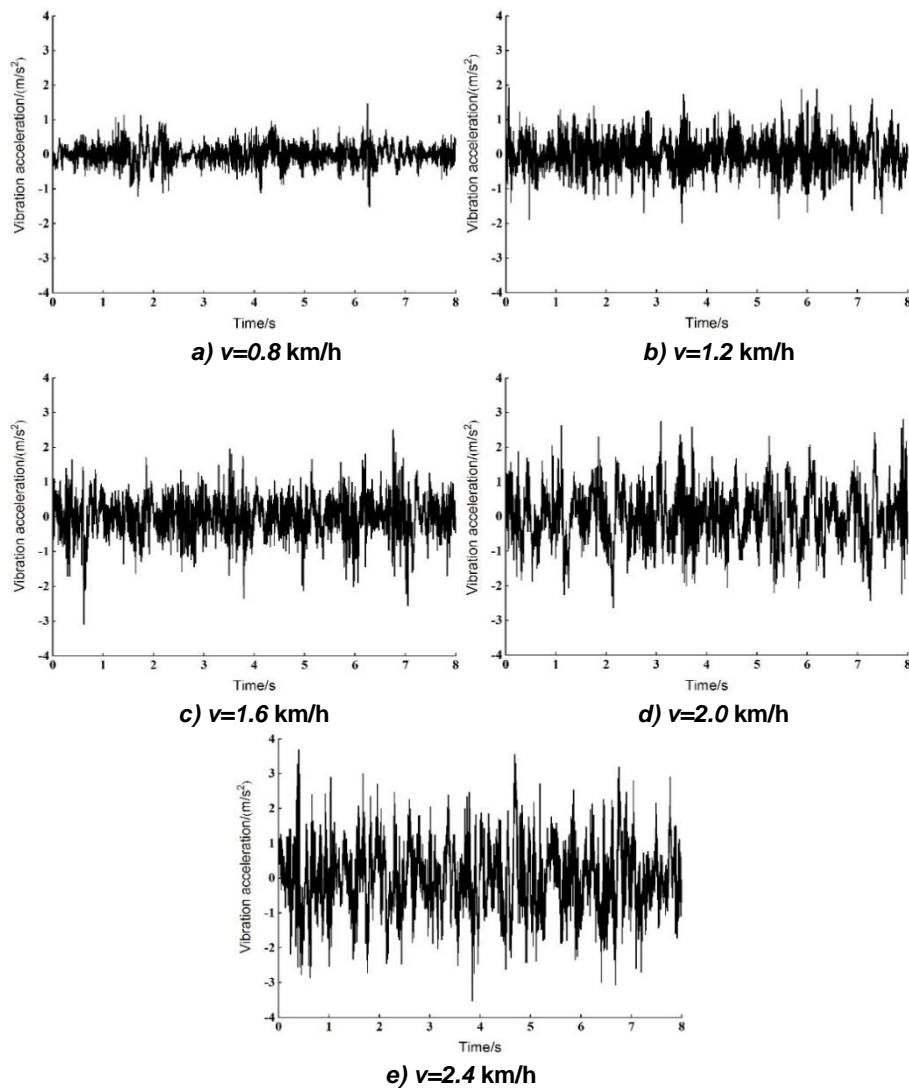
e) v=2.4 **km/h**
Fig. 5 - Vibration time domain diagram at different speeds

The power spectrum represents the energy component of the vibration signal in the specific frequency band. The power spectrum density curve in Figure 6(a) shows that the main frequency components of the vertical vibration energy for the transplanter concentrate in a low-frequency range of 0~10 Hz, there is also high vibration energy near the 50 Hz frequency band. At the same time, the greater the forward speed of the transplanter, the more intense the vibration. It does not affect the frequency distribution of vibration energy.
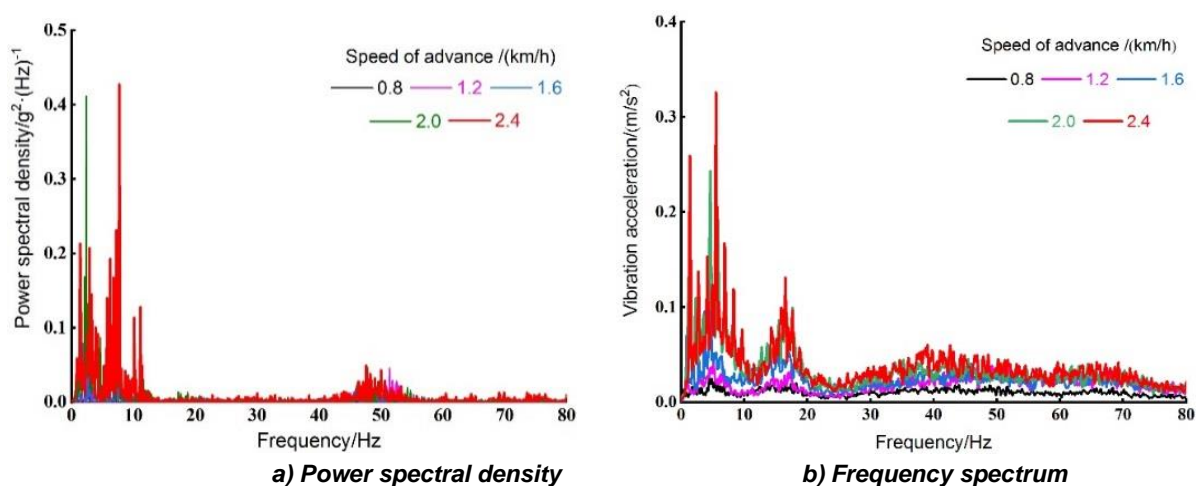
a) Power spectral density   *b) Frequency spectrum*
Fig. 6 - Vibration frequency analysis of cup transplanter

The vibration characteristics at different speeds can be extracted from the spectrogram of Figure 6(b), as shown in Table 5. When the forward speed is in the range of 0.8~2.4 km/h, the central frequency of vibration is distributed between 4.5~5.5 Hz. As the forward speed increases. The acceleration range corresponding to the primary frequency of oscillation is 0.03~0.33 m/s^2.

Table 5

Vibration characteristics corresponding to different velocity levels

Forward speed	Vibration frequency	Vibration acceleration
[km/h]	[Hz]	[m/s^2]
0.8	4.5	0.03
1.2	5.0	0.04
1.6	4.6	0.12
2.0	4.6	0.24
2.4	5.5	0.33

CONCLUSIONS

1) The mathematical model for transplanting machine-soil vibration under complex excitation is established and obtains the steady-state response of the transplanter. According to the vibration equation and the derivation process of the steady-state response, the forward speed of the transplanter determines the vibration characteristics, the external excitation, the soil surface condition, the machine structure characteristics, and other factors.

2) The vibration test shows that the vertical vibration of the transplanter is the strongest. According to the RMS value for vibration acceleration under different working conditions, the main factors influencing vertical vibration are the forward speed of the transplanter, surface solidity, and planting depth.

3) When the forward speed changes in the range of 0.8~2.4 km/h, the forward speed of the transplanter increases. The vertical vibration acceleration also increases, according to the analysis for the power spectral density curve and the spectrum curve. The main frequency components of sheer vibration energy during transplanting operation are between 0 and 10 Hz. The central frequency of transplanting vibration is in the range of 4.5~5.5 Hz, and the acceleration range corresponding to the primary frequency of oscillation is 0.03~0.33 m/s^2.

REFERENCES

[1]   Geng Lingxin, Li Kang, Pang Jing, et al. (2021). Test and analysis of vibration characteristics of transplanting machine based on time frequency and power spectral density (基于时频和功率谱密度的移栽机振动特性测试与分析), *Transactions of the Chinese Society of Agricultural Engineering*, 37(11), 23-30. https://doi.org/10.11975/j.issn.1002-6819.2021.11.003

[2]   Hu Fei, Guo Dong, Chen Cairong, et al. (2021). Design and experiment on compound crank Rocker double-row planting device of vegetable plug seedling up-film transplanter (复合曲柄摇杆式蔬菜膜上双行栽植装置设计与试验). *Transactions of the Chinese Society for Agricultural Machinery*, 1-11. http://kns.cnki.net/kcms/detail/11.1964.S.20210712.1439.027

[3]   Hildebrand R., Keskinen E., Romero J.N. (2008) Vehicle vibrating on a soft compacting soil half-space: Ground vibrations, terrain damage, and vehicle vibrations. *Journal of Terramechanics*, 45, 121-136. https://doi.org/10.1016/j.jterra.2008.09.003

[4]   Jin Seok Jo, Frank Gyan Okyere, et al. (2018). A study on improving the performance of the planting device of a vegetable transplanter, *Journal of Biosystems Engineering*, 43(3), 202-210. https://i.org/10.5307/JBE.2018.43.3.202

[5]   Kumara G.V.P., Raheman H. (2011). Development of a walk-behind type hand tractor powered vegetable transplanter for paper pot seedlings, *Biosystems Engineering*, 110(2), 189-197. https://doi.org/10.1016/j.biosystemseng.2011.08.001

[6]   Liu Yang, Mao Hanping, Wang Tao, et al. (2018). Collision optimization and experiment of tomato plug seedling in basket-type transplanting mechanism (吊杯式移栽机构中番茄穴盘苗运动分析优化与试验). *Transactions of the Chinese Society for Agricultural Machinery*, 49(5), 143-151. https://doi.org/10.6041/j.issn.1000-1298.2018.05.016

[7]   Liu Yang, Wang Shiguo, Mao Hanping, et al. (2019). Trajectory optimization and test of basket-type planting devices (吊杯式栽植器运动轨迹优化与试验). *Agricultural Research in the Arid Areas*, vol. 37(3), 291-298. https://doi.org/10.7606/j.issn.1000-7601.2019.03.38

[8]   Liu Xuening, Li Xuying, Zhang Yongzhi. (2019). The design and experimental research of measuring device about 3D surface topography of tillage soils (耕作土壤地表三维形貌测量装置设计与试验研究). *Journal of Agricultural Mechanization Research*, 41(7), 85-89. https://doi.org/10.3969/j.issn.1003-188X.2019.07.016

[9]   Liu Yueqin, Liu Fei, Zhao Manquan, et al. (2016), Analysis of vibration test and vibration theory of air-suction no-tillage planter (气吸式免耕播种机的振动测试与振动理论分析), *Journal of China Agricultural university*, 21(10), 109-116. https://doi.org/10.11841/j.issn.1007-4333.2016.10.14

[10]   Rabbani M A, Tsujimoto T, Mitsuoka M, et al. (2011). Prediction of the vibration characteristics of half-track tractor considering a three-dimensional dynamic model, *Biosystems Engineering*, 110(2):178-188. https://doi.org/10.1016/j.biosystemseng.2011.07.013.

[11]   Wang Yongwei, Tang Yanhai, Wang Jun, et al. (2016). Parameters optimization for the dibble-type planting apparatus of vegetable pot seedling transplanter in high-speed condition (蔬菜钵苗高速移栽机吊杯式栽植器参数优化). *Transactions of the Chinese Society for Agricultural Machinery*, 47(1), 91-100. https://doi.org/10.6041/j.issn.1000-1298.2016.01.013

[12]   Wout W, John L, Christof D., et al. (2014). Dealing with periodical loads and harmonics in operational modal analysis using time-varying transmissibility functions, *Mechanical Systems and Signal Processing*, 49(1/2), 154-164. https://doi.org/10.1016/j.ymssp.2014.04.008

[13]   Wang Qi, Zhu Longtu, Li Mingwei, et al. (2019). Vibration characteristics of corn no-tillage finger-type precision planter and its effect on seeding performance (指夹式玉米免耕精密播种机振动特性及对排种性能的影响). *Transactions of the Chinese Society of Agricultural Engineering*, 35(9), 9-18. https://doi.org/10.11975/j.issn.1002-6819.2019.09.002

[14]   Wang Li, Li Shuo, Lv Dianji, et al. (2021). Multi-sensor signal acquisition and data processing analysis of combine harvester. *INMATEH Agricultural Engineering*, 63(2), 335-344. https://doi.org/10.35633/inmateh-63-34

[15]   Xu Gaowei, Qiu Xuyun, Zhu Mengxia et al. (2021). Research progress and analysis of transplanting machinery on film (膜上移栽机械研究进展及与分析) *Agricultural equipment and vehicle engineering*, 59(02): 23-26+30. https://doi.org/10.3969/j.issn.1673-3142.2021.02.006

[16]   Zhao Xiong, Cui Haiyang, Dai Li, et al. (2017). Kinematic Analysis and Experimental Research on the Seedling Pick-Up Mechanism of a Second-Order Free Noncircular Planetary Gear System, *Applied Engineering in Agriculture*, 33(2): 169-179. https://doi.org/10.13031/aea.11852

[17]   Zhang Xiaodong, Li Chenghua, Li Jianqiao, et al. (2014). Mathematic Vibration Model of Spade Punch Planter of Maize (铲式玉米精密播种机振动特性模型建立与试验). *Transactions of the Chinese Society for Agricultural Machinery*, 45(2), 88-93. https://doi.org/10.6041/j.issn.1000-1298.2014.02.015.

[18]   Zhang Shuo, Chen Qingyu, Liu Jinyi, et al. (2021). Research on design and experiment of multifunctional vegetable field machine. *INMATEH Agricultural Engineering*, 63(2), 434-442. https://doi.org/10.35633/inmateh-63-44

DESIGN AND EXPERIMENT OF 5TG-85 BUCKWHEAT THRESHER
/
5TG-85 型荞麦脱粒机的设计与试验

Qi LU[1,2], Decong ZHENG[1], Lihong LI[1], Yun LIU*[1]

[1] College of Agricultural Engineering, Shanxi Agricultural University, Taigu 030801, China
[2] Chinese Academy of Agricultural Mechanization Sciences, Beijing 100083, China
Tel: +86-13593060095; E-mail: liuyun9010@163.com

ABSTRACT

A 5TG-85 buckwheat thresher was designed to solve the problems of low mechanical harvesting level of buckwheat in hilly and mountainous areas, high work intensity of threshing and grain cleaning, and few available machines and tools. The machine adopts rasp bar-nail tooth combined threshing device and air screen cleaning device, which can complete threshing and grain cleaning at one time. In the paper, the structure, transmission system and key components of the thresher were designed, the parameters were calculated, and the threshing performance test was carried out. The results show that when the moisture content of buckwheat stem is 75%, the moisture content of grain is 17%, and the grass grain ratio is 4.4, when the rotating speed of the threshing drum of the thresher is 500r/min, the threshing gap is 10mm, the feeding amount is 0.8kg/s, the air speed of suction mouth is 8m/s, and the vibration frequency of vibrating screen is 25.12 rad·s^{-1}. The crushing rate Z_p is 1.13%, the impurity content Z_z is 2.73%, the unthreshed loss rate S_w is 0.07%, the entrainment loss rate S_j is 1.77%, the cleaning loss rate S_q is 1.96%, the spatter loss rate S_f is 0.62% and the total loss rate S is 4.42%. The threshing effect is good, which meets the requirements of buckwheat threshing. The development of this machine will reduce the manual cost of buckwheat threshing, improve the work efficiency, improve the mechanized harvest level of buckwheat, and promote the development of buckwheat industry.

摘 要

针对丘陵山区荞麦机械收获水平不高，脱粒和清粮作业工作强度大，可用的机具少等问题，设计了一种 5TG-85 型荞麦脱粒机。该机采用纹杆——钉齿组合式脱粒装置和风筛式清选装置，可一次完成脱粒和清粮作业。文章对该脱粒机的整机结构、传动系统和关键部件进行了结构设计和参数计算，并开展了脱粒性能试验。试验结果表明，当荞麦茎秆含水率为 75%，籽粒含水率为 17%，草谷比为 4.4 时，调整脱粒机的脱粒滚筒转速为 500 r/min、脱粒间隙为 10 mm、喂入量为 0.8kg/s、吸杂口风速为 8m/s、振动筛振动频率为 25.12 rad·s^{-1} 的条件下，脱粒机的破碎率 Z_p 为 1.13%、含杂率 Z_z 为 2.73%、未脱净损失率 S_w 为 0.07%、夹带损失率 S_j 为 1.77%、清选损失率 S_q 为 1.96%、飞溅损失率 S_f 为 0.62%、总损失率 S 为 4.42%，脱粒效果良好，满足荞麦脱粒要求，可以进行脱粒作业。本机的研制将减少荞麦脱粒环节的人工作业成本高，提高工作效率，提升荞麦机械化收获水平，促进荞麦产业的发展。

INTRODUCTION

Buckwheat belongs to the buckwheat genus of Polygonaceae *(Gim é Nez Bastida, 2015; Ye S.B. et al, 2021)*. It is an annual herb and belongs to small-scale miscellaneous grain crops. It is mainly distributed in alpine or hilly mountainous areas in China *(Xiang D.B. et al, 2013)*. It is internationally recognized as a multi-purpose miscellaneous grain cash crop with nutrition, health care, medicine, feed and honey *(Zhang R.M. et al, 2016)*. It has the growth characteristics of cold tolerance, drought tolerance, barren tolerance, strong stress resistance and short growth period. It is of great significance in stable grain income, crop rotation, soil fertilization and regulation of people's diet in mountainous and dry lands *(Xu B., 2021; Hang X.N. et al, 2018)*. Because the topography of its growing area is mainly mountain or sloping land, the large-scale modern combine harvester is very difficult to work, resulting in a low level of buckwheat harvest mechanization, which affects the development of buckwheat industry *(Ji J.T. et al, 2016; LU Q. et al, 2020)*. Threshing and grain cleaning are the main links in the harvest process, therefore it is of great significance to develop a small buckwheat thresher suitable for use in hilly and mountainous areas or family farms.

---

[1] *Qi Lu, Ph.D. Stud. Eng.; Decong Zheng, Prof. M.S. Eng.; Lihong Li, Lec. M.S. Eng. Yun Liu*, Lec. M.S. Eng.*

In recent years, some scholars have studied and explored the buckwheat threshing device or harvester, and made some progress. *Zhang Kunkun* designed a buckwheat harvester, studied and analysed the layout of the main working parts, and established a multi-body dynamic model of the whole machine layout. The results show that when the slope increases to 30°, the tipping angle of the harvester reaches the limit *(Zhang K.K., 2019). Huang Xiaona* improved the design of a shear-transverse axial flow threshing device and carried out bench tests *(Hang X.N., 2020). Dang Weilong* improved and designed a double-drum buckwheat threshing device, the front drum is a bar drum, and the rear drum is a combined drum of bar and rod tooth, and the bench test is carried out *(Dang W.L., 2018). Wang Jiawei et al*. designed an internal and external drum buckwheat separation device, and analysed the overall situation of the threshed materials, the content of each component in the mixture and the axial distribution along the threshing drum *(Wang J.W. et al, 2019, Wang J.W. et al, 2020). Morishita T*. and *Suzuki K*. analysed the loss rate of combine harvester in the process of harvesting buckwheat *(Morishita T. et al, 2012)*.

In order to solve the problem of mechanized harvesting of buckwheat in small plots in hilly and mountainous areas, a smaller buckwheat threshing machine is developed in the paper. It adopts rasp bar - nail tooth combined threshing device and air-sieve type grain cleaning device, which integrates threshing and grain cleaning as a whole. It can greatly reduce the labour intensity, improve the production efficiency and improve the mechanized harvest level of buckwheat.

MATERIALS AND METHODS
Overall structure design and working principle
● **Overall structure and working principle**
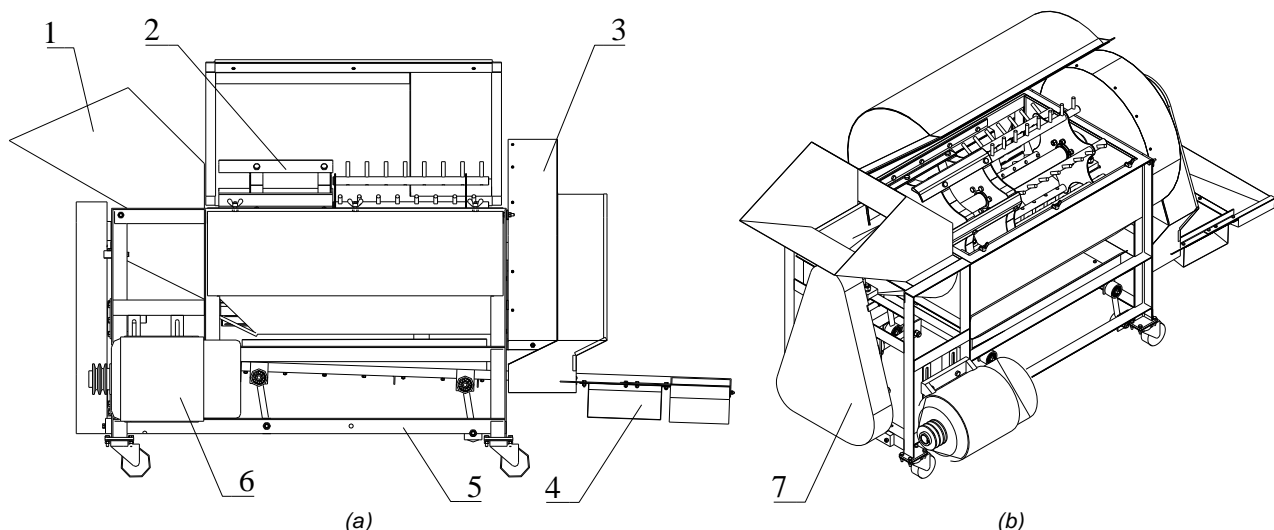
Fig. 1 - Schematic diagram of the whole machine structure
a) Upright view; b) Axonometric drawing
1. Feeding device; 2. Threshing device; 3. Fan; 4. Reciprocating vibrating screen; 5. Rack; 6. Motor; 7. Transmission system

As shown in figure 1, 5TG-85 buckwheat thresher is mainly composed of feeding device, threshing device, fan, reciprocating vibrating screen, rack, transmission system, etc. During operation, the buckwheat plant enters the rasp bar-nail tooth combined threshing device from the feeding device. Under the combined action of the threshing drum and the concave plate, the buckwheat grain and stem are separated through its impact, rubbing and impact. The grain and part of the miscellaneous residue fall on the reciprocating vibrating screen and enter the air screen cleaning system.

During the conveying process of vibrating screen transportation, the light miscellaneous residue and chaff on the screen surface are sucked in and blown out of the machine through the air suction of the centrifugal fan, and the clean grains on the sieve surface are collected into the material-bearing device. In the process of threshing, long stalks and residual ears are gradually transported to the discharge outlet, and discharged out of the machine.

The technical parameters of the whole machine structure are shown in Table 1.

Table 1

Technical parameter of 5TG—85 buckwheat thresher

Project		Parameters
Matching power [kW]		5.5
Motor type		Y132M-4
Size (length × width × height) [mm × mm × mm]		2160×878×1380
Total weight [kg]		300
Feeding quantity [kg/s]		0.8
Transmission type		Belt drive
Threshing device	Structural pattern	rasp bar-nail tooth
	Drum diameter [mm]	450
	Drum speed [r/min]	500
	Speed regulating device	APH- 5 continuously variable transmission
Vibrating screen	Structural pattern	Reciprocating vibrating screen
	Installation angle [°]	2
	Vibration frequency [rad·s^{-1}]	25.12
Grain cleaning fan	Cleaning type	Suction type
	Structural pattern	Centrifugal type
	Leaf number [set]	3
	Rotational speed [r/min]	1036

● **Design of transmission system of the whole machine**
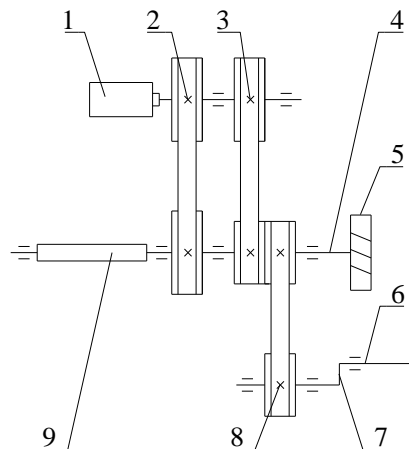
Fig. 2 - Schematic diagram of the whole machine transmission

1. Motor; 2. Belt drive of threshing device; 3. Belt drive of centrifugal fan; 4. Drive shaft of centrifugal fan; 5. Centrifugal fan;
6. Reciprocating vibrating screen drive connecting rod; 7. Eccentric device; 8. Reducer belt drive; 9. Threshing drum drive shaft.

As shown in figure 2, the power of the whole machine comes from the motor. The motor transfers the power to the threshing device and the cleaning device through belt transmission, because the connecting force between buckwheat grain and stem is small and it is easy to thresh. The rotating speed of the threshing device is low, while the rotating speed of the air screen cleaning system is high. Therefore, in the design of the transmission system, the driving shaft of the threshing device and the driving shaft of the centrifugal fan are arranged coaxially and driven separately. The driving shaft of the threshing device adopts the hollow shaft, and the driving shaft of the centrifugal fan adopts the solid shaft. The solid shaft is installed inside the hollow shaft, to realize coaxial and independent transmission. The structure is shown in figure 3. Due to the low vibration frequency of the reciprocating vibrating screen, the power transmitted by the fan drive shaft needs to be transmitted through the reducer belt and decelerated by the reducer output shaft, and through the eccentric device, the power is transferred to the reciprocating vibrating screen drive connecting rod, the rotary motion is transformed into reciprocating linear motion, and the reciprocating motion of the vibrating screen is realized.
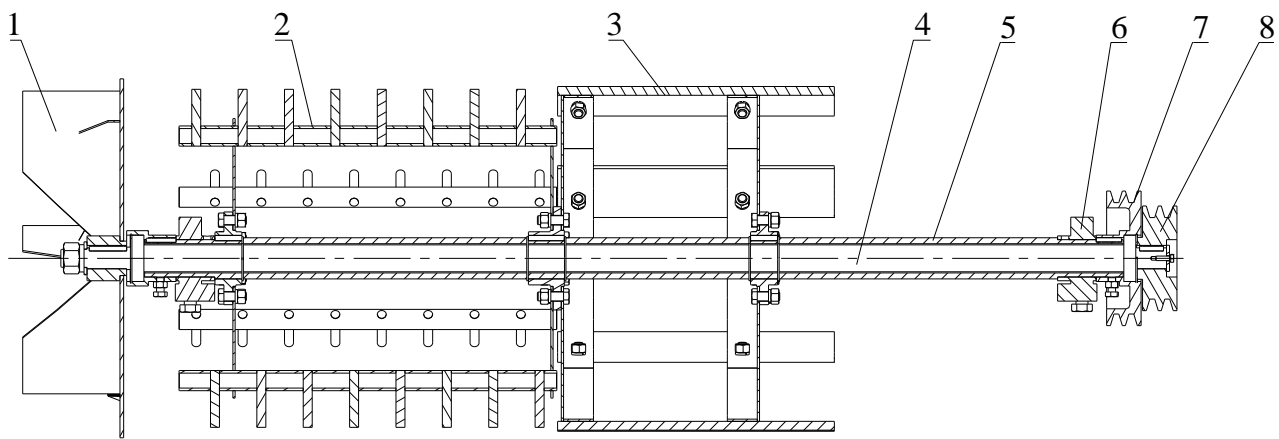
Fig. 3 - Transmission assembly drawing
1. Fan; 2. Nail tooth threshing device; 3. Rasp bar threshing device; 4. Inner drive shaft; 5. Outer drive shaft;
6. Bearing seat; 7. Threshing device drive pulley; 8. Fan drive pulley

Design of threshing device

● **Arrangement of threshing drum**

According to the direction of crop movement along the drum, the common arrangement of threshing drum can be divided into tangential flow type and axial flow type. The advantages of tangential threshing device are relatively simple structure, short threshing time, and relatively low energy consumption, but the purification rate is not high and the separation capacity is poor. The axial flow threshing device has the advantages of long threshing and separation time, high removal rate and good separation effect, but the power consumption is relatively large. As shown in figure 4, the axial flow threshing drum process has four main forms according to the feeding and discharge modes *(Di Z.F., et al, 2018; Ling S.Y. et al, 2021)*. In order to enhance the threshing and separation effect of buckwheat and improve the work efficiency and quality, combined with the structural layout of the whole machine, the technical scheme of axial feeding and radial discharge is adopted in this design, which is shown in figure 4 (c).
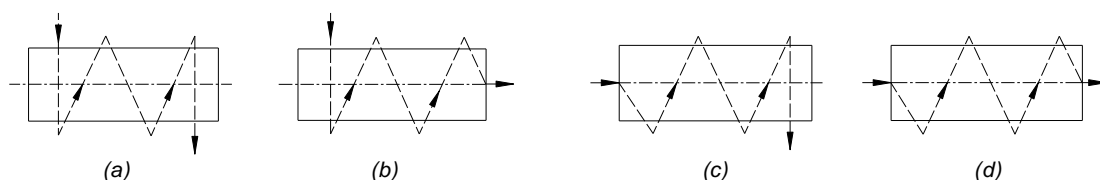
Fig. 4 - Arrangement of axial flow threshing device
a. Radial feeding, radial discharge; b. Radial feeding, axial discharge; c. Axial feeding, radial discharge; d. Axial feed, axial discharge

● **Structural design of threshing drum**

(1) Determination of drum diameter

The diameter of the drum directly affects the effect of threshing. If the diameter is too small, it is easy to wind the crop, and the separation area of the concave plate is reduced. If the drum diameter is large, it can adapt to large feeding amount and high working efficiency. However, if the diameter is too large, the structural size of the whole machine becomes larger and the weight increases, which is not conducive to the operation of small plots and road transfer. Combined with the Chinese standard (NJ105-75), the diameter of roller is 450 mm in this paper.

(2) Determination of drum length

The length L of the threshing drum is determined according to the productivity and is calculated according to the following formula *(China Academy of Agricultural Mechanization Sciences, 2007)*:

$$L \geq q/q_0 \tag{1}$$

where, q is the feeding amount of the threshing device (kg/s); q_0 is the allowable feeding amount per unit length of the drum (kg/(s m)). Generally, the longitudinal feeding thresher is $q_0 =1.5$ kg/(s m).

The feeding amount of threshing device is equal to the design feeding amount of thresher, taking q = 0.8 kg/s. $L \geq 530$ mm is calculated from formula (1). Considering that the thresher is mainly suitable for individual farmers and small plots in hilly and mountainous areas, the model should not be too large, and the drum length L = 850 mm is comprehensively considered.

(3) Determination of the type and structure of threshing elements

The common threshing components of full-feeding harvester mainly include rasp bar type and nail tooth type. Rasp bar threshing has relatively soft effect, weak striking effect, strong kneading effect, high production efficiency, but weak separation ability. The nail-tooth threshing element mainly relies on impact to complete threshing, with high grain crushing rate, strong stirring capacity and strong separation capacity. However, due to the impact of nail teeth on the stem, the protruded stem is broken, resulting in more impurities in the mixture, which increases the load on the subsequent cleaning device. At present, the drum is a transverse axial flow drum, and most of the threshing elements are nail tooth. Because the buckwheat is easy to thresh, but the stems are brittle, if the impact force is too large, the stems are short and broken too much, resulting in an increase in the burden of the air-sieve cleaning system. In order to comprehensively consider the effect of threshing and cleaning, the threshing device designed in this paper is "rasp bar - nail tooth" combination type. The front section is a rasp bar type threshing device, and the rear section is a nail tooth type threshing device. Its structure type is shown in figure 3.
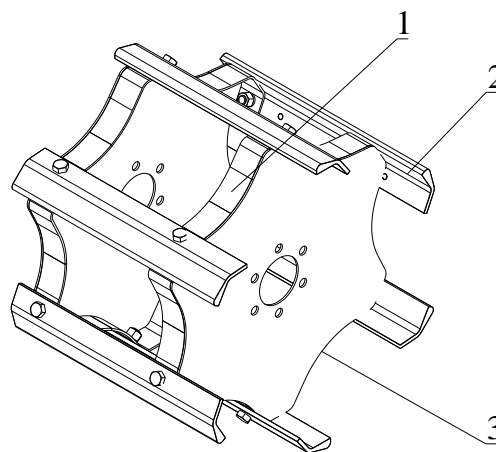
Fig. 5 - Rasp bar threshing device
1. Rasp bar connecting plate; 2. Rasp bar; 3. Spoke plate

The rasp bar threshing device is shown in figure 5, and its main structure is composed of a spoke plate, a rasp bar connecting plate and a D-shaped rasp bar. Its drum diameter is D=450 mm, drum length L_1 = 350, and the form of the drum is an open drum. In order to facilitate the balance of the drum, the number of stripes is usually even. According to the Chinese standard NJ105-75, the number of stripes is Z=6. In order to facilitate the movement of materials from the feed port to the grass outlet, the twill bars are installed in the same direction.
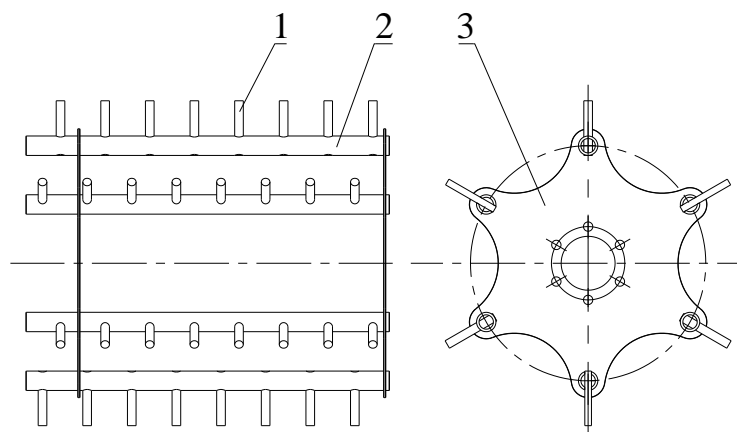
Fig. 6 - Nail tooth threshing device
1. Nail tooth; 2. Nail tooth connecting pipe; 3. Spoke plate

As shown in figure 6, the nail tooth type threshing device is mainly made of nail tooth fixing tube, nail tooth drum spoke plate and nail tooth welding. Its drum diameter D = 450 mm, drum length L_2 = 500. The screw tooth fixing pipe is an empty pipe with Φ = 27 mm and thickness 3.5 mm. The nail tooth is a solid steel pipe with Φ = 12 mm and 76 mm length. In order to balance with the threshing device of the grain bar, the number of tooth rows is 6, and the total number of teeth is 48 teeth. In order to ensure that the material has the ability of conveying backward, the nail teeth are arranged according to the helix with the number of screw heads as 3, the tooth trace distance as 62 mm and the pitch as 182 mm.

(4) Productivity calculation

In order to verify whether the productivity of the designed threshing device can meet the designed feeding capacity of the threshing machine, it is necessary to calculate the designed "rasp bar-nail tooth" combined threshing device. The productivity is determined by the productivity of the rasp bar threshing device and the nail-tooth threshing device.

Productivity of rasp bar threshing device q_1 *(China Academy of Agricultural Mechanization Sciences, 2007)*:

$$q_1 = \frac{ZnL_1\mu_0}{60} \tag{2}$$

where, Z is the number of striated bars, taking 6; n is the rotational speed of drum, taking 500 r/min; L_1 is the length of roller, taking 350 mm; μ_0 is the threshing ability per unit length of striated rod, which is usually 0.018~0.024 kg/m, taking 0.02 kg/m.

Substituting the corresponding data, the productivity of the rasp bar threshing device is calculated to be 0.35 kg/s.

Productivity of nail tooth threshing device q_2 *(China Academy of Agricultural Mechanization Sciences, 2007)*:

$$q_2 \leq \frac{0.6zq_d}{1-\beta} \tag{3}$$

where, β is the weight ratio of grain fed into crops. According to standard T/NJ 1217-2020, the grass-grain ratio of buckwheat crops is generally 1.5~6, taking 0.25; q_d is the threshing ability of each nail tooth, taking 0.02; z is the number of nailed teeth on the drum, taking 48.

Substituting the corresponding data, it is calculated that the productivity of the nail-tooth threshing device is q_2 ≤0.72 kg/s.

Productivity of the designed threshing device Q:

$$Q \leq q_1 + q_2 \tag{4}$$

The calculated Q ≤ 1.07 kg/s. That is, the maximum productivity of the designed threshing device is Q = 1.07 kg/s, which is larger than the designed feeding capacity q = 0.8 kg/s of the thresher. Therefore, the structure design of the threshing device is reasonable.

● **Threshing speed and threshing clearance**

Because of the biological characteristics of buckwheat, it is easy to thresh. According to the reference [15-16], it is determined that the threshing interval is 10 mm and the threshing speed is 500 r/min.

Concave design

The length of the concave is generally determined by the length of the drum. At the same time, within a certain range, the larger the wrapping angle α, the better the effect of threshing and separation, and the wrapping angle is generally 150°~ 240°. In this paper, the wrapping angle is 180°.

The main function of the concave plate is to cooperate with the threshing device to complete buckwheat grain threshing and stem separation. The common concave plate forms include grid screen type, punching screen type and braided screen type. Among them, the grid screen has high strength and good rigidity, while the braided screen has the highest porosity and the highest screening efficiency, but it has low strength and easy to deform. This design comprehensively considers its strength requirements and screening efficiency, and adopts the combined concave plate of "grid format concave frame + braided screen". As shown in figure 7, the grid format concave frame is mainly composed of a concave mounting frame, a concave grid and a screen connecting plate, and the grid size is 145 mm × 137 mm. The mesh with diameter of Φ = 2.5 mm and spacing of 3 mm is installed on the connecting plate of concave screen by bolting.
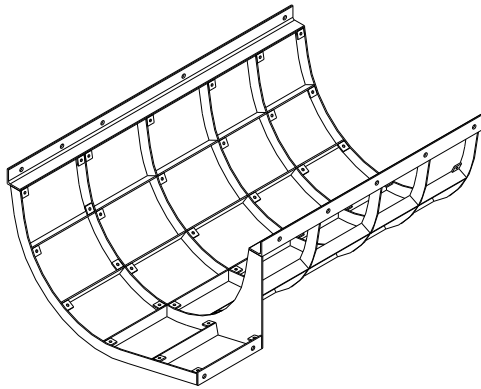
Fig. 7 - Grid format concave frame
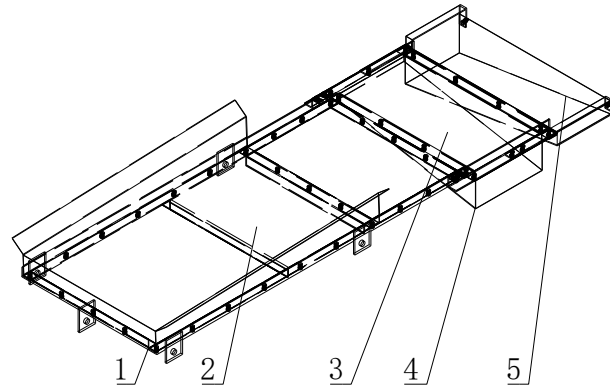
Fig. 8 -The body structure of vibrating screen
1. Screen frame; 2. Conveyor screen; 3. Separating screen;
4. Grain collector; 5. Impurity collector

Vibrating screen design
- **Structural design**

The structure and motion characteristics of the vibrating screen determine the cleaning effect of grain and impurity residue *(Tang Z. et al, 2010)).* In this paper, a reciprocating vibrating screen is designed. The vibrating screen body is connected to the frame through four equal rockers with a length of 220 mm, and the installation angle of the screen surface is α = 2°. The structure of the vibrating screen is shown in figure 8, which is mainly composed of a sieve frame, a conveying sieve plate, a grain collector, a separation screen and a miscellaneous collector. The sieve frame adopts 30 mm × 30 mm × 3 mm angle steel to form the welded structure. The conveying sieve plate and collector are welded on the sieve frame with 1 mm thick steel plate. The braided sieve with wire diameter of 0.5 mm and mesh number of 3 is selected to meet the screening requirements of buckwheat grains.

- **Motion analysis and test of grain on the sieve surface**

In the reference [12], the force and motion characteristics of the vibrating screen grain on the screen surface are analysed and calculated, and the motion simulation analysis is carried out by using ADAMS software. The analysis results show that the motion of connecting rod and rocker changes periodically, each angular displacement, angular velocity and angular acceleration change gently, there is no obvious inflection point in the curve, and the curve has no obvious inflection point, violent vibration and large impact. The vibrating screen has reasonable structure design and good performance. The experimental results show that when the vibration frequency of the vibrating screen is 25.12 rad·s⁻¹, the installation inclination angle of the screen surface is 2°, and the vibration direction angle is 23°, the screening efficiency is 89.8% and the conveying speed is 0.133 m·s⁻¹.

Design of air suction centrifugal fan
- **Overall structural design**
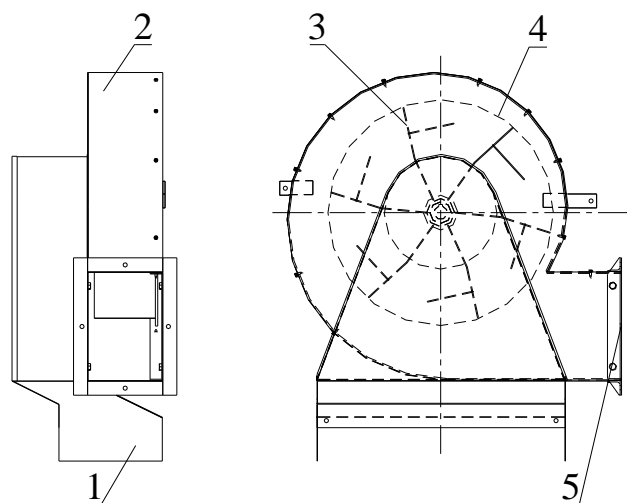
Fig. 9 - Schematic diagram of fan structure
1. Suction mouth; 2. Volute; 3. Leaf; 4. Spoke plate; 5. Air outlet

As shown in figure 9, the air suction centrifugal fan is mainly composed of blades, volutes, suction vents, air vents and so on. Six blades were evenly distributed and welded on the spoke plate with a thickness of 5 mm. The spoke plate is connected with the fan transmission shaft through the flange, and the volute is composed of a thin plate with a thickness of 1 mm. During operation, the fan transmission shaft drives the fan blade to rotate, and the air flow enters the fan through the suction port, forming a pressure difference. When the air speed of the suction port is greater than the suspension speed of the impurity, the impurity will be sucked into the fan through the suction port. Under the action of centrifugal force, the impurity is discharged through the exhaust outlet to complete the cleaning operation.

● **Shell design**
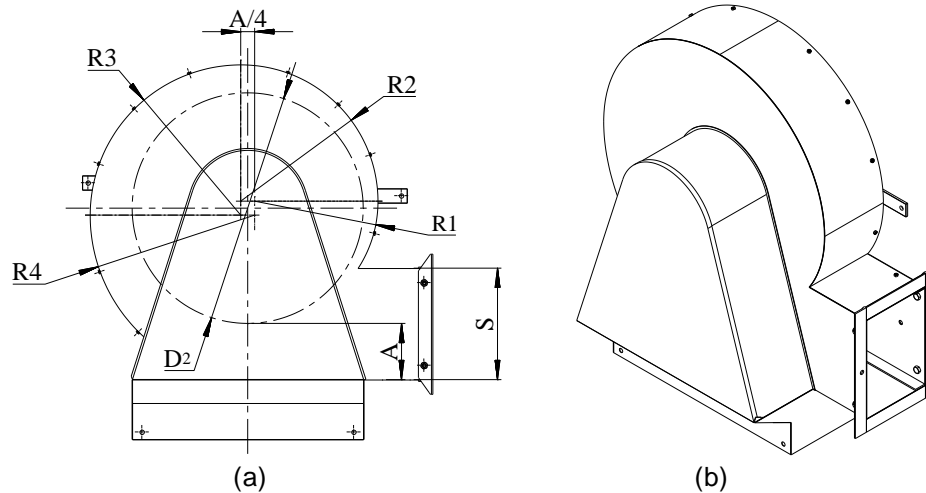
Fig.10 - Shell structure
(a) Shell size; (b) Axonometric drawing

The shell of the air suction centrifugal fan adopts a spiral volute. According to the reference (*China Academy of Agricultural Mechanization Sciences, 2009*), the spiral drawing method of the shell is shown in figure 10(a). The side length of the square in figure 10(a) is $A/4$. The connected arcs are drawn from the four vertex corners of the square with the radius of R_1, R_2, R_3 and R_4 respectively, which is the shape of the spiral case.

$$\begin{cases} R_1 = \dfrac{D_2}{8} + (1/8)A \\[2mm] R_2 = \dfrac{D_2}{2} + (3/8)A \\[2mm] R_3 = \dfrac{D_2}{2} + (5/8)A \\[2mm] R_4 = \dfrac{D_2}{2} + (7/8)A \end{cases} \tag{5}$$

where, D_2 is the impeller diameter (mm), for suction fans, the impeller diameter D_2 is mostly 250~500 mm, in this paper, taking 480 mm; A is taken as the spiral volute shell expansion size (mm), generally A = (0.1 ~ 0.2) D_2, taking 80 mm.

It is calculated that R_1, R_2, R_3 and R_4 are 72 mm, 276 mm, 300 mm and 324 mm.

S is the height of the air outlet, S = (0.35-0.45) D_2, taking 192 mm.

● **Parameter design of suction port**

The size of the suction port directly affects the gas flow of the fan, and the minimum air volume V_0 required for air separation is related to the impurity content. The calculation is as follows:

$$V_0 = \beta Q / \mu\rho \tag{6}$$

where, Q thresher feed volume (kg/s), Q = 0.8 kg/s; β is taken as the ratio of removing impurities to machine feed, β = 20% *(Cheng F., 2021)*; ρ is air density (kg/m³), ρ = 1.225 kg/m³; μ is the mixed concentration ratio of impurity flow, about 0.2 ~ 0.3, taking 0.2. Calculated V_0=0.653 m³/s.

In order to ensure that the residue in the buckwheat extract entering the vibrating screen can enter the air separation device through the impurity suction port, the minimum wind speed of the suction port should not be lower than the suspension speed of the residue. The results of suspension velocity of buckwheat exudates show that the suspension velocities of grains, branches, stems and leaves of buckwheat are 4.47 ~ 10.18, 1.85 ~ 5.18, 2.80 ~ 8.37 and 0.76~ 2.99 m/s, respectively *(Hou H.M. et al, 2018)*. The suspension speed of light miscellaneous residue such as leaves is lower, and easy to be separated. The suspension speed of branches and stems has a great relationship with the physical characteristics of diameter and length of stems. The suspension speed of stems and branches with small diameter and short length is lower, and easy to separate from grains *(Liao Q.X. et al, 2015)*. Because the concave plate screening uses a braided screen with a mesh number of 5, there are fewer long stems and branches in the extrudates on the vibrating screen, mainly light residue such as leaves, in order to ensure the cleanliness of the air separation, comprehensively consider the suspension speed of stems and rods as the design basis, so as to ensure that short stems, branches, leaves and light miscellaneous residue are cleaned.

The minimum air intake area S_0 of the suction port is calculated as follows:

$$S_0 = \frac{V_0}{v_1} \tag{7}$$

where, v_1 is the wind speed of the suction mouth, and the maximum suspension speed of the stem is about 8 m/s, and the $S_0 = 0.0816$ m^2 is calculated.

Considering the combination of suction port and vibrating screen, the structure of suction port is rectangular and its size is 482×220 mm. It is calculated that the actual air intake area is $S_1 = 0.105$ m^2, which is larger than S_0, which meets the requirement of the minimum air intake area, and the actual air intake of the suction port is $V_1 = 0.84$ m^3/s.

Test and result analysis

In order to verify whether the working performance of the thresher can meet the use requirements, the production assessment of the designed 5TG-85 buckwheat thresher was carried out on October 25, 2021. The test site is the Agricultural Machinery Laboratory of Shanxi Agricultural University. The photo of the test site is shown in figure 11.

Fig.11 - Threshing performance test

● **Materials**

The test materials were Shanxi Hongshan buckwheat planted in Shenfeng experimental base of Shanxi Agricultural University. During the experiment, the moisture content of buckwheat stem was 75%, the grain moisture content was 17%, and the grass grain ratio was 4.4.

● **Method**

According to the Chinese standard《Test method of Thresher》(GB/T 5982-2017), it is necessary to determine the crushing rate Z_p, impurity content Z_z, unremoved net loss rate S_w, entrainment loss rate S_j, cleaning loss rate S_q, spatter loss rate S_f and total loss rate S. The parameters are calculated as follows:

$$\begin{cases} Z_p = \dfrac{m_p}{m_x} \times 100\% \\[2ex] Z_z = \dfrac{m_{xz}}{m_{xh}} \times 100\% \\[2ex] S_w = \dfrac{m_w}{m} \times 100\% \\[2ex] S_j = \dfrac{m_j}{m} \times 100\% \\[2ex] S_q = \dfrac{m_q}{m} \times 100\% \\[2ex] S_f = \dfrac{m_f}{m} \times 100\% \\[2ex] S = S_w + S_j + S_q + S_f \\[1ex] m = m_c + m_w + m_j + m_q + m_f \end{cases} \tag{8}$$

where:

m_p is the broken grain mass in the sample (g);

m_x is the grain mass in the sample (g);

m_{xz} is the impurity mass in the sample (g);

m_{xh} is the grain mixture weight in the sample (g);

m_w is unpurged grain mass (g);

m is total grain mass (g);

m_j is entrainment loss grain mass (g);

m_q is cleaning loss grain mass (g);

m_f is splash loss grain mass (g);

m_c grain mass at outlet (g).

The specific operation was as follows: at the grain outlet, 1 kg of small samples were taken randomly each time, the samples were screened and selected, and m_p, m_x, m_{xz} and m_{xh} were obtained respectively. Within the specified time of the experiment, the grain mixture and the lost grains of each part (m_j, m_q, m_f) were collected, and the m_c was obtained by sieving the grain mixture. The performance indexes were calculated according to the formula (8). Each group of data was repeated for 5 groups, the average value was taken, and the results were recorded.

RESULTS

Combined with the requirements of mechanized threshing of coarse grain crops in hilly and mountainous areas, it is required that the crushing rate Z_p, impurity content Z_z and total loss rate S should be less than or equal to 5%. *(Shi R.J., 2021).* According to the test scheme and calculation method, when the threshing drum speed of the thresher is adjusted to 500 r/min, the threshing gap is 10 mm, the feeding amount is 0.8 kg/s, the air speed of the suction port is 8 m/s, and the vibration frequency of the vibrating screen is 25.12 rad·s⁻¹. The test results are shown in Table 2. The test results show that all the performance indexes of 5TG-85 buckwheat threshing machine meet the requirements, with good threshing effect and small loss, and can be used for buckwheat threshing.

Test results of threshing performance   **Table 2**

Test index	Standard values	Test result
Z_p	≤5%	1.13%
Z_z	≤5%	2.73%
S_w	≤5%	0.07%
S_j	≤5%	1.77%
S_q	≤5%	1.96%
S_f	≤5%	0.62%
S	≤5%	4.42%

CONCLUSIONS

(1) In view of the low level of mechanized threshing of buckwheat in Hilly and mountainous areas, a 5tg-85 buckwheat thresher was designed, the structure and transmission system of the whole machine were designed, and the structure selection and parameter calculation of key components such as threshing device, vibrating screen and centrifugal fan were carried out. The design results show that the design scheme of the thresher is feasible and the structural design is reasonable.

(2) The performance test shows that when the moisture content of buckwheat stem is 75%, the moisture content of grain is 17%, and the grass grain ratio is 4.4, when the rotating speed of the threshing drum of the thresher is 500 r/min, the threshing gap is 10 mm, the feeding amount is 0.8 kg/s, the air speed of suction port is 8 m/s, and the vibration frequency of vibrating screen is 25.12 rad·s^{-1}. The crushing rate Z_p is 1.13%, the impurity content Z_z is 2.73%, the unthreshed loss rate S_w is 0.07%, the entrainment loss rate S_j is 1.77%, the cleaning loss rate S_q is 1.96%, the spatter loss rate S_f is 0.62% and the total loss rate S is 4.42%. The threshing effect is good, which meets the requirements of buckwheat threshing and can be used for threshing.

ACKNOWLEDGEMENT

REFERENCES

[1] Cheng F., (2021). *The design and research of grain granulation machine in grain crop area*. Shanxi Agricultural University, Taigu / P.R.C.;

[2] Dang W.L., (2018). *Design and experiment of test platform for windrow harvesting of buckwheat*. Northwest A & F University, Yangling / P.R.C.;

[3] Di Z.F., (2018). Design and experiment of rasp bar and nail tooth combined axial flow corn threshing cylinder. *Transactions of the Chinese Society of Agricultural Engineering* (*Transactions of the CSAE*), Vol.34, Issue 1, pp. 28-34, Beijing / P.R.C.;

[4] Giménez-Bastida J.A. et al. (2015), Buckwheat as a Functional Food and Its Effects on Health. *J Agric Food Chem*, Vol. 63, Issue 36, pp. 896-913, Washington DC / USA;

[5] Hou H.M., (2018). Design and test of air-sweeping suspension velocity testing device for cleaning threshed materials of grain and oil crops [J]. *Transactions of the Chinese Society of Agricultural Engineering (Transactions of the CSAE)*, Vol.34, Issue 16, pp. 43-19, Beijing / P.R.C.;

[6] Hang X.N., (2018). Research status and development trend of Buckwheat harvesting Machinery. *Agricultural machinery*, Issue 10, pp. 84-90, Beijing / P.R.C.;

[7] Hang X.N., (2020). Design and experimental research on tangential and transverse axial flow threshing system of windrow harvesting for buckwheat. Northwest A & F University, Yangling / P.R.C.;

[8] Ji J.T., (2016). Present situation technical analysis and equipment demand of harvesting mechanization for characteristic coarse cereals. *Agricultural Engineering*, Vol.6, Issue 6, pp. 1-3, Beijing / P.R.C.;

[9] Liao Q.X., (2015). Design and experiment on cyclone separating cleaning system for rape combine harvester. *Transactions of the Chinese Society of Agricultural Engineering (Transactions of the CSAE),* 2015, 31(14): 24－31. Vol.31, Issue 14, pp. 24-31, Beijing / P.R.C.;

[10] Lin S.Y., (2021). Structure design of 5TG-100A rape thresher. *Journal of Anhui Agricultural Sciences*, Vol.49, Issue 7, pp. 208-211, Anhui / P.R.C.;

[11] Lu Q., (2020). Problems and thoughts on mechanized harvesting technology of buckwheat in China. *Agricultural Engineering*, Vol.10, Issue 1, pp. 6-9, Beijing / P.R.C.;

[12] Morishita T and Suzuki K, (2012). *The evaluation of harvest loss in shattering resistant common buckwheat using combine harvester*. Report of the Hokkaido Branch, the Japanese Society of Breeding and Hokkaido Branch, the Crop Science Society of Japan, Issue 53, pp.49-50, Tokyo/Japan;

[13] Tang Z., (2010). Analysis on the eddy current of the air-and-screen cleaning device. *Transactions of the Chinese Society for Agricultural Machinery*, Vol.41, Issue 12, pp. 62-66, Beijing / P.R.C.;

[14] Wang J.W., (2020). Design and threshing outputs study of internal and external rotary roller buckwheat thresher. *INMATEH-Agricultural Engineering*, Vol.60, Issue 1, pp.173-182, Bucharest / Romania;

[15] Wang J.W., (2020). Performance experiment of buckwheat threshing device with inner and outer roller rotation. *International Agricultural Engineering Journal*, Vol.29, Issue 2, pp.173-182, Beijing / P.R.C.;

[16] Xiang D.B., (2013). Research progress on cultivation in buckwheat [J]. *Crops*, Issue 3, pp.1-6, Beijing / P.R.C.;

[17] Xu B., (2021). Construction of a discrete element model of buckwheat grain and calibration of parameters. *INMATEH-Agricultural Engineering*, Vol.64, Issue 2, pp.175-184, Bucharest / Romania;

[18] Ye S.B., (2021). Design and test of negative pressure chamber rotary buckwheat seed metering device. INMATEH-*Agricultural Engineering*, Vol.64, Issue 2, pp.185-194, Bucharest / Romania;

[19] Zhang K.K., (2019). *Research on dynamics simulation and layout of buckwheat picking harvester*. Northwest A & F University, Yangling / P.R.C.;

[20] Zhang R.M. (2016). Cloning and epitope analysis of a novel allergy protein TBW17 from Tartary buckwheat. *Genomics and Applied Biology*. Vol.35, Issue 12, pp.3481-3486, Guangxi / P.R.C.;

[21] Shi R.J., (2019). Design and test of full-feed flax thresher. *Journal of China Agricultural University*, 2019, 24(08):120-132. Vol.24, Issue 08, pp. 120-132, Beijing / P.R.C.;

[22] *** China Academy of Agricultural Mechanization Sciences. (2007). Agricultural Machinery Design Manual. China Agricultural Science and Technology Press;

[23] *** Chinese Society of Agricultural Machinery. (2020). Whole-feed buckwheat combine harvester. T/NJ 1217-2020, Chinese Standard Press, Beijing / P.R.C.

DESIGN AND STUDY ON THE ADAPTIVE LEVELING CONTROL SYSTEM OF THE CRAWLER TRACTOR IN HILLY AND MOUNTAINOUS AREAS
/
丘陵山区履带式拖拉机自适应调平控制系统的设计与研究

Xiaohu CHEN [1], **Xiaolian LÜ** [2,3], **Xiao WANG** [1], **Xinye TU** [1], **Xiaorong LÜ** [1*] [1]

[1] College of Machinery & Electronics, Sichuan Agricultural University, Yaan, Sichuan, 625014, China
[2] Nanjing Research Institute for Agricultural Mechanization, Ministry of Agriculture and Rural, Nanjing, Jiangsu, 210014, China
[3] College of Machinery and Automotive Engineering, Chuzhou University, Chuzhou, Anhui, 239000, China
E-mail: lxrxj2008@163.com
DOI: https://doi.org/10.35633/inmateh-66-30

ABSTRACT

In order to improve the automation level of the crawler tractor leveling system, an adaptive leveling control system was designed for the developed crawler tractor leveling device. The overall hardware of the leveling control system was determined and the software system of the leveling device was designed using the proportional algorithm. The designed leveling control system is composed of the real-time detection part, control part, driving part and display part. The system can realize the real-time detection of the tractor inclination angle, and complete rapid leveling of the leveling device. The test results of the leveling control system show that the leveling accuracy and leveling time of the lateral and longitudinal slope increase with the increase of the tractor inclination angle. The leveling accuracy and stability of the longitudinal slope are better than that of lateral slope leveling, and the leveling speed is higher than that of the lateral slope. The coordination leveling accuracy is higher than the independent leveling accuracy of the lateral slope and longitudinal slope, and the collaborative leveling accuracy of the longitudinal slope is better than that of the independent leveling accuracy. The developed leveling control system can independently complete the leveling work under the actual working conditions of the crawler tractor. The leveling accuracy can be in 1° and the leveling time is in 0-6 s. The leveling accuracy and time can meet the design requirements.

摘要

为了提高履带式拖拉机调平系统的自动化水平,针对开发的调平装置进行了自适应调平控制系统的设计与研究。设计了调平装置控制系统硬件设备的整体方案,并采用比例算法对调平控制系统的软件部分进行了设计。设计开发的调平控制系统主要由实时检测部分、控制部分、驱动部分及显示部分组成。通过该系统能够实现对拖拉机作业中车身倾斜角度的实时检测,并基于检测信息实现调平装置的快速调平。调平控制系统性能测试结果表明:系统在调平作业中横坡、纵坡调平精度及时间均随车身倾角增加而增加,纵坡调平精度及平稳性均好于横坡调平、调平速度高于横坡调平,协同调平中横坡、纵坡调平精度较横坡、纵坡独立调平精度均有所提升,纵坡协同调平精度明显优于其独立调平精度,同时调平控制系统能够根据机具实际作业情况自主完成调平工作,调平精度均能达到1°以内,调平时间在0-6s以内,调平精度及时间均能满足设计要求。

INTRODUCTION

In Hilly and mountainous areas, the working quality and mechanization level of machines are reduced due to large topographic conditions, and the machine is at risk of overturning. In recent years, researchers have done a lot of research on the automatic leveling technology of agricultural tractors, mainly through the processing of external information to realize the automatic leveling of tractors *(Li et al., 2021; Li et al., 2019; Pijuan et al., 2012; Wang et al., 2021; Wang et al., 2019).* The early leveling system was mainly controlled by the integrated circuits, and many advanced technologies were gradually introduced *(Kwon et al., 2020; Marcelo et al.,2018; Pawin et al., 2016; Phu et al., 2020; Rabiet al., 2020; Yin et al., 2020).* Qi et al., (2019) designed an autonomous adjustment system for tractors in Hilly and mountainous areas.

---

[1]*Xiaohu Chen, M.S. Stud; Xiaolian Lü, Prof.; Xiao Wang, M.S. Stud; Xinye Tu, M.S. Stud; Xiaorong Lü, Prof..*

This system used the PID and closed-loop fuzzy PID algorithms to effectively reduce the overshoot and leveling time. Zhang*, (2019)* designed a leveling system of parallel four-bar mechanism for the power chassis of agricultural machinery in Hilly and mountainous areas. The system takes PLC (programmable logic controller) as the control core and uses electromagnetic proportional control valve to control the expansion and contraction of the hydraulic cylinder. *Peng et al., (2018) and Wang et al., (2017)* designed a four-point hydraulic support and hydraulic driven leveling system for hilly and mountainous wheeled tractor. This control system adopts fuzzy PID control algorithm to realize the leveling of the device. Moreover, *Xu et al., (2017)* designed an automatic leveling system controlled by PLC, and the inclination sensor was used to detect the tractor inclination. PLC was used to control the expansion and contraction of the hydraulic cylinders on both sides of the tractor to drive the parallel four-bar mechanism and complete the real-time leveling. The leveling control system of the leveling device designed in this paper can detect the road conditions and process dates in real time. It meets the requirements of leveling accuracy and response time under the normal operation conditions of the leveling control system.

MATERIALS AND METHODS

OVERALL SCHEMES AND WORKING PRINCIPLE

The overall scheme of the leveling control system is shown in Figure 1, including detection part, control part, driving part and display part.
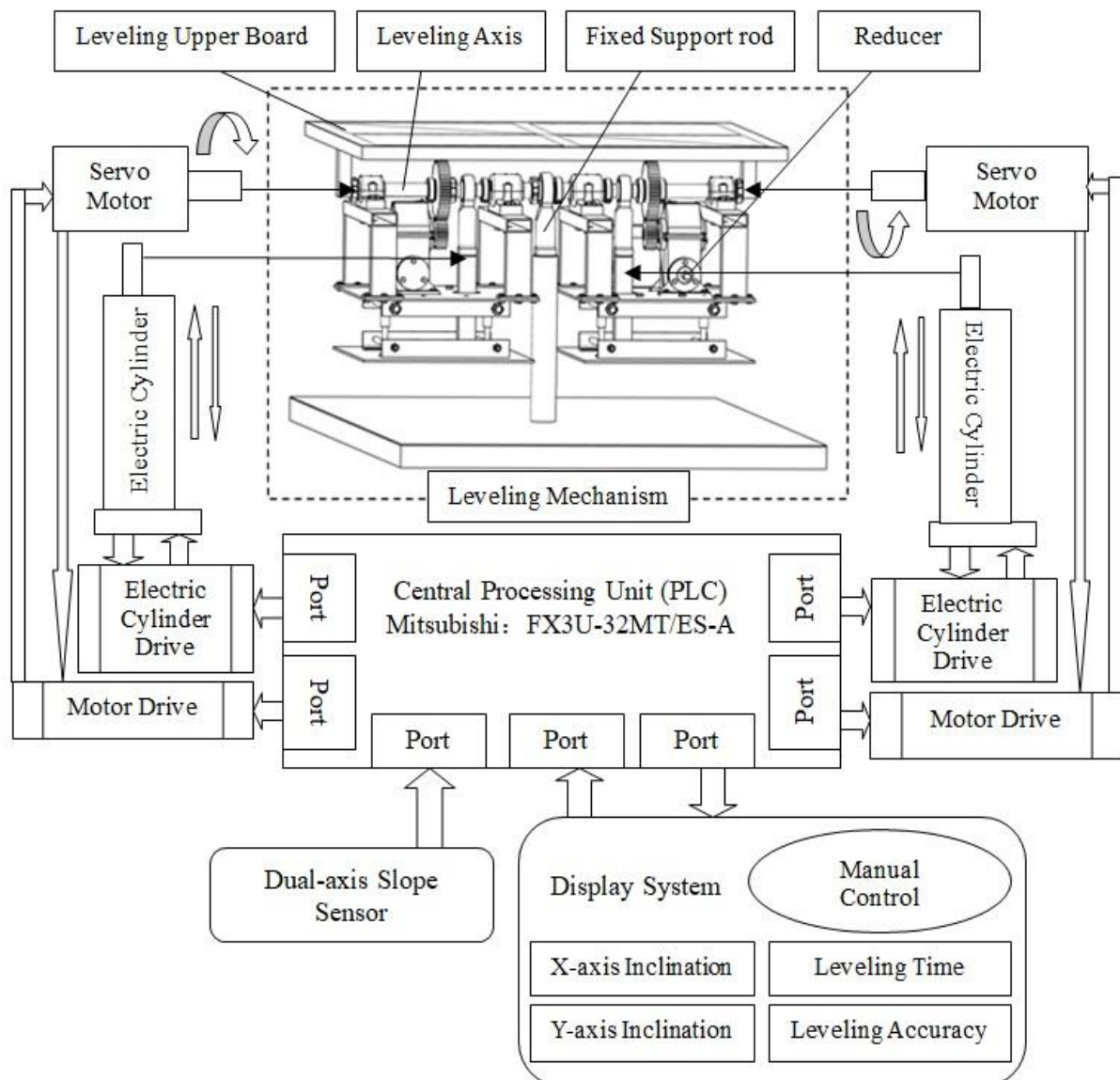

Fig. 1- Overall scheme diagram of the leveling control system

The tractor battery converts 12V DC into 220V AC via an inverter to power the entire leveling control system. In the detection part, the inclination of the tractor is detected by the dual-axis inclination sensor and fed back to the control system for real-time processing. The leveling is realized by driving the servo motor and servo electric cylinder in real time. The display part mainly monitors the working conditions of the leveling system in real time, and displays the inclination angle of the lateral slope and longitudinal slope of the leveling device, as well as the leveling time and leveling accuracy. The leveling control system is divided into manual control and automatic control. The manual control is realized through the human-computer Interactive function of the display. It is mainly to level one side separately when there is a problem with the leveling system or special circumstances, if system is stopped in case of an emergency. The leveling mechanism is mainly composed of the longitudinal and lateral slope leveling mechanism. The longitudinal slope direction is controlled by the rotation of the servo motor, and the lateral slope direction is controlled by the expansion and contraction of the servo electric cylinder. These two parts are adjusted independently. During the leveling process, the servo motor and servo electric cylinder are automatically leveled with the inclination angle of the tractor in real time, so as to keep the tractor within the preset inclination range. The machines and tools are installed on the leveling upper plate when operating. The leveling control system detects the inclination angle of the tractor through the dual-axis inclination sensor in real time, and transmits the detection information to the central processing unit (PLC) through the data line. The PLC controller processes the detected real-time inclination angle signal through the control algorithm, and sends the result command to the driving part in real time. The servo motor drives the horizontal axis to rotate radially through the reducer to complete longitudinal adjustment. The servo driver controls the expansion and contraction of the left and right electric cylinders and drives the leveling shaft to swing axially to complete the lateral adjustment.

DESIGN OF LEVELING CONTROL SYSTEM
CONTROL ALGORITHM

The leveling control system adjusts the speed by controlling the expansion of the servo electric cylinder and the servo motor to complete the tractor leveling. The proportional algorithm is used for the designed control system, and the inclination angle (*a*) of the tractor is used as the control parameter. The leveling accuracy error is *e*, and the output parameter is the servo motor speed *n*. The longitudinal slope is the forward direction of the tractor in the Y-axis direction, and the lateral slope is the forward vertical direction of the tractor in the X-axis direction. The leveling accuracy of the longitudinal slope is set in $-1° < a_y < 1°$, and that of the lateral slope is in $-1° < a_x < 1°$. $a(t)$ is the inclination angle function of the tractor, which is the input function of the proportional controller. $e(t)$ is the error function, and $n(t)$ is the speed function of the servo motor, which is the output function of the proportional controller. During the sampling period, the error function is as follows:

$$e(t) = \begin{cases} a(t) - 1° & (a(t) \geq 0) \\ a(t) + 1° & (a(t) < 0) \end{cases}$$ (1)

After calculation, the speed function of the longitudinal slope leveling servo motor is

$$n_y(t) = \frac{1}{6}k_1 e(t) = \begin{cases} \frac{1}{6}k_1 e[a_y(t) - 1°] & (a_y(t) \geq 0) \\ \frac{1}{6}k_1 [a_y(t) + 1°] & (a_y(t) < 0) \end{cases}$$ (2)

The speed function of the servo electric cylinder is:

$$n_x(t) = \frac{1}{6}k_2 e(t) = \begin{cases} \frac{1}{6}k_2 e[a_x(t) - 1°] & (a_x(t) \geq 0) \\ \frac{1}{6}k_2 [a_x(t) + 1°] & (a_{yx}(t) < 0) \end{cases}$$ (3)

where: k_1- the preset ratio of the longitudinal slope function;

k_2- the preset ratio of the lateral slope function.

During the control process, the sensor detects the inclination range of the tractor. The real-time inclination angle of the tractor is displayed on the screen, and it is determined whether the inclination angles in the Y-axis and X-axis directions are in the set accuracy range. When the inclination angle is not in the accuracy range, the inclination angle a_y (or a_x) is input into the proportional controller for proportional calculation. The calculated signals are transmitted to the servo motor driver or servo electric cylinder driver to control the movement of relevant leveling mechanism. The leveling is not ended until the leveling accuracy requirements are met. The flowchart of the leveling control system is shown in Figure 2.
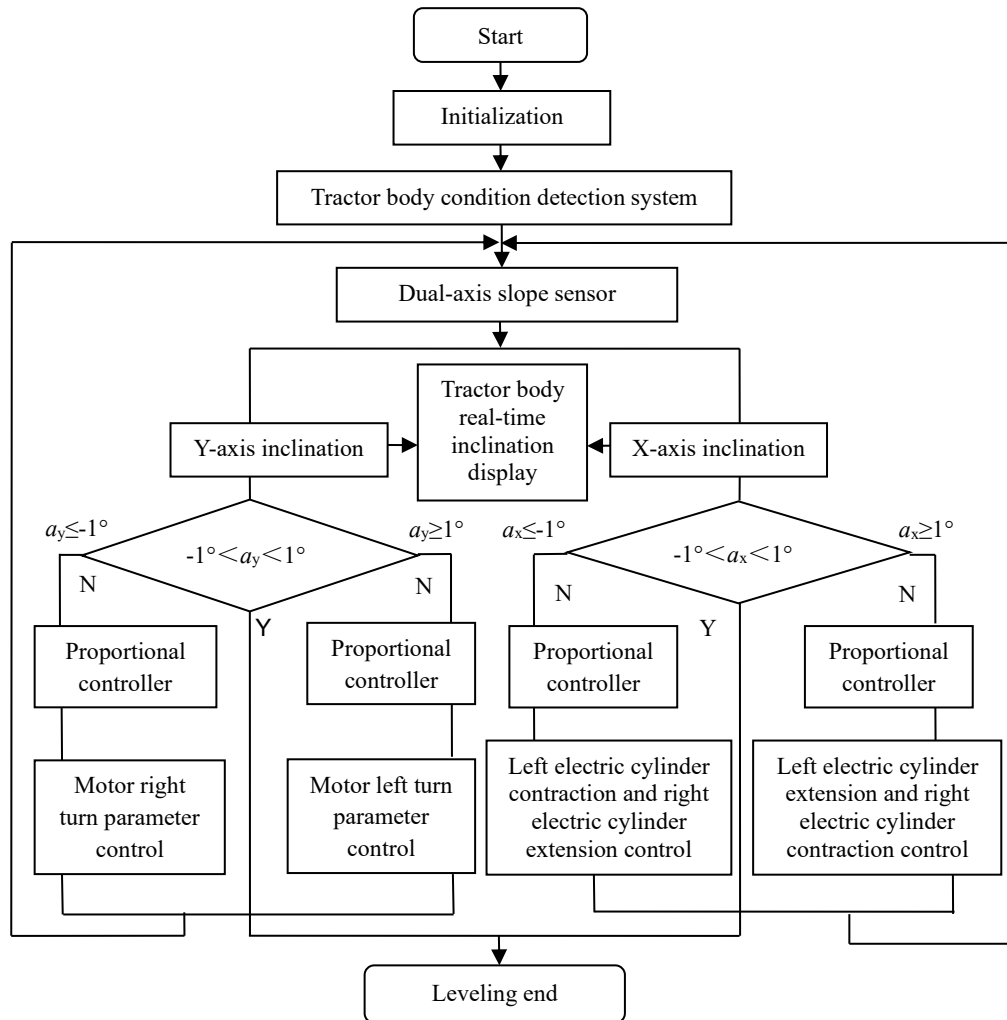
Fig. 2 - Program flow chart

PLC CONTROLLER

According to the design requirements of the control system, PLC adopts Mitsubishi FX3U-32MT/ES-A with transistor output. The PLC port is shown in Figure 3.

X_0 is set as the emergency switch to control the main switch and emergency stop of the leveling system. X_1 is set as the longitudinal slope leveling switch to control the servo motor, X_2 as the lateral slope leveling switch to control the servo electric cylinder.

Y_0 is set as pulse 1 (the pulse sending interface of the servo motor). Y_1 is set as pulse 2 (as the pulse sending interface of the servo electric cylinder). Y_5 is set as enable 1 with opening and closing port (the enable opening or closing interface of the servo motor). Y_6 is set as direction 1 with positive and negative port (the positive and negative direction control interface of the servo motor). Y_{10} is set as enable 2 with opening and closing port (the enabling opening or closing interfaces of the servo electric cylinder driver). Y_{11} is set as the positive and negative change port of direction 2 (the positive and negative direction control interface of the servo electric cylinder driver).

The pulse 1, enable 1 opening and closing, direction 1 positive and negative of the PLC ports are set as the driving programming wiring port of servo motor, which can control the longitudinal slope leveling and the opening and closing state of the servo motor. The pulse 2, enable 2 opening and closing, direction 2 positive and negative of the PLC ports are set as the driving programming wiring port of the servo electric cylinder, which can control lateral slope leveling and the opening and closing state of the servo electric cylinder.
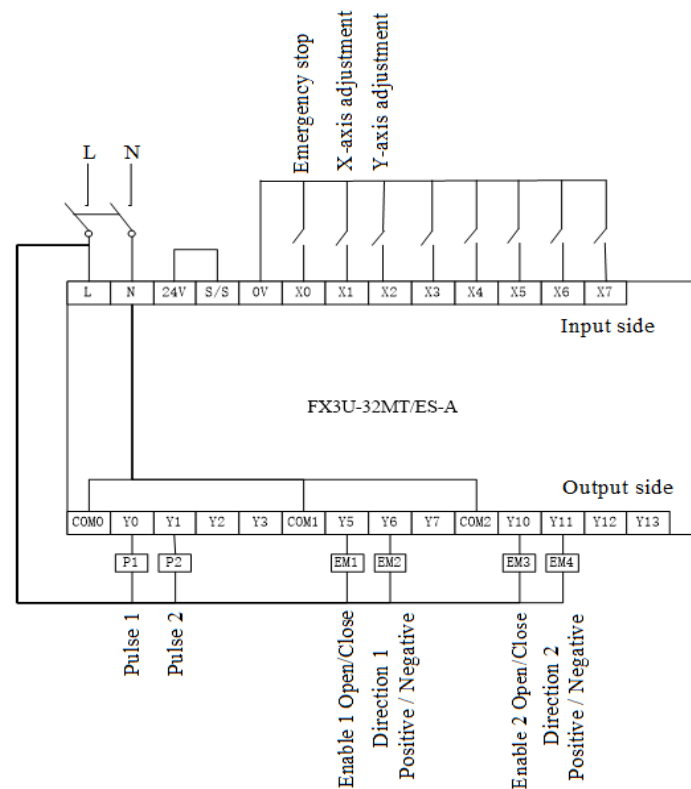
Fig. 3 - PLC port settings

SERVO MOTOR AND DRIVE

The drive controls the servo motor to adjust the longitudinal slope. According to the design requirements, the motor driver adopts MBDLN25SE and the servo motor adopts MSMF042L1U2M. The leveling system adopts the position control mode, and the connection between the driver and peripheral equipment is shown in Figure 4.
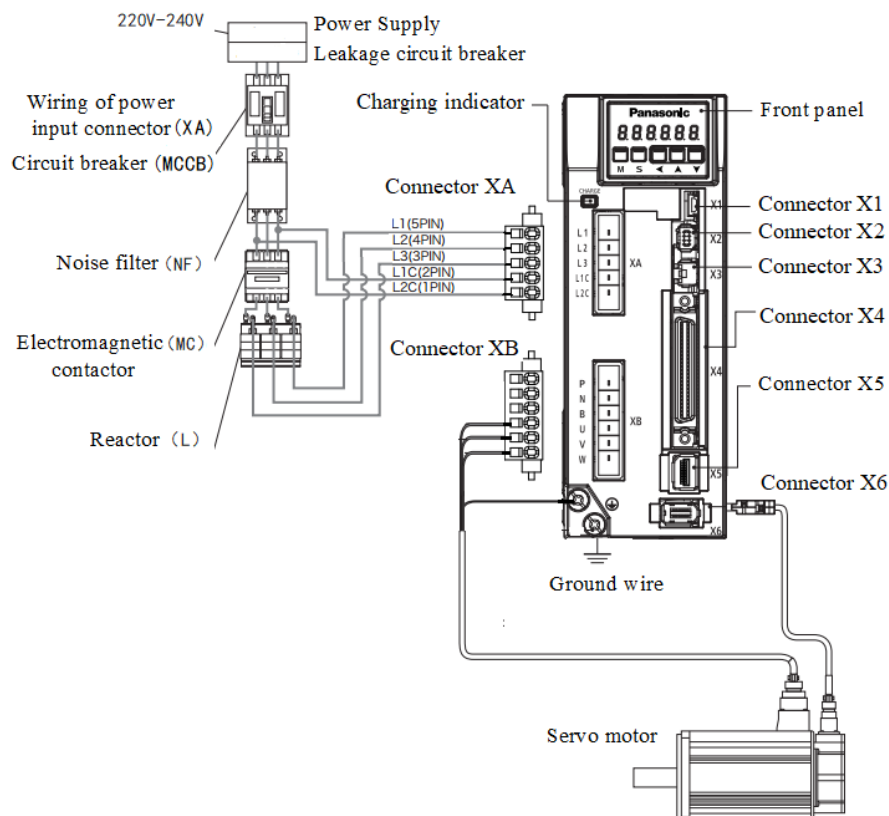
Fig. 4 - Motor driver and peripheral equipment connection diagram

The connector X_A on the driver is the wiring of the power input port, and the power line is protected by the circuit breaker. The noise interference from the driver is reduced by the noise filter, and the electromagnetic contactor is used to connect or disconnect the main power supply of the driver. In addition, the reactor is also used to reduce the high-order harmonic current of the power supply. Connector X_B and X_4 are connected with the servo motor and the coding line of the servo motor, respectively, and the connector X_4 is used to control the coding of the servo driver. Before leveling programming control, the motor should be tested to check the working state of the driver. First, the connector X_4 is connected and the power supply of the driver is turned on to confirm the standard setting value of the parameter. Then, "on state" of the servo is set and the motor is put in the excitation state. Finally, the low-frequency pulse signal from the upper device is input to make the motor run in low-speed, and the motor speed is confirmed in monitoring mode.

SERVO ELECTRIC CYLINDER AND DRIVE

The driver controls the servo electric cylinder to adjust the lateral slope. According to the design requirements, the driver adopts DS3E-21P2-PFA and the servo electric cylinder adopts MS-1100ST-M04030BZ-21P2. The leveling control system adopts the position control mode, and the leveling control uses single phase AC electrical 220V. The power wires are connected to the R and T interfaces, and the wiring ports of the driver are connected with the corresponding terminals of the electric cylinder. The built-in resistance is used for the regenerative resistance terminal, short circuit P+ and D terminals, disconnect P + and C, and p_0-24=0. CN_0 is input and output signal terminal of the pulse, direction and enable, and it is also the coding line interface of the driver. CN_0 is connected with PLC to control the driver coding. CN_1 terminal is used for expansion module. CN_2 is the driver encoder terminal and connected with the coding line of the servo electric cylinder. The connection between the driver and peripheral equipment is shown in Figure 5. CN_0 terminal is connected with PLC, and terminal 1 and terminal 4 are respectively used as the pulse and direction inputs to control the expansion and contraction speed of the electric cylinder. SI1 terminal is used as the enabling input and the switch of the electric cylinder.
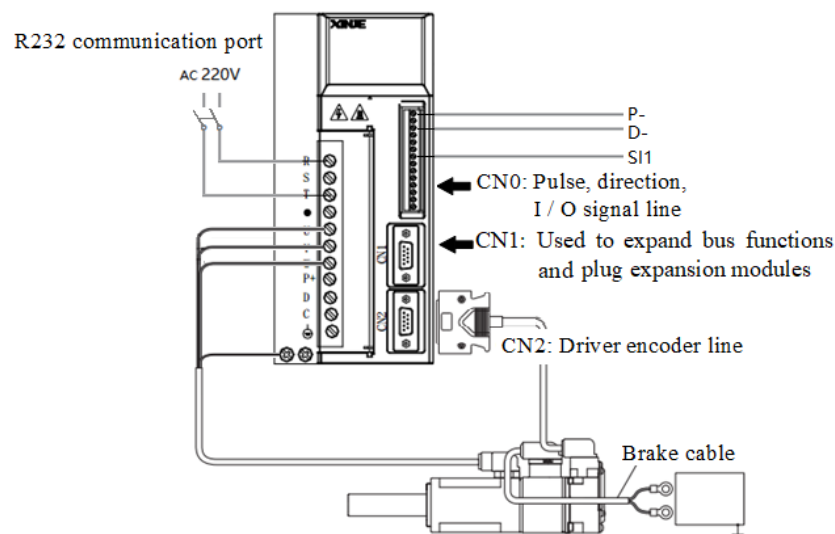
Fig. 5 - Electric cylinder driver and peripheral equipment connection diagram

INCLINATION DETECTION PART

The inclination detection circuit is used to detect and feedback the inclination angle of the tractor. The detection element adopts dual-axis inclination sensor HVT826T, and the wiring is shown in Figure 6. The output interface of the sensor is 5 lines. Two lines are the power lines, where the red is the positive line of power supply (AC11~36V), and white is the negative line of power supply. The black is the grounding wire, and yellow and green are the communication lines. The yellow send data terminal (TXD) is connected the receive data interface (RXD) of the PLC communication. The green receive data terminal (RXD) is connected the send data interface (TXD) of the PLC communication. Before using the inclination sensor, the power test and parameter setting are carried out. The corresponding product model HVT826T and the corresponding COM port of the equipment are selected to open the software interface.

The current address code of the sensor is 00, and the current baud rate of the sensor is selected as 9600 bit/s. Then the corresponding parameters are set for initialization and information detection. When the leveling control system works, the PLC sends the inclination reading command. The sensor verifies whether the command is correct and then sends the inclination information, which is the compressed BCD code. The PLC needs to read the inclination values of lateral slope and longitudinal slope according to the BCD code reading rules. In the communication program, the PLC uses the timer T command to read the inclination information once, and then the inclination information is read through RS command and the sensor communicating. The maximum output frequency of the sensor is 50Hz, and the sampling period is 80ms.
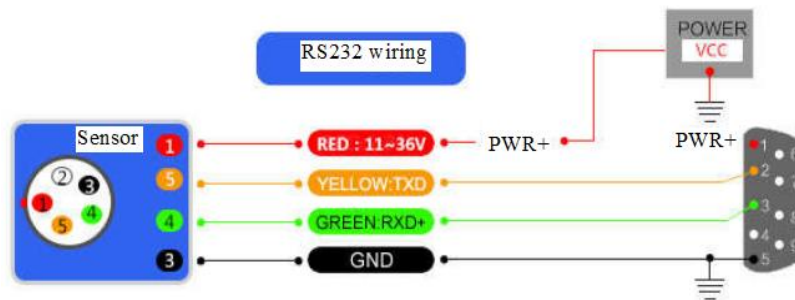
Fig. 6 - Sensor wiring diagram

DISPLAY PART

According to the design requirements of the leveling control system, the display is Xinjie OP320-A-S. The display operation interface is designed by the editing software "Xinjie 6.5". During the display programming, the USB-to-RS232 driver is installed on the PC port and the display is connected with the PC port. The corresponding display model OP320-A-S in the editing software is selected and the communication type "Mitsubishi (FX) between the display and PLC. Then the display content is written. The display interface includes emergency stop switch, lateral slope adjustment switch, longitudinal slope leveling switch, real-time inclination angle, current leveling time and historical leveling time. The display is connected with PLC 485-BD communication port through the BD9-pin serial port line to realize communication with PLC. Before the display works, it is necessary to set PLC communication to ensure that the communication format between the display and PLC is consistent. Through the buttons on the operation interface, the leveling of Y-axis and X-axis directions of the tractor can be controlled manually, so as to realize the independent axis direction leveling test, clear historical data and register cached data.

PERFORMANCE TEST OF LEVELING CONTROL SYSTEM
CONTENT AND METHOD

When the tractor was driving in the experimental field of Sichuan Agricultural University, the accuracy and time of the leveling control system were tested for the tractor inclination. The developed adaptive leveling system is shown in Figure 7.
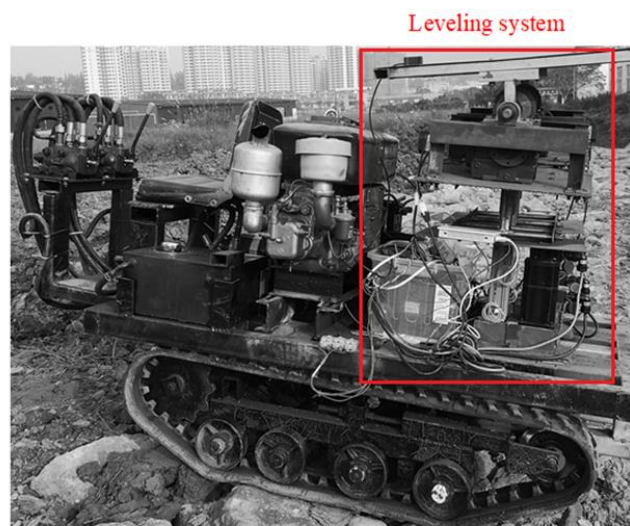
Fig. 7 - The adaptive leveling system testing prototype

The testing is divided into three groups: (1) Independent leveling performance of the longitudinal slope; (2) Independent leveling performance of the lateral slope; (3) Coordinated leveling performance of lateral slope and longitudinal slope. Before each testing group, the leveling device was set on the horizontal plane, so that the angles of the lateral slope and longitudinal slope were 0°. In the first testing group, the lateral slope leveling switch was off to test the independent leveling accuracy and time of the longitudinal slope of the system. In the second testing group, the longitudinal slope leveling switch was off to test the independent leveling accuracy and time of the lateral slope of the system. In the third testing group, the leveling switches of the lateral slope and longitudinal slope were set "on state" to test the leveling accuracy and time of the coordinated leveling of the system.

RESULTS AND ANALYSIS

During the test, the dual-axis inclination sensor was used to test the inclination angles of the tractor in the directions of the lateral slope (X-axis) and longitudinal slope (Y-axis). The inclination angles are recorded and processed in real-time, and the leveling (leveling accuracy) and leveling time are displayed on the screen at the same time. The test results are shown in Table 1, Table 2 and Table 3.

Table 1

X-axis leveling test results

Absolute value of X-axis slope /°	Absolute value of leveling accuracy /°	Leveling time /s
3.45	0.49	0.97
7.63	0.69	1.63
9.88	0.55	2.87
12.04	0.85	3.75
14.13	0.96	4.98

Table 2

Y-axis leveling test results

| Absolute value of Y-axis slope /°	Absolute value of leveling accuracy /°	Leveling time /s
5.49	0.69	0.85
8.99	0.72	1.48
14.16	0.76	2.68
18.78	0.93	3.25
22.55	0.98	4.13

Table 3

X-axis and Y-axis coordinated leveling test results

Absolute value of slope /°		Absolute value of leveling accuracy /°		Leveling time /s
X-axis	Y-axis	X-axis	Y-axis	
3.88	4.48	0.55	0.36	0.89
8.75	10.38	0.73	0.48	1.50
10.86	12.47	0.39	0.57	2.17
12.49	15.47	0.95	0.89	3.45
14.68	18.56	0.79	0.92	5.27

It can be seen from the results that the designed leveling control system can maintain the leveling accuracy within 1° under no-load conditions, and the leveling time is between 0 and 6s. The performance parameters of the leveling control system can usually meet the objectives and requirements of the system design. Nevertheless, the self-vibration of the tractor in operation will increase the leveling time, and result in the overshoot of the system and oscillation around the leveling angle. From Figure 8, it can be seen that during the leveling, the leveling accuracy and leveling time of X-axis and Y-axis increase with the increase of the tractor inclination. The leveling accuracy and stability of Y-axis are better than that of X-axis, and its leveling speed is higher than that of X-axis. The collaborative leveling accuracy of X-axis and Y-axis is higher than the independent leveling accuracy of X-axis and Y-axis. The collaborative leveling accuracy of Y-axis is significantly better than its independent leveling accuracy, and the collaborative leveling speed of X-axis and Y-axis slopes is lower than that of X-axis slope. The reason is that the vibration of the tractor has a great impact on the inclination signal detected by the inclination sensor.

The control system cannot effectively filter the noise model of the tractor, and the vibration of the tractor has a great impact on the electric cylinder in the leveling system. The Y-axis leveling is controlled by the servo motor through the reducer with self-locking function to reduce the accumulation of errors during the leveling process. The motion conversion efficiency of the servo motor is also higher than that of the servo electric cylinder. As such, the real-time operation can be completed accurately and in time, and the influence of over-leveling and vibration can be effectively prevented. The interaction between the leveling of X-axis and Y-axis is significant, and the collaborative leveling can effectively improve the effect of the control system.
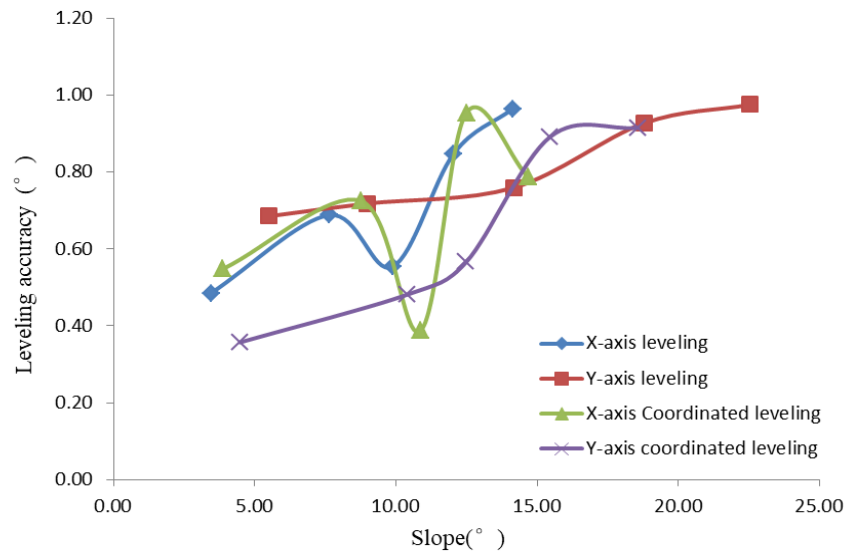
(a) Leveling accuracy

(b)
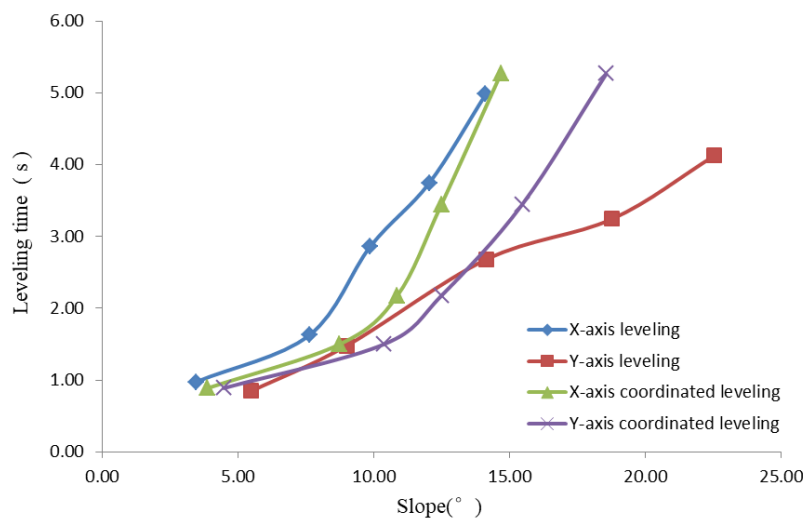
(b) Leveling time

Fig. 8 - Change chart of leveling time with variable frequency parameters

CONCLUSIONS

(1) The system adopts the Mitsubishi FX3U-32MT/ES-A as the core of the signal processing and control system, and uses the double axis inclination sensor HVT826T to detect the inclination of the tractor. The designed leveling control system adopts the position control mode, and the servo motor is controlled by the driver to adjust the longitudinal slope, so as to adjust the lateral slope and the servo electric cylinder. The display OP320-A-S is adopted. Through the editing software "Xinjie 6.5", the design of the display interface of the leveling control system and the real-time communication function with PLC are completed on the computer. The basic test parameter display and human-computer interactive functions of the control system are realized.

(2) The test results of the leveling control system shows that the designed leveling control system can work normally. Under different operating conditions, the leveling accuracy can be maintained in 1°, and the leveling time is in 0-6 s. The leveling accuracy and timeliness can meet the design objectives and requirements. The leveling control system has simple structure, good timeliness and stability. It cannot only improve the accuracy, safety and automation of the agricultural tractor, but also provide a certain theoretical basis and technical reference for improving the stability and quality of agricultural machines in Hilly and Mountainous areas.

ACKNOWLEDGEMENT

REFERENCES

[1] Kwon, B. S., Hyun, Y. J., Yi, K. (2020). Mode control of electro-mechanical suspension systems for vehicle height, leveling and ride comfort. *Proceedings of the Institution of Mechanical Engineers, Part D: Journal of Automobile Engineering*, 234(2-3), 792-809.

[2] Li, L. L., Deng, G. R., Lin, W. G., Cui, Z. D. (2021). Development Status and Trend of Agricultural Machinery Automatic Leveling Technology. *Modern Agricultural Equipment*, 42(5), 2-7, 35.

[3] Li, Z., Fan, C. J., Zhang, H., Qin, F. (2019). Analysis on the present situation and tendency of automatic leveling in agricultural machinery. *Journal of Chinese Agricultural Mechanization,* 40(4), 48-53.

[4] Marcelo, M. M., Manh, Q. N., Olivier, S., Luc, D. (2018). Design of a fast real-time LPV model predictive control system for semi-active suspension control of a full vehicle. *Journal of the Franklin Institute*, 356(3), 1196-1224.

[5] Pawin, T., Tofael, A., Tomohiro, T. (2016). Navigation of autonomous tractor for orchards and plantations using a laser range finder: Automatic control of trailer position with tractor. *Biosystems Engineering*, 147, 90-103.

[6] Peng, H., Ma, W. X., Zhao, E. P., Lu, X. Q., Feng, X. (2018). Design and physical model experiment of body leveling system for roller tractor in hilly and mountainous region. *Transactions of the CSAE*, 34(14), 36-44. https://doi.org/10.1016/j.inpa.2020.02.004

[7] Phu, N. D., Hung, N. N., Ahmadian, A., Senu, N. (2020). A New Fuzzy PID Control System Based on Fuzzy PID Controller and Fuzzy Control Process. *International Journal of Fuzzy Systems,* 22(7), 2163-2187.https://doi.org/10.1007/s40815-020-00904-y

[8] Pijuan, J., Comellas, M., Nogues, M. (2012). Active bogies and chassis leveling for a vehicle operating in rough terrain. Journal of Terramechanics, 49(3), 161-171.

[9] Qi, W. C., Li, Y. M., Zhang, J. H., Qin, C. J., Liu, C. L., Yin, Y. P.(2019). Double Closed Loop Fuzzy PID Control Method of Tractor Body Leveling on Hilly and Mountainous Areas. *Transactions of the Chinese Society for Agricultural Machinery,* 50(10), 17-23, 34.

[10] Rabi, N. M., Kanungo, B. M. (2020). Development and implementation of induction motor drive using sliding-mode based simplified neuro-fuzzy control. *Engineering Applications of Artificial Intelligence,* 91(C), 103593-103593.

[11] Wang, Z. Z., Yang, J., Liu, P. Y., Long, X. J. (2019). Development of an agricultural vehicle leveling system based on rapid active leveling. *Biosystems Engineering*, 186(C), 337-348.

[12] Wang, J. J., Zhao, J. Y., Cai, W., Li, W. L., Francesco, D. O. (2021). Leveling Control of Vehicle Load-Bearing Platform Based on Multisensor Fusion. *Journal of Sensors*, DOI: 10.1155/2021/8895459

[13] Wang, Z. S., Ma, W. X., Li, H. L., Wang, J. X. (2017). Design and Analysis of Hydraulic Leveling System in Hillside Tractor Body. *Hydraulics Pneumatics & Seals,* 37(10), 76-80.

[14] Xu, F., Li, G. Y., Gao, M. R. (2017). Design of leveling control system for mountain tractor body. *Agriculture and Technology*, 37(17), 59-61.

[15] Yin, H. Q., Yi, W. J., Li, C. C., Wang, K. J., Wu, J. T. (2020). The fuzzy adaptive PID control of brushless DC motor. *Journal of Physics: Conference Series,* DOI:10.1088/1742-6596/1507/5/052005

[16] Zhang, L., Xu, F., Li, G. Y, Yang, S. Q. (2019). Design of Control System for Self-moving Chassis-body Leveling. *Journal of Northeast Agricultural Sciences*, 44(6), 107-110. DOI: 10.16423/j.cnki.1003-8701.2019.06.024

DESIGN AND EXPERIMENT OF ROTARY PRECISION HILL DIRECT SEED-METERING DEVICE FOR RICE
/
转勺式水稻精量穴直播排种器设计与试验

Liquan TIAN [1,2), Zhao DING [1, 2), Zhan SU[1, 2), Lizhen LI [3), Zhiming WANG[*1, 2)   [1]
[1) Key Laboratory of Crop Harvesting Equipment Technology of Zhejiang Province, Jinhua, 321017, China
[2) Mechanical & Electrical Engineering College, Jinhua Polytechnic, Jinhua, 321017, China
[3) Jinhua Electromechanical Product Simulation Technology Research Institute, Jinhua, 321017, China
E-mail: jhcwzm@163.com

Keywords: Rotary seed-metering device; Mechanical hill direct seeding; Rice bud seeds; Design; Test

ABSTRACT

In order to realize the mechanical direct seeding of precision rows and hills in rice field, a rotary precision hill direct seed-metering device for rice was designed. Through designing the key components of seed-metering device and analyzing its working principle, the main factors and critical conditions affecting the seed-metering performance were obtained. Using the secondary rotation combination test, taking the rotation speed of seed-metering disc and seed capacity height as the test factors, and the re-broadcasting rate, seed-metering qualified rate and miss-seeding rate as the indexes, the seed-metering performance was experimentally studied by using the JPS-12 seed-metering device tested. Design-Expert 6 0.10 software was used to analyze the test data to obtain the mathematical model between factors and indexes. The test results show that when the speed of the seed-metering plate was 24.60 r/min and the seed capacity height was the radius of the seed-metering disc, the qualified rate of seed-metering was 94.83%, the re-broadcasting rate was 3.43%, and the miss-seeding rate was 1.74%. The seeding performance meets the agronomic requirements of rice seeding, and provides a reference for the design of the whole machine.

摘要

为实现水稻田间精量成行成穴机械直播，设计了一种转勺式水稻田间精量穴直播排种器。通过设计排种器关键部件，并对其工作原理进行分析，得到影响排种性能主要因素和临界条件。采用二次旋转组合试验以排种盘转速、容种高度为试验因素，重播率、排种合格率和漏播率为性能指标，利用 JPS-12 排种器检测试验台对排种性能进行试验研究，并运用 Design-Expert6.0.10 软件对试验数据进行分析，得到因素与指标之间的数学模型。试验结果表明：排种盘转速为 24.60r/min、容种高度为排种盘半径时，排种合格率为 94.83%，重播率为 3.43%，漏播率为 1.74%，排种性能满足水稻田间播种的农艺要求，并为整机设计提供参考。

INTRODUCTION

Rice direct seeding technology is different from the seedling raising and transplanting technology *(He and Zhao et al, 2019; Arzu and Adnan, 2014)*. It saves the work of conventional cultivation, seedling raising, seedling transportation and transplanting, and the seedling field operation *(Andrade et al, 2019; Hevko et al, 2008)*. It is also a cost-saving and efficient planting technology suitable for the development of economics *(Blümmel et al, 2020; Yin, 2020)*. The mechanical direct seeding of rice has the advantages of high efficiency, low labor intensity and low production cost, and is suitable for large-scale promotion *(Yazgi et al, 2017; Vasylkovska et al, 2019)*. Rice direct seeding does not have the recovery stage caused by seedling and transplanting, which is conducive to promoting tillering and increasing the effective panicles of the rice plant *(Dai et al, 2020; Ibrahim et al, 2018)*. It is also an important way to improve the level of mechanized planting in the whole process *(Poncet et al, 2018; Yang, 2020)*.

Seed-metering device is an important part of the precision seeder *(Huang et al, 2020; Andre et al, 2020)*. Rice precision seeding is a little difficult. Currently, Heilongjiang Province mostly adopts the drilling method, and most of the drilling tools are the outer groove wheel or the hill wheel seed-metering device. Due to the limitation of the structure, the seed-metering device has low accuracy, poor uniformity and easily damage of seeds, and a large number of fine rice seeds are wasted. It is difficult to achieve the purpose of reasonable hill spacing required by agronomy *(Zhou et al, 2016)*.

---

[1] *Tian Liquan, Associate Professor; Ding Zhao, Ph.D; Su Zhan, Ph.D; Li Lizhen, Ph.D; Wang Zhiming, Ph.D*

In order to meet the needs of precision mechanical hill direct seeding for rice, realize the uniform seeding of bud seeds in rows and hills, and reduce the damage to bud seeds during the seeding, a rotary precision hill direct seed-metering device for rice is designed in this paper. It adopts the operation modes of rotary seed-picking, gravity seed-cleaning, rotary seed-delivery and secondary seed-feeding to explore the structural parameters of key components and analyze its working principle. The best combination of various factors was obtained through bench test to provide reference for the design of the whole machine.

MATERIAL AND RESEARCH METHODS
MAIN STRUCTURE

The structure of the seed-metering device is shown in Fig. 1. It is mainly composed of seed filling cover, seed-metering shaft, bearing, bearing end cap, separator (track and seed delivery port), seed groove wheel, seed-metering shell and more. The rotary spoon disc is composed of 18 seed-picking rotary spoons, which are connected with the slider through the torsion spring. Each seed-spoon makes a circular motion with the rotary spoon disc and rotates in the assembly hole under the control of the torsion spring and the slider. The separator is fixedly assembled with the pin hole of the seed-metering shell by means of a fixed pin. The separator is made of a 1.5 mm thick steel plate with a triangular groove on the edge, which is provided with a track groove and a seed delivery port. The track is welded in the track groove, and the track, the slider and the torsion spring jointly control the rotation of the seed-spoon in the assembly hole. The seed groove wheel rotates synchronously with the rotary spoon disc, and its circumference is evenly distributed. The seed groove corresponds to the seed-picking rotary spoon one by one, and forms 18 seed guiding chambers with the diaphragm and seed-metering shell.
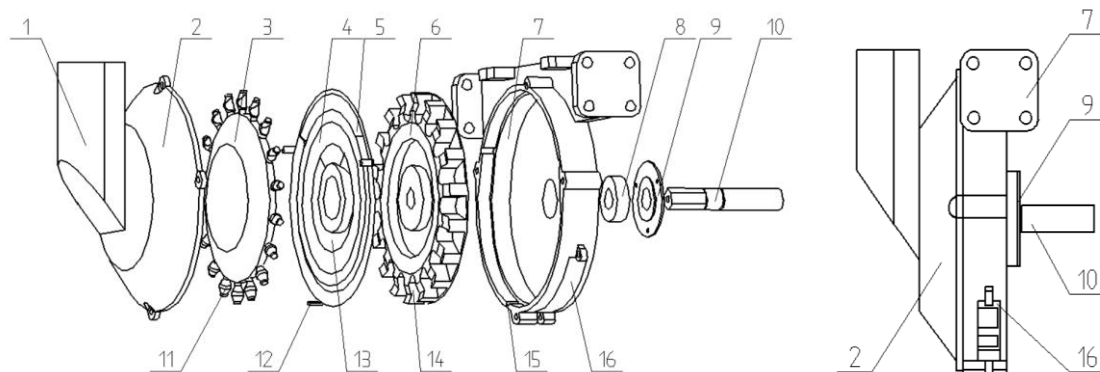
Fig. 1 - Rotary seed-metering device
1. Feed opening; 2. Seed filling cover; 3. Rotary spoon disc; 4. Separator; 5. Seed-delivery port; 6. Seed groove wheel;
7. Seed-metering shell; 8. Bearing; 9. Bearing end cap; 10. Seed-metering shaft; 11. Pickup finger; 12. Fixed pin;
13.Track groove; 14. Seed groove; 15. Housing pin hole; 16. Seeding port.

The working process of seed-metering device is mainly divided into five stages: seed-picking, seed-clearing, seed-delivery, seed-guiding and seed-feeding. During operation, the bud seeds are filled into the seed filling cover through the feed opening, and the machines and tools transmit the power to the seed-metering shaft through the chain to drive the rotary spoon disc and seed guiding groove wheel to rotate. The track in the separator and groove is fixed, and the seed-picking spoon is controlled to rotate regularly in the assembly hole with the slider and torsion spring. In the seed-picking area, the bud seeds fill the seed capsule space formed by the seed-picking rotary spoon and the triangular groove of the separator, and leave the seed-picking area driven by the rotary spoon disc to complete the seed-picking process. When the seed-picking rotary spoon pushes the bud seeds to the seed clearing area, the bud seeds in the unstable state of seed capsule space fall back to the seed filling area to complete the seed-clearing process. Driven by the rotary spoon disc, the seed-picking rotary spoon continues to move to the seed-delivery port. Under the joint action of the track, slider and torsion spring, the seed-picking rotary spoon rotates around the axis of the seed-picking rod to push the fixed bud seeds of the seed capsule space into the seed guiding chamber through the seed-delivery port of the separator to complete the seed-delivery process. The seed-guiding groove wheel and the rotary spoon continue to rotate to send the bud seeds in the seed guiding chamber to the seed-feeding port. The bud seeds are separated from the seed-metering device and thrown out under the action of gravity and centrifugal force *(Zhang et al, 2021).*

In order to reduce the height and improve the uniformity of seed-feeding, the seed-metering device has the function of secondary seed-feeding, that is, when the bud seeds in the seed capsule space reaches the seed-delivery port, it is pushed into the corresponding seed guiding chamber to complete one seed feeding. The bud seeds in the seed-guiding room rotate with the seed-guiding groove wheel, turns to the seed-feeding port and are thrown out to complete the secondary seed-feeding.

SEED-PICKING ROTARY SPOON

The seed-picking rotary spoon is composed of a seed-spoon, a torsion spring, a seed-picking rod, a slider and a positioning pin, as shown in Fig. 2. During operation, the seed capsule space composed of the seed-spoon and triangular groove of the separator to scoop the bud seeds. The positioning pin combines the torsion spring and the seed-picking rod into a whole, and positions the seed-picking rotary spoon in the assembly hole at the same time. The slider contacts and rubs with the track, controls the seed-picking rotary spoon to rotate around the axis of the seed-picking rod in the assembly hole, and then controls the seed-spoon to scoop, hold and push the bud seeds.
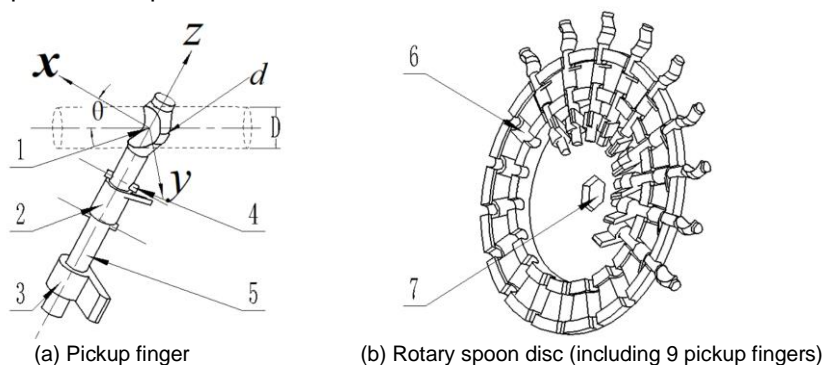
(a) Pickup finger   (b) Rotary spoon disc (including 9 pickup fingers)
Fig. 2 - Diagram of pickup finger
1. Seed-spoon; 2. Torsion spring; 3.Slider; 4. Positioning pin; 5. Seed-picking rod;
6. Assemble hole; 7. Shaft fastening hole.

The seed-spoon is a curved body formed by the intersection of the drum column at the top of the seed-picking rod and the cylindrical surface, and the curved surface is surrounded by the triangular groove of the separator to form a seed capsule space. The maximum diameter d of the drum column and the inclination angle θ of the cylindrical surface relative to the separator, and the diameter D of the cylindrical surface determine the space of the seed capsule space. If the seed space is too small, the bud seeds are difficult to enter the spoon, which is easy to cause miss-seeding. If the seed capsule space is too large, many bud seeds will enter the spoon, and it is easy to cause re-broadcasting. In order to improve the scope of seed selection, three kinds of direct seeding rice, Longjing 26, Kenjiandao 6 and Konyu 131 in Heilongjiang Province were selected. After soaking the seeds to promote germination until the chest was broken and white, 1000 seeds were randomly selected to measure the overall dimensions of bud seeds. The average value of statistical data is shown in Table 1.

Table 1

Statistical Results of Dimensions of Rice bud seeds

Variety	Length L / mm	Width W / mm	Thickness T / mm
Longjing 26	7.08	3.96	2.39
Kenjian rice 6	6.68	3.62	2.54
Konyu 131	7.35	3.88	2.47

According to the statistical results in Table 1, the shape and size of seed-spoon surface should meet $W_{max}<d<D<L_{max}$. The structural parameters of the spoon are 7 mm of the cylindrical diameter D, 30° of the inclination angle θ and 4.5 mm of the maximum diameter d of the drum.

SEPARATOR TRACK

According to the needs of seed-metering, the circumferential angle of the separator track is divided into four parts: seed-spoon opening, seed-picking duration, seed-spoon delivery and delivery duration, as shown in Fig.3. In the seed-spoon opening area, the track height gradually decreases, and the slider gradually disengages from the track. Under the action of torsion spring, the pickup finger rotates in the assembly hole, and the seed capsule space is opened to the maximum.

     After the pickup finger turns over the seed-picking continuation area, the slider contacts the closed slope of the track and enters the seed-spoon delivery area. The height of the guiding rail increases gradually, and the slider overcomes the action of the torsion spring to control the rotation of the pickup finger in the assembly hole. The seed capsule space gradually decreases, and the bud seeds in the seed–spoon are pushed into the seed-guiding chamber through the seed-delivery port. The slider enters the delivery continuous area. Under the action of track lifting, the pickup finger maintains the pushing state of bud seeds at the seed-delivery port.
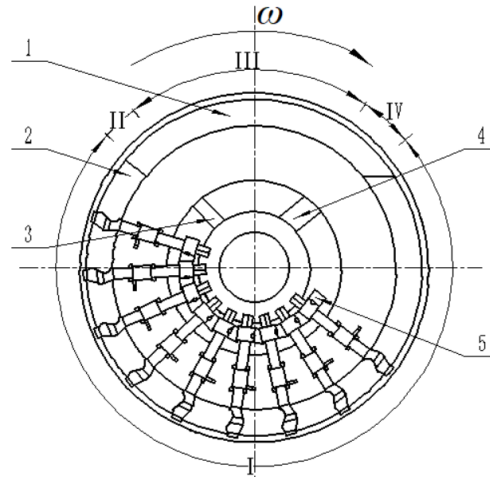
Fig. 3 - Diagram of the separator track
I. Seed-picking duration; II. Seed-spoon delivery; III. Delivery duration; IV. Seed-spoon opening.
1. Seed-delivery port; 2. Triangular groove; 3. Closed slope; 4. Involute slope; 5. Slider

     According to the position of seed-delivery port and the position of bud seed population, the opening angle of seed-spoon orbit circumference is designed to be 30°, the seed-picking duration angle is 250°, the seed-spoon delivery angle is 20° and the delivery duration angle is 60°.

SEED-PICKING AND SEED-CLEARING PROCESS

     When the seed-metering device works, the rotary spoon disc rotates at an angular speed ω to drive the pickup fingers to scoop the bud seeds, and the bud seeds are lifted from the population by the seed spoon to complete the seed-picking operation. When the pickup fingers rise to a certain height, the bud seeds in the unstable state of seed capsule space fall back to the seed-filling area under the action of gravity to complete the seed-clearing operation.

     As shown in Fig. 4, when there are too few bud seeds, the seed capacity height H is small and the seed-filling probability is small. When there are too many bud seeds, the seed capacity height H is large and the seed-filling probability is large. However, when the starting angle β of seed-clearing is exceeded, there are still bud seeds filling in the capsule seed space, which would affect the seed-clearing performance. The highest point of AB on the population surface should not exceed the seed-clearing starting point. Turning the spoon to dig into the bud seeds until they leave the population surface, and the central angle ζ corresponding to the population surface AB is the seed angle, then:
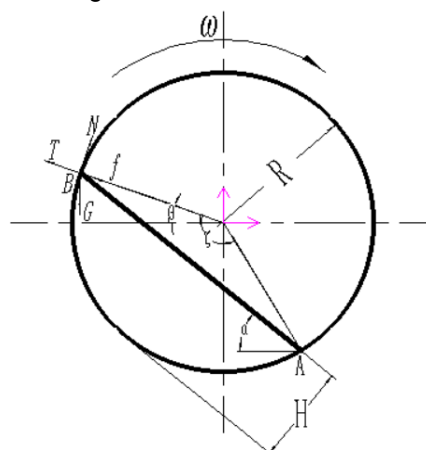
Fig. 4 - Diagram of the force applied to the moving seeds

$$\varsigma = 2\arccos\frac{R-H}{R} \tag{1}$$

where, R - the distance from the bud seeds to the center of the seed-spoon disc, mm

H - seed height in the filling cap of the seed-metering device, mm

ζ - seed-picking angle corresponding to the population surface, (°)

With the rotation of the spoon disc, the seed capsule space gradually decreases. A bud seed B is selected as the research object. There are mainly frictional force f, seed-spoon support force N, gravity G and centrifugal force T acting on the bud seeds to establish the force equation.

$$\begin{cases} G\sin\beta + f = T \\ N = G\cos\beta \\ f = N\tan\varphi \\ T = m\omega^2 R \\ G = mg \end{cases} \tag{2}$$

where: ω - the speed of the rotary spoon disc, r/min,

φ - the sliding friction angle between bud seed and seed-spoon, (°),

β - the starting angle of seed-clearing, (°),

m - the quality of bud seeds, g.

With the rotation of the spoon disc, the seed-picking ends and the seed-clearing process begins. The clearing start angle β is:

$$\beta = \arcsin\left(\frac{\omega^2 R}{g}\cos\varphi\right) - \varphi \tag{3}$$

The starting and ending positions of the seeds are determined by the angle α between the population plane AB and the horizontal direction.

$$\alpha = \frac{\pi}{2} + \arcsin(\frac{\omega^2 R}{g}\cos\varphi) - \varphi - arccoa(\frac{R-H}{R}) \tag{4}$$

where, α - the angle between the population plane and the horizontal direction, (°).

As the angular velocity ω of the rotary spoon disc increases, the distance R from the bud seed to the center of the rotary spoon disc increases, and the included angle α also increases. The highest point of the population surface increases as well, resulting in an excessively large seed filling area and a small clearing area, which is easy to re-broadcast.

ANALYSIS OF SEED-DELIVERY PROCESS

The *xoyz* coordinate system is established, and the center *O* of the seed-spoon surface is the coordinate origin. The xOy coordinate plane is perpendicular to the axis direction of the seed-picking rod, and the z-axis is the axis direction of the seed-picking rod, as shown in Fig. 5. The distance between the bud seed Q and the axis of the seed-picking rod is r, and the distance from the axis of seed-metering is R'.
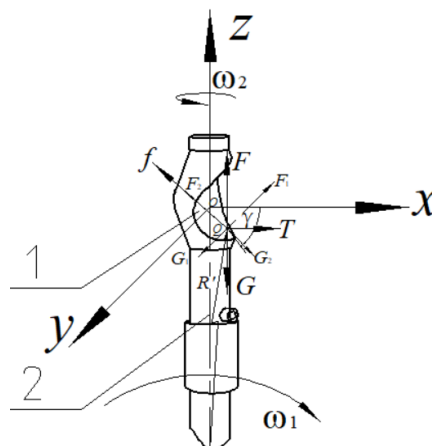
Fig. 5 - Stress analysis of bud seeds in the process of seed-delivery
1. Seed-spoon;   2.Seed-picking rod axis

In the process of seed-delivery, the bud seed Q is subjected to the gravity G, the support force N of the seed-scoop on the bud seed, the centrifugal force F received by the bud seed with the seed-picking spoon rotating around the seeding axis at an angular velocity ω_1, the centrifugal force T received by the bud seeds rotating around the axis of the seed-picking rod with the angular velocity ω_2 and the friction f. The bud seeds subjected to the gravity G can be decomposed into the positive pressure G_1 of the bud seeds on the surface of the seed-spoon and the sliding force G_2 along the surface of the seed-spoon:

$$\begin{cases} G_1 = G\cos\gamma \\ G_2 = G\sin\gamma \end{cases} \tag{5}$$

where, γ - the sliding angle of bud seeds along the surface of the seed-spoon, (°),

The bud seed Q rotates around the seed-picking spoon axis at an angular velocity ω_1 with the rotary spoon, and the received centrifugal force $F=m\,\omega_1^2\,R'$ can also be decomposed into two component forces F_1 and F_2 in the opposite direction of gravity,

$$\begin{cases} F_1 = F\cos\gamma \\ F_2 = F\sin\gamma \end{cases} \tag{6}$$

The bud seed Q slides down the surface of the seed-spoon, and the friction force is:

$$f = \mu(G_1 - F_1) \tag{7}$$

where, μ - the friction coefficient between bud seed and seed-spoon surface.

During the seed delivery process, the bud seed Q rotates with the seed spoon around the axis of the seed-picking rod at an angular velocity ω_2, and is also affected by the centrifugal force T. Its direction is the tangential direction of the circle with the z-axis as the center and r as the radius, pointing to the seed-delivery port of the separator, and its value is:

$$T = mr\,\omega_2^2 \tag{8}$$

where, r - the distance between the seed-spoon and the bud seed from the axis of the seed-picking rod, mm,

ω_2 - the rotational angular velocity of bud seeds around the axis of the seed rod, r/min.

The bud seed Q is pushed into the seed guiding chamber through the seed-delivery port by the resultant force. Its pushing acceleration can be calculated by the following formula:

$$\eta = \frac{\sqrt{(G_2 - F_2 - f)^2 + T^2}}{m} \tag{9}$$

Substituting each known quantity into Equation (9):

$$\eta = \sqrt{(g - \omega_1^2 R')^2 (\sin\gamma - \mu\cos\gamma)^2 + (\omega_2^2 r)^2} \tag{10}$$

where: η - bud seed pushing acceleration, m/s²,

ω_1 - angular velocity of bud seeds around the seed-metering axis, r/min.

Assuming that the length of the bud seed Q is L, the time t required for the bud seed to pass through the seed-delivery port of the partition to reach the seed-guiding chamber can be obtained from the following formula.

$$t = \sqrt{\frac{2L}{\eta}} \tag{11}$$

where: L - the bud seed length, mm,

t - Time of the bud seed passing through the seed-delivery port, s.

From formula (10) and formula (11), the spread angle ρ of the seed-delivery port can be calculated, namely:

$$\rho = \frac{255\,\omega_1\sqrt{L}}{\pi\sqrt[4]{(g - \omega_1^2 R')^2(\sin\gamma - \mu\cos\gamma)^2 + (\omega_2^2 r)^2}} \tag{12}$$

where: ρ - the spread angle of the seed-delivery port, (°)

Substituting L=0.012 m (length of rice bud seeds), ω_1=24 r/min, R'=0.12 m, γ=55°, r=0.001 m, ω_2=108 r/min and μ=0.47 into formula (12), it is determined that the minimum value of the spread angle ρ of the seed-delivery port is 36°. In order to ensure the smooth passage of the bud seeds through the seed-delivery port, the spread angle of the seed-delivery port is selected to be 90°.

SEED GUIDING GROOVE WHEEL

Under the combined centrifugal force F_e, self-gravity G and frictional force f, the bud seeds move toward the seed-delivery port, where they are finally forced to be thrown out when they reach it, and then the process of seed-guiding and seed-delivery is completed.

The state of bud seeds in the seed-guiding chamber is analyzed, and a Cartesian coordinate system is established. The coordinate origin O is set to coincide with the rotation center of the seed-guiding groove wheel, as shown in Fig. 6. The critical conditions for bud seeds in the seed-guiding chamber are:
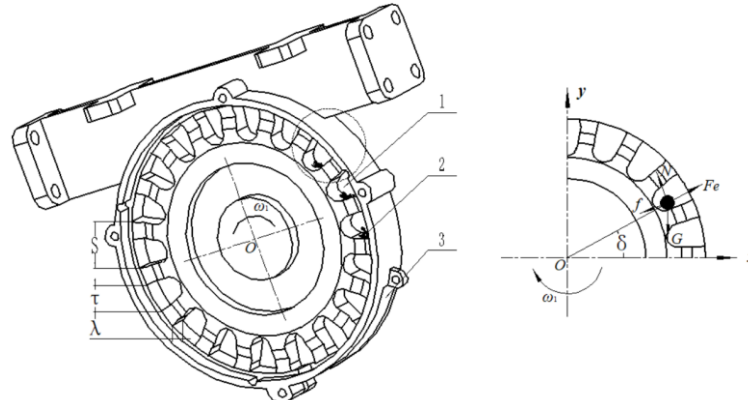
Fig. 6 - Analysis diagram of seed-guiding movement
1. Seed guiding chamber; 2. Rice bud seeds; 3. Seed-delivery port

$$\begin{cases} F_e = \dfrac{mV_1}{K} \\ V_1 = 2\pi nK \\ f = \lambda G \cos\delta \\ f + G\sin\delta \leq F_e \end{cases} \tag{13}$$

Where, δ - the angle of circumference of the seed guiding groove wheel, (°),

K - distance from the bud seeds to the metering axis in the seed-guiding chamber, mm,

λ - friction coefficient between the bud seeds and the side wall of seed-guiding chamber,

V_1 - the linear speed of the seed-guiding groove wheel, m/s.

Through the analysis of the seeding process, the seed guiding grooves passing through the seed-guiding chamber is Z in time t. In this design, $Z=1$, that is:

$$Z\frac{V_0 t}{P} = \frac{V_1 t}{S} \tag{14}$$

Combining formula (13) and formula (14), it is obtained:

$$S = \frac{2\pi nKP}{ZV_0} \tag{15}$$

where, V_0 - forward speed of sowing tool, m/s,

P - spacing of rice planting hill, mm,

S - distance of seed-guiding groove, mm.

In this design, the radius K of the seed-guiding groove wheel is 120 mm, the distance P between the rice seeding hills is 110 mm-130 mm, and the forward speed V_0 of the seed-metering device is 0.86 m/s. Substituting the above parameters into the formula (15), the distance S between the seeding chambers can be obtained as 42 mm. The parameters of the seed-guiding chamber need to consider the external dimensions of the bud seeds, and take the minimum value under the condition that the seeds are not stuck. Therefore, the width τ of the seed guiding groove is 14 mm, and the depth λ of the guiding groove is 12 mm.

EXPERIMENTAL DESIGN AND ANALYSIS

In order to check the working quality of the seed-metering device, referring to the "Testing methods of single seed drills (precision drills)" (GB/T6973-2005), 2 to 6 bud seeds in the hill are selected and the hill diameter is not more than 50 mm as the qualified standard for seed-metering. Design-Expert software was used for data processing.

TEST CONDITIONS AND MATERIALS

The experimental material was Longjing 26, and the rice seeds were soaked and germinated. The test instrument was the JPS-12 seed-metering device test bench, which is adjusted to make the seed-metering shaft run smoothly at 10-150 r/min, as shown in Fig. 7(a):

(a) *Seed-metering test bench*   (b) *Seed-metering effect diagram*
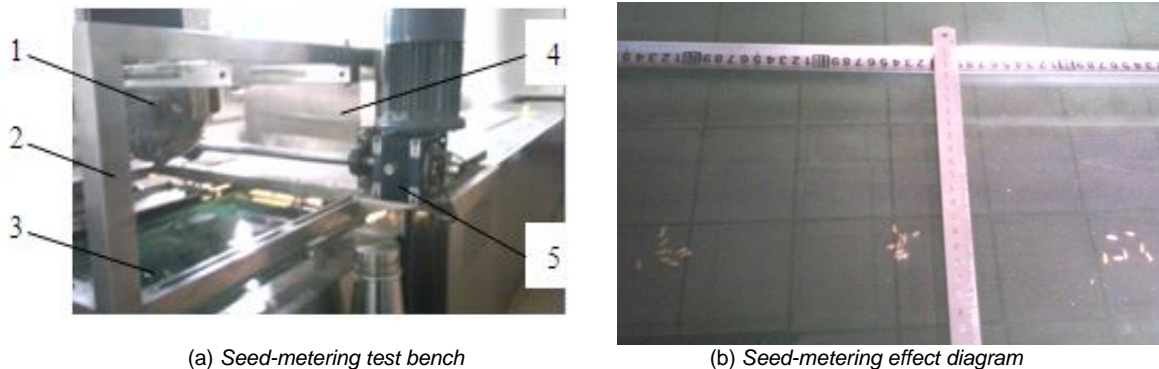
Fig. 7 -Test bench of seed-metering performance
1. Seed-metering device; 2. Mounting frame; 3. Seed bed belt; 4. Camera box; 5. Electrical machinery

The seed-metering device is fixed on the mounting frame, and the seed bed belt rotates in the opposite direction relative to the seed-spoon disc to simulate the forward motion state of the seed-metering device. The oil injection pump sprays the sticky seed oil on the surface of the seed bed belt with a fixed width, and the bud seeds are dropped from the seed-metering device to the sticky seed oil layer of the seed bed belt, as shown in Fig. 7(b).

TEST CONTENT AND METHOD

A single factor pre-test was carried out to determine the variation range of each factor on the effects of the speed of the seed-spoon and the seed capacity height on the performance were determined. On this basis, a two-factor five-level quadratic rotation combination design test was used to determine the optimal combination parameters of the seed-metering device. The test factor level coding is shown in Table 2.

Table 2

Coding table of test factor level

Code No.	Speed of rotary spoon disc	Seed capacity height
	x_1 (r/min)	x_2 (mm)
1.414	45	134.40
1	40	120.00
0	28	84.00
-1	16	48.00
-1.414	11	33.60

TEST RESULTS AND ANALYSIS

The experimental plan and results are shown in Table 3. The regression analysis of the experimental data was carried out by Design-Expert software. x_1 is the speed of the rotary spoon, x_2 is the seed capacity height, y_1 is the qualified rate of seed-metering, y_2 is the re-broadcasting rate, and y_3 is the miss-seeding rate.

Table 3

Results and design of tests

No.	Test factors		Performance indexes		
	x_1	x_2	y_1	y_2	y_3
	(r/min)	(mm)	(%)	(%)	(%)
0	1	2	3	4	5
1	16	48.00	76.13	12.28	11.59
2	40	48.00	84.09	8.21	7.70
3	16	120.00	86.24	6.40	7.36
4	40	120.00	73.56	8.17	18.27
5	11	84.00	75.74	17.51	6.75

0	1	2	3	4	5
6	45	84.00	71.41	19.66	8.93
7	28	33.60	95.10	2.40	2.50
8	28	134.40	94.07	4.60	1.33
9	28	84.00	92.32	6.15	1.53
10	28	84.00	95.41	3.01	1.58
11	28	84.00	97.13	1.90	0.97
12	28	84.00	95.31	2.55	2.14
13	28	84.00	95.20	3.37	1.43
14	28	84.00	93.04	4.20	2.76
15	28	84.00	94.38	4.84	0.78
16	28	84.00	92.63	7.05	0.32

$$y_1 = 7.26 + 5.34x_1 + 39.35x_2 - 1.43x_1x_2 - 0.08x_1^2 \tag{16}$$

$$y_2 = 48.48 - 2.86x_1 - 12.53x_2 + 0.41x_1x_2 + 0.05x_1^2 \tag{17}$$

$$y_3 = 44.26 - 2.48x_1 - 26.83x_2 + 1.03x_1x_2 + 0.03x_1^2 \tag{18}$$

In order to intuitively analyze the relationship between the test indicators and factors, the response surface is obtained by using the Design-Expert software, as shown in Fig.8:
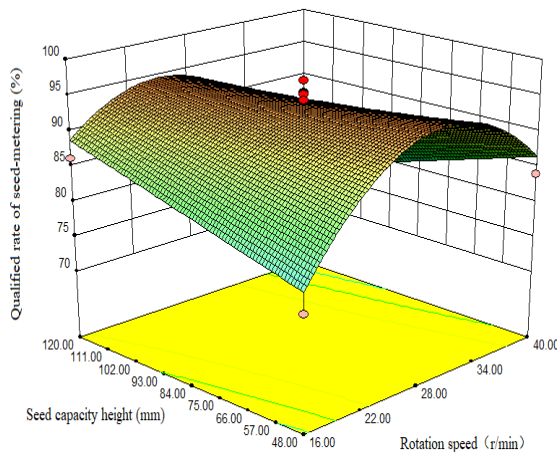
(a) The qualified rate of seed-metering
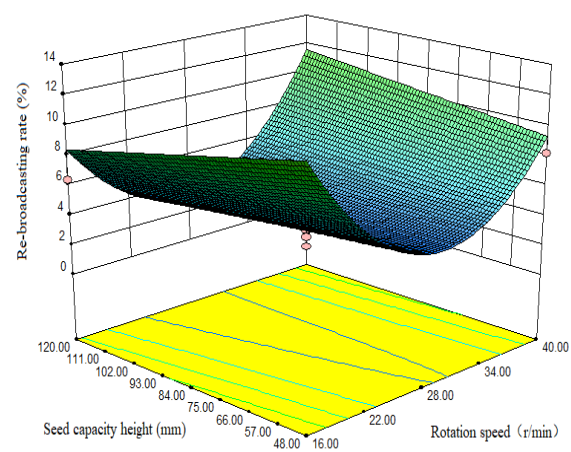
(b) Re-broadcasting rate
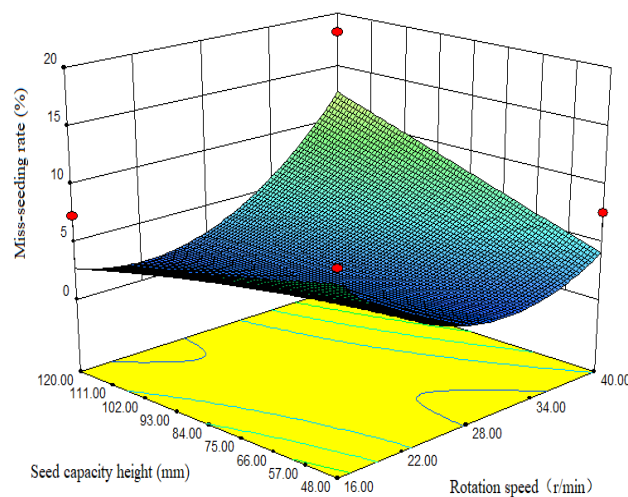
(c) Miss-seeding rate

Fig. 8 - Response surfaces of all factors to the test index

According to the above formulas (16), (17) and (18), and Fig. 8, it can be seen that there is an interaction between the speed of the rotary spoon and the seed capacity height. It can be seen from Fig. 8(a) that when the seed capacity height is constant, the qualified rate first increases and then decreases with the increase of the speed of the rotary spoon. When the speed of the rotary spoon disc is constant, the qualified rate increases with the increase of the seed capacity height. The variation range of the qualified rate is large when the speed of rotary spoon disc changes. Thereby, the speed of the rotary spoon is the main factor affecting the qualified rate of seed-metering. It can be seen from Fig. 8(b) that when the seed capacity height is constant, the re-broadcasting rate first decreases and then increases with the increase of the rotation speed. When the rotation speed is low, the re-broadcasting rate gradually decreases with the increase of the seed capacity height. However, when the rotation speed is larger, the re-broadcasting rate gradually increases. When the rotating speed changes, the variation range of the re-broadcasting rate is large, so the rotation speed is an important factor affecting the re-broadcasting rate. It can be seen from Fig. 8(c) that when the rotation speed is constant, the miss-seeding rate increases with the seed capacity height and the miss-seeding rate gradually decreases.

SEED-METERING ADAPTABILITY TEST

In order to study the adaptability of the seed-metering device to different rice bud seeds, the test seed-metering was carried out. Three kinds of rice bud seeds were selected as the research objects, and the sizes are shown in Table 1. Five repeated tests were carried out when the rotation speed of the seed-spoon disc was 24.6 r/min and the forward speed was 0.86 m/s. The data was processed to obtain the average value, as shown in Table 4.

Table 4

Adaptation test results

Variety	Performance index		
	Qualified rate %	Re-broadcasting rate %	Miss-seeding rate %
Longgeng 26	94.83	3.43	1.74
Kenjiand 6	94.26	3.18	2.56
Kongyu 131	93.32	4.40	2.28

It can be seen from Table 4 that the adaptability of the seed-metering device to the three kinds of rice bud seeds meets the agronomic requirements of precision seeding. Among them, Longjing 26 has better fluidity, is stable in the seed capsule space, and is easy to clear seeds, thus its performance index is the best. In the process of seed filling, Kongyu 131 is prone to the phenomenon that many seeds are in the capsule seed space. The bud seed has poor fluidity, the seed clearing is not thorough, and re-broadcasting is easy to occur. The seeding indexes of Kenjian 6 were better.

CONCLUSIONS

(1) In this paper, a rotary precision mechanical hill direct seed-metering device for rice is designed, and its working principle is analyzed. The structural parameters of key components are optimized to meet the requirements of precision hill direct seeding.

(2) Taking the rotation speed of the rotary spoon disc and the seed capacity height as independent variables, and the seed-metering qualified rate, re-broadcasting rate and miss-seeding rate as objective functions, the influence relationship between the working and structural parameters of the rotary spoon precision hill direct seed-metering device and the performance index of seed-metering was determined.

(3) Through the analysis and optimization of the test results using Design-Expert software, it is concluded that when the speed of the rotary spoon disc was 24.6 r/min, and the seed capacity height was the seed filling cover radius R, the qualified rate of seed-metering was 94.83%, the re-broadcasting rate was 3.43%, and the miss–seeding rate was 1.74%.

ACKNOWLEDGEMENT

REFERENCES

[1]   Arzu Y., Adnan D. (2014). Measurement of seed spacing uniformity performance of a precision metering unit as function of the number of holes on vacuum plate. *Measurement*, vol. 56, pp. 128-135. https://doi.org/10.1016/j.measurement.2014.06.026

[2]   Arzu Yazgi, Erdem Aykas, Zeynep Dumanoglu, Gulcan Demiroglu Topcu. (2017). Seed Mixture Flowing Characteristics of a Seed Drill for Mixed Seeding. *Applied Engineering in Agriculture*, vol.33, no.1, pp.63-71. DOI: 10.13031/aea.11606.

[3]   Aurelie M. Poncet, John P. Fulton, Timothy P. McDonald, Thorsten Knappenberger, Joey N. Shaw, Rees W. Bridges. (2018): Effect of Heterogeneous Field Conditions on Corn Seeding Depth Accuracy and Uniformity. *Transactions of the ASABE*. vol. 34, no. 4, pp. 819-830. DOI: 10.13031/aea.12238.

[4]   Blümmel, M., Duncan, A. J., Lenné, J. M. (2020) Recent advances in dual purpose rice and wheat research: A synthesis. *Field Crops Research*. vol. 253, pp. 107823.

[5]   Coelho A.L.F., Queiroz D.M., Valente D.S.M., Valente, Pinto F., (2020): Development of a Variable-Rate Controller for a Low-Cost Precision Planter. *Applied Engineering in Agriculture*. vol.36, no.2, pp. 233-243. DOI: 10.13031/aea.13784.

[6]   Dai, Y. Z., Luo, X. W., Zhang, M. H. (2020) Design and experiments of the key components for centralized pneumatic rice dry direct seeding machine. *Transactions of the Chinese Society of Agricultural Engineering (Transactions of the CSAE)*. vol. 36, no. 10, pp. 1-8. DOI:10.11975/j.issn.1002-6819.2020.10.001.

[7]   Edreira., Rattalino. J. I., Conley. (2019). Assessing the influence of row spacing on soybean yield using experimental and producer survey data. *Field crops research*. vol. 230, pp. 98-106. https://doi.org/10.1016/j.fcr.2018.10.014

[8]   He, L. N., Zhao, M. M., Zhao, T. C., Hao, X. G., Zhang, X.Z., He, R. Y. (2019) Design and experimental of the spiral trough seed-metering for rice and wheat. *Journal of Hunan Agricultural University*. vol.45, no.6, pp.657-663. DOI:10.13331/j.cnki.jhau.2019.06.015.

[9]   Hevko R.B., Baranovsky V.M., Lyashuk O.L. Pohrishchuk, B.V., Gumeniuk, Y.P., Klendii, O. M., Dobizha N. V. (2008). The influence of bulk material flow on technical and economic performance of a screw conveyor. *INMATEH - Agricultural Engineering,* vol.56, no.3, pp.175-184. Bucharest / Romania https://inmateh.eu/volumes/old-volume/volume-56-no-3-2018/article/the-influence-of-bulk-material-flow -on-technical-and-economical-performance-of-a-screw-conveyor

[10]   Huang, M., Fang, S.L., Cao F.B., Chen, J.N., Shan, S.L., Liu, Y., Lei T., Tian, A.L., Tao, Z., Zou Y.B., (2020). Early sowing increases grain yield of machine-transplanted late-season rice under single-seed sowing. *Field Crops Research*. No. 253, pp.107832. https://doi.org/10.1016/j.fcr.2020.107832

[11]   Ibrahim E J, Liao Q X, Wang L, Liao Y T, Yao L. (2018) Design and experiment of multi-row pneumatic precision metering device for rapeseed. *Int J Agric & Biol Eng*, 11(5): 116-123. https://www.ijabe.org/index.php/ijabe/article/view/3544

[12]   Vasylkovska K.V., Vasylkovskyi O.M., Sc. Sviren M.O. (2019) Determining the parameters of the device for inertial removal of excess seed. *INMATEH - Agricultural Engineering*, vol. 57, no.1, pp.135-140. Bucharest / Romania. https://inmateh.eu/volumes/old-volume/volume-57-no-1-2019/article/determining-the-parameters-of-th e-device-for-inertial-removal-of-excess-seed

[13]   Yang, Y. (2020) Rice cultivation status and high yield cultivation suggestions（水稻栽培现状及高产栽培技术意见分析）. *Modern Agricultural Science and Technology*. vol. 10, pp. 50-51. *(In Chinese)* http://www.xdnykj.com/ch/reader/view_abstract.aspx?file_no=20200213005&flag=1

[14]   Yin, Z. K. (2020) Experimental study on fixed distance and precision sowing of rice. *Hybrid rice*. vol. 50, no. 1, pp.38-40. DOI:10.16170/j.cnki.1673-6737.2020.01.009.

[15]   Zhang, K., Yi, S. J., Liu, H. J., Sun, H., Ma, Y.C. (2021). Optimization Design and Test of Suction Performance of Air Suction Cylinder Type Precise Seeding Device for Maize with Plant Material Bowl-tray. *Transactions of the Chinese Society for Agricultural Machinery*. vol.52, no.4, pp. 62-69. DOI: 10.6041/j.issn.1000-1298.2021.04.006

[16]   Zhou, H. B., Liang, Q. Y., Wei, T. L., Ma, X., Jiao, C. L. (2016). Design and experiment of quantitative seed supply device with fluted roller used for double-vibrating precision seed meter. *Transactions of the Chinese Society for Agricultural Machinery*. vol. 47, no.10, pp. 57-61, 83. DOI:10.6041/j.issn.1000-1298.2016.S0.009

DETECTION OF CUCURBITS' FRUITS BASED ON DEEP LEARNING

/

基于深度学习检测葫芦科果实

Fan ZHAO , Jiawei ZHANG, Na ZHANG, Zhiqiang TAN, Yonghao XIE, Song ZHANG, Zhe HAN, Mingbao LI [*)]

College of mechanical and Electronic Engineering, Northeast Forestry University, Haerbin/China
Tel: +86-0450-82190397; E-mail: lmbnefu@126.com
DOI: https://doi.org/10.35633/inmateh-66-32

ABSTRACT

Cucurbitaceae is widely planted and its fruits have great economic value. Object detection is one of the key aspects of cucurbit harvesting. In this paper, four models, YOLOv3, YOLOv4, YOLOv5s and improved Resnet_YOLO, were used to detect mixed bitter melon, cucumber, white melon, and "Boyang 9" melon fruits. Fruit images of bitter melon, cucumber, white melon and "Boyang 9" melon were collected under different natural conditions for model training. The results showed that "Boyang 9" melon had the best overall detection results among the four cucurbit species, with the highest AP and F1, 0.99 and 0.94 respectively. The YOLOv5s model performed best among the four models: the best weights size was the smallest at 14 MB; the better mAP value of 0.971 for all classes of cucurbits; and the fastest detection speed with fps of 90.9. This paper shows that four types of cucurbit fruit images, bitter melon, cucumber, white melon, and "Boyang 9" melon, can be detected based on deep learning methods for hybrid detection.

摘要

葫芦科种植面积广泛，其果实具有巨大的经济价值。目标检测是葫芦科采摘的关键环节之一。本人采用 YOLOv3、YOLOv4、YOLOv5s 和改进的 Resnet_YOLO 四种模型对苦瓜、黄瓜、白皮甜瓜、"博洋9"甜瓜果实进行混合检测。采集不同自然情况下的苦瓜、黄瓜、白皮甜瓜、"博洋9"甜瓜的果实图像进行模型训练。结果表明，在 YOLOv3、YOLOv4、YOLO5、Resnet_YOLO 四种模型检测苦瓜、黄瓜、白皮香瓜和"博洋9号"甜瓜时，"博洋9号"甜瓜检测结果整体最优，AP 和 F1 最高，分别为 0.99、0.94；YOLOv5 模型表现最优：最佳权重内存最小，为 14MB； 具有很好的 mAP 值，达到了 0.971；检测速度最快，fps 为 90.9 。此方法表明苦瓜、黄瓜、白皮香瓜、"博洋9"甜瓜四类葫芦科果实图像可进行混合检测。

INTRODUCTION

Fruits provide people with a rich source of minerals, vitamins and dietary fibre. However, fruit picking is not an easy task. Fruit picking is an important part of cucurbit fruit production that is labour intensive and highly seasonal. An example is the cucurbit fruit. Cucurbitaceae is widely cultivated with about 113 genera and 800 species (*Tzortzakis N. et al., 2018*). Among them there are 32 general and 154 species in China (*Ren Chunmei et al., 2014*). Cucurbitaceae fruits include important vegetables and melons such as bitter melon, cucumber, melon, and sweet gourd. Bitter melon has medicinal values such as being purgative and low in sugar (*Huang H. et al., 2019*). Cucumber is rich in protein and various vitamins and has diuretic, sore throat relief and weight loss properties (*Wang Chen et al., 2020*). Melon contains nutrients such as sugar, aromatic substances, and proteins (*Sánchez E. et al., 2021*). However, cucurbit fruit picking is also difficult.

Fan Zhao, As Lec. Ph.D. Eng.; Jiawei Zhang, Prof. Ph.D. Eng.; Mingbao Li, Prof. Ph.D. Eng.

The reason is that some cucurbit fruits are similar in shape and some cucurbit fruits are similar in colour, which makes it difficult to distinguish and locate them when the machine performs object detection.

| Cucumber | Bitter melon | White melon | "Boyang 9" melon |

Fig. 1 - Different cucurbit fruits

In recent years, with the rise of artificial intelligence, deep learning has developed rapidly, and great breakthroughs have been made in target detection algorithms. The more popular algorithms can be divided into two categories. One category is the two-stage algorithm based on the R-CNN system of Region Proposal, which divides the target detection task into two steps, target category and target region (*Li Z et al., 2017; Wimmer G et al., 2021; Ren S et al., 2017*), and the other category is the one-stage algorithm such as YOLO and SSD, which directly predicts the category and location of different targets. As the first class of algorithms, R-CNN and Faster RCNN methods have high target detection accuracy, but convolutional neural networks are very computationally large and slow. And as one of the two-stage second class algorithms, YOLO (You Only Look Once) algorithm was proposed by *Redmon et al. (2016),* which guarantees the detection speed and the target detection accuracy (*Redmon J et al., 2016*). This algorithm has been widely used in the field of target detection and has undergone v1-v5 development (*Redmon J et al., 2017; Bochkovskiy A et al., 2020*).

YOLOv1 takes the whole image as the network input and regresses the position and category of the bounding box directly in the output layer. Its disadvantages are: the output layer is a fully connected layer, the YOLOv1 training model only supports the same input resolution as the training image; each cell can only predict one object, and the prediction of small objects is poor. The YOLOv2 network model was adopted from Darkent_19 (*Xiong Juntao et al., 2018*). And the YOLOv3 model is more complex than the YOLOv1 and YOLOv2 models and can predict small targets (*Redmon J et al., 2018; He K, Zhang X et al., 2016*). YOLOv4 improves various parts of YOLOv3 to make the AP value rise, for example, mosaic data enhancement on the input, CSPDarknet53 on the backbone, Mish activation function, etc (*Qingshu W et al., 2021*). There are four versions of YOLOv5s, YOLOv5m, YOLOv5l, and YOLOv5x models in the YOLOv5 target detection network, and the YOLOv5s network model is the smallest, the fastest, and the AP accuracy is not low.

Shilei Lu used YOLOv3-LITE lightweight neural network for citrus recognition with 91.13% AP and 87.32% average IoU for the whole test set (*Lü Shilei et al., 2019*). *Lawal O.M.* developed a YOLO fig detection model based on deep learning, with an average accuracy and speed of 89.3% and 96.8 fps for the optimal model (*Lawal O.M.,2021*). *Juntao Xiong* used UAV vision to detect green mangoes on trees in a natural environment, and the average time to detect one image was 0.08 s, and the correct recognition rate of the test set was 90.64% (*Xiong Juntao et al., 2018*). *Xiaoyang Liu et al.* performed instance segmentation, based greenhouse cucumber detection with an improved mask RCNN F1 of 89.47% and a running time of 0.3461 s (*Liu X et al., 2019*). *Anna Kuznetsova et al.* used YOLO3 combined with pre-processing and post-processing for apple detection by fruit harvesting robot (*Kuznetsova A. et al., 2020*).

The above-mentioned scholars have conducted different fruit detection studies based on deep learning, but the studies on the differentiation and identification of the fruits of Cucurbitaceae plants have not been reported. To solve different cucurbit classification and recognition problems, this paper uses YOLO deep learning algorithms for cucurbit fruit image classification and recognition.

MATERIALS AND METHODS

Image Acquisition

The datasets used in this research work were collected from the bitter melon, cucumber, white melon, and "Boyang 9" melon greenhouses at the Juxin Venture Park in Taigu County, Jinzhong City, Shanxi Province, China. The images were taken using a smartphone with 2340X1080-pixel resolution, RGB colour space and JPG storage format. Images were captured in a natural light environment, including the complexity of the growing environment: light changes, shading and overlap. A total of 2469 pictures were collected. Among them, 665 pictures of bitter melon, 664 pictures of cucumber, 404 pictures of white melon and 736 pictures of "Boyang 9" melon. The four species were randomly divided into an 80% training set and a 20% test set, respectively (Table 1). Randomly, the captured images included a single target without shading, a single target with stem and leaf shading, multiple targets without shading, multiple targets with stem and leaf shading, and targets near the land, among others. The images in different environments are shown in Figure 2.

Table 1

Number of pictures of different Cucurbitaceae fruits

Class	Training set	Validation set	Total number
Bitter melon	532	133	665
Cucumber	532	132	664
White melon	324	80	404
"Boyang 9" melon	588	148	736

a) Single object with no occlusion	b) Multiple objects with occlusion	c) Objects close to land
d) Shading conditions	e) Illumination variation	f) Cluster objects

Fig. 2 - Cucurbits samples under different growing environments

Data Annotation

Before the YOLO detection model is trained, the data needs to be labelled, i.e., category labels and detection target locations. The open source tool Labelling is used to manually label all the data, and the label file is saved in txt format with the name corresponding to the image one by one. The bounding boxes are as small as possible while being able to cover the target, which helps to reduce the chance of human error (*Lawal M.O., 2021*). For shaded fruits, the shape is marked according to what the person thinks it is.

YOLO Algorithm

(1) YOLOv3

The backbone of YOLOv3 is Darknet-53, YOLOv3 adds a residual networks every two layers based on YOLOv2, i.e. short cut layer, which can solve the problem of gradient disappearance or gradient explosion. The number of residual blocks is 1, 2, 8, 8, 4. YOLOv3 uses the K-means clustering approach with 9 anchor frames. Each size of feature map uses 3 anchor frames with multi-scale prediction for small targets. Neck of YOLOv3 uses FPN (Feature Pyramid Network). FPN is fast like Single feature map and Pyramidal feature hierarchy, but it is more accurate. In the whole YOLOv3 network, there is only convolutional layer, no pooling layer. The size of the output feature map is controlled by adjusting the convolutional step, so there is no limitation on the image input size.

(2) YOLOv4

YOLOv4 splits the target detection framework into: input, backbone, neck, head. YOLOv4=CSPDarknet53+spp+PAN+YOLOv3. YOLOv4 is an efficient and powerful target detection model with the goal of finding the optimal balance between the network input resolution, the number of convolutional layers, the number of parameters and the number of layer outputs optimal balance.

(3) YOLOv5s

The network structure of YOLOv5s mainly consists of Backbone, Neck, and Head, where Backbone mainly uses CSPdarknet + SPP structure, Neck uses PANet junction, and Head uses YOLOv3 head. The weight of YOLOv5s is much smaller than that of YOLOv4, and the speed is very fast, while the accuracy is comparable to that of YOLOv4. In this paper, YOLOv5s is used, and the network structure is shown in Figure 3.
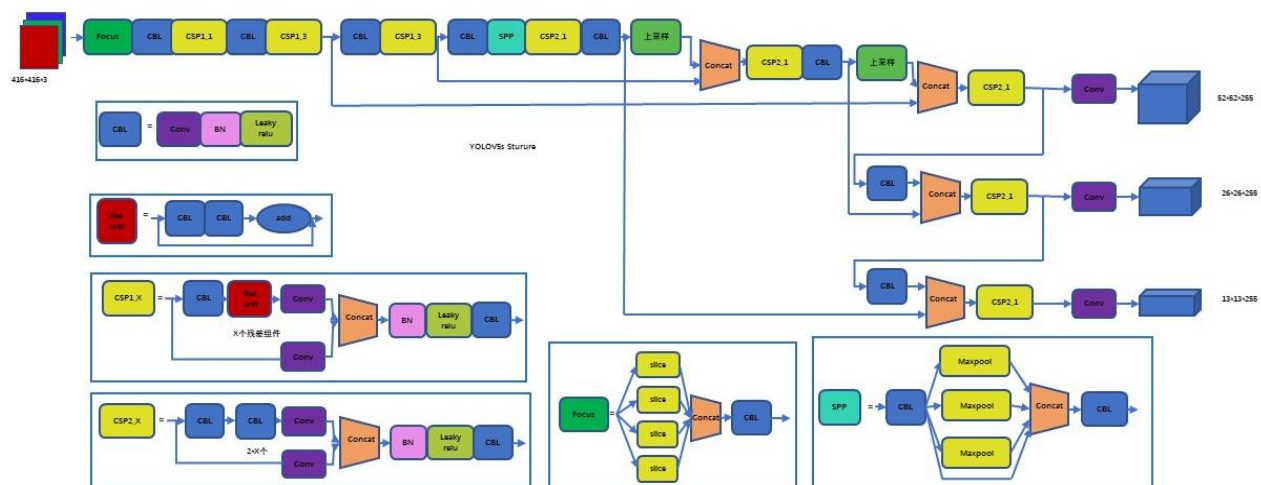
Fig. 3 - YOLOv5s model

(4) Resnet_YOLO

The backbone network of the Resnet_YOLO model is composed of ResNet43, which replaces DarkeNet53. Using ResNet43, the network depth is deeper and gradient disappearance does not occur; the classification accuracy is deepened due to the use of a deeper network; and the problem of deep network degradation is solved. The number of residual blocks of ResNet43 is 2,3,4,3,2, as shown in Fig.4(a).

The structure of residual blocks used by Resnet43 is shown in Fig. 4(b). Each layer of ResNet43 uses the Leaky activation function. The fruit detection optimization is performed by adding SPPNet as part of the Resnet_YOLO model to the ResNet43 backbone network. SPPNet is a feature enhancement network that simultaneously extracts global features of multiple dimensions and local features of the same detection stage. The application of SPPNet helps to avoid missed and inaccurate detection of the extracted fuzzy feature maps. The three scales of Resnet_YOLO are provided through 13×13, 26×26 and 52×52 feature vectors, as shown in Figure 4(a).
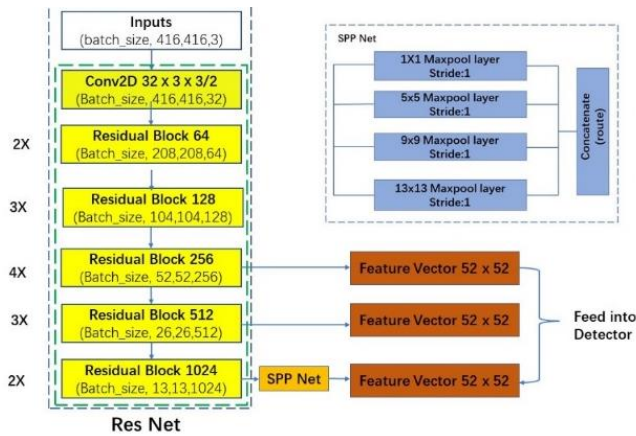
Fig. 4(a) - ResNet structure   **Fig.4 (b) - Resnet_YOLO model**
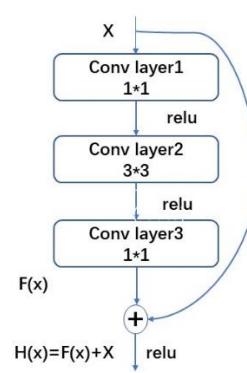
Resnet_YOLO model uses DIoU-NMS (The non-maximum suppression) algorithm to remove the redundant detection of multiple bounding boxes and find the best matching bounding box from multiple overlapping entities. DIoU-NMS considers not only the IOU but also the distance between the centre points of two boxes to avoid missing detection. In the Resnet_YOLO model, the original 6 layers of the YOLOv3 head are cropped to 4 layers in order to improve the detection speed using FPN (Feature Pyramid Networks). As the neck, FPN is a feature pyramid network that upsamples the top-level features and fuses them with the bottom-level features to obtain high-resolution, strongly semantic features. FPN can handle the multi-scale variation of object detection with a very small increase in computational effort. Finally, the Resnnet_YOLO model uses a full IOU (CIoU) loss function with fast convergence and good performance.

Model training and testing

Experimental platform

The experimental platform for this study is built as follows: Computer: Lenovo Legion R90000P 2021H, Operation system: Windows 10 (Professional edition), CPU: AMD Ryzen 7 5800H 3.2GHz, GPU:RTX3060 , RAM:16GB, CUDA v11.1, cuDNN v8.0.4, OpenCV v4.2.0.

Image training

Before training and testing, it is necessary to find out the most likely size of the anchor box from the dataset instead of using the default anchor box provided by YOLOv, which can reduce the convergence time of the model and improve the accuracy of the generated coordinate boxes. In this paper, The K-mean clustering algorithm was used to generate 9 clusters at 416 × 416 pixels according to 3 scales of detection layer.

The input image size of the model is 416X416 pixels. the number of samples per batch for the model hyper hyperparameters is 64, the momentum factor is 0.949, the initial learning rate is 0.001, the learning rate decreases by 10 times after every 8000 iterations of training, and the model saves the weights once every 1000 training sessions.

Model Evaluation

In order to verify the merits of the four models YOLOv3, YOLOv4, YOLOv5s and Resnet_YOLO, using Precision, Recall, F1score, AP value (average precision),mAP(mean Average Precision) as evaluation parameters, the formulas were calculated as follows.

$$P = \frac{TP}{TP + FP}$$

$$R = \frac{TP}{TP + FN}$$

$$F1 = \frac{2PR}{P + R}$$

$$AP = \int_0^1 P(R)\mathrm{d}R$$

$$mAP = \frac{\sum AP}{C}$$

where:

P is the accuracy rate, R is the recall rate;
TP is the number of true positive samples;
FP is the number of false positive samples;
FN is the number of false negative samples,
mAP is the average precision mean;
C is the total number of target species.

RESULTS AND ANALYSIS
Analysis of the results of different models

In order to verify the performance of target detection of bitter melon, cucumber, white melon and melon "Boyang 9" in this paper, four models, YOLOv3, YOLOv4, YOLOv5s and Resnet_YOLO, were used for target detection, comparing the advantages and disadvantages of the models, focusing on the accuracy and detection speed of the models. The F1 score is a trade-off between balanced precision P and recall R. The AP value is a more comprehensive measure between precision and recall. YOLOv3, YOLOv4, YOLOv5s, and Resnet_YOLO four model detection results are shown in Tables 2, 3, 4, and 5, respectively.

Table 2

YOLOv3 detection model results

Class	Precision	Recall	F1	AP
Bitter melon	0.91	0.85	0.89	0.91
Cucumber	0.77	0.88	0.82	0.90
White melon	0.95	0.81	0.87	0.88
"Boyang 9" Melon	0.88	0.94	0.91	0.98

In the YOLOv3 model, white melon had the highest P of 0.95; "Boyang 9" melon had the highest Recall, F1 score and AP value of 0.94, 0.91 and 0.98, respectively; while cucumber and white melon did not perform well in the detection results.

Table 3

YOLOv4 detection model results

Class	Precision	Recall	F1	AP
Bitter melon	0.90	0.88	0.89	0.97
Cucumber	0.82	0.89	0.85	0.95
White melon	0.91	0.90	0.90	0.98
"Boyang 9" Melon	0.92	0.96	0.94	0.99

In the YOLOv4 model, P, Recall, F1, and AP of "Boyang 9" melon were the highest in the four fruit types tested, at 0.92, 0.96, 0.94, and 0.99, respectively; The P, F1, and AP of cucumber were the lowest in all four fruit types. The recall of bitter melon was the lowest in all four fruit types.

Table 4

YOLOv5s detection model results

Class	Precision	Recall	F1	AP
Bitter melon	0.91	0.87	0.89	0.98
Cucumber	0.68	0.92	0.78	0.94
White melon	0.92	0.87	0.89	0.97
"Boyang 9" Melon	0.91	0.97	0.94	0.99

In the YOLOv5s model, Recall, F1, and AP of "Boyang 9" melon were the highest among the four fruit types detected, with 0.97, 0.94, and 0.99, respectively; "Boyang 9" melon had the highest P value, as did Bitter melon, at 0.91. P, F1, and AP of cucumber were the lowest. The best detection results were obtained for the "Boyang 9" melon, followed by the bitter melon.

Table 5

Resnet_YOLO detection model results

Class	Precision	Recall	F1	AP
Bitter melon	0.89	0.90	0.90	0.94
Cucumber	0.72	0.91	0.80	0.93
White melon	0.87	0.91	0.89	0.94
"Boyang 9" Melon	0.84	0.97	0.90	0.98

In the Resnet_YOLO model, bitter melon had the highest P, reaching 0.89; "Boyang 9" melon had the highest Recall and AP values, 0.97 and 0.98; bitter melon and "Boyang 9" melon had similar F1 value of 0.90; cucumber had the lowest P, F1, and AP. In short, "Boyang 9" melon had the best general detection results and cucumber had the worst detection results.

Among the four models, "Boyang 9" melon had the best overall detection results, with the highest AP and F1 values of 0.99 and 0.94, respectively.

Comparison of the results of different models

The IoU threshold is set to 50% in the four modes of YOLOv3, YOLOv4, YOLOv5s, and Resnet_YOLO. The P-R curves of the above four models are shown in Figure 5, and the comparison of the best weights size, mAP, speed for the four models are shown in Table 5.
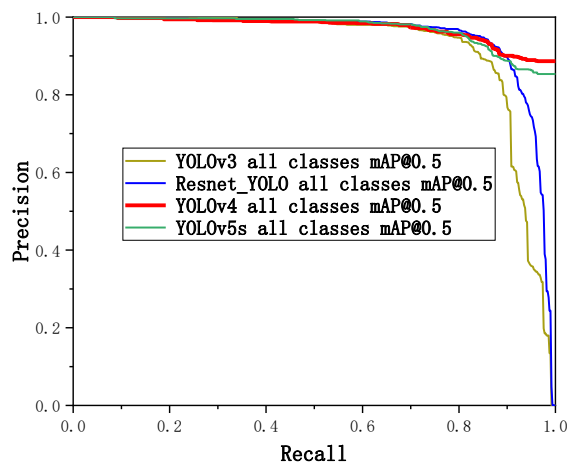
Fig. 5 - P-R curves for different modifications of cucurbits detection model

Table 5

Comparison of results of different models

Methods	Best Weights size (MB)	All classes mAP	fps
YOLOv3	234	0.92	31.9
YOLOv4	115	0.973	55.6
YOLOv5s	14	0.971	90.9
Resnet_YOLO	98	0.95	32.0

In terms of best weights size, the YOLOv5s model has the smallest best weights size of 14 MB. The best weights size for Resnet_YOLO is 98 MB and for YOLOv4 is 115 MB. YOLOv3 has the largest best weights size at 234 MB.

In terms of accuracy, YOLOv3 has the lowest mAP but also reaches 0.92. Resnet_YOLO has a higher mAP than YOLOv3 but lower than YOLOv4 and YOLOv5s, with a mAP of 0.95. YOLOv5s has an mAP of 0.971, while YOLOv4 has the highest mAP at 0.973. Correspondingly, the P-R curves of the YOLOv4 models perform better because it has the largest area under curve (area under curve, AUC).

In terms of speed, the fps values of the YOLOv3 and Resnet_YOLO models are close to each other, around 30. The fps of YOLOv4 is 55.6. The fps value of YOLOv5s reaches 90.9, which is a very fast detection speed.

The mAP of YOLOv5s is not the highest, but the speed and the best weights size are optimal. In a combined comparison, YOLOv5s is best among the four types of models: YOLOv3, YOLOv4, YOLOv5s, and Resnet_YOLO.

The images of bitter melon, cucumber, white melon and "Boyang 9" melon were combined into one image and detected by YOLOv3, YOLOv4, YOLOv5s and Resnet_YOLO models respectively, and the results are shown in Figure 6. The results indicate that the YOLOv4 and YOLOv5s models have the better detection results, but YOLOv5s is the fastest.

YOLOv3

YOLOv4

Resnet_YOLO

YOLOv5s
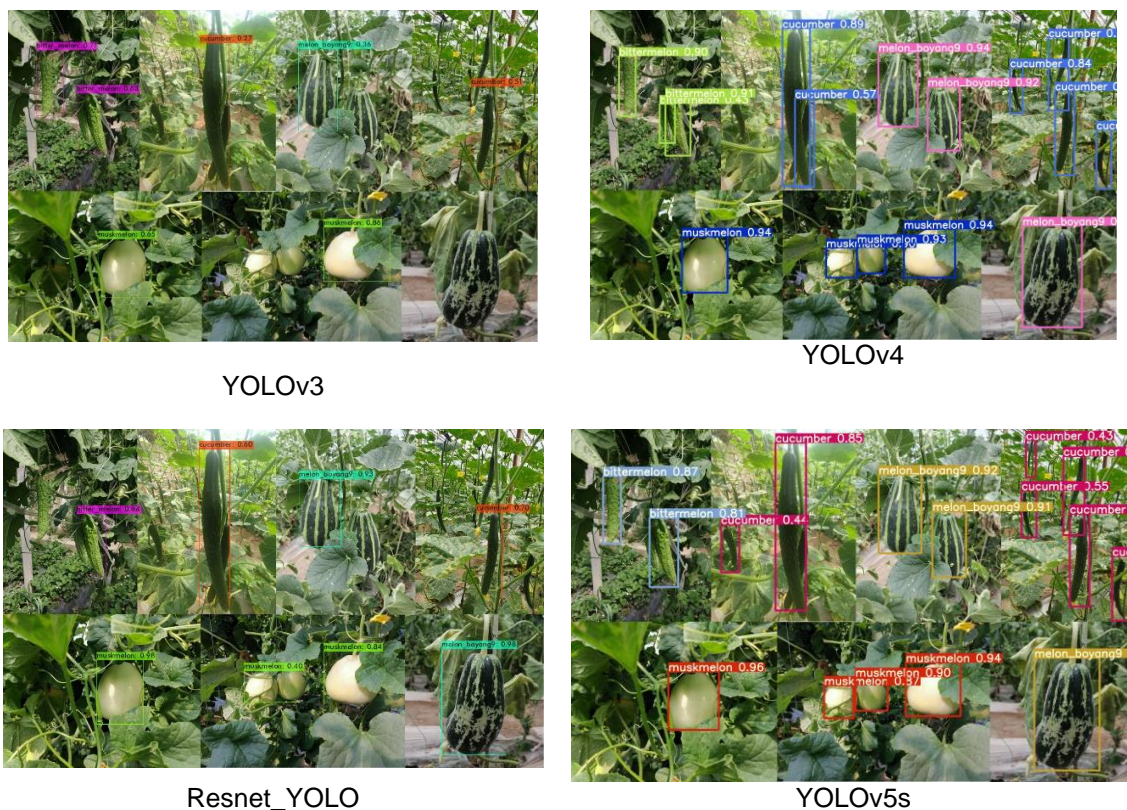
Fig. 6 - Four model image test results

CONCLUSIONS

In the paper, four models, YOLOv3, YOLOv4, YOLO5s and Resnet_YOLO, were used to detect cucurbits, including bitter melon, cucumber, white melon and "Boyang 9" melon varieties.

(1) In the four models of YOLOv3, YOLOv4, YOLO5s and Resnet_YOLO for bitter melon, cucumber, white melon and "Boyang 9" melon, the overall best results were obtained for "Boyang 9" melon, with the highest AP and F1 was the highest, with 0.99 and 0.94, respectively.

(2) YOLOv3, YOLOv4, YOLO5s and Resnet_YOLO models detect bitter melon, cucumber, white melon and "Boyang 9" melon, among them, YOLOv5s model has the best performance: the best weights have the smallest size, 14MB; the better mAP value, 0.971; the fastest detection speed with fps of 90.9.

REFERENCES

[1]   Bochkovskiy, A., Wang, C., Liao, H., (2020). YOLOv4: Optimal Speed and Accuracy of Object Detection. *arXiv*, Cornell / USA.

[2]   He, K., Zhang, X., Ren, S., (2016). Deep Residual Learning for Image Recognition. *IEEE*, pp.770-778, New York /USA.

[3]   Huang, H., Chen. F., Long R., (2019). The antioxidant activities in vivo of bitter gourd polysaccharide. *International Journal of Biological Macromolecules*, Vol.145, pp.141-144. Amsterdam / Netherlands.

[4]   Kuznetsova, A., Maleva, T., Soloviev V., (2020). Using the YOLOv3 algorithm with pre and post-processing procedures for fruit detection by an apple-picking robot. *Agronomy*, Vol.10, pp.1016-1034, Basel / Switzerland.

[5]   Lawal, M., (2021). Tomato detection based on modified YOLOv3 framework. *Scientific Reports*, 2021,11:1447. Vol.11, pp1447-1457, London / England.

[6]   Lawal, M., (2021). YOLOFig detection model development using deep learning. *IET Image Processing,* Vol.15, Issue.13, pp.3071-3079. Hertford/ England.

[7]   Li, Z, Peng, C, Yu, G., (2017). Light-Head R-CNN: In Defense of Two-Stage Object Detector. *arXiv*, Cornell / USA.

[8]   Liu, X., Zhao, D., Jia, W., (2019). Cucumber Fruits Detection in Greenhouses Based on Instance Segmentation. *IEEE Access*, vol. 7, pp. 139635-139642, New York / USA.

[9]   Lü, S., Lu, S., Li, Z., Hong, T., Xu, Y., Wu, B., (2019). Orange recognition method using improved YOLOv3-LITE lightweight neural network (基于改进 YOLOv3-LITE 轻量级神经网络的柑橘识别方法). *Transactions of the Chinese Society of Agricultural Engineering (Transactions of the CSAE)*, Issue.17, pp.205-214, Beijing / China.

[10]   Qingshu, W., Jianfeng, H., Pengfei, Z., (2021). Crayfish quality detection method based on YOLOv4 (神经网络的小龙虾质量检测方法). *Food and machinery*, Vol.37, Issue.3, pp.120-124+194, Changsha/China.

[11]   Redmon, J., Divvala, S., Girshick, R., (2016). You Only Look Once: Unified, Real-Time Object Detection. *IEEE computer society*, pp.779-788, New York / USA.

[12]   Redmon, J., Farhadi, A., (2017). YOLO9000: Better, Faster, Stronger, *IEEE*, pp.6577-6525, New York / USA.

[13]   Redmon, J, Farhadi, A., (2018). YOLOv3: An Incremental Improvement. *arXiv e-prints*, Vol. 4, Cornell / USA.

[14]   Ren, C., Cheng, Y., Yang, L., (2014). Multiplex RT-PCR method for detecting multiple viruses in Cucurbitaceae crops by two-step method (两步法检测葫芦科作物多种病毒的多重 RT-PCR 方法). *Proceedings of 2014 annual academic meeting of China Plant Protection Society*, Xiamen / China.

[15]   Ren, S., He, K., Girshick, R., (2016). Faster R-CNN: Towards Real-Time Object Detection with Region Proposal Networks. *IEEE Transactions on Pattern Analysis & Machine Intelligence*, Vol. 39, Issue.6, pp.1137-1149, New York / USA.

[16]   Sánchez E., Pollock, R., Elkner, T., (2021). Fruit Yield and Physicochemical Quality Evaluation of Hybrid and Grafted Field-Grown Muskmelon in Pennsylvania. *Horticulturae*, 2021, 7(4):69. Vol.7, Issue.4, pp.69, Basel / Switzerland.

[17]   Tzortzakis, N., Chrysargyris, A., (2018), Petropoulos S A. Phytochemicals Content and Health Effects of Cultivated and Underutilized Species of the Cucurbitaceae Family. ISBN 9781681087399. *Bentham Science Publishers*, Sharjah / UAE.

[18] Wang, C., (2020). Cultivation and management techniques of pollution-free, high-quality and high-yield cucumber (黄瓜无公害优质高产栽培管理技术). *Jilin Vegetable,* Vol. 2, pp.12-13, Jilin/ China.

[19] Wimmer, G., Schraml, R., Hofbauer, H., (2021). Two-stage CNN-based wood log recognition. *Computational Science and Its Applications-ICCSA2021*, Vol.12955, pp.115-125, Cagliari/Italy.

[20] Xiong, J., Liu, Z., Lin, R., (2018). Unmanned Aerial Vehicle Vision Detection Technology of Green Mango on Tree in Natural Environment (自然环境下树上绿色芒果的无人机视觉检测技术). *Journal of agricultural machinery*, Vol.49, Issue 11, pp. 23-29, Islamic Republic of Iran.

THE ROLE OF VOLATILE COMPONENTS IN THE PROCESS OF THERMAL DESTRUCTION AND IGNITION OF THE SUNFLOWER HUSK BIOMASS
/
РОЛЬ ЛЕТКИХ КОМПОНЕНТІВ У ПРОЦЕСІ ТЕРМАЛЬНОЇ ДЕСТРУКЦІЇ ТА ЗАПАЛЮВАННЯ БІОМАСИ ЛУШПИННЯ СОНЯШНИКА

Olena ZOLOTOVSKA[1]; **Mykola KHARYTONOV**[1*]; **Iryna RULA**[1]; **Nadia MARTYNOVA** [2]; **Hynek ROUBÍK**[3]

[1] Dnipro State Agrarian and Economics University, Dnipro, Ukraine;
[2] Dnipro National University, Dnipro, Ukraine;
[3] Czech University of Life Sciences Prague, Prague, Czech Republic
Tel: 0973456227; E-mail: envteam@ukr.net, S.Yefremova st. 25, Dnipro, Ukraine
DOI: https://doi.org/10.35633/inmateh-66-33

ABSTRACT
The final composition of volatile components in the process of oxidative pyrolysis depends on the temperature level of the process. The gas output increases with the growth of hydrogen, methane and heavy hydrocarbons concentration in the process of pyrolysis in the range of 200-500°C. In this case, there is a noticeable decrease in undesirable impurities in the output of carbon dioxide and nitrogen in the fuel gas. The obtained data on the dynamics of thermal decomposition of biomass under heating conditions reflect the complex dependence of the yield of total gas individual components both on time and on the temperature of the process. The more volatiles contained in the source fuel, (the other things being equal) the faster the gas mixture ignites, and the more intensely it burns out. The composition and temperature of the gas mixture affects the pressure drop and auto-ignition temperature in the pyrolysis chamber. It was found that the lowest self-ignition temperature of a gas mixture is 490°C. A series of experiments to determine the critical condition for self-ignition at a constant temperature of 490°C and various initial pressures of the mixture (100-300 kPa) was carried out. It was found that the transition from a smooth increase in pressure of 90 kPa to an explosive one (up to 300-400 kPa) depends on the composition and temperature of the gas mixture. Therefore, the composition of the gas and its ignition temperature can be controlled by adjusting the mode of pressure increase in the reactor.

ТЕЗИ
Кінцевий склад летких компонентів у процесі окисного піролізу залежить від температурного рівня процесу. Вихід газу збільшується із зростанням концентрації водню, метану та важких вуглеводнів у процесі піролізу в діапазоні 200-500 °С. При цьому на виході помітно зменшується кількість небажаних домішок вуглекислого газу та азоту в паливному газі. Отримані дані про динаміку термічного розкладання біомаси в умовах нагрівання відображають складну залежність виходу окремих компонентів газової суміші як від часу, так і від температури процесу. Чим більше летких речовин міститься в вихідному паливі, тим (за інших рівних умов) швидше запалюється газова суміш і тим інтенсивніше вона вигорає. Склад і температура газової суміші впливає на перепад тиску і температуру самозаймання в пірозлізній камері. Встановлено, що найнижча температура самозаймання газової суміші становить 490°С. Була проведена серія експериментів з визначення критичного стану самозаймання при постійній температурі 490°С і різних початкових тисках суміші (100-300 кПа). Встановлено, що перехід від плавного підвищення тиску 90 кПа до вибухового (до 300-400 кПа) залежить від складу та температури газової суміші. Отже, склад газу і температуру його займання можна регулювати, змінюючи режим підвищення тиску в реакторі.

INTRODUCTION
During last decades sunflower has occupied significant sown areas among industrial crops in Ukraine, which are mainly located in agricultural enterprises of the Steppe and Forest-Steppe *(Cherednichenko, 2020)*. It is known that raw sunflower husk has several disadvantages such as low heating value and bulk density, high moisture, and volatile matter contents *(Bala-Litwiniak and Zajemska, 2020)*. Several case studies have shown that for effective use of biomass as energy, feedstock in thermochemical conversion processes requires pretreatment *(Zajemska et al., 2017; Isemin et al., 2017; Islamova et al., 2021)*.

Crop residues biomass can also be processed in torrefaction, gasification and liquefaction processes *(Zolotovska et al., 2016; Kaczynska et al., 2019)*.

The pellets application for heat production allows diminishing the atmospheric burden of greenhouse gases *(Kuznetsova, 2012)* and creates the conditions for sustainable economic development *(Cui et al., 2019)*. It was shown that in terms of price, sunflower seed husk pellet fuel is 71% cheaper than natural gas and 75% cheaper than coal. Meanwhile, there is still uncertainty in the assessment of the impact of pollutant emissions caused by the burning of biomass on air quality caused by the lack of emission factors that would characterize real combustion *(Pastorello et al., 2011; Zajqc et al., 2019)*.

At the same time, biomass contains lower sulfur and ash amount than non-renewable sources, such as fossil fuels, and, therefore, it generates lower NO_x and SO_x emissions *(Klason and Bai, 2007; Perea-Moreno et al., 2018)*. As a rule, sulfur content in the biomass does not exceed 0.2% and only certain biomass fuels reach 0.5-0.7% (for brown coal 0.7-7%) *(Demirbas, 2004; Parmar, 2017)*. Meanwhile, biomass is characterized by a high proportion of volatile parts and high humidity content *(Zolotovska et al., 2016)*. The amount of ash, active carbon and volatile matter contained in sunflower seed husk briquettes is about 2.4%, 22.7% and 72% accordingly *(Spirchez et al., 2019)*. The content of combustible matter (C, S and H) significantly decreases after thermal processing, while the contents of oxygen (O) and volatile matter significantly rise after drying *(Matin et al., 2019)*.

It is known that the high volatility of the biomass material provides numerous advantages associated with a low ignition temperature and retention of ignition over a longer period of time *(Sivabalan et al., 2021)*. An increase in volatile substances led to increase the heating value of the feedstock. The sunflower husk calorific value is 3500-4000 Cal/kg being supplied through burning *(Popescu et al, 2013)*. The thermal reactivity of the sunflower seed husk is extremely higher than that for the other samples (hazelnut shell, rice husk, and olive refuse) under investigated conditions *(Haykiri-Acma and Yaman, 2011)*. The volatilization stage is characterized by the release of volatiles caused by the decomposition of hemicellulose and cellulose and partial decomposition of lignin *(Tibola et al., 2022)*.

This work aims to study the role and composition of volatile components in the process of thermal destruction and ignition of the sunflower seed husk biomass.

MATERIALS AND METHODS

The thermal analysis of sunflower seed husk biomass was carried out using the derivatograph Q-1500D of the "F. Paulik-J. Paulik-L. Erdey" system. Differential mass loss and heating effects were recorded. Samples of biomass were analyzed dynamically at a heating rate of 10°C/min in an air atmosphere. The mass of samples was 100 mg. The reference substance was aluminum oxide. The activation energy of thermo-oxidation destruction samples is determined by the method of Broido *(Broido, 1969)*.

The value of the double logarithm for each temperature was calculated using the dependence:

$$\ln\left(\ln\frac{100}{100-\Delta m}\right) = -\frac{E}{R}\cdot\frac{1}{T}$$

(1)

where:

m is the sample mass, %;

E – the activation energy, kJ/kmol;

R – universal gas constant, 8.314 J (mol.K);

T – temperature, K.

High performance capillary gas chromatography was used to separate hydrocarbons in fuel gas using a flame ionization detector. A glassy highly permeable polymer, polytrimethylylpropyne (PTMSP), was chosen as the stationary phase for the separation of hydrocarbon gases. A quartz capillary column with an outer metal protective coating, 10 m long and 0.35 mm in inner diameter, filled with PTMSP was used. The thickness of the adsorption layer was 30 μm. The polymer was dissolved in toluene. The capillary was filled with this solution under pressure. It was removed by heating the column and passing a flow of carrier gas. The following analysis conditions were chosen: column oven temperature - 55°C, evaporator and detector temperatures - 130°C. The carrier gas is nitrogen. The specified flow rate of nitrogen was controlled by a rheometer at a level of 18 cm^3/s. The analysis time was 10 min.

The presence of inorganic components of the pyrolysis gas was determined on a gas chromatograph using a conductometric detector. Separation was carried out at a temperature of 45°C on two packed columns.

A column 2 m long and 4 mm in diameter filled with 5A molecular sieves was used to determine H_2, N_2, CO, H_2, O_2. It is noticed that at higher temperatures their crystal structure is destroyed. The second column of the same size with a polymeric sorbent, a copolymer of styrene and divinylbenzene, was used to determine CO_2, and H_2S. The carrier gas, grade A helium, was used for both columns. The temperature of the evaporator and the thermostat of the detector is 110°C. Gas samples with a volume of 3 cm^3 were introduced through a sampling probe. The ignition temperature was determined by the method of inlet of a pre-prepared gas mixture into an evacuated (residual pressure no more than 0.4 kPa) heated flask, 200 cm^3 in volume, made of quartz glass. The test equipment is shown in fig.1. The reaction vessel (127 mm long and 127 mm in diameter) was placed in a horizontal steel cylinder of an electric furnace. The stainless-steel cylinder is inserted into the ceramic body. Three Chromel-Alumel thermocouples were used to measure the furnace temperature. The temperature measurement error under static conditions did not exceed 3-6°C in the range of 220-490°C.

The supplied mixture of gases was prepared in a 3-liter cylinder. The prepared mixture was kept in the cylinder for at least 10 hours before the start of the experiment to complete mixing of the reagents.
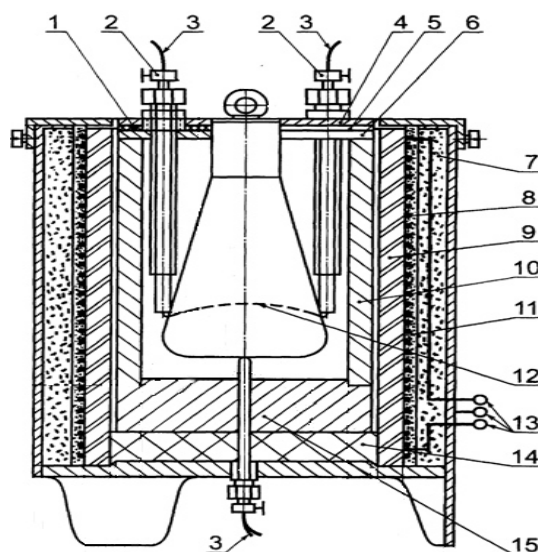
Fig. 1 - Test equipment for determining the ignition temperature of a gas
1 - high-temperature insulation; 2 - clamping sleeves; 3 - thermocouples; 4 - upper part of the cover; 5 - insulating ring; 6 - lower part of the cover; 7 - thermal insulation; 8 - heater; 9 - ceramic tube; 10 - steel cylinder; 11 - high-temperature mastic; 12 - control points; 13 - heater connection for voltage 220 V; 14 - insulating disk; 15 - metal base

The prepared mixture was admitted into the reaction vessel using a 200 cm^3 sealed glass syringe equipped with a three-way valve and connecting tubes (Fig. 2).
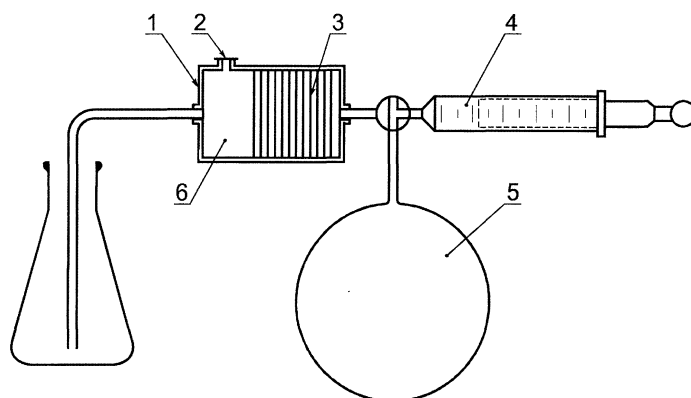
Fig. 2 - Introduction of a gas sample
1 - flame arrester; 2 - safety membrane; 3 - sintered glass plates; 4 - sealed syringe; 5 - tank with gas; 6 – pre-chamber

Eight volumetric gaseous samples (20-55 cm^3) were taken in the temperature range of 220-600°C to be tested at various initial pressures of the mixture (from 100 to 400 kPa).

The pressure of the mixture in the reaction vessel after the inlet was determined by the pressure in the dosing tank before the inlet, taking into account the valve opening time (0.07–1 s).

The pressure in the reactor was recorded by a fast inertia inductive pressure sensor. All the results obtained were treated by statistical methods using the StatGraphics Plus5 software package at significance level of 0.95% (p-value < 0.05).

RESULTS

Thermal destruction of sunflower husks begins at a temperature of 29-30°C. The main decomposition of volatile components and evaporation of water occurs in the range of 40-150°C. The process speed is low, on average 5.5%/min. The maximum rate (8.7-8.84%/min) was observed at a temperature of 79-91°C (Fig. 3, curve 3). The weight loss at this stage is small and amounts to 8.3% (Fig. 3, curve 1). The process of volatile components decomposition is accompanied mainly by endothermic reactions with the most pronounced effects in the temperature range of 61-79°C (Fig. 3, curve 2).
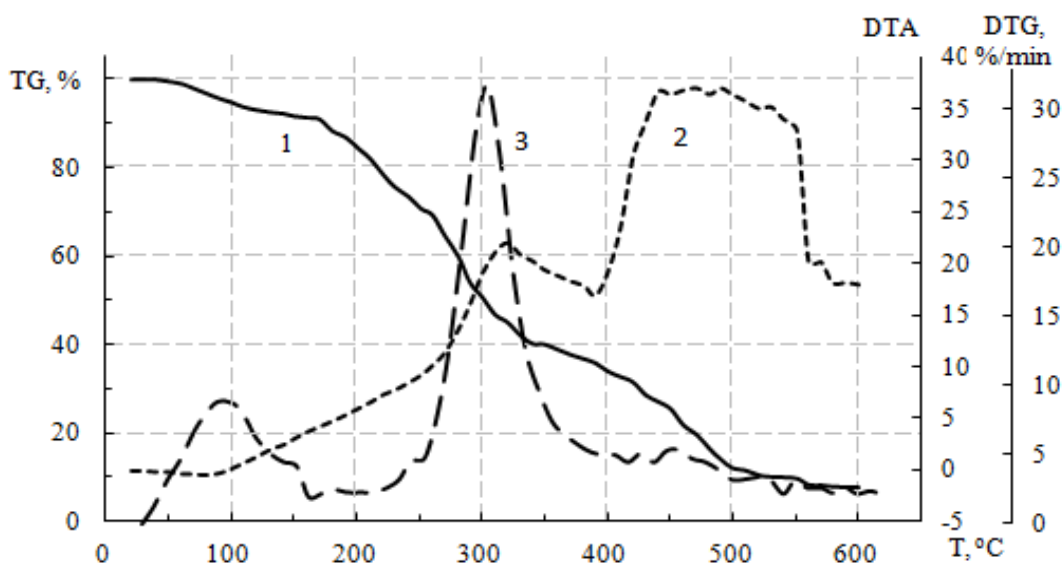
Fig. 3 - Curves of thermogravimetric (1), differential thermal (2) and differential thermogravimetric (3) analysis of sunflower husk

The process of decomposition of the main components of sunflower husk takes place in the temperature range of 151-400°C. The degradation ranges of hemicelluloses (220-320°C) and cellulose (300-380°C) partially overlap. That is why only one peak is observed on the DTG curve at a temperature of 300°C (Fig. 3, curve 3). The average speed of the process is 13.7-14.2%/min, the maximum is 31.7%/min. The mass loss at this stage is the largest and amounts to 57.8% (Fig. 3, curve 1). Decomposition reactions of hemicelluloses and cellulose are exothermic with the greatest thermal effects in the temperature range of 280-300°C.

The process of lignin destruction begins at a temperature of 250-280°C. However, the bulk of lignin decomposes in the range of 400-550°C. Typically, the decomposition rate is 3.5-4.0%/min (maximum 5.4%/min). One small peak is observed at a temperature of 430-440°C (Fig. 3, curve 3). The weight loss was 26.3%. Decomposition reactions are exothermic with pronounced thermal effects in the temperature range of 440-500°C (Fig. 3, curve 2). Combustion of sunflower husk ends in the range of 550-600°C. The fireproof residue was 7.6% of the total mass.

According to the activation energy data, the heat resistance of sunflower husks is low (Fig. 4). The activation energy was 33.7 kJ/mol at the initial stage of decomposition. Its value at the stage of destruction of the main components was 32.1 kJ/mol. Low activation energy values are explained by a rather large amount of pentosans (27-28%) and a relatively small amount of cellulose (31-38%) in sunflower husk *(Yadav et al., 2016)*. During the process, pyrolysis produces both solid and liquid products (bio-oils, tars, and water), and a gas mixture composed mainly of CO_2, CO, H_2, and CH_4 *(Castello et al., 2017; Uddin et al., 2018)*.

Fig. 4 - Diagram of the process of non-isothermal decomposition of sunflower husk

The results of assessing the release of volatile substances from the particles of sunflower husk biomass are shown in Figures 5 and 6.

Fig. 5 - Emission of volatiles from sunflower husk biomass

a) hydrogen; b) methane; c) heavy hydrocarbons; c) carbon monoxide; d) carbon dioxide; f) nitrogen
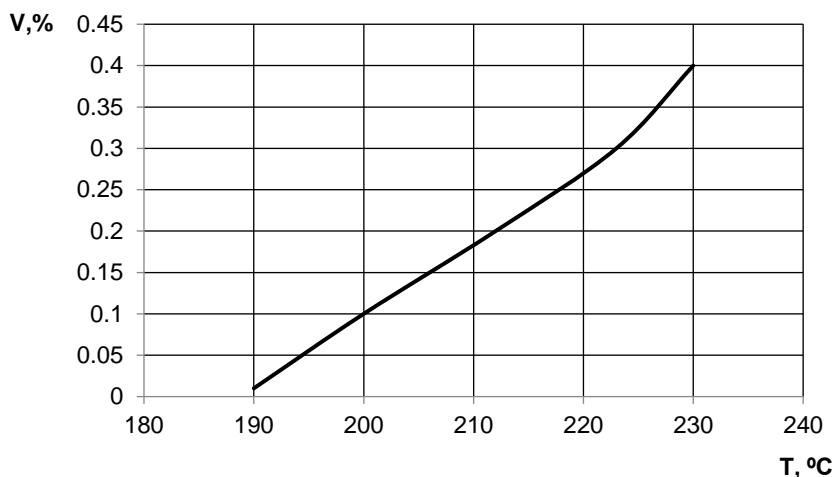
Fig. 6 - Hydrogen sulfide emission from sunflower husk biomass

The growth of gas emission is directly caused by the rise in the pyrolysis temperature in the range of 200-500°C. This is due to an increase in the concentration of hydrogen and methane and to a lesser extent it depends on heavy hydrocarbons. The roots of this effect are associated with a more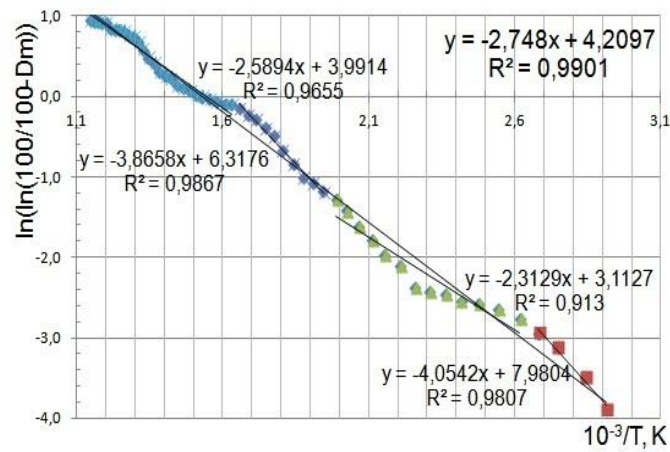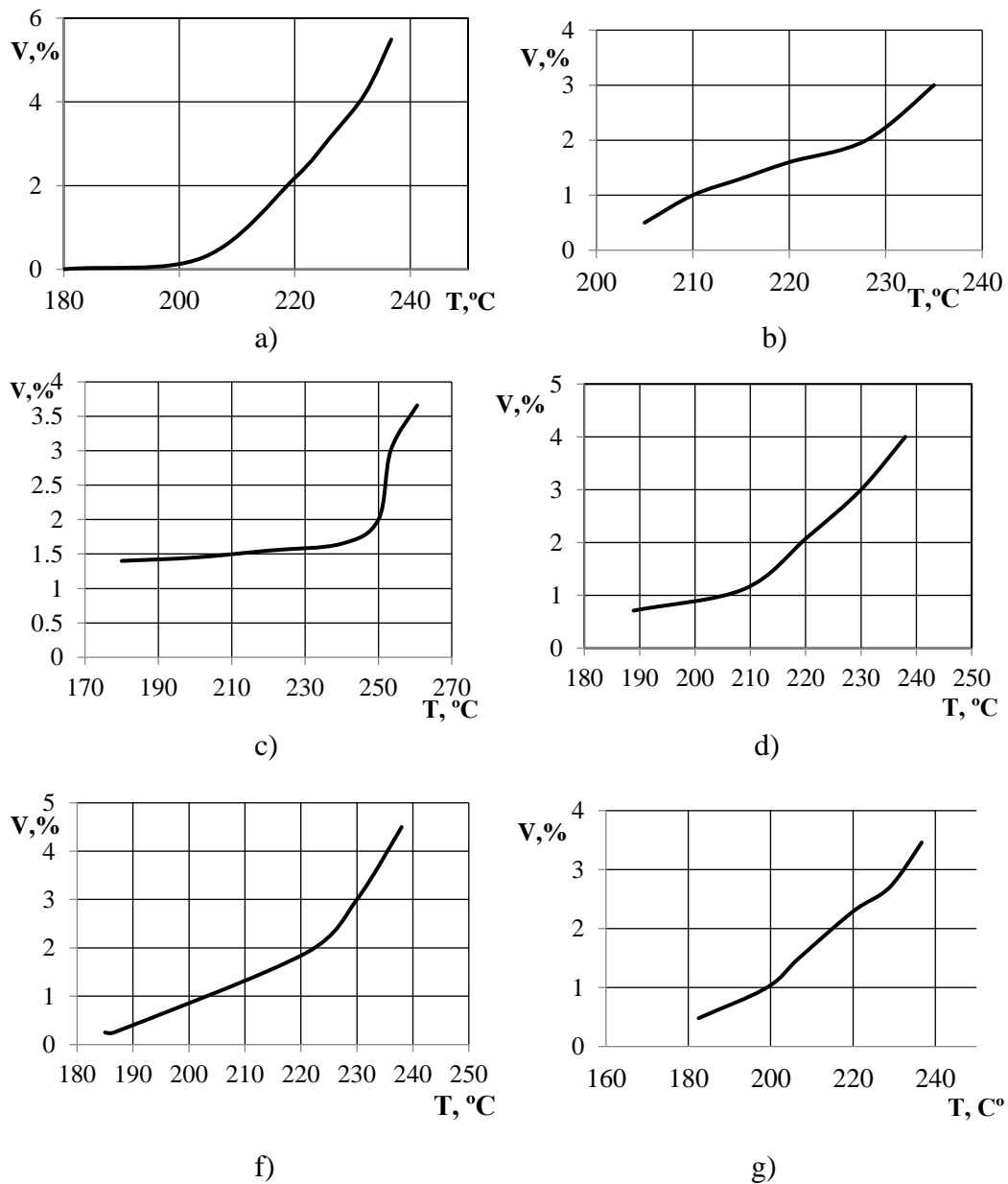 complete decomposition of biomass particles. The volume of pyrolysis gas increases by 1.04; 1.21; 1.3 and 1.61 times at temperatures of 260, 320, 380 and 420, respectively, compared with the volume of the gas mixture at a temperature of 220°C.

Meanwhile, a noticeable decrease in the yield of carbon dioxide and nitrogen (undesirable impurities in the fuel gas) occurs in the temperature range of 280-500°C. The amount of hydrocarbons in the resulting gas mixture also increases with increasing temperature and reaches a maximum at a temperature of 420°C, exceeding this value corresponding to a temperature of 200°C by 2.1 times. The chemical content of the test gas is shown in Table 1.

Table 1

Chemical content of pyrolysis gas

Components	H_2	CH_4	CO	CO_2	N_2	C_nH_m	H_2S	A
	[%]	[%]	[%]	[%]	[%]	[%]	[%]	[%]
Concentration	22.70	16.20	20.80	19.12	2.29	15.54	2.65	0.70

It is known that the thermal decomposition of xylan produces furfural, which quickly ignites and causes a sharp increase in temperature and self-heating of biomass *(Zaichenko et al., 2020)*. An ignition risk ranking is estimated using both kinetic parameters and characteristic temperatures *(Jones et al., 2015)*. Some crop residues, olive cake and sunflower husk are predicted to have a high risk of low temperature ignition. The determination of the critical condition for self-ignition was carried out at a constant temperature of 490°C and various initial pressures of the mixture (100-300 kPa). Typical barograms are shown in figure 7. The analysis of thermo-barograms showed that the heating of the gas mixture occurs mainly in the process of puffing. Insufficient heating of the gas to the level of the reactor temperature at the moment of closing the valve was 1-2% and depended both on the pressure and the diameter of the reactor. The completion time of gas heating after closing the valve did not exceed the ignition delay in the entire studied temperature range of 200-600°C (Fig. 8).

The transition from a smooth increase in pressure of 90 kPa to an explosive one (in the range of 300-400 kPa) occurred when the initial pressure of the mixture after the injection into the reactor changed by 1-10%. This transition depends on the chemical content and temperature of the gas mixture. The composition of the gas can be controlled by adjusting the pressure pulsations and the ignition temperature of the gas mixture. The flash point changes with increasing pressure (Fig. 9).
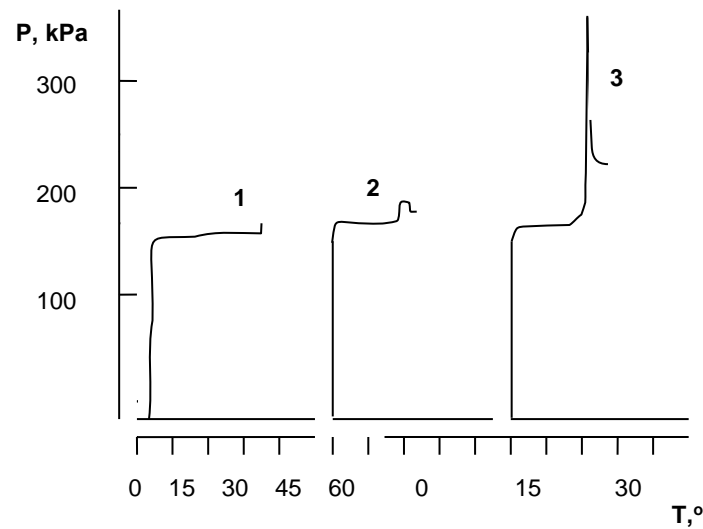
Fig. 7 - Barograms of studies at a temperature of 490°C with $O_2 = 42.3\%$
1 - no ignition; 2 - degenerate ignition; 3 - self-ignition

Fig. 8 - Dependence of the autoignition temperature on pressure

Fig. 9 – The dependence of the autoignition temperature on pressure for a gas mixture with air

A change in pressure from 100 to 200 kPa leads to an increase in the flash point to 300-500°C. As can be seen, the pyrolysis process occurs at varying pressure. Ignition of pyrolysis gas is possible when the limit temperature is reached.

CONCLUSIONS

Decomposition reactions of hemicelluloses and cellulose are exothermic with the greatest thermal effects in the temperature range of 280-300°C. The process of lignin destruction begins at a temperature of 250-280°C. However, the bulk of lignin decomposes in the range of 400-550°C. Combustion of sunflower husk ends in the range of 550-600°C. The fireproof residue was 7.6% of the total mass. The activation energy value at the stage of destruction of the main components was 32.1 kJ/mol. Gas emission increases with an increase in the pyrolysis temperature in the range of 200-500°C due to an increase in the composition of hydrogen, methane and slightly from heavy hydrocarbons. The amount of pyrolysis gas in the gas mixture increases with increasing temperature. The amount of hydrocarbons in the resulting gas mixture also increases with increasing temperature and reaches a maximum at a temperature of 420°C. The analysis of thermo-barograms showed that the heating of the gas mixture occurs mainly in the process of puffing. Insufficient heating of the gas to the level of the reactor temperature at the moment of closing the valve was 1-2% and depended both on the pressure and the diameter of the reactor. The completion time of gas heating after closing the valve did not exceed the ignition delay in the entire studied temperature range of 200-600°C. The composition of the gas can be controlled by adjusting the pressure and the gas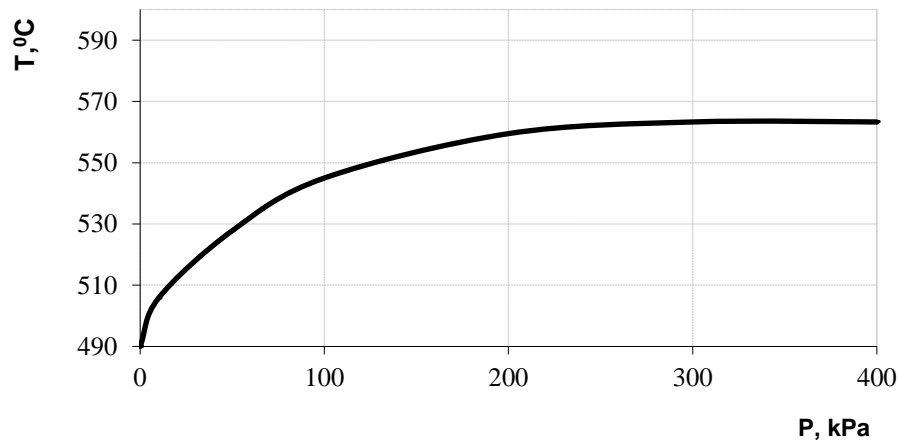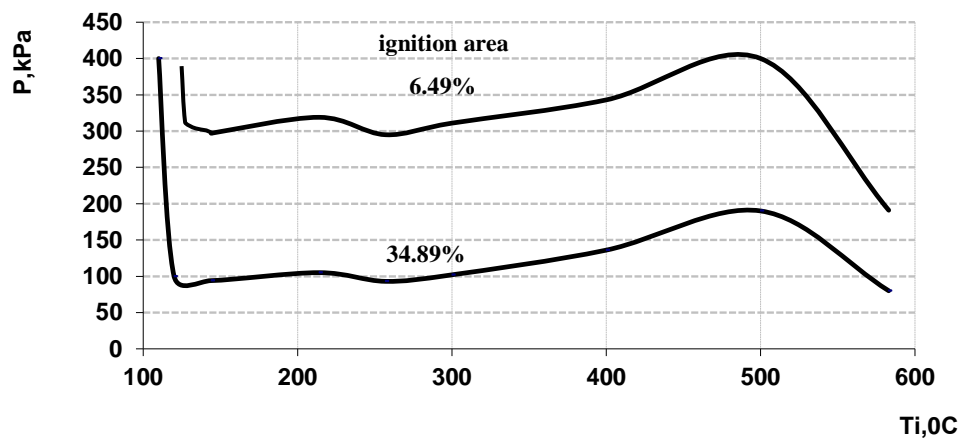 mixture temperature of the ignition. A change in pressure from 100 to 200 kPa leads to an increase in the flash point to 300-500°C.

ACKNOWLEDGEMENT

REFERENCES

[1] Anca-Couce, A., Zobel, N., Berger, A., Behrendt, F., (2012). Smoldering of pine wood: Kinetics and reaction heats, *Combustion and Flame*, Vol. 159 (4), pp. 1708-1719, doi:10.1016/j.combustflame.2011.11.015 Pittsburgh / USA.

[2] Bala-Litwiniak, A. & Zajemska, M., (2020). Computational and experimental study of pine and sunflower husk pellet combustion and co-combustion with oats in domestic boiler. *Renew Energ*, Vol. 162, pp. 151-159. https://doi.org/10.1016/j.renene.2020.07.139, Netherlands.

[3] Broido, A.A., (1969). A simple, sensitive graphical method of treating thermogravimetric analysis data. *Journal Polymer of Science*, Vol. 7 (10), pp.1761–1763, Hoboken / USA.

[4] Castello, D., Rolli, B., Kruse, A., Fiori, L., (2017). Supercritical water gasification of biomass in a ceramic reactor: Long - time batch experiments. *Energies*, Vol.1*0*, 1734, Basel / Switzerland.

[5] Cherednichenko, O., (2020). Current state and development of specialized enterprises – producers of sunflower. *Modern management review*. Vol. XXV, 27 (2), pp.7-13, doi: 10.7862/rz.2020.mmr.11, Rzeszów / Poland.

[6] Cui, X., Yang, J., Shi, X., Lei, W., Huang, T., Bai, C., (2019). Pelletization of Sunflower Seed Husks: Evaluating and Optimizing Energy Consumption and Physical Properties by Response Surface Methodology (RSM). *Processes*, Vol. *7*, 591, https://doi.org/10.3390/pr7090591. Basel / Switzerland.

[7] Demirbas, A., (2004). Combustion characteristics of biomass fuels. Progress Energy Combustion Science. 30, 219–230. https://doi.org/10.1016/j.pecs.2003.10.004, Amsterdam / Netherlands.

[8] Di Blasi, C., (2008). Modeling chemical and physical processes of wood and biomass pyrolysis. Progress in Energy and Combustion Science, Vol. 34, pp. 47-90, Amsterdam / Netherlands.

[9] Haykiri-Acm, H. & Yaman, S., (2011). Comparison of the combustion behaviors of agricultural wastes under dry air and oxygen. World Renewable Energy Congress. *Bioenergy Technology (BE)*, pp.251-256, Linkbping / Sweden

[10] Isemin, R, Mikhalev, A Klimov, D., Panagiotis, G., Margaritis, N., Kourkoumpas, D.S., Zaichenko, V.M., (2017). Torrefaction and combustion of pellets made of a mixture of coal sludge and straw. *Fuel, Vol.*210, pp.859-865, doi:10.1016/j.fuel.2017.09.032, Netherlands.

[11] Islamova, S.I., Ermolaev, D.V., Bulygina, K.S., (2022). Oxidative Torrefaction of Sunflower Husk Pellets in the Kaolin Layer. *BioEnergy Research journal.* Vol. 15**,** pp. 183–192, https://doi.org/10.1007/s12155-021-10280-6. USA.

[12] Jones, J.M., Saddawi, A., Dooley, B., Mitchell, E.J.S., Werner, J., Waldron, D.J., Weatherstone, S., Williams, A., (2015). Low temperature ignition of biomass. *Fuel Processing Technology* Vol. 134, pp. 373-377, http://dx.doi.org/10.1016/j.fuproc.2015.02.019. Netherlands.

[13] Klason, T. & Bai, X. S., (2007). Computational study of the combustion process and NO formation in a small-scale wood pellet furnace. *Fuel*, Vol. 86 (10), pp. 1465-1474, doi: 10.1016/j.fuel.2006.11.022. Netherlands.

[14] Kuznetsova, A., (2012). Pellet production in Ukraine: a profitable option for sustainable development? *German-Ukrainian Agricultural Policy Dialogue (APD).* 20 p., Wageningen, Netherlands.

[15] Matin, A., Majdak, T., Kricka, T., Grubor, M., (2019). Valorization of sunflower husk after seeds convection drying for solid fuel production. *Journal of Central European Agriculture*, Vol. 20(1), pp. 389-401,

[16] Parmar, K., (2017). Biomass - An overview on composition characteristics and properties. *IRA - International J. Appl. Sci.,* Vol.7, pp. 42-51, http://dx.doi.org/10.21013/jas.v7.n1.p4. Zelena Gura / Poland.

[17] Pastorello, C., Caserini, S., Galante, S., Dilara, P., Galletti, F., (2011). Importance of activity data for improving the residential wood combustion emission inventory at regional level. *Atmospheric Environment*, Vol. 45 (17), pp. 2869-2876, Netherlands.

[18] Perea-Moreno, M.A., Manzano-Agugliaro, F., Perea-Moreno, A.J., (2018). Sustainable Energy Based on Sunflower Seed Husk Boiler for Residential Buildings. *Sustainability,* Vol. 10(10), 3407, doi:10.3390/su10103407. Basel / Switzerland.

[19] Popescu, B., Senila, L., Varaticeanu, C., Simon, G.N., (2013). Cellulosic bioethanol from sunflower seed hulls – a renewable energy source. *Studia ubb ambientum*, LVIII, Vol.1-2, pp.105-110, Cluj-Napoca / Romania.

[20] Schwarzer, L., Jensen, P. A., Glarborg, P., Holm, J. K., & Dam-Johansen, K., (2017). Biomass ignition in mills and storages - is it explained by conventional thermal ignition theory? *DTU Library*, pp.1-10, Stockholm / Sweden.

[21] Sivabalan, K., Hassan, S., Ya, H., Pasupuleti, J., (2021). A review on the characteristic of biomass and classification of bioenergy through direct combustion and gasification as an alternative power supply. *Journal of Physics: Conference Series*, Vol.1831, pp.1-23, doi:10.1088/1742-6596/1831/1/012033. United Kingdom.

[22] Spirchez, C., Lunguleasa, A., Croitoru, C., (2019). Ecological briquettes from sunflower seed husk. *E3S Web of Conferences,* Vol. 80, pp. 1-5, https://doi.org/10.1051/e3sconf/20198001001. Paris / France.

[23] Tibola, F.L., de Oliveira, T.J. P., Ataide, C.H., Cerqueira, D.A., Sousa, N.G., Cardoso, C.R., (2022), Temperature - programmed pyrolysis of sunflower seed husks: application of reaction models for the kinetic and thermodynamic calculation. *Biomass Conversion and Biorefinery*. pp. 1-18, https://doi.org/10.1007/s13399-021-02297-w. Germany.

[24] Uddin, M. N., Techato, K., Taweekun, J., Mofijur, M., Rasul, M. G., Mahlia, T. M. I., Ashrafur, S.M., (2018). An Overview of Recent Developments in Biomass Pyrolysis Technologies. *Energies,* Vol. 11, 3115, doi:10.3390/en11113115. Basel / Switzerland.

[25] Weatherstone, S. & Williams, A., (2015). Low temperature ignition of biomass. *Fuel Processing Technology,* Vol.134, pp. 373-377, Netherlands.

[26] Wystalska, K., (2018). Effects of pyrolysis parameters on the yield and properties of biochar from pelletized sunflower husk. *E3S Web of Conferences,* Vol.44, pp.1-7, Polanica-Zdroj / Poland.

[27] Yadav, S.P., Ghosh, U.K., Ray, A.K., (2016). A Fresh Look at the Kinetics of Pentosan Removal from Lignocellulosic Biomass. *American Journal of Chemical Engineering.* 4(6), pp. 161-169, USA.

[28] Zaichenko, V.M., Krylova, A.Y., Sytchev, G.A., Shevchenko, A.L., (2020). Thermal effects during biomass torrefaction. *Solid Fuel Chem.* Vol. 4, pp. 228 – 231, Netherlands.

[29] Zajemska, M., Urbanczyk, P., Poskart, A., Urbaniak, D., Radomiak, H., Musial, D., Golanski, G., Wylecial, T., (2017). The impact of co-firing sunflower husk pellets with coal in a boiler on the chemical composition of flue gas. *E3S Web of Conferences,* Vol. 14, pp.1-7, Krakow, Poland.

[30] Zajqc, G., Szyszlak-Barglowicz, J., Slowik, T., (2019). Comparison and Assessment of Emission Factors for Toxic Exhaust Components During Combustion of Biomass Fuels. *Rocznik Ochrona Srodowiska.* Vol. 21(1), pp. 378-394, Koszalin / Poland.

[31] Zolotovs'ka, O., Kharytonov, M., Onyshchenko, O., (2016). Agricultural residues gasification, dependency of main operational parameters of the process on feedstock characteristics. *INMATEH Agricultural Engineering*, Vol.50 (3), pp. 119-126. Bucharest / Romania.

LOW COST TELEMONITORING TECHNOLOGY OF SEMISPHERICAL SOLAR DRYER FOR DRYING ARABICA COFFEE BEANS
/
TEKNOLOGI TELEMONITORING BERBIAYA RENDAH PADA PENGERING SURYA TIPE *SEMI-SPHERICAL* UNTUK PENGERINGAN BIJI KOPI ARABIKA

Eko Kuncoro PRAMONO [1)], Mirwan Ardiansyah KARIM [1)], Ahmad FUDHOLI [2, 3)], Ramayanty BULAN [*4)],
Ravipat LAPCHAROENSUK [5)], Agustami SITORUS [1, 5)]

[1)] Research Centre for Appropriate Technology, National Research and Innovation Agency, Indonesia
[2)] Research Centre for Electrical Power and Mechatronics, National Research and Innovation Agency, Indonesia
[3)] Solar Energy Research Institute, Universiti Kebangsaan Malaysia, Malaysia
[4)] Department of Agricultural Engineering, Syiah Kuala University, Indonesia
[5)] Department of Agricultural Engineering, King Mongkut's Institute of Technology Ladkrabang, Thailand
Tel: +62 812-8343-9334; E-mail: ramayantybulan@gmail.com
Corresponding author: Ramayanty Bulan
DOI: https://doi.org/10.35633/inmateh-66-34

ABSTRACT

This study focusses on the development of a low-cost Internet of Things (IoT) system for semispherical solar dryers to dry arabica coffee beans. The temperatures and relative humidity (Rh) of a solar dryer room are measured using a DHT22 sensor module. The moisture content of hard arabica coffee beans is calculated by measuring the mass of the dried product using the load cell sensor module. All detected data are then sent using wireless networks and saved on a database cloud server. Tests are conducted to evaluate the uniformity of the DHT22 sensor module in a semispherical solar dryer, measure the temperature and Rh and reduce the mass of the dried coffee beans. The performance of the DHT22 sensor module at the uniformity testing stage shows promising results in terms of temperature and Rh, with standard deviations of 0.46 and 3.55, respectively. In addition, the performance of the semispherical solar dryer in relation to the drying kinetics of arabica coffee beans is evaluated. Arabica coffee beans are dried from 49.59% (w.b.) to 10% (w.b.) moisture content within 69 h. In addition, the drying kinetics of coffee arabica beans are investigated. Three models are compared with experimental data on arabica coffee beans dried in a semispherical solar dryer. The Page model is selected to represent the thin layer drying behaviour of arabica coffee beans.

ABSTRAK

Dalam penelitian ini, kami fokus pada pengembangan sistem internet of things (IoT) berbiaya rendah untuk alat pengering surya semi-spherical biji kopi arabika. Suhu dan kelembapan relatif ruang pengering diukur menggunakan modul sensor DHT22. Kadar air biji kopi arabika dihitung dengan mengukur massa produk kering menggunakan modul sensor load cell. Semua data yang diukur kemudian dikirim menggunakan jaringan internet dan disimpan di server cloud database. Pengujian dilakukan untuk mengevaluasi keseragaman modul sensor DHT22 dalam pengering surya semi-spherical, mengukur suhu dan kelembapan relatif serta pengurangan massa biji kopi yang dikeringkan. Kinerja modul sensor DHT22 pada tahap pengujian keseragaman menunjukkan hasil yang menjanjikan dalam hal suhu dan kelembapan relatif dengan standar deviasi masing-masing sebesar 0.46 dan 3.55. Selain itu, evaluasi kinerja alat pengering surya semi-spherical dalam kaitannya dengan kinetika pengeringan biji kopi arabika juga dilakukan. Biji kopi arabika dikeringkan dari 49.59% (b.b.) hingga 10% (b.b.) kadar air dalam waktu 69 jam. Selain itu, kinetika pengeringan biji kopi arabika juga diselidiki. Tiga model dibandingkan dengan data eksperimen pada biji kopi arabika yang dikeringkan dalam pengering surya semi-spherical. Model Page ditemukan dapat mewakili perilaku pengeringan lapisan tipis biji kopi arabika dalam alat pengering ini.

INTRODUCTION

Monitoring and control systems are being considered in modern drying equipment technology to enable the control of dryer performance. *Zhang et al.* (2018) and *Sitorus et al.* (2020) investigated the acquisition of data on the moisture content of products that are dried in a non-invasive fluidisation dryer. Information on the percentage of moisture content is crucial in controlling the quality of dried products and the performance of

dryers. However, relevant monitoring systems are rarely integrated into solar dryers, mainly because they are likely to increase the costs of solar dryers.

Goud et al. (2019) and *Lingayat et al.* (2020a) used six RTD Pt−100 sensors (accuracy of 1%) to measure temperature with 16 channel data loggers. The reduction in the mass of the dried product was measured with a weight balance (Model: OHAUS PA 214) with an accuracy of ±0.2 mg. In their experimental procedure, the proposed indirect solar dryer with inlet fans powered by solar PV panels was obviously not integrated with a data acquisition system (*Goud et al.*, 2019; *Lingayat et al.*, 2020a). *Vijayan et al.* (2020) used K-type thermocouples connected to a digital temperature indicator with a resolution of 0.1 °C. Relative humidity was observed using a thermo-hygrometer with an accuracy of ±2% and a resolution of 0.01%. The weights of the samples were checked using a digital weighing machine with a resolution of 1 g. According to the experimental setup described in their study (*Vijayan et al.*, 2020), the process of recording dryer performance data is not integrated into the solar dryer. Therefore, the recording of performance data from the developed solar dryer remains offline and is not performed in real time.

The use of monitoring technology based on the internet of things (IoT), i.e. telemonitoring, is growing rapidly. Several researchers have highlighted the use of this technology in agriculture (*Villa-Henriksen et al.*, 2020; *Tzounis et al.*, 2017), fishery (*Wang et al.*, 2020; *Kumar and Sivaperumal*, 2020; *Chen et al.*, 2017) and animal husbandry (*Zhou et al.*, 2019; *Stojkoska et al.*, 2018; *Babalola G. et al.*, 2018) so that data can be accessed anywhere and at any time. On the one hand, the tools for developing systems towards the use of IoT have developed rapidly. Such tools make devices easy and inexpensive to use in various fields. On the other hand, monitoring equipment for drying technology, especially solar dryers, still uses devices that are scientific and are thus expensive (*Lakshmi et al.*, 2019; *Lingayat et al.*, 2020a; *Goud et al.*, 2019; *Vijayan et al.*, 2020). Therefore, monitoring technology is generally not integrated into solar dryer units. In such a case, the monitoring instruments are removed from the solar dryers after the drying performance is tested.

Solar dryers can be used for low temperature drying. In particular, greenhouse dryers are widely popular, especially in remote areas. In the last two and half decades, greenhouse dryers have been used for low temperature drying with the aid of solar radiation (Prakash et al., 2016). The popularity of solar dryers in remote areas can be attributed to the abundance of solar energy and the need to dry and thereby preserve agricultural materials. Therefore, these devices are beneficial, especially in Indonesia. Scientific studies aiming to optimise solar dryer technology have also been carried out; examples include the works of *Ekka et al.* (2020) on black ginger, *Lingayat et al.* (2020a) on apple and watermelon, *Djebli et al.* (2020) on potatoes and *Ouaabou et al.* (2020) on Moroccan sweet cherry. Other researchers have conducted relevant reviews (*Lingayat et al.*, 2020b; *Vijaya. et al.*, 2012). Meanwhile, several studies have focused on drying kinetics, thin-layer drying models and the evaluation of the performance of solar dryers for red chili (*Fudholi et al.*, 2014b; *Fudholi et al.*, 2013), seaweed (*Fudholi et al.*, 2014a), salted silver jewfish (*Fudholi et al.*, 2016) and palm oil fronds (*Fudholi et al.*, 2015a).

Solar dryers can be classified into four groups: direct, indirect, mixed, and hybrid solar dryers. Solar dryers can be also categorised as tent dryers, cabinet dryers and greenhouse dryers according to the type of drying chamber. *Fudholi et al.* (2015b) and *Fudholi et al.* (2015c) reviewed air- and water-based types of solar dryers in Malaysia. In Indonesia, *Yahya et al.* (2016) developed a solar dryer system for cassava and rice paddies (*Yahya et al.*, 2018; *Yahya et al.*, 2017). However, existing research is still focused on finding an optimal method for harvesting solar energy and studying the kinetic drying modeling of dried products. Therefore, the objective of the current study is to compare suitable mathematical drying models for Arabic coffee beans and to analyse the performance of a semispherical solar dryer for Arabic coffee beans. The main objective of this study is to develop a low-cost IoT system for monitoring semispherical solar dryers. The proposed system is expected to complement solar drying by allowing drying performance to be monitored anywhere and at any time.

MATERIALS AND METHODS

This research was carried out at the Research Centre for Appropriate Technology, National Research and Innovation Agency, Subang. The solar dryer equipped with a telemonitoring system is located at 6°33'16.0"S–107°45'41.6"E at an altitude of 87 m asl. The telemonitoring system performance test was carried out in August 2019. The development of the telemonitoring system was carried out in three stages, namely, (i) designing the telemonitoring system, (ii) testing the uniformity of temperature and relative humidity sensors and (iii) testing the performance of the telemonitoring system integrated into the solar dryer.

The telemonitoring system integrated into a solar dryer is presented in Figure 1. The solar dryer developed at the Research Centre for Appropriate Technology is of the semispherical type (*Uğur et al.*, 2018). The dryer has a width of 2.8 m, length of 4.2 m and height of 3.1 m. It comprises three layers, each of which has two racks on which to place the products to be dried. The solar dryer frame is made of galvanized iron with a diameter of 38.1 mm and its walls and roof are coated with 14% UV plastic with a thickness of 170 microns. The floor of the solar dryer is made of bricks that are attached directly to the ground.

1–chimney
2–rotary wind ventilator
3–exit vent
4–tray
5–frame tray
6–air duct
7–air intake
8–telemonitoring system
☆–DHT22 sensors
○–load-cells sensors
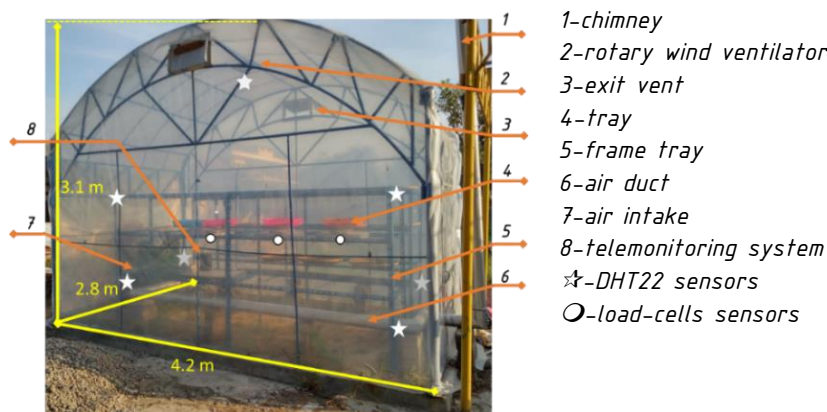
Fig. 1 – Solar dryer developed in this study

When designing the telemonitoring system, the cost and availability of materials used for the construction were considered. The system consists of a temperature telemonitoring unit and a product mass telemonitoring unit. The temperature telemonitoring unit uses seven DHT22 sensor modules to measure temperature and relative humidity (Figure 2). The product mass telemonitoring unit comprises three racks equipped with load cell sensors which measure the changes in the mass of the products being dried. This unit indicates the decreases in the mass of the products that are dried in the solar dryer (*Sitorus et al.*, 2020). All sensor data are recorded and sent to the NodeMcu Esp8266 microcontroller via WLAN every 2 s. A datasheet of the DHT22 sensor modules and load cells is presented in Table 1. The list of components used in the design of the telemonitoring unit is shown in Table 2. The capital cost for the construction and installation of this system is 130.70 USD. This cost is not much higher than that of other low-cost systems, such as *Putra* (2020), which is a portable sensing system integrated with an on-the-go fertilizer application system.
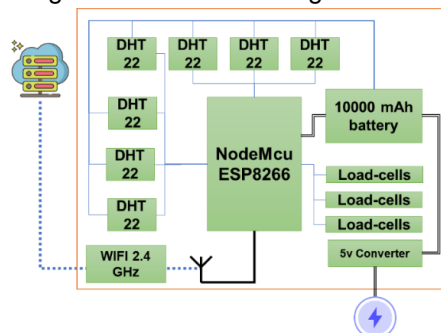
Fig. 2 – Telemonitoring system architecture

The performance testing of the telemonitoring system was carried out in two stages. The first stage involved testing the level of uniformity of the DHT22 temperature sensors and their sensitivity to temperature changes in the solar dryer. For this stage, the DHT22 sensor modules in the middle of the solar dryer room were collected. Then, the system was turned on for three days.

The level of measurement uniformity was indicated by the standard deviation parameters of the seven DHT22 sensors that are calculated using Equation 1. At this stage, the DHT22 temperature sensors were placed at several points in the solar dryer room. The drying racks were also equipped with load cell sensors. The second stage involved the use of wet coffee beans with hard skins (Java Preanger Arabica coffee, Indonesia) (*Happyana et al.*, 2020) with a water content of 49.80% (w.b.). All data were sent to the database using the internet network. The selected coffee type is one of the oldest agricultural products that is continuously preserved in West Java Province, Indonesia. Even today, extensibility continues to meet market demands.

$$S = \sqrt{\frac{\sum_{i=1}^{n}(x_i - \mu)^2}{n-1}} \qquad (1)$$

Where S is the standard deviation, x_i denotes the data sent to i, μ is the mean and n is the amount of data.

Table 1

Datasheet of DHT22 and load-cells sensor

Parameter	DHT22 sensor module		Load-cells sensor
	Temperature	Relative humidity	
Operating Voltage	5 V		3.3 V – 5 V
Operating Current	1.5 mA		1.5 mA
Operating Temperature	-20 °C – +80 °C		-35 °C – +80 °C
Range measurement	-40 °C – +80 °C	0 – 100%	0 – 5 kg
Deviation	±0.5 °C	± 2.0%	0.05%
Resolution	0.1 °C	0.1%	1.0±0.15 mv/V

Table 2

List of components of the low-cost system and their price (as of November 2021)

No	Component	Quantity	Price unit (USD)	Remark
1	NodeMCU Lolin V3	3	7.29	ESP8266
2	Temperature and Rh Sensor	7	37.80	DHT22 DFRobot
3	Loadcell + Amplifier	3	6.43	HX711
4	Sensor cable	1	21.43	AWM 24x3
5	Connector	10	3.57	USB male-female
6	Electronic box	1	2.54	
7	Battery	1	11.79	10000 mAh
8	Switch	1	0.14	
9	PCB	1	0.29	
10	Spacer	10	0.86	
11	Indicator LED	1	0.07	
12	Pin Header	1	0.07	
13	Jumper	1	0.36	
14	Plastic Basket	3	3.21	
15	Metal sheet	3	8.57	
16	Internet network	1	32.14	
17	5-VDC Adapter	1	1.43	
Total cost of developing telemonitoring system		**~130.70**		

Table 3

Uncertainties of the parameters during the experiment

Parameter	Unit	Comment
Uncertainty in the temperature measurement		
Drying room temperature	°C	±0.2872
Ambient air temperature	°C	±0.2872
Uncertainty in the time measurement		
Uncertainty in the time measurement	min	±0.1000
Temperature values	min	±0.1000
Uncertainty in the mass loss measurement	g	±0.5123
Uncertainty of the measurement of relative humidity of air	%	±0.1414
Calculated values		
Total uncertainty for moisture rate	%	±0.5220
Total uncertainty for drying rate	%	±0.5220

Uncertainty analysis focuses on uncertainties or errors in experimental data. In general, errors can be particularly systematic errors or random errors. According to *Akpinar* (2010), errors and uncertainties in experiments on solar dryers can arise from instrument selection, condition, calibration, environment, observation, reading and test planning. Therefore, the uncertainty analysis of the experimental measurement and results is a powerful tool when used in the planning and design of experiments. In the current study, an uncertainty analysis was performed using Equation 2 (*Akpinar*, 2010; *Holman*, 2001).

$$\omega_R = \left[\left(\frac{\partial R}{\partial x_1} \omega_1 \right)^2 + \left(\frac{\partial R}{\partial x_2} \omega_2 \right)^2 + ... + \left(\frac{\partial R}{\partial x_n} \omega_n \right)^2 \right]^{1/2} \qquad (2)$$

where: R- is the function of the independent variables $x_1, x_2, x_3, ..., x_n$,; w_R-uncertainty in the result and w_1, $w_2, ..., w_n$.

Total uncertainties of the measured parameters and calculated experimental parameters are presented in Table 3. Each uncertainty value was considered to be within a suitable range.

Table 4 and Table 5 show the equations of the drying analysis, including the drying rates, moisture contents of the arabica coffee beans and drying mathematical models. Four drying mathematical models were fitted with the experimental data of the semispherical solar dryer for arabica coffee beans: Newton model, Page model, Henderson and Pabis model and the modified Page model. These models were calculated using Excel, and the constants were determined using a curve method. The values of determination (R^2), mean bias error (MBE) and root-mean-square error ($RMSE$) coefficient were used to select the most suitable drying mathematical models. The model that produced the highest R^2 and the lowest $RMSE$ in describing the drying curve was considered the best model. The statistical parameters were calculated using the following Equations 3 and Equations 4.

$$MBE = \frac{1}{N}\sum_{i=1}^{N}\left(MR_{pre,i} - M R_{exp,i}\right)^2 \tag{3}$$

$$RMSE = \sqrt{\frac{1}{N}\sum_{i=1}^{N}\left(MR_{pre,i} - M R_{exp,i}\right)^2} \tag{4}$$

where: $MR_{exp,i}$ is experimental value of moisture ratio, $MR_{pre,i}$ is simulated value of moisture ratio, and

N is number of data points (observations).

Table 4

Drying analysis equations

Drying analysis	Unit	Comment	Equation	
Drying rate (DR)	(g/g)/h	M_t is moisture content at time t, and M_{t+dt} is moisture content at time $t + dt$	$DR = \frac{M_{t+dt} - M_t}{dt}$	(5)
Moisture content wet basis	(% w.b.)	$w(t)$ is mass of wet materials at instant t (kg), d is mass of dry materials (kg)	$M = \frac{w(t) - d}{w}$	(6)
Moisture content dry basis	(g/g)		$M = \frac{w(t) - d}{d}$	(7)
Moisture ratio (MR)		M is the moisture content at any time t, M_e is equilibrium moisture content, and M_i is initial moisture content.	$MR = \frac{M - M_e}{M_i - M_e}$	(8)

Table 5

Drying mathematical model

Model name	Model solution with Excel solver	Model equation	
Newton	The exponential curve of Newton's model, which represents the correlation between MR and drying time	$MR = \exp(-kt)$	(9)
Page	$ln (-ln\ MR) = ln\ (k) + n\ ln\ (t)$, The correlation $ln\ (-ln\ MR)$ with t, which is the curve of the logarithmic equation	$MR = \exp(-kt^n)$	(10)
Henderson and Pabis	$ln\ MR = -kt + ln\ (a)$, a plot of $ln\ MR$ versus drying time produced a straight line with intercept $ln\ (a)$ and slope k	$MR = a \cdot \exp(-kt)$	(11)

The heat utilisation factor (HUF) and coefficient of performance (COP) were evaluated for the semispherical solar dryer for arabica coffee beans. HUF is defined as the ratio between temperature decrease due to cooling air during drying and temperature increase due to heating of air, as shown in Equation 12. COP is calculated by Equation 13 (*Prakash et al.*, 2016; *Sayyad et al., 2015*).

$$HUF = \frac{(T_d - T_e)}{(T_d - T_a)} \tag{12}$$

$$COP = \frac{(T_e - T_a)}{(T_d - T_a)} \tag{13}$$

$$HUF + COP = 1 \tag{14}$$

where:

T_a, T_d and T_e are the ambient temperature, drying temperature and exhaust air temperature, respectively.

RESULTS

A telemonitoring system was successfully developed and integrated into the solar dryer (Figure 3). The telemonitoring unit consisted of two control boxes, each of which comprised seven temperature sensors; each mass sensor had three control boxes. Telemonitoring systems can record and send data to servers via WLAN.

The data can then be accessed wherever and whenever using devices such as smartphones to monitor the performance of solar dryer units and dried products. Telemonitoring devices are expected to improve the process of identifying the performance of solar dryers and dried products. The resulting data are important for drying agricultural and food products because according to some studies, agricultural and food products are highly perishable (*Sivakumar et al.*, 2016; *Bruce et al.*, 2019; *Ogawa et al.*, 2017) due to various factors, including improper drying temperature monitoring.

1-tray product
2-loadcells frames
3-control box telemonitoring system

Fig. 3 – Telemonitoring devices integrated into the solar dryer

Open-source software (Arduino IDE) was used to develop a logarithm for the telemonitoring system. Open-source software Notepad++ was used to design the data recording information system for web logging. An example of a data recording page is presented in Figure 4.
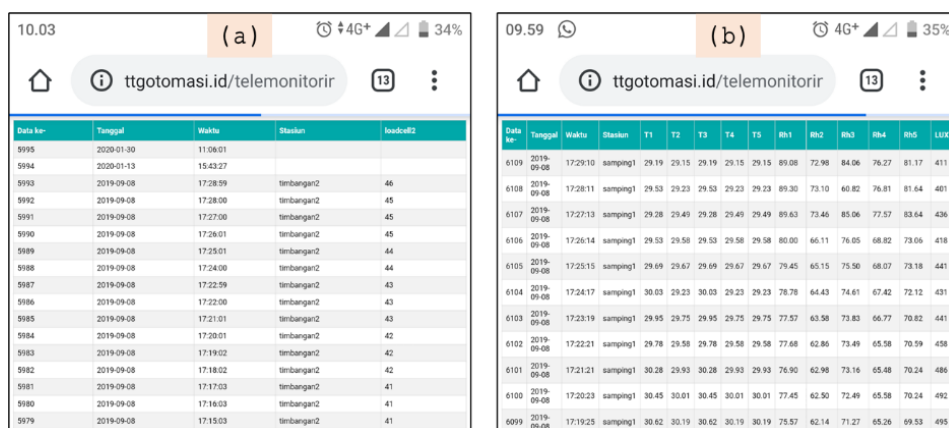
Fig. 4 – Data pages accessed via smartphone

Temperature and relative humidity are important parameters in the drying process. Therefore, it is important to ensure that every sensor used meets reliability requirements. Seven DHT22 sensors were used in the uniformity test. Each sensor was placed at one point in the solar dryer room. The setup was aimed at determining the differences in sensor readings of changes in temperature and relative humidity.

The average temperature readings of the DHT22 sensors followed by standard deviations are presented in Figure 5a. The tests were carried out from August 3 at 10:45:53 am to August 6 at 02:24:51 am. A total of 3276 temperature recordings followed the patterns of temperature changes in the solar dryer. However, from the seven temperature recording sensors, the NAN data recorded were 7.94%, 7.78%, 7.84%, 9.13%, 12.52%, 3.24% and 11.48%. The presence of NAN data, which are called unsuccessfully recorded data, is in line with the research by *Dahlan et al.* (2018), who found similar results from the use of DHT22 sensors. However, their work did not mention the percentages; therefore, no comparison could be made. The highest, lowest, and average temperatures during the uniformity test were 52.07±10.24 °C, 18.86±0.04 °C and 30.42±0.46 °C, respectively. The results of the test indicated that the standard deviations of the temperature sensors tended to increase with increasing temperature of the solar dryer room, and vice versa.

The average relative humidity readings from the DHT22 sensors followed the standard deviations and are presented in Figure 5b. The test was carried out from 3 August at 10:45:53 am to 6 August at 02:24:51 am. A total of 3276 relative humidity recordings followed the patterns of relative humidity changes in the solar dryer. However, from the seven relative humidity recording sensors, the NAN data were 7.94%, 7.78%, 7.84%,

9.13%, 12.52%, 3.24% and 11.48%. The highest, lowest, and average relative humidity during uniformity testing were 85.05%±24.47%, 20.27%±1.29% and 58.14%±3.55%, respectively. The results of this test indicated that the standard deviation of the relative humidity sensor tended to decrease with increasing relative humidity in the solar dryer room, and vice versa.
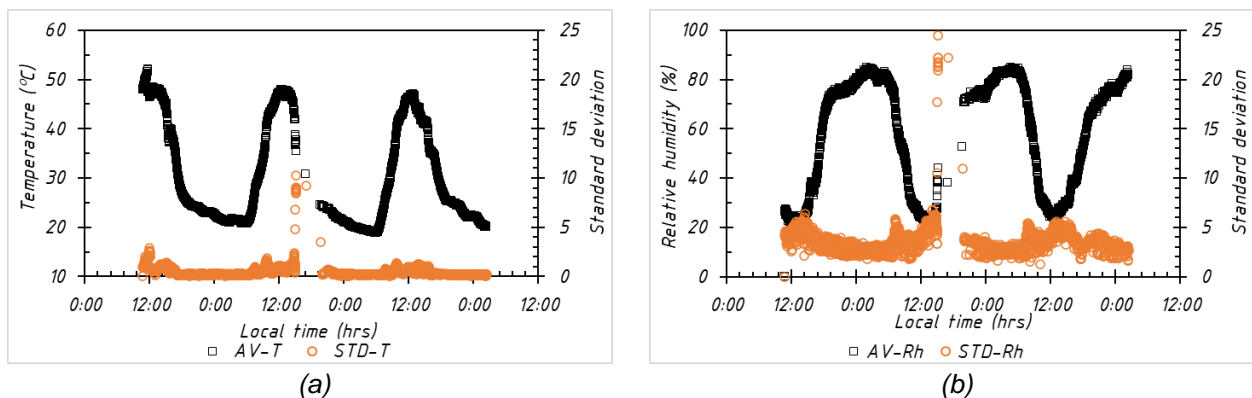

(a)   *(b)*

Fig. 5 – Sensor uniformity test from 3 to 6 August 2019 (a) temperature (b) relative humidity

In the DHT22 sensor uniformity test on August 4, the unstable temperature and relative humidity data readings (sensor 1 and sensor 2) lasted 16907 s. Therefore, the standard deviations of the temperature and relative humidity data at the time of measurement increased to 10.24 and 24.47, respectively. The instability of the temperature data measurements was marked by a decrease in the temperature readings of sensor 1 (from 44.40 °C to 23.90 °C) and sensor 2 (from 42.30 °C to 24.50 °C) within 618 s; the other sensors did not follow the same trend. As for the relative instability of the measurement of relative humidity data, it was marked by an increase in relative humidity readings by sensor 1 (from 43.60% to 68.70%) and sensor 2 (from 48.00% to 71.80%) within 618 s; the other sensors did not follow the same trend. Thereafter, all sensors were turned off for 16289 s. This incident was attributed to the power outage and the exhaustion of the backup power from the telemonitoring system before the power was restored. The measurements of temperature and relative humidity of all sensors returned to normal on their own at 19:41:28 pm after the power was restored.

(a)   *(b)*
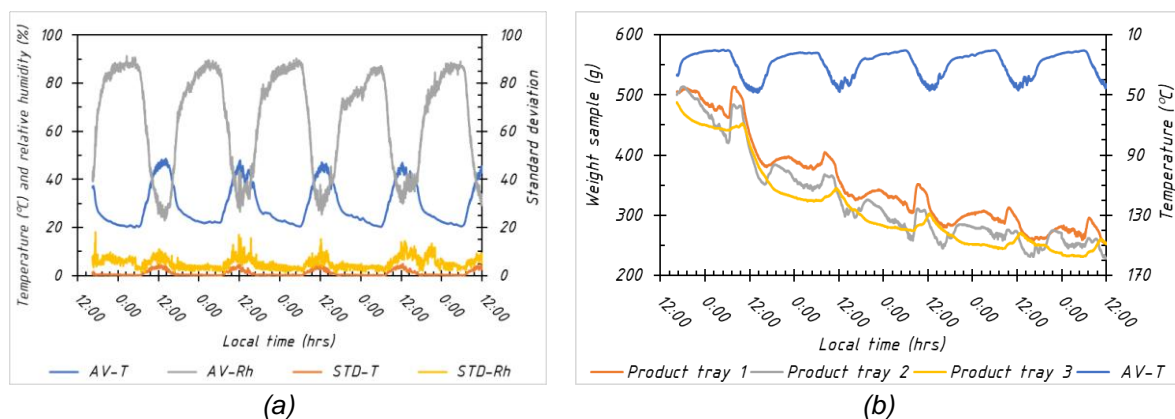
Fig. 6 – Testing solar dryer on 7 to 12 August 2019 (a) temperature and relative humidity (b) mass reduction

The average temperature and relative humidity readings of the DHT22 sensors following the standard deviations in the test using coffee products are presented in Figure 6a. The experiments were carried out from 7 August at 16:25:16 pm to 12 August at 11:59:38 am or for 115.57 h. A total of 6740 temperature and relative humidity readings were recorded, and they followed the patterns of the changes in temperature and relative humidity in the solar dryer. The percentages of NAN data for the temperature and relative humidity recorded from the seven sensors were 14.57%, 9.54%, 14.85%, 9.88%, 19.58%, 7.8%, and 12.66%. The highest, lowest, and average temperatures during the test were 48.57±4.9 °C, 20.00±0.00 °C and 29.30±1.06 °C, respectively. The highest, lowest, and average relative humidity during the test were 91.30%±18.10%, 22.94%±1.03% and 65.84%±5.33%, respectively. The performance test indicated that increasing the temperature increased the temperature measurement errors, and vice versa. Meanwhile, increasing the relative humidity decreased the errors from measuring relative humidity, and vice versa.

The decrease in product mass due to the evaporation of the moisture content in the test is presented in Figure 6b. Three trays with the same product of the same initial relative mass showed distinct differences in drying behaviour throughout the drying process. The percentage decrease in the mass of the dried product during the first stage of testing was 50.84%. In general, when the temperature in the solar dryer increased, the mass of the dried product decreased sharply. However, as the temperature decreased, the mass of the dried product increased. This result is in line with that of *Lakshmi et al.* (2019), who explained that it was caused by evaporation of moisture from the surface and the latter decrease in the rate of moisture removal was mainly due to the diffusion of moisture from the interior to the surface of the product.

With reference to Table 5, the results of the drying analysis, including the drying rate curve, characteristic drying curve, drying kinetic curves and drying curve of the semispherical solar dryer for arabica coffee beans are showed. The drying curve showed the change in profile in moisture content versus drying time (t). Figure 7a describes a reduction in moisture content (dry basis and wet basis). The drying rate with an average of 0.01 (g/g)/h and a maximum of 0.11 (g/g)/h, was calculated using Equation (5).

(a)

(b)

(c)

(d)
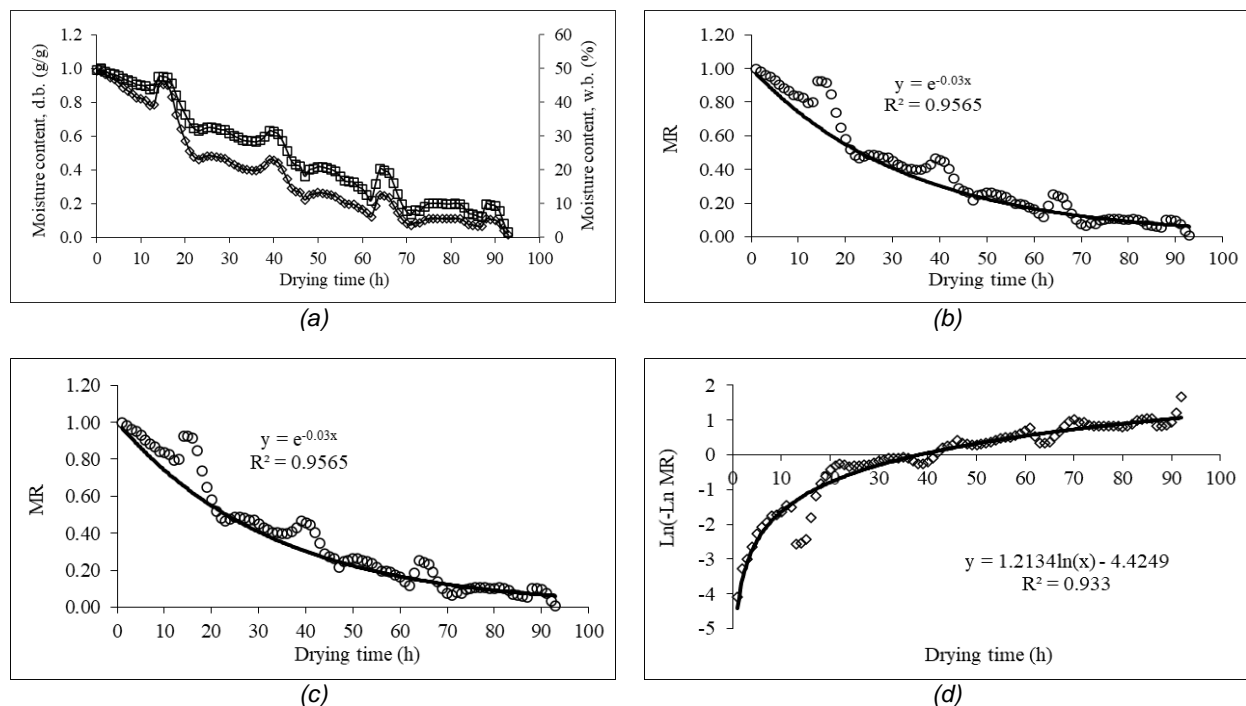
Fig. 7 – (a) Moisture content variation (b) Newton drying model (c) Page drying model (d) Henderson and Pabis drying model

Drying mathematical model curve of the semispherical solar dryer for arabica coffee beans are shown in Figure 7b until Figure 7d. Figure 7b shows Newton's model, which represents the correlation between the *MR* and drying time. Figure 7b shows that the exponential curve with k constant is 0.03. Figure 7c shows Page's model, which represent the correlation *ln (−ln MR)* with *t*, which is the curve of the logarithmic equation. Figure 7c shows that *n* constant is 1.2134 and the obtained value for *k* constant is 0.012. Figure 7d shows that a plot of *ln MR* versus drying time produced a straight line the intercept of which is *ln a* and the slope is *k* (0.0334) and the obtained value of *a* constant (1.242).

The results presented in Table 6 show that the Page drying model exhibited the highest value of R^2 (0.933) and the lowest values of *RMSE* (0.0581) and *MBE* (0.0034) compared to the Newton model and the Henderson and Pabis model. Accordingly, the Page model was selected to represent the drying mathematical model behaviour of arabica coffee beans. This selection is in accordance with the findings of *Fudholi et al.* (2014a), who reported that the Page model had a better fit in drying seaweeds than the Newton and Henderson and Pabis models. Also, it was reported that the Page model exhibited a better fit than other models in accurately simulating the drying curves of rapeseed, kiwi, okra, green beans, chili pepper, and others.

The performance characteristics of the semispherical solar dryer for arabica coffee beans, including *HUF* and *COP*, were calculated. The average *HUF* was 0.79. The average *COP* was 0.21, and the total *HUF* and *COP* was 1.

Table 6

Results of drying mathematical model analyses

Model	a	k	n	R^2	MBE	RMSE
Newton		0.03		0.8699	0.0066	0.0811
Page		0.012	1.2134	0.9596	0.0034	0.0581
Henderson and Pabis	1.242	0.0334		0.8854	0.0050	0.0706

CONCLUSIONS

A telemonitoring system as add-on equipment for solar dryers was realised using a low-cost IoT system, and the results of this work show its promising performance. The performance of a solar dryer unit when applied to product drying can be known in real time and online using the developed telemonitoring system. Solar dryer performance data can be logged and then accessed anytime and anywhere. The reduction in the moisture content of dried products can also be known online and in real time. Improving the performance of the proposed system requires an advanced and detailed understanding of the mechanism of the telemonitoring system. Such a requirement entails obtaining experimental results on the basis of real conditions and applying many types of product drying conditions. In sum, when a solar dryer is equipped with a telemonitoring system, it can be used as a high-performance technology system that can be considered intelligent technology. In this study a semi-spherical solar dryer was evaluated to dry Arabica coffee beans using kinetic curves. The Page model clearly showed a better fit to the experimental data compared to the Newton and Henderson–Pabis models. This model had the highest *R^2* and the lowest *RMSE* and *MBE*. At the average ambient temperature of approximately 28 °C, the *HUF* and *COP* were 0.79 and 0.21, respectively. The semispherical solar dryer to dry Arabica coffee beans took 69 h to reduce the moisture content of the product from approximately 50% (w.b.) to 10% (w.b.).

REFERENCES

[1] Akpinar, E. K. (2010). Drying of mint leaves in a solar dryer and under open sun: modelling, performance analyses. *Energy convers. and manag.*, 51(12). 2407-2418, https://doi.org/10.1016/j.enconman.2010.05.005

[2] Babalola G., O., Kehinde O., Abiodun O. (2018). Implementing an Internet of Things Livestock Strain and Stray Monitoring System. *International J. of Inf.*, 7(6). 41-47,

[3] Bruce, R. M., Atungulu G. G., Sadaka S. (2019). Impacts of size fractionation, commingling, and drying temperature on physical and pasting properties of broken rice kernels. *Cereal Chem.*, 97(2). 256-269, https://doi.org/10.1002/cche.10241

[4] Chen, Y., Zhen Z., Yu H., Xu J. (2017). Application of fault tree analysis and fuzzy neural networks to fault diagnosis in the Internet of Things (IoT) for aquaculture. *Sensors*, 17(1). 153-168, https://doi.org/10.3390/s17010153

[5] Dahlan, N., Halid A. I., Hashim T. J., Sakimin S. (2018). Temperature based control of ventilation system for optimum climate in tomato greenhouse. *Indonesian J. of Electrical Eng. and Comput. Sci.*, 12(2). 655-661, https://doi.org/10.11591/ijeecs.v12.i2.pp655-661

[6] Djebli, A., Hanini S., Badaoui O., Haddad B., Benhamou A. (2020). Modeling and comparative analysis of solar drying behavior of potatoes. *Renew. Energy*, 145. 1494-1506, https://doi.org/10.1016/j.renene.2019.07.083

[7] Ekka, J. P., Bala K., Muthukumar P., Kanaujiya D. K. (2020). Performance analysis of a forced convection mixed mode horizontal solar cabinet dryer for drying of black ginger (Kaempferia parviflora) using two successive air mass flow rates. *Renew. Energy*, 152. 55-66, https://doi.org/10.1016/j.renene.2020.01.035

[8] Fudholi, A., Bakhtyar B., Saleh H., Ruslan M. H., Othman M. Y., Sopian K. (2016). Drying of salted silver jewfish in a hybrid solar drying system and under open sun: modeling and performance analyses. *International J. of green energy*, 13(11). 1135-1144, https://doi.org/10.1080/15435075.2016.1175347

[9] Fudholi, A., Othman M. Y., Ruslan M. H., Sopian K. (2013). Drying of Malaysian Capsicum annuum L.(red chili) dried by open and solar drying. *International J. of Photoenergy*, 2013. https://doi.org/10.1155/2013/167895

[10] Fudholi, A., Sopian K., Alghoul M., Ruslan M. H., Othman M. Y. (2015a). Performances and improvement potential of solar drying system for palm oil fronds. *Renew. Energy*, 78. 561-565, https://doi.org/10.1016/j.renene.2015.01.050

[11] Fudholi, A., Sopian K., Bakhtyar B., Gabbasa M., Othman M. Y., Ruslan M. H. (2015b). Review of solar drying systems with air based solar collectors in Malaysia. *Renew. and Sustainable Energy Rev.*, 51. 1191-1204, https://doi.org/10.1016/j.rser.2015.07.026

[12]   Fudholi, A., Sopian K., Gabbasa M., Bakhtyar B., Yahya M., Ruslan M. H., Mat S. (2015c). Techno-economic of solar drying systems with water based solar collectors in Malaysia: a review. *Renew. and Sustainable Energy Rev.*, 51. 809-820, https://doi.org/10.1016/j.rser.2015.06.059

[13]   Fudholi, A., Sopian K., Othman M. Y., Ruslan M. H. (2014a). Energy and exergy analyses of solar drying system of red seaweed. *Energy and Buildings*, 68. 121-129, https://doi.org/10.1016/j.enbuild.2013.07.072

[14]   Fudholi, A., Sopian K., Yazdi M. H., Ruslan M. H., Gabbasa M., Kazem H. A. (2014b). Performance analysis of solar drying system for red chili. *Sol. Energy*, 99. 47-54, https://doi.org/10.1016/j.solener.2013.10.019

[15]   Goud, M., Reddy M. V. V., V.P C., S S. (2019). A novel indirect solar dryer with inlet fans powered by solar PV panels: Drying kinetics of Capsicum Annum and Abelmoschus esculentus with dryer performance. *Sol. Energy*, 194. 871-885, https://doi.org/10.1016/j.solener.2019.11.031

[16]   Happyana, N., Hermawati E., Syah Y. M., Hakim E. H. (2020). Discrimination of the Indonesian roasted arabica coffees using1H NMR-based metabolomics. *Curr. Res. in Nutr. and Food Sci.*, 8(2). 479-488, https://doi.org/10.12944/CRNFSJ.8.2.13

[17]   Holman, J. P., (2001). Experimental methods for engineers

[18]   Kumar, Y. P., Sivaperumal S. (2020). Iaas level Internet of Things based Aquaculture Data Monitoring System with Network Topology Analysis. *TEST Eng. & Manag.*, 82. 8813-8819,

[19]   Lakshmi, D. V. N., Muthukumar P., Layek A., Nayak P. K. (2019). Performance analyses of mixed mode forced convection solar dryer for drying of stevia leaves. *Sol. Energy*, 188. 507-518, https://doi.org/10.1016/j.solener.2019.06.009

[20]   Lingayat, A., Chandramohan, Raju, Kumar A. (2020a). Development of indirect type solar dryer and experiments for estimation of drying parameters of apple and watermelon. *Therm. Sci. and Eng. Prog.*, 16. 100477-100493, https://doi.org/10.1016/j.tsep.2020.100477

[21]   Lingayat, A. B., Chandramohan V. P., Raju V. R. K., Meda V. (2020b). A review on indirect type solar dryers for agricultural crops – Dryer setup, its performance, energy storage and important highlights. *App. Energy*, 258. 114005-114027, https://doi.org/10.1016/j.apenergy.2019.114005

[22]   Ogawa, T., Chuma A., Aimoto U., Adachi S. (2017). Effects of drying temperature and relative humidity on spaghetti characteristics. *Dry. Technol.*, 35(10). 1214-1224, https://doi.org/10.1080/07373937.2016.1236812

[23]   Ouaabou, R., Nabil B., Ouhammou M., Idlimam A., Lamharrar A., Ennahli S., Hanine H., Mahrouz M. (2020). Impact of solar drying process on drying kinetics, and on bioactive profile of Moroccan sweet cherry. *Renew. Energy*, 151. 908-918, https://doi.org/10.1016/j.renene.2019.11.078

[24]   Prakash, O., Kumar A., Laguri V. (2016). Performance of modified greenhouse dryer with thermal energy storage. *Energy reports*, 2. 155-162,

[25]   Putra, B. T. W. (2020). New low-cost portable sensing system integrated with on-the-go fertilizer application system for plantation crops. *Measurement*, 155. 107562-107572, https://doi.org/10.1016/j.measurement.2020.107562

[26]   Sayyad, F., Sardar N., Rathod J., Baria U., Yaduvanshi B., Solanki B., Chavda J. (2015). Design and development of solar cooker cum dryer. *Curr. World Environ*, 10(3). 985-993,

[27]   Sitorus, A., Novrinaldi N., Bulan R. (2020). Non-invasive moisture content measurement system based on the ESP8266 microcontroller. *Bull. of Electrical Eng. and Inform.*, 9(3). 924-932, https://doi.org/10.11591/eei.v9i3.2178

[28]   Sivakumar, R., Saravanan R., Perumal A. E., Iniyan S. (2016). Fluidized bed drying of some agro products–A review. *Renew. and Sustainable Energy Rev.*, 61. 280-301, https://doi.org/10.1016/j.rser.2016.04.014

[29]   Stojkoska, B. R., Bogatinoska D. C., Scheepers G., Malekian R. (2018). Real-time internet of things architecture for wireless livestock tracking. *Telfor J.*, 10(2). 74-79, https://doi.org/10.5937/telfor1802074R

[30]   Tzounis, A., Katsoulas N., Bartzanas T., Kittas C. (2017). Internet of Things in agriculture, recent advances and future challenges. *Biosyst. Eng.*, 164. 31-48, https://doi.org/10.1016/j.biosystemseng.2017.09.007

[31]   Uğur, Ç., Erol Ş., Kemal Ç., Ayşegül Ç. K. (2018). 'Solar calculations of modified arch (Semi-spherical)-type greenhouse system for Bayburt City.' in, *Exergy for A Better Environment and Improved Sustainability 2* (Springer)

[32]   Vijaya., V., Iniyan S., Goic R. (2012). A review of solar drying technologies. *Renew. and Sustainable Energy Rev.*, 16(5). 2652-2670, https://doi.org/10.1016/j.rser.2012.01.007

[33]   Vijayan, S., Arjunan T. V., Kumar A. (2020). Exergo-environmental analysis of an indirect forced convection solar dryer for drying bitter gourd slices. *Renew. Energy*, 146. 2210-2223, https://doi.org/10.1016/j.renene.2019.08.066

[34] Villa-Henriksen, A., Edwards G. T. C., Pesonen L. A., Green O., Sørensen C. A. G. (2020). Internet of Things in arable farming: Implementation, applications, challenges and potential. *Biosyst. Eng.*, 191. 60-84, https://doi.org/10.1016/j.biosystemseng.2019.12.013

[35] Wang, J., Cheng H., Yuan S., Wang Q., Shu L., Zhang C. (2020). 'Design and Research of the Intelligent Aquaculture Monitoring System Based on the Internet of Things.' in, *Data Processing Techniques and Applications for Cyber-Physical Systems (DPTA 2019)* (Springer)

[36] Yahya, M., Fahmi H., Fudholi A., Sopian K. (2018). Performance and economic analyses on solar-assisted heat pump fluidised bed dryer integrated with biomass furnace for rice drying. *Sol. Energy*, 174. 1058-1067, https://doi.org/10.1016/j.solener.2018.10.002

[37] Yahya, M., Fudholi A., Hafizh H., Sopian K. (2016). Comparison of solar dryer and solar-assisted heat pump dryer for cassava. *Sol. Energy*, 136. 606-613, https://doi.org/10.1016/j.solener.2016.07.049

[38] Yahya, M., Fudholi A., Sopian K. (2017). Energy and exergy analyses of solar-assisted fluidized bed drying integrated with biomass furnace. *Renew. Energy*, 105. 22-29, https://doi.org/10.1016/j.renene.2016.12.049

[39] Zhang, W., Cheng X., Hu Y., Yan Y. (2018). Measurement of moisture content in a fluidized bed dryer using an electrostatic sensor array. *Powder Technol.*, 325. 49-57, https://doi.org/10.1016/j.powtec.2017.11.006

[40] Zhou, K., Chen X., Gao W., Shi W., Li J. (2019). "Design and Implementation of Intelligent Management System for Livestock Farm Based on Internet of Things." In *International Conference on Frontier Computing*, 593-603. Springer

DESIGN AND TEST OF REAL-TIME MONITORING SYSTEM FOR NON-CONTACT FERTILIZATION FLOW
/
非接触施肥流量实时监测系统的设计与试验

L.M. ZHOU[1], K. NIU[1], K.K. CHEN[1, 2], Y.W. YUAN[1,*], B. XUE[1] and L.L. WANG[1]　[1]
[1] The State Key Laboratory of Soil, Plant and Machine System Technology, Chinese Academy of Agricultural Mechanization Sciences, Beijing, 100083, China
[2] College of Engineering, China Agricultural University, Beijing, 100089, China
E-mail: yyw215@163.com

Keywords: Fertilizer applicator, Capacitive sensor, CAN bus, Flow monitoring

ABSTRACT

Precision fertilization is one of the important links in the precision agricultural operation system. In recent years, the demand for precision fertilization in facility greenhouse has become more and more urgent. As such, this paper designs an accurate and practical fertilization on-line monitoring system. The system adopts capacitance conversion chip PCAP01 and SCM STM32F103C8T6 to build a capacitance detection circuit. The effective acquisition of differential capacitance sensor microcapacitor signal output under this system is realized. The response relationship between the mass flow and the sensor capacitance output was studied, and a linear fitting model of fertilization was established. According to the prediction, the model determination coefficient was 0.9997. The experiment shows that the system has good adaptability to ambient temperature. The average measurement error is 1.13%, which meets the technical requirements of flow measurement. The capacitive fertilization online measurement system provides an effective way for the on-line acquisition of fertilization flow. It is of great significance for the implementation of high-precision variable fertilization.

摘要

精准施肥是精准农业运营体系中的重要环节之一。近年来，人们对设施温室精准施肥的需求越来越迫切。本文主要设计了一套准确实用的施肥在线监测系统。系统采用电容转换芯片 PCAP01 和单片机 STM32F103C8T6 搭建电容检测电路，实现了差分电容传感器微电容信号输出的有效采集。研究了质量流量与传感器电容输出的响应关系，建立了线性拟合模型。模型确定系数为0.9997，并通过预测验证了模型。实验表明，该系统对环境温度具有良好的适应性，平均测量误差为 1.13%，可以满足流量技术要求。电容式施肥量在线测量系统为施肥机施肥流量的在线获取提供了有效途径，对实现高精度变量施肥作业具有重要意义。

INTRODUCTION

Excessive application of chemical fertilizer has become one of the important factors leading to agricultural non-point source pollution (*Huang, 2016; Hou, 2015; Qi et al, 2016; Zhang et al, 2006*). Precise variable fertilization technologies can apply fertilizer as needed as needed, so as to improve the utilization rate of fertilizer and reduce water and soil pollution (*Yuan et al, 2016; Kuş, 2021*). The online measurement of fertilizer application is critical for high precision variable fertilization (*Dan et al, 2021; Song, 2012*). The biggest difficulty is the complex characteristics of fertilization and non-contact measurement without destroying the drain pipe. The research on online monitoring of the seeding rate of precision seeders is relatively mature (*Wang, 2013; Zhou, 2013; Cheng, 2012; Zhang and Zhao, 2013; Liu, 2013; Wang et al, 2013)*. However, the online measurement of the mass flow of solid particle fertilizer is less. The main measurement methods are the weighing method, indirect measurement of fertilizer discharge axis and the photoelectric method. *Peng and Wei, (2012),* designed a belt-scale-based fertilization test device to measure the flow at the fertilizer discharge port and the fertilizer application rate per unit area.

Zhao et al., (2010), used the dynamic weighing method to obtain the mass flow rate of fertilizer. Combined with location information, the rational application of fertilizer based on spatial distribution was realized.

---

[1]Zhou Liming, Researcher; Niu Kang, Senior engineer; Chen Kaikang, Ph.D.Stud.; Yuan Yan Wei, Researcher;
Xue Bing, Master student; Wang Lili, Senior Engineer

Maet al., (2015), applied the Hall sensors and encoders to measure the rotation cycle and angle of the fertilizer discharge shaft indirectly. This method has simple structure, but the measurement error is relatively large. Some scholars used the photoelectric method to measure the fertilizer flow rate online. *Swisheret al., (2002),* adopted the laser light source, and transmitted the light through a trapezoidal light chamber to the array detection unit with 32 photodiodes. According to the shading intensity of granular fertilizers, the instantaneous flow rate of fertilizers in the air-transported fertilizer machine was obtained. *Griftet al., (2001),* studied the relationship model between the output pulse width of the near-infrared photodetector and the fertilizer flow rate. Under laboratory conditions, the accuracy of the photoelectric flow sensor at different flow rates and densities was realized. *Backet al., (2014),* used the CCD camera to obtain the falling image of the fertilizer particles. Through the image recognition method, the diameter and quantity of fertilizer particles were obtained. Combined with the fertilizer density, the online monitoring of the mass flow rate of fertilizer discharge was realized. The photoelectric imaging method has high measurement accuracy, but it is easily affected by the fertilizer powder covering the probe. The measurement results are poor.

In this paper, an on-line measurement method of fertilizer mass flow rate based on the principle of capacitance detection is presented. A differential capacitive fertilizer flow sensor is designed, and an on-line measurement system of fertilization is constructed. Using nitrogen, phosphorus and potassium fertilizers commonly used in agriculture, the relationship model between fertilizer flow and capacitance response was established and verified. The measurement and display of fertilizer application and the whole-process monitoring of fertilizer pipe clogging were realized.

MATERIALS AND METHODS
MECHANICAL STRUCTURE OF THE FERTILIZER APPLICATOR AND THE PRINCIPLE OF FERTILIZERATION DETECTION

Fertilizer applicator is mainly composed of fertilizer box, fertilizer application device, transmission bearing, controller, soil covering device, press wheel, rotating chain, press spring and seed row box, as shown in Figure 1.
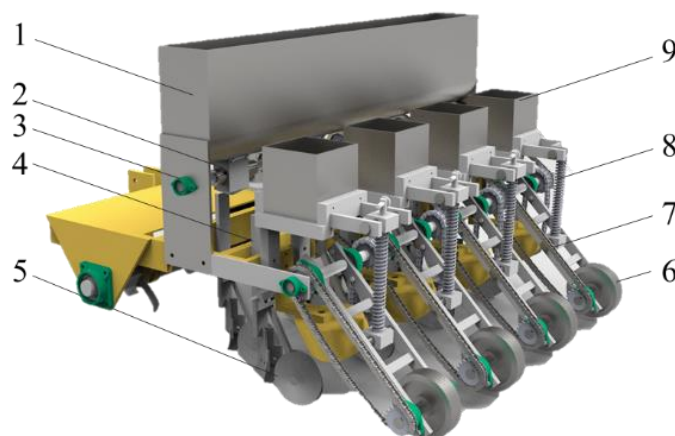
Fig. 1 - Mechanical structure diagram of the fertilizer applicator
1. Fertilizer box; 2. Fertilizer discharger; 3. Transmission bearing; 4.Controller; 5. Press wheel;
6. Ground wheel; 7. Rotary chain; 8. Press spring; 9. Seed metering box

Before using the fertilizer applicator, the sensor needs to be calibrated. Relevant parameters of the machine are calibrated and entered into the database of the circuit control module. Then, the fertilization of the fields is also input into the circuit control module. The fertilizer spreader is driven by an engine and a speed sensor is installed on the driving wheel. The sensor monitors the moving speed of the fertilizer applicator in real time, and transmits the speed information to the circuit control module. The circuit control module analyzes the data, calculates the rotational pulse frequency of the stepping motor and transmits it to the driver. The stepping motor is driven to control the rotational speed of the transmission shaft. Quantitative chemical fertilizer will ensure that it is deeply applied in the fertilizer ditch, so as to achieve quantitative and accurate fertilization.

During the normal operation of the fertilizer applicator, the fertilizer falls freely in the closed fertilizer pipe. Due to different dielectric constants of fertilizer and air, the equivalent dielectric constant of the material between the plates will change. When the fertilizer falls through the capacitor plate, it causes a change in the output capacitance. At this time, the change of the sensor output capacitance is:

$$\Delta C = C - C_0 = \frac{s\,(\varepsilon_1 - \varepsilon_2)}{\rho_1 dV} m_1 \tag{1}$$

where ΔC is the capacitance change when the fertilizer passes through the sensor, F; S is the plate area, m²; ε_1 is the dielectric constant of the fertilizer, F/m; ε_2 is the air dielectric constant, F/m; ρ_1 is the fertilizer density, kg/m³; D is the plate spacing, m; V is the detection field volume between the plates of the capacitive sensor, m³, and m_1 is the mass of fertilizer in the sensor, kg.

On the basis of obtaining fertilizer flow rate, the amount of fertilizer per unit area can be further obtained according to the working width and advancing speed of the fertilizer applicator.

$$M(t) = \frac{Q(t)}{DV(t)} \tag{2}$$

where $M(t)$ is the fertilizer applied per unit area, kg/m²; D is the operation width of the fertilization machine and tool, m; $V(t)$ is the forward speed of the machine and tool, m/s; $Q(t)$ is the mass flow rate of the fertilizer, kg/s.

CONSTRUCTION OF SENSOR TEST SYSTEM

The online detection system of fertilizer amount is mainly composed of capacitive fertilizer flow sensor, forward speed sensor and vehicle-mounted terminal, as shown in Figure 2.
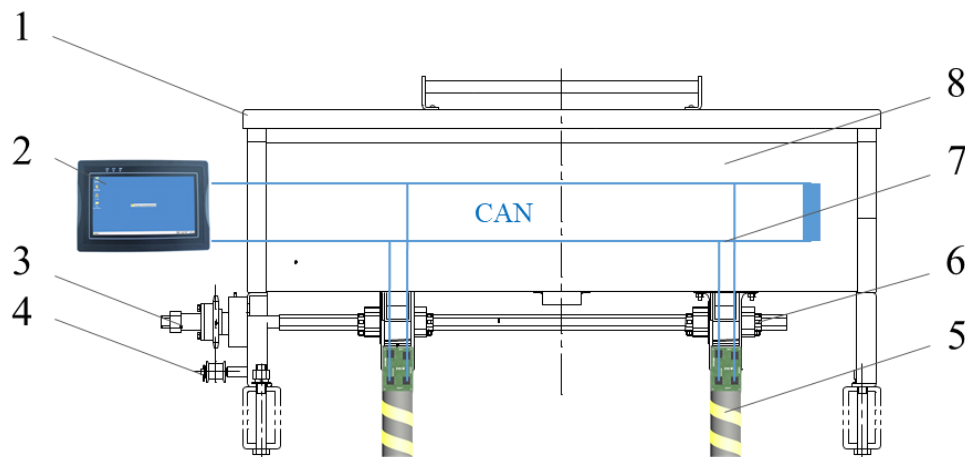

Fig. 2 - Structure diagram of fertilizer application quantity detection system
1. Frame; 2. Vehicle display terminal; 3. Transmission shaft; 4. Speed sensor;
5. Flow sensor; 6. Fertilizer exhauster; 7. CAN bus; 8. Fertilizer box

The system adopts the Controller Area Network (CAN) bus structure, which can realize the distributed on-line detection of each fertilization pipeline and facilitate the node expansion of fertilizer applicators with different widths. The capacitive fertilizer flow sensor is installed on the fertilizer discharge disk to obtain the online mass flow rate of fertilizer. The forward speed sensor is located on the forward wheel to obtain the forward speed of the machine and tools. The on-board terminal is located in the cab. It can receive the real-time information through the built-in CAN bus adaptation module, and display the fertilizer after information processing. In addition, the fertilizer flow sensor can judge the clogging state of the pipeline according to the state of fertilizer, and display the alarm state through the alarm light on the sensor.

TYPES AND SELECTION OF FERTILIZER DRAINERS

The commonly used fertilizer dischargers include external groove wheel fertilizer dischargers, planetary wheel fertilizer dischargers and spiral fertilizer dischargers. Sheave spreaders are especially common in seeding spreaders because of their simple structure and easy cleaning. When the outer groove wheel fertilizer discharger works, the groove wheel rotates with the rotation of the fertilizer discharge shaft. The fertilizer is filled in the groove wheel and accompanied by the rotation of the wheel. The outermost layer of fertilizer is discharged from the sheave box by friction and conveyed to the fertilizer ditch through the discharge pipe. The fertilizer can be adjusted by adjusting the effective working length of the sheave, which can be used for fertilizer removal in different working environments.
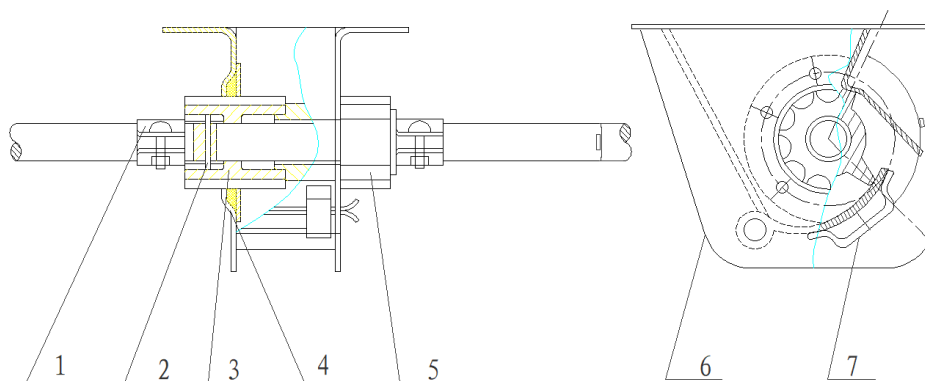
Fig. 3 - External grooved wheel fertilizer spreader
1. Clamp; 2. Shaft pin; 3.Fertilizer wheel; 4.Taper pin; 5. Block box; 6. Fertilizer box; 7. Fertilizer tongue

STRUCTURAL DESIGN OF THE FLOW SENSOR

According to the preliminary experimental results, the structure of the fertilizer flow sensor has been improved this year, mainly focusing on the systematic improvement of the sensor from the plate structure and overall IP protection. The new fertilizer flow sensor adopts the spiral plate structure, and the internal fertilizer guide tube is made by 3D printing.

In order to ensure the consistency of the structure parameters of the spiral plate, the guide plate is directly designed and pasted on the guide tube, so that the guide plate is pasted along the guide structure. In addition, PCB mounting table is designed on the fertilizer guide tube and connected to the plate by short thread. The integrated design of capacitor plate, PCB board and fertilizer guide tube can reduce the influence of stray capacitance on the test results.

In order to realize the IP67 protection design of the sensor, the shell is processed by CNC (Computerized Numerical Control Machine) as a whole. Meanwhile, the sealing groove is designed on the upper and lower end cover, and the sealing ring is matched to meet the protection requirements.
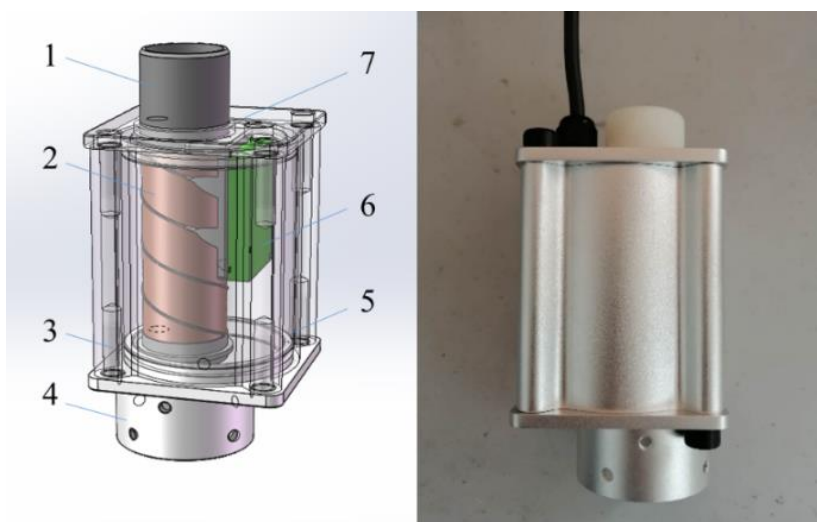
Fig. 4 - Structure diagram and physical object of flow sensor of the screw fertilizer
1. Fertilizer input pipe; 2. Spiral capacitance plate; 3. Fixing bolt; 4. Fertilizer output pipe;
5. Alloy housing; 6. PCB circuit board; 7. Fixed bushing;

MICROCAPACITOR SIGNAL CONDITIONING CIRCUIT

Capacitor signal conditioning circuit is the key to obtain high-precision capacitor signals. The commonly used microcapacitor detection circuit mainly includes a DC charge-discharge conversion circuit, an AC capacitive conversion circuit, and a microcapacitor detection circuit based on capacitor digital conversion (*Zhou et al, 2010; Jin et al, 2019; Jin et al, 2020; Jin et al, 2018; Zhou et al, 2017; Bergeijka et al, 2001; Zhou et al, 2014*). Among them, the capacitive digital conversion method based on integrated detection chip is widely used (*Bai et al, 2020; Xiong et al, 2020*).

When the fertilizer passes through the capacitive sensor, the capacitance change is 0.1pF. In order to ensure the accuracy and reliability of the measurement, this paper uses the capacitance-to-digital conversion method to design the conditioning circuit of the sensor. The capacitive-to-digital conversion chip PCAP01 and the microcontroller STM32F103C8T6 were used to form a microcapacitor signal measurement circuit.

PCAP01 is a capacitance-to-digital conversion chip launched by German ACAM Company with DSP processing unit, which is specially used for microcapacitor measurement. The TDC conversion module and environmental compensation function are integrated on the chip, with the highest measurement precision and frequency up to 6aF and 500 kHz, respectively. Furthermore, the protocol control pin IIC_EN of PCAP01 is grounded and SPI transmission mode is selected. In order to eliminate the influence of environmental factors on the measurement results as much as possible, PCAP01 takes the ratio of the sensor capacitance to the reference capacitance as the calculation result. The measurement result is output as a 24bit digital signal, which is convenient for subsequent conversion processing. Since the measurement result of PCAP01 is the output ratio relative to the reference capacitance, the measurement result needs to be converted.

The conversion formula is as follows:

$$C = \frac{C_{mear}}{2^{21}} \times C_{ref} \tag{3}$$

where C is the measured capacitance after conversion, pF; C_{mear} is the measured output ratio, dimensionless; C_{ref} is the reference capacitance value, pF.

When the electrode plate of the fertilizer flow sensor is connected to PCAP01, the drift connection mode is adopted. Electrode plate 1 is connected to PC2; electrode plate 2 is connected to PC3, and electrode plate 3 is connected to PC4. At the same time, the ceramic capacitors of the same order of magnitude as the basic capacitance of the sensor are connected to PC0 and PC1 as the reference capacitances.

SIGNAL ACQUISITION AND PROCESSING

The vehicle-mounted terminal is the hardware platform for the software operation of the fertilizer rate detection system. It is responsible for receiving the information and forward speed of each sensor in real time, so as to complete the calculation and statistics of the fertilizer rate at each pipeline. Taking the X86 architecture based Atom motherboard as the core, the terminal integrates the solid state storage module, data communication module, LIQUID crystal display and input and output module. The real-time data on the bus is obtained through the built-in USB-CAN communication adaption module. The terminal can be well compatible with Windows operating system, and is convenient for the development of upper computer software.

Under the Keil MDK software development environment, C language is used to write part of the software MCU (Microcontroller Unit). The software design adopts the modular programming method, and its functions mainly include system initialization, PCAP01 firmware writing CAN module initialization, capacitor data acquisition and preprocessing. Its program flow is shown in Figure 5.

After the system is on, the single-chip microcomputer executes the initialization program to complete the configuration of each IO port. After that, the firmware information of internal EEPROM is read, and the SRAM region inside PCAP01 is written through SPI bus to enter the configuration state of PCAP01, where the sampling rate is configured at 10kHz and the blocking alarm threshold is 0.5PF. When the capacitance measurement is completed, the MCU reads the results of PCAP01 to obtain the capacitance information. On the one hand, the data is sent to the on-board terminal through CAN bus, and the real-time capacitance is compared with the blocking threshold. Once the blocking threshold is exceeded, the corresponding IO port is driven by MCU, so that the alarm indicator light is always on to realize the local alarm.

The upper computer software was developed by LabWindows/CVI 2012 of National Instrument (NI). Lab windows software adopts interactive programming technology and integrates powerful function library and graphical interface control, which is suitable for the development of measurement and control system. The software functions of the developed fertilizer rate detection system mainly include communication parameter setting, system operation, data processing, data display and playback.

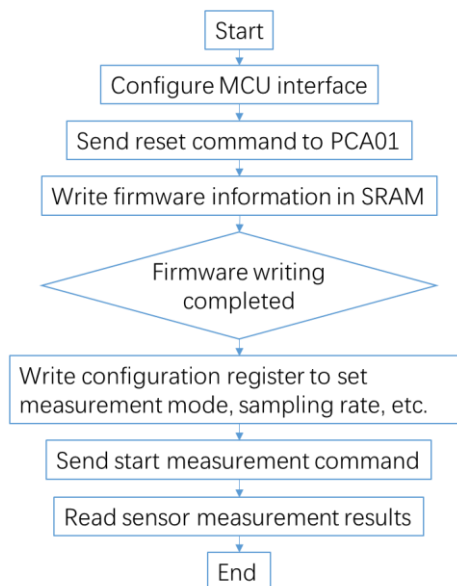The software interface is shown in Figure 5.

Fig. 5 - Flow chart of MCU software program

After the software receives the real-time data sent by the sensor through CAN bus, the capacitance value is calculated and the filtering algorithm is used to filter the acquired original capacitance. According to the pre-calibrated capacitor-mass flow signal, the mass flow rate of fertilizer in the drainage tube is obtained. In order to ensure the real-time performance of data acquisition and display, multi-thread method is adopted to carry out data acquisition, processing and display. The main thread is used to create, display and run the interface. The data acquisition thread is used to complete capacitor information acquisition and data processing, and the display thread is used to complete the display and playback of all data.

Granular fertilizer and compound fertilizer N-P commonly used in agriculture were used in the experiment $_2O_5$-K_2. The ratio of O content is 24-14-9, and the fertilizer particles are uniform without agglomeration. In order to check the reliability and accuracy of the capacitive fertilizer rate sensor, the fertilizer rate measurement experiment was carried out on the fertilization test bench. The test bed was mainly composed of fertilizer box, fertilizer discharge shaft, servo motor, reducer and fertilizer discharge pipe. The test bed was driven by a servo motor to rotate the fertilizer discharging shaft. The input voltage of the analog quantity under the speed control mode of the servo motor can be changed by the upper computer to realize the automatic control of the motor speed. Then the speed of the fertilizer discharging shaft can be continuously adjusted to achieve on-line adjustment.

RESULTS
INFLUENCE OF TEMPERATURE ON FERTILIZER FLOW SENSOR

Ambient temperature is one of the important factors affecting the performance of the capacitance sensor. Considering the field working environment of the detection system, the temperature of the fertilizer rate sensor was tested in the range of 15-55°C.

First, the test sensor was put into the thermostatic control box (type 202FBX-0, Shanghai Lishu Instrument Co., LTD., ±1°C). Then the measurement system was started and preheated for 5 min to enter the detection state after the measurement data was stable. Taking 5°C as the change gradient, the temperature inside the temperature control box was adjusted to 55°C. After each adjustment, wait for 5min after the temperature display was stable. The detected and reference capacitances and the current actual temperature were recorded, and the influence relationship between the differential capacitance (the difference between the detected and reference capacitance) and the temperature were obtained. The test results are shown in Figure 6.

From Figure 6, when the temperature gradually rises from 15°C to 55°C, the difference between the sensor and its zero-base capacitance increases from 0.02 pF to 0.33 pF. Compared with the initial value of the detection capacitance, the change rate is close to 8%. However, the difference between the detection and reference capacitances is always in the range of 0-0.019 pF. This indicates that differential capacitance sensing can effectively improve the influence of ambient temperature on the measurement, which is conductive to improving the accuracy of measurement.
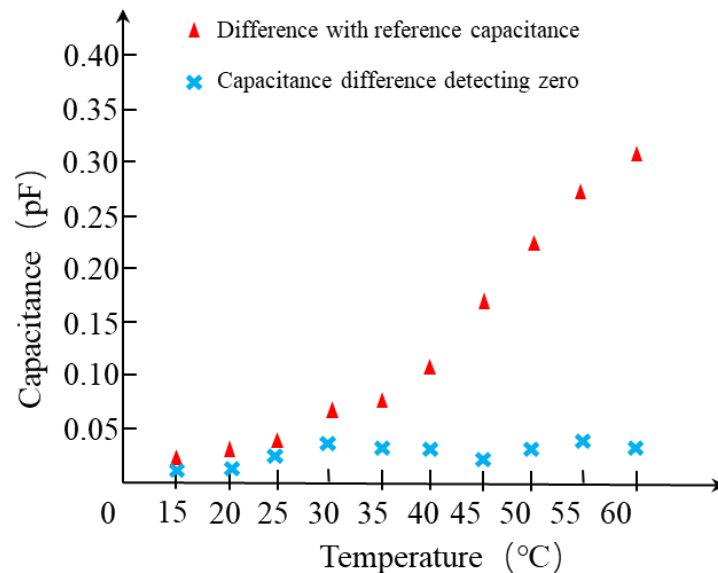
Fig. 6 - Influence of temperature on capacitance output

INFLUENCE OF FERTILIZATION ON THE FERTILIZER FLOW SENSOR

A feeding box is placed at the fertilizer outlet of the measuring device, and the sensor calibration is carried out by the weighing method. The rotation speed of the fertilizer discharging shaft was set at 20 r/min. The rotation time of the fertilizer discharging shaft was controlled by the upper computer to obtain different fertilizer discharge according at different operation time. After each fertilizer discharge, an electronic balance (SL4001, Shanghai Minqiao Electronic Instrument Factory, 4000±0.1 g) was used to weigh the fertilizer in the receptacle. The cumulative capacitance value of the difference between the measured and reference capacitance sensors was recorded at the same time. Calibration tests were performed for each fertilization by the Matlab software. The response curve of fertilizer mass and capacitance value was obtained as shown in Figure 7.
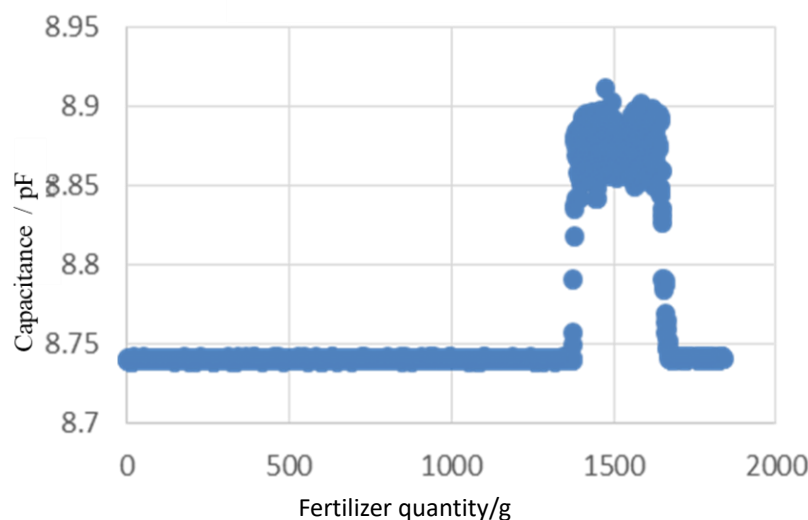
Fig. 7 - Signal response of the compound fertilizer passing through the sensor

It can be seen that when the fertilizer passes through the sensor, its capacitance value will change from 8.75 pF to 8.87 pF. Through linear fitting and normalization, the relationship model between capacitance and mass obtained is as follows:

$$Q(t) = 20.644C(t) + 2.6815 \qquad (4)$$

It can be seen that there is a linear relationship between the capacitive output value of the granular fertilizer flow sensor and the fertilizer application. With the increase of fertilizer application, the capacitive output will increase correspondingly, and the coefficient determined by the model is $R^2=0.9997$.

VERIFICATION OF THE FERTILIZATION TESTING SYSTEM

In order to verify the accuracy of the fertilization test system under different discharge speed, the system was tested at Shengfa Family farm in Dubolan Town, Qingdao from September 18 to 20, 2020.

Fig. 8 - The developed prototype of granular fertilizer flow sensor

In order to verify the accuracy of the fertilization detection system under different discharge flows, the rotating speed of the fertilizer discharging shaft was set as 15 r/min, 21 r/min, 27 r/min and 31 r/min, respectively. A feeding dish was placed under the discharge port to compare the measured value of the fertilizer obtained by the detection system with the actual weighing value of the fertilizer in the receiving dish. The results are shown in Table 1.

Table 1

Test results of the fertilization detection system

Rotation rate (r/min)	Measuring mass (g)	Real mass (g)	Relative error (%)
15	849.2919	864	1.70
	857.756	857	0.09
	345.5783	333	3.78
	643.2648	642	0.20
21	766.0966	776	1.28
	949.4153	961	1.21
	1424.021	1417	0.50
	1799.742	1786	0.77
27	1232.238	1231	0.10
	328.2374	327	0.38
	906.4758	913	0.71
	1919.064	1928	0.46
31	663.4959	650	2.08
	1223.774	1201	1.90
	2191.152	2157	1.58
	1901.723	1875	1.43

It can be seen from Table 1 that the system can accurately measure the fertilizer under different speed of fertilizer discharge. The average measurement error is 1.13%, which meets the actual requirements. Therefore, it is feasible to measure the fertilizer online by the capacitance method.

CONCLUSIONS

1) In this paper, a differential capacitive fertilizer flow sensor based on ring pipelines was designed. A micro-capacitance detection circuit composed of STM32F103C8T6 and PCAP01 was built, and a fertilizer amount detection system based on LabWindows/CVI was constructed to realize the online detection of fertilizer.

2) The response relationship between the mass flow and the sensor capacitance output was studied. The linear fitting models of three fertilizers were established, and the model determination coefficients were 0.9889, 0.9898 and 0.9935, respectively. Moreover, the model was predicted and verified.

3) The test shows that the fertilization detection system has good adaptability to the environmental temperature. It can accurately measure the fertilization and timely alarm the failure of the fertilizer pipe clogging. The maximum measurement error of the fertilization was 3.75%, which can meet the actual production needs.

This paper mainly discusses the feasibility of using capacitive sensing method to measure the fertilizer online. Currently, the moisture content of fertilizers when leaving the factory is required to be no more than 1%. Therefore, the influence of changes in the moisture content of fertilizer on the sensor is not considered in the preliminary test. In the actual production, the condensation and agglomeration of fertilizer will occur, indicating that the moisture content will change to a certain extent. In the future work, the change of moisture content of fertilizer and the influence of environmental humidity on the sensor measurement should be considered to improve the adaptability of the detection system.

ACKNOWLEDGEMENT

REFERENCES

[1]   Back, S. W., Yu, S. H., Kim, Y. J., Chung, S. O., Lee, K. H., (2014). An image based application rate measurement system for a granular fertilizer applicator. *Transactions of ASABE*, *57*(2), 679-687, 2014. Doi: 10.13031/trans.57.10605

[2]   BaduaS.A., Sharda A., Strasser R., CiampittiI.(2021). Ground speed and planter downforce influence on corn seed spacing and depth. *Precision Agriculture*, (22), 1154-1170. Doi:10.1007/S11119-020-09775-7.

[3]   Bergeijka J., Goense D., WilligenburgaL.G., Speelman L., (2001). PA-Precision Agriculture: Dynamic Weighing for Accurate Fertilizer Application and Monitoring. *Journal of Agricultural Engineering Research*, *80*(1), 25-35. https://doi.org/10.1006/jaer.2001.0714

[4]   Cujbescu D., Gageanu I., Persu C., Matache M., Vladut V., Voicea I., Gigel, Paraschiv G., Biriş S.S., Ungureanu N., Voicu Gh., Ipate G., (2021). Simulation of Sowing Precision in Laboratory Conditions. *Appl. Sci.* 2021, 11(14), 6264, https://doi.org/10.3390/app11146264

[5]   Emrah K. (2021). Field-scale evaluation of parameters affecting planter vibration in single seed planting. *Measurement*, 184,109959. doi:10.1016/J.MEASUREMENT.2021.109959.

[6]   Grift, T. E., Walker, J. T., Hofstee, J. W., (2001). Mass flow measurement of granular materials in aerial application part 2: experimental model validation. *Transactions of the American Society of Agricultural Engineers*, *44*(1): 27-34, doi:10.13031/2013.2300

[7]   Hou H.D., (2015). *Application and popularization of maize no tillage precision seeder*. Jilin Agricultural University.

[8]   Huang J.Y., (2016). Design of the fertilizing and seeding module of the small multifunctional agricultural machinery. *Modern Machinery*, (3), 53-57, DOI: 10.13667/j.cnki.52-1046/th.2016.03.017

[9]   Jin X., Chen K.K., Ji J.T., Zhao K.X., Du X.W., Ma H., (2019). Intelligent vibration detection and control system of agricultural machinery engine. *Measurement*, 145, 503-510. https://doi.org/10.1016/j.measurement.2019.05.059

[10]   KimB., JangJ., KimS., Hwang S., ShinM. (2021). Design of an ICT convergence farm machinery for an automatic agricultural planter. *International Journal of Computational Vision and Robotics*. 11(4), 448-460. doi:10.1504/IJCVR.2021.116561.

[11]   Liu H.M., (2013). Discuss the development status of corn precision seeding machinery. *Beijing Agriculture*, (6), 141.

[12]   Ma X.L., Yi S.J., Zhao B., Gao J., Ren S.H., Liu K., (2015). Research on fertilization operation performance of the real time monitoring system of corn precision seeder. *Journal of Agricultural Mechanization Research*, *37*(12), 20-22. DOI: 10.13427/j.cnki.njyi.2015.12.005

[13]   Ovtov V.A., Mitin K.M., Tsurenko P.D.(2021). The pulse stepless onion planter gear reducer. *IOP Conference Series: Earth and Environmental Science*, 868, 012009. doi:10.1088/1755-1315/868/1/012009.

[14]   Peng B., Wei M., (2012). The design of a small multifunctional precision planter. *Science and Technology Information*, (33), 168-169.

[15]   Qi X.Y., Zhou Z.Y., Yang C., Luo X.W., Gu X.Y., Zang Y., Liu W.L., (2016). Design and experiment of key parts of pneumatic variable rate fertilizer applicator for rice production. *Transactions of the Chinese Society of Agricultural Engineering*, 32(6), 20-26+316. DOI: 10.11975/j.issn.1002-6819.2016.06.003

[16]   Song G.P., (2012). Research and design of 2BMS-2 double-row no-tillage precision seeder. *Agricultural Development and Equipments*, (6), 79-80+95.

[17]   Swisher D.W., Borgelt S.C., Sudduth K.A., (2002). Optical sensor for granular fertilizer flow rate measurement. *Transactions of the ASAE*, 45(4), 881-888. Doi: 10.13031/2013.9934

[18]   Wang J.L., Wang, X.J., Cao, S.L., Wang, M., (2013). The Status and Development Trend of Cultivator and Fertilizer Mechanization Technique. *Journal of Anhui Agricultural Sciences*, *41*(4), 1814-1816+1825.DOI: 10.13989/j.cnki.0517-6611.2013.04.110

[19]   Wang K., (2013). *Multi-function Wheat Planter Design and 3D Modeling*. Shandong Agricultural University.

[20]   Sawant C.P., Singh K.P., Singh R.S., Lakaria BrijLal, Patel Anurag, Gupta Ajita, Kumar Manoj. (2020). Comparative evaluation of maize planters in conservation agriculture under black cotton soil of central India. *BhartiyaKrishi Anusandhan Patrika*. (35), 39-44.doi: 10.18805/BKAP201.

[21]   Strasser R., BaduaS. A., Sharda A., Rothmund M..(2021). Development of a test stand to quantify the response of a planter's automatic downforce control system. *Transactions of the ASABE. 64*(5), 1533-1543, doi:10.13031/TRANS.14047.

[22]   Yuan L.H., Gu D.D., Wang W.Z., Zhong D.F., Wang M.S. Chen J., (2016). Design and Experiment of Variable Rate Fertilization System of Tri-wheel High Frame Operation Vehicle. *Transactions of the Chinese Society for Agricultural Machinery*, *47*(s1), 170-175. DOI: 10.6041/j.issn.1000-1298.2016.S0.026

[23]   Yuan Y.W., Li S.J. Fang X.F., Wei L.G., Liu Y.C., (2013). Decision support system of N, P and K ratio fertilization. *Transactions of the Chinese Society for Agricultural Machinery*, *44*(8), 240-244+223. DOI: 10.6041/j.issn.1000-1298.2013.08.041

[24]   Zhou, L.M., Zhang, X.C., Yuan, Y.W., (2010). Capacitive Seed rate Sensor of Wheat Planter. *Transactions of the Chinese Society of Agricultural Engineering*, *26*(10), 99-103. doi:10.3969/j.issn.1002-6819.2010.10.015

[25]   Zykin E., Kurdyumov V., Lazutkina S., (2021). Substantiation of the Absolute Velocity of the Soil Thrown by a Spherical Disc of the Roller of a Ridge Roller Planter. *MATEC Web of Conferences*, (346), 03101. doi:10.1051/MATECCONF/202134603101.

DESIGN AND EXPERIMENT OF FINGER-CHAIN GRAIN LIFTER FOR RATOON RICE STUBBLE ROLLED BY MECHANICAL HARVESTING
/
再生稻机收碾压稻茬扶正机设计与试验

Xiongfei CHEN, Xuehai LIANG, Muhua LIU, Jiajia YU, Huilong LI, Zhaopeng LIU [*)] [1]
Key Laboratory of Modern Agricultural Equipment of Jiangxi Province, Nanchang, Jiangxi 330045, China
E-mail: 314134582 @qq.com

ABSTRACT

For rice ratooning, the lateral bud germination of the rice stubble after the first harvesting can be used to continue the next growing season, but the first harvesting machinery will crush and damage the rice stubble, resulting in the reduction of yield in the ratooning season. Lifting the rolled stubble can reduce this loss, and thus a double-chain finger grain lifter was designed in this study. Then, a kinematic model and motion trajectory curve of the grain lifter was established. The influence law of the chain speed, chain spacing and the number of fingers of the rear lifting chain was determined. Furthermore, taking into account the success rate and the rate of secondary damage of the lifting, a full-factor bench test was performed. The best operating characteristics of the grain lifter are: chain speed of 345 r/min, adjacent chain spacing of 300 mm, and the number of gears and fingers on the rear lifting chain of 3. The success rate and the secondary damage rate of the lifting is 90.05% and 1.72%, respectively. A field verification test was conducted, with an average success rate of 55%. The results of this study can provide valuable reference for the lifting technology of rolled rice stubble and promote the whole mechanized production of ratoon rice.

摘要

再生稻可利用头季收割后稻茬的侧芽再萌发继续完成下一个生长季，但头季稻机械收获会碾压和损伤稻茬造成再生季减产。扶正被碾压的稻茬能够减小这种损失。为此本研究设计了双链排扶正装置，构建了扶正齿爪运动学模型及其运动轨迹曲线，确定了影响扶正装置工作性能的主要因素为链排转速、相邻链排间距和后扶正链排齿爪个数；进而以扶正成功率和扶正二次损伤率为评价指标，开展全因素台架试验，确定扶正装置最优工作参数组合为链排转速345r/min、相邻链排间距300mm和后扶正链排齿爪数3个，其扶正成功率为90.05%，扶正二次损伤率为1.72%；通过田间试验验证了田间平均扶正成功率为55%。本研究结果可为再生稻机收碾压稻茬扶正装置研发提供参考。

INTRODUCTION

Rice ratooning is a kind of rice production mode, which uses the lateral bud germination characteristics of rice stubble after harvesting to promote lateral bud growth, regenerated tillers and earings again through irrigation and fertilization, so as to achieve the purpose of one planting and two harvests. Agronomic experts labeled the rice varieties with strong lateral bud germination ability as ratoon rice and optimized their cultivation. *(Mamun et al., 2019; Munda et al., 2009; Faruq et al., 2014; Bahar et al., 1977; Shamiul et al., 2008; Thi et al., 2017)* However, in the mechanized production of ratoon rice, its mechanical harvesting in the first season will crush and seriously damage the stubble, resulting in the reduction of the second harvest yield, which is one of the main problems affecting the mechanized production of ratoon rice and preventing its large-scale adoption and utilization, at present.

This problem was addressed by the relevant scholars through research on the damage reduction technology and equipment for harvesting rice, both in terms of improving or redesigning the special harvester for ratooning rice and harvesting path planning. For the new type of rice combine harvester, the academic team of Luo Xiwen of South China Agricultural University *(Zeng et al., 2018a; Zeng et al., 2018b; Yang et al., 2019)* explored how to minimize the rolled rate by shifting the distance between walking wheels and by adopting narrow wheels with large ground gaps.

Chen Xiongfei, Associate Professor; Liang Xuehai, Postgraduate; Liu Muhua, Professor; Yu Jiajia, Lecturer;
Li Huilong, Postgraduate; Liu Zhaopeng, Lecturer

The narrow wheel and high-ground gap ratooning grain header, broad full-tracked double-header ratooning rice harvester, and double-channel feeding ratooning rice harvester were created by Professor Zhang Guozhong of Huazhong Agricultural University *(Zhang et al., 2016; Lu et al., 2017; Fu et al., 2020)*. The ratooning rice harvester was lightened by Professor Li Yaoming of Jiangsu University *(Wang et al., 2021; Huang et al., 2020)* to prevent harm to rolled rice stubble. Path planning navigation and machine vision navigation were used by Shi Huojie and Guo Hanlin from Fujian Agriculture and Forestry University *(Guo et al., 2016)* to minimize the stubble rolled rate of ratoon rice harvesting machines. However, due to constraints imposed by planting patterns, agronomic requirements, working environment, and other factors, there are few application reports in actual production, and the technical equipment for harvesting and rolled rice stubble in the first season of ratoon rice requires additional study.

In order to address the aforementioned issues, this paper developed a double-layer chain gear-finger grain lifter based on the single-layer chain finger grain lifter previously designed for rice ratooning *(Zhang, 2019)*, and the kinematic model and motion trajectory curve were constructed during the working process of lifting finger. To better understand how the grain lifter affects the harvesting of rice stubble, we conducted bench and field experiments in order to identify the optimal combination of working parameters. The results of the experiment will serve as a guide for future research and development of rice stubble-related grain lifter for rolled ratoon rice machine harvesting, as well as for the widespread popularization and application of rice ratooning in suitable areas.

MATERIALS AND METHODS
Overall structure and working principle

The double-chain finger grain lifter used for lifting the ratooning rice stubble rolled by harvesting process is primarily composed of the following components: front lifting chain finger mechanism, rear lifting chain finger mechanism, lifting chain finger transmission mechanism, adjacent chain spacing adjustment, finger buried angle adjustment mechanism and other components as necessary. The lifting unit was formed by the front and rear lifting chain, gear unit, fingers, as illustrated in figure 1. Lifting chain and finger, driven sprocket, active sprocket, rubber block, finger retraction setting assembly, finger unfolding guide, gear finger arc transition ejection mechanism, chain support plate, etc., as illustrated in figure 2, are the major components of the grain lifter.
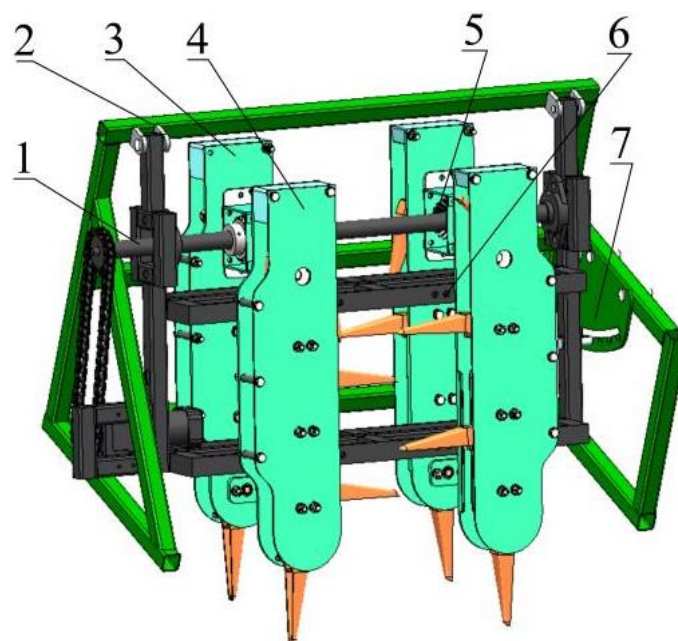

Fig. 1 - **Structure diagram of double-chain finger grain lifter**
1. Power input shaft; 2. Lifting rack; 3. Front lifting chain finger mechanism; 4. Rear lifting chain finger mechanism;
5. Lifting chain finger transmission mechanism; 6. Chain spacing adjustment mechanism;
7. Finger buried angle adjustment mechanism

External power drives the power input shaft to rotate, which drives the axle drive bevel pinion in the lifting chain finger transmission mechanism to rotate, and then drives two groups of passive bevel gears in the lifting chain finger transmission mechanism to rotate during the lifting operation. In this way, the chain in the front and rear lifting chain finger mechanism and the lifting fingers mounted on the chain are driven to rotate, so as the rolled rice stubble lifting operation may be accomplished.

According to different operations, the rotation of the chain in a cycle can be divided into five stages: unfolding process, reeling process, lifting process, retraction process and hollow travel process. As shown in Figure 2, the unfolding and reeling process refers to the process in which the fingers pass around the bottom driven sprocket *2* and start moving up along the chain *3*. In this possess, under the action of transition component *8*, the fingers change from the tangential direction of the chain to the outer normal direction and roll up the lodging stubble. The lifting process is that after the reeling stage, under the action of the unreeling guide rail *7*, the fingers always keep the outward normal direction when moving upward along the chain, so as to ensure that the lodging stubble is lifted until it is separated from the end of the stubble. The fingers continue to move upward along the chain and enter the retraction process until it disengages from *7* guide rail. Then under the action of gravity, the fingers rotate downward from the outer normal direction to the tangent direction. When the fingers continue to go up around the upper drive sprocket *4* of the chain, it maintains the tangent direction under the constraint of the *5,* rubber block. After that, the fingers go around the upper sprocket and move down under the drive of the chain to enter the hollow travel process. During the hollow travel, the fingers still maintain the tangential direction of the chain until it encounters the transition component *8*, and then enters the reeling process. Since then, a lifting cycle is completed.
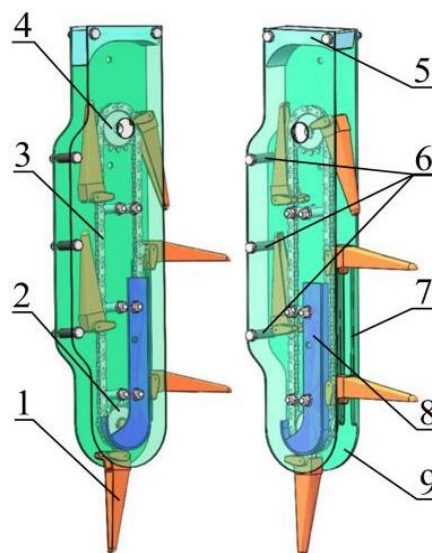
Fig. 2 - **Structure diagram of lifting chain finger mechanism**
1. Lifting finger; 2. Driven sprocket; 3. Chain; 4. Drive sprocket; 5. Rubber block; 6. Finger retraction setting assembly;
7. Finger unfolding guide; 8. Finger ejection transition component; 9. Chain support plate

KINEMATIC ANALYSIS OF LIFTING FINGERS

Taking the ground projection point of the driven sprocket center as the origin O, taking the forward direction of the machine as the X axis, and the vertical upward direction of the O point as the Z axis, a spatial rectangular coordinate system is established, as shown in the Figure 3. Among them, the inclination angle of chains is θ; the centers of driving sprocket and driven sprocket of rear chains are O_1 and $O_{1'}$, respectively. The center of driving sprocket and driven sprocket of front chains are O_2 and $O_{2'}$, respectively. The distance between the centers of driving sprocket and driven sprocket is L; The distance between the driven sprocket center and the rotation center of finger on the meshing sprocket is R_1; the distance from any point A on the lifting finger to the rotation center of the finger is R_2; the distance from point A to the center of the driven sprocket is R; the distance between the center of the driven sprocket and the ground is L_1; the distance between the front and rear chains in the x-axis direction is L_2. The forward speed is VM, the chain speed is N, and the chain speed is VT.

Furthermore, if the analysis object is any point A on the lifting finger, the one cycle rotation of point A around the chain is recorded as a cycle, and the duration of one cycle rotation is specified as T, a is the number of cycles of finger rotation. A motion trajectory equation of point A is then established by t_1, t_2, t_3, t_4, and t_5 being the total time of the lifting finger unfolding process, reeling process, lifting process, retraction process, and the hollow travel process, as shown in the formula (1)-(5).
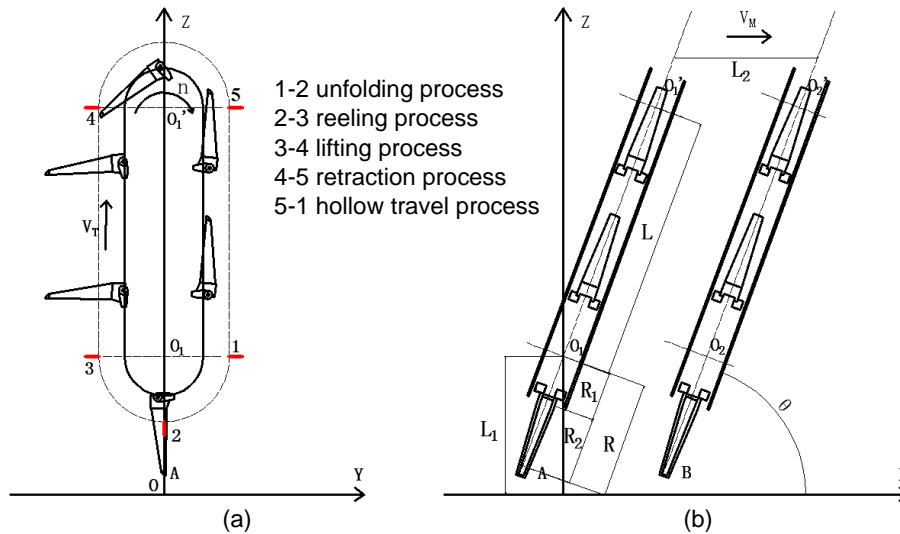

Fig. 3 - Kinematic model of working process
a) Front view of lifting chain; b) Diagram of location relationship for the front and rear chain location

During the unfolding process, the motion trajectory equation of point A is as follows:

$$\left.\begin{cases} X_A = \big[R_2\cos[12n[t_1-\lambda_5]] - R_1\sin[6n[t_1-\lambda_5]]\big]\cos\theta + V_m t_1 \\ Y_A = R_2\sin[12n[t_1-\lambda_5]] + R_1\cos[6n[t_1-\lambda_5]] \\ Z_A = L_1 - \big[R_2\cos[12n[t_1-\lambda_5]] - R_1\sin[6n[t_1-\lambda_5]]\big]\sin\theta \end{cases}\right\} \; t_1 \in (\lambda_5,\lambda_6) \tag{1}$$

During the reeling process, the motion trajectory equation of point A is as follows:

$$\left.\begin{cases} X_A = -R\cos[6n(t_2-\lambda_1)]\cos\theta + V_m t_2 \\ Y_A = -R\sin[6n(t_2-\lambda_1)] \\ Z_A = L_1 - R\cos[6n(t_2-\lambda_1)]\sin\theta \end{cases}\right\} \; t_2 \in [\lambda_1,\ \lambda_2] \tag{2}$$

During the lifting process, the motion trajectory equation of point A is as follows:

$$\left.\begin{cases} X_A = V_T[t_3-\lambda_2]\cos\theta + V_m t_3 \\ Y_A = -R \\ Z_A = V_T[t_3-\lambda_2]\sin\theta + L_1 \end{cases}\right\} \; t_3 \in (\lambda_2,\lambda_3] \tag{3}$$

During the retraction process, the motion trajectory equation of point A is as follows:

$$\left.\begin{cases} X_A = \big[R_1\sin[6n[t_4-\lambda_3]] + R_2\sin[3n[t_4-\lambda_3]] + L\big]\cos\theta + V_m t_4 \\ Y_A = -\big[R_1\cos[6n[t_4-\lambda_3]] + R_2\cos[3n[t_4-\lambda_3]]\big] \\ Z_A = \big[R_1\sin[6n[t_4-\lambda_3]] + R_2\sin[3n[t_4-\lambda_3]] + L\big]\sin\theta + L_1 \end{cases}\right\} \; t_4 \in (\lambda_3,\ \lambda_4) \tag{4}$$

During the hollow travel process, the motion trajectory equation of point A is as follows:

$$\left.\begin{cases} X_A = \big[L + R_2 - V_T[t_5-\lambda_4]\big]\cos\theta + V_m t_5 \\ Y_A = R_1 \\ Z_A = \big[L + R_2 - V_T[t_5-\lambda_4]\big]\sin\theta + L_1 \end{cases}\right\} \; t_5 \in (\lambda_4,\ \lambda_5] \tag{5}$$

In the formula (1)-(5),

$$\lambda_1 = aT, \quad \lambda_2 = \frac{\pi R_1}{2V_T} + aT, \quad \lambda_3 = \frac{\pi R_1 + 2L}{2V_T} + aT, \quad \lambda_4 = \frac{3\pi R_1 + 2L}{2V_T} + aT, \quad \lambda_5 = \frac{3\pi R_1 + 4L}{2V_T} + aT, \quad \lambda_6 = \frac{2\pi R_1 + 2L}{V_T} + aT.$$

In order to obtain the movement trajectory of the lifting finger end in the process of machine movement, the influence characteristics of the structural parameters of the lifting mechanism on the lifting process are analyzed by taking the rotational speed of the chains, the distance between the left and right adjacent chains and the number of the finger in the rear lifting chains as variables. Among them, the structural parameters of the centralizer designed in this study are R_1=0.06 m, R=0.177 m, θ = 70, V_m=0.75 m/s, L=0.405m, L_1=0.17m, L_2=0.233m.

1) The influence of the speed of the chains on the trajectory of finger

Based on formulas (1)-(5), the rotational speeds of chains are 100 r/min, 200 r/min and 300 r/min respectively, and the motion trajectory curves of different rotational speeds for the process of finger unreeling, hugging, lifting, retracting and hollow travel are constructed, as shown in Figure 4.
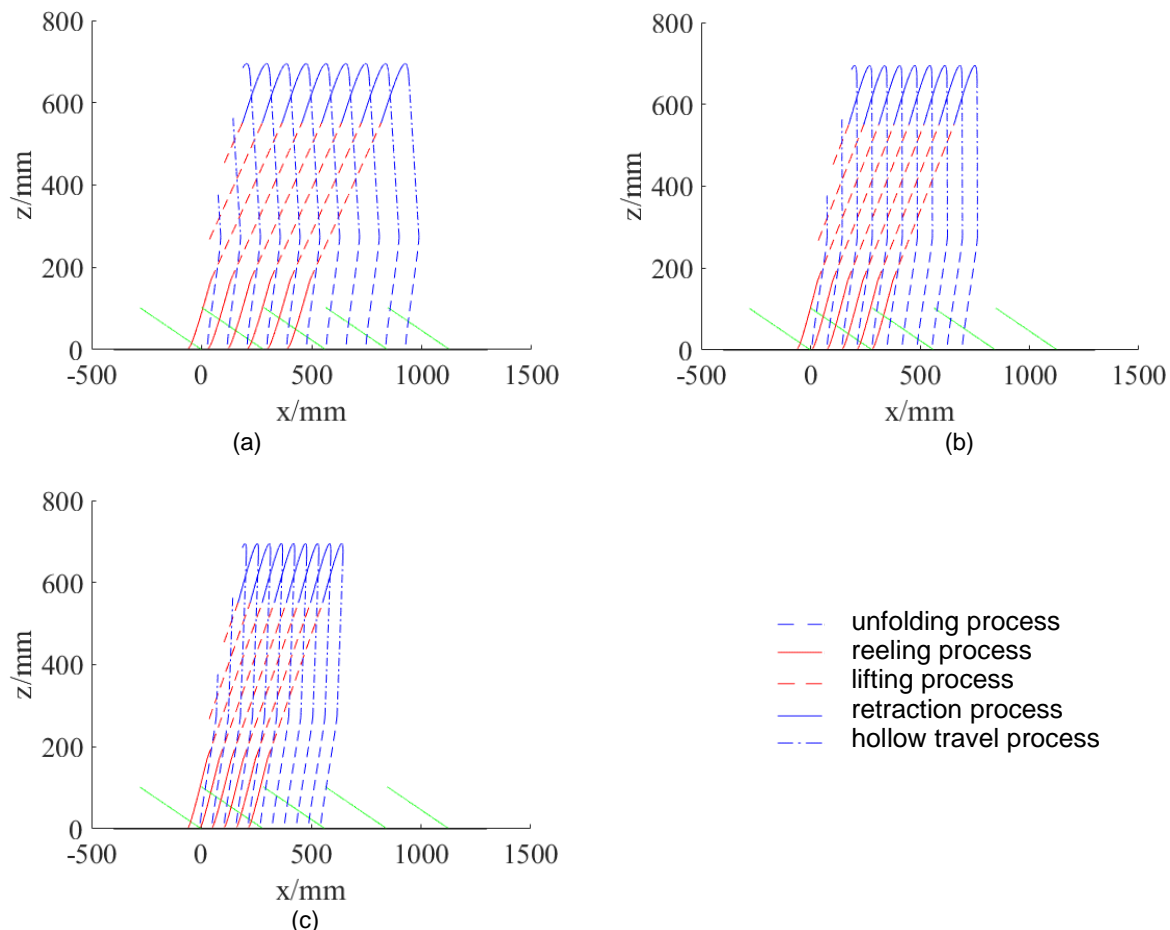
Fig. 4 - Finger motion trajectory of different chain rotational speed
a) Chain rotational speed 100 r/min; b) Chain rotational speed 200 r/min; c) Chain rotational speed 300 r/min

As can be seen from Figure 4, the greater the speed of chains is, the denser the trajectory curves of fingers are. In the case of the same number of fingers, the faster speed of the chain, the more times the fingers focus on the rice stubble, and the higher the success rate of improvement. However, the greater the speed of the chains is, the greater the impact kinetic energy of the fingers on the rice stubble is, which will cause secondary damage to the rice stubble in the process of lifting. Therefore, the determination of chain speed needs to comprehensively consider the centralization rate and secondary damage. In addition, the rotational speeds of the chains and the number of fingers on the chains are the main factors that determine the lifting times of rice stubble. Appropriate combination of the rotational speed of the chains and the number of fingers can coordinate the relationship between the success rate of lifting and the secondary damage rate of lifting.

2) The influence of the distance between adjacent chains on the double-chain lifting breadth

The spacing between chains determines the effective area of lifting process. According to formulas (1)-(5), the motion trajectories of left and right adjacent chains are constructed respectively, and the adjacent spacing is set as 240 mm, 300 mm and 360 mm, respectively. The motion trajectory curves of left and right chains in the process of unfolding, reeling, lifting, retracting and hollow travel are shown in Figure 5.

As can be seen from Figure 5, the distance between adjacent chains is inversely proportional to the overlapping area of left and right finger trajectories and directly proportional to the working area of left and right finger. However, when the distance between adjacent chains exceeds twice the length of finger, missing support will occur, and too close distance will cause too small lifting area. Ideally, the distance between adjacent chains is exactly equal to twice the length of fingers, which can realize the maximum lifting area without leaking support. However, the field ground situation is complex, and the different lifting resistance of adjacent fingers will cause asynchronism, that is, missing support will still occur. Therefore, the maximum adjacent distance between left and right chains without missing support still needs to be obtained through experiments.
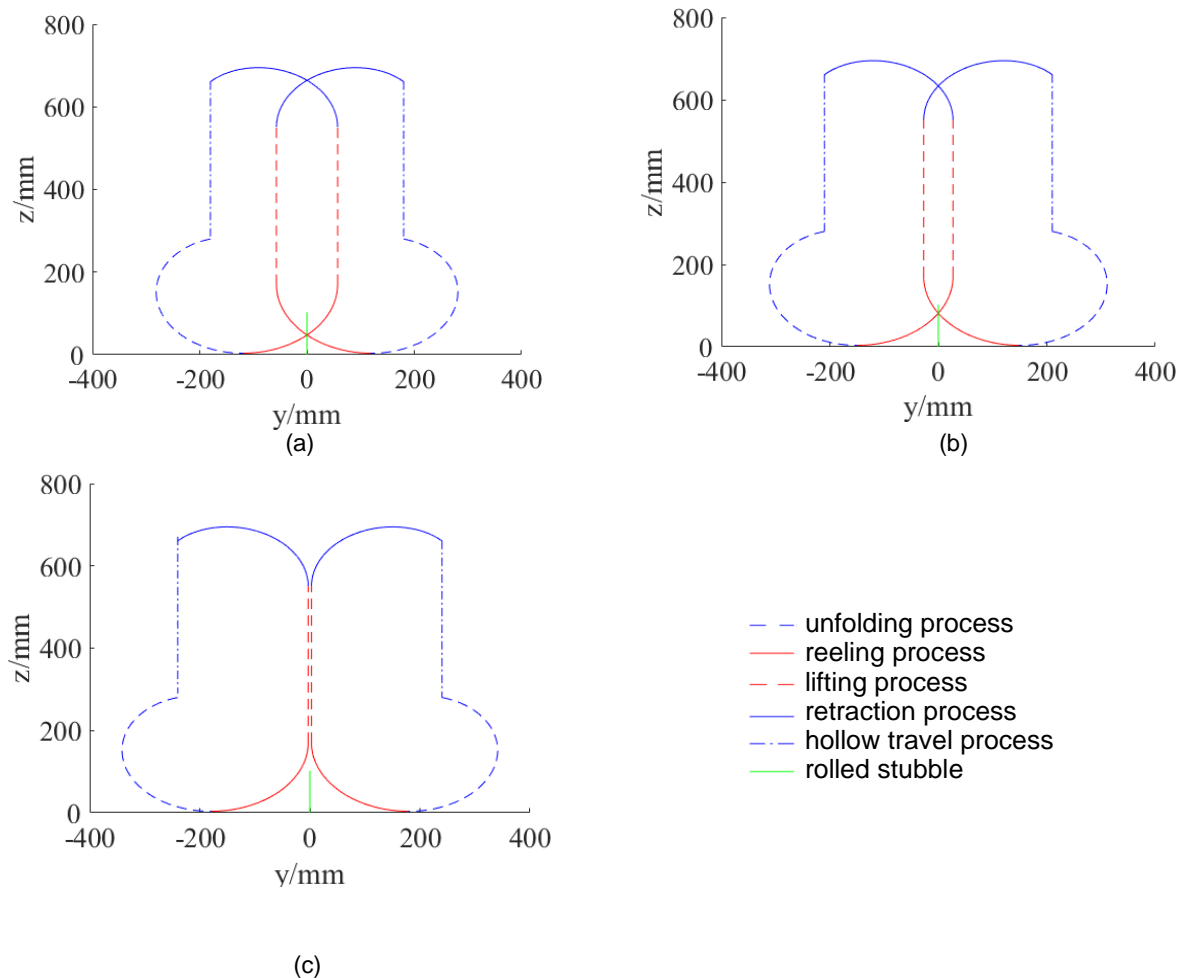
Fig. 5 - Finger motion trajectories with different distances between adjacent chains
a) Space 240 mm; b) Space 300 mm; c) Space 360 mm

Bench test

In the field, the rice stubble was randomly selected according to the average number of rice tillers, the stubble height was 350 mm, and the soil column of 200 mm long ×200 mm wide × 250 mm deep was dug by the field soil column method. The ratoon rice variety was Kenliangyou 801. A double-chain finger lifting test bench is built, which is mainly composed of double-chain finger grain lifter, speed regulating motor, installation frame, H80-70 guide rail, rolled rice stubble and test soil tank, etc. Fifteen bags of rolled rice stubble soil column samples are prepared in the test soil tank, as shown in Figure 6.

Based on the previous studies, the forward speed of the centralizer is 0.75 m/s, the front chains finger is 6, and the chains speed is 263 r/min, 345 r/min and 431 r/min respectively *(Zhang, 2019)*. Taking the speed of chains, the distance between adjacent chains and the number of fingers in the rear lifting chains as test factors, and the success rate of lifting and the secondary damage rate as evaluation indexes, the all-factor bench test of lifting performance was carried out. Among them, the distance between adjacent chains is 240 mm, 300 mm and 360 mm, and the number of fingers in the rear chains is 0, 3 and 6, respectively.

Fig. 6 - **Performance test rack of double-layer chain finger grain lifter**
1. Layer chain finger grain lifter; 2. Adjustable-speed motor; 3. Installation rack;
2. 4. H80-70-type guide rail; 5. Rolled rice stubble 6. Test soil trough

Field test

In order to verify the actual operation effect of the optimal combination of working parameters in bench test, a field test was carried out in Yangwan Village, Duchang County, Jiujiang City, Jiangxi Province in August 2020, and the traction power was the transplanter head. The experimental field area is 1334 m², the variety is Kenliangyou 801, the planting density is 140 mm × 300 mm, and the average stubble height is 350 mm. The operation effect is shown in Figure 7. After mechanical lifting, 10 stumps were randomly selected to roll lifting rice stubble, and the success rate of lifting was counted, with 5 repetitions. Because the straightening machine has transplanter head traction, it is inevitable that rice stubble will be rolled again during the traveling process, and the causes of secondary damage in the straightening process are difficult to define clearly, so the secondary damage rate is not counted in the field test in this paper.

Fig. 7 - **Field verification test**
a) Harvesting and rolled rice stubble lifting prototype of ratoon rice;
b) Mechanical lifting effects drawing of field rolled rice stubble;
1. Raising rice stubble after milling; 2. Rice stubble chain without being rolled; 3. No rice stubble after milling;

Tests evaluation index

If the angle between the rolled rice stubble and the ground after lifting is ≥ 45°, the rolled rice stubble is considered to be successfully righted, and if the rolled rice stubble is broken during the lifting process, it is considered secondary damage to the rolled rice stubble, as illustrated in figure 8.
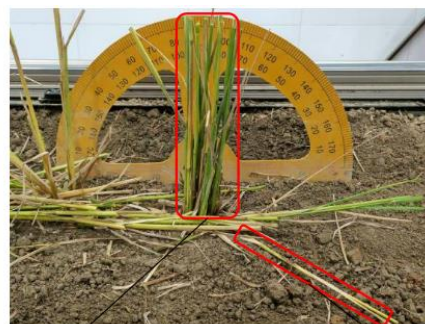
Fig. 8 - Lifting effect of rolled rice stubble

Then, the following formulas are used to calculate the lifting success rate F and the secondary damage rate S:

$$F = \frac{M_C}{M_Z} \times 100\% \tag{7}$$

$$F = \frac{N_D}{M_Z} \times 100\% \tag{8}$$

Wherein:

F -- lifting success rate, %

S — secondary damage rate of lifting, %

M_C — Number of rolled rice stubble after lifting,

N_D — The number of rolled rice stubble broken after lifting,

M_Z — Total number of rolled rice stubble

RESULTS
BENCH TEST

(1) Effect of different factors on lifting success rate of rolled rice stubble.

As can be seen from Table 1, when the distance between adjacent chains and the number of fingers in the rear chains is consistent, the lifting success rate is proportional to the rotational speed of the chains. When the rotational speed of the chains and the number of fingers of the rear chains are the same, the success rate of lifting first increases and then decreases with the increase of the distance between adjacent chains, and the success rate of lifting is the highest when the distance between adjacent chains is 300 mm, which is consistent with the previous theoretical analysis. When the distance between adjacent chains is the same, the relationship between the success rate of lifting and the number of fingers in the rear chains is affected by the speed of the chains, and the success rate of lifting is positively correlated with the number of fingers in the rear chains when the speed of the chains is 263 r/min and 345 r/min; at 431 r/min, the success rate of lifting no longer increased with the increase of the number of fingers in the subsequent chains, but showed a downward trend. It was considered that the single-layer chains could fully lift the rolled rice stubble at a higher chains speed, and the increase of the number of fingers in the later lifting chains caused a secondary negative effect on the lifted rice stubble. The results showed that when the rotational speed was 431 r/min, the distance between left and right adjacent chains was 300 mm, the number of fingers in the rear chains was 0, and the highest success rate of lifting rice stubble was 95.05%.

Table 1

Success rate/% of lifting for rolled rice stubble

chain speed/r·min⁻¹	distance between adjacent chains/mm	number of rear lifting chain fingers/piece		
		0	3	6
	240	62.44±6.19aA	63.76±2.91aA	68.26±2.80aA
263	300	65.72±7.79aA	69.67±3.10aA	77.68±4.47aA
	360	50.59±6.47aA*	63.30±5.74aA	73.70±4.77aA*
	240	83.80±4.52bA	84.99±4.56bAB	85.01±3.40bAB
345	300	85.74±4.12bA	90.05±2.37 bB	89.77±3.11bB
	360	73.63±5.88bA	74.30±4.60aA	75.22±5.19aA
	240	94.72±1.33bA	88.33±2.77bA	90.19±2.60bA
431	300	95.05±1.64bA	91.14±2.04bA	90.95±1.29bA
	360	87.95±3.43bA	87.90±2.60bA	87.52±2.23bA

Note: When p=0.05, the lowercase letters a and b in the table indicate that different chain rotational speed has a significant impact on lifting success rate; The uppercase letters A and B in the table indicate that different chain spacing has a significant effect on the success rate of lifting when p=0.05; "" in the table indicates that the success rate of lifting is significantly influenced by the number of fingers that are used.*

(2) Effects of different factors on secondary damage rate of rolled rice stubble lifting.

It can be seen from Table 2 that when the distance between adjacent chains and the number of fingers in the rear chains are the same, the secondary damage rate of lifting increases with the increase of chains speed. When the rotational speed of the chains and the number of fingers of the rear chains are the same, the secondary damage rate of lifting decreases first and then rises with the increase of the distance between adjacent chains. When the distance between adjacent chains is consistent, the secondary damage rate of lifting increases greatly with the increase of chains speed; the relationship with the number of fingers in the rear chain is affected by the speed of the chain. The secondary damage rate increases with the number of fingers in the rear chain when the speed of the chain is 263 r/min and 345 r/min, but the opposite trend appears at 431 r/min, namely the number of fingers in the rear chain decreases with the increase of the number of fingers in the rear chain. The results showed that the lowest secondary damage rate was 1.20% when the rotational speed was 263 r/min, the distance between left and right adjacent chains was 300 mm, and the number of fingers in the rear chains was 0.

Table 2

Secondary damage rate of rolled roll stubble lifting

chain speed/r·min⁻¹	distance between adjacent chains/mm	number of rear lifting chain fingers/piece		
		0	3	6
263	240	1.43±0.81aA	1.44±0.78aA	2.06±0.99aA
	300	1.20±0.65aA	1.37±0.93aA	1.46±0.82aA
	360	1.37±0.74aA	1.54±0.86aA	2.16±0.97aA
345	240	1.81±1.07aA	2.13±1.19aA	3.05±1.24aA
	300	1.58±0.89aA	1.72±0.79aA	1.94±1.34aA
	360	1.62±1.10aA	1.93±1.06aA	3.68±1.09aA
431	240	4.32±1.63aA	4.23±1.71aA	3.49±1.38aA
	300	3.83±1.22aA	3.15±1.11aA	2.93±1.34aA
	360	4.79±1.25bA	5.57±1.51bA	4.24±1.71aA

Note: The lowercase letters a and b in the table indicate that varying chain rotational speed has a significant effect on the secondary damage rate when p=0.05; the uppercase letters A and B in the table indicate that varying chain spacing has a significant effect on the secondary damage rate when p=0.05.

(3) Inter-subject effect inspection of lifting success rate and secondary damage rate

As shown in tables 3 and 4, the distance between the adjacent chains and the number of fingers of the rear lifting chain all affect the success rate and secondary damage rate.

Table 3

Inter-subject effect inspection of lifting success rate

Source of variance	Type III Sum of Squares	df	Mean Square	F	P	Partial Eta squared	Eta squared
Corrected Model	.322ᵃ	6	0.054	25.742	0.000	0.885	
Intercept	17.142	1	17.142	8217.932	0.000	0.998	
Rotational speed of the chains	0.276	2	0.138	66.226	0.000	0.869	0.759
Spacing of adjacent chains	0.037	2	0.019	8.956	0.002	0.472	0.103
Number of tooth fingers	0.009	2	0.004	2.045	0.156	0.170	0.023
Within groups Error	0.042	20	0.002				
Total	17.506	27					
Corrected Total	0.364	26					

a. R^2 = 0.885 (After adjustment R^2= 0.851)

In conclusion, the secondary damage rate of rolled rice stubble lifting increases with the increase of lifting success rate as a whole. According to the results of inter-agent effect test, it can be concluded that the biggest factor affecting the success rate of lifting and the secondary damage rate is the speed of chains, which directly affects the contact lifting kinetic energy and the contact lifting frequency of rolled rice stubble, and the number of fingers in the rear chains also affects the contact lifting frequency of rolled rice stubble. Because the secondary damage mainly comes from two aspects: the kinetic energy produced by the contact between the rotation of the lifting chain finger and the lifting of the rolled rice stubble, and the contact lifting frequency of the rolled rice stubble, considering the success rate of lifting and the secondary damage rate comprehensively, the optimal working parameter combination of the grain lifter is as follows: the speed of the chains is 345 r/min, the distance between adjacent chains is 300 mm, and the number of fingers of the rear lifting sprocket is 3.

Table 4

Inter-subject effect inspection of lifting secondary damage rate

Source of variance	Type III Sum of Squares	df	Mean Square	F	P	Partial Eta squared	Eta squared
Corrected Model	.003a	6	0.001	17.651	0.000	0.841	
Intercept	0.018	1	0.018	556.271	0.000	0.965	
Rotational speed of the chains	0.003	2	0.002	46.967	0.000	0.824	0.746
Spacing of adjacent chains	0.000	2	0.000	5.164	0.016	0.341	0.082
Number of tooth fingers	5.371E-05	2	2.685E-05	0.822	0.454	0.076	0.013
Within groups Error	0.001	20	3.267E-05				
Total	0.022	27					
Corrected Total	0.004	26					

a. R^2= 0.841 (After adjustment R^2= 0.793)

Field test

It can be seen from Table 5 that the average lifting success rate of the double-chain finger grain lifter developed in this study in the field operation is 55%. It is quite different from the bench test results. On the one hand, the operation trajectories of mechanical planting and harvesting machines are irregular, resulting in an inconsistent lodging direction of the rolled stubble. This makes it difficult for the grain elevator to align with the lodging stubble that part of the lodging stubble outside the lifter and cannot be lifted. On the other hand, the grain lifter designed in this study does not consider the ground copying mechanism. Due to the rough ground, the fingers cannot touch into the stubbles or get buried in the soil, which can easily lead to the disengagement of the chain and sprocket. During this process, the grain lifter fails to work effectively. To this end, this study will introduce the unmanned driving technology for rice planting in the future to ensure the straight end of the rice field distribution and harvesting rolled path, so as to realize the high-precision improvement of the rice stubble grain lifter. In addition, a copying device and an elastic lifting finger are designed to reduce the tooth jumping and jamming of the lifting finger.

Table 5

Success rate of field lifting

targets of test	test number					average value
	1	2	3	4	5	
lifting success rate	40%	60%	65%	60%	50%	55.00%

CONCLUSIONS

1) A double-chain finger grain lifter for lifting the rolled ratoon rice stubble in mechanical harvesting is designed; the kinematics model and its trajectory curve of the process of unfolding, reeling, lifting, retracting and hollow travel of the finger are constructed by establishing the kinematics analysis of the lifting chain. The main factors affecting the lifting performance are analyzed and determined, such as the rotational speed of the chain, the distance between adjacent chains and the number of fingers on the rear lifting chain.

2) Bench test was carried out with the success rate of lifting and the secondary damage of lifting as indexes. The results show that the speed of the chains, the distance between adjacent chains and the number of fingers in the rear chains all significantly affect the centralization performance of the device. When the speed of the chains is 345 r/min, the distance between adjacent chains is 300 mm and the number of fingers in the rear lifting sprocket is 3, the success rate of lifting is 90.05%, and the secondary damage rate of lifting is 1.72%.

3) The field test validates the effectiveness of lifting operations; the average success rate of lifting operations in the field is 55%, which shows that the double-chain finger grain lifter designed in this study has a good potential for lifting the ratoon rice stubble rolled by mechanical harvesting.

REFERENCES

[1] Bahar, F. A., & De Datta, S. K. (1977). Prospects of Increasing Tropical Rice Production through Ratooning. *Agronomy Journal*, 69(4), 536-540.

[2] Faruq, G., Taha, R. M., & Prodhan, Z. H. (2014). Rice ratoon crop: A sustainable rice production system for tropical hill agriculture. *Sustainability,* 6, 5785-5800; doi:10.3390/su6095785.

[3] Fu, J. W., Zhang, G. X., Xie, G., Wang, Y., Gao, Y., Zhou, Y. (2020). Development of double-channel feeding harvester for ratoon rice. *Transactions of the Chinese Society of Agricultural Engineering, 36*(03), 11-20. DOI:10.11975/j.issn.1002-6819.2020.03.002

[4] Guo, H. L., Lin, J., Shi, H. J., Zhang, X. (2016). Current Situation and Development Trend of Harvest Mechanization in the First Season of Regenerated Rice. *Fujian Agricultural Machinery,* (01), 16-18. Doi: 10.3969/j.issn.1004-3969.2016.01.007

[5] Harrell, D. L., Bond, J. A., & Blanche, S. (2009). Evaluation of main-crop stubble height on ratoon rice growth and development. *Field Crops Research,* 114(3), 396-403. https://doi.org/10.1016/j.fcr.2009.09.011

[6] Huang, M.S., Wang, H. H., Li, Y. M., Xu, L. Z., Ma, Z. (2020). Simulation and experiment of air flow field in the cleaning device of ratooning rice combine harvesters. *Transactions of the Chinese Society of Agricultural Engineering, 36*(20): 84-92. DOI: 10.11975/j.issn.1002-6819.2020.20.011

[7] Lu, K., Zhang, G. Z., Peng, S. B., Lei, Z. Q., Fu, J. W., Zha, X. T., Zhou, Y. (2017). Design and performance of tracked harvester for ratoon rice with double-headers and double-threshing cylinders. *Journal of Huazhong Agricultural University, 36*(05): 108-114. DOI: 10.13300/j.cnki.hnlkxb.2017.05.016

[8] Mamun, A. F. M., Mazumder, S. K., Suvo, T. P., & Akter, S. (2019). Productivity of boro ratoon rice under different levels of nitrogen. International Journal of Agricultural Research, *Innovation and Technology, 9*(1), 48-57. DOI: 10.3329/ijarit.v9i1.42949

[9] Munda, G. C., Das, A., & Patel, D. P. (2009). Evaluation of transplanted and ratoon crop for double cropping of rice (Oryzct sativa L.) under organic input management in mid altitude sub-tropical Meghalaya. Current Science (00113891), 96(12). 1620-1627. http://www.ias.ac.in/currsci

[10] Oad, F. C., Samo, M. A., Hassan, Z. U., Pompe, S. C., & Oad, N. L. (2002). Correlation and path analysis of quantitative characters of rice ratoon cultivars and advance lines. *Int. J. Agric. Biol,* 4(2), 204-207. https://www.researchgate.net/publication/230846595_Correlation_and_path_analysis_of_quantitative_characters_of_rice_ratoon_cultivars_and_advance_lines

[11] Shamiul Islam, M., Hasanuzzaman, M., & Rokonuzzaman, M. (2008). Ratoon rice response to different fertilizer doses in irrigated condition. *Agriculturae Conspectus Scientificus*, 73(4), 197-202. https://hrcak.srce.hr/31230

[12] Thi Hoa Sen, L., & Bond, J. (2017). Agricultural adaptation to flood in lowland rice production areas of Central Vietnam: understanding the 'regenerated rice'ratoon system. *Climate and Development*, 9(3), 274-285. https://doi.org/10.1080/17565529.2016.1149440

[13] Toorminaee, V., Allahyari, M. S., Damalas, C. A., & Aminpanah, H. (2017). RETRACTED: Double cropping in paddy fields of northern Iran: Current trends and determinants of adoption, *Land Use Policy*, 62, 59-67. DOI: 10.1016/j.landusepol.2016.12.013

[14] Wang, H. H., Li, Y. M., Xu, L. Z., Huang, M. S. (2021). Design and Experimental Study of Cleaning Device of Small-scale Ratooning Rice Combine Harvester. *Journal of Agricultural Mechanization Research, 43*(05), 85-90. DOI: 10.13427/j.cnki.njyi.2021.05.014

[15] X. F. Chen, H. L. Li, M. H. Liu, J. J. Yu, X. Y. Zhang, Z. X._Liu, Y. F. Peng. (2021). Stubble Lifting Increases the Grain Yield of Ratooning Rice After the Mechanical Harvest of Primary Rice. *Journal of Plant Growth Regulation*, https://doi.org/10.1007/s00344-021-10416-0

[16] Yang, Y. K., Liu, J., Huang, D. P., ZENG, S., LAI, Q. X. (2019). Design of full-feeding ratoon rice combine harvester Design of full-feeding ratoon rice combine harvester. *Hubei Agricultural Sciences, 58*(18), 129-132. DOI: 10.14088/j.cnki.issn0439-8114.2019.18.031

[17] Zeng, S., Ling, S. Y., Liu, J., et al. (2018a). *A Regenerative Rice Harvester with Variable Wheel Distance* [P]. 201810169020.X. 2018.09.21. (China)

[18] Zeng, S., Ling, S. Y., Luo, X. W., et al. (2018b). *A Four - Drive Low Rolled Regenerative Rice Harvester* [P]. 201820287659.3. 2018.10.12. (China)

[19] Zhang, G. Z., Zhang, Y. X., Huang J. L., Qu K .Y., Zhou, Y., Huang, H. D., Fan, Q. Z. (2016). Designing and performance testing a novel head spike harvester of ratoon rice. *Journal of Huazhong Agricultural University, 35*(01): 131-136. DOI: 10.13300/j.cnki.hnlkxb.2016.01.021

[20] Zhang, X. Y. (2019), *Design and experiment of regenerative rice chains finger type grain lifter*. Nanchang: Jiangxi Agricultural University, 2019. DOI: 10.27177/d.cnki.gjxnu.2019.000373

OPTIMIZATION OF STIRRING PARAMETERS FOR MILLET FLUID SEED METERING BASED ON RESPONSE SURFACE METHODOLOGY
/
基于响应面法的谷子流体排种器搅拌技术参数优化

Yanqing ZHANG, Qingliang CUI[*), Shaobo YE, Can WANG, Zhiyong ZHANG [1]
College of Agricultural Engineering, Shanxi Agricultural University, Taigu/China
Tel: +86-0354-6288339; E-mail: qlcui@126.com
DOI: https://doi.org/10.35633/inmateh-66-37

ABSTRACT

Fluid seeding is a new technology for drought resistance, water saving and yield increase in modern agriculture. To improve the uniformity of fluid seed metering of millet, the mechanical stirring device was added to the metering device, and the single-factor tests were carried out on the size parameters of the pump tube, the installation position and the parameters of mechanical stirring. The stirring speed, the ratio between the length of stirring paddle and the diameter of seed box and distance between the pump tube and the stirring paddle were selected as independent variables, and the right rate of hill distance, right rate of seeds per hill and rate of no seed hill were selected as response values. According to the test design principle of Central Composite Design, a response surface analysis method was used to establish mathematical models between each experimental factor and performance index, and the influencing factors of fluid seed metering were analyzed. The single-factor test results showed that when the pump tube was installed on the side of the seed box, and its inner diameter and wall thickness were 4.8 mm and 1.6 mm, respectively, the seeding performance was better. The response surface test results showed that the selected factors all have an influence on the performance of millet fluid seed metering, and the optimal stirring parameters were the stirring speed of 30 r/s, the ratio between the length of stirring paddle and the diameter of seed box of 0.69, and distance between the pump tube and the stirring paddle of 0.11 cm. The verification test was conducted under these parameters, and the right rate of hill distance, right rate of seeds per hill and rate of no seed hill were 94.14%, 84.24%, and 2.21%, respectively, and the error from the predicted values was less than 4%. The performance indexes of fluid seed metering were improved compared with the fluid seed metering device without stirring device, indicating that the optimized stirring parameters can improve the performance indexes of millet fluid seed metering. This study can provide a reference for the research and development of key technologies and equipment for precision fluid seed metering of millet.

摘要

　　流体播种是现代农业抗旱、节水和增产的一种新技术。为提高谷子流体排种均匀性，在现有输送泵式谷子流体排种器的基础上增设了机械搅拌装置，对泵管尺寸参数、安装位置及搅拌技术参数进行了单因素试验。选取搅拌速率、搅拌桨-种箱直径比和泵管-搅拌桨垂直距离为自变量，以穴距合格率、穴粒数合格率和空穴率为响应值，按照 *Central Composite Design* 试验设计原理，采用三因素五水平响应面分析方法建立了各试验因素与性能指标之间的数学模型，并对各因素进行分析。单因素试验结果表明：当泵管安装于种箱侧面，其内径和壁厚分别为 4.8 mm、1.6 mm 时，排种性能较优。响应面试验结果表明：搅拌速率、搅拌桨-种箱直径比和泵管-搅拌桨垂直距离均对谷子流体排种性能有一定影响，且流体排种器最佳搅拌参数为搅拌速率 30 r/s、搅拌桨-种箱直径比 0.69、泵管-搅拌桨垂直距离 0.11cm。该参数下进行验证试验得到谷子流体排种穴距合格率、穴粒数合格率和空穴率分别为 94.14%、84.24%、2.21%，与预测值误差小于 4%。通过与未加搅拌装置的流体排种器进行对比试验，流体排种性能指标均有明显改善，说明增设的搅拌装置及其最优技术参数可提高谷子流体排种性能指标。该研究可为谷子精量流体排种关键技术与装备的研发提供参考。

[1] *Yanqing Zhang, As Prof. Ph.D. Eng.; Qingliang Cui*, Prof. Ph.D. Eng.; Shaobo Ye, Prof. Ph.D. Eng.;*
Can Wang, Prof. Ph.D. Eng.; Zhiyong Zhang, Prof. Ph.D. Eng.

INTRODUCTION

Millet is a coarse grain crop grown in arid regions of northern China. In recent years, the realization of precise mechanized sowing of millet has been one of the problems to be solved urgently with the gradual development of the millet industry *(Du et al., 2015; Li et al., 2014).* Millet is often sown in dry land with little rain, and it is difficult to germinate after sowing in the hilly and mountainous areas of northern China *(Tian et al., 2013).* At the same time, the traditional mechanical sowing technology and equipment were used by most farmers to sow millet, which resulted in poor uniformity of sowing, large sowing amount, irregular seedling emergence, heavy thinning workload, and even the phenomenon of seedling shortage *(Zhang et al., 2017).* Fluid seeding is a new technology for modern agriculture to resist drought, save water and increase production, that is to say, a method of quantitative machine seeding by evenly distributing seeds in a water solution with the water retaining agent *(Pill, 1991).* The water retaining agent has a high viscosity, water absorption and water retention. It can slowly release water for crop absorption and utilization. In the case of drought, the purpose of seedling growth and stable yield can be achieved *(Chen et al., 2010; Hayes et al., 2010).* Therefore, using the fluid seeding method can not only improve the uniformity of seeding, but also promote the growth of millet in dry land.

At present, spray seeding is mainly used for fluid seeding of small seeds, such as pneumatic fluid seeder, *KangdaCPB8* spray seeder and *SL-PBJ* spray seeder, which are mainly applied to the drill and broadcast sowing for forage grass and flower seeds *(Currah et al., 2010).* A precise fluid seeding device controlled by a microcomputer has been developed in America and Japan, but it is still in the stage of experimental research and has not been popularized yet *(Wu, 1995).* A study showed that the structure of the seed box was optimized by the stirring system of pressurized air, and the corn seeds tended to be uniformly suspended by air stirring of high pressure *(Xin et al., 2008).* The Scholars analyzed the interaction mechanism of seeds, water retaining agent and bubbles in the multiphase flow, revealed the theory of uniform suspension of seeds in the multiphase flow and invented three kinds of fluid seeding device, such as roller type, groove type, cable tray type, which provides a key technology for quantitative sowing of large seeds *(Xin et al., 2016a; Xin et al., 2016b).* Millet seeds are small in size and light in weight, belonging to small seeds *(Sun et al., 2021),* and there are still problems such as a large amount of sowing and poor uniformity in the field. So it is necessary to develop the fluid seeding equipment which should meet the requirements of precision seeding.

The seed metering device is the core component of the seeder. Our project initially developed a fluid metering device of the delivery pump for millet seeds, but it has the problem of uneven seed metering. Mechanical stirring is an important method to promote the uniformity of solid-liquid mixture *(Li et al., 2021).* In this study, a mechanical stirring device was added to the seed box, the effects of the size parameters of the pump tube, installation position and stirring technical parameters on the seed metering performance were analyzed, and the optimal stirring parameters were obtained. The performance of the fluid seed metering device was improved through mechanical stirring, providing a reference for the development of fluid seed metering technology for millet seeds.

MATERIALS AND METHODS
Materials and equipment

Jingu No. 21 millet seed were selected, which is widely grown locally. The 1000-grain weight of millet seed was 3.31 g (13.2%, w.b.), and its average length, width and thickness were 3.14 mm ,1.92 mm and 1.50 mm, respectively. *Anxin* water retaining agent was used to prepare solid-liquid mixture, and the rate of water absorption was 450-500. The mass ratio of water retaining agent, millet seeds and water in a solid-liquid mixture was 1.1:10:200, and the viscosity of the solid-liquid mixture was 1.62 Pa·s *(Zhang et al., 2017).*

The self-made test bench, fluid seed metering device, had been adopted to the performance test, and its structure is shown in Fig.1. Its operation process is that negative pressure was generated inside the pump tube and the solid-liquid mixture was extracted from the seed box under the extrusion pressure of the delivery pump. The seeds passed through pump tube, three-way tube, long bent tube and short bent tube, and were finally discharged from the end drainage tube. The delivery pump provided power for the seed delivery, and the amount of seed metering could be adjusted by changing the speed of the delivery pump. The combination of the three-way tube, long bent tube and short bent tube can improve the uniformity of the seed metering, and the limiting clip was used to prevent the pump tube from moving *(Zhang et al., 2017).*

In order to improve the performance of the fluid seed metering device, a cylindrical barrel was used as a seed box, and a mechanical stirring device was added in this study, as shown in Fig.2. The speed of the mechanical stirring device R can be adjusted by the motor controller, and its adjustment range is 0-3000 r/min. The stirring paddle can be replaced in different tests, and the ratio of the stirring paddle length t to the diameter of the seed box T was 0.5-0.9. The width of the stirring paddle d and its distance from the bottom of the seed box h were 10 mm and 45 mm, respectively. The pump tube could be installed at the bottom, top and side of the seed box, so as to facilitate seed metering performance tests at different installation positions of the pump tube. Meanwhile, the position of the pump tube on the side of the seed box can be adjusted, and its vertical distance from the stirring paddle D was -4 - +4 cm ('-' represents the position below the stirring paddle, and '+' represents the position above the stirring paddle). All fluid metering performance tests were carried out on a mobile platform with a speed adjustment range of 0.5 – 1 m/s. *(Zhang et al., 2017).* The other test tools were mass balance (500 g, 0.01 g), rulers (500 cm, 0.1 cm), and the pump tubes with different size parameters. In this study, the speed of the delivery pump and mobile platform were 40 r/min and 0.5 m/s, respectively.
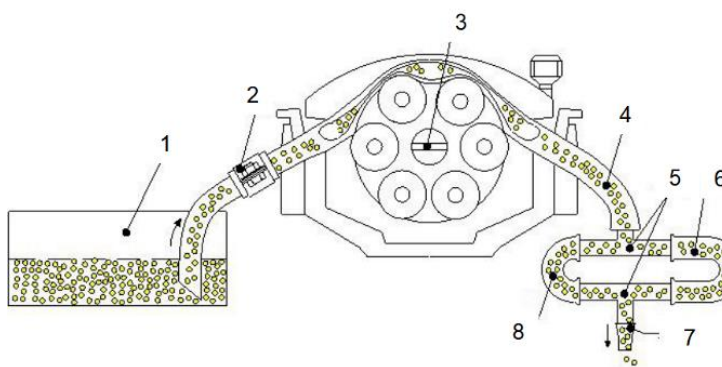

Fig. 1 - Fluid seed metering device
1.Seed box; 2.Limiting clip; 3.Delivery pump; 4.Pump tube;
5.Three-way tube; 6.Long bent tube; 7.End drainage tube;
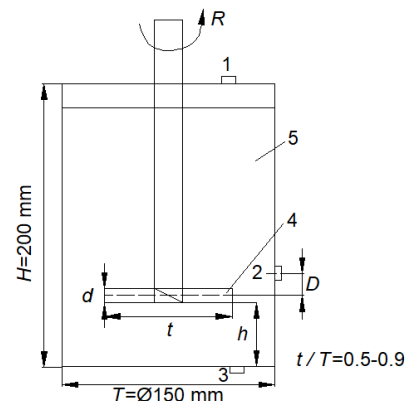*8.Short bent tube*

Fig. 2 - Mechanical stirring device
1.Top entrance of pump tube; 2.Side entrance of
pump tube; 3. Bottom entrance of pump tube;
4. Stirring paddle; 5. Seed box

Test evaluation index

The NY/T 987-2006 "Operating quality grains film-covering hill-drop drill" was referenced for fluid seeding performance tests *(China Agriculture Press, 2006).* The seed number of 51 holes was recorded in each experiment, and the distance between 50 holes was measured continuously. According to the agronomic requirements of millet sowing, the theoretical hill distance value ± 1.5cm was the qualified hill distance, and the reasonable seed number per hill was 2-4 *(Cui et al., 2017; Ren et al., 2014).* The experiment was repeated for 3 times, and the evaluation indexes of the right rate of hill distance Y_1, right rate of seeds per hill Y_2 and rate of no seed hill Y_3 were calculated as follows:

$$Y_1 = \frac{P}{e-1} \times 100\% \tag{1}$$

$$Y_2 = \frac{Q}{e} \times 100\% \tag{2}$$

$$Y_3 = \frac{W}{e} \times 100\% \tag{3}$$

Where: P is the number of qualified hill distances, Q is the number of right seeds range, W is the number of no seeds per hill, e is the total number of hills determined in the test.

The undamaged millet seeds were selected for static tests of fluid seed metering, and 200 mL solid-liquid mixture was collected to calculate the rate of seed breakage Z.

The experiment was repeated for 3 times, and the formula of Z is as follows:

$$Z = \frac{M}{N} \times 100\% \tag{4}$$

Where: Z is the rate of seed breakage, M is the number of damaged seeds, N is the total number of seeds.

Test design

The test device is shown in Fig.3. The single-factor performance tests of fluid seeding were carried out by selecting the different size parameters of the pump tube, installation position of the pump tube, stirring speed and ratio between the length of stirring paddle and the diameter of seed box as the factors. The vertical distance between the pump tube and the stirring paddle was selected as a factor to carry out the fluid seeding performance test after the installation position of the pump tube was determined, and test factors and levels are shown in Table 1.

In order to further study the influence factors on the performance of fluid seeding and optimize technical parameters of mechanical stirring, Central Composite Design (CCD) was used for response surface test design based on the single-factor tests, and the relation of practical and coding values with CCD is shown in Table 2.
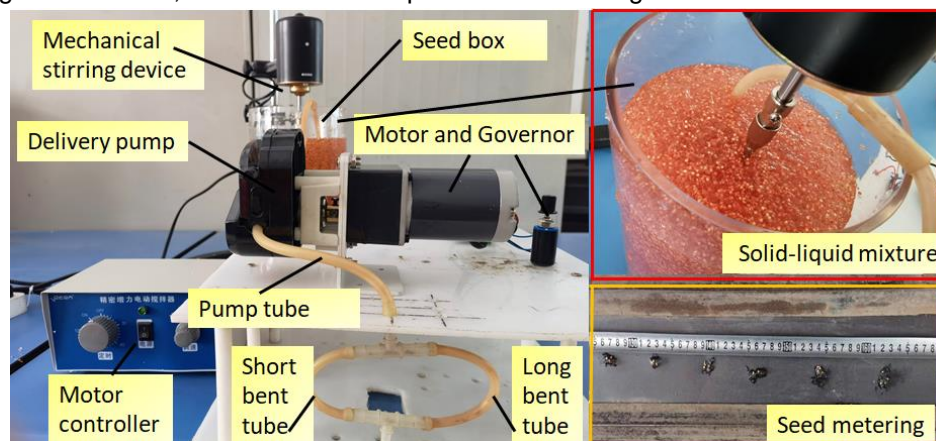

Fig. 3 - Test of fluid seed metering

Table 1

Factors and levels of single-factor tests

Levels	Inner diameter (thickness) of pump tube / mm	Stirring speed R / (r/s)	Ratio between the length of stirring paddle and the diameter of seed box A	Installation position	Distance between the pump tube and the stirring paddle D / cm
1	4 (1)	20	0.5	/	-4
2	4 (2)	25	0.6	Top	-2
3	4.8 (1.6)	30	0.7	Side	0
4	6 (1)	35	0.8	Bottom	+2
5	6 (2)	40	0.9	/	+4

Table 2

Relation of practical and coding values with CCD

Coding values	Practical values		
	Stirring speed R / (r/s)	Ratio between the length of stirring paddle and the diameter of seed box A	Distance between the pump tube and the stirring paddle D / cm
-1.682	21.59	0.53	-3.36
-1	25	0.6	-2
0	30	0.7	0
+1	35	0.8	+2
+1.682	38.41	0.87	+3.36

RESULTS

Results of single-factor test

The performance tests of fluid seed metering were carried out by replacing the pump tube of different size parameters when the seeds were discharged from the side of the seed box and the *R, A* and *D* were determined as 30 r/s, 0.7 and 0 cm, respectively.

Exploring the effect of the installation position, the inner diameter and wall thickness of the pump tube were 4.8 mm and 1.6 mm, respectively. As shown in Table 3, the seeds could not move smoothly in the pump tube, and the pump tube was clogged when the inner diameter of the pump tube was 4 mm. It was related to the size of the millet seed, and the agglomeration of multiple seeds caused the clogging and seed breakage in the pump tube. The right rate of hill distance, right rate of seeds per hill and rate of seed breakage improved obviously when the inner diameter of the pump tube increased to 4.8 – 6 mm, but the rate of no seed hill of the pump tube with a 6 mm inner diameter was higher than that of the pump tube with a 4.8 mm inner diameter. This is mainly because in the process of seed filling, more liquid was pumped and the seeds were not extracted proportionally.

In the case of the installation position of the pump tube, all the values of the evaluation indexes showed that the pump tube could be installed on the side of the seed box. Therefore, the pump tube with a 4.8 mm inner diameter was selected and installed on the side of the seed box for the best performance of the millet fluid seed metering.

In this study, the performance tests of fluid seed metering under different stirring speeds were conducted when A and D were 0.7 and 0 cm, respectively. It can be obtained from Table 4 that the right rate of hill distance Y_1 and right rate of seeds per hill Y_2 generally increased first and then decreased with the increase of the stirring speed, and the rate of no seed hill Y_3 first decreased and then increased. This reason may be that the viscosity of the solid-liquid mixture is relatively high, and a slow stirring speed cannot promote the uniform flow of the seeds. Similarly, the larger stirring speed causes the liquid flow to be accelerated in the solid-liquid mixture, resulting in an increase of the rate of no seed hill and a decrease of the right rate of seeds per hill.

Table 3

Effects of the size parameters and installation position of pump tube on fluid seed metering

Factor	Value	Y_1 / %	Y_2 / %	Y_3 / %	Z / %	Whether the clogging
Inner diameter (thickness) of pump tube / mm	4 (1)	85.72	80.58	3.89	0.01	Yes
	4 (2)	87.14	81.30	3.14	0.005	Yes
	4.8 (1.6)	95.12	86.23	2.38	0	No
	6 (1)	94.13	85.44	3.53	0	No
	6 (2)	95.33	86.14	3.47	0	No
Installation position	Top	93.55	83.12	3.14	0	No
	Side	95.12	86.23	2.38	0	No
	Bottom	93.71	84.54	3.22	0	No

Under the condition that the R and D were 30 r/s and 0 cm, respectively, the A was changed by installing different stirring paddles to conduct the fluid seed metering tests. The evaluation indexes were the optimum when the ratio between the length of the stirring paddle and the diameter of seed box A was 0.7. The main reason is that the high-viscosity mixture and the short stirring paddle could not make the seeds flow faster on the side of the seed box, and the long stirring paddle made the centrifugal force of millet seed increase, causing a large amount of liquid without seeds to be discharged.

Table 4

Effects of the stirring parameters on fluid seed metering of millet

Factor	Value	Y_1 / %	Y_2 / %	Y_3 / %	Z /%
Stirring speed R / (r/s)	20	90.35	80.54	3.04	0
	25	92.14	83.21	2.54	0
	30	95.33	86.78	2.15	0
	35	95.12	81.24	2.28	0
	40	95.20	78.25	2.33	0
Ratio between the length of stirring paddle and the diameter of seed box A	0.5	89.23	79.55	2.89	0
	0.6	93.00	81.23	2.54	0
	0.7	95.13	86.74	2.21	0
	0.8	91.23	86.41	2.23	0
	0.9	88.26	87.55	2.34	0

Factor	Value	Y1 / %	Y2 / %	Y3 / %	Z / %
Distance between the pump tube and the stirring paddle *D* / cm	-4	91.23	81.53	2.74	0
	-2	94.12	84.35	2.39	0
	0	95.66	86.87	2.15	0
	+2	91.03	84.47	2.29	0
	+4	88.76	80.65	2.36	0

The performance tests of fluid seed metering under the different distances between the pump tube and the stirring paddle were conducted when *R* and *A* were 30 r/s and 0.7, respectively. We can see from Table 4 that these indexes were optimal when the pump tube was installed on the side of the seed box and the closer the pump tube was to the stirring paddle. During the stirring process of the solid-liquid mixture, the main flow modes are circulating flow and turbulent flow, and the latter can promote the seeds to mix evenly in the liquid *(Blais B.et al., 2017; Xin et al., 2008)*. At the same time, we observed that millet seeds were not broken at a rapid stirring speed, and this is mainly due to the high viscosity of the solid-liquid mixture resulted in a faster stirring speed that does not cause the seeds to be broken.

Results of response surface test

In order to obtain the optimal stirring parameters for fluid seed metering of millet, a response surface test was carried out after determining the size parameters and installation position of the pump tube, and Table 5 shows the results of the response surface test.

Table 5

Response surface analysis data of fluid seed metering test

Testing number	Factor levels			Y_1 / %	Y_2 / %	Y_3 / %
	R	*A*	*D*			
1	−1	−1	−1	92.28	80.28	2.24
2	−1	−1	1	96.01	86.79	2.18
3	−1	1	−1	95.65	86.54	2.14
4	−1	1	1	91.43	84.70	2.45
5	1	−1	−1	92.06	82.97	2.36
6	1	−1	1	94.08	82.27	2.40
7	1	1	−1	93.53	83.85	2.43
8	1	1	1	96.39	86.11	2.16
9	−1.682	0	0	95.78	87.78	2.07
10	1.682	0	0	94.16	83.22	2.50
11	0	−1.682	0	91.25	81.04	2.27
12	0	+1.682	0	91.64	81.92	2.42
13	0	0	−1.682	93.46	82.00	2.30
14	0	0	+1.682	95.23	86.82	2.14
15	0	0	0	92.45	81.31	2.37
16	0	0	0	95.37	86.80	2.17
17	0	0	0	93.09	82.93	2.39
18	0	0	0	92.46	82.66	2.39
19	0	0	0	93.07	84.26	2.17
20	0	0	0	94.11	81.93	2.35

Design Expert 11.0 was conducted to analyze the test results to reveal the relationships between the factors and the evaluation indexes of fluid seed metering, and the regression equations were determined as follows:

$$Y_1 = -0.06R^2 - 85.21A^2 - 0.19D^2 + 3.38R + 118.63A - 0.16D + 0.14RA + 0.02RD - 0.36AD + 1.60 \quad (5)$$

$$Y_2 = -0.08R^2 - 127.75A^2 - 0.28D^2 + 4.27R + 160.30A - 2.42D + 0.5RA + 0.05RD - 1.25AD - 30.07 \quad (6)$$

$$Y_3 = 0.0027R^2 + 4.17A^2 + 0.029D^2 - 0.22R - 7.70A - 0.07D + 0.07RA + 0.001RD + 0.06AD + 8.13 \quad (7)$$

Table 6

Regression equation analysis of variance results

Source of variation	Right rate of hill distance Y_1 / %			Right rate of seeds per hill Y_2 / %			Rate of no seed hill Y_3 / %		
	DOF	F-Value	*p*-Value	DOF	*F*-Value	*p*-Value	DOF	*F*-Value	*p*-Value
Model	9	20.39	<0.0001**	9	10.55	<0.0001**	9	19.43	<0.0001**
R-R	1	3.02	0.11	1	17.58	0.0018**	1	13.47	0.0043**
A-A	1	6.56	0.03*	1	4.66	0.0562	1	7.51	0.02*
D-D	1	13.62	0.004**	1	0.30	0.60	1	0.96	0.35
RA	1	0.15	0.71	1	1.36	0.27	1	6.33	0.03*
RD	1	1.52	0.25	1	5.44	0.04*	1	0.61	0.45
AD	1	0.16	0.70	1	1.36	0.27	1	0.61	0.45
R^2	1	112.90	<0.0001**	1	154.03	<0.0001**	1	38.27	0.0001**
A^2	1	40.18	<0.0001**	1	63.93	<0.0001**	1	15.06	0.0031**
D^2	1	32.13	0.0002**	1	49.31	<0.0001**	1	113.06	<0.0001**
Residual	10			10			10		
Lack of fit	5	1.89	0.25	5	1.45	0.35	5	1.15	0.44
Error	5	R^2=0.9483		5	R^2=0.9627		5	R^2=0.9459	
Total	19			19			19		

*Note: * represents significant (p<0.05), ** represents highly significant (p<0.01).*

Table 6 shows the variance analysis of regression models of the right rate of hill distance, right rate of seeds per hill and rate of no seed hill. The response surface models of these evaluation indexes were significant ($p<0.01$). The lack of fit *F*-value was not significant ($p>0.05$) and the fitting degrees R^2 were larger than 0.94, indicating that the regression models were valid.

The significance of the influence of each factor on the evaluation indexes in the regression equation was determined by the *F* test. The evaluation index of the right rate of hill distance showed that the quadratic terms of *R*, *A* and *D* and the linear term of *D* were highly significant ($p<0.01$), and the linear term of *A* was significant ($p<0.05$), but the linear term of *R* had no significant effect on the right rate of hill distance ($p>0.05$). The primary and secondary orders of each factor that affected the right rate of hill distance were *D*, *A* and *R*. The evaluation index of the right rate of seeds per hill showed that the quadratic terms of *R*, *A* and *D* were extremely significant ($p<0.01$), and the linear term of *R* was highly significant ($p<0.01$), and the interaction term between *R* and *D* were significant ($p<0.05$). The primary and secondary orders of each factor that affected the right rate of seeds per hill were *R*, *A* and *D*.

The evaluation index of the rate of no seed hill showed that the quadratic terms of *R*, *A* and *D* and the linear term of *R* were extremely significant ($p<0.01$), and the linear term of *A* and the interaction term between *R* and *A* were significant ($p<0.05$). The primary and secondary orders of each factor that affected the rate of no seed hill were *R*, *A* and *D*.
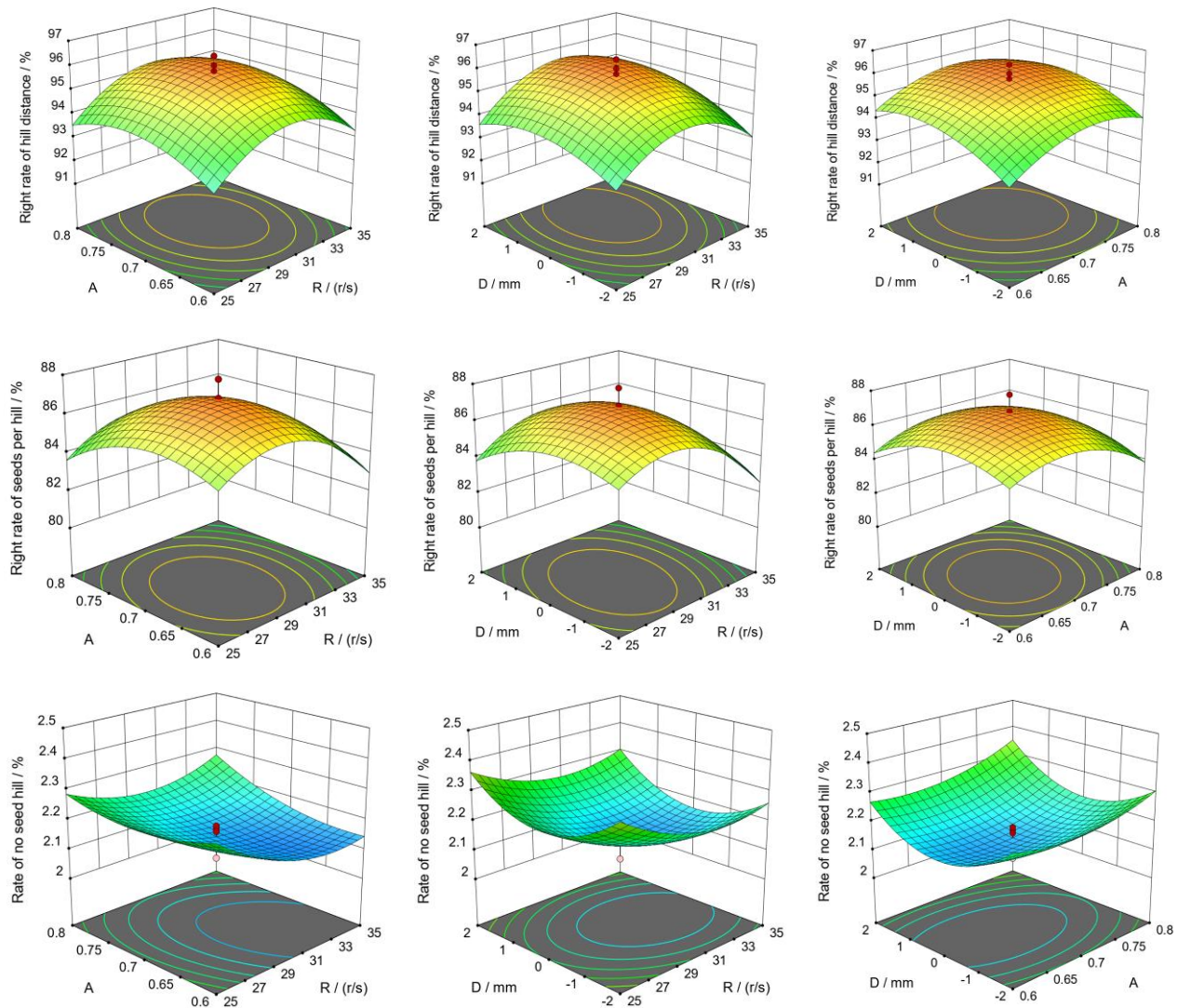
Fig. 4 - Response surface of various factors on the evaluation indexes of fluid seed metering test

Any two factors were fixed to 0 level, and the response surface was obtained according to regression equations (5), (6) and (7), respectively (Fig. 4).

The response surface figures showed that the change of the fluid seeding performance indexes were consistent with the single-factor experiment, and the interaction terms R and D was significant for Y_2, which indicated that the combined effect of stirring speed and the ratio between the length of stirring paddle and the diameter of seed box could improve the right rate of seeds per hill. Meanwhile, the interaction terms R and A were significant for Y_3, which indicated that the combined effect of the stirring speed and the distance between the pump tube and the stirring paddle could decrease the rate of no seed hill.

The Design expert 11.0 was adopted to the optimization of the fluid seed metering performance indexes to get the technical parameters of stirring, and the optimization equation is as follows：

$$\begin{cases} \max Y_1(R, A, D) \\ \max Y_2(R, A, D) \\ \min Y_3(R, A, D) \\ -1.682 \leq R \leq 1.682 \\ -1.682 \leq A \leq 1.682 \\ -1.682 \leq D \leq 1.682 \end{cases} \qquad (8)$$

The stirring parameters (R, A and D) for the maximization of Y_1 and Y_2, and the minimization of Y_3 predicted from the response surface models were as follows: the stirring speed of 30.21 r/s, the ratio between the length of stirring paddle and the diameter of seed box of 0.69, and the distance between the pump tube

and the stirring paddle of 0.11 cm. Under these parameters, the predicted values of the right rate of hill distance, right rate of seeds per hill and rate of no seed hill were 95.76%, 86.77% and 2.14%, respectively. The feasibility of the optimization results was validated through a verifying test. The test results are shown in Table 7. The error of Y_1, Y_2 and Y_3 between the actual results and the predicted values were less than 4%, indicating that the response surface model determined in this research was reliable. It can also be seen from Table 7 that the performance indexes of fluid seed metering have been improved after adding the stirring device, which has a reference value for improving the performance of millet fluid seeding.

Table 7

Results of verifying tests

Testing	Results			Error of Y_1 / %	Error of Y_2 / %	Error of Y_3 / %
	Y_1 / %	Y_2 / %	Y_3 / %			
Predicted values with stirring device	95.76	86.77	2.14	1.69	2.92	3.27
Measured values with stirring device	94.14	84.24	2.21			
Measured values without stirring device	90.02	80.55	3.19	/	/	/

CONCLUSIONS

The mechanical stirring device was added to the performance test of millet fluid seed metering, and the optimal stirring parameters of fluid seed metering were obtained based on the response surface test method, and the following conclusions were drawn:

(1) The inner diameter (thickness) of the pump tube suitable for millet fluid seed metering was 4.8 (1.6) mm, and the seeding performance indexes were the best when it was installed on the side of the seed box.

(2) According to the response surface test, the stirring speed, ratio between the length of stirring paddle and the diameter of seed box and distance between the pump tube and the stirring paddle have an influence on the seeding performance indexes of the right rate of hill distance, right rate of seeds per hill and rate of no seed hill.

(3) The optimal stirring parameters predicted from the response surface model were the stirring speed of 30.21 r/s, the ratio between the length of stirring paddle and the seed box diameter of 0.69 and the distance between the pump tube and the stirring paddle of 0.11 cm. The right rate of hill distance, right rate of seeds per hill and rate of no seed hill were 95.76%, 86.77% and 2.14%, respectively, and the error of these evaluation indexes from the actual results were less than 4%.

(4) Compared with the seed metering performance without the stirring device, the uniformity of the indexes with the addition of the stirring device were improved, which can provide references for improving the uniformity of the millet fluid seeding.

REFERENCES

[1] Blais B., Bertrand F., (2017), CFD-DEM investigation of viscous solid-liquid mixing: Impact of particle properties and mixer characteristics, *Chemical Engineering Research & Design*, Vol. 2017, Issue 118, pp. 270-285, London/England;

[2] Chen P., Zhang W., Luo W., et al.,(2010), Synthesis of super absorbent polymers by irradiation and their applications in agriculture, *Journal of Applied Polymer Science*, Vol. 93, Issue 4, pp. 59-65, San Hoboken/USA;

[3] Cui Q.L., Hou H.M., Zheng D.C., et al.,(2017), Design and test of tilt dise-type fine and small-amount seed metering device for foxtail millet, *Transactions of the Chinese Society of Agricultural Engineering* Vol. 32, Issue 12, pp.17-23, Beijing/P.R.C.;

[4] Currah I.E., Gray D., Thomas T.H.,(2010), The sowing of germinating vegetable seeds using a fluid drill, *Annals of Applied Biology*, Vol. 76, Issue 3, pp. 311-318, New Jersey/USA;

[5] Du W.J., Li P., Zhang X.W., et al.,(2015), Research progress and development direction of Shanxi millet seeding technology and equipment, *Journal of Agricultural Mechanization Research*, Vol. 2015, Issue 7, pp.6-10, Harbin/P.R.C.;

[6] Hayes M.J., Williams E.D.,(2010), Some effect fluid-sowing, pre-germination, irrigation and soil covering on the establishment and growth of seedlings of white clover slot-seeded into permanent pasture, *Grass & Forage Science*, Vol. 41, Issue 2, pp. 151-157, Blackwell/England;

[7] Li S.G., Liu F., Liu M., et al., (2014), The current industry situation, development trend, and suggestions for the future of foxtail millet in China, *Research of Agricultural Modernization*, Vol. 35, Issue 5, pp. 531-535, Changsha/P.R.C.;

[8] Li S.M., Lv H.M., (2021), Study on flow field distribution characteristics of a new type of vertical double impeller agitator, *Journal of Qingdao University of Science and Technology*, Vol. 42, Issue 6, pp. 89-110, Qingdao/P.R.C.;

[9] Pill W.G., (1991), Advances in fluid drilling, *HortTechnology*, Vol. 1, Issue 1, pp. 59-65, San Diego/USA;

[10] Ren L.M., Huang X.F., Cui Q.L.,(2014), Effect of different leaving seedling number each hole on hybrid millet yield and yield components, *Journal of Shanxi Agricultural Sciences*, Vol. 42, Issue 8, pp.842-844, Taiyuan/P.R.C.;

[11] Sun J.X., Yang L.Q., Xu B.H., et al.,(2021), Design and experiment of centrifugal collision test device for millet and sweet buckwheat grain, *INMATEH Agricultural Engineering*, Vol. 65, Issue 3, pp. 193-202, Bucharest/Romania;

[12] The Ministry of Agriculture of the People's Republic of China, (2006), Operating quality grains film-covering hill-drop drill, NY/T 987-2006, *China Agriculture Press*, Beijing/P.R.C.;

[13] Tian G., Wang Y. W., Li H.X. ,et al.,(2013), Current situation and development measures for millet industry in Shanxi province, *Journal of Shanxi Agricultural Sciences*, Vol. 41, Issue 2, pp. 299-300, Taiyuan/P.R.C.;

[14] Wu D.Y., (1995), Discussion on fluid seeding, *Crops*, Vol. 1995, Issue 1, pp. 31-32, Beijing/P.R.C.;

[15] Xin M.J., Liu L.X., Song Y.Q., et al., (2016), Experimental study on parameters of maize fluid hill-drop seeding, *Agricultural Research in the Arid Areas*, Vol. 34, Issue 1, pp.154-158, Yangling/P.R.C.;

[16] Xin M.J., Liu S.W., Su X.H., et al.,(2016), Structural optimization on metering mechanism of fluid hill-seeder, *Journal of Shenyang Agricultural University*, Vol. 34, Issue 1, pp. 154-158, Shenyang/P.R.C.;

[17] Xin M.J., Song Y.Q., Ren W.T., et al., (2008), Study on maize fluid hilling mechanism and metering device, *Journal of Agricultural Mechanization Research*, Vol. 2008, Issue 3, pp. 165-167, Harbin/P.R.C.;

[18] Zhang Y.Q., Cui Q.L., Wang F., et al.,(2017), Design and test of fluid and small-amount seed metering device for foxtail millet, *Transactions of the Chinese Society of Agricultural Engineering*, Vol. 33, Issue 12, pp. 20-27, Beijing/P.R.C..

DESIGN AND EXPERIMENT OF A COMBINED ROOT-CUTTING AND DITCHING DEVICE
/
组合式切根开沟装置的设计与试验

Xuening ZHANG, Yong YOU *), Decheng WANG *), Jie LV [1]
China Agricultural University, College of Engineering, Beijing / China
Tel: +86 10 010-62737977; +86 10 010-62737208; E-mail: youyong@cau.edu.cn; wdc@cau.edu.cn
Corresponding authors: Yong You, Decheng Wang
DOI: https://doi.org/10.35633/inmateh-66-38

ABSTRACT

To improve the ditching performance of high-firmness grassland, a bionic root cutter based on the contour curve model of Prosopocoilus astacoides' jaw was designed, as well as a grassland root-cutting and ditching device combining the bionic root cutter with the core-share opener. The grassland ditching experiment investigated the horizontal working resistance, ditching stability, and soil disturbance of the three ditching parts. According to the trial results, when the core-share opener was used for ditching in high-firmness grassland, the ditching stability was poor, the working resistance was high, and the grassland was severely damaged. Compared with the independent configuration of the core-share opener, the ditching performance can be significantly improved by installing a root cutter in front of the core-share opener, and the effect of installing the bionic root cutter was better than that of an ordinary triangular root cutter. When the ditching depth was 5 cm, 10 cm, and 15 cm, the ditching stability coefficient of the root-cutting and ditching device increased by 16.67%, 9.54%, and 6.18%, respectively, the horizontal working resistance reduced by 58.73%, 28.15%, and 19.84%, respectively, and the soil disturbance area reduced by 30.58%, 23.73%, and 20.21%, respectively.

摘要

为提高高坚实度草地的开沟性能，依据前锹甲上颚轮廓曲线模型，设计了一种新型仿生切根刀，并研制了一种将仿生切根刀与芯铧式开沟器相组合的草地切根开沟装置。通过草地开沟试验，对三种开沟部件的水平工作阻力、开沟稳定性以及草地扰动情况进行了比较分析。试验结果表明，芯铧式开沟器在高坚实度草地进行开沟作业时，其开沟稳定性较差、耕作阻力较大，对草地破坏严重。相较于芯铧式开沟器单独配置，在其前方加装切根刀可以显著提升开沟性能，且加装仿生切根刀比普通三角切根刀的效果更佳；加装仿生切根刀的芯铧式开沟器在 5cm、10cm、15cm 开沟深度时的开沟稳定性系数分别提高了 16.67%、9.54%、6.18%，水平工作阻力分别降低了 58.73%、28.15%、19.84%，土壤扰动面积分别降低了 30.58%、23.73%、20.21%。

INTRODUCTION

The subterranean roots of *Leymus Chinensis* are intertwined with soil to form the soil–root composites. The formation of the composites enhanced grassland firmness and decreased grassland permeability, which became the direct cause of natural grassland degradation in China (*You et al., 2011; You et al., 2011; He et al., 2016*). When ditching on natural grassland, the traditional ditching parts frequently fail to create the desired ditching effect. The ditching resistance is excessive, and the grassland vegetation and roots are seriously damaged. At the same time, the excessive disturbance created by traditional ditching parts makes the grassland susceptible to wind erosion, resulting in the deterioration of natural grassland. Therefore, developing ditching parts appropriate for high-firmness grassland is critical.

The current ditching parts of natural grassland are mostly improved by traditional farming parts, such as hoe-shovel openers, arrow-shovel openers, wing-shovel openers, core-share openers, disc openers, etc. (*Zhao et al., 2014*). Its application in farmland is quite mature, but it has great limitations as a ditching part of natural grassland (*He et al., 2015*).

---

[1] *Xuening Zhang, Ph.D. Stud. Eng; Yong You, As. Prof. Ph.D. Eng.; Decheng Wang, Prof. Ph.D. Eng.; Jie Lv, M.S. Stud. Eng.*

Scholars have studied the ditching of high-firmness grassland and reached some conclusions. *He et al. (2019)* investigated the coupling failure characteristics including surface disturbance and profile, disturbed cross-section area, soil over-turning rate, and coupling forces between the soil layer of natural grassland and selected passive subsoiler-type openers. *Liang et al. (2021)* achieved steady ditching of shallow grassland layer using a double-disc opener.

To address problematic ditching in high-firmness grassland, this paper designed a root-cutting and ditching device that combines the bionic root cutter with the core-share opener. It could ditch the grassland based on the grooves cut out by the root-cutting operation. The ditching performance of three ditching parts: core-share opener, triangular root cutter + core-share opener, bionic root cutter + core-share opener were compared and analyzed. The findings of the study can be used to generate fresh ideas and references for the design of ditching parts of natural grassland.

MATERIALS AND METHODS

● **Experimental site description**

The grassland ditching experiment was conducted on September 26, 2020. The experiment site was located in typical natural grassland in the Chabei district of Hebei province (41°28'31.649″N, 115°1'28.733″E). A flat topography and uniform grassland vegetation characterized the trial region. Leymus Chinensis was the dominant grass species in this area. The average of physical parameters of grassland obtained by field measurements were as follows: water content 9.98 %, bulk density 1.41 g/cm^3, firmness 2864 KPa, and porosity 50.47%.

● **Design of bionic root cutter**

Prosopocoilus astacoides feeds on the nutrient solution found in the plant's rhizome. The developed jaw and sharp edges of the *Prosopocoilus astacoides* enable it to cut the plant rhizome to access the nutrient solution. In this paper, the jaw of *Prosopocoilus astacoides* was taken as the research object, and its contour curve was fitted to the edge of the root cutter for the optimization design of the root cutter. The jaw contour of the *Prosopocoilus astacoides* was shown in Fig. 2 (a). Import the image of the *Prosopocoilus astacoides*' jaw into the MATLAB software, take points successively for the jaw contour of the *Prosopocoilus astacoides* by tracing points, and recording the coordinate values of each point (*Zhao et al., 2017*).

The fitting precision of the curve cannot be guaranteed using the low-order polynomial fitting method due to a large number of data points obtained, while the high-order polynomial fitting method would increase the difficulty of calculation and even distortion. Therefore, the full jaw contour curve of *Prosopocoilus astacoides* was obtained using the piecewise polynomial fitting method (*Liu et al., 2014*). The inner and outer contour curves of the *Prosopocoilus astacoides*' jaw were split into five stages for fitting in this article. The fitting equations of each stage were shown in table 1, and the determination coefficient for all equations were more than 0.9, indicating that the fitting effect of all equations was good.

Table 1

The fitting equations of each stage

Each stage		Fitting equation	Determination coefficient
Inner contour curve	Stage 1	$y = 0.106x^3 - 21.04x^2 + 1396x - 3.086e+04$	0.996
	Stage 2	$y = 7.32x^3 - 1.38e+03x^2 + 8.68e+04x - 1.82e+06$	0.999
	Stage 3	$y = -3.27x^3 + 626x^2 - 3.99e+04x + 8.49e+05$	0.985
	Stage 4	$y = -0.0087x^3 + 1.9x^2 - 1.4e+02x + 3.7e+03$	0.992
	Stage 5	$y = -0.00022x^3 + 0.074x^2 - 8.8x + 3.8e+02$	0.978
Outer contour curve	Stage 1	$y = -25x^3 + 1.4e+03x^2 - 2.5e+04x + 1.5e+05$	0.998
	Stage 2	$y = -0.021x^3 + 1.8x^2 - 52x + 6.2e+02$	0.985
	Stage 3	$y = -0.0032x^3 + 0.36x^2 - 16x + 3.1e+02$	0.992
	Stage 4	$y = -0.0013x^3 + 0.19x^2 - 11x + 2.6e+02$	0.998
	Stage 5	$y = -4.3e-05x^3 + 0.018x^2 - 2.5x + 1.3e+02$	0.935

The fitting curves of the inner and outer contours of the *Prosopocoilus astacoides*' jaw were shown in Fig. 1.
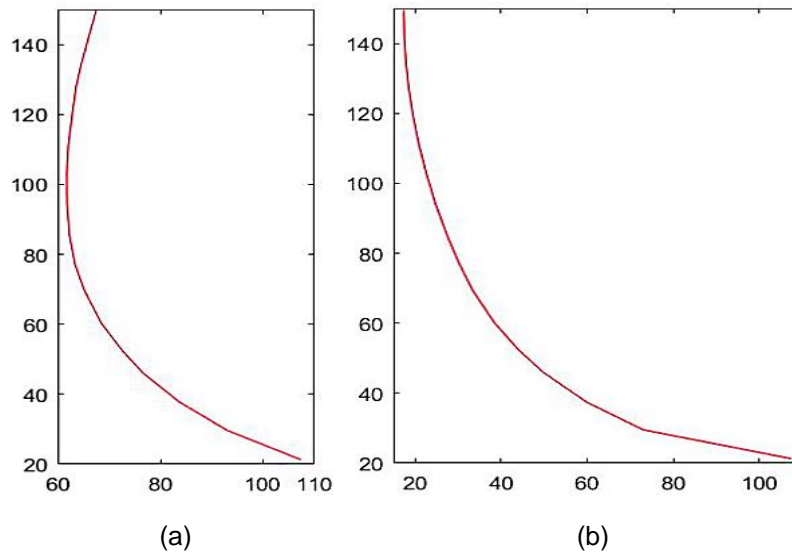

| (a) | (b) |

Fig. 1 - The fitting curves of the inner and outer contours of the *Prosopocoilus astacoides*' jaw:
(a) Fitting curve of the inner contour;   (b) Fitting curve of the outer contour

The simulation model of the bionic root cutter was established based on the fitting equations of the *Prosopocoilus astacoides*' inner and outer contour, as shown in Fig. 2 (b). The bionic root cutter model was scaled up and manufactured, as shown in Fig. 2 (c). According to the requirements of the grassland root-cutting operation and the processing size of the test bench, the penetration angle of the root cutter was set to 28.6 °, the penetration gap angle was set to 5.2 °, the blade length was set to 200 mm, the handle width was set to 50 mm, and the total length of the root cutter was set to 775 mm.
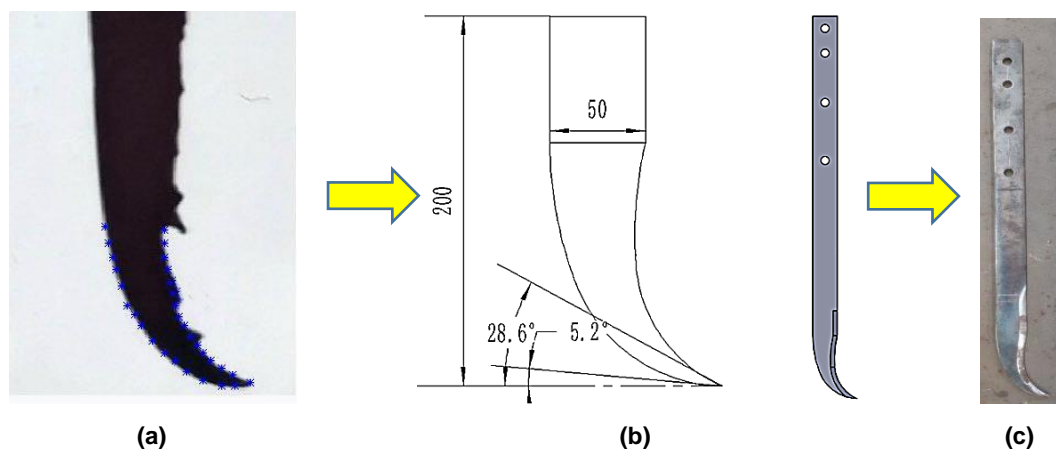

| (a) | (b) | (c) |

Fig. 2 - The bionic root cutter: (a) The jaw contour of the *Prosopocoilus astacoides*;
(b) Fitting contour and simulation model of root cutter; (c) Physical tool

● **Design of core-share opener**
The core-share opener is simple in structure and reliable in operation, and its main structure includes core-share, share handle, and wing plate. It can squeeze the soil on both sides along the ditch gap cut by the root cutter and expand it to seed ditches, which can better cooperate with the root cutter to complete the root-cutting and ditching operation.

The parameters of the core-share opener were selected by referring to the agricultural machinery design manual and other literature (*CAAMS, 2007; Cao et al., 2016*). A small penetration angle lengthens the share-tip and reduces the opener's strength, while a large penetration angle increases the opener's working resistance. Therefore, the opener's penetration angle α was set to 24°. A small penetration gap angle lowers the penetration performance of the opener, while a large penetration gap angle readily leads to an uneven ditch bottom. Therefore, the penetration gap angle ε of the opener was set to 9 °. Due to the small size of forage seeds, the width B of the opener was set to 40 mm.

The chamfer angle affects the slippage of the grassland soil, and the opener's chamfer angle γ was set to 60° to reduce soil disturbance. The ridge curvature radius affects the structural compactness of the opener, and the ridge curvature radius R of the opener was set to 300 mm. A high share-height increases the working resistance of the opener, and the share-height H of the opener was set to 110 mm. The structural parameters and physical objects of the core-share opener were shown in Fig. 3.
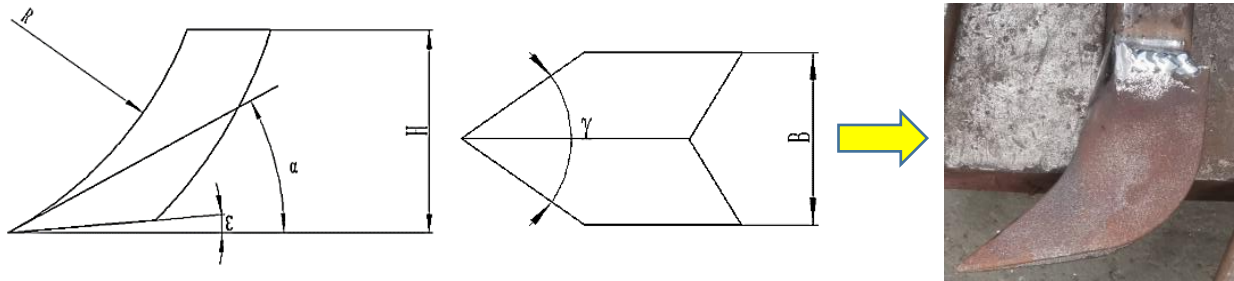

Fig. 3 - The core-share opener

● **Combined root-cutting and ditching device**

The combined root-cutting and ditching device was shown in Fig. 4. The main structure includes a traction frame, bionic root cutter, core-share opener, depth-limiting wheel, pressure sensor, and data collector. The test bench was linked with a tractor by three-point hydraulic suspension frames, and the power output shaft provides the operating power.
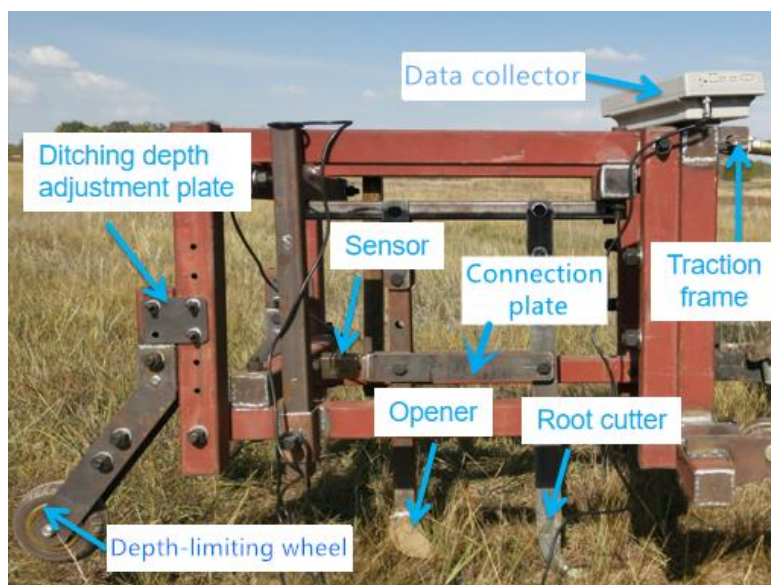

Fig. 4 - Combined root-cutting and ditching device

The connection plate connected the bionic root cutter to the core-share opener, and the machine penetrated the soil layer through its gravity. The pressure sensor was installed directly behind the connection plate, and received the horizontal working resistance from the ditching parts, which was then recorded by the data collector. To satisfy varied test requirements, the device can be equipped with the bionic root cutter and the core-share opener at the same time or individually. The ditching depth was adjusted by the depth-limiting wheel and ditching depth adjustment plate.

● **Experimental procedure and calculation**

To investigate the operating effectiveness of the combined root-cutting and ditching device, the grassland ditching experiment was carried out. There were three kinds of ditching parts: core-share opener, bionic root cutter + core-share opener, triangular root cutter + core-share opener. The triangular root cutter's penetration angle, penetration gap angle, and blade length were consistent with those of the bionic root cutter. The structural parameters of the triangular root cutter were shown in Fig. 5.

The device was operated at a forward speed of 1.08±0.14 km/h pulled by the tractor moving at a slow speed of No.2 level (*He et al., 2020*). The operating depth was 5 cm, 10 cm, and 15 cm, respectively. The evaluation indicators of the experiment were ditching stability coefficient, horizontal working resistance, and soil disturbance area.
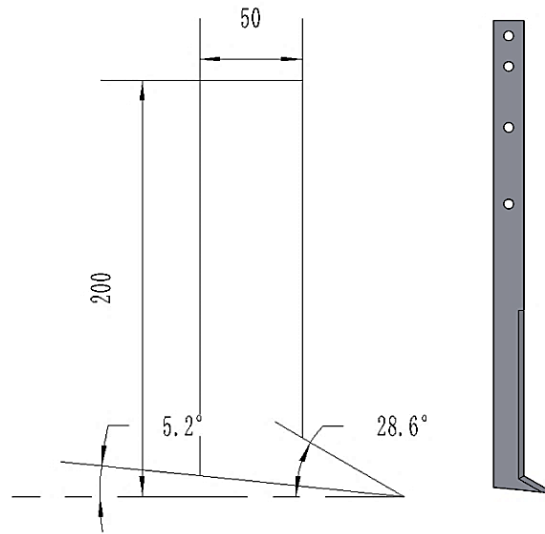

Fig. 5 - The structural parameters of the triangular root cutter

The ditching stability coefficient was used to describe the stability of working depth during the tillage movements of the ditching parts (*Pan et al., 2016; Yang et al., 2019*), calculated as follows:

$$S = \sqrt{\frac{\sum_{i=1}^{n}(h_i - h)^2}{N-1}} \tag{1}$$

$$V = \frac{S}{h} \times 100\% \tag{2}$$

$$U = (1-V) \times 100\% \tag{3}$$

where:
  U is the ditching stability coefficient;
  V is the coefficient of variation;
  S is the standard deviation of depth;
  h is the average value of depth;
  h_i is the measured depth value at the point i;
  N and n are the numbers of the measurement points.

The working resistance curve of each ditching part in the horizontal direction was collected by the pressure sensor. The stable stage of the curve was selected and its average value was calculated as the horizontal working resistance of each ditching part (*Hasimu et al., 2014; Ding et al., 2017*).

The soil disturbance area was utilized to assess the disturbance of each ditching part on natural grassland. The pit contour and ridge contour constitute the disturbance contour of the soil cross-section (*Huang et al., 2016*), as shown in Fig. 6.

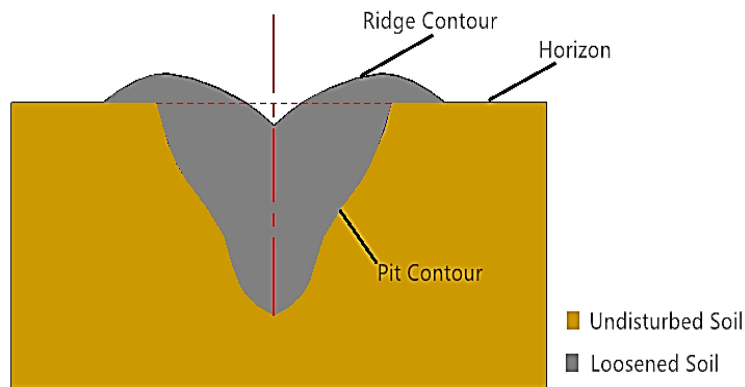The gray figure contour is the soil cross-section disturbance contour, and its area is the soil disturbance area.

Fig. 6 - Schematic diagram of the soil cross-section disturbance contour

The disturbed area of soil was measured by a profiler, as shown in Fig. 7. The profiler was composed of a connection ruler, strip slider, and fixed block. The strip slider could slide up and down along the connection ruler, and was held in place by the fixed block. The soil cross-section disturbance contour measured by the profiler was plotted on the coordinate paper, and the soil disturbance area was calculated.
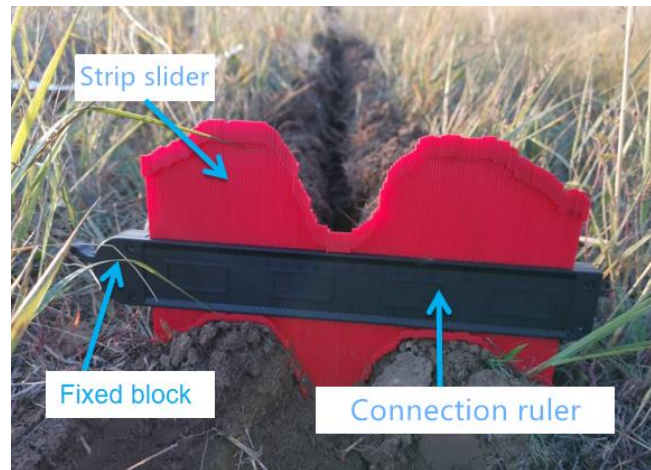

Fig. 7 - Determination of soil disturbance area

RESULTS

- **Ditching stability**

After each group's ditching test was completed, the actual ditching depth was measured every 1 m for a total of 8 times. The ditching stability coefficient was computed once the measurement was completed. The computation results were shown in Table 2. The ditching stability coefficient increased with the ditching depth increasing.

Table 2

Ditching stability coefficient

Type of ditching parts	Design ditching depth /cm	Actual ditching depth /cm	Relative error/%	Ditching stability coefficient /%
Core-share opener	5	3.7±0.966	26	71.82
	10	7.0±1.365	30	79.22
	15	12.1±1.581	19.3	86.10
Triangular root cutter + Core-share opener	5	4.6±0.994	8	76.65
	10	8.1±1.172	19	84.53
	15	12.3±1.612	18	86.03
Bionic root cutter + Core-share opener	5	5.1±0.545	2	88.49
	10	9.7±1.022	3	88.76
	15	13.9±1.003	7.3	92.28

The relative error between the actual and design ditching depth of the core-share opener was the largest. The relative error of the three ditching depths was more than 19%, making it impossible to satisfy the expected requirements of the design ditching depth. The ditching stability of the core-share opener was the worst, and its ditching stability coefficient varied obviously at different ditching depths, which was greatly affected by the ditching depth.

When the ditching depth was 5 cm or 10 cm, installing the triangular root cutter in front of the core-share opener increased the ditching stability coefficient by 4.83% and 5.31%, respectively. When the ditching depth was deepened to 15 cm, the ditching stability coefficients of the two became nearly identical. Under this ditching depth, installing the triangular root cutter would not help the core-share opener improve ditching stability.

The ditching stability increased even further when the bionic root cutter was installed in front of the core-share opener. The ditching stability coefficient increased by 16.67%, 9.54%, and 6.18% for ditching depths of 5 cm, 10 cm, and 15 cm, respectively. The ditching stability of the core-share opener could still be increased at a deeper ditching depth by installing the bionic root cutter. At varied ditching depths, the relative error between the actual and design ditching depths was less than 8%, and the ditching stability coefficients were all more than 88%. Furthermore, its ditching stability coefficients changed little at different ditching depths, implying that ditching depth has less of an influence on ditching stability.

- **Horizontal working resistance**

The horizontal working resistance of each ditching part at different ditching depths was shown in Fig. 8. The horizontal working resistance of ditching parts increased with the actual ditching depth increase. At the same ditching depth, the horizontal working resistance of the core-share opener was the highest. By installing a root cutter in front of the core-share opener, the horizontal working resistance of the ditching part considerably decreased, and the drag reduction effect of installing the bionic root cutter was superior to the triangular root cutter.

Each curve showed a high degree of fit with the R^2 value exceeding 0.96. Because the actual ditching depth of each ditching part varied, the horizontal working resistance of each ditching part was calculated by the fitting curve for comparative analysis when the ditching depth was 5 cm, 10 cm, and 15 cm. Compared with the single configuration of the core-share opener, when the ditching depth was 5 cm, 10 cm, and 15 cm, installing the triangular root cutter reduced the horizontal working resistance by 22.26%, 7.32%, and 3.25%, respectively, while installing the bionic root cutter reduced it by 58.73%, 28.15%, and 19.84%, respectively. The drag reduction effect of installing a root cutter steadily diminished with the ditching depth increasing. When the ditching depth was 15 cm, the drag reduction effect of installing the triangular root cutter was limited, while the drag reduction effect of installing the bionic root cutter was still close to 20%. The bionic root cutter still has a significant drag reduction effect when the ditching depth was deep.
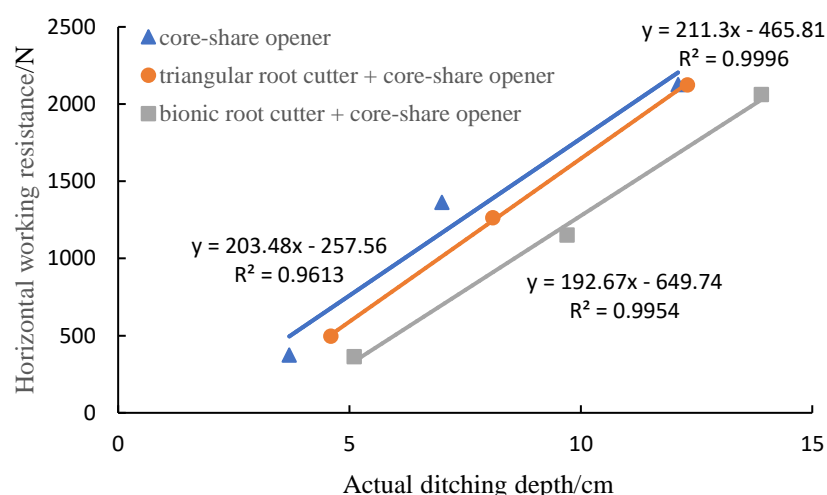

Fig. 8 - Horizontal working resistance of ditching parts

- **Soil disturbance area**

The soil disturbance area of each ditching part at different ditching depths was shown in Fig. 9. The soil disturbance area of each ditching part increased with the actual ditching depth increase. At the same ditching depth, the soil disturbance area of the core-share opener was the highest.

Installing the root cutter in front of the core-share opener considerably reduced the soil disturbance area, and the soil disturbance area caused by installing the bionic root cutter was significantly smaller than that generated by installing the triangular root cutter.

Each curve showed a high degree of fit with the R^2 value exceeding 0.98. Because the actual ditching depth of each ditching part varied, the soil disturbance area of each ditching part was calculated by the fitting curve for comparative analysis when the ditching depth was 5 cm, 10 cm, and 15 cm. Compared with the single configuration of the core-share opener, installing the triangular root cutter reduced the soil disturbance area by 23.09%, 9.46%, and 2.45% when the ditching depth was 5 cm, 10 cm, and 15 cm, respectively, while installing the bionic root cutter reduced it by 30.58%, 23.73%, and 20.21%, respectively. When the ditching depth was shallow, installing the triangular root cutter or the bionic root cutter in front of the core-share opener could significantly reduce the soil disturbance area. However, when the ditching depth was deepened to 10 cm, the effect of installing the triangular root cutter was considerably reduced. When the ditching depth was deepened to 15 cm, the soil disturbance area was reduced by just 2.45% by installing the triangular root cutter, but it was reduced by 20.21% by installing the bionic root cutter. Even though the ditching depth was deep, the bionic root cutter greatly reduced the soil disturbance area.
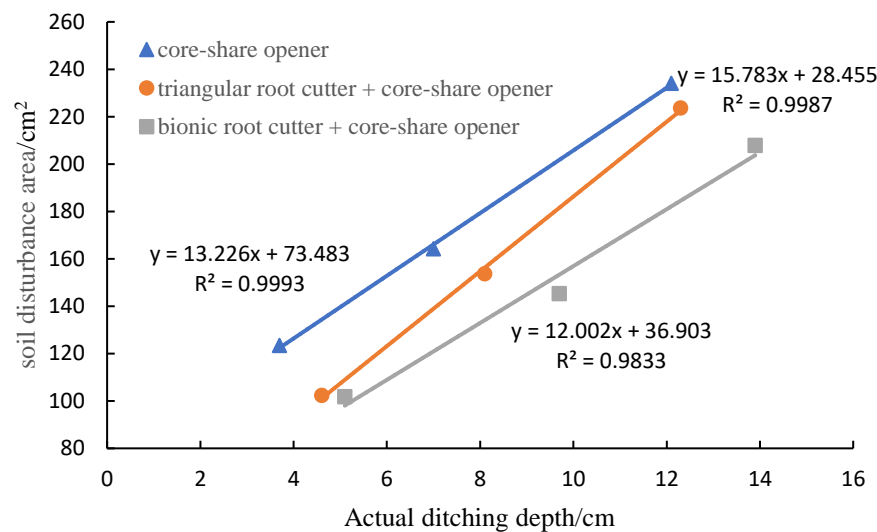

Fig. 9 - Soil disturbance area of ditching parts

The disturbance of the grassland surface by the ditching parts was shown in Fig. 10. The grassland surface displayed the phenomenon of big clods being overturned along the furrow after the ditching operation was completed by the core-share opener. The roots of the grassland were turned out with the soil, inflicting significant damage to the natural grassland. After the ditching operation of the core-share opener equipped with the triangular root cutter or the bionic root cutter was completed, no large clods were overturned and the damage to the grassland was insignificant.
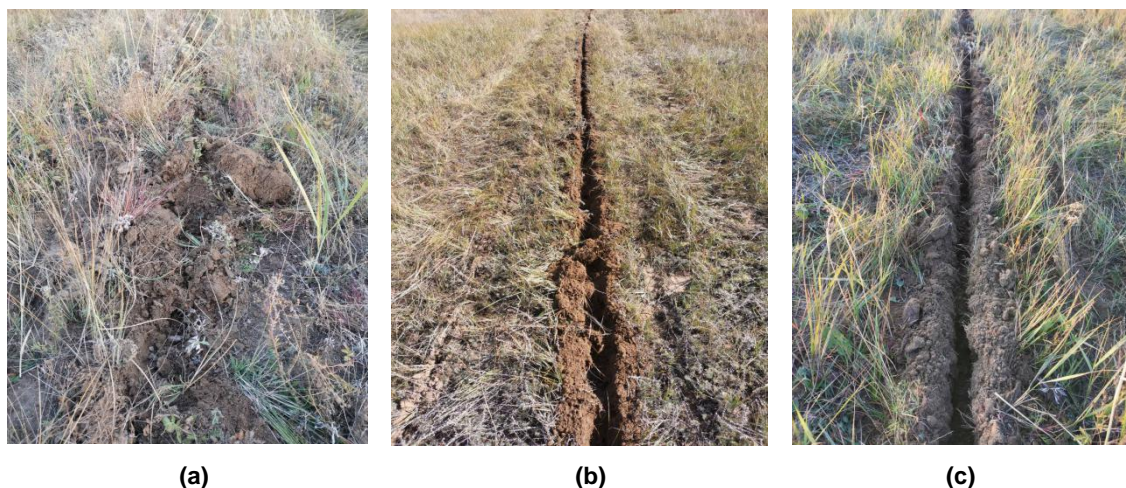

(a)   **(b)**   **(c)**

Fig. 10 - Disturbance of grassland surface: (a) Core-share opener;
(b) Triangular root cutter + Core-share opener; (c) Bionic root cutter + Core-share opener

As shown in Fig. 11 (a), the core-share opener squeezed out the soil through the core-share during the ditching operation. Due to its large width and poor soil-breaking performance, the core-share opener not only destroyed the grassland vegetation and roots seriously but also created big clods on the surface of the grassland. During the operation of the combined root-cutting and ditching device, the root cutter cut out the grooves on the surface of the grassland and cut off the roots at the same time. Then, the core-share opener squeezed the soil with the grooves cut out by the root cutter. The operation process reduced the pulling of the core-share opener on the roots, so the combined root-cutting and ditching device has less disturbance during ditching operation, as shown in Fig. 11 (b).

(a)   (b)

Fig. 10 - Coupling procedure between the grassland surface and ditching parts:
(a) Core-share opener; (b) Root cutter + Core-share opener

CONCLUSIONS

(1) Because of its poor ditching stability, high ditching resistance, and substantial damage to grassland vegetation and roots, the core-share opener was not suitable for grassland ditching alone. The combined root-cutting and ditching device improved ditch stability and reduced the working resistance and grassland damage.

(2) When the ditching depth was 5 cm, 10 cm, and 15 cm, compared with the core-share opener, the combined root-cutting and ditching device increased the ditching stability by 16.67%, 9.54%, and 6.18%, respectively, and the horizontal working resistance reduced by 58.73%, 28.15%, and 19.84%, respectively, and the soil disturbance area decreased by 30.58%, 23.73%, and 20.21%, respectively.

(3) The ditching depth has a great influence on the ditching effect of the ditching parts. When the ditching depth was deep, the ditching stability of the ditching parts improved, but the horizontal working resistance of the ditching parts and the disturbance damage to the grassland increased. When the ditching depth was shallow, the ditching effect could be significantly improved by installing the triangular root cutter or the bionic root cutter in front of the core-share opener. When the ditching depth was deep, the ditching effect improved by installing the triangular root cutter was limited, but the ditching effect could still be significantly improved by installing the bionic root cutter.

ACKNOWLEDGEMENT

REFERENCES

[1]   CAAMS (Chinese Academy of Agricultural Mechanization Sciences), (2007). *Agricultural machinery design manual.* pp. 377, Beijing/China.

[2]   Cao X., Zhao S., Liu H., Yang Y., Zhou Y., (2016). Design and Experiment of Winter-wheat No-tillage Seeder for Inter-planting (垄间套播冬小麦免耕播种机设计与试验). *Journal of Agricultural Mechanization Research*, Vol. 38, pp. 157-161, Heilongjiang/China.

[3]   Ding Q., Ge S., Ren J., Li Y., He R., (2017). Characteristics of Subsoiler Traction and Soil Disturbance in Paddy Soil (水稻土深松阻力与土壤扰动效果研究). *Transactions of the Chinese Society for Agricultural Machinery*, Vol. 48, pp. 47-56, Beijing/China.

[4] Hasimu A., Chen Y., (2014). Soil disturbance and draft force of selected seed openers. *Soil & Tillage Research*, Vol. 140, pp. 48-54, Amsterdam/Netherlands.

[5] He, C., Wang, D., Wang, G., You Y., Liang F., Liu L., Shao C., (2015). The development of grassland mechanical restoration technology research (天然草地机械化改良技术研究进展). *Journal of Agricultural Mechanization Research*, Vol. 37, pp. 258-263, Heilongjiang/China. (in Chinese with English abstract)

[6] He C., You Y., Wang D., He G., Wu H., Ye B., (2019). Effect of tine geometry on penetration resistance during vertical movement on natural grassland. *INMATEH-Agricultural Engineering*, Vol. 59, pp.19-26, Bucharest / Romania.

[7] He C., You Y., Wang D., Wang G., Wu H., Gong S., (2016). Mechanical characteristics of soil-root composite and its influence factors in degenerated grassland (退化草地复合体力学特性与影响因素研究). *Transactions of the Chinese Society for Agricultural Machinery*, Vol. 47, pp. 79-89, Beijing/China.

[8] He C, You Y, Wang D, Wu H., Ye B., (2020). An experimental investigation of soil layer coupling failure characteristics on natural grassland by passive subsoiler-type openers. *INMATEH - Agricultural Engineering*, Vol. 60, pp. 293-302, Bucharest / Romania.

[9] Huang Y., Hang C., Yuan M., Wang B., Zhu R., (2016). Discrete Element Simulation and Experiment on Disturbance Behavior of Subsoiling (深松土壤扰动行为的离散元仿真与试验). *Transactions of the Chinese Society for Agricultural Machinery*, Vol. 47, pp. 80-88, Beijing/China.

[10] Liang F., Wang D., You Y., Wang G., Wang Y., Zhang X., Feng J., (2021). Design and experiment of root-cutter with fertilization and reseeding compound remediation machine for grassland (草地切根施肥补播复式改良机设计与试验). *Journal of Jilin University (Engineering and Technology Edition)*, pp. 1-10, Jilin/China.

[11] Liu X., Wang Y., (2014). Research of Automatically Piecewise Polynomial Curve-fitting Method Based on Least-square Principle (基于最小二乘法的自动分段多项式曲线拟合方法研究). *Science Technology and Engineering*, Vol. 14, pp. 55-58, Beijing/China.

[12] Pan S., Cao Z., Yang Y., Zhao W., (2016). The Design n of Furrow Opener Based on Discrete Element Method (基于离散元法的芯铧式开沟器设计). *Journal of Agricultural Mechanization Research*, pp. 23-27, Heilongjiang/China.

[13] Yang W., Wu B., Peng Z., Tan S., (2019). Estimation of the Operation Quality of Vertical Helix Furrow Openers Based on the Discrete Element Method (基于离散元法立式螺旋开沟器开沟质量的评价). *Journal of Southwest University(Natural Science)*, Vol. 41, pp. 1-7, Chongqing/China.

[14] You Y., Wang D., Liu J., (2011). A device for mechanical remediation of degraded grasslands. *Soil & Tillage Research*, Vol. 118, pp. 1-10, Amsterdam/Netherlands.

[15] You Y., Wang D., Wang G., (2011). 9QP-830 Soil-gashing and Root-cutting Mechanism (9QP-830 型草地破土切根机). *Transactions of the Chinese Society for Agricultural Machinery*, Vol. 42, pp. 61-67, Beijing/China.

[16] Zhao S., Liu H., Tan H., Cao X., Zhang X., Yang Y., (2017). Design and performance experiment of opener based on bionic sailfish head curve (仿旗鱼头部曲线型开沟器设计与性能试验). *Transactions of the Chinese Society of Agricultural Engineering (Transactions of the CSAE)*, Vol. 33, pp. 32-39, Beijing/China.

[17] Zhao J., Yang X., Zhou J., Liu L., Yang H., (2014). Analysis the Current Situation about Furrow Opener and its Performance Test Device (播种机开沟器及其性能测试装置的现状分析). *Journal of Agricultural Mechanization Research*, Vol. 1, pp. 238-241, Beijing/China.

DESIGN AND EXPERIMENT OF IMPURITY REMOVAL DEVICE OF POTATO COMBINE HARVESTER
/
马铃薯联合收获机除杂装置的设计与试验

Danyang LV[1)], Jiayi REN[1)], Meng ZHANG[2,3)], Xiangyou WANG[1,*)], Pengxiang MENG[2,3)], Xueqiang LI[2,3)], Xiaohui YANG[1)]
[1)]School of Agricultural Engineering and Food Science, Shandong University of Technology, Zibo 255091, China
[2)]Shandong Provincial Intelligent Engineering and Technology Research Center for Potato Production Equipment, Dezhou 253600, China
[3)]Shandong Star Agricultural Equipment Co., Ltd., Dezhou 253600, China
Tel: +86-13806481993; E-mail: wxy@sdut.edu.cn

ABSTRACT
Because of the low impurity removal rate and high damage rate of the potato combine harvester during the working process, a new type of impurity removal device for the potato combine harvester was designed. The device was mainly composed of retaining plates, impurity removal rollers, smooth rollers, and a control system. To determine the best working parameters of the device, the rotational speed of the rollers, the distance between two rollers, and the inclination angle of the device were used as the test factors. The impurity removal rate and damage rate were employed as the evaluation indexes. Then, the single factor test and the second rotation orthogonal regression test were performed. The optimum combination after parameter optimization was determined to be as follows: rotational speed of the rollers was 113.4 r/min, the distance between the two rollers was 97.5 mm and the inclination angle of the device was 10.4°. The corresponding impurity removal rate was 95.12%, and the damage rate was 0.54%. The device can better meet the requirements of impurity removal operations.

摘要
针对马铃薯联合收获机除杂过程中除杂率低、伤薯率高的情况，设计了一种用于马铃薯联合收获机的新型除杂装置。该装置主要由挡土板、除杂辊、光辊、控制系统等组成。为确定装置的最佳工作参数，以辊速、辊距和装置倾角为试验因素，以除杂率和伤薯率为评价指标，进行了二次旋转正交回归试验。获取了最优参数组合为辊速113.4r/min、辊距为97.5mm和装置倾斜角度为10.4°。最优参数下的验证试验结果表明，平均除杂率为95.12%、平均伤薯率为0.54%。该装置能较好地满足马铃薯除杂作业要求。

INTRODUCTION

China is one of the largest potato-producing countries in the world (*Jia et al. 2021; Ji et al. 2020*). In 2021, the total planting area of potatoes in China reached 57,000 hectares and the output exceeded 90 million tons (*Wen et al. 2022; Duan et al. 2022*). The harvested potatoes contain a large number of impurities such as soil and weeds, which cannot be removed well by traditional debris removal devices alone (*Wei et al. 2019; Geng et al. 2021*). At present, there is less research on the impurity removal device in China (*Sun et al. 2017; Zhang et al. 2021*), and the existing impurity removal rollers have a single structure, which has the problems of low impurity removal rate and high damage rate of potatoes.

In recent years, the research on impurity removal equipment mainly had focused on the shape, arrangement, and rotation speed of the rollers (*Wei et al. 2019; Yang et al. 2021*). For example, some scholars changed the arrangement of the rollers and used double rows of rollers to remove impurities (*Yang et al. 2014*). Some scholars chose nylon as the material of the rollers and carried out comparative experiments (*Zhang et al. 2021*). The results showed that the new type of roller has a better effect of removing impurities than the traditional one. In order to improve production efficiency, some scholars designed a machine that can both remove impurities and grade potatoes (*Wang et al. 2017*). Some scholars analyzed the impurity removal process and optimize the design of the rollers based on the analysis results (*Lv et al. 2021*).

---

[1] *Danyang Lv, M.S. Stud. Eng.; Jiayi Ren, M.S. Stud. Eng.; Meng Zhang, Ph.D. Stud.; Xiangyou Wang, Prof. Ph.D. Eng.; Pengxiang Meng, M.S. Eng.; Xueqiang Li, PE.; Xiaohui Yang, M.S. Stud. Eng.*

According to the conclusions of the above research and combined with the current research status of the potato combine harvester, a new type of impurity removal device for potato combine harvester was designed in this study. The device adopted the form of an alternate arrangement of impurity removal rollers and smooth rollers, which can effectively remove impurities and reduce the damage rate of potatoes. Then, single factor test and second rotation orthogonal regression test were performed on the device. After several tests, the optimal working parameters were obtained. The research results provide a theoretical basis and reference for the optimal design of the impurity removal device.

MATERIALS AND METHODS

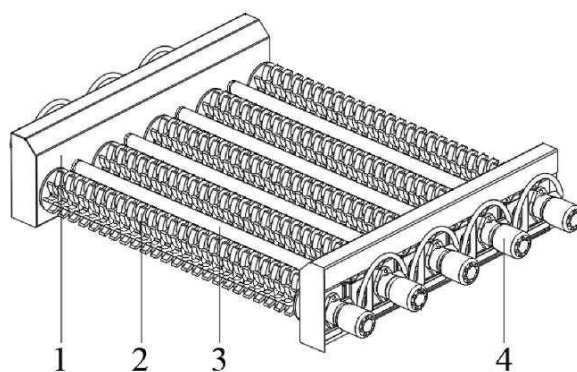### Whole structure and working principle

Fig. 1 – Overall structure of the impurity removal device
1. Retaining plate; 2. Impurity removal rollers; 3. Smooth rollers; 4.Control system

As shown in Fig. 1, the device was mainly composed of retaining plates, impurity removal rollers, smooth rollers, and a control system. The rotational speed and direction of rotation of the impurity removal rollers and the smooth roller were the same. The device removed impurities through the frictional collision between the rollers and the potatoes. Smaller clods and weeds fell out of the unit from the gap between the rollers, and cleaned potatoes fall to the conveyor belt. The rotational speed of the rollers, the distance between the rollers, and the inclination angle of the device can be adjusted to meet the needs of the operation under different soil conditions. The main technical parameters of the whole machine are shown in Table 1.

Table 1

Technical parameters of impurity removal device

Parameters	Value
Overall dimensions (Length × Width × Height) [mm]	1630×1295×350
Rated pressure of hydraulic motor [M Pa]	8
Electric motor power of hydraulic power system [kW]	6
Rotational speed of the rollers [r/min]	80~120
Distance between two rollers [mm]	100~160
Inclination angle of the device [°]	8~16

Design analysis of key mechanisms

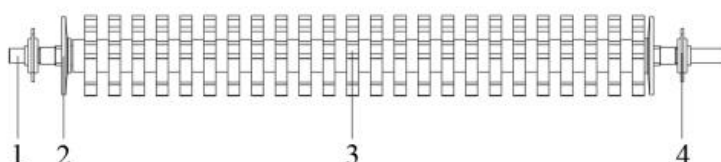### The design of impurity removal rollers

Fig. 2 – Structure of impurity removal roller
1.Axle; 2. Baffle; 3. Rubber sleeve; 4. Bearing blocks

As shown in Fig. 2, the impurity removal roller consists of an axle, baffles, a rubber sleeve, and bearing blocks. To reduce the damage to the potato between the two rollers, referring to the potato damage law of the research, the material of the sleeve is rubber (*Chen et al. 2020*).

To increase the number of contact friction between the impurity removal rollers and the surface of the potatoes, and have a better impurity removal effect, the structure of the rubber sleeve is shown in Fig. 3.

To reduce the rate of potato injury, the edge *1* (shown in Figure 3) in the rubber sleeve was designed as a concave arc, and the edge *2* was designed as an external convex arc. The shape of the potato is ellipsoid, so the edge of the rubber sleeve consists of 4 arcs of tangent transition.
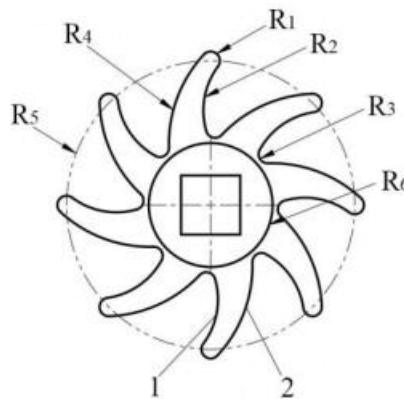

Fig. 3 – Structure of impurity removal wheel

The radii of the arcs are: R1=5 mm; R2=40 mm; R3=10 mm; R4=70 mm. Also, R5=78.5 mm; R6=33.5 mm. To comply with the potato combine harvester, referring to the existing structure and size of the impurity removal roller, the length of the impurity removal roller was designed to be 1200 mm.
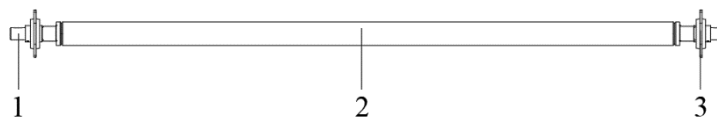
The design of smooth rollers

Fig. 4 – Structure of smooth roller
1. Inner shaft; 2. Outer shaft; 3. Bearing blocks

To improve the impurity removal rate, a smooth roller was installed between adjacent impurity removal rollers. Among them, the rotational speed and direction of rotation of the smooth rollers were consistent with the impurity removal rollers. As shown in Fig. 4, the smooth roller consists of an inner shaft, an outer shaft, and bearing blocks. To improve the crushing effect of the clods and reduce the resistance of the potatoes to pass over the smooth rollers, the material of the smooth roller was selected from alloy steel with high strength and low friction coefficient. Referring to the structural parameters of the impurity removal roller, it is determined that the diameter of the outer shaft of the smooth roller is 48 mm, the diameter of the inner shaft is 25 mm, and the length is 1190 mm.
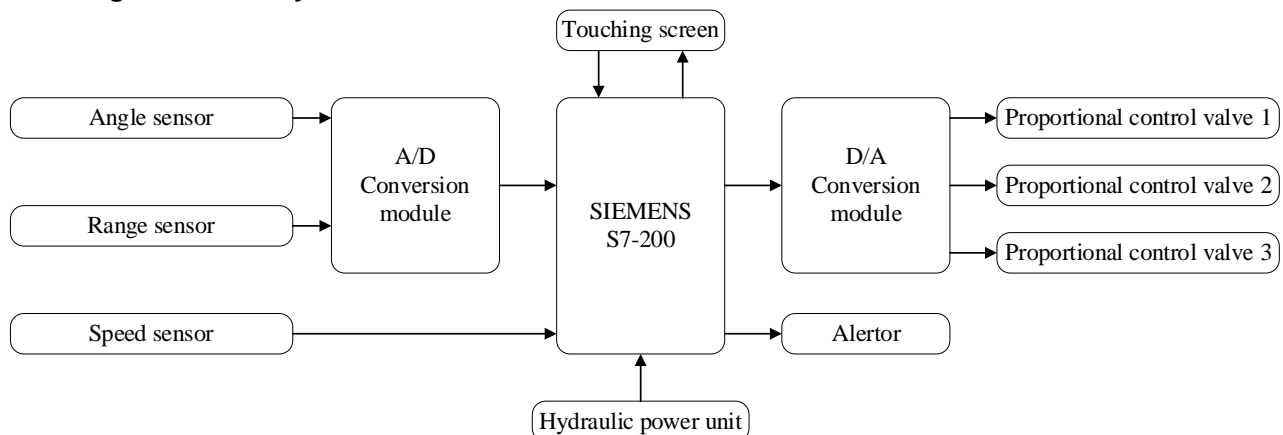
The design of control system

Fig. 5 – Schematic diagram of the control principle

To meet the working requirements of the impurity removal device, the control system for the device was designed. The schematic diagram of the control principle is shown in Fig. 5. It mainly includes detection module, control module, and alarm module.

CBN hydraulic power unit was selected as the power source of the impurity removal device. The speed of the rollers was controlled by BMR-160 hydraulic motor. The distance between two rollers and the inclination angle of the device were controlled by HSG-40 hydraulic cylinder. The main control module of the system was Siemens PLC S7-200. The system hardware was mainly composed of the main controller, TPC7062Ti touching screen, C12-10NO speed sensor, JUB500-30GM-E5-V15 distance sensor, MPU-6050 angle sensor, EFBF-03-160-H proportional control valve, etc. The system controlled the work of each actuator by collecting the rotational speed of the rollers, the distance between two rollers, and the inclination angle of the device.

Experimental design

To obtain the optimal working parameters combination of the impurity removal device, the rotational speed of the rollers, the distance between two rollers, and the inclination angle of the device, which has a great influence on the impurity removal effect, were selected as the test factors, and the influence of the three factors on the performance of the impurity removal device was analyzed. The three factors were adjusted in the following manner:

1. Rotational speed of the rollers: the rotational speed was regulated by the hydraulic motor.
2. Distance between two rollers: the distance was regulated by the distance adjustment device.
3. Inclination angle of the device: the angle was regulated by the hydraulic cylinder.

Fig. 6 – Test prototype

The test contents and methods are as follows. Firstly, the parameter ranges of the rotational speed of the rollers, the distance between two rollers, and the inclination angle of the device were obtained by using single factor tests. Then, the distance between two rollers, and the inclination angle of the device were used as the test factors. And the impurity removal rate and the damage rate were employed as the evaluation indexes. Finally, the orthogonal test of three factors and five levels was carried out.

The test was carried out in Dezhou City, Shandong Province. The test material was the Xisen No. 4 potatoes harvested on the same day. The average diameter of the potatoes was 47.2 mm, the average length was 82.4 mm, the average moisture content was 84.6%, and the average mass was 95.3 g. The test photo is shown in Fig. 6.

Performance evaluation of the impurity removal device

The test indicators were based on the relevant requirements in the Chinese national standards NY/T 648—2015 "Technical Specification for Quality Evaluation of Potato Harvesters"(Wei et al. 2019; Zhang et al. 2020). The selected test response indicators were the impurity removal rate y_1, and damage rate y_2.

The calculation formula is as follows:

$$y_1 = \frac{m_1}{m_1 + M} \times 100\% \tag{1}$$

$$y_2 = \frac{m_2}{m_1} \times 100\% \tag{2}$$

Where:

m_1—is the total potato mass after harvest operation, kg;

M—is the total mass of impurities, kg;

m_2—is the quality of damaged potatoes after harvesting, kg;

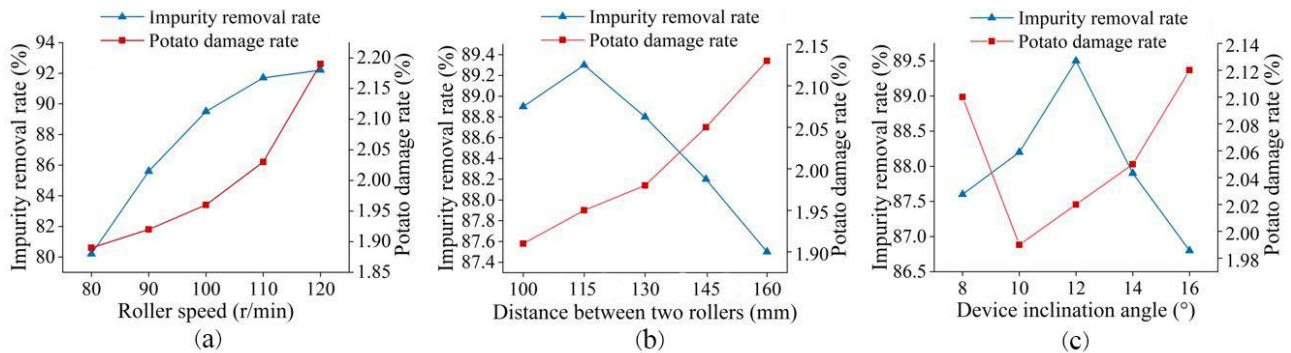## RESULTS AND ANALYSIS
Single factor test

Fig. 7– Impact of rotational speed of the rollers on evaluation indexes

The distance between the two rollers was set to 130 mm; the inclination angle of the device was set to 12°; the rotational speed of the rollers was adjusted to 80, 90, 100, 110, and 120 r/min respectively. It can be seen from Fig. 7a that with the increase of the rotational speed of the rollers, both the impurity removal rate and the damage rate showed an upward trend. When the rotational speed of the rollers reached 110 r/min, the impurity removal rate increased slowly, but the damage rate increased rapidly. Overall, the device worked better when the speed of the rotational speed of the rollers was in the range of 100 to 110 r/min.

The rotational speed of the rollers was set to 100 r/min; the inclination angle of the device was set to 12°; the distance between the two rollers was adjusted to 100, 115, 130, 145, and 160 mm, respectively. It can be seen from Fig. 7b that with the increase of the distance between the two rollers, the impurity removal rate first increased slowly and then decreased rapidly, but the damage rate had been on the rise. When the distance between the two rollers was in the range of 100 to 130 mm, the impurity removal rate was higher than 88%, the damage rate was lower than 2%. It showed that the device works well.

The distance between the two rollers was set to 130 mm; the rotational speed of the impurity removal rollers was 100 r/min; the inclination angle of the device was adjusted to 8, 10, 12, 14, and 16° respectively. As shown in Fig. 7c, when the inclination angle of the device was in the range of 8 to 12°, the impurity removal rate increased with the increase of the inclination angle. When the inclination angle of the device was in the range of 12 to 16°, the impurity removal rate decreased with the increase of the inclination angle of the device, but the damage rate first decreased and then increased. This results in the best overall performance of the device when the inclination angle was 10 to 14°.

Orthogonal experiment results and analysis

Through the single factor test analysis, it was obtained that the range of factors with good performance was that the rotational speed of the rollers was 100 to 110 r/min, the distance between the two rollers was 100 to 130 mm, and the inclination angle of the device was 10 to 14°. The orthogonal test was designed with the ranges obtained by the single factor test. The level of each factor was determined as shown in Table 2.

Table 2

Experimental factors and levels

levels	Factors		
	Rotational speed of the rollers A	**Distance between two rollers B**	**Inclination angle of the device C**
	[r/min]	**[mm]**	**[°]**
1.68	113.4	140.2	15.4
1	110	130	14
0	105	115	12
-1	100	100	10
-1.68	96.6	89.8	8.6

According to the test scheme, 23 groups of tests were performed, and each group of tests was repeated three times. Take the average value as the test results. And the test results are shown in Table 3.

Table 3

The experiment results

Test number	A	B	C	Impurity removal rate Y_1	Potato damage rate Y_2
	[R/min]	[mm]	[°]	%	%
1	-1	-1	-1	94.21	0.53
2	1	-1	-1	95.94	0.62
3	-1	1	-1	93.95	0.49
4	1	1	-1	96.35	0.95
5	-1	-1	1	95.43	0.74
6	1	-1	1	96.32	1.08
7	-1	1	1	94.71	0.85
8	1	1	1	97.02	1.25
9	-1.68	0	0	94.21	0.53
10	1.68	0	0	96.47	0.84
11	0	-1.68	0	96.13	0.72
12	0	1.68	0	95.28	1.03
13	0	0	-1.68	94.57	0.56
14	0	0	1.68	95.28	1.03
15	0	0	0	96.47	0.97
16	0	0	0	96.41	1.03
17	0	0	0	95.68	1.08
18	0	0	0	95.83	1.01
19	0	0	0	96.24	0.96
20	0	0	0	96.02	0.97
21	0	0	0	96.35	1.02
22	0	0	0	96.41	0.94
23	0	0	0	96.52	1.07

Variance analysis

Analysis of variance (ANOVA) was performed using Design Export 10.0 for the impurity removal rate and damage rate, and the results are shown in Tables 4-5. It can be seen from the two tables that the model terms are all significant (P < 0.01), and the lack of fit terms is not significant (P > 0.1). This indicates that the regression equation fits well and can represent the mathematical relationship between the three factors and the two response indicators.

Table4

Variance analysis results of impurity removal rate

Source	Sum of Squares	DF	Mean Square	F Value	P Value
Model	15.17	9	1.69	14.77	<0.0001**
A	9.07	1	9.07	79.48	<0.0001**
B	0.12	1	0.12	1.08	0.3169
C	1.31	1	1.31	11.45	0.0049**
AB	0.55	1	0.55	4.78	0.0476*
AC	0.11	1	0.11	0.95	0.3482
BC	0.004	1	0.004	0.032	0.8615
A^2	1.10	1	1.19	9.64	0.0084**
B^2	0.29	1	0.29	2.50	0.1377
C^2	2.67	1	2.67	23.38	0.003**
Residual	1.48	13	0.11		
Lack of Fit	0.76	5	0.15	1.67	0.2464
Pure Error	0.73	8	0.091		
Cor Total	16.66	22			

*Note: P < 0.01 (extremely significant, **), 0.01<P < 0.05 (significant, *).*

It can be seen from Table 4 that A, C, A^2 and C^2 have extremely significant effects on the impurity removal rate (P<0.01), and AB has a significant effect on the impurity removal rate (0.01<P<0.05).

Other factors had no significant effect on the impurity removal rate (P>0.1). After removing insignificant terms, the fitted regression equation is:

$$y_1 = 96.13 + 0.82A + 0.31C + 0.26AB - 0.26A^2 - 0.41C^2 \tag{3}$$

Variance analysis results of damage rate

Source	Sum of Squares	DF	Mean Square	F Value	P Value
Model	0.92	9	0.10	22.06	<0.0001**
A	0.24	1	0.24	51.66	<0.0001**
B	0.065	1	0.065	13.91	0.0025**
C	0.33	1	0.33	70.79	<0.0001**
AB	0.023	1	0.023	4.97	0.0441*
AC	0.004	1	0.004	0.97	0.3426
BC	1.25×10^{-5}	1	1.25×10^{-5}	2.68×10^{-3}	0.9594
A²	0.16	1	0.16	35.06	<0.0001**
B²	0.040	1	0.040	8.55	0.0118*
C²	0.062	1	0.062	13.31	0.0029**
Residual	0.060	13	4.65×10^{-3}		
Lack of Fit	0.041	5	8.2×10^{-3}	3.38	0.0617
Pure Error	0.019	8	2.42×10^{-3}		
Cor Total	0.98	22			

Note: P < 0.01 (extremely significant, **), 0.01<P < 0.05 (significant, *)

It can be seen from Table 5 that A, B, C, A² and C² have extremely significant effects on the damage rate (P<0.01), and B²、AB have a significant effect on the damage rate (0.01<P<0.05). Other factors had no significant effect on the damage rate (P>0.1). After removing insignificant terms, the fitted regression equation is:

$$y_2 = 1 + 0.13A + 0.069B + 0.16C + 0.054AB - 0.1A^2 - 0.05B^2 - 0.062C^2 \tag{4}$$

Response surface analysis

Response surface analysis of impurity removal rate

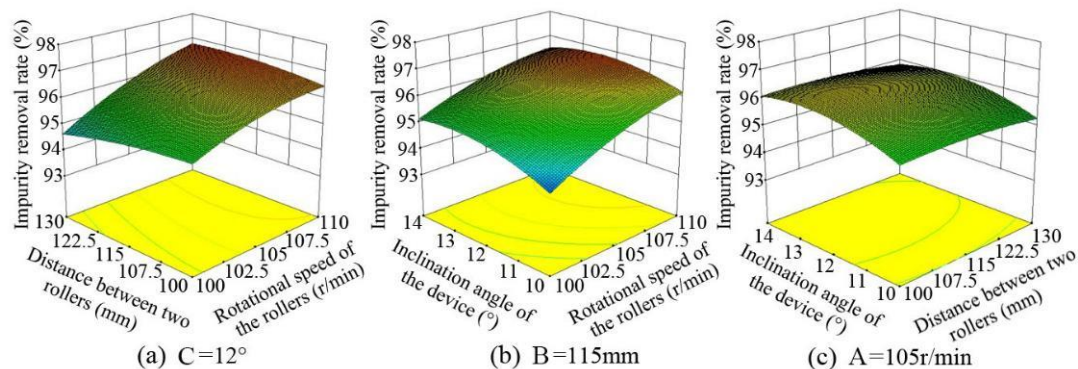(a) C=12°   (b) B=115mm   (c) A=105r/min

Fig. 8 – Response surface of impurity removal rate

As shown in Fig. 8a, when the inclination angle of the device was 12°, the impurity removal rate decreased with the increase of the distance between two rollers and increased with the increase of the rotational speed of the rollers. As shown in Fig. 8b, when the distance between the two rollers was 115 mm, the impurity removal rate increased with the increase of the inclination angle of the device. However, the impurity removal rate increased and then decreased slowly with the rotational speed of the rollers. As shown in Fig. 8c, when the rotational speed of the rollers was 105 r/min, the impurity removal rate first increased and then decreased slowly with the increase of the inclination angle of the device and the distance between the two rollers.

The overall influence trend of the experimental factors on impurity removal rate was as follows: when the distance between the two rollers and the inclination angle of the device were moderate and the rotational speed of the rollers was high, the impurity removal rate was high. When the distance between the two rollers is larger or smaller, the contact area between the surface of the potatoes and the impurity removal rollers will

be reduced, resulting in a decrease in the impurity removal rate. When the rotational speed of the impurity removal roller increases, the number of contacts between the potatoes and the impurity removal rollers increases, so that impurities can be effectively removed.
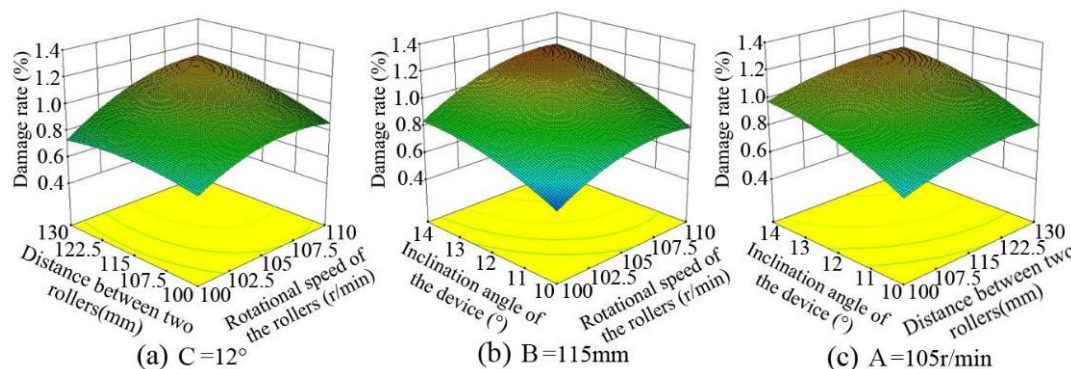
Response surface analysis of damage rate

Fig. 9 – Response surface of damage rate

As shown in Fig. 9a, when the inclination angle of the device was 12°, the damage rate first increased and then decreased slowly with the increase of the distance between the two rollers. But the damage rate increased with the increase of the rotational speed of the rollers. As shown in Fig. 9b, when the distance between the two rollers was 115 mm, the damage rate increased with the increase of the device inclination angle and the rotational speed of the rollers. As shown in Fig. 9c, when the rotational speed of the rollers was 105 r/min, the damage rate increased with the increase of the inclination angle of the device and the distance between the two rollers.

The overall influence trend of the experimental factors on damage rate was as follows: when the distance between the two rollers was moderate and the rotational speed of the rollers and the inclination angle of the device were large, the damage rate was high. The main reason is that when the distance between the two rollers is larger or smaller, the number of collisions between the potatoes and the impurity removal rollers will be reduced, resulting in a lower damage rate. And when the speed of the impurity removal rollers increases, the number of collisions between the potato and the impurity removal roller will be increased, resulting in a higher damage rate. In addition, when the inclination angle of the device increases, the height of the potatoes falling to the next-level impurity removal roller will increase, thereby increasing the contact force with the impurity removal roller, resulting in an increase in the damage rate.

Parameter optimization and validation

To obtain the best working parameters of the impurity removal device for potato combine harvester, taking the maximum impurity removal rate and the minimum damage rate as the optimization objectives, the optimization module in Design-Export 10.0.3 was used to solve the optimal parameters.

The objective function and constraints conditions are as follows:

$$\begin{cases} \max y_1(A,B,C) \\ \min y_2(A,B,C) \\ \\ s.t.\begin{cases} 96.6r/\min < A < 113.4r/\min \\ 89.8mm < B < 140.2mm \\ 8.6° < C < 15.4° \end{cases} \end{cases} \quad (5)$$

After optimization calculation, the optimal working parameters were obtained as follows: the rotational speed of the rollers was 113.4 r/min, the distance between two rollers was 97.5 mm and the inclination angle of the device was 10.4°. The predicted value of impurity removal rate was 95.85%, and the predicted value of damage rate was 0.49%.

Five replicate experiments were carried out with the above optimization parameters, and the test results were averaged. The results showed that the impurity removal rate was 95.12%, and the damage rate was 0.54%, which was consistent with the prediction results of the model, and the prediction errors were less than 3%.

CONCLUSIONS

1. A new type of impurity removal device for potato combine harvester was designed in this study. The device adopted the form of an alternate arrangement of impurity removal rollers and smooth rollers, which can effectively remove impurities and reduce the damage rate of potatoes.

2. To determine the best working parameters of the device, the second rotation orthogonal regression test was carried out with the rotational speed of the rollers, the distance between two rollers, and the inclination angle of the device as the test factors. Furthermore, the impurity removal rate and damage rate are employed as evaluation indexes. Through the response surface analysis of the impurity removal rate and damage rate, the influence of three factors on the two response indicators was obtained.

3. The best working parameters were obtained taking the maximum impurity removal rate and the minimum damage rate as the optimization objectives. The optimal parameters obtained were as follows: the rotational speed of the rollers was 113.4 r/min, the distance between two rollers was 97.5 mm and the inclination angle of the device was 10.4°. At this time, the impurity removal rate was 95.85% and the damage rate was 0.49%. The results of the verification test showed that the relative error between the measured value and the predicted value was less than 3%, which indicates that the regression model was reliable.

REFERENCES

[1] Chen, Z., Duan, H., Cai, X., et al. (2020). Distribution characteristics of potato contact stress during the drop impact(马铃薯跌落碰撞时的接触应力分布特性). *Journal of South China Agricultural University*, Vol. 41, No. 5, 99-108.

[2] Deng, W., Wang, C., Xie, S., (2019), Test research on the impact peak force and damage depth of potato. *INMATEH - Agricultural Engineering*, Vol. 61, Issue 2, pp. 105-114.

[3] Geng, D., Su, G., Wei, Z., et al. (2021). Design and Experiment of Potato-stone Separator Based on Airflow Suspension Technology (马铃薯清选机气力悬浮薯石分离装置设计与试验), *Transactions of the Chinese Society for Agricultural Machinery*, Vol. 52, No. 5, 102-110.

[4] Ji, L., Xie, H., Yan, J., et al. (2020). Current Situation and Prospect of Potato Cleaner Equipment Research (马铃薯清洗设备研究现状及展望). *Journal of Chinese Agricultural Mechanization*, Vol. 41, No. 4, 98-104.

[5] Jia, W., Diao, P., Zhang, H. et al. (2021). Current Situation of Potato Production and Mechanized Harvest in China (中国马铃薯生产及机械化收获现状), *Agricultural Equipment & Vehicle Engineering*, Vol. 59, No. 4, pp 18-22.

[6] Liu, S., Zhang, G., Li, G., et al. (2022). Design and Experiment on the Monitoring and Reseeding Device of Potato Sower (马铃薯播种漏播检测自动补种装置设计与试验), *Journal of Agricultural Mechanization Research*, Vol. 44, No. 3, 78-83.

[7] Lv, J., Du, C., Liu, Z., et al. (2021). Design and Test of Impurity Removal Device of Potato Receiving Hopper (马铃薯料斗机除杂装置设计与试验). *Transactions of the Chinese Society for Agricultural Machinery*, Vol. 52, No. 1, 82-90+61.

[8] Meng, J., Zhao, X., Wang, K., et al. (2022). Research Status of Potato Harvesters in China in the Past Decade (近十年我国马铃薯收获机研究现状), *Journal of Agricultural Mechanization Research*, Vol. 44, No. 2, pp 1-8.

[9] Su, Q., Naoshi, K., Minzan, L., et al, (2018), Potato quality grading based on machine vision and 3D shape analysis. *Computers and Electronics in Agriculture*, Vol. 152, pp. 261–268.

[10] Sun, J., Wang, X., Hang, Z., et al, (2017), Classification，Integration of Storage and Transportation Engineering Technologies in Potato Producing Areas of China (中国马铃薯产地贮运工程技术分类与集成). *Hubei Agricultural Science*, Vol. 65, No. 2, pp. 314-319+324.

[11] Wang, X., Sun, J., Xu, Y., et al. (2017). Design and Experiment of Potato Cleaning and Sorting Machine(拨辊推送式马铃薯清选分选机设计与试验), *Transactions of the Chinese Society for Agricultural Machinery*, Vol. 48, No. 10, 316-322.

[12] Wei, Z., Li, H., Sun, C., et al. (2019). Design and Experiment of Potato Combined Harvester Based on Multi-stage Separation Technology (基于多段分离工艺的马铃薯联合收获机设计与试验), *Transactions of the Chinese Society for Agricultural Machinery*, Vol. 50, No. 1, 129-140+112.

[13] Wei, Z., Li, H., Su, G., et al. (2019). Development of potato harvester with buffer type potato-impurity separation sieve (缓冲筛式薯杂分离马铃薯收获机研制). *Transactions of the Chinese Society of Agricultural Engineering*, Vol. 35, No. 8, 1-11.

[14] Wei, Z., Li, H., Sun, C., et al. (2019). Experiments and Analysis of a Conveying Device for Soil Separation and Clod-Crushing for a Potato Harvester. *Applied Engineering in Agriculture*, Vol. 35, Issue 6.

[15] Yang, H., Xie, H., Wei, H., et al, (2021), Development and Testing of Soil Impurities Removing Apparatus for Potato. *INMATEH-Agricultural Engineering*, Vol. 65, Issue 3, pp. 485-494.

[16] Yang, X., Shi, M., Wei, H., et al. (2014). Design and Simulation of Grading Device on Potato Combine Harvester (马铃薯联合收获机分级装置的设计与仿真), *Journal of Shenyang Agricultural University*, Vol. 45, No. 2, 241-244.

[17] Zhang, Y., Li, X., Gao, S (2014). Design and Test of Roller Nylon Brush Potato Cleaning and Classifying Machine (辊式尼龙刷马铃薯清选分级机的设计与试验), *Journal of Agricultural Mechanization Research*, Vol. 43, No. 6, 152-155+160.

[18] Zhang, Y., Li, X., Gao, S., et al, (2020), Design and Response Surface Analysis and Optimization of Roller Type Nylon Brush Potato Cleaning Classifier (辊式尼龙刷马铃薯清选分级机的设计及响应面分析与优化). *Chinese Potato Journal*, Vol. 34, No. 3, pp. 171-179.

[19] Zhang, T., Peng, Y., Song, S., et al. (2021). Design of Separation Mechanism of Potato Soil under Heavy Clay Soil (马铃薯土薯分离机构现状及敲打辅助分离机构设计). *Agricultural Technology & Equipment*, Vol. 31, No. 11, 20-22.

COMPARATIVE STUDY OF THE PERFORMANCE OF WATER-WATER HEAT PUMP BETWEEN R407C AND OTHER NEW ECO-FRIENDLY REFRIGERANTS
/
STUDIUL COMPARATIV AL PERFORMANȚEI POMPEI DE CĂLDURĂ APĂ-APĂ ÎNTRE R407C ȘI ALȚI AGENȚI FRIGORIFICI ECOLOGICI

Claudia IONIȚĂ[1]); Elena Eugenia VASILESCU*[1]); Lucreția POPA [2)   1]

Faculty of Mechanical Engineering and Mechatronics, University Politehnica of Bucharest / Romania
[2)] INMA Bucharest / Romania
Tel: +04722765949 E-mail: eev_ro@yahoo.com
Corresponding author: Vasilescu Elena Eugenia
DOI: https://doi.org/10.35633/inmateh-66-40

ABSTRACT
In the paper we presented a comparative analysis of the effect of the refrigerant used on the operation and performance of a heat pump with water-water and heat regeneration. Various sensitivity studies are presented comparatively for some eco-friendly refrigerants (R290, R600a, R454C, R152a) and R407C. Based on the exergetic analysis, the exergy destruction and loss were estimated for each device, depending on the destination and the operating regime. Graphic and numerical results are presented. In conclusion, a comparative analysis of the defined performance coefficient based on energy and exergetic efficiency is presented. The interest of the study is important due to the applicability of geothermal heat pumps in the field of air conditioning of residential and industrial buildings but also in agriculture for animal farms, for drying some agricultural products in a climate with controlled temperature and relative humidity, in addition the water can be used in summer for irrigation.

ABSTRACT
În lucrare este prezentata o analiză comparativă a efectului agentului frigorific utilizat, asupra funcționării si performanțelor unei pompe de caldură cu regenerarea caldurii de tip apa-apa (geotermală). Diverse studii de sensibilitate sunt prezentate comparativ pentru câțiva agenți frigorifici eco-friendly (R290, R600a, R454C, R152a) și R407C în vederea reducerii emisiilor de seră. Pe baza analizei exergetice s-au estimat pentru fiecare aparat, în funcție de destinație și de regimul de funcționare, distrugerea de exergie si pierderea de exergie. Sunt prezentate rezultate grafice și numerice. În concluzie, se prezintă o analiză comparativă a coeficientului de performanță definit pe baza energetică și a randamentului exergetic. Interesul studiului este important datorita aplicabilității pompelor de caldură geotermale în domeniul climatizării clădirilor rezidențiale și industriale dar și în agricultură pentru fermele de animale, pentru uscarea unor produse agricole în climat cu temperatură și umiditate relativă controlate, dar și pentru irigare.

INTRODUCTION

This paper deals with a comparative analysis of the refrigerant impact on a heat pump with water-to-water heat recovery. The situation of heating and air conditioning for residential, commercial, industrial spaces must be seen in the current context of reducing fossil fuel consumption and using renewable and recoverable energy sources, but also reducing CO2 emissions to limit global warming. This fossil fuel reduction program was set after two weeks of negotiations between world leaders at the 26th United Nations Climate Change Conference (COP26) held in Glasgow in October-November 2021 *(United Nations Climate Change Conference, 2021).*

Heat pumps are generally recognized as an efficient method of saving energy and are widely used for heating and cooling industrial, commercial and residential spaces, for the production of domestic hot water, *in agriculture* in farms for maintaining an adequate indoor thermal environment and air quality. The use of heat pumps offers energy savings, economic benefits but also a positive effect on the environment by reducing CO_2 emissions in the atmosphere. The heat pump is an ecological and renewable energy technology that

---

[1] *Claudia Ionita, Lecturer Ph D. Eng.; Elena Eugenia Vasilescu, Assoc.Prof. Ph.D. Eng.; Popa Lucretia, Ph.D. Eng.*

transforms renewable thermal energy from soil, air or water into useful heat for space heating and cooling, domestic hot water production, reversing the natural heat flow from a lower useful temperature to a higher one. This transformation is achieved with the help of an inverted cycle of a refrigerant *(Gaigalis et al., 2016).* Due to the ratification of the Kyoto Protocol, the use of refrigerants with high GWP (GWP - Global Warming Potential) is gradually restricted and they will be phased out in use for heat pump systems. For this reason, the lack of future for hydrofluorocarbon (HFC) refrigerants due to their high global warming potential (GWP) has directed research interest to natural and low GWP refrigerants.

As a result, in 2017 a comparative study was carried out between two heat pump systems for the production of domestic hot water using different natural refrigerants (CO_2 and R290). Comparing these two systems, it was concluded that the subcritical propane systems presented a higher performance coefficient (between 5% and 20%, depending on the increase in water temperature) and that the subcritical propane system is able to heat water from 30º C to 90º C with up to 11% COP improvement compared to CO_2 systems (*Pitarch et al., 2017*).

In the same year a study was carried out that presents a detailed analysis of the feasibility of successfully replacing high GWP refrigerants with low GWP refrigerants with acceptable performance. Thus the hydrofluoroolefin (HFO) refrigerants R1234yf and R1234ze(E) have been considered for use in several heating, ventilation, air conditioning and refrigeration applications due to their very low GWP. Both R1234yf and R1234ze(E) have been shown to replace R134a with comparable performance and without substantial changes to the original system *(Nawaz et al., 2017).*

In 2021, researchers showed that the high-temperature heat pump cycle based on R1233zd(E) has excellent performance and broad application prospects, which plays a positive role in the further development of heat pumps (*Jiang et al., 2021*).

To compare the performance of different heat pumps, six refrigerants were selected and simulated in an ideal cycle, including natural refrigerant (R718), HCs (R600, R601), HFO (R1234ze(Z), R1336mzz(Z)) and HFCs (R245fa). The simulation results showed that R718 has the best system performance and Carnot efficiency (COP/COPCarnot) among all these refrigerants. The experimental comparison also showed that R718 has its unique advantages in heat pump applications (*Wu et al., 2020*).

In 2020, researchers also conducted a comprehensive review of geothermal source heat pumps (GSHP) and air source heat pumps (ASHP). They are studied from different aspects, including with refrigerant change, single-stage heat pump and economizer heat pump. These cycles are analyzed using energy, exergy and from an environmental but also an economic point of view (4E analysis). The results show that the coefficient of performance (COP) and exergetic efficiency values for the GSHP cycle are higher than the ASHP cycle, and the best refrigerant for both is R134A. The economic and environmental analysis also reveals that using the GSHP cycle can save electricity to 239 MWh/year, which reduces CO_2 emissions to 140 tons/year and saves costs by $27,280/year compared to ASHP. Moreover, by using an economizer in the heat pump cycle, the COP of the GSHP cycle improved by 9%, the exergetic efficiency by about 6.8%, and the COP of the ASHP cycle increased by about 7.5%, and its efficiency exergetic by 7.4%. It is concluded that the economizer has a significant impact on the GSHP cycle (*Maddah et al., 2020*).

In 2017 another study evaluated the performance of R290 (propane) and R600a (isobutane) as a replacement for R134a (an HFC) for heat pump water heating. The results of the analysis suggest that both alternative refrigerants could provide comparable system performance to the base system containing R134a, with a caveat that the alternative, R290, was found to be a better replacement for R134a, while R600a it is expected to provide similar performance if the compressor size is increased to provide a similar heating capacity (*Nawaz et al., 2017*).

Another work evaluates the low GWP refrigerants R600a, R1234ze(Z) and R1233zd(E) as alternatives to traditional low-pressure HFC refrigerants such as R245fa for heat pump (HP) and organic Rankine cycle (ORC) applications. Thermodynamic and heat transfer evaluation results show that R600a, R1234ze(Z) and R1233zd(E) are valuable long-term low-GWP replacements for traditional low-pressure HFC refrigerants in both HP and ORC applications. (*Longo et al., 2020*)

In 2022, a study of high-temperature heat pumps was made through a multiparametric optimization based on low-GWP refrigerants. The mixtures based on R-1233zd(E) and R-1336mzz(Z) were the most promising ones, as they also comply with the environmental restriction (*Moreno et al., 2022*).

R410A refrigerant has a GWP of 1924, so its impact on global warming is significant. For this reason, various lower GWP alternatives to R410A have been proposed in recent years. Two of them are R452B and R454B with GWP values of 675 and 466, respectively. In this context, studies of the performance of introducing

R452B and R454B refrigerants into a heat pump to replace R410A have been developed. This study identified R-452B and R-454B as potential candidates, respectively. In addition, both refrigerants showed similar COP and cooling (or heating) capacities to systems operating with R-410A, as well as lower TEWI (Total Equivalent Warming Impact) values for most of the studies analyzed. Compared to R410A, the lower GWP alternatives show higher discharge temperatures, lower heating and compression powers and similar COPs. (*Sieres et al, 2021; Guilherme et al, 2022*).

Also, in another investigation carried out in 2020, the impact of five HFC refrigerants such as R125, R134A, R404A, R407C and R507A on the efficiency of geothermal heat pump operation was studied. Energetic and exergetic analysis is used to investigate the influence of temperature variations of the geothermal source exhaust fluid on the operation of the heat pump. The coefficient of performance (COP), exergetic efficiency and exergy destruction were determined for different components. The results show that, in the geothermal heat pump cycle, refrigerants R134A and R125 have the highest and lowest COP, respectively. In addition, increasing the temperature of the exhaust fluid from the geothermal source results in an improvement in the COP. For the mentioned refrigerants, the exergy destruction due to the compressor, as the primary energy-consuming equipment, is between 26.7 and 27.3%, compared to the whole system (*Dashtebayaz et al., 2020*).

Another paper (*Tarlea et al., 2020*) compared the operating performance of a heat pump system using R407CA refrigerant to one using R290. The conclusion was that the heat pump that uses the R290 refrigerant achieves an energy saving of 971kWh, which represents, at the annual consumption level of the heat pump that uses the R407C refrigerant, a saving of 22%, and the ecological performance of R290 is absolute.

It should also be emphasized the research direction that studies the importance of applying geothermal heat pumps in the agro-zootechnical sector, where they are rarely applied but necessary and thus their potential must be verified (*Alberti et al., 2018; Blázquez et al., 2022*).

MATERIALS AND METHODS
System description

We considered a water-water type heat pump (geothermal heat pump) that works in the cycle with mechanical vapor compression in one step, with heat regeneration between the superheating and sub-cooling processes, as shown in Fig. 1. The heat pump works with the R407C refrigerant. The condenser thermal load is $\dot{Q}_{W,h}$ = 13kW and the cold source is groundwater with temperature at the evaporator inlet $t_{wc,1}$=10°C and providing a temperature of the water at the exit from the condenser $t_{wh,2}$=35°C. In this case, the electrical power consumed by the heat pump is P_{el}=2,07 kW and the superheating degree is 10°C.
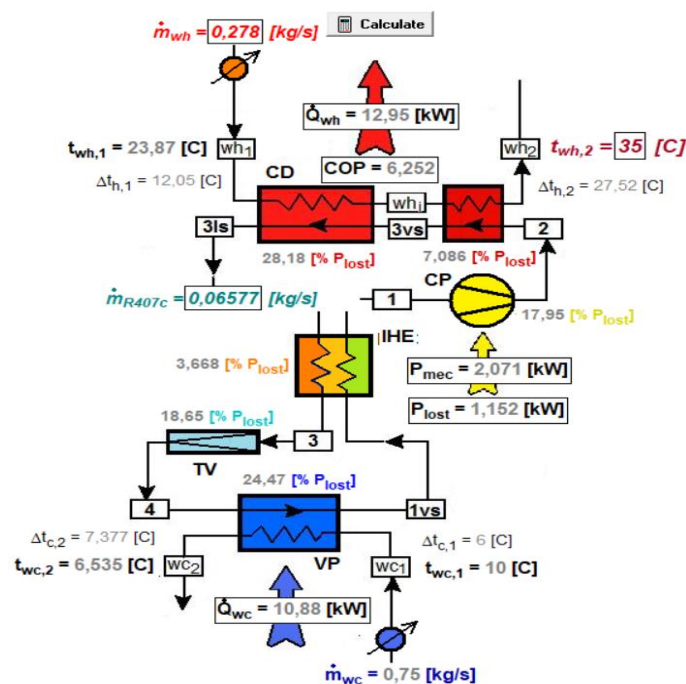

Fig. 1 – Heat Pump with internal heat exchanger
CP-compressor, CD-condenser, VC-vapors cooler, TV-throttle valve,
VP-evaporator, IHE-Internal heat exchanger

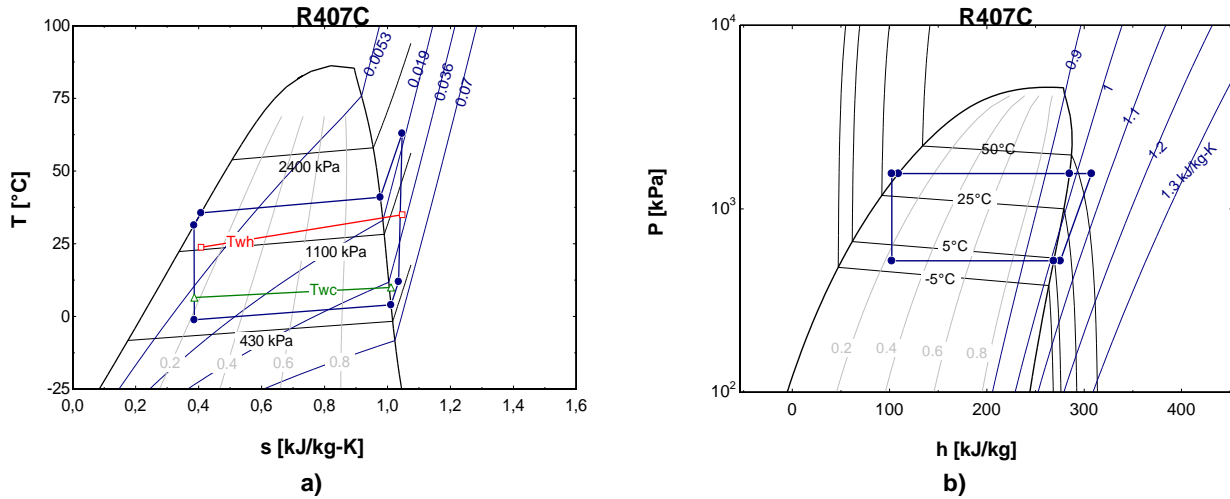The heat pump cycles are represented in T-s and p-h coordinates in Fig.2.

Fig. 2 – Operating cycle
a) p-h coordinates and b) T-s coordinates

Mathematical model

The system is analyzed both from energetic and exergetic points of view.

Energy analysis is based on the First Law of thermodynamics.

a) Heat transfer rate in condenser:

$$\dot{Q}_C = \dot{m} \cdot (h_{3ls} - h_2) \tag{1}$$

Where: $\dot{m}$ is refrigerant flow rate in [kg/s]; h is specific enthalpy in [kJ/kg].

b) Heat transfer rate in evaporator:

$$\dot{Q}_0 = \dot{m} \cdot (h_{1vs} - h_4) \tag{2}$$

c) The power consumption of compressor can be estimated by:

$$\dot{W}_{Cp} = \dot{m} \cdot (h_1 - h_2) \tag{3}$$

d) For the throttling valve (throttle process, is enthalpic):

$$\dot{m} \cdot h_3 = \dot{m} \cdot h_4 \tag{4}$$

e) For the Internal heat exchanger (IHE):

$$h_3 - h_{3ls} = h_{1vs} - h_1 \tag{5}$$

f) The energetic efficiency of the system is measured by the coefficient of performance (COP):

$$COP = \frac{usefulleffect}{Consumption} = \frac{|\dot{Q}_C|}{|\dot{W}_{Cp}|} \tag{6}$$

g) The volumetric heat capacity (VHC) is used to estimate the heat capacity per volume:

$$VHC = \frac{h_2 - h_{3ls}}{v_1} \tag{7}$$

where: v_1 is the specific volume at the compressor inlet [m³/kg].

By applying the Second Law of Thermodynamics to each control volume, one could find the entropy generation in the system. By applying to each device of the system, one gets:

a) For the vapors cooler:

$$\dot{S}_{gen,VC} = \dot{m} \cdot (s_3 - s_2) + \dot{m}_{wh} \cdot (s_{wh2} - s_{whi}) \tag{8}$$

Where: s is the specific enthalpy in [kJ/kg K] and $\dot{m}_{wh}$ is water flow rate at condenser.

b) For the condenser:

$$\dot{S}_{gen,Cd} = \dot{m} \cdot (s_{3ls} - s_{3vs}) + \dot{m} \cdot (s_{whi} - s_{wh1}) \tag{9}$$

c) For the evaporator:

$$\dot{S}_{gen,Vp} = \dot{m} \cdot (s_{1vs} - s_4) + \dot{m}_{wc} \cdot (s_{wc2} - s_{wc1}) \tag{10}$$

d) For the compressor:

$$\dot{S}_{gen,Cp} = \dot{m} \cdot (s_2 - s_1) \tag{11}$$

e) For the throttling valve:

$$\dot{S}_{gen,VL} = \dot{m} \cdot (s_4 - s_3) \tag{12}$$

f) For the Internal heat exchanger:

$$\dot{S}_{gen,Rec} = \dot{m} \cdot (s_1 - s_{1vs} + s_3 - s_{3ls}) \tag{13}$$

These state parameters (h, s, v) of the refrigerant are determined in each state during the operating cycle by means of the Engineering Equation Solver (EES).

Exergy analysis is based on the Second Law of thermodynamics.

According to Guy-Stodola theorem, the exergy destruction rate is computed by:

$$I = T_0 \cdot \dot{S}_{gen} \tag{12}$$

where I is the exergy destructions rate, [W].

In thermodynamics, the exergy destruction represents a major inefficiency and a quantity to be minimized when the overall system efficiency should be maximized (*Tsatsaronis et al., 2011*)

Total the exergy destructions rate in the whole system can be calculated as:

$$I_{TOT} = I_{VC} + I_{Cd} + I_{TV} + I_{VP} + I_{IHE} \tag{13}$$

The share of the exergy destructions rate of the component k, in the total exergy destructions rate of the system:

$$\Psi_k = \frac{I}{I_{TOT}} \text{ [-]} \tag{14}$$

The exergetic efficiency measures the behavior of the system in relation to the corresponding Carnot cycle. Exergy measures the irreversibility developed in relation to theoretical models.

$$COP_{ex} = \frac{\dot{Ex}_{Q_{Cd}}^{T_c}}{\left| \dot{W}_{Cp} \right|} \tag{15}$$

Thermal exergy transfer associated with heat transfer $\dot{Q}_c$ is:

$$\dot{Ex}_{Q_c} = \dot{Q}_c \left(1 - \frac{T_0}{T} \right) \tag{16}$$

Whre: T_0 - temperature of the heat source, K; T - temperature of the heat sink, K.

The dead state temperature for the exergetic analysis is considered to be equal to that of the ambient environment which is equal to the temperature of the groundwater $t_0 = 10°C$.

The analysis was performed with the software program Engineering Equation Solver (EES).

RESULTS

Obviously, by its nature, the refrigerant of the cycle in turn influences the performance of the heat pump. The five refrigerants used in the comparative analysis of the heat pump are described in table 2. The thermodynamic agent of the cycle influences the performance of the heat pump and for this purpose we have carried out a sensitivity study. The hot water outlet temperature is the varied parameter for evaluating the performance of the five refrigerants described in Table 2. Following the diagrams 4-14 the different behavior of the five investigated refrigerants can be observed.

Table 2

Some characteristics of refrigerants

Ashrae Number	IUPAC Name	ODP	net GWP 100-yr	Molar mass g/mol	Normal Boiling Point (s) °C	Critical Temp. °C	Critical Pressure (absolute) kPa
R-290	Propane	0	3.3	44.1	-42.1	96.7	4,248
R-600a	Isobutane	0	3.0	58.1	-11.7	134.7	3,640
R-152a	1,1- Difluoroethane (R-152a)	0	124	66,051	-24,7	113,15	44,96
R454C	R32/R1234yf 21.5/78.5	0	146	90.8	--45,9	82.4	38.6
R407C	Tetrafluoroethane	0	1530	86.2	-43.6	86.1	4,62

Regarding irreversibilities, in Fig. 3 one may see the repartition of exergy destruction rates on each component of heat pump system (VC-vapors cooler, Cd-condenser, IHE-internal heat exchanger, Vp-evaporator, TV-throttling valve) for the five refrigerants. The highest exergy destruction rate is in the Condenser for R290, R600a and for R125a. The lower exergy destruction rate is in Vapors Cooler end Internal heat exchanger (IHE) for all the refrigerators.
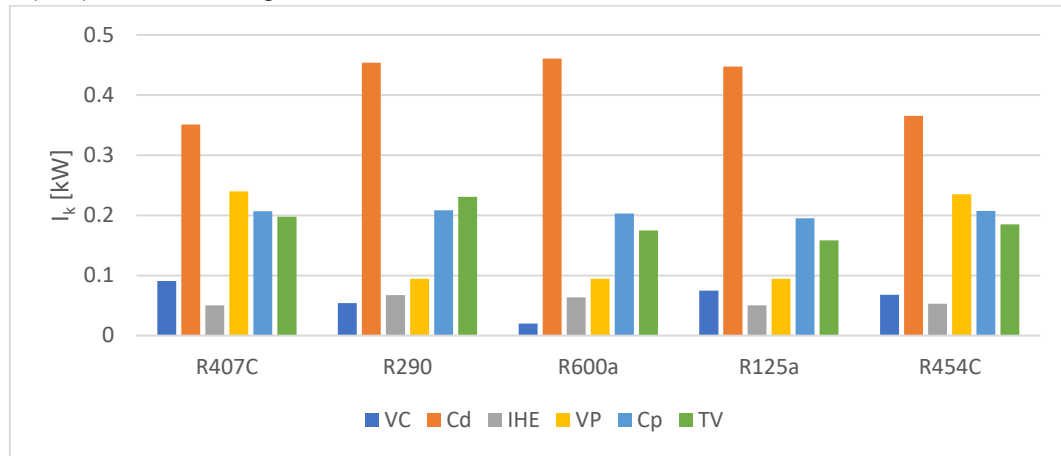

Fig. 3 – Refrigerant effect on the exergy destruction rates for each component of heat pump system
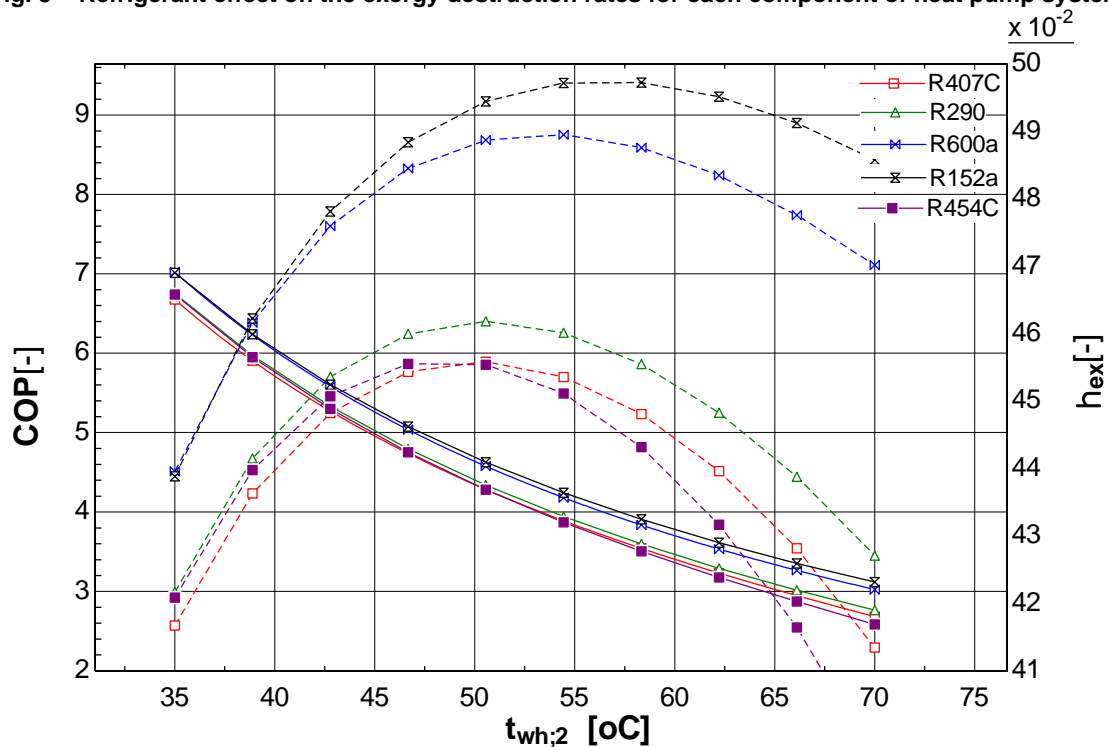
Fig. 4 – Change of COPen and COPex (η_ex)
for various refrigerants with the hot water outlet temperature

According to Fig. 4, the heat pump cycles using R152a and R600a refrigerants have the highest COP among the compared refrigerants. Due to the increasing temperature of the hot water outlet temperature, the heat output from the panel decreases more than the work of the compressor, thus decreasing the COP. Also, as illustrated, increasing the hot water outlet temperature worsen the COP of the cycle for all the refrigerants. In the same figure, the exergy efficiency calculated by Eq. (5) is shown with hot water outlet temperature from sink source for various refrigerants. R152a and R600a refrigerants have the highest exergy efficiency, and, then, the exergy efficiency decreases for R407C, R290, R507A, and R454C refrigerants, respectively. Increasing the hot water outlet temperature increases the exergy efficiency of the cycle for all the refrigerants between 35 and 55, after that the exergy efficiency decreases for all refrigerants, but has the most significant effect on R152a coolant, after which, R600a, R290, R407A and R545C refrigerants have a greater effect with the hot water temperature of the exhaust from sink source. Refrigerants R407C, R290 and R454C have the

lowest exergy efficiency, therefore also the highest exergy destruction. R152a and R600a, the refrigerants having the lowest exergy destruction, also have the best exergy efficiency.

It was presented COPen and COPex in a only figure because the antagonistic situation is interesting: COPen decreases with the increase in temperature t_{w2} and COPex increases and even shows a maximum. Of course, a compromise between the two situations must be found, which can only be achieved on the basis of a technical-economic study.

In Fig. 5, the work of compressor with the temperature of the hot water outlet from the condenser for R290, R600a and R152a, R407C, and R454C refrigerants is plotted. As shown in Fig. 5, R290, R600a and R152a refrigerants have a higher work. Also, R407C and R454C refrigerants have moderate compressor work. It is also observed that, with the increment of the temperature of the hot water outlet, the compressor work is accordingly augmented.
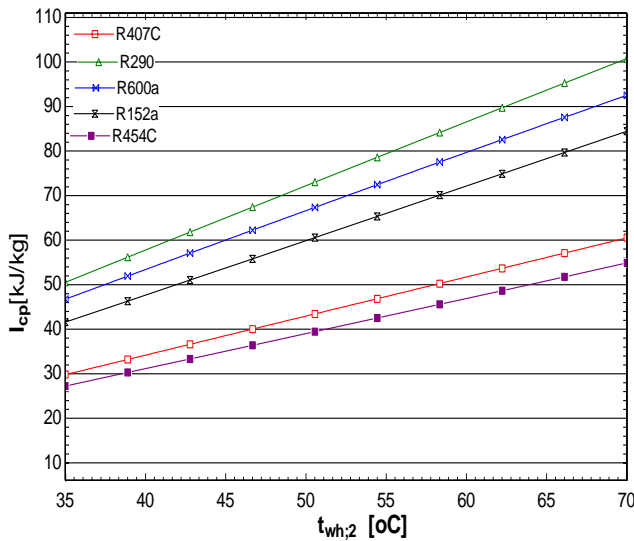
Fig. 5 – Change of the compressor work for various refrigerants with the hot water outlet temperature
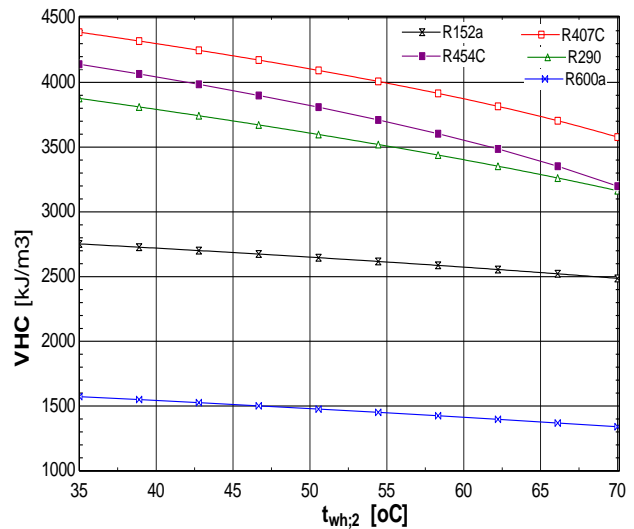

Fig. 6 – Change of volumetric heat capacity for various refrigerants with the hot water outlet temperature
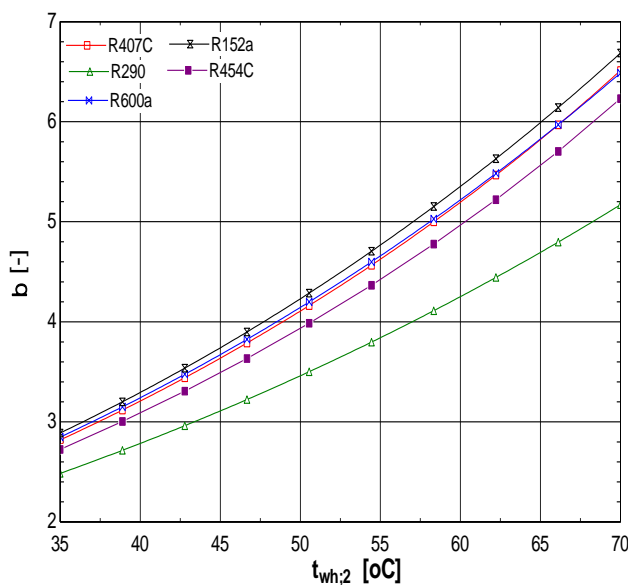

Fig. 7 – Change of the compressor ratio for various refrigerants with the hot water outlet temperature
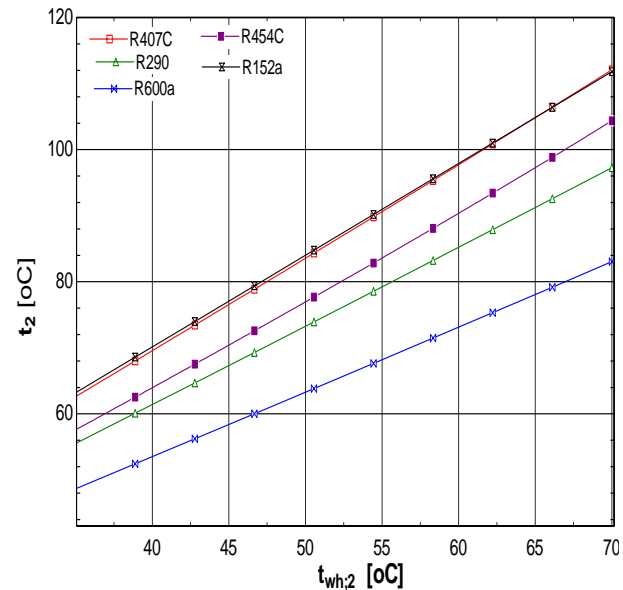

Fig. 8 – Change of discharge temperature for various refrigerants with the hot water outlet temperature

Fig. 6 further shows a comparison of the volumetric heat capacity of different refrigerants. According to the calculation results, the volumetric heat capacity of R407C, R454C and R290 is obviously larger than that of other refrigerants and at least twice the volumetric heat capacity of R600a.

The Volumetric Heat capacity is an indicator of the required compressor size. In order to have a small value for VHC (like refrigerant R290) a big size of the compressor is desirable.

When the hot water outlet temperature increases, the condensation temperature and pressure increase. The increased condensation temperature leads to an increase of the pressure ratio, which correspondingly causes the reduction of the volumetric efficiency and the mass flow rate (Fig.7). The final discharge temperature has also been evaluated in Fig. 8.
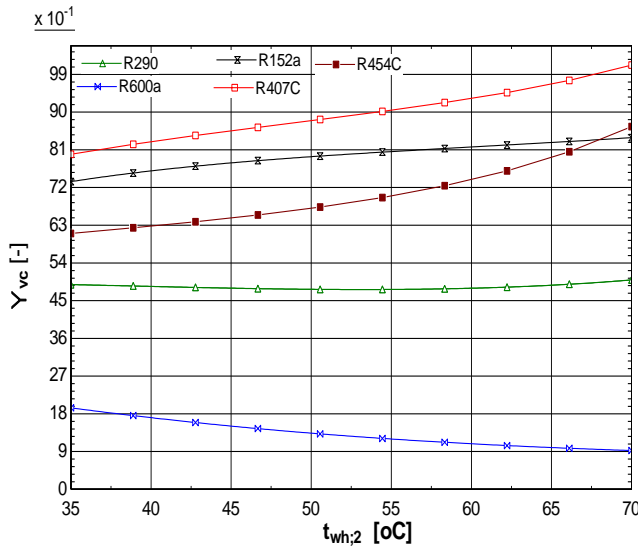
Fig. 9 – Change of the exergy destruction share in Vapor Cooler for various refrigerants with the hot water outlet temperature
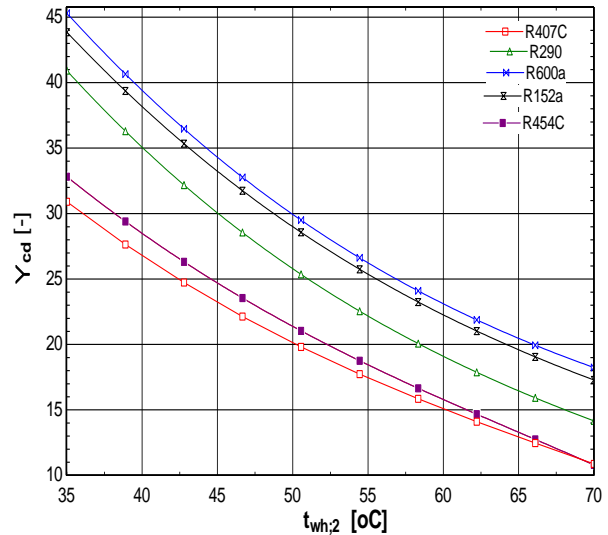

Fig. 10 – Change of the exergy destruction share in Condenser for various refrigerants with the hot water outlet temperature
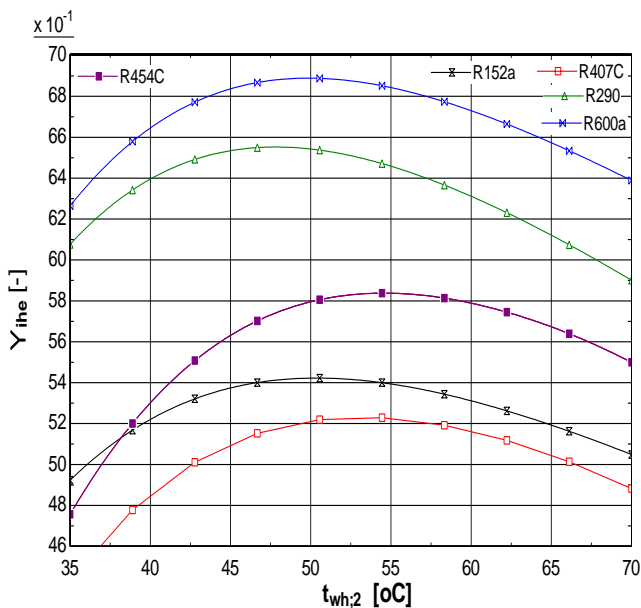

Fig. 11 – Change of the exergy destruction share in Internal Heat Exchanger for various refrigerants with the hot water outlet temperature
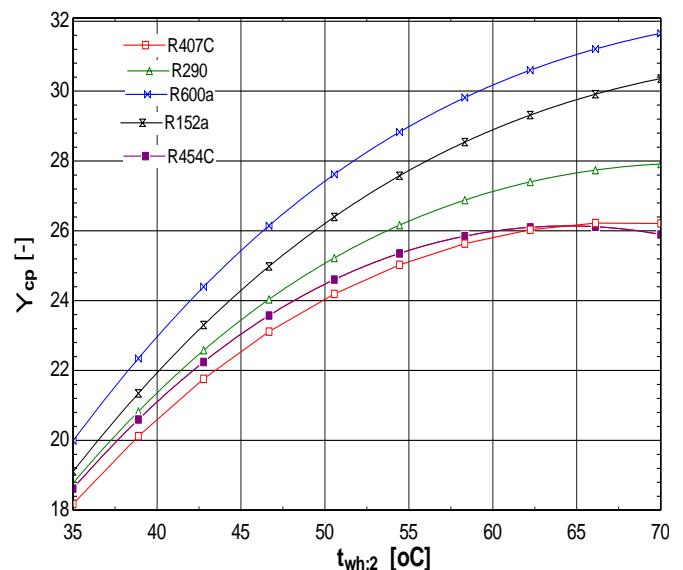

Fig. 12 – Change of the exergy destruction share in Compressor for various refrigerants with the hot water outlet temperature

From Fig.10, it can be seen that, at a temperature of 35°C of the hot water, the share of exergy destruction in the condenser is minimal for the R 407C and R 454C freons. The greatest destruction is observed with R600a and R152a freon. As the hot water temperature increases, the share of exergy destruction in the condenser decreases, which is valid for all refrigerants.

The share of exergy destruction at the internal heat recuperator is shown in Fig. 11 and it is observed that it has the lowest value for R407C freon; followed by the freons R152a and R454C. The other two freons show a greater destruction.

From Fig. 12 it can be seen that the share of exergy destruction at the compressor is the lowest for R407C, R454C, R290. R600a refrigerant has a special characteristic, the trend being the following: when the temperature of the hot water increases, the loss in the compressor also increases.
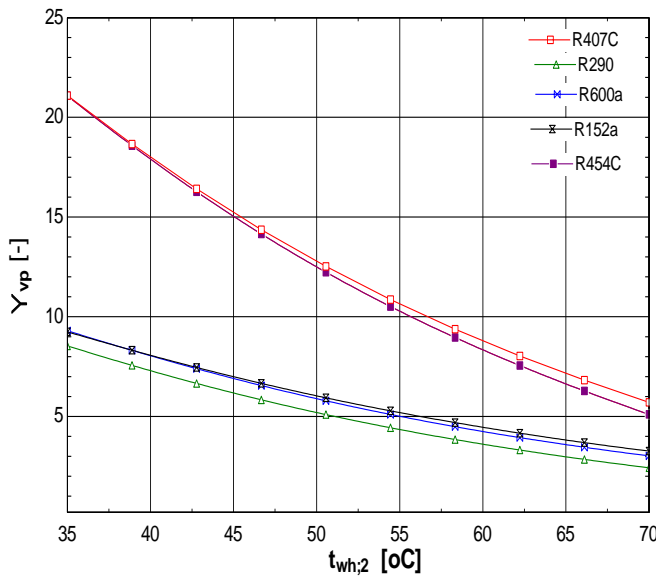
Fig. 13 – Change of the exergy destruction share in Evaporator for various refrigerants with the hot water outlet temperature
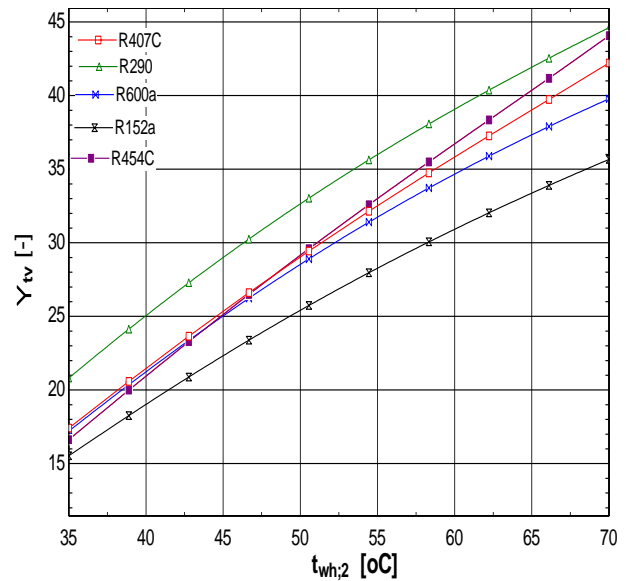

Fig. 14 – Change of the exergy destruction share in Throttle Valve for various refrigerants with the hot water outlet temperature

Following the diagrams in figures 9-14 it is observed that the working agent R600a has a reduced exergy destruction at the level of the vaporizer, but regarding the condensation behaviour, the values of the exergy destruction present due to the heat transfer at the finite temperature difference are high, so following this analysis, it can be seen that the choice of any working agent represents a compromise.

CONCLUSIONS

A comparative analysis of the impact of different refrigerants on the performance of a heat pump was presented. In this paper, current low-GWP refrigerants for conventional heat pumps with a hot water output temperature of 35–70 °C are discussed. The system performance was simulated for different hot water outlet temperatures. Hot water outlet temperature has a remarkable impact on system performance. As the hot water outlet temperature increases from 35°C to 70°C, the COP decreases by 27%, and the heating capacity decreases by 20%.

Based on the exergy analysis, the exergy destructions were estimated for each component of the system in a comparative manner for four ecofriendly refrigerants (R290, R600a, R454C, R152a) proving a different behavior and therefore bringing important information about the optimization of the heat pump system when working with a certain refrigerant. The results obtained in the present research can provide instructions for the design and optimization of efficient geothermal heat pump systems.

The low-GWP refrigerants (R290, R600a, R152a, and R454C) are valid replacements for existing R-407C with comparable, and, in some cases, improved performance metrics. From the ecological point of view, operation with the R290 and R600a refrigerants are the ideal ecological options. Following the COPen and COPex performance indices, it is possible to identify for each of the five investigated agents an optimal point where the equipment performance is maximum.

Finally, further investigations are always needed to find long-term alternative refrigerants that are efficient, environmentally safe and non-flammable.

ACKNOWLEDGEMENT

REFERENCES

[1] Alberti, L., Antelmi, M., Angelotti, A., Formentin, G., (2018). Geothermal heat pumps for sustainable farm climatization and field irrigation. *Agricultural Water Management*, Vol. 195, pp. 187-200.

[2]   Blázquez, C.S.; Borge-Diez, D.; Nieto, I.M.; Maté-González, M.Á.; Martín, A.F.; González-Aguilera, D., (2022). Geothermal Heat Pumps for Slurry Cooling and Farm Heating: Impact and Carbon Footprint Reduction in Pig Farms. *Sustainability*, *14*, 5792.

[3]   Dashtebayaz, M., D., Maddah, S., Goodarzi, M., Maddah, O., (2020). Investigation of the effect of using various HFC refrigerants in geothermal heat pump with residential heating applications, *Journal of Thermal Analysis and Calorimetry*, Vol.141, pp. 361–372, Hungary.

[4]   Gaigalis, Y., Skema, R., Marcinauskas, K., Korsakiene,I., (2016). A review on Heat Pumps implementation in Lithuania in compliance with the National Energy Strategy and EU policy. *Renewable and Sustainable Energy Reviews*, Vol. 53, pp. 841-858, Lithuania.

[5]   Guilherme, I., F., Marcucci Pico, D., F., Dall'Onder dos Santos, D., Filho, E., P., B., (2022). A review on the performance and environmental assessment of R-410A alternative refrigerants, *Journal of Building Engineering*, Vol. 47, Brazil.

[6]   Jiang, J., Hu, B., Wang, R., Z., Liu, H., Zhang, Z., Li, H., (2021). Theoretical performance assessment of low-GWP refrigerant R1233zd(E) applied in high temperature heat pump system. *International Journal of Refrigeration*, Vol. 131, pp. 897-908, China.

[7]   Longo, G., Mancin, S., Righetti, G., Zilio, C., Brown, J., S., (2020). Assessment of the low-GWP refrigerants R600a, R1234ze(Z) and R1233zd(E) for heat pump and organic Rankine cycle applications, *Applied Thermal Engineering*, Vol. 167, Italy.

[8]   Maddah, S., Goodarzi, M., Safaei M., R., (2020). Comparative study of the performance of air and geothermal sources of heat pumps cycle operating with various refrigerants and vapor injection, *Alexandria Engineering Journal*, Vol. 59, Issue 6, pp. 4037-4047, Iran.

[9]   Moreno, A., F., Babiloni, A., Giménez-Prades, P., Navarro-Esbrí, J., (2022). Optimal refrigerant mixture in single-stage high-temperature heat pumps based on a multiparameter evaluation, *Sustainable Energy Technologies and Assessments*, Vol. 52, Part A, Spain.

[10]   Nawaz, K., Shen, B., Elatar, A., Baxter, V, Abdelaziz,O., (2017). R1234yf and R1234ze(E) as low-GWP refrigerants for residential heat pump water heaters. *International Journal of Refrigeration*, Vol. 82, pp. 348-365, United States.

[11]   Nawaz, K., Shen, B., Elatar, A., Baxter, V., Abdelaziz, O., (2017). R290 (propane) and R600a (isobutane) as natural refrigerants for residential heat pump water heaters, *Applied Thermal Engineering*, Vol. 127, pp. 870-883, United States.

[12]   Pitarch, M., Navarro-Peris, E., Gonzálvez-Maciá, J., Corberán, J., (2017). Evaluation of different heat pump systems for sanitary hot water production using natural refrigerants. *Applied Energy*, Vol. 190, pp.911-919, Spain.

[13]   Sieres, J., Ortega, I., Cerdeira, F., Álvarez, E., (2021). Drop-in performance of the low-GWP alternative refrigerants R452B and R454B in an R410A liquid-to-water heat pump, *Applied Thermal Engineering*, Vol. 182, Spain.

[14]   Tarlea, G., Mardare, G., Tarlea, A.,(2020). Ecological and Energy Efficiency Study of Heat Pumps with Capillary Evaporators*, Rehva Journal*, pp. 10-15, Romania.

[15]   Tsatsaronis, G., Morosuk, T., (2011). Exergy-based methods for computer-aided design of energy conversion systems, *Computer Aided Chemical Engineering*, Vol. 29, pp. 1949-1953, Germany.

[16]   Wu, D., Hu, B., Wang, R., Z., Fan, H., Wang, R., (2020). The performance comparison of high temperature heat pump among R718 and other refrigerants, *Renewable Energy*, Vol. 154, pp. 715-722, China.

[17]   *** 2021 United Nations Climate Change Conference, https://ukcop26.org/

[18]   ***EES: Engineering Equation Solver | F-Chart Software : Engineering; *www.fchart.com/ees/*.

ENERGY AND EXERGETIC ANALYSIS OF AN AIR-CONDITIONING SYSTEM FOR A FRUIT WAREHOUSE
/
ANALIZA ENERGETICĂ ȘI EXERGETICĂ A UNUI SISTEM DE CLIMATIZARE PENTRU UN DEPOZIT DE FRUCTE

Claudia IONIȚĂ[1)]; Elena Eugenia VASILESCU[*1)]; Lucreția POPA[2)], Horatiu POP [*1)]   [1]
Faculty of Mechanical Engineering and Mechatronics, University Politehnica of Bucharest / Romania
[2)] INMA Bucharest / Romania
Corresponding author: Vasilescu Elena Eugenia; Tel: +04722765949; E-mail: eev_ro@yahoo.com
Corresponding author: Pop Horatiu; E-mail: pophoratiu2001@yahoo.com
DOI: https://doi.org/10.35633/inmateh-66-41

ABSTRACT
In the paper, a thermodynamic analysis of an air conditioning system necessary to store a quantity of 500 kg of apricots at a temperature of 10°C and a humidity of 90% in a fruit warehouse was aimed at. The storage facility is cooled by means of an air handling unit (AHU). The energetic and exergetic analysis was carried out on the air conditioning system that treats a mixture of fresh air and recirculated air for various fractions of fresh air ranging from 0 to 100%, thus being able to perform a finer analysis of the operation of the installation under different working conditions. Based on the exergy analysis, the exergy loss was estimated for each device, depending on their destination and operating mode. Numerical and graphical results are presented related to the necessary mass flow rates of the air, the refrigeration load, the necessary treatment and evolution of humid air in the system, as well as the exergy loss in the main components of the air conditioning system. This theoretical study was carried out to obtain quantitative information that will lead to a better understanding of the air conditioning irreversibility process and their distribution amongst the system component and minimizing them for optimal air conditioning cycle.

REZUMat
Această lucrare prezintă analiza termodinamică a unui sistem de aer condiționat necesar pentru păstrarea într-un depozit de fructe a unei cantități de 500 kg de caise la o temperatură de 10°C și o umiditate de 90%. Spațiul de stocare este răcit prin intermediul unei centrale de tratare a aerului (CTA). A fost efectuată analiza energetică și exergetică a sistemului de aer condiționat care tratează un amestec de aer proaspăt și aer recirculat pentru diverse fracțiuni de aer proaspăt variind de la 0 la 100%, putându-se realiza astfel o analiză mai fină a funcționării instalației în diferite condiții de lucru. Pe baza analizei exergetice au fost estimate pierderile de exergie pentru fiecare aparat, în funcție de destinație și de regimul de funcționare. Sunt prezentate rezultate grafice și numerice legate de debitele de aer necesare, puterea frigorifică necesară, procedeele de tratare ale aerului umed în sistemul de aer condiționat precum și pierderile de exergie din procesele principale. Acest studiu teoretic s-a realizat pentru a obține informații cantitative care să conducă la o mai bună înțelegere a ireversibilitatilor aerului condiționat și a distribuției acestora între componentele sistemului și la minimizarea acestora pentru un ciclu optim de climatizare.

INTRODUCTION

Damage of the fruits and vegetables during their picking, handling, packaging, storage and sale, can be generated in part by too high temperatures that cause over-ripening, decay, as well as loss of quality and nutritional value. Other damages can be caused on the contrary, by a temperature that is too low or they can be of a mechanical nature, due to the carelessness of those who handle the products. The cold processing technologies of fruits and vegetables, the appropriate packaging, make it possible for them to arrive in a fresh state in markets that can be geographically very far from the place where they were picked. As a result, the variables to be controlled and monitored in the refrigeration of fruits and vegetables are temperature, relative humidity and ventilation.

---

[1]*Claudia Ionita, Lecturer Ph D. Eng.; Elena Eugenia Vasilescu, Assoc.Prof. Ph.D. Eng.; Lucretia Popa, Ph.D. Eng.; Horatiu Pop, Assoc.Prof. Ph.D. Eng.*

Fresh fruits and vegetables are alive and require fresh air to allow breathing. Without ventilation during storage, respiratory gases can accumulate and damage products. Ventilation must be done in such a way as to have control over temperature, humidity and energy consumption. All vegetables and fruits are alive and continue to breathe and metabolize. The metabolic process produces carbon dioxide and metabolic heat. There is a clear relationship between the heat of metabolism and the evolution of CO_2, and for every 2.96 watts of metabolic heat, 1 g of is generated. Respiration may also release water vapor and ethylene. The level of respiration depends on the type of product and the temperature. It also varies depending on the maturity of the product (*Heap et al., 2003*).

Cold storage is a refrigerated warehouse where fruits and vegetables can be stored for a long period of time without any deterioration of the products stored. Optimum storage temperature and relative humidity are necessary to maximize shelf life and maintain the quality of the products stored. The results showed that the shelf life of each vegetable can be increased by 50–60% when they are kept inside the cold storage prototype (*Parida et al., 2020*).

Food storage conditions, including storage time, temperature and light can have an influence on the retention of phytochemicals. In 2018, a study was conducted to investigate the effect of processing methods (freezing, preservation and drying) and storage periods on the physical-chemical and antioxidant properties of three varieties of apricots. It can be concluded from the study that canning and freezing can preserve apricot pulp for 12 months and significantly retain bioactive compounds (*Wani et. al., 2018*). A review was also made related to the thermo-physical properties of fruits which are vital for the study and optimization of post-harvest handling processes. However, the data available in the literature are not always consistent and should not be used directly. It is crucial to examine the accuracy and reliability of property data. The purpose of this review is to show gaps in fruit property data, with a focus on those properties that are important during post-harvest handling (*Mukama et al., 2020*).

Another research presented the applicability of wind and solar energies for cooling a fruit warehouse in the hot and dry Yazd region of Iran. The studied fruit warehouse had an area of 4240 m^2, resulting in a storage capacity of approximately 1000 tons. For this purpose, the heat gain of the warehouse is determined, and the obtained cooling load is then used to examine the solar and wind energy to power a conventional warehouse system (*Mostafaeipour et al., 2020*).

As part of the management of fruit refrigeration systems, it is essential to control the atmosphere with adequate ventilation. The influence of basket stacking arrangements and fan position on air flow in an industrial apple storage room was studied in this sense. Three fans situated above the vertical gaps were more effective for the ventilation of bins than four fans above the bin rows. A wide distance between stack and wall opposite to fans increased flow uniformity (*Praeger et al., 2021*). In another research, a k-ε simulation model was developed to evaluate the airflow pattern in a refrigerated container loaded with bananas, where k is the kinetic turbulent energy (k) and (ε) is the turbulent dissipation rate. The simulation results predict the location of hot spots. Moreover, it was found that the cooling distribution is improved by changing the layout of the pallets in the container, the so-called chimney layout (*Issa et al., 2014*).

The results of another study demonstrated the importance of room humidification for preserving fruit quality. Storage of fruits in a room at 95% RH (relative humidity) minimized weight loss and best preserved fruit color, firmness, size and chemical quality attributes of pomegranate. Therefore, fruit water losses can be reduced by proper packaging, control temperature and humidification of the storage room (*Mukama et al, 2019*). Another study was taken in three varieties of apricots grown in the same farm and placed in storage after sorting, the preliminary phase of storage. Storing was carried out in three different conditions: ambient temperature (+20…+22°C), refrigerated spaces (+10…+12°C) and cold conditions (+3...+5°C). The duration of preservation and level of weight (mass) and decay losses, as well as the evolution of some chemical components during storage were determined. The best results were obtained for storage in refrigerated conditions (*Vintila et al., 2015*).

Starting from the fact that storage requires a climate controlled by temperature and humidity, it is particularly important to use an efficient installation from an energy point of view. Research studies such as those presented below have been developed in this direction. So, in another study an energy and exergy analysis is made of moist air, it is used the psychometrics charts. A Visual Basic program is used to generate psychometrics charts. These charts are used to analyze the air thermodynamic behavior, considering the environmental variations, pressure, temperature and relative humidity. Also, the available energy in the cooling processes at constant enthalpy, humidification at constant temperature and heating with constant relative humidity is analyzed (*Pereyra et al., 2011*).

The following general conclusions could be drawn in another research paper: exergy efficiency is more rational than energy efficiency; exergy analysis is more helpful than energy analysis for locating and evaluating available energy saving potentials, identifying opportunities for improvements in system design and establishing cost effective system maintenance programs (*Chengqin et al., 2002*). Also, in another paper, researchers have discussed thermodynamic analysis of various psychrometric processes using the concept of exergy. They noticed that a decrease in mass flow rate of fresh air (second incoming stream) in the case of adiabatic mixing decreases the second-law efficiency of the process (*Bilal et al., 2003*).

MATERIALS AND METHODS
System description

The following analysis refers to a particular case of a fruit and vegetable cold store composed of a refrigeration chamber designed to refrigerate a quantity of products, in our case 0.5 tons of apricots. The room is provided with an access door, it is insulated with polyurethane. The external dimensions of the refrigerated warehouse are 4 m long, 3 m wide and 2.5 m high. The ambient air is at 38°C at 30% RH- relative humidity, the internal air is at 10°C at 90% RH. The walls, roof and floor are all insulated with 0.08 m polyurethane with a overall heat transfer coefficient k value of 0.308W/m²K. The ground temperature is 15°C. The purpose of the air handling unit (AHU) in Fig.1 is to remove the stale air from inside the space and introduce fresh air into it. Several modules can be present inside a central unit depending on how the air is desired to be when it is introduced into the room. The modules included in the AHU are: filter module, fans, mixing module and cooling module, i.e. BRS (surface cooling battery). With the help of fans, the air is extracted from the room and the air from outside is introduced, and the amount of air introduced or extracted from the room can also be regulated, with the help of the mixing chamber, the stale air can be recirculated if it is not toxic. The cooling module helps to cool the air with water or refrigerant (depending on its supply system) before it is introduced into the room. The air coming from the mixing house will go into a cooling battery system (BRS). The air is cooled through the refrigerant medium until it reaches a lower temperature of the mixed air resulting in convection and conduction heat transfer. The entire process is shown in the Mollier (h, x) diagram (enthalpy-humidity ratio diagram) in Fig.2 and Fig.3.
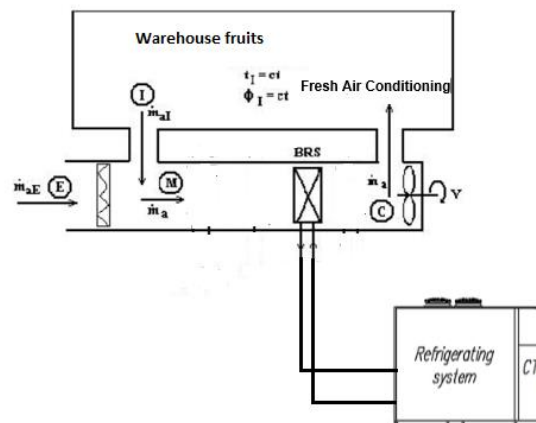

Fig. 1 –Schematic representation of the air-handling unit (AHU) serving the Warehouse
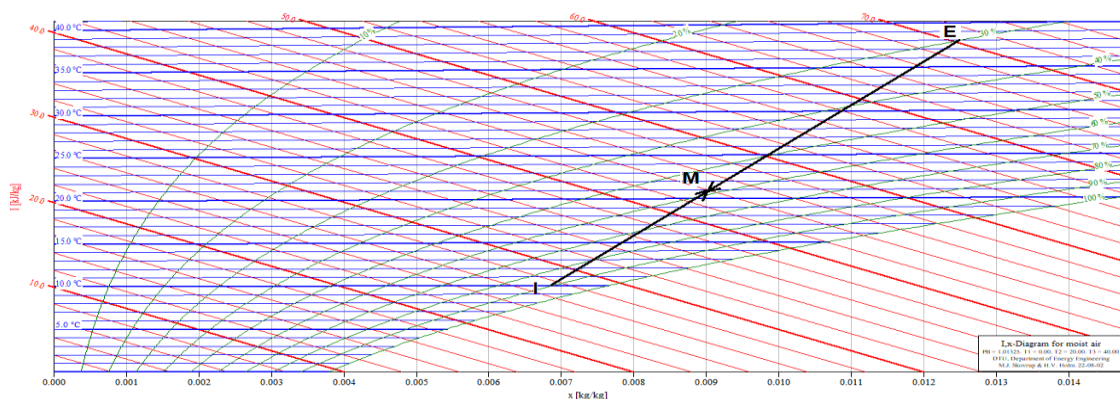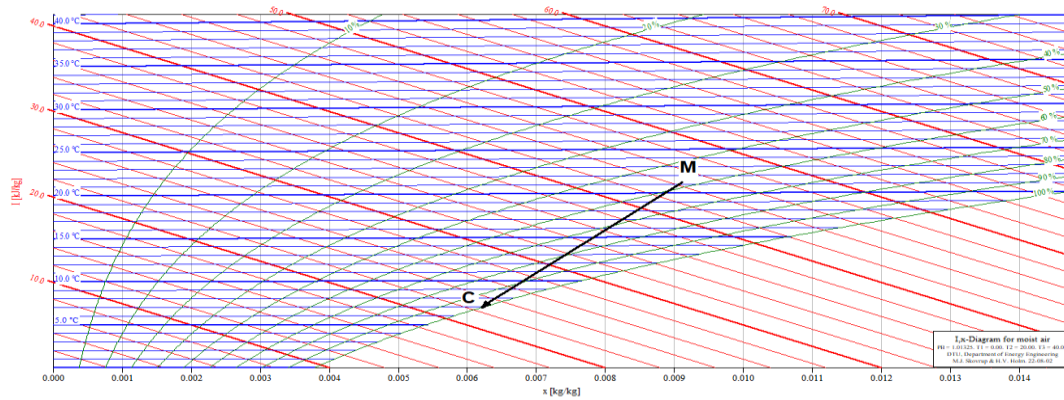

Fig. 2 – Process of mixing with 40% fresh air

Fig. 3 – Cooling process in BRS

Mathematical model

Cooling and humidity load analysis

<u>Calculation of thermal loads</u> of warehouses adapted for cooling in summer is important for the accuracy of the design and the appropriate choice of equipment for the adaptation of air and air handling units in order to meet the requirements of operation.

The cold requirement for the vegetable and fruits store represents the total heat flow that must be extracted from the cold storage whose temperature must be maintained at 10^oC and a relative humidity of 90% *(Pop et al., 2016; Cooling Load Calculation, 2017)*:

$$\dot{Q}_{nec} = \dot{Q}_{walls} + \dot{Q}_{floor} + \dot{Q}_{lightening} + \dot{Q}_{products} [kW] \tag{1}$$

- Heat flow through walls and roof:

$$\dot{Q}_{walls} = \sum_{i=5} \dot{Q}_{wall,i} [kW] \tag{2}$$

where $\dot{Q}_{wall,i}$ is the heat flow coming in through wall i

$$\dot{Q}_{wall} = k_{wall} \cdot S_{wall} \cdot \Delta T_{wall} \tag{3}$$

where:

k_{wall} - is the overall heat exchange coefficient, $\left[\dfrac{W}{m^2 K}\right]$;

S_{wall} - is the heat exchange area, $\left[m^2\right]$;

ΔT_{wall} is temperature difference over wall, $\left[K\right]$.

The overall heat exchange coefficient is expressed as:

$$k_{wall} = \cfrac{1}{\dfrac{1}{\alpha_{int}} + \sum\limits_{i=1}^{n} \dfrac{\delta_i}{\lambda_i} + \dfrac{1}{\alpha_{ext}}} \tag{4}$$

where:

α_{int} is the indoor convection coefficient, $\left[\dfrac{W}{m^2 K}\right]$;

α_{ext} is the outdoor convection coefficient, $\left[\dfrac{W}{m^2 K}\right]$;

δ wall thickness, $\left[m\right]$;

λ thermal conductivity coefficient, $\left[\dfrac{W}{mK}\right]$.

- The heat load of the floor:

$$\dot{Q}_{Floor} = k_{Floor} \cdot S_{Floor} \cdot \Delta T_{Floor} \tag{5}$$

$$k_{floor} = \cfrac{1}{\cfrac{1}{\alpha_{int}} + \sum_{i=1}^{n} \cfrac{\delta_i}{\lambda_i}}$$

(6)

- The heat generated by the lighting devices is:

$$\dot{Q}_{lighting} = n \cdot \dot{Q}_{lamp}$$

(7)

where n is number of lamps within the cold room.

- The heat load from stored products:

$$\dot{Q}_{Products} = \dot{m} \cdot c \cdot \Delta T$$

(8)

c is the specific heat capacity of product (kJ/kgK)

$\dot{m}$ = the mass flow of products (kg/s)

ΔT = temperature difference between the temperature of the products and the temperature within the store (K)

The heat load of the walls, roof and floor of the room dedicated to storing apricots at the temperature of 10 °C is shown in Table 1.

Table 1

Heat load of the walls, roof, floor dedicated to storing apricots

Title	A	k	ΔT	$\dot{Q}$
	[m²]	[W/m²K]	[K]	[W]
North Wall	10	0.3081	28	86.26
South Wall	10	0.3081	28	86.26
East Wall	7.5	0.3081	28	64.7
West Wall	7,5	0.3081	28	64.7
Roof	12	0.3081	28	103.5
Floor	12	0.2816	5	16.89
Total				422.3

To calculate the total cooling load, we will just sum all the values calculated:

$$\dot{Q}_{nec} = \dot{Q}_{walls} + \dot{Q}_{floor} + \dot{Q}_{lightening} + \dot{Q}_{products} \cong 1kW$$

Further the system is analyzed both from energy and exergy points of view. The analysis was performed with the Mathcad software program.

Energy analysis

The thermodynamic properties at each point should be specified in order to apply the energy and exergy analysis. Calculation of the physical quantities, which determine the states of the moist air, is performed using the equations given below.

Specific enthalpy, *h(t,x),* of the moist air is defined by the following equation:

$$h(t,x) = 1.004 \cdot t + x \cdot (2500 + 1.88 \cdot t) \left[\frac{kJ}{kgdryair} \right]$$

(9)

t is temperature of the moist air [°C].

The vapour pressure of water in saturated moist air (in bar) - $p_S(t)$ is expressed by the following equation (*ASHRAE Handbook, Fundamentals, 2009*):

$$A1_t(t) = 5.865604 \cdot 10^{-3} - 3.142305 \cdot 10^3 \cdot \left(\frac{1}{t+273.15} - \frac{1}{373.15} \right)$$

(10)

$$A2_t(t) = 8.2 \cdot \log \left(\frac{373.15}{t+273.15} \right) - 2.4804 \cdot 10^{-3} - (373.15 - t - 273.15)$$

(11)

$$p_S(t) = 10^{A1_t(t) + A2_t(t)}$$

(12)

Correlation between relative humidity and humidity ratio x, can be expressed:

$$x(t, \varphi) = 0.622 \, \frac{\varphi \cdot p_S(t)}{p_B - \varphi \cdot p_S(t)} \quad \text{[kg water vapor/kg dry air]} \tag{13}$$

The state parameters of the outdoor air, state E (from STAS 6648/2-82 page 3 for the month of July, Bucharest, Romania) are:

t_E=38°C x_E=12.5·10⁻³ kg vapours/kg dry air

The state parameters of the indoor air (fruit storage conditions) state I:

t_I=10°C and relative humidity φ_I=0.90

The state parameters of air conditioning with state C

An air conditioning temperature of t_C = 7°C is chosen, and then, using the angular direction of the CI process, in which the air conditioning evolves towards to state I taking over $\dot{Q}_T = \dot{Q}_{nec}$ and $\dot{m}_w$, respectively:

$$\varepsilon_{CI} = \frac{\dot{Q}_{nec}}{\dot{m}_w} \tag{14}$$

The moisture content of state C can be calculated using the formula:

$$x_C = \frac{h_I - 1.004 \cdot t_C - \varepsilon_{CI} \cdot x_I}{2500 + 1.84 \cdot t_C - \varepsilon_{CI}} \tag{15}$$

The moisture released by the products (apricots) is: $\dot{m}_w = 0.00014$ kg um /s (*Wells, 1962*).

Calculation of air flow rates

Total flow rate of dry air $\dot{m}_a$ [kg dry air/s] from the moist air is:

$$\dot{m}_a = \frac{\dot{Q}_{nec}}{h_I - h_C} \tag{16}$$

As it can be seen in Fig.1, the total flow rate is made up of recirculated air *I* and outdoor fresh air *E*, which are combined in the mixing room. The fresh air flow is the variable in relation to which the thermodynamic analysis of the system is performed.

During the analysis, the fresh air flow will be varied from 0 to 100% of the total air flow.

Recirculated air flow $\dot{m}_{aI}$ [kg dry air/s]:

$$\dot{m}_{aI} = \dot{m}_a - \dot{m}_{aE} \tag{17}$$

State of the mixed air M

Applying the mass balance as well as the energy balance, the thermodynamic properties at the outlet of the mixing chamber are obtained (parameters of mixed air under *M* state). The position and state parameters of point *M* depend on the ratio between fresh air flow and recirculated air flow.

$$h_M = \frac{\dot{m}_{aI} \cdot h_I + \dot{m}_{aE} \cdot h_E}{\dot{m}_{aE} + \dot{m}_{aI}} \tag{18}$$

$$x_M = \frac{\dot{m}_{aI} \cdot x_I + \dot{m}_{aE} \cdot x_E}{\dot{m}_{aE} + \dot{m}_{aI}} \tag{19}$$

setting the moist air treatment process from M to C.

In the particular case studied, the line MC intersects the saturation curve φ=1. Cooling in BRS (surface cooling battery) is chosen, and this battery must have a wall temperature:

$$t_p = t_C - 5grd = 2°C \tag{20}$$

The refrigerating power of the refrigerating installation that ensures the cooling of the moist air, so that the flow air $\dot{m}_a$ and the *M* state reach the *C* state, results from the heat flow that must be extracted from the air:

$$\dot{Q}_{MC} = \dot{m}_a \cdot \left(h_M - h_C \right)$$
$$\dot{Q}_{BRS} = \dot{Q}_{MC} \tag{21}$$

Condensate flow rate discharged from the system is:

$$\dot{m}_{condens} = \dot{m}_a \cdot \left(x_M - x_C \right) \quad \text{[kg/s]} \tag{22}$$

The results are shown in table 2.

Table 2

The states of the moist air

Condition	x (humidity ratio)	h (specific enthalpy)	t (temperature)	φ (relative humidity)
	[kg vap/kg dry air]	[kJ/kg]	[ºC]	[-]
Outdoor Air (E)	$12.5 \cdot 10^{-3}$	70.295	38	0,301
Air (C)	$6.856 \cdot 10^{-3}$	22.622	7	0,999
Mixed Air (M)		44.50	21.27	
Room Air (I)	$6.856 \cdot 10^{-3}$	27.309	10	0,90

Exergy analysis

The **exergetic analysis** method allows determining the cause and magnitude of inefficiencies in an energy process or system. Exergy represents the maximum fraction of a form of unordered energy that can be transformed into mechanical work, in the ideal, reversible thermodynamic evolution of the system up to a state of reference called "dead state", chosen most of the time as the state of thermodynamic equilibrium with the ambient environment (*Dobrovicescu, 2000*). Therefore, the value assigned to the exergy of a material flow depends on the correct selection of the reference medium. The fundamental dead state is that state that would be reached if each constituent of the substance were reduced to complete equilibrium with the stable components in the environment.

The dead state temperature for the exergetic analysis is considered to be equal to that of the ambient environment:

E: $p_o = p_E = 1$ bar; $t_o = t_E = 38 °C$; $x_o = x_E = 0.0125$ kg vap/kg dry air; $\varphi_o = \varphi_E = 0.301$.

According to *Bejan et al., (1988),* the exergy carried by a current of moist air contains the follwing components:

Thermal exergy of moist air, ex_{th} is:

$$ex_{th} = \left(c_{pa} + x \cdot c_{pv}\right)\left[T - T_o - T_o \cdot \ln\left(\frac{T}{T_o}\right)\right] \tag{23}$$

Mechanical exergy of moist air, ex_{mec}:

$$ex_{mec} = \left(1 + 1.608 \cdot x\right)R_a \cdot T_o \cdot \ln\left(\frac{p}{p_o}\right) \tag{24}$$

Chemical exergy of moist air, ex_{ch}:

$$ex_{ch} = R_a \cdot T_o\left[\left(1 + 1.608 \cdot x\right) \cdot \ln\left(\frac{1 + 1.608 \cdot x_o}{1 + 1.608 \cdot x}\right) + 1.608x \cdot \ln\left(\frac{x}{x_o}\right)\right] \tag{25}$$

with:

$c_{pa} = 1.004$ kJ/kg.K mass specific heat of dry air;

$c_{pv} = 1.88$ kJ/kg.K mass specific heat of water vapours;

$R_a = 0.287$ kJ/kg.K mass specific constant of dry air.

Total exergy of moist air will be:

$$ex = ex_{th} + ex_{mec} + ex_{ch} \qquad \text{[kJ/kg dry air]} \tag{26}$$

Exergy flow $\dot{Ex}$ transported by the moist air will be calculated with the formula:

$$\dot{Ex} = \dot{m}_a \cdot ex \qquad \text{[kW]} \tag{27}$$

In the exergy analysis of the air conditioning systems, the exergy flow carried by the humidity, ex_w given off by the moist air must also be taken into consideration. It can be calculated using the formula:

$$ex_w \cong -R_v \cdot T_o \cdot \ln\left(\varphi_o\right) \qquad \text{[kJ/kg water]} \tag{28}$$

$$\dot{Ex}_w = \dot{m}_w \cdot ex_w \qquad \text{[kW]} \tag{29}$$

$R_v = 0.461$ kJ/kgK is the mass constant of the water vapours.

The exergetic balance equation is given by the relation:

$$\frac{d(E-T_oS)}{d\tau} = \sum Ex(\dot{Q}_i) - \dot{W} - (\dot{Ex}_{out} - \dot{Ex}_{in}) - \dot{Ex}_D \tag{30}$$

where:

E is the total energy of the system, [J];

T_0 - reference temperature in exergetic analysis, usually ambient temperature, [K]

S – the system entropy, [J/K];

τ - the time, [s].

$\sum \dot{Ex}(\dot{Q}_i) = \sum \left(1 - \frac{T_0}{T_i}\right)\dot{Q}_i$ represents the exergy of the heat flows $\dot{Q}_i$ [W] exchanged by the system at the

temperature level of the outer sources T_i [K];

$\dot{W}$ is the mechanical power produced or consumed [W];

$\dot{Ex}_{in}$ and $\dot{Ex}_{out}$ are the exergy flows carried by thermal agents (the working fluids circulating in the system), [W].

In thermodynamics, the exergy destruction represents a major inefficiency and a quantity to be minimized when the overall system efficiency should be maximized (*Tsatsaronis et al., 2011*).

According to Guy-Stodola theorem, the exergy destruction rate is computed by:

$$\dot{Ex}_D = T_0 \cdot \dot{S}_{gen} \tag{31}$$

where $\dot{Ex}_D$ is the exergy destruction rate, [W].

Typical irreversible processes in installations (heat transfer at finite temperature difference, flow with friction and pressure loss, throttling, mixing) lead to a high rate of entropy generation, directly proportional to the destruction of exergy in each device and in the system as a whole. In conclusion, the exergy destruction rate in a device or in a plant is the best indicator of the operating efficiency.

Generally, the flow of exergy destroyed in a device can be calculated using the formula:

$$\dot{Ex}_D = \sum \dot{Ex}_{in} - \sum \dot{Ex}_{out} \tag{32}$$

and the exergy efficiency is:

$$\eta_{ex} = \frac{\sum \dot{Ex}_{out}}{\sum \dot{Ex}_{in}} = 1 - \frac{\dot{Ex}_D}{\sum \dot{Ex}_{in}} \tag{33}$$

RESULTS

Next, the influence of the ratio between the fraction of fresh air and that of recirculated air is presented both on the energy consumption of the installation and on the exergy destroyed in the system.

The obtained results are graphically illustrated in Fig. 4…9. The variable in relation to which the graphic representations are made is the ratio between the flow of fresh, outside air and the total flow of air circulated in the system.
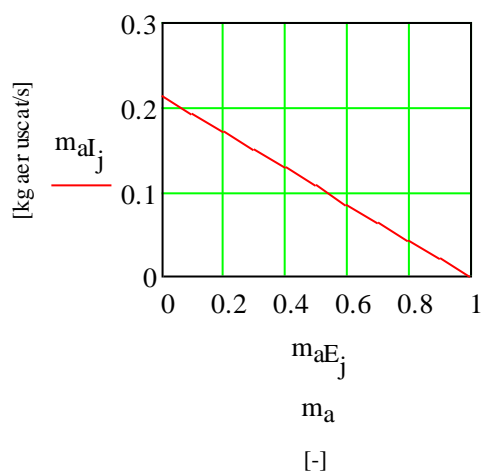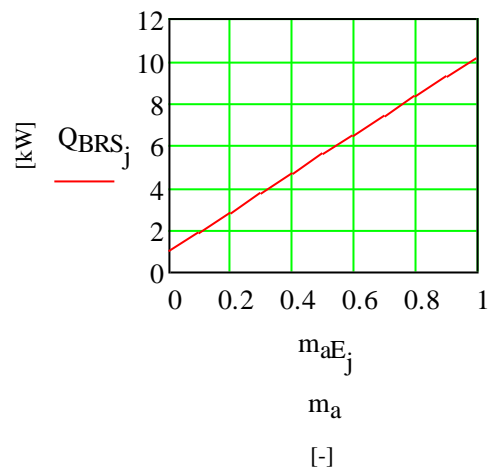

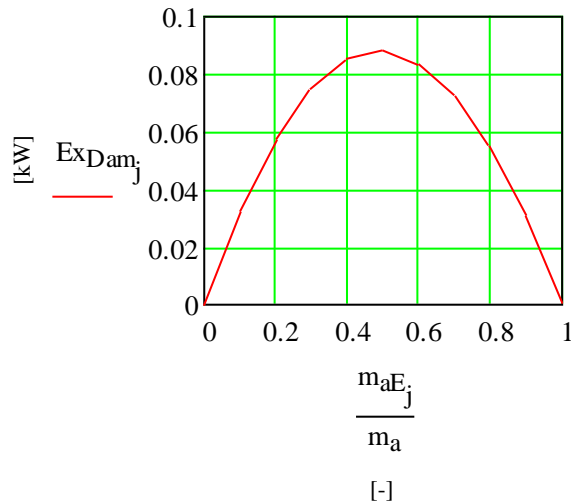**Fig. 4 – Recirculated air flow**   **Fig. 5 – Refrigerating power necessary to cool**

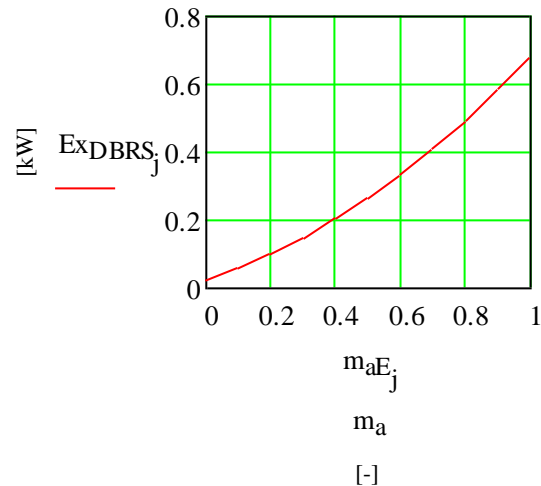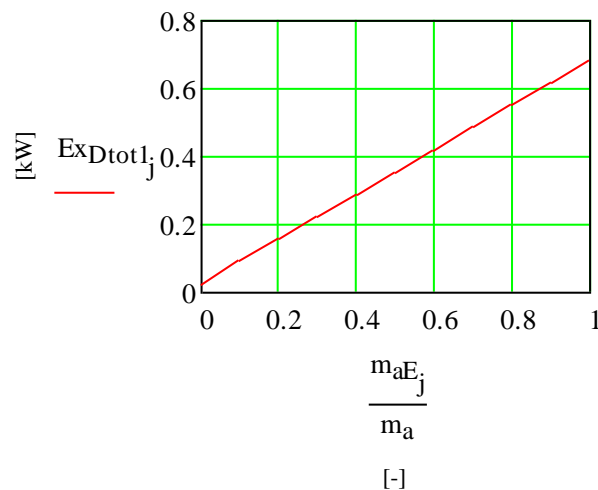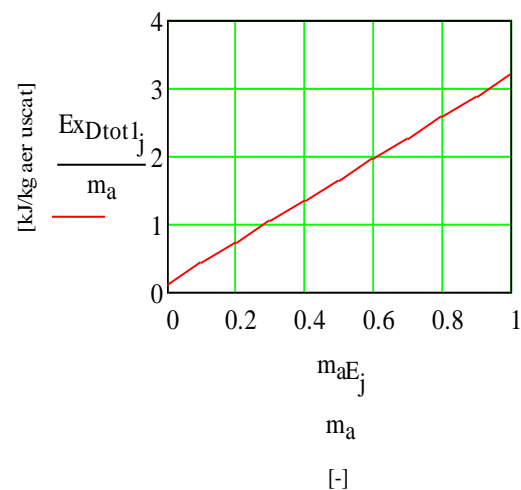**Fig. 6 – Exergy destroyed in the mixing process**

**Fig. 7 – Exergy destroyed in the process
of cooling the moist air**

**Fig. 8 – Total destroyed exergy
- mixing and treating in BRS**

**Fig. 9 - Total specific destroyed exergy
- mixing and treating in BRS**

According to Fig. 5, the refrigeration power required to cool the moist air increases with the increase in the ratio between the fresh air and the total air introduced into the system. The fact that the refrigerating power increases from 1 kW to 10 kW is due to the fact that it introduces fresh air, the higher the flow of fresh air, the higher the required refrigerating power and also the exergy destruction according to Fig.7.

Through mixing, it can be seen that the high exergy destruction is reached when the proportion of air is 50%, then as the fresh air flow increases, it starts to decrease according to Fig.6.

CONCLUSIONS

The energetic and exergetic analysis applied to the concrete case of a summer air conditioning system for a refrigerated storage facility for fruit-vegetables was presented. The changes introduced by the variation of the proportion of fresh air in the total flow of air circulated by the system in the humid air treatment variant with only BRS were shown.

The results indicate that the exergy destruction during the mixing process between fresh and recirculated air reaches a maximum value when the two flow rates are equal (Fig.6). The value of the exergy destroyed in mixing is, however, much lower than that in the cooling battery (Fig.7). It is also noticed that the global intensity of exergy destruction increases with the increase of the fresh recirculated air fraction, the plant also requiring a higher energy consumption to cool the moist air in BRS (Fig.8.and Fig.9).

Likewise, the refrigeration power in the BRS starts to decrease when the proportion of one of the components, either fresh air or recirculated air, decreases. The higher the proportion of fresh air, the higher the temperature of the mixture and therefore the higher the exergy destruction.

REFERENCES

[1] Bejan A. (1988). *Advanced Engineering Thermodynamics*. John Wiley & Sons, New York;

[2] Bilal A., Zubair S., (2003). Application of exergy analysis to various psychrometric processes. *Int. J. Energy*, vol.27, pp. 1079–1094, South Africa;

[3] Chengqin R., Guangfa T., Nianping L., Jing Y., (2002). Discussion Regarding the Principles of Exergy Analysis Applied to HVAC Systems. *Journal of Asian Architecture and Building Engineering*/March 2002/141, China.

[4] Dobrovicescu A., (2000). *Exergetic and thermoeconomic analysis of refrigeration and cryogenic systems (Analiza exergetica si termoeconomica a sistemelor frigorifice si criogenice). Agir Printing House*, Romania.

[5] Heap R., Marshall R., (2003). Ventilation effects and requirements in containerised refrigerated transport. *International Congress of Refrigeration 2003*, Washington. D.C.

[6] Issa S., Lang W. (2016). Airflow Simulation Inside Reefer Containers*. In: Kotzab, H., Pannek, J., Thoben, KD. (eds) Dynamics in Logistics. Lecture Notes in Logistics.*, Germany.

[7] Mostafaeipour A., Nasiri A., (2020). Economic Evaluation of Cooling Storage Warehouses in Hot and Dry Regions for Fruits Using Different Renewable Energies. *Journal of Renewable Energy and Environment*, Vol.7, pp. 18-32, Iran.

[8] Mukama M., Ambaw A., Opara U.L., (2020). Thermophysical properties of fruit-a review with reference to postharvest handling. *Journal of Food Measurement and Characterization,* South Africa.

[9] Mukama M., Ambaw A., Berry T.M., Opara U.L., (2019). Analysing the dynamics of quality loss during precooling and ambient storage of pomegranate fruit. *Journal of Food Engineering*, Vol. 245, pp. 166-173, South Africa.

[10] Parida S., Roy A., Anjankar P., (2018). Design and experimental study of prototype cold storage for various vegetables stored*. Techno-Societal 2018,* pp 447–455, India.

[11] Pop H., Apostol V., Popescu Gh., Dobrovicescu A., Prisecaru M., Ionita C., (2016). *Refrigeration and air conditioning installations. Applications. (Instalatii frigorifice si de climatizare. Aplicatii). Printech Printing House*, Romania.

[12] Praeger U., Jedermann R., Sellwig M., Neuwald D., Truppel I., Scaar H., Hartgenbusch N., Geyer M., (2021). Influence of room layout on airflow distribution in an industrial fruit store. *International Journal of Refrigeration*, Vol. 131, pp 714-722, Germany.

[13] Pereyra M.S., Velázquez M.T., Eslava G.T., Lugo-Leyte R., Rosas C.R., (2011). Energy and Exergy Analysis of Moist Air for Application in Power Plants*. Energy and Power Engineering*, Vol. 3, pp. 376-381, Mexico.

[14] Tsatsaronis G., Morosuk T., (2011). Exergy-based methods for computer-aided design of energy conversion systems, *Computer Aided Chemical Engineering*, Vol. 29, pp. 1949-1953, Germany.

[15] Vintila M., Niculescu F.A., Veringa D., (2015). Study of post-harvest storage for variety apricots in the family farms. *The14th International Symposium "Prospects for the 3rd Millennium Agriculture,* Romania.

[16] Wani S.M., Masoodi F.A., Ahmad M., Mir S.A., (2018). Processing and storage of apricots: effect on physicochemical and antioxidant properties, *J. Food Sci Technol,* vol.55(11):4505-4514.

[17] Wells, A., W.,(1962). Effects of storage temperature and humidity on loss of weight by fruit. *Print book : National government publication* .[Washington, D.C.] : U.S. Department of Agriculture, Agricultural Marketing Service, Market Quality Research Division

[18] ***https://www.academia.edu/39168321/, 2009, ASHRAE Handbook, Fundamentals, *Inch Pound Edition.*

[19] ***https://theengineeringmindset.com/cooling-load-calculation-cold-room/ Evans, P., 2017. Cooling Load Calculation – Cold Room.

WRITING INSTRUCTIONS

Article Types

Three types of manuscripts may be submitted:

1. **Regular articles:** These should describe new and carefully confirmed findings, and experimental procedures should be given in sufficient detail for others to verify the work. The length of a full paper should be the minimum required to describe and interpret the work clearly (max.10 pages, <u>even number</u>);

2. **Reviews:** Submissions of reviews and perspectives covering topics of current interest are welcome and encouraged (max.12 pages, <u>even number</u>).

Manuscripts should be written in English (American or British usage is accepted, but not a mixture of these) and submitted **electronically** at the following e-mail addresses: *inmatehjournal@gmail.com*
Please be sure to include your full affiliation and e-mail address (see Sample manuscript)
The authors are responsible for the accuracy of the whole paper and references.
There are allowed 2 papers by each first author.
The text layout should be in single-column format. To avoid unnecessary errors it is strongly advised to use the "spell-check" and "grammar check" functions of your word processor.

Review Process

All manuscripts are reviewed by 2 members of the Scientifically Review Office. Decisions will be made as rapidly as possible and the journal strives to return reviewers' comments to authors in approx.3 weeks.
The editorial board will re-review manuscripts that are accepted pending revision.

NOTE:

Submission of a manuscript implies: that the work described has not been published before (excepting as an abstract or as part of a published lecture or thesis) that it is not under consideration for publication elsewhere.

1. REGULAR ARTICLES

- Manuscripts should be concise, in *1.15 line spacing*, and should have 2 cm all over margins. The font should be *Arial 10 pt.* Ensure that each new paragraph is clearly indicated, using **TAB at 1 cm**.
- Title will be *Arial 12 pt*. and explicit figures will be *Arial 9 pt*.
- Text will be written in English.
- Chapters' titles are written by *Arial 10 pt, Bold, Uppercase* (e.g. **INTRODUCTION, MATERIALS AND METHODS**), between chapters is left a space for 10 pt. At the beginning of each paragraph, TAB of 1 cm.
- The paper body will be written in *Arial 10 pt., Justify alignment*.

<u>**TITLE**</u> *Arial 12 pt., Uppercase, Bold, Center (in English language)* and *Bold Italic (in native language)*.
Should be a brief phrase describing the contents of the paper. Avoid long titles; a running title of no more than 100 characters is encouraged (without spaces).

<u>**AUTHORS**</u> *ARIAL 9, Bold, Centre alignment*
Under the paper's title, after a space (enter) 9 pt., write *authors' names* and *affiliations (Arial 8 pt.-Regular)*
When the paper has more than one author, their name will be followed by a mark (Arabic numeral) as superscript if their affiliation is different. Less than 6 authors.
Corresponding author's name (next row), *(Arial 8 pt.).* Should be added also: phone, fax and e-mail information, for the paper corresponding author (*font: 8 pt., Italic*).

<u>**KEYWORDS**</u> *(In English)* about 4 to 7 words that will provide indexing references should be listed (<u>title</u>: *Arial 10pt, bold italic,* <u>text</u> *Arial 10 pt., italic*).

A list of non-standard *Abbreviations* should be added. In general, non-standard abbreviations should be used only when the full term is very long and used often. Each abbreviation should be spelled out and introduced in parentheses the first time it is used in the text. Standard abbreviations (such as ATP and DNA) need not to be defined.
<u>**ABSTRACT**</u> *(in English and Native language, Arial 10 pt.)*, the title *bold*; the text of abstract: *italic*) should be informative and completely self-explanatory, briefly present the topic, state the scope of the experiments, indicate significant data, and point out major findings and conclusions. The Abstract should be max.250 words. Complete sentences, active verbs, and the third person should be used, and the abstract should be written in the past tense. Standard nomenclature should be used and abbreviations should be avoided. No literature should be cited.
<u>**INTRODUCTION**</u> (*Arial 10 pt.*) should provide a clear statement of the problem, the relevant literature on the subject, and the proposed approach or solution. It should be understandable to colleagues from a broad range of scientific subjects. We should refer to the current stage of researches performed in the field of the paper to be published, by quoting up-to-date specialty studies, preferably published after 2006, excepting certain referential specialty

books/studies, especially papers issued in magazines/journals/conferences/ISI quoted symposia or in other international data bases, which are well known and available.

MATERIALS AND METHODS (*Arial 10 pt.)* should be complete enough to allow experiments to be reproduced. However, only truly new procedures should be described in detail; previously published procedures should be cited, and important modifications of published procedures should be mentioned briefly. Methods in general use need not be described in detail.

RESULTS (*Arial 10 pt.)* should be clarity presented. The results should be written in the past tense when describing findings in the authors' experiments. Results should be explained, but largely, without referring to the literature. Discussion, speculation and detailed interpretation of data should not be included in the Results, but should be put into the Conclusions section.

CONCLUSIONS (*Arial 10 pt.)* The main conclusions drawn from results should be presented in a short Conclusions section. Do not include citations in this section.

Formulae, symbols and abbreviations: Formulae will be typeset in Italics (preferable with the Equation Editor of Microsoft Office 2003) and should be written or marked as such in the manuscript, unless they require a different styling. They should be referred to in the text as Equation (4) or e.g. (4). The formulae should be numbered on the right side, between brackets *(Arial 10 pt.)*:

$$P = F \cdot v \tag{1}$$

Terms of the equation and the unit measure should be explained, e.g.

        P is the power, [W];
        F – force, [N];
        v – speed, [m/s]

SI units must be used throughout.

Tables should be self-explanatory without reference to the text. The details of the methods used in the experiments should preferably be described in the legend instead of in the text. The same data should not be presented both in table and graph form or repeated in the text.
Table's title will be typed *Arial 9 pt, Bold, Centered*
In the table, each row will be written Arial 9 pt, single-spaced throughout, including headings and footnotes.
The table should be numbered on the right side, *Arial 10 pt.*

Figures (Arial 9 pt., Bold, Center) should be typed in numerical order (Arabic numerals). Graphics should be high resolution (e.g.JPEG).Figure number is followed by what represent the figure or graph e.g.:

Fig.1 – Test stand

Legend: Arial 8 pt, Italic, Center, e.g.:
        1 - plansifter compartments; 2- break rolls; 3 – semolina machines; 4 – reduction rolls; 5 – flour

ACKNOWLEDGMENTS (*Arial 10 pt.)* of people, grants, funds etc should be brief (*if necessarily*).

REFERENCES (*Arial 10 pt.)*
        (In alphabetical order, in English and in the original publication language).
        Minimum 10 references, last 10 years, minimum 3 references from the last 2 years

It can be used "*References*" tool from the *Word Editor*. **APA Style (American Psychological Association)** https://apastyle.apa.org/style-grammar-guidelines/references/examples

All references must be provided in English
Authors are fully responsible for the accuracy of the references.

References should be **alphabetically**, with complete details, as follows:

Examples:

Books: https://apastyle.apa.org/style-grammar-guidelines/references/examples/book-references

Jackson, L. M. (2019). *The psychology of prejudice: From attitudes to social action* (2nd ed.). American Psychological Association. https://doi.org/10.1037/0000168-000
Kesharwani, P. (2020). *Nanotechnology based approaches for tuberculosis treatment*. Academic Press.
Sapolsky, R. M. (2017). *Behave: The biology of humans at our best and worst*. Penguin Books.

Torino, G. C., Rivera, D. P., Capodilupo, C. M., Nadal, K. L., & Sue, D. W. (2019). *Microaggression theory: Influence and implications*. John Wiley & Sons. https://doi.org/10.1002/9781119466642
In text:
- ***Parenthetical citations***: (Jackson, 2019; Sapolsky, 2017)
- ***Narrative citations***: Jackson (2019) and Sapolsky (2017)

Journal Article:
https://apastyle.apa.org/style-grammar-guidelines/references/examples/journal-article-references

Grady, J. S., Her, M., Moreno, G., Perez, C., & Yelinek, J. (2019). Emotions in storybooks: A comparison of storybooks that represent ethnic and racial groups in the United States. *Psychology of Popular Media Culture*, *8*(3), 207–217. https://doi.org/10.1037/ppm0000185
In text:
- ***Parenthetical citation***: (Grady et al., 2019)
- ***Narrative citation***: Grady et al. (2019)

Conference or Symposium:
https://apastyle.apa.org/style-grammar-guidelines/references/examples/conference-proceeding-references

Duckworth, A. L., Quirk, A., Gallop, R., Hoyle, R. H., Kelly, D. R., & Matthews, M. D. (2019). Cognitive and noncognitive predictors of success. *Proceedings of the National Academy of Sciences*, *USA*, *116*(47), 23499–23504. https://doi.org/10.1073/pnas.1910510116
In text:
- ***Parenthetical citation***: (Duckworth et al., 2019)
- ***Narrative citation***: Duckworth et al. (2019)

Dissertation / Thesis:
https://apastyle.apa.org/style-grammar-guidelines/references/examples/published-dissertation-references

Zambrano-Vazquez, L. (2016). *The interaction of state and trait worry on response monitoring in those with worry and obsessive-compulsive symptoms* [Doctoral dissertation, University of Arizona]. UA Campus Repository. https://repository.arizona.edu/handle/10150/620615
In text:
- ***Parenthetical citations***: (Kabir, 2016; Miranda, 2019; Zambrano-Vazquez, 2016)
- ***Narrative citations***: Kabir (2016), Miranda (2019), and Zambrano-Vazquez (2016)

https://apastyle.apa.org/style-grammar-guidelines/references/examples/unpublished-dissertation-references

Harris, L. (2014). *Instructional leadership perceptions and practices of elementary school leaders* [Unpublished doctoral dissertation]. University of Virginia.
In text:
- ***Parenthetical citation***: (Harris, 2014)
- ***Narrative citation***: Harris (2014)

Patents: Names and initials of authors, year (between brackets), patent title (Italic), patent number,country:
Grant, P. (1989). *Device for Elementary Analyses*. Patent. No.123456. USA.

Legal regulations and laws, organizations:
https://apastyle.apa.org/style-grammar-guidelines/references/examples/iso-standard-references

International Organization for Standardization. (2018). *Occupational health and safety management systems— Requirements with guidance for use* (ISO Standard No. 45001:2018). https://www.iso.org/standard/63787.html
Occupational Safety and Health Administration. (1970). *Occupational safety and health standards: Occupational health and environmental control: Occupational noise exposure* (OSHA Standard No. 1910.95). United States Department of Labor.
https://www.osha.gov/laws-regs/regulations/standardnumber/1910/1910.95
In text:
- ***Parenthetical citations***: (International Organization for Standardization, 2018; Occupational Safety and Health Administration, 1970)
- ***Narrative citations***: International Organization for Standardization (2018) and Occupational Safety and Health Administration (1970)

Web references: The full URL should be given in text as a citation, if no other data are known. If the authors, year, and title of the documents are known and the reference is taken from a website, the URL address has to be mentioned after these data.

Citation in text

Please ensure that every reference cited in the text is also present in the reference list (and vice versa).

Do not cite references in the Abstract and Conclusions !.

Unpublished results, personal communications as well as URL addresses are not recommended in the references list.

Making personal quotations (one, at most) should not be allowed, unless the paper proposed to be published is a sequel of the cited paper. Articles in preparation or articles submitted for publication, unpublished, personal communications etc. should not be included in the references list.

Citations style

Text: All citations in the text may be made directly (or parenthetically) as bellow.

- **single author**: the author's name (without initials, unless there is ambiguity) and the year of publication:
      "as previously demonstrated *(Brown, 2010)*".

- **two authors**: both authors' names and the year of publication: *(Adam and Brown, 2008; Smith and Hansel, 2006; Stern and Lars, 2009)*

- **three or more authors**: first author's name followed by "et al." and the year of publication: "As has recently been shown *(Werner et al., 2005; Kramer et al., 2000)* have recently shown ...."

Citations of groups of references should be listed first alphabetically, then chronologically.

Units, Abbreviations, Acronyms

  ▪ Units should be metric, generally SI, and expressed in standard abbreviated form.
  ▪ Acronyms may be acceptable, but must be defined at first usage.

2. REVIEWS

Summaries, reviews and perspectives covering topics of current interest in the field, are encouraged and accepted for publication. Reviews do not have the requirements for regular articles. However, should include: (*) an introductory chapter, (**) a careful and critical presentation of the relevant aspects of the topic approached and (***) emphasis of the aspects that aren't known and require further research to progress. Reviews should be concise (max. 12 pages).